AFRL-RQ-WP-TR-2015-0160

HIGH-FIDELITY NUMERICAL MODELING OF COMPRESSIBLE FLOW

Nicholas J. Bisek

Hypersonic Sciences Branch
High Speed Systems Division

NOVEMBER 2015
Final Report

AIR FORCE RESEARCH LABORATORY
AEROSPACE SYSTEMS DIRECTORATE
WRIGHT-PATTERSON AIR FORCE BASE, OH 45433-7541
AIR FORCE MATERIEL COMMAND
UNITED STATES AIR FORCE

NOTICE AND SIGNATURE PAGE

Using Government drawings, specifications, or other data included in this document for any purpose other than Government procurement does not in any way obligate the U.S. Government. The fact that the Government formulated or supplied the drawings, specifications, or other data does not license the holder or any other person or corporation; or convey any rights or permission to manufacture, use, or sell any patented invention that may relate to them.

This report was cleared for public release by the USAF 88th Air Base Wing (88 ABW) Public Affairs Office (PAO) and is available to the general public, including foreign nationals.

Copies may be obtained from the Defense Technical Information Center (DTIC) (http://www.dtic.mil).

AFRL-RQ-WP-TR-2015-0160 HAS BEEN REVIEWED AND IS APPROVED FOR PUBLICATION IN ACCORDANCE WITH ASSIGNED DISTRIBUTION STATEMENT.

*//Signature//

NICHOLAS J. BISEK
Program Manager
Hypersonic Sciences Branch
High Speed Systems Division

//Signature//

MICHAEL S. BROWN, Branch Chief
Hypersonic Sciences Branch
High Speed Systems Division

//Signature//

THOMAS A. JACKSON
Principal Scientist
High Speed Systems Division
Aerospace Systems Directorate

This report is published in the interest of scientific and technical information exchange, and its publication does not constitute the Government's approval or disapproval of its ideas or findings.

*Disseminated copies will show "//Signature//" stamped or typed above the signature blocks.

REPORT DOCUMENTATION PAGE

Form Approved
OMB No. 0704-0188

1. REPORT DATE *(DD-MM-YY)*	2. REPORT TYPE	3. DATES COVERED *(From - To)*
November 2015	Final	01 January 2014 – 30 September 2015

4. TITLE AND SUBTITLE
HIGH-FIDELITY NUMERICAL MODELING OF COMPRESSIBLE FLOW

5a. CONTRACT NUMBER
In-house

5b. GRANT NUMBER

5c. PROGRAM ELEMENT NUMBER
61102F

6. AUTHOR(S)
Nicholas J. Bisek

5d. PROJECT NUMBER
3002

5e. TASK NUMBER
N/A

5f. WORK UNIT NUMBER
Q05P

7. PERFORMING ORGANIZATION NAME(S) AND ADDRESS(ES)
Hypersonic Sciences Branch (AFRL/RQHF)
High Speed Systems Division
Air Force Research Laboratory, Aerospace Systems Directorate
Wright-Patterson Air Force Base, OH 45433-7541
Air Force Materiel Command, United States Air Force

8. PERFORMING ORGANIZATION REPORT NUMBER
AFRL-RQ-WP-TR-2015-0160

9. SPONSORING/MONITORING AGENCY NAME(S) AND ADDRESS(ES)
Air Force Research Laboratory
Aerospace Systems Directorate
Wright-Patterson Air Force Base, OH 45433-7541
Air Force Materiel Command
United States Air Force

10. SPONSORING/MONITORING AGENCY ACRONYM(S)
AFRL/RQHF

11. SPONSORING/MONITORING AGENCY REPORT NUMBER(S)
AFRL-RQ-WP-TR-2015-0160

12. DISTRIBUTION/AVAILABILITY STATEMENT
Approved for public release; distribution unlimited.

13. SUPPLEMENTARY NOTES
PA Case Number: 88ABW-2015-5548; Clearance Date: 12 Nov 2015.
Three other published documents for work unit Q05P cover the time period between 01 October 2007 to 01 January 2014: AFRL-RB-WP-TP-2009-3231, AFRL-RB-WP-TR-2012-0040, and AFRL-RQ-WP-TR-2014-0079.

14. ABSTRACT
This report describes numerical modeling work carried out on high Mach number flows. Three main technical areas were addressed: seamless transition of implicit large eddy simulation to direct numerical simulation, the development of secondary motion in corner flows, and large-scale unsteadiness of separated shock-wave/boundary-layer interactions. High-order numerical simulations of a Mach 2.3 turbulent equilibrium boundary-layer flow were performed with increasing resolution until all fluid scales in the domain were fully resolved. It was found that the high-fidelity implicit large-eddy simulations converged seamlessly to direct numerical simulation and the turbulent statistics were found to be essentially independent of the domain width for values greater than twice the maximum boundary layer thickness. Numerical simulations of turbulent equilibrium boundary layer flow in the presence of a second wall yielded the development of secondary motion, which significantly increased the three-dimensionality of the subsequent shock boundary-layer interaction in the system. Inclusion of both sidewalls was required to accurately predict the separation location. Introduction of the quadratic relationship into Reynolds-averaged Navier-Stokes models did generate secondary motion for compressible corner flows. However, the improved low-fidelity results did not fully match the high-fidelity implicit large eddy simulations. These results emphasize the need for and use of higher fidelity methods to reduce uncertainty and risk.

15. SUBJECT TERMS
computational fluid dynamics, CFD, computational, shock boundary-layer interaction, SBLI, hypersonics

16. SECURITY CLASSIFICATION OF:			17. LIMITATION OF ABSTRACT:	18. NUMBER OF PAGES	19a. NAME OF RESPONSIBLE PERSON (Monitor)
a. REPORT	b. ABSTRACT	c. THIS PAGE			Nicholas J. Bisek
Unclassified	Unclassified	Unclassified	SAR	215	19b. TELEPHONE NUMBER *(Include Area Code)* N/A

TABLE OF CONTENTS

Section Page

LIST OF FIGURES ..... **ii**

ACKNOWLEDGEMENTS ..... **iii**

1 SUMMARY **1**

2 INTRODUCTION **2**

2.1 Background 2
2.1.1 Fluid Modeling 2
2.2 Approach 3
2.3 Scope 4

3 RESULTS AND DISCUSSION **5**

3.1 Resolution Effects 5
3.2 Corner Flows 7
3.2.1 Implicit Large-Eddy Simulations 7
3.2.2 Reynolds-averaged Navier-Stokes Modeling 8
3.3 Shock Boundary-Layer Interaction 10
3.3.1 Implicit Large-Eddy Simulations 11
3.3.2 Detached-Eddy Simulations 13

4 CONCLUSIONS **15**

5 REFERENCES **16**

APPENDIX A RESOLUTION EFFECTS **17**

APPENDIX B CORNER FLOWS **76**

APPENDIX C SHOCK BOUNDARY-LAYER INTERACTION **122**

LIST OF SYMBOLS, ABBREVIATIONS, AND ACRONYMS **209**

LIST OF FIGURES

Figure 1: Instantaneous Density Fields (ρ/ρ_∞) in the x/δ_0 = 100 Plane for Mach 2.3 Turbulent Boundary Layer Flow.....6
Figure 2: Effect of Spatial Resolution on Spectra at x/δ_0 = 100, y/δ = 0.5 for Mach 2.3 Turbulent Boundary Layer Flow.....7
Figure 3: Instantaneous Iso-surfaces of the Q-criterion Colored by Streamwise *u*-velocity for Mach 2.3 Turbulent Boundary-layer Flow near Two Adjoining Walls.....8
Figure 4: Time Mean Cross-velocity Contours and Streamlines for Mach 2.3 Turbulent Boundary Layer Flow near a 90^o Corner at Reθ = 2750.....9
Figure 5: Coefficient of Skin Friction versus Distance from a 90^o Corner for Mach 2.3 Turbulent Boundary Layer Flow at Reθ = 2750.....10
Figure 6: Iso-surfaces of the Q-criterion over Half of the Span, Colored by the *u*-velocity for Mach 2.3 Turbulent Flow over a 24° Compression-ramp between Two Sidewalls...11
Figure 7: Top Down View of Skin Friction Fields for Mach 2.3 Flow over a 24° Ramp.....12
Figure 8: Normalized Density Field Contours for Mach 2.9 Flow over a Backward Facing Step13
Figure 9: Surface Pressure Statistics for Mach 2.9 Turbulent for over a Backward Facing Step / Compression Ramp.....14

ACKNOWLEDGEMENTS

Work at AFRL under this project was sponsored in part by grants from the Air Force Office of Scientific Research (monitored by I. Leyva, AFOSR/RSA), and by grants of High Performance Computing (HPC) time from the Air Force Research Laboratory (AFRL), Army Research Laboratory (ARL), and the U.S. Army Engineer Research and Development Center (ERDC) DoD Supercomputing Resource Centers (DSRC).

The author would like to acknowledge helpful discussions of this ongoing work with D. Gaitonde, D. Garmann, M. Visbal, and M. White. G. Candler provided the hypersonic computational fluid dynamics code US3D for use in this project.

1 SUMMARY

This report describes work carried out on numerical modeling of high Mach number flows. Three main technical areas were addressed: seamless transition of implicit large eddy simulation to direct numerical simulation, the development of secondary motion in the turbulent system, and the large-scale unsteadiness of separated shock-wave/boundary-layer interactions.

High-order numerical simulations of a Mach 2.3 turbulent equilibrium boundary-layer flow were performed with increasing resolution until all fluid scales in the domain were fully resolved. It was found that the high-fidelity implicit large-eddy simulations (HFILES) converged seamlessly to direct numerical simulation (DNS) and the turbulent statistics were found to be essentially independent of the domain width for values greater than twice the maximum boundary layer thickness. These findings confirmed that the HFILES methodology was an appropriate simplification to the compressible turbulent flows within this body of work.

High-fidelity numerical simulations of the same Mach 2.3 turbulent equilibrium boundary layer were carried out in the presence of a second wall. The inclusion of the second wall led to the development of secondary motion due to anisotropy of the turbulence from the two adjoining turbulent boundary-layers. In a subsequent simulation, a compression ramp was added to the floor of the computational domain leading to the development of the turbulent shock boundary-layer interaction (SBLI). This SBLI scenario had been studied previously without the sidewall and was discussed in a prior interim report. It was found that the SBLI was significantly more three-dimensional when the sidewalls were included and that it was necessary to simulate the entire width of the configuration to accurately predict the SBLI separation and reattachment locations. These findings show the importance of secondary motion on accurately predicting the entire shock system.

Detached-eddy simulations (DES) were performed for a Mach 2.9 backward facing step / compression ramp configuration. DES directly computes the large-scale unsteadiness of the turbulence (LES), but requires Reynolds-averaged Navier-Stokes (RANS) to explicitly model the near wall turbulence. The influence of boundary layer thickness at separation on the reattachment shock system was explored and the results collapsed when scaled by the reattachment location and boundary layer thickness.

Introduction of the quadratic relationship into lower-fidelity Reynolds-averaged Navier-Stokes (RANS) models provided a mechanism to obtain secondary motion in the corner flow systems. However, it was found that the additional parameter was unable to be tuned to fully match the HFILES predictions. While lower-fidelity RANS predictions can quickly and cheaply provide an estimate of the flow pattern, higher fidelity approaches are still required to reduce uncertainty in the results.

2 INTRODUCTION

2.1 Background

Hypersonic flight is an enabling factor for long-range strike and reconnaissance in contested airspace. A common phenomenon associated with hypersonics is turbulent shock boundary-layer interaction which typically occurs for both internal flows (such as high-speed inlets as the incoming air is rapidly slowed and vectored into the combustor) and external flows (such as fin-body junctures). They are associated with large-scale unsteadiness, extreme thermo-mechanical loads, and engine operability problems. The work reported here has focused on developing and applying high-fidelity numerical tools on increasing complex configurations in order to accurately predict heating and large-scale unsteadiness typically experienced in this flight regime.

The numerical methods used are described here.

2.1.1 Fluid Modeling

For the work reported here, simulations were carried out with four independently implemented computer codes (OVERFLOW, US3D, FDL3DI, and HOPS). While OVERFLOW and US3D have high-order spatial schemes available, they were primarily used for their built-in RANS capabilities with second-order spatial and first-order temporal accuracy.

OVERFLOW is a well-validated, finite-difference, time-marching, implicit Navier-Stokes solver for structured and overset grids. It was developed as a joint effort between NASA's Johnson Space Flight and Ames Research Centers. Central differencing was used for the right hand side Euler terms, along with the ARC3D diagonalized Beam-Warming scalar pentadiagonal scheme on the left hand side.

The US3D code is an unstructured, finite volume solver developed by G. Candler's group at the University of Minnesota. The code solves the compressible Navier-Stokes equations using a cell-centered, finite-volume formulation. For the calculations of both the inviscid and viscous fluxes, gradients of flow variables are computed using a weighted least squares method. The DES results presented in this report where achieved using a hybrid version of the code. The RANS portion of the domain was obtained with second-order spatial accuracy. The LES portion of the hybrid simulation was performed by combing a fourth-order spatially accurate symmetric flux evaluation with the dissipative portion of the shock-capturing modified Steger-Warming flux vector splitting scheme. The viscous fluxes were evaluated using a second-order accurate central difference scheme. The current computations were carried out using the perfect gas assumption. Second-order accurate, implicit time integration was employed when DES was used.

Two codes developed at AFRL were also used in this study. The FDL3DI code was named for the Flight Dynamics Laboratory, a precursor organization to AFRL. This code uses a sixth-order accurate spatial differencing, structured-grid, finite-difference solver for the perfect-gas, compressible-flow Navier- Stokes equations. The HOPS code includes several physical models, but here it is employed as a single-fluid gasdynamics code. Employed in this way, the two codes represent independent implementations of essentially the same numerical approach. Both codes include the option of switching to a third-order, upwind scheme in the vicinity of a shock.

Time integration of the conservation equations was carried out in the baseline approach using a second-order implicit scheme, based on a three-point backward difference of the time terms. The general formulation is similar to the standard technique of Beam and Warming. Approximate factoring and quasi-Newton subiterations were employed, with three applications of the flow solver per time step. The implicit terms were evaluated using the scalar pentadiagonal formulation of Pulliam and Chaussee. For comparison, a fourth-order, explicit Runge-Kutta method was employed for some of the calculations.

The baseline spatial differencing scheme was based on compact differencing and filtering. In one dimension, the finite difference approximation to the first derivative ϕ'_i at Node *i* is evaluated by solving a tridiagonal system of the form:

$$\alpha\phi'_{i-1} + \phi'_i + \alpha\phi'_{i+1} = a\frac{\phi_{i+1} - \phi_{i-1}}{2} + b\frac{\phi_{i+2} - \phi_{i-2}}{2} \tag{1}$$

where α, *a*, and *b* are constants chosen to give a certain order of accuracy and set of spectral properties for the scheme.

Numerical stability was enforced using a low-pass, Padé-type, nondispersive spatial filter. The filtering approach replaces the computed value ϕ_i at a particular node with a filtered value $\hat{\phi}_i$:

$$\alpha_f\hat{\phi}_{i-1} + \hat{\phi}_i + \alpha_f\hat{\phi}_{i+1} = \sum_{n=0}^{N}\frac{a_n}{2}\left(\phi_{i+n} - \phi_{i-n}\right) \tag{2}$$

where the constants α_f , a_0, ... a_N are chosen to give appropriate filter properties. The filter was applied to the solution vector, sequentially, in each of the three computational directions, following each sub-iteration for implicit time integration, or each time-step for explicit integration. The order of the filtering operation was permuted at each time step.

The hybrid compact-Roe shock-capturing scheme of Visbal and Gaitonde was employed for flows containing strong shocks. During each sub-iteration of the solver, the shock location was identified by the pressure gradient detector developed by Swanson and Turkel. The metrics were evaluated using the method of Thomas and Lombard.

2.2 Approach

The technical approach for modeling neutral gas flows focused on turbulence and large-scale unsteadiness primarily without the use of explicit models. In particular, direct numerical simulation was applied to a compressible turbulent equilibrium boundary layer, and implicit large-eddy simulation was applied to turbulent flows in the presence of strong shocks. In the latter approach, the effect of unresolved turbulent scales is replicated using the filtering effect of the numerical scheme discussed in Section 2.1.1. A secondary aspect of the work emphasized the use of lower-fidelity numerical approaches, such as detached-eddy simulations and Reynolds-averaged Navier-Stokes, which do use explicit closure models. While these lower-order approaches provide significant computational saving due to a large reduction in spatial and temporal resolution requirements, the explicit models neglect some key physics in the flow.

Improvements were made to enhance the capability of the lower-fidelity approached and then tuned using the high-fidelity implicit large-eddy simulation results.

The personnel involved in this work were Nicholas Bisek of AFRL/RQHF, Jonathan Poggie of AFRL/RQHF, and Timothy Leger of Ohio Aerospace Institute.

2.3 Scope

The main technical objective of this program was to develop techniques for the prediction of supersonic flows in a range up to Mach 6. This regime is important for the development of Air Force systems with short response time and high survivability. The low supersonic regime is relevant for internal flows in scramjet engines, whereas the higher Mach number range is relevant for external flow over a vehicle.

Particular attention has been given to heat transfer and large-scale unsteadiness in separated, turbulent flow and accurately predicting the turbulence using high-fidelity numerical methods and very large grid systems to fully support all relevant fluid structures.

The primary challenges to computational simulation of air vehicles in the hypersonic regime are the disparate length and time scales present in problem. Scales range from the molecular, to the component level, and to the flight profile. These disparate scales make the problems very stiff, and encourage the development of new, more efficient numerical algorithms to attack these problems. It also motivates the use of large-scale computing systems and highly scalable algorithms to reduce the wall time needed to perform the complex simulations. In addition, these requirements have motivated the use of lower-order approaches with improved closure models. These lower-order approaches allow for the exploration of a larger range of scenarios, but understanding and quantifying their limitations are critical to quantifying uncertainty when using any numerical methods.

3 RESULTS AND DISCUSSION

The following subsections review the work that was done under this project to explore high-speed flow. Additional details can be found in publications reproduced in Appendices A through C. The work can be divided into three main categories: resolution effects (Section 3.1 and Appendix A), corner flows (Section 3.2 and Appendix B), shock-wave/boundary-layer interaction (Section 3.3 and Appendix C).

In 2014, work was carried out on corner flows using high-fidelity implicit large-eddy simulations (Ref. [1], Appendix B), resolution effects with implicit large eddy simulations (Ref. [2], Appendix A), detached-eddy simulations of shock boundary-layer interaction on a backward-facing step (Ref. [3], Appendix C), and implicit large-eddy simulations of shock boundary-layer interaction on a corner / ramp configuration (Ref. [4], Appendix C). Work in 2015 used detached-eddy simulations to perform scaling studies on the backward facing step / ramp flow (Ref. [5], Appendix C), high fidelity implicit large-eddy simulations of shock boundary-layer interact on a ramp with both sidewalls (Ref. [6], Appendix C), additional resolution studies of a turbulent boundary layer with strict direct numerical simulation (Ref. [7], Appendix A), and Reynolds-averaged Navier-Stokes simulations of corner flows (Ref. [8], Appendix B).

3.1 Resolution Effects

This project explored turbulent boundary layer flow in the context of direct numerical simulation and implicit large-eddy simulation. In particular, the present work focused on assessing how well models at these different levels of approximation serve as tools for predicting the properties of turbulent boundary layer flow, and, given large-scale computing resources, whether high-resolution methods can be used in design.

Here DNS designates an approach where all fluid length scales are resolved in the simulation. Implicit large-eddy simulation is a general approach in which the additional dissipation needed to account for the unresolved scales is provided directly by the numerical scheme. The terminology HFILES is intended to be more specific than ILES; the HFILES approach uses high-order spatial differencing with a higher order filter, and numerical dissipation is added only at the smallest, under-resolved, spatial scales. In RANS, all turbulent fluctuations are modeled, and only the mean flow is computed. Intermediate levels of modeling, employing subgrid-scale closure models, were not considered in this study.

Typical resolution recommendations for wall-resolving large-eddy simulation are $50 \leq \Delta x^+ \leq 150$, $\Delta y_w^+ < 1$, $15 \leq \Delta z^+ \leq 40$, where y_w is the grid spacing at the wall in the wall normal direction. Corresponding recommendations for direct numerical simulation further restrict the streamwise and spanwise resolution: $10 \leq \Delta x^+ \leq 20$, $5 \leq \Delta z^+ \leq 10$. A wide range of spatial resolutions, spanning the range of LES and DNS, were reported in previous studies: $\Delta x^+ = 1.3$–59, $\Delta y_w^+ = 0.1$–3.6, $\Delta z^+ = 1.2$–29. Unfortunately, the grid resolution at the boundary layer edge Δy_e^+ has not been well documented. The reported domain width, relative to the maximum boundary layer thickness, has ranged over $L_z/\delta = 0.84$-3.8. With the exception of the temporal simulation of Maeder *et al.* at Mach 6 on a very small domain ($2.3\delta_0 \times 3.0\ \delta_0 \times 1.4\ \delta_0$), no

previous study appears to have approached direct numerical simulation in the strictest sense, where the maximum mesh spacing in inner scaling is $\Delta s^+ \leq 1$.

To address this deficiency, the present work examined the effects of spatial resolution on spectra and other flow statistics for a supersonic turbulent boundary layer flow at Mach 2.3 and $\delta+ \approx$ 600. The finest grid in the spatial resolution study consisted of 3.3×10^{10} points, and maintained max (Δx^+, Δy^+, Δz^+) ≤ 1 everywhere on a domain.

As detailed in Refs. [2] and [7], the effects of spatial resolution were carefully explored using the high-fidelity computational fluid dynamics code HOPS, as described in Section 2.1.1 and Appendix A. Direct numerical simulations and HFILES were carried out for turbulent boundary layers at Mach 2.3. Transition to turbulence was promoted with an artificial body-force trip. In the simulations, the spatial resolution was systematically increased until all fluid length scales within the domain were fully supported (Δx^+, Δy^+, $\Delta z^+ \leq 1$), which is the definition of DNS in the strictest sense. For comparison, the minimum value of the Kolmogorov length scale occurs at the wall, and has a value of $\eta^+ \approx 1.5$. Figure 1 shows instantaneous density field contours for both the coarsest HFILES grid and the DNS grid. The view corresponds to the end-plane of the resolved region of the computational domain; flow is into the page. The effect of resolution is obvious. Motions in the outer layer are highly smeared in the coarsest HFILES grid, whereas DNS resolution captures the sharp vortical-irrotational interface of the viscous superlayer.

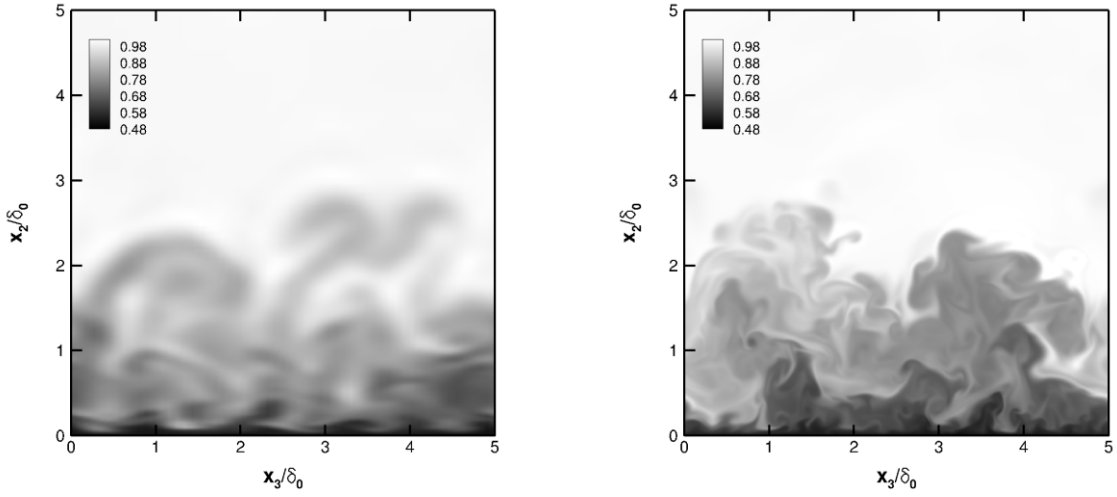

Figure 1: Instantaneous Density Fields (ρ/ρ_∞) in the x/δ_0 = 100 Plane for Mach 2.3 Turbulent Boundary Layer Flow

The left sub-figure is the coarse HFILES grid: Δx^+=45,Δy^+=0.9-19,Δz^+=9, whereas the right sub-figure is the fine DNS grid: Δx^+=1,Δy^+=0.9,Δz^+=1. The DNS grid has 3,300 times more grid points than the coarse HFILES grid.

The effects of spatial resolution on spectra and other flow statistics were also studied. Examining spanwise velocity spectra in detail, Figure 2 shows HFILES results converge seamlessly to DNS as the spatial resolution was increased. The black dashed line is Pope's model spectrum. In the simulation, the turbulent Reynolds number is $Re_L \approx 800$. Further, turbulence statistics were found to be essentially independent of the domain width for values between two and eight times the maximum boundary layer thickness.

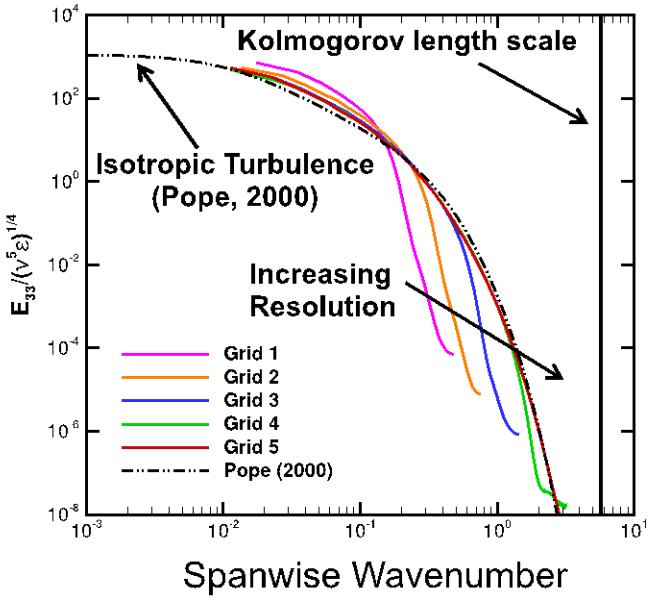

Figure 2: Effect of Spatial Resolution on Spectra at $x/\delta_0 = 100$, $y/\delta = 0.5$ for Mach 2.3 Turbulent Boundary Layer Flow

The wavenumber corresponding to the Kolmogorov length scale is $k_i\eta = 2\pi \approx 6$.

3.2 Corner Flows

Corners are a common feature in the design of both internal and external aerodynamic configurations. In turbulent flows, the anisotropy of turbulence causes such corners to generate secondary flow. Prandtl was the first to document this and in 1926 he classified it as secondary flow of the second kind. Secondary flow is characterized by a pair of counter rotating vortices that transfer momentum from the mean flow into the corner. While the velocity of the secondary flow is relatively weak, being only 1% to 3% of the freestream velocity, the vortex pair can have a significant effect on wall shear stress and heat transfer in the corner.

For external corners, such as the junction between a wing and fuselage, this results in interference drag. In internal flows, such as rectangular ducts and isolators, corner flows significantly distort the primary flow field, which may lead to "unstart" conditions in air breathing engine flowpaths. In addition, corner flows can have a significant effect on the behavior of a SBLI. It is therefore important to gain a better understanding and improve predictions of corner flow effects for the design and development of future air vehicles.

3.2.1 Implicit Large-Eddy Simulations

The investigation described in Ref. [1] was performed to determine an efficient way for generating turbulent boundary-layer flow near a corner, and if the HFILES methodology would result in the production of secondary motion in a Mach 2.3 turbulent flow in a duct. Previous studied had been performed on similar configurations, but had previously only considered incompressible flows.

Three grids of increasing resolution were used in the study, with the finest grid having the recommended resolution requirements for DNS as mentioned in Section 3.1 ($\Delta x^+ = 17.6$, $\Delta y_w^+ =$

Δz_w^+ =0.35, $\Delta y_e^+ = \Delta y_e^+$ = 5.9). The simulations were performed using the HFILES methodology and the FDL3DI code, as discussed in Section 2.1.1 and Appendix B. Figure 3 shows instantaneous results of the incompressible Q-criterion, colored by the streamwise (u) velocity. The Q-criterion is the second invariant of the velocity gradient tensor, which compares the vorticity to the strain-rate. The Q-criterion is commonly used to highlight organized structures in turbulence, especially for wall-bounded turbulent flows where the large streamwise velocity gradient can hide vorticity due to vortex motion.

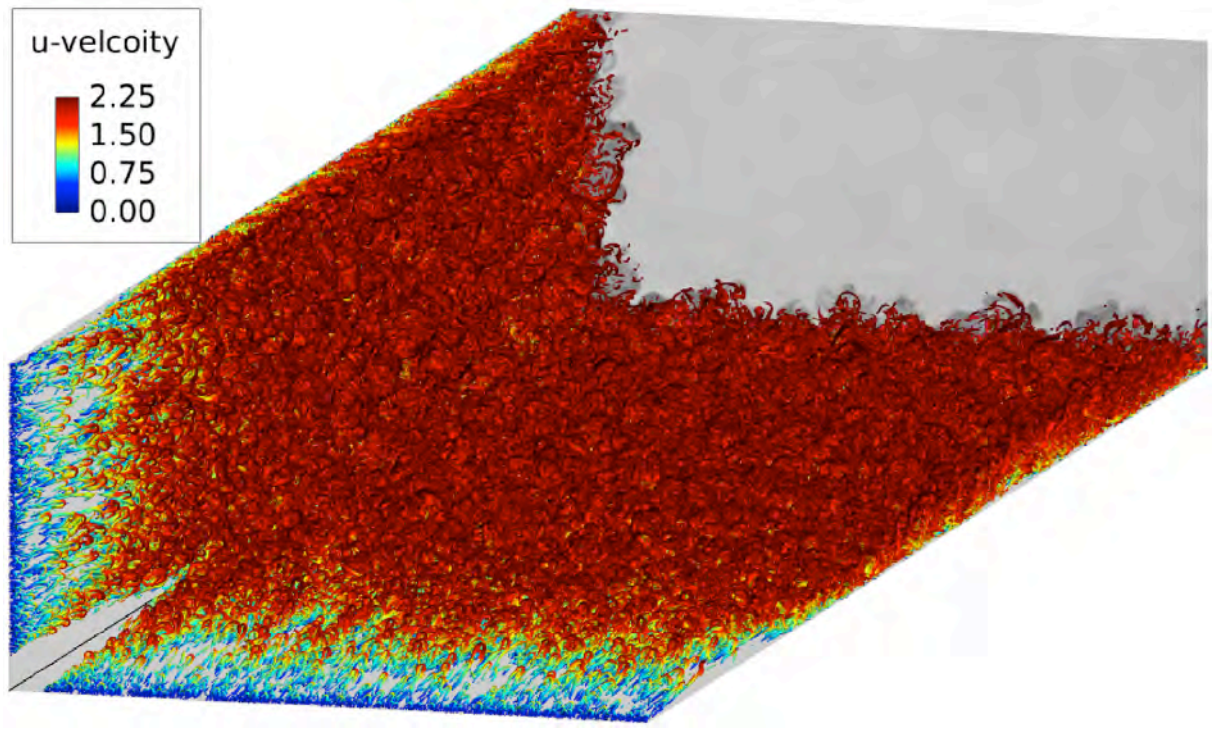

Figure 3: Instantaneous Iso-surfaces of the Q-criterion Colored by Streamwise *u*-velocity for Mach 2.3 Turbulent Boundary-layer Flow near Two Adjoining Walls

The flow is into the page. Only ¼ of the duct is shown. The blue structures at the beginning of the domain correspond to an artificial body-force trip.

The location of the artificial body-force trip (i.e., the bypass-transition method) is apparent at the beginning of Figure 3. It is worth noting that the trip was excluded from the near corner region ($y/\delta_0 < 1.25$, $z/\delta_0 < 1.25$), to ensure that the trip model did not drive the transition process and subsequent secondary motion in the near corner region. As such, the disturbances introduced by the trip grow along each flat plate wall until they have convected a sufficient distance downstream (≈10 δ_0 from the trip), to transition to a fully turbulent flow. As the transitional flow travels downstream, the turbulent structures spread into the corner, which aids in its transition to a turbulence state. Farther downstream, anisotropy from the turbulent boundary layers feeds into the corner leading the to development of secondary motion in the time-mean solution.

3.2.2 Reynolds-averaged Navier-Stokes Modeling

The investigation described in Ref. [8] was conducted to evaluate the effectiveness of RANS modeling of secondary motion via the inclusion of the quadratic constitutive relation (QCR).

Without QCR, the RANS predictions do not yield any secondary motion in the presence of a corner. This is because most commonly used RANS models linearize the Boussinesq approximation to provide a simple explicit closure model. Spalart recognized this deficiency in the closure model and proposed the QCR as a relatively simple modification to account for the anisotropic, non-linear Reynolds-stress behavior present in corner flows. The QCR modification involves adding a non-linear term to the Boussinesq approximation, with the strength of this non-linear term being adjustable via the constant C_{cr1} in the formulation.

Figure 4 shows the normalized cross-velocity fields ($\overline{v \cdot w} / \overline{u_\infty^2}$) and streamlines for the HFILES results discussed in Section 3.2.1 and the QCR adjusted RANS, where $C_{cr1} = 0.3$. Spalart suggested a value of 0.3 for the tunable constant C_{cr1}, which is based on a scenario where $u'^2 > v'^2 > w'^2$. Since some flows do not satisfy this scenario, and Spalart's work was focused on subsonic flow, the present study explored the effects of QCR for a one-to-one duct, with the high-fidelity implicit large-eddy simulations discussed in Section 3.2.1.

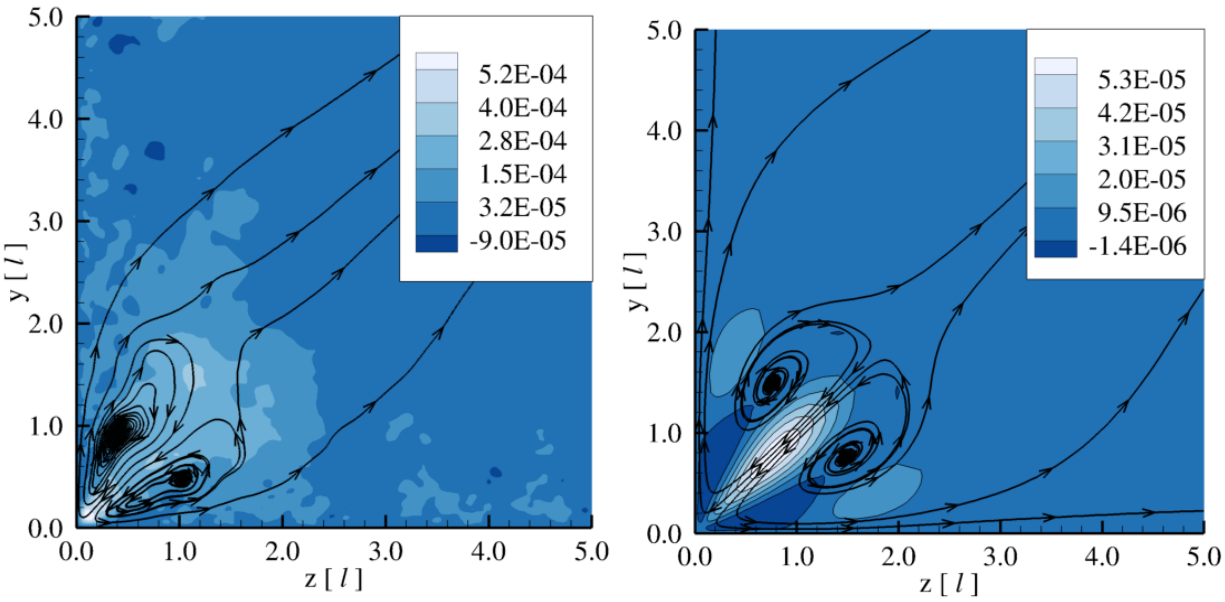

Figure 4: Time Mean Cross-velocity Contours and Streamlines for Mach 2.3 Turbulent Boundary Layer Flow near a 90° Corner at $Re_\theta = 2750$

The left figure is from the LES results. The right figure is from the RANS simulation that included the quadratic constitutive relation with the constant set to $C_{cr1} = 0.3$.

Several quantities were investigated, primarily focused on the size and strength of the corner vortex pair. This vortex pair is responsible for the change in surface skin-friction and heating rates in the near corner region when secondary motion is present. Figure 5 shows the coefficient of skin friction for several values of QCR's C_{cr1} parameter along with the HFILES results. As seen in the figure, the highest values of C_{cr1} best match the rapid change in skin friction predicted by the HFILES, yet, the high C_{cr1} parameter leads to the creation of additional (non-physical) vortex pairs away from the corner. The additional vortices produce an appreciable undershoot in skin friction near $z = 1.6\ \delta_0$.

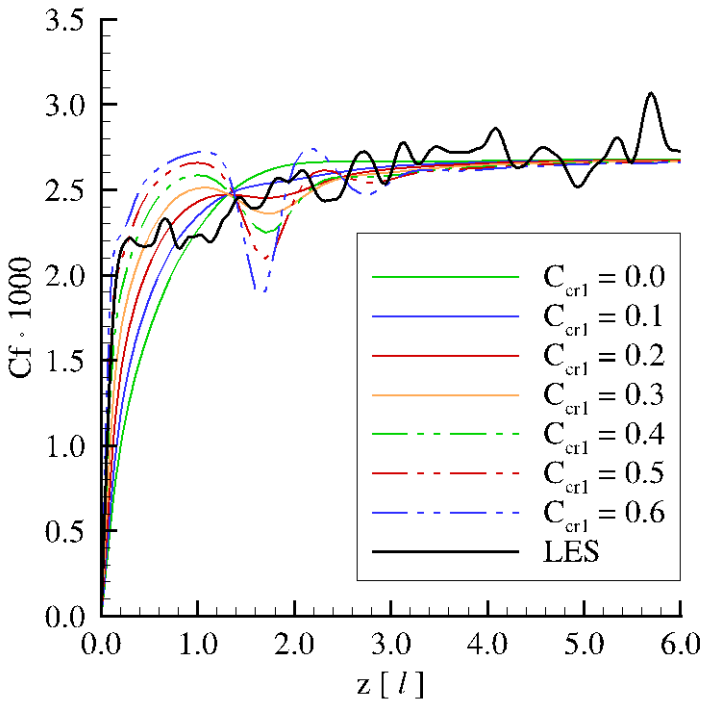

Figure 5: Coefficient of Skin Friction versus Distance from a 90° Corner for Mach 2.3 Turbulent Boundary Layer Flow at $Re_\theta = 2750$

The figure shows results from both the LES and the RANS for several values of the quadratic constitutive relation. The original RANS results are recovered with the constant set to $C_{cr1} = 0.0$.

Overall, QCR provides a mechanism for RANS simulations to develop secondary motion, but only the angle from the vortex core to the nearest wall and skin friction could be tuned by QCR to match the HFILES. These results suggest that while QCR provides a mechanism for generating secondary motion in corner flow, it does not improve the RANS predictions for some quantities.

3.3 Shock Boundary-Layer Interaction

Shock boundary-layer interactions, or (more broadly) inviscid-viscous interactions, are common phenomena that drive many of the design difficulties associated with flight at high Mach number. They occur wherever the vehicle shape deviates from a simple, smooth surface. Such flows are typically characterized by flow separation, large-scale unsteadiness, and extremely high heat transfer rates. They are the source of much of the aero-thermo-acoustic load that a high-speed vehicle must resist.

In recent work, we have addressed several aspects of the prediction of shock-wave/boundary-layer interaction. We have explored the limitations of conventional turbulence models in predicting heat transfer rates in strongly perturbed, separated flow. We have also investigated large-scale unsteadiness in these interactions, both from the standpoint of prediction and from control.

3.3.1 Implicit Large-Eddy Simulations

The investigation described in Refs. [4] and [6] expanded the HFILES corner flow simulations discussed in Section 3.2.1, by introducing a 24° ramp to the bottom plate. The ramp rapidly changes the flow angle resulting in a shock boundary-layer interaction, which when combined with the secondary motion due to the sidewall boundary layer, leads to a highly three-dimensional shock front. Figure 6 shows the instantaneous iso-surfaces of the Q-criterion, colored by *u*-velocity for half the domain.

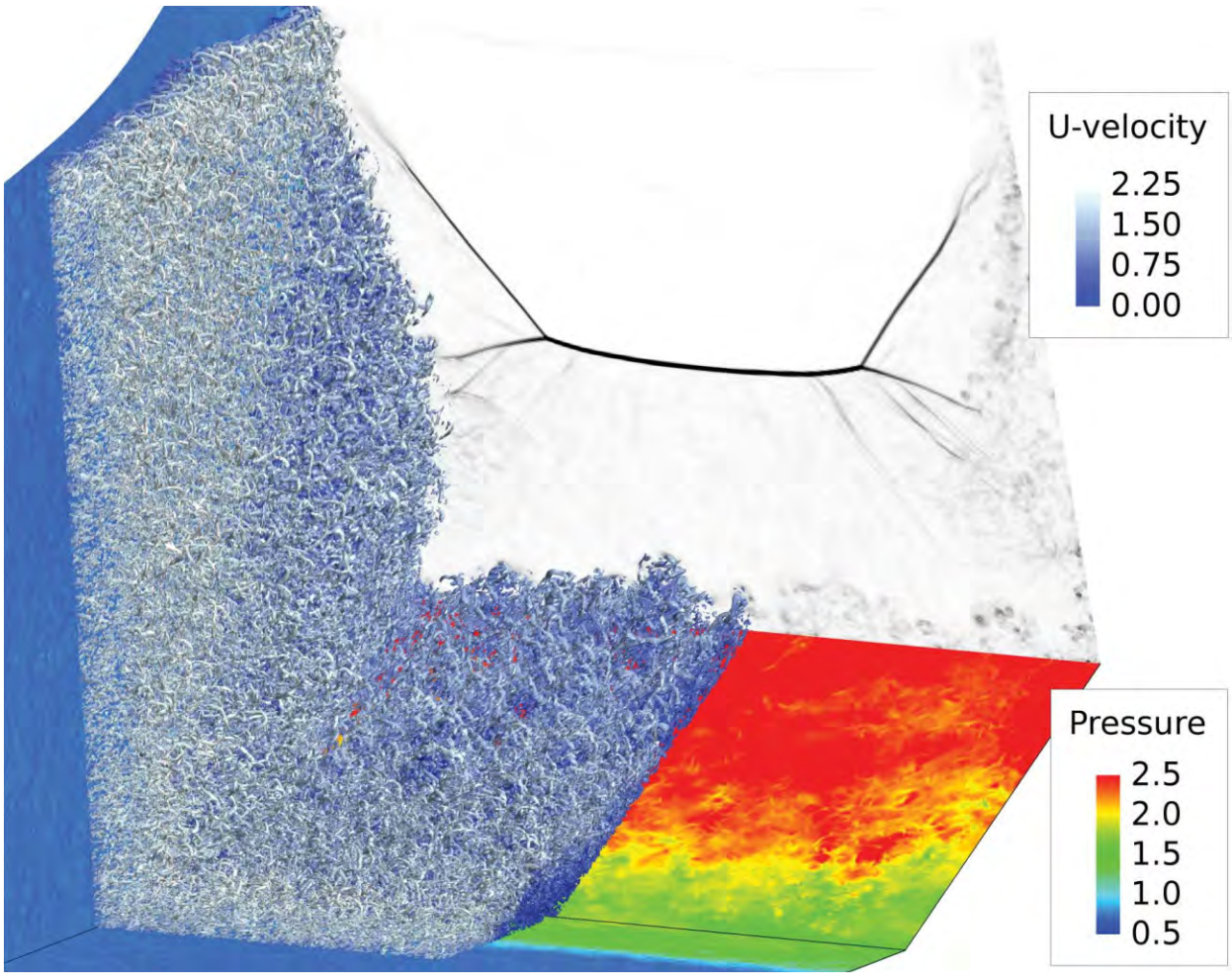

Figure 6: Iso-surfaces of the Q-criterion over Half of the Span, Colored by the *u*-velocity for Mach 2.3 Turbulent Flow over a 24° Compression-ramp between Two Sidewalls
The figure also includes surface pressure contours (colored) and a streamwise slice of pressure gradient magnitude (gray-scale).

The simulation discussed in Ref. [4] used a symmetry boundary condition at the midspan, whereas Ref. [6] conducted the full width simulation. The full width simulation showed that the symmetry boundary condition was not able to accurately predict the separation location near the midspan symmetry plane. Figure 7 shows the coefficient of skin friction for both the full span scenario and a scenario which assumed the flow was spanwise periodic. Since the full span domain is very wide relative to the boundary layer thickness just upstream of separation ($L_z/\delta \approx$

16δ), previous theory suggested that eh flow in the middle of the domain should be quasi two-dimensional, and thus, consistent with the spanwise periodic scenario.

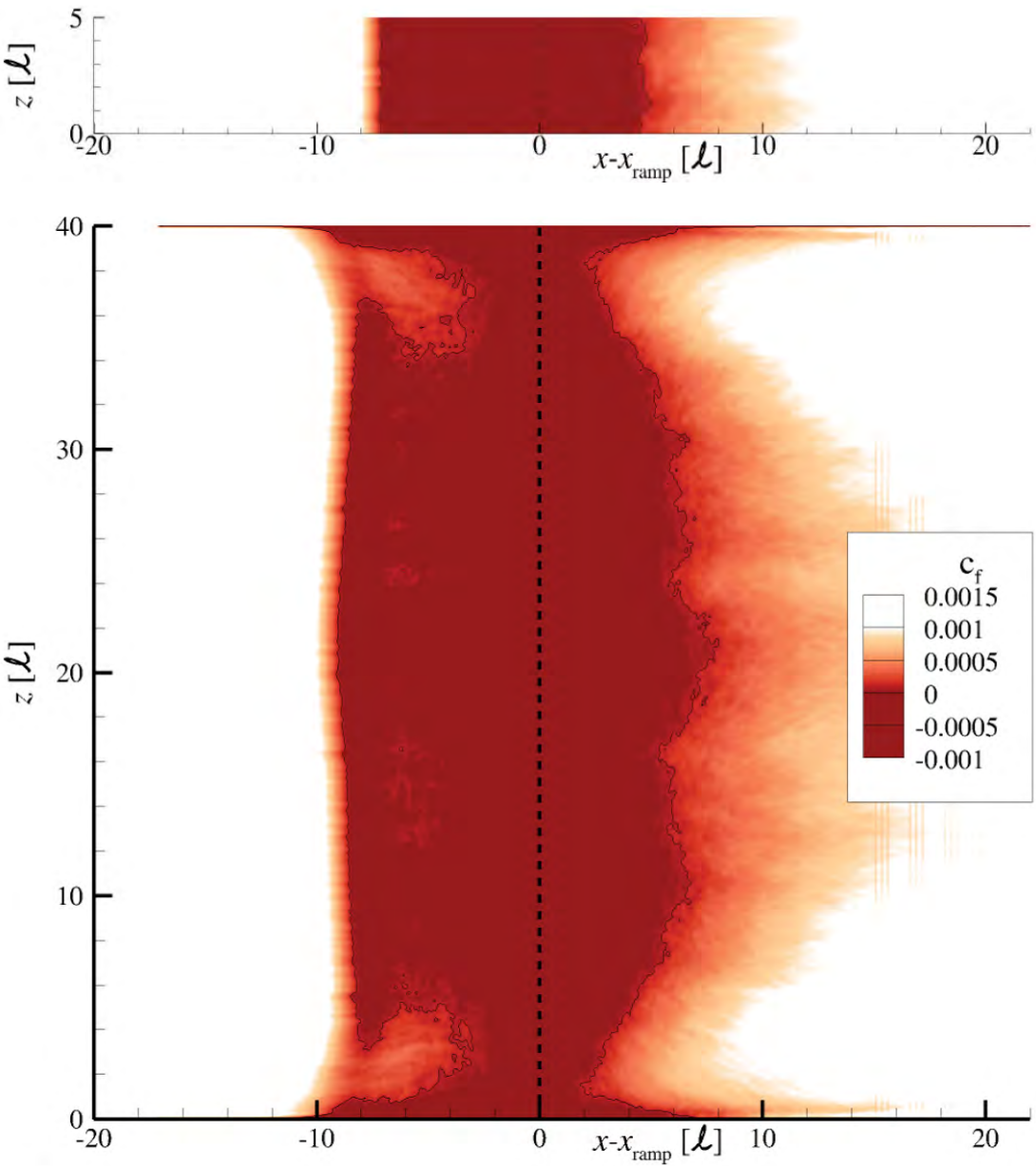

Figure 7: Top Down View of Skin Friction Fields for Mach 2.3 Flow over a 24° Ramp
The top figure was spanwise periodic, whereas the bottom grid contains the full span (i.e., it has both side walls).

As seen in Figure 7, the separation location for the spanwise periodic separation is about 7 δ_0 upstream of the corner and reattachment occurred approximately 4 δ_0 downstream for a total separation length of approximately 11δ_0. Conversely, the simulation with both sidewalls included in the simulation predicts that the separation location continues to move upstream to the midspan, with a max separation location of 10 δ_0 upstream of the corner. Likewise, reattachment at the midspan occurred approximately 7 δ_0 downstream of the corner location for a total separation length of approximately 17 δ_0, which is approximately 35% larger than the spanwise

periodic scenario. Since the separation length has been shown to correlate with the low frequency unsteadiness of the shock motion, accurately predicting this motion required the inclusion of both sidewalls in order to accurately account for the influence of the secondary motion from both sides of the domain.

3.3.2 Detached-Eddy Simulations

During preliminary design work of hypersonic and supersonic vehicles, RANS models provide a relatively quick and robust way to obtain the major mean flow features upon which early design decisions are often based. However RANS models, by their very nature, cannot provide information about the instantaneous flow field or unsteady flow phenomena, such as shear layer separation and reattachment. The Detached- Eddy Simulation (DES) method can provide the next level of fidelity in the design process. While DES requires a significantly larger amount of computational resources compared to a RANS simulation, it is still several orders of magnitudes less than HFILES. This benefit is also true when it comes to simulation run times since the limiting time step for most turbulent boundary-layer simulations is located at the wall. In the DES approach, the bulk of the flow is modeled with a Large Eddy Simulation (LES), so large scale turbulence is resolved. However in the near wall regions of the flow, where the resolution requirements of LES quickly become prohibitive, a RANS model with turbulence closure is utilized and greatly reduces the computational cost when compared to HFILES on a similar configuration.

The investigation described in Refs. [3] and [5] used the DES methodology to model Mach 2.9 turbulent boundary layer flow over a backward facing step and subsequent compression ramp. Figure 8 illustrates the scenario and the major flow features present in the system.

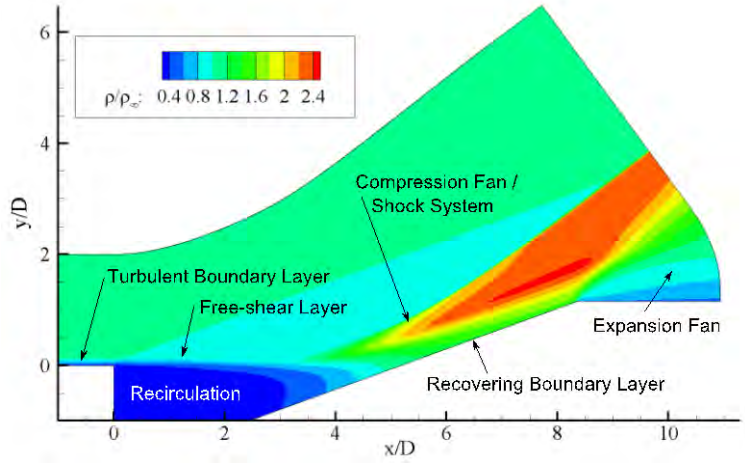

Figure 8: Normalized Density Field Contours for Mach 2.9 Flow over a Backward Facing Step

In these simulations, the inflow profile was obtained from the turbulent RANS solutions so the inflow did not have any fluctuations. The baseline case was constructed to match the configuration of Shen *et al*. A second scenario, with double the boundary layer thickness just upstream of the separation point ($2\delta_0$), was also performed and compared with the baseline case. The results, as seen in Figure 9, show that the mean surface pressure and resulting spectral

analysis of the surface pressure signal collapse for the two scenarios when the incoming boundary layer height and the separating length were used in the scaling.

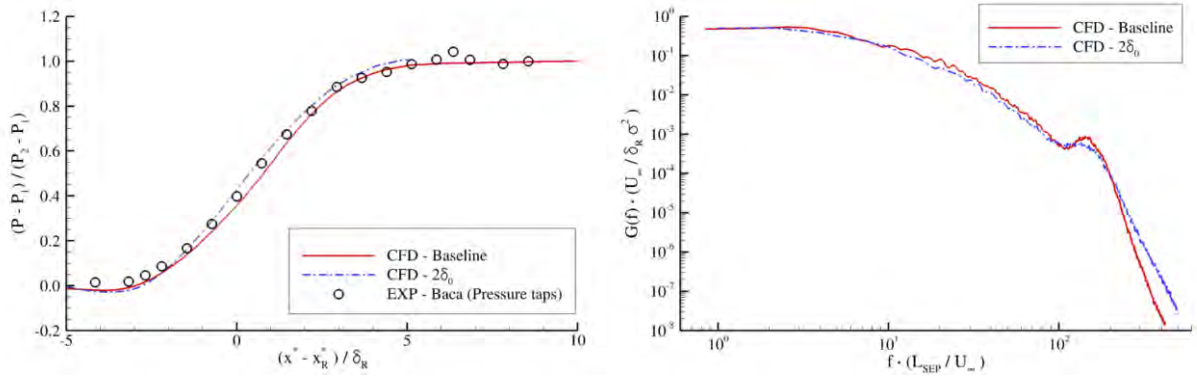

Figure 9: Surface Pressure Statistics for Mach 2.9 Turbulent for over a Backward Facing Step / Compression Ramp

The left figure shows mean surface pressure distribution. The right figure shows the nondimensional auto-spectra of the wall pressure fluctuations along the ramp wall downstream of reattachment

4 CONCLUSIONS

High fidelity numerical modeling of high Mach number flows was carried out to address large-scale unsteadiness and turbulent heating rates on increasingly three-dimensional configurations using high-performance large-scale computing.

High-order numerical simulations of a Mach 2.3 turbulent equilibrium boundary-layer flow were performed with increasing resolution until all fluid scales in the domain were fully resolved for a wall-bounded compressible flow. This was the first time in the reported literature that the simulations resolution was systematically increased to the strictest definition of direct numerical simulation for a supersonic turbulent boundary-layer flow. Comparison of the high-fidelity implicit large-eddy simulation results with the direct numerical simulation showed excellent agreement. The findings confirmed that the implicit large-eddy simulation method was a suitable approach for the compressible turbulent flows study within this body of work.

Secondary motion was predicted near the juncture of two walls due to anisotropy from the adjoining turbulent equilibrium boundary layers. These calculations were performed using high-fidelity implicit large-eddy simulations. Lower fidelity Reynolds-averaged Navier-Stokes simulations were also carried out with the inclusion of the quadratic constitutive relation which models the anisotropic, non-linear Reynolds-stress behavior present in corner flows. A tuning constant in the relationship was adjusted to best match the implicit large-eddy simulations. The modified Reynolds-averaged Navier-Stokes results agreed well for some parameters of interest, but showed poor agreement for other quantities. The results suggests that while the quadratic constitutive relation does provide a straight-forward mechanism for producing secondary motion, the model does not fully capture the physics in compressible flows so higher fidelity approaches are needed to reduce uncertainty in the fluid model predictions.

Large-scale unsteadiness was examined for a full span supersonic turbulent duct flow with a compression ramp added to the floor. The configuration led to the development of a highly three-dimensional turbulent shock boundary-layer interaction. Inclusion of the sidewalls lead to secondary motion in the corners prior to the main shock interaction, which yielded a significantly more three-dimensional shock front than prior simulations without the sidewalls present. In addition, each sidewall boundary layer developed its order glancing shock boundary-layer interaction and exhibited its own low frequency unsteadiness corresponding to the sidewall separation length scale.

5 REFERENCES

1. N. J. Bisek, “High-Order Implicit Large-Eddy Simulations of Supersonic Corner Flow” AIAA Paper 2014-0588, American Institute of Aeronautics and Astronautics, January 2014.

2. J. Poggie, “Large-Scale Structures in Implicit Large-Eddy Simulation of Compressible Turbulent Flow” AIAA Paper 2014-3328, American Institute of Aeronautics and Astronautics, June 2014.

3. T. Leger and J. Poggie, “Detached-Eddy Simulation of a Reattaching Shear Layer in Compressible Turbulent Flow” AIAA Paper 2014-3329, American Institute of Aeronautics and Astronautics, June 2014.

4. N. J. Bisek, “High-Order Implicit Large-Eddy Simulations of Supersonic Corner Flow over a Compression Ramp” AIAA Paper 2014-3335, American Institute of Aeronautics and Astronautics, June 2014.

5. T. Leger and J. Poggie, “Spectral Scaling in a Supersonic Reattaching Shear Layer” AIAA Paper 2015-1972, American Institute of Aeronautics and Astronautics, January 2015.

6. N. J. Bisek, “Sidewall Interaction of Supersonic Corner Flow over a Compression Ramp” AIAA Paper 2015-1976, American Institute of Aeronautics and Astronautics, January 2015.

7. J. Poggie, “Compressible Turbulent Boundary Layer Simulations: Resolution Effects and Turbulent Modeling” AIAA Paper 2015-1983, American Institute of Aeronautics and Astronautics, January 2015.

8. T. Leger, N. Bisek, and J. Poggie, “Supersonic Corner Flow Predictions using the Quadratic Constitutive Relation” AIAA Paper 2015-3432, American Institute of Aeronautics and Astronautics, June 2015.

APPENDIX A
RESOLUTION EFFECTS

AIAA Aviation
16-20 June 2014, Atlanta, GA
7th AIAA Theoretical Fluid Mechanics Conference

Large-Scale Structures in Implicit Large-Eddy Simulation of Compressible Turbulent Flow

Jonathan Poggie*
Air Force Research Laboratory, Wright-Patterson AFB, Ohio 45433-7512 USA

High-fidelity, implicit large-eddy simulations were performed for two supersonic turbulent boundary layers with Mach numbers of 2.3 and 2.9, and momentum thickness Reynolds numbers based on wall viscosity of 2.0×10^3 and 2.5×10^3, respectively. Transition to turbulence was promoted with an artificial body force trip. Four computational meshes were considered for each case. The resolution of the coarsest mesh met the requirements for implicit large-eddy simulation: $\Delta x^+ < 50$, $\Delta y_w^+ < 1$, $\Delta z^+ < 15$, and $\Delta t^+ < 1$, whereas the resolution of the finest mesh approached that required for direct numerical simulation: $\max(\Delta x^+, \Delta y^+, \Delta z^+) < 10$, $\Delta y_w^+ < 1$, and $\Delta t^+ < 1$. The computational results were compared for the same flow state, at a station where the skin friction coefficient and Reynolds number agreed within 10% on all grids. At this station, mean velocity and Reynolds stress agreed within 10% for Grids 2–4, but the calculations on Grid 1 did not appear to produce a fully-developed turbulent boundary layer flow. Comparing frequency and wavenumber spectra of mass flux fluctuations at this station, additional mesh resolution revealed additional spectral content, and an extension of the inertial subrange to smaller scales. These results suggest that even the finest mesh remains in the large-eddy simulation regime, rather than direct numerical simulation regime. Nonetheless, good convergence of the turbulence statistics and agreement with experiment permitted detailed examination of the behavior of large-scale structures and of parameters used in turbulence modeling. In particular, the strong Reynolds analogy, the ratios of Reynolds stresses, and the near-wall behavior of the turbulent energy transport were evaluated for the two flows. Further, the effects of wall temperature on the turbulent heat flux were examined, as were correlations characterizing large-scale structures. The results were in general agreement with assumptions employed in turbulence models for compressible flow.

*Senior Aerospace Engineer, AFRL/RQHF. Associate Fellow AIAA.

Nomenclature

Variables

L	=	length scale
M	=	Mach number
p	=	pressure
R	=	auto-correlation
$\mathrm{Re}_\theta = \rho_\infty U_\infty \theta / \mu_\infty$	=	momentum thickness Reynolds number
$\mathrm{Re}_{\theta i} = \rho_\infty U_\infty \theta / \mu_w$	=	momentum thickness Reynolds number based on wall viscosity
T	=	temperature
t	=	time
u	=	streamwise component of velocity
v	=	wall-normal component of velocity
w	=	spanwise component of velocity
x	=	streamwise coordinate
y	=	wall-normal coordinate
z	=	spanwise coordinate
δ	=	boundary layer thickness
θ	=	boundary layer momentum thickness, or angle
ρ	=	density
μ	=	viscosity
ν	=	kinematic viscosity
τ	=	shear stress, or time scale
ϵ	=	viscous dissipation
η	=	Kolmogorov microscale

Subscripts

∞	=	freestream
0	=	reference station
e	=	boundary layer edge
i	=	incompressible flow equivalent
x	=	position
w	=	wall
θ	=	momentum thickness

Superscripts

$+$	=	turbulent boundary layer 'inner' coordinates
$\prime$	=	fluctuating component

I. Introduction

The structure of turbulence in high Reynolds number, compressible, turbulent boundary layer flow cannot be considered well-understood, because neither experiments nor simulations can currently resolve the full range of space and time scales.[1–3] Thus, much of the understanding of the structure of turbulence in this regime comes from extrapolation of ideas developed for low-Reynolds-number, incompressible flow.

In the low-speed regime, coherent structures are believed to be the primary mechanism for the transport of mass, momentum, and energy across the boundary layer,[1] and for the entrainment of irrotational freestream fluid into the vortical boundary layer flow.[4,5] The inner part of the boundary layer ($y^+ < 100$) is characterized by alternating streaks of high and low speed fluid.[6] These streaks are persistent in space and time, and tend

to be spaced about $\Delta z^+ \approx 100$ apart in the spanwise direction. The streaks have been observed to lift up from the wall, oscillate, and break up between $y^+ = 10$ and $y^+ = 30$. This inner layer burst cycle is believed to be the dominant mechanism for turbulence energy production in the boundary layer.[7]

Bulges are the dominant structure in the outer part of the boundary layer, from the beginning of the wake region to beyond the mean boundary layer edge ($y/\delta \approx 1.2$). The bulges are on the order of the boundary layer thickness in scale, and freestream fluid tends to penetrate close to the wall between the bulges. Studies of outer layer structure have found that a strong shear layer exists on the upstream side of these bulges, formed when high-speed freestream fluid impacts onto slow-moving fluid within the bulges.[8]

In supersonic flow, the large-scale structures have been studied using hotwires,[9–12] particle image velocimetry,[13] wall pressure transducers,[14] and flow visualization.[15,16] A number of previous simulations of compressible, turbulent boundary layers have been carried out with a resolution that approached the DNS regime.[17–30]

The primary effect of compressibility on turbulent boundary layers is the conversion of mechanical energy to heat through compression and viscous dissipation.[2,3] Near the wall, these factors cause the temperature to increase and the density to drop. The Reynolds number near the wall tends to decrease rapidly with increasing Mach number, a change that may have a strong effect on the turbulence structure in that region.[2,3,31]

If the fluctuating Mach number is small, the turbulence structure is believed to be similar to that of the incompressible case, with the primary difference being the property variation across the boundary layer.[2,3,32,33] The principal support for this hypothesis is that a coordinate transform accounting for the fluid property variation succeeds in collapsing profiles of both mean velocity and turbulence statistics onto corresponding incompressible flow profiles. When the fluctuating Mach number is larger, the turbulence structure may be significantly modified by compressible flow phenomena like eddy shocklets and sound radiation.

Turbulent boundary layers are important as inflow boundary conditions of more complex flows. Recent experiments and large-eddy simulations[34–38] have supported a model of separation unsteadiness[39] in which the separation bubble acts as an amplifier of large-scale disturbances in the incoming turbulent flow. Accurate characterization of these structures in large-eddy simulation is essential in order for computations to be used to make engineering estimates of the fatigue loading associated with separation unsteadiness.

One of the fundamental parameters used to characterize the large-scale structures in turbulent flow is the convection velocity. For example, Poggie et al.[16] used flow visualization to measure convection velocities of δ-scale structures in boundary layers and mixing layers at Mach 3 and Mach 8. Thurow et al.,[40] however, have shown that measurements of convection velocity based on flow visualization of large-scale structures differ substantially from those based on planar Doppler velocimetry. These results motivate a reexamination of the metrics used to characterize large-scale turbulent structures in both experiment and computation.

The present project aims to explore turbulent boundary layer flow in the context of high-fidelity, implicit large-eddy simulation. The work focuses on assessing the accuracy of large-eddy simulation as tool for predicting the properties of large-scale structures, and on investigating how the omission of the small scales affects the structure of the flow turbulence. In particular, the boundary between implicit large-eddy simulation and direct numerical simulation is investigated. Spatial and temporal resolution are varied at fixed momentum thickness Reynolds numbers, and the effect of these changes in resolution is explored. Comparison to experiment is carried out for turbulence statistics and for parameters characterizing large-scale boundary layer structures.

II. Procedure

Two supersonic turbulent boundary layer flows at Mach 2.3 and 2.9 were explored using high-fidelity, implicit large-eddy simulation. The numerical scheme was based on sixth-order compact spatial differences, second-order implicit time advancement, and eighth-order filtering. Rectangular grids with smooth stretching were employed, and transition from laminar to turbulent flow was promoted through a trip based on an artificial body force.

A. Physical Model

The calculations were carried out using the code HOPS (Higher Order Plasma Solver), developed by the author.[41–46] The code includes several physical models and numerical schemes. Here, the physical model

consists of the perfect-gas, compressible-flow Navier-Stokes equations. The conservation of mass, momentum, and energy are expressed as:

$$\frac{\partial \rho}{\partial t} + \nabla \cdot (\rho \mathbf{u}) = 0 \tag{1}$$

$$\frac{\partial}{\partial t}(\rho \mathbf{u}) + \nabla \cdot (\rho \mathbf{u}\mathbf{u} - \mathbf{\Sigma}) = \mathbf{f} \tag{2}$$

$$\frac{\partial \mathcal{E}}{\partial t} + \nabla \cdot (\mathbf{u}\mathcal{E} - \mathbf{\Sigma} \cdot \mathbf{u} + \mathbf{Q}) = \mathbf{f} \cdot \mathbf{u} + S \tag{3}$$

where ρ is the gas density, $\mathbf{u}$ is its velocity, $\mathbf{\Sigma}$ is the total stress tensor, $\mathcal{E} = \rho(\epsilon + u^2/2)$ is the total fluid energy, ϵ is the internal energy, and $\mathbf{Q}$ is the heat flux. An optional body force $\mathbf{f}$ and energy source term S are included on the right hand side of the equations.

The total stress tensor $\mathbf{\Sigma}$ is given by the usual constitutive equation for a Newtonian fluid, and the heat flux $\mathbf{Q}$ follows Fourier's heat conduction law:

$$\Sigma_{ij} = -p\delta_{ij} + \mu \left(\frac{\partial u_i}{\partial x_j} + \frac{\partial u_j}{\partial x_i} \right) - \frac{2}{3}\mu \frac{\partial u_k}{\partial x_k}\delta_{ij} \tag{4}$$

$$Q_i = -k\frac{\partial T}{\partial x_i} \tag{5}$$

where p is the pressure, μ is the viscosity, and k is the thermal conductivity. The transport coefficients were evaluated using the correlations given in Ref. 47. The working fluid (air) was assumed to be a calorically and thermally perfect gas: $\epsilon = c_v T$ and $p = \rho R T$, where T is the temperature, c_v is the specific heat, and R is the ideal gas constant.

B. Numerical Methods

The numerical approach was based on compact spatial differencing, filtering, and an implicit time-marching scheme. Employed in this manner as a perfect-gas, compressible-flow Navier-Stokes solver, the HOPS code is similar to the AFRL code FDL3DI.[48,49] A previous publication[50] showed good comparison between the HOPS and FDL3DI codes in a large-eddy simulation of a supersonic turbulent boundary layer flow. (See Pirozzoli[51] for alternative approaches, and for a general review of numerical methods for high-speed flows.)

The conservation laws were solved using an approximately-factored, implicit scheme, related to those developed by Beam and Warming[52] and Pulliam.[53] All calculations were carried out using double-precision arithmetic. Applying the standard transformation from physical coordinates (x, y, z) to grid coordinates (ξ, η, ζ), the conservation equations (1)–(3) can be written in the form:

$$\frac{\partial \overline{U}}{\partial t} + \frac{\partial \overline{E}}{\partial \xi} + \frac{\partial \overline{F}}{\partial \eta} + \frac{\partial \overline{G}}{\partial \zeta} = \frac{\partial \overline{E}_v}{\partial \xi} + \frac{\partial \overline{F}_v}{\partial \eta} + \frac{\partial \overline{G}_v}{\partial \zeta} + \overline{S} \tag{6}$$

where the usual notation[54] is used. For example, $U = [\rho, \rho\mathbf{u}, \mathcal{E}]^T$ is the the vector of dependent variables, E is a flux, $\overline{U} = U/J$, $\overline{E} = (\xi_x E + \xi_y F + \xi_z G)/J$, and J is the Jacobian of the grid transformation.

Writing Eq. (6) as $\partial \overline{U}/\partial t = R$, and discretizing in time, we have:

$$(1+\theta)\overline{U}^{n+1} - (1+2\theta)\overline{U}^{n} + \theta \overline{U}^{n-1} = \Delta t R^{n+1} \tag{7}$$

where $\theta = 0$ for an implicit Euler scheme and $\theta = 1/2$ for a three point backward scheme. We introduce subiterations such that $\overline{U}^{n+1} \rightarrow \overline{U}^{p+1}$, with $\Delta \overline{U} = \overline{U}^{p+1} - \overline{U}^{p}$. The right hand side R^{n+1} is linearized in the standard thin layer manner. Collecting the implicit terms on the left hand side, and introducing approximate

factoring and a subiteration time step $\Delta\hat{t}$ gives:

$$\begin{aligned}
&\left[I - \frac{\Delta\hat{t}}{1+\theta}(B + \delta_\xi A_1 + \delta_\xi R_1 \delta_\xi + D_{i\xi})\right] \times \\
&\left[I - \frac{\Delta\hat{t}}{1+\theta}(\delta_\eta A_2 + \delta_\eta R_2 \delta_\eta + D_{i\eta})\right] \times \\
&\left[I - \frac{\Delta\hat{t}}{1+\theta}(\delta_\zeta A_3 + \delta_\zeta R_3 \delta_\zeta + D_{i\zeta})\right] \Delta\overline{U} = \\
&- \frac{\Delta\hat{t}}{1+\theta}\left\{\frac{(1+\theta)\overline{U}^p - (1+2\theta)\overline{U}^n + \theta\overline{U}^{n-1}}{\Delta t} - R^p\right\}
\end{aligned} \tag{8}$$

where B is the source Jacobian, and A_{1-3} and R_{1-3} are flux Jacobians. The spatial derivatives on the left-hand-side are evaluated using second order central differences. The symbol D_i represents the implicit damping operator described by Pulliam.[53] The implicit terms were evaluated using the scalar pentadiagonal formulation of Pulliam and Chaussee.[55] The metrics were evaluated using the method of Thomas and Lombard.[56]

The spatial differencing scheme for the right-hand-side was based on compact differencing.[48,57] In one dimension, the finite difference approximation to the first derivative ϕ'_i is evaluated by solving a tridiagonal system of the form:

$$\alpha\phi'_{i-1} + \phi'_i + \alpha\phi'_{i+1} = a\,\frac{\phi_{i+1} - \phi_{i-1}}{2} + b\,\frac{\phi_{i+2} - \phi_{i-2}}{4} \tag{9}$$

where α, a, and b are constants chosen to give a certain order of accuracy and set of spectral properties for the scheme. Second derivatives were found by applying the first derivative operator twice.

Numerical stability was enforced using a low-pass, Padé-type, non-dispersive spatial filter.[48,57] The filtering approach replaces the computed value ϕ_i at a particular node with a filtered value $\overline{\phi}_i$:

$$\alpha_f\overline{\phi}_{i-1} + \overline{\phi}_i + \alpha_f\overline{\phi}_{i+1} = \sum_{n=0}^{N}\frac{a_n}{2}(\phi_{i+n} + \phi_{i-n}) \tag{10}$$

where the constants α_f, a_0, ... a_N are chosen to give appropriate filter properties. The filter was applied to the solution vector, sequentially, in each of the three computational directions, following each sub-iteration for implicit time integration. The order of the filtering operation was permuted at each time step.

The code includes the shock capturing methods[49] of Visbal and Gaitonde, but this additional complexity was found to be unnecessary for the weak compression waves in the turbulent boundary layers studied here.

In the implementation of the computer code, multi-level parallelism is exploited by using vectorization, multi-threading with OpenMP commands,[58] and multi-block decomposition implemented through MPI commands.[59] Typical runs were carried out by decomposing the domain into blocks of $65^3 \approx 2.7 \times 10^5$ points, each executed with an MPI task and up to eight OpenMP threads. Additional details on these aspects of the implementation were reported in an earlier paper by Poggie.[42]

C. Flowfield

Two flat-plate turbulent boundary layer flows were investigated here. The flow conditions are listed in Tables 1 and 2. The conditions for the Mach 2.3 case are similar to those employed in several previous numerical investigations.[17,21,22,60] Corresponding experimental data are available from a 1955 experiment by Shutts et al., documented as Case 55010501 in Fernholz and Finley.[61] The flow conditions for the Mach 2.9 case correspond to those reported for the experiments of Bookey et al.,[62] and studied in a number of previous computations.[63] The conditions in the experiments of Spina[64] are similar, but correspond to an order of magnitude higher Reynolds number.

For each case, the inflow boundary condition was provided by a similarity solution of the compressible, laminar boundary layer equations. No-slip conditions were imposed on the flat-plate surface, with zero normal pressure gradient enforced to third-order accuracy. Periodic boundary conditions were imposed in the spanwise direction. Grid stretching and extrapolation were used to provide outflow boundary conditions at the top and the end of the domain.

The boundary layer was tripped to turbulence using a body-force trip method.[65] An artificial body force $\mathbf{f}$ was added to the momentum equation (2), and its corresponding work $\mathbf{f}\cdot\mathbf{u}$ was added to the total energy equation (3). The magnitude of this body force was taken to be:

$$f_0 = \frac{2D_c}{\pi x_r y_r} \sin^2\left(2\pi \frac{z-z_1}{z_r}\right) \exp\left[-\left(\frac{x-x_1}{x_r}\right)^2 - \left(\frac{y-y_1}{y_r}\right)^2\right] \tag{11}$$

The smooth variation in the form of the trip function obviated the need for grid clustering around the trip, and the sinusoidal variation in the spanwise direction was found to promote more rapid transition. (Previous work[50] used a force distribution for the trip that was triangular in the x-y-plane, and uniform in the spanwise direction.) Note that this spatial distribution is scaled so that:

$$\int_0^{z_r} \int_{-\infty}^{\infty} \int_{-\infty}^{\infty} f_0 \, dx \, dy \, dz = D_c \tag{12}$$

The components of the force were:

$$\begin{aligned} f_x &= f_0 \cos\theta \\ f_y &= f_0 \sin\theta \\ f_z &= 0 \end{aligned} \tag{13}$$

The parameters were chosen to be $x_1 = 2.5\,\delta_0$, $y_1 = 0$, $z_1 = 0$, $x_r = 0.17\,\delta_0$, $y_r = 0.01\,\delta_0$, $z_r = 1.0\,\delta_0$, $\theta = 179$ deg, and $D_c = 0.015$. (Here δ_0 is the thickness of the laminar boundary layer imposed at the inflow boundary.) For this choice of parameters, only the $y \geq 0$ half of the force magnitude distribution, Eq. (11), acts on the flow.

D. Numerical Resolution

The computational meshes consisted of 1.0×10^7 to 1.1×10^9 cells. The streamwise extent of the resolved region was $100\delta_0$, where δ_0 is the thickness of the laminar boundary layer imposed at the inflow plane. The wall-normal extent of the resolved region was $5\delta_0$ for the Mach 2.3 case, and $6\delta_0$ for the Mach 2.9 case. The spanwise extent was $5\delta_0$ for most cases, but additional test cases were run with $10\delta_0$ and $20\delta_0$ to examine the effect of domain width on the computational results. Details for each case are presented in Table 3 for the Mach 2.3 boundary layer flow, and in Table 4 for the Mach 2.9 boundary layer flow.

Typical resolution recommendations[66,67] for wall-resolving large-eddy simulation are $50 \leq \Delta x^+ \leq 150$, $\Delta y_w^+ < 1$, $15 \leq \Delta z^+ \leq 40$, and $\Delta t^+ < 1$. (The conventional inner variable scaling is used here: $\Delta t^+ = u_\tau^2 \Delta t/\nu_w$, $\Delta y_w^+ < u_\tau \Delta y_w/\nu_w$, where $u_\tau = \sqrt{\tau_w/\rho_w}$ is the friction velocity.) Following these guidelines, the resolution at the wall for initial runs was set with the proportions $\Delta x : \Delta y : \Delta z = 50 : 1 : 10$. Based on the results of these initial calculations, Grid 1 was generated for each Mach number case to meet the restriction $\Delta x^+ < 50$, $\Delta y_w^+ < 1$, $\Delta z^+ < 15$. Grids 2 and 3 were then generated to carry out a conventional grid resolution study, in which resolution was doubled twice for the same pattern of the distribution of mesh points. Finally, an additional case (Grid 4) was developed that increased the streamwise resolution of Grid 2 until the overall resolution was comparable to a level reported as direct numerical simulation (DNS) in the literature.[30,68] From Tables 3-4, we see that the requirements for wall-resolved large-eddy simulation are met for all cases, and the Grid 4 case could be considered near-DNS.

Grids 5 and 6 were employed for the domain width study at Mach 2.3 (see Table 3). These grids maintained the spatial resolution of Grid 4, but respectively doubled and quadrupled the spanwise extent of the computational domain.

For direct numerical simulation in the strictest sense, the Kolmogorov microscale[67,69] $\eta = (\nu^3/\epsilon)^{1/4}$ and its associated time scale $\tau = (\nu/\epsilon)^{1/2}$ must be resolved everywhere in the flow. The most stringent spatial resolution requirement occurs at the wall, where the viscous dissipation is highest. Estimating the dissipation as $\epsilon_w = \nu_w (\partial\overline{u}/\partial y)_w^2$ and the friction velocity as $u_\tau = \sqrt{\nu_w (\partial\overline{u}/\partial y)_w}$, we find $\eta^+ = 1$ and $\tau^+ = 1$. To meet the requirements for true direct numerical simulation at the wall, the mesh size would have to be increased from the Grid 4 case by a factor of about 25 at Mach 2.3 and 35 at Mach 2.9.

III. Results

The present work focuses on the turbulent fluxes and properties of the large-scale structures in the region of fully-developed turbulent boundary layer flow. To illustrate the region of the flow under consideration,

cross-sections of the instantaneous flowfield for the Mach 2.3 turbulent boundary layer are given in Figs. 1–2. All the plots correspond to the same instant in time, and were obtained from the results of the computations on Grid 4.

Figure 1 shows instantaneous contours of the density ρ. Three planes are shown: an end view in the $x/\delta_0 = 100$ plane, a plan view in a plane about halfway through the boundary layer, and a side view plane at the center of the domain. In all the plots, the highly convoluted interface between the boundary layer and the freestream is apparent. Boundary layer fluid appears to be ejected beyond the mean boundary layer edge and freestream fluid often reaches close to the wall. Within the sectional planes, islands of freestream fluid are sometime visible wholely surrounded by boundary layer fluid, as are disconnected islands of boundary layer fluid in the freestream. These results are qualitatively consistent with flow visualization experiments.[16]

Corresponding plots of quantities at the wall are shown in Fig. 2. Figure 2a shows the instantaneous wall pressure and Fig. 2b shows the magnitude of the wall shear stress. Structures in the pressure field appear relatively isotropic, whereas structures in the shear stress are highly elongated in the streamwise direction.

A. Effects of Numerical Resolution

A comparison of the turbulence statistics was carried out for the different grids and Mach numbers. For each case discussed here, averaging was carried out over 6×10^4 time steps, corresponding to a non-dimensional time of $U_\infty t/\delta_0 = 300$ or $t^+ > 3 \times 10^3$.

Figure 3 shows the mean skin friction profile for each case. Here the skin friction coefficient is $C_f = 2\tau_w/(\rho_\infty U_\infty^2)$, where τ_w is the mean wall shear stress. The shear stress was computed in an auxiliary routine, using the same compact difference scheme and order of accuracy as the main flow solver. The shear stress distribution on the wall was stored as a function of time in a log file. The results were averaged in time, and across the spanwise direction, to produce the figures shown. The results show general agreement for the different grids, with a moderate variation in transition location with mesh resolution.

Figure 4 shows profiles of streamwise velocity in van Driest transformed[70] inner coordinates at $x/\delta_0 = 100$ for each case. The results were obtained by averaging over time and over the spanwise direction. The following closed-form expression was used for the van Driest effective velocity (see White,[47] pp. 544–546):

$$\begin{aligned} \frac{u_{vD}}{U_e} &= \frac{1}{a}\left[\sin^{-1}\left(\frac{2a^2\overline{u}/U_e - b}{Q}\right) + \sin^{-1}\left(\frac{b}{Q}\right)\right] \\ a &= \sqrt{\frac{\gamma-1}{2}M_e^2\frac{T_e}{T_w}} \\ b &= \frac{T_{aw}}{T_w} - 1 \\ Q &= \sqrt{b^2 + 4a^2} \end{aligned} \tag{14}$$

The adiabatic wall temperature was estimated as:

$$\frac{T_{aw}}{T_e} = 1 + r\frac{\gamma-1}{2}M_e^2 \tag{15}$$

with a recovery factor of $r = 0.89$. The data are presented in the form $u^+ = u_{vD}/u_\tau$ versus $y^+ = u_\tau y/\nu_w$. The flow appears to be transitional at this station on Grid 1 for both the Mach 2.3 and 2.9 cases. Nonetheless, good agreement is obtained for Grids 2 through 4.

Figure 5 shows profiles of the streamwise Reynolds normal stress in inner coordinates at $x/\delta_0 = 100$ for each case. Again, the data were averaged over time and the spanwise direction. Following Morkovin's hypothesis,[32] the data are scaled by the local mean density and the friction velocity: $\overline{\rho}\overline{u'^2}/(\rho_e u_\tau^2)$. The streamwise fluctuation intensity varies with grid resolution, with the Grid 1 case displaying particularly high values. For the cases showing grid convergence, peak values of the normal Reynolds stress occur at $y^+ \approx 13$, and scaling with the local density collapses the data for the two Mach numbers.

Figure 6 shows corresponding profiles of the Reynolds shear stress component $-\overline{\rho}\overline{u'v'}/(\rho_e u_\tau^2)$ for each case. In contrast to the results for the Reynolds normal stress, general agreement is obtained on all meshes for the Reynolds shear stress. For both Mach number cases, peak values of the Reynolds shear stress occur at $y^+ \approx 45$. Again, scaling with the local density collapses the data for the two Mach numbers.

Figure 7 shows the spectra of the mass flux fluctuations for the different cases. Figures 7a–b show frequency spectra $E(f)$, and Figs. 7c–d show spanwise wavenumber spectra $E(k_z)$. The momentum thickness Reynolds number varies by less than 10% between solutions on the different grids (Tables 3–4), and the skin friction profiles for Grids 2–4 show a similar state of boundary layer development (Fig. 3). The differences in the spectra can thus be attributed to differences in numerical resolution. The results are that expected for implicit large-eddy simulation: as the grid resolution is increased, the calculations capture an increasing portion of the inertial subrange. As mentioned earlier, the grid resolution of Grid 4 would have to be increased by a factor of 25–35 to achieve direct numerical simulation in the strictest sense, that is $\max(\Delta x^+, \Delta y^+, \Delta z^+) < 1$ at the wall.

A time resolution study was also carried out. Figure 8 shows the effect of changing the time step in the range $U_\infty \Delta t/\delta_0 = 2.5 \times 10^{-3}$, 5.0×10^{-3}, and 1.0×10^{-2} ($\Delta t^+ \approx 2.7 \times 10^{-2}$, 5.3×10^{-2}, and 1.1×10^{-1}) for the Mach 2.3 case on Grid 4. The turbulence statistics are seen to be independent of the time step for the range considered here.

B. Effect of Domain Width

Additional calculations were carried out for the turbulent boundary layer flow at $M = 2.3$, $\mathrm{Re}_{\theta i} = 2.0 \times 10^3$, using the resolution level of Grid 4, but varying the spanwise extent of the computational domain ($L_z/\delta_0 = 5$, 10, and 20). Sample density contours in the $x/\delta_0 = 100$ plane shown in Fig. 9 illustrate that the results are qualitatively the same for all three domain widths.

The quantitative effect on the numerical solution is shown in Fig. 10. The skin friction (Fig. 10a) and the mean velocity profiles (Fig. 10b) are indistinguishable on the three grids. Spanwise wavenumber spectra of mass flux (Fig. 10c) and wall pressure (Fig. 10d) are identical at high frequency, but increasing the domain width brings additional spectral content at low wavenumber (large spanwise scale). Such large-scale content is expected to play an important role in large-scale unsteadiness,[38] and merits additional study in that context.

C. Comparison to Experiment

Comparisons to experimental data are shown in Fig. 11. The data sets of Alving[71] ($M = 0$, $\mathrm{Re}_\theta = 5.0 \times 10^3$), Shutts et al.[61] ($M = 2.3$, $\mathrm{Re}_{\theta i} = 3.6 \times 10^3$), Éléna and Lacharme[72] ($M = 2.3$, $\mathrm{Re}_{\theta i} = 2.6 \times 10^3$), and Spina[64] and Konrad[73] ($M = 2.9$, $\mathrm{Re}_{\theta i} = 3.6 \times 10^4$) are compared to the large-eddy simulations ($M = 2.3$, $\mathrm{Re}_{\theta i} = 2.0 \times 10^3$ and $M = 2.9$, $\mathrm{Re}_{\theta i} = 2.5 \times 10^3$).

Mean velocity profiles are shown in van Driest[70] transformed inner and outer coordinates in Figs. 11a and 11b, respectively. The experimental data were obtained with either Pitot probes or single-component laser Doppler anemometry (LDA), and the measurement uncertainty is on the order of the symbol size used in the plots. As expected, the van Driest transform collapses the data for the different Mach numbers very effectively, and the primary differences are due to variation in Reynolds number.

In inner coordinates, the inner part of the profiles collapses, with differences in the wake region due to the differing Reynolds numbers. Of particular note is the agreement of the computations with the experimental data of Alving in the buffer region (Fig. 11a, $y^+ = 20$–40). The data of Éléna and Lacharme very nearly match the Reynolds number of the Mach 2.9 large-eddy simulations, and this is borne out in the close agreement between these data sets in inner coordinates for the wake region (Fig. 11a, $y^+ = 500$–1000).

In outer coordinates, the wake region collapses for all the profiles, and variation due to Reynolds number is displayed in the inner part of the profiles (Fig. 11b). Agreement between computation and experiment in the logarithmic region is evident in this plot.

Various components of the Reynolds stress tensor are shown in Figs. 11c–11f. The data of Alving and Konrad were obtained with hotwire probes, whereas the data of Éléna and Lacharme were obtained with laser Doppler anemometry. Error bars corresponding to the statistical uncertainty reported by Éléna and Lacharme are included on the plots. There is an additional bias error in two-component LDA data that causes the Reynolds stress measured in this manner to be systematically low.[72] The results are plotted in outer coordinates, and collapse of the data should be expected for the outer portion of the profiles (say $y/\delta > 0.2$).

For the streamwise component of the Reynolds normal stress ($\overline{\rho}\widetilde{u''^2}$, Fig. 11c), computation and experiment agree within the measurement uncertainty. The agreement is not as good for the transverse normal stress ($\overline{\rho}\widetilde{v''^2}$, Fig. 11d) or the spanwise normal stress ($\overline{\rho}\widetilde{w''^2}$, Fig. 11e). The computational results tend to be

somewhat higher than the values measure by Alving and by Éléna and Lacharme, and differ substantially from the crosswire measurements of Konrad. The quantities $\overline{v'^2}$ and $\overline{w'^2}$ are difficult to measure, and their proper scaling is matter of debate (see Smits and Dussauge,[3] pp. 238–239). In particular, their peak values may vary with Reynolds number.

The Reynolds shear stress $-\overline{\rho}\overline{u'v'}$ is shown in Fig. 11f. Good agreement is obtained between the computations and the incompressible flow measurements of Alving. Considering the large statistical uncertainty in the data of Éléna and Lacharme, and the tendency for the LDA data to be biased low, agreement for these data can also be considered reasonably good.

D. Turbulence Modeling

Several turbulence closure parameters[74] were evaluated using the results of the simulations. The results are shown in inner coordinates in Fig. 12 for the two Mach number cases.

Figure 12a shows profiles of the parameters predicted by the classical strong Reynolds analogy.[3,21,32] Neglecting total temperature fluctuations and assuming uniform mean total temperature, the classical strong Reynolds analogy predicts $\mathrm{Pr}_T = 1$, $R_{uv} = -R_{vT}$, and $R_{uT} = -1$. Here the turbulent Prandtl number is defined as:

$$\mathrm{Pr}_T = \frac{\overline{u'v'}}{\overline{v'T'}} \frac{\partial \overline{T}/\partial y}{\partial \overline{u}/\partial y} \tag{16}$$

and each of the correlations R has a form analogous to:

$$R_{uv} = \frac{\overline{u'v'}}{\left[\overline{u'^2}\ \overline{v'^2}\right]^{1/2}} \tag{17}$$

In the results of the large-eddy simulations, $0.7 \leq \mathrm{Pr}_T \leq 1.0$, $-0.8 \leq R_{uT} \leq -0.5$, and $R_{uv} \approx -R_{vT} \approx 0.4$, indicating reasonable agreement with the classical strong Reynolds analogy. Similar results were obtained by Pirozzoli and Bernardini[51] for simulations at $M_\infty = 2$ and $\mathrm{Re}_{\theta i} = 4 \times 10^3$.

The structure parameter, the ratio of Reynolds shear stress to turbulent kinetic energy, is an important closure parameter in turbulence modeling.[21,74] Figure 12b compares the structure parameter to the following closure model:[74]

$$\frac{\tau_{xy}^T}{\overline{\rho} k^T} = \frac{-2\ \overline{u'v'}}{\overline{u'^2} + \overline{v'^2} + \overline{w'^2}} = a_1 \left(1 - e^{-y^+/A^+}\right) \tag{18}$$

Here τ_{xy}^T is the Reynolds stress, k_T is the turbulent kinetic energy, $a_1 = 0.28$, and $A^+ = 26.0$. Relatively good agreement is obtained between the results of the present simulations, the prediction of the theory, and the results of other published simulations.[21]

Another closure model parameter, the ratio τ_{xy}^T/τ_{yy}^T, is presented in Fig. 12c. This ratio is compared to the theoretical relation:[74]

$$\frac{\tau_{xy}^T}{\tau_{yy}^T} = \frac{\overline{u'v'}}{\overline{v'^2}} = -\frac{C}{1 - e^{-y^+/A^+}} \tag{19}$$

where $C = 0.68$. Again, reasonable agreement is obtained between the results of the present simulations and the predictions of the theory.

Since the prediction of wall heat transfer rates is one of the primary motivations for numerical simulations of supersonic turbulent flow, accurate modeling of the turbulent energy flux is of strong interest. The leading terms in a Taylor series expansion[74,75] for the turbulent energy flux in the vicinity of the wall are as follows:

$$q_y^T = f_1 y^3 + f_2 y^4 \tag{20}$$

where $f_1 = 0$ for an adiabatic wall. The turbulence model of Bowersox[74] assumed $f_1 = 0$ in general. Figure 12d shows the near-wall behavior of the turbulent energy flux for the present simulations on logarithmic axes. A curve proportional to y^4 is shown for reference. The results show the fourth-power scaling with distance from the wall expected for the adiabatic case.

The adiabatic wall temperature for the Mach 2.3 flow is about $T_w = 323$ K; additional calculations were carried out for a slightly cold wall ($T_w = 303$ K) and a slightly hot wall ($T_w = 343$ K). These moderate changes in boundary conditions allowed wall temperature effects to be explored without significant changes in grid resolution requirements.

Figure 13 shows the effects of varying wall temperature on the flow. Mean temperature profiles for the three cases are shown in Fig. 13a. They illustrate the change in temperature gradient that occurs for the different wall boundary conditions. Figure 13b shows the turbulent energy flux. Bowersox's assumption[74] of $f_1 = 0$ is seen to hold well for all three cases; the near-wall turbulent energy flux follows $q_y^T \sim y^4$ quite closely.

E. Correlations

Time series of the fluctuations of mass flux generated by the simulations were saved in order to carry out a correlation analysis. The analysis is intended to be similar to that of the classic hotwire measurements of Kovasznay et al.[8] in a low-speed turbulent boundary layer and of Spina et al.[10,11,64] in a supersonic boundary layer.

Spatial correlations are shown in Fig. 14. (See Fig. 1 for plots of the instantaneous mass-flux in the same planes.) Figures 14a–b show correlations for the $x/\delta_0 = 100$ plane, corresponding to an end view with flow into the page. Plan views at $y/\delta = 0.5$ are shown in Figs. 14c–d; here the view is from above and flow is left to right. Finally, Figs. 14e–f show side views for the center of the domain ($z/\delta_0 = 2.5$), with flow left to right. In each case, the origin of the x and z axes has been shifted to the reference point for the correlations ($x/\delta_0 = 100$, $y = 0$, $z/\delta_0 = 2.5$), but the origin for the y-coordinate is kept at the wall for clarity.

The scale and orientation of the large-scale structures in the simulated boundary layer are similar to those observed in experiments.[8,10,11,16] The mass flux is well-correlated over a length scale on the order of the mean boundary layer thickness δ, and the correlation contours are roughly ellipsoidal. The characteristic length scales in the spanwise direction ($\sim 0.4\delta$) and wall-normal direction ($\sim 0.5\delta$) are somewhat smaller than that in the streamwise direction ($\sim 0.8\delta$). Contours in the x-y-plane are oriented at an angle of about 45 deg from the wall. These results are generally consistent with the appearance of the instantaneous mass-flux field seen in Fig. 1. Moderate differences are seen between the Mach 2.3 and 2.9 cases, and further exploration of compressibility effects on the large-scale structures is warranted.

Another flow variable that has been extensively studied experimentally is the fluctuating wall pressure.[14] Time series of the computed wall pressure fluctuations were saved for correlation analysis. Spatial correlations of the fluctuating wall pressure are shown in Fig. 15. The correlation contours are roughly circular, with a slight elongation in the spanwise direction. The characteristic diameter is about 0.3δ for the $R = 0.3$ correlation contour. These results are qualitatively consistent with the features of the instantaneous wall pressure field shown in Fig. 2a. The results are also qualitatively consistent with the experimental results of Spina,[64] but the spatial scales in the present simulations are about a factor of three smaller than those observed experimentally.

Another quantity of interest is the wall shear stress. Spatial correlations of fluctuations in the magnitude of the wall shear stress are shown in Fig. 16. Note how the correlation contours are elongated in the streamwise direction ($\sim 0.6\delta$ streamwise scale vs. $\sim 0.1\delta$ spanwise scale), consistent with the long streaks seen in the instantaneous skin friction field (Fig. 2b).

F. Convection Velocity

Convection velocities derived from space-time correlations of the fluctuating wall pressure are shown in Fig. 17a. The broadband convection velocity is seen to be $U_c/U_e \approx 0.60$, in agreement with experimental results.[64] Broad-band convection velocities, derived from space-time cross-correlations of the mass flux fluctuations, are shown in Fig. 17b. The convection velocity for both Mach numbers closely follows the mean velocity profile. Based on hotwire measurements in a Mach 2.9 turbulent boundary layer, Spina et al.[11] reported $U_c/U_e = 0.9 \pm 0.1$ across the outer part of the boundary layer. (The experimental uncertainty was primarily due to temporal discretization, the sampling rate of the analog-to-digital converter.) Note that, in the present work, the broadband convection velocity extracted from the wall pressure fluctuation data is consistent with the convection velocity in the near-wall region ($y/\delta < 0.2$) determined from the mass flux fluctuations.

IV. Conclusions

High-fidelity, implicit large-eddy simulations were performed to examine large-scale structures in compressible, turbulent flow. Calculations were carried out for turbulent boundary layers at Mach 2.3 and 2.9,

with momentum thickness Reynolds numbers based on wall viscosity of 2.0×10^3 and 2.5×10^3, respectively.

Four computational meshes were considered for each Mach number case. The coarsest mesh met the recommended resolution for implicit large-eddy simulation, whereas the finest mesh corresponded to a level of resolution commonly called direct numerical simulation. The computational results were compared at a station where the skin friction coefficient and Reynolds number agreed within 10% for all cases, so that the flow state could be considered the same for each grid. Comparing statistical results between the grids, the nondimensionalized mean velocity and Reynolds stress was found to agree within 10% for Grids 2–4. The calculations carried out on Grid 1 did not appear to produce a fully developed turbulent boundary layer flow. A time resolution study indicated that a time step of $\Delta t^+ \approx 0.05$ is well resolved.

Despite the convergence of statistics like the mean velocity and Reynolds stress, differences were observed on all grids for frequency and wavenumber spectra. Comparing all cases for a fixed flow state, increasing the mesh resolution led to additional spectral content, and to an extension of the inertial subrange to smaller scales. These results suggest that the simulations are better described as implicit large-eddy simulations than direct numerical simulations. To achieve strict direct numerical simulation at the wall, the resolution there would have to be increased by a factor of 25–35 from the present grids.

Nonetheless, good agreement was obtained between computation and experiment for profiles of mean velocity and several components of the Reynolds stress. Further, convection velocity, scale, and orientation of large-scale structures extracted from space-time correlations also were in good agreement with experiment.

Convergence of the turbulence statistics permits the examination of a number of parameters used in turbulence modeling. In particular, the strong Reynolds analogy, the ratios of Reynolds stresses, and the near-wall behavior of the turbulent energy transport were evaluated for the two flows. Further, the effects of wall temperature on the turbulent heat flux were examined. The results support assumptions made in turbulence modeling for compressible flow.

Acknowledgments

This project was sponsored in part by the Air Force Office of Scientific Research, under tasks monitored by F. Fahroo and J. Schmisseur. It was also supported by grants of High Performance Computing time from the Department of Defense Supercomputing Resource Centers at the Air Force Research Laboratory, the Army Research Laboratory, and the Army Engineer Research and Development Center. Additional computer hours were provided under a Department of Defense, High-Performance Computation Modernization Program Frontier Project (R. Gosse, Principal Investigator).

References

[1]Robinson, S. K., "Coherent Motions in the Turbulent Boundary Layer," *Annual Review of Fluid Mechanics*, Vol. 23, 1991, pp. 601–639.

[2]Spina, E. F., Smits, A. J., and Robinson, S. K., "The Physics of Supersonic Turbulent Boundary Layers," *Annual Review of Fluid Mechanics*, Vol. 26, 1994, pp. 287–319.

[3]Smits, A. J. and Dussauge, J.-P., *Turbulent Shear Layers in Supersonic Flow*, Springer, New York, 2nd ed., 2006.

[4]Corrsin, S. and Kistler, A. K., "Free-Stream Boundaries of Turbulent Flow," Technical Report NACA-TR-1244, National Advisory Committee for Aeronautics, January 1955.

[5]Hussain, A. K. M. F., "Coherent Structures – Reality and Myth," *Physics of Fluids*, Vol. 26, No. 10, 1983, pp. 2816–2850.

[6]Kline, S. J., Reynolds, W. C., Schraub, F. A., and Runstadler, P. W., "The Structure of Turbulent Boundary Layers," *Journal of Fluid Mechanics*, Vol. 30, 1967, pp. 741–773.

[7]Offen, G. R. and Kline, S. J., "A Proposed Model of the Bursting Process in Turbulent Boundary Layers," *Journal of Fluid Mechanics*, Vol. 70, 1975, pp. 209–228.

[8]Kovasznay, L. S. G., Kibens, V., and Blackwelder, R. F., "Large-Scale Motion in the Intermittent Region of a Turbulent Boundary Layer," *Journal of Fluid Mechanics*, Vol. 41, 1970, pp. 283–325.

[9]Owen, F. K. and Horstman, C. C., "On The Structure of Hypersonic Turbulent Boundary Layers," *Journal of Fluid Mechanics*, Vol. 53, 1972, pp. 611–636.

[10]Spina, E. F. and Smits, A. J., "Organized Structures in a Compressible, Turbulent Boundary Layer," *Journal of Fluid Mechanics*, Vol. 182, 1987, pp. 85–109.

[11]Spina, E. F., Donovan, J. F., and Smits, A. J., "On the Structure of High-Reynolds-Number Supersonic Turbulent Boundary Layers," *Journal of Fluid Mechanics*, Vol. 222, 1991, pp. 293–327.

[12]Smith, D. R. and Smits, A. J., "Simultaneous Measurement of Velocity and Temperature Fluctuations in the Boundary Layer of a Supersonic Flow," *Experimental Thermal and Fluid Science*, Vol. 7, No. 3, 1993, pp. 221–229.

[13]Tichenor, N. R., Humble, R. A., and Bowersox, R. D. W., "Response pf a Hypersonic Turbulent Boundary Layer to Favorable Pressure Gradients," *Journal of Fluid Mechanics*, Vol. 722, 2013, pp. 187–213.

[14]Beresh, S. J., Henfling, J. F., Spillers, R. W., and Pruett, B. O. M., "Fluctuating Wall Pressures Measured Beneath a Supersonic Turbulent Boundary Layer," *Physics of Fluids*, Vol. 23, 2011, pp. 075110.

[15]Smith, M. W. and Smits, A. J., "Visualization of the Structure of Supersonic Turbulent Boundary Layers," *Experiments in Fluids*, Vol. 18, 1995, pp. 288–302.

[16]Poggie, J., Erbland, P. J., Smits, A. J., and Miles, R. B., "Quantitative Visualization of Compressible Turbulent Shear Flows using Condensate-Enhanced Rayleigh Scattering," *Experiments in Fluids*, Vol. 37, 2004, pp. 438–454.

[17]Rai, M. M., Gatski, T. B., and Erlebacher, G., "Direct Simulation of Spatially Evolving Compressible Turbulent Boundary Layers," AIAA Paper 95-583.

[18]Guarini, S. E., Moser, R. D., Shariff, K., and Wray, A., "Direct Numerical Simulation of a Supersonic Turbulent Boundary Layer at Mach 2.25," *Journal of Fluid Mechanics*, Vol. 414, 2000, pp. 1–33.

[19]Maeder, T., Adams, N. A., and Kleiser, L., "Direct Simulation of Supersonic Turbulent Boundary Layers by an Extended Temporal Approach," *Journal of Fluid Mechanics*, Vol. 429, 2001, pp. 187–216.

[20]Stolz, S. and Adams, N. A., "Large-eddy Simulation of High-Reynolds-Number Supersonic Boundary Layers Using the Approximate Deconvolution Model and a Rescaling and Recycling Technique," *Physics of Fluids*, Vol. 15, No. 8, 2003, pp. 2398–2412.

[21]Pirozzoli, S., Grasso, F., and Gatski, T. B., "Direct Numerical Simulation and Analysis of a Spatially Evolving Supersonic Turbulent Boundary Layer at $M = 2.25$," *Physics of Fluids*, Vol. 16, No. 3, 2004, pp. 530–545.

[22]Rizzetta, D. P. and Visbal, M. R., "Large-Eddy Simulation of Supersonic Boundary-Layer Flow by a High-Order Method," *International Journal of Computational Fluid Dynamics*, Vol. 18, No. 1, 2004, pp. 15–27.

[23]Xu, S. and Martin, M. P., "Assessment of Inflow Boundary Conditions for Compressible Turbulent Boundary Layers," *Physics of Fluids*, Vol. 16, No. 7, 2004, pp. 2623–2639.

[24]Martín, M. P., "Direct Numerical Simulation of Hypersonic Turbulent Boundary Layers. Part 1. Initialization and Comparison with Experiments," *Journal of Fluid Mechanics*, Vol. 570, 2007, pp. 347–364.

[25]Ringuette, M. J., Wu, M., and Martín, M. P., "Coherent Structures in Direct Numerical Simulation of Turbulent Boundary Layers at Mach 3," *Journal of Fluid Mechanics*, Vol. 594, 2008, pp. 59–69.

[26]Duan, L., Beekman, I., and Martín, M. P., "Direct Numerical Simulation of Hypersonic Turbulent Boundary Layers. Part 2. Effect of Wall Temperature," *Journal of Fluid Mechanics*, Vol. 655, 2010, pp. 419–445.

[27]Duan, L., Beekman, I., and Martín, M. P., "Direct Numerical Simulation of Hypersonic Turbulent Boundary Layers. Part 3. Effect of Mach Number," *Journal of Fluid Mechanics*, Vol. 672, 2011, pp. 245–267.

[28]Lagha, M., Kim, J., Eldredge, J. D., and Zhong, X., "A Numerical Study of Compressible Turbulent Boundary Layers," *Physics of Fluids*, Vol. 23, 2011, pp. 015106.

[29]Marco, A. D., Camussi, R., Bernardini, M., and Pirozzoli, S., "Wall Pressure Coherence in Supersonic Turbulent Boundary Layers," *Journal of Fluid Mechanics*, Vol. 732, 2013, pp. 445–456.

[30]Pirozzoli, S. and Bernardini, M., "Probing High-Reynolds Number Effects in Numerical Boundary Layers," *Physics of Fluids*, Vol. 25, 2013, pp. 021704.

[31]Bradshaw, P., "Compressible Turbulent Shear Layers," *Annual Review of Fluid Mechanics*, Vol. 9, 1977, pp. 33–52.

[32]Morkovin, M. V., "Effects of Compressibility on Turbulent Flows," *Méchanique de la Turbulence*, edited by A. Favre, CNRS, Paris, France, 1962, pp. 367–380.

[33]Smits, A. J., Spina, E. F., Alving, A. E., Smith, R. W., Fernando, E. M., and Donovan, J. F., "A Comparison of the Turbulence Structure of Subsonic and Supersonic Boundary Layers," *Physics of Fluids*, Vol. 1, No. 11, 1989, pp. 1865–1875.

[34]Poggie, J. and Smits, A. J., "Shock Unsteadiness in a Reattaching Shear Layer," *Journal of Fluid Mechanics*, Vol. 429, 2001, pp. 155–185.

[35]Poggie, J. and Smits, A. J., "Experimental Evidence for Plotkin Model of Shock Unsteadiness in Separated Flow," *Physics of Fluids*, Vol. 17, 2005, pp. 018107.

[36]Ganapathisubramani, B., Clemens, N. T., and Dolling, D. S., "Effects of Upstream Boundary Layer on the Unsteadiness of Shock-Induced Separation," *Journal of Fluid Mechanics*, Vol. 585, 2007, pp. 369–394.

[37]Touber, E. and Sandham, N. D., "Low-Order Stochastic Modelling of Low-Frequency Motions in Reflected Shock-Wave / Boundary-Layer Interactions," *Journal of Fluid Mechanics*, Vol. 671, 2011, pp. 417–465.

[38]Poggie, J., Bisek, N. J., Kimmel, R. L., and Stanfield, S. A., "Spectral Characteristics of Separation Shock Unsteadiness," *AIAA Journal*, 2014, Accepted for publication. DOI: 10.2514/1.J053029.

[39]Plotkin, K. J., "Shock Wave Oscillation Driven by Turbulent Boundary-Layer Fluctuations," *AIAA Journal*, Vol. 13, No. 8, 1975, pp. 1036–1040.

[40]Thurow, B. S., Jiang, N., Kim, J.-H., Lempert, W., and Samimy, M., "Issues with Measurements of the Convection Velocity of Large-Scale Structures in the Compressible Shear Layer of a Free Jet," *Physics of Fluids*, Vol. 20, 2008, pp. 066101.

[41]Poggie, J., "Discharge Modeling for Flow Control Applications," AIAA Paper 2008-1357.

[42]Poggie, J., "Control of Shock-Wave / Boundary-Layer Interaction Using Volumetric Energy Deposition," AIAA Paper 2008-1090.

[43]Poggie, J., "High-Order Compact Difference Methods for Glow Discharge Modeling," AIAA Paper 2009-1047.

[44]Poggie, J., "Compact Difference Methods for Discharge Modeling in Aerodynamics," AIAA Paper 2009-3908.

[45]Poggie, J., "Role of Charged Particle Inertia in Pulsed Electrical Discharges," AIAA Paper 2010-1195.

[46]Poggie, J., "High-Order Numerical Methods for Electrical Discharge Modeling," AIAA Paper 2010-4632.

[47]White, F. M., *Viscous Fluid Flow*, McGraw-Hill, New York, 2nd ed., 1991.

[48]Visbal, M. R. and Gaitonde, D. V., "On the Use of Higher-Order Finite-Difference Schemes on Curvilinear and Deforming Meshes," *Journal of Computational Physics*, Vol. 181, 2002, pp. 155–185.

[49]Visbal, M. R. and Gaitonde, D. V., "Shock Capturing Using Compact-Differencing-Based Methods," AIAA Paper 2005-1265.

[50]Poggie, J., Bisek, N. J., Leger, T., and Tang, R., "Implicit Large-Eddy Simulation of a Supersonic Turbulent Boundary Layer: Code Comparison," AIAA Paper 2014-0423, 2014.

[51]Pirozzoli, S., "Numerical Methods for High-Speed Flows," *Annual Review of Fluid Mechanics*, Vol. 43, 2011, pp. 163–194.

[52]Beam, R. and Warming, R., "An Implicit Factored Scheme for the Compressible Navier-Stokes Equations," *AIAA Journal*, Vol. 16, No. 4, 1978, pp. 393–402.

[53]Pulliam, T. H., "Implicit Finite-Difference Simulations of Three-Dimensional Compressible Flow," *AIAA Journal*, Vol. 18, No. 2, 1980, pp. 159–167.

[54]Hoffmann, K. A. and Chiang, S. T., *Computational Fluid Dynamics*, Engineering Educational System, Wichita KS, 4th ed., 2000.

[55]Pulliam, T. H. and Chaussee, D. S., "A Diagonal Form of an Implicit Approximate-Factorization Algorithm," *Journal of Computational Physics*, Vol. 39, 1981, pp. 347–363.

[56]Thomas, P. D. and Lombard, C. K., "Geometric Conservation Law and Its Application to Flow Computations on Moving Grids," *AIAA Journal*, Vol. 17, No. 10, 1979, pp. 1030–1037.

[57]Gaitonde, D. V. and Visbal, M. R., "High-Order Schemes for Navier-Stokes Equations: Algorithm Implementation into FDL3DI," Technical Report AFRL-VA-WP-TR-1998-3060, Air Force Research Laboratory, Wright-Patterson Air Force Base, Ohio, August 1998.

[58]Chandra, R., Dagum, L., Kohr, D., Maydan, D., McDonald, J., and Menon, R., *Parallel Programming in OpenMP*, Academic Press, San Diego, 2001.

[59]Gropp, W., Lusk, E., and Skjellum, A., *Using MPI: Portable Parallel Programming with the Message-Passing Interface*, The MIT Press, Cambridge, MA, 2nd ed., 1999.

[60]Bisek, N. J., Rizzetta, D. P., and Poggie, J., "Plasma Control of a Turbulent Shock Boundary-Layer Interaction," *AIAA Journal*, Vol. 51, No. 8, 2013, pp. 1789–1804.

[61]Fernholz, H. H. and Finley, P. J., "A Critical Compilation of Compressible Turbulent Boundary Layer Data," AFARDograph 223, NATO Advisory Group for Aerospace Research and Development, Neuilly-sur-Seine, France, 1977.

[62]Bookey, P., Wyckham, C., Smits, A., and Martin, M. P., "New Experimental Data of STBLI at DNS/LES Accessible Reynolds Numbers," AIAA Paper 2005-309.

[63]Wu, M. and Martin, M. P., "Direct Numerical Simulation of Supersonic Turbulent Boundary Layer over a Compression Ramp," *AIAA Journal*, Vol. 45, No. 4, 2007, pp. 879–889.

[64]Spina, E. F., *Organized Structures in a Supersonic Turbulent Boundary Layer*, Ph.D. Dissertation, Princeton University, Princeton NJ, October 1988.

[65]Mullenix, N. J., Gaitonde, D. V., and Visbal, M. R., "Spatially Developing Supersonic Turbulent Boundary Layer with a Body-Force Based Method," *AIAA Journal*, Vol. 51, No. 8, 2013, pp. 1805–1819.

[66]Georgiadis, N. J., Rizzetta, D. P., and Fureby, C., "Large-Eddy Simulation: Current Capabilities, Recommended Practices, and Future Research," *AIAA Journal*, Vol. 48, No. 8, 2010, pp. 1772–1784.

[67]Choi, H. and Moin, P., "Grid-Point Requirements for Large Eddy Simulation: Chapman's Estimates Revisited," *Physics of Fluids*, Vol. 24, 2012, pp. 011702.

[68]Pirozzoli, S. and Bernardini, M., "Turbulence in Supersonic Boundary Layers at Moderate Reynolds Number," *Journal of Fluid Mechanics*, Vol. 688, 2011, pp. 120–168.

[69]Tennekes, H. and Lumley, J. L., *A First Course in Turbulence*, The MIT Press, Cambridge MA, 1972.

[70]van Driest, E. R., "On the Turbulent Flow Near a Wall," *Journal of the Aeronautical Sciences*, Vol. 23, 1956, pp. 1007–1011.

[71]Alving, A. E., *Boundary Layer Relaxation from Convex Curvature*, Ph.D. dissertation, Princeton University, Princeton NJ, 1988.

[72]Éléna, M. and Lacharme, J. P., "Experimental Study of a Supersonic Turbulent Boundary Layer Using a Laser Doppler Anemometer," *Journal Mécanique Théorique et Appliquée*, Vol. 7, 1988, pp. 175–190.

[73]Konrad, W., *A Three-Dimensional Supersonic Turbulent Boundary Layer Generated by an Isentropic Compression*, Ph.D. Dissertation, Princeton University, Princeton NJ, 1993.

[74]Bowersox, R. D., "Extension of Equilibrium Turbulent Heat Flux Models to High-Speed Shear Flows," *Journal of Fluid Mechanics*, Vol. 633, 2009, pp. 61–70.

[75]Abe, K. and Suga, K., "Towards the Development of a Reynolds-Averaged Algebraic Turbulent Scalar-Flux Model," *International Journal of Heat and Fluid Flow*, Vol. 22, 2001, pp. 19–29.

Parameter	Value
δ_0	0.610 mm
U_∞	588 m/s
p_∞	23.8 kPa
T_∞	170 K
T_w	323 K
M	2.25
$U_\infty \delta_0 / \nu_\infty$	1.5×10^4

Table 1. Flow conditions for Mach 2.3 turbulent boundary.

Parameter	Value
δ_0	5.38 mm
U_∞	605 m/s
p_∞	2.30 kPa
T_∞	108 K
T_w	270 K
M	2.90
$U_\infty \delta_0 / \nu_\infty$	3.2×10^4

Table 2. Flow conditions for Mach 2.9 turbulent boundary.

Quantity	Grid 1	Grid 2	Grid 3	Grid 4	Grid 5	Grid 6
N_x	526	1026	2026	4026	4026	4026
N_y	151	276	526	276	276	276
N_z	130	255	505	255	505	1005
N	1.0×10^7	7.2×10^7	5.4×10^8	2.8×10^8	5.6×10^8	1.1×10^9
L_x/δ_0	100	100	100	100	100	100
L_y/δ_0	5	5	5	5	5	5
L_z/δ_0	5	5	5	5	10	20
$\Delta x/\delta_0$	2.0×10^{-1}	1.0×10^{-1}	5.0×10^{-2}	2.5×10^{-2}	2.5×10^{-2}	2.5×10^{-2}
$\Delta y_w/\delta_0$	4.0×10^{-3}	2.0×10^{-3}	1.0×10^{-3}	2.0×10^{-3}	2.0×10^{-3}	2.0×10^{-3}
$\Delta z/\delta_0$	4.0×10^{-2}	2.0×10^{-2}	1.0×10^{-2}	2.0×10^{-2}	2.0×10^{-2}	2.0×10^{-2}
Δx^+	45	23	11	5.6	5.6	5.6
Δy_w^+	0.89	0.45	0.23	0.45	0.45	0.45
Δy_e^+	19	8.9	4.3	8.6	8.6	8.6
Δz^+	8.9	4.5	2.3	4.5	4.5	4.5
$U_\infty \Delta t/\delta_0$	5.0×10^{-3}	5.0×10^{-3}	5.0×10^{-3}	5.0×10^{-3}	5.0×10^{-3}	5.0×10^{-3}
Δt^+	5.3×10^{-2}	5.5×10^{-2}	5.4×10^{-2}	5.3×10^{-2}	5.3×10^{-2}	5.3×10^{-2}
δ^+	660	580	560	570	570	570
Re_θ	3.0×10^3	3.3×10^3	3.3×10^3	3.4×10^3	3.4×10^3	3.4×10^3
$\mathrm{Re}_{\theta i}$	1.8×10^3	1.9×10^3	1.9×10^3	2.0×10^3	2.0×10^3	2.0×10^3

Table 3. Mach 2.3 turbulent boundary layer: properties of the computational mesh, nondimensionalized using conditions at the reference station $x/\delta_0 = 100$.

Quantity	Grid 1	Grid 2	Grid 3	Grid 4
N_x	526	1026	2026	4026
N_y	151	276	526	276
N_z	130	255	505	255
N	1.0×10^7	7.2×10^7	5.4×10^8	2.8×10^8
L_x/δ_0	100	100	100	100
L_y/δ_0	6	6	6	6
L_z/δ_0	5	5	5	5
$\Delta x/\delta_0$	2.0×10^{-1}	1.0×10^{-1}	5.0×10^{-2}	2.5×10^{-2}
$\Delta y_w/\delta_0$	3.3×10^{-3}	1.7×10^{-3}	8.3×10^{-4}	1.7×10^{-3}
$\Delta z/\delta_0$	4.0×10^{-2}	2.0×10^{-2}	1.0×10^{-2}	2.0×10^{-2}
Δx^+	53	27	14	6.6
Δy_w^+	0.88	0.45	0.23	0.45
Δy_e^+	27	12	5.4	11
Δz^+	11	5.3	2.7	5.3
$U_\infty \Delta t/\delta_0$	5.0×10^{-3}	5.0×10^{-3}	5.0×10^{-3}	5.0×10^{-3}
Δt^+	6.3×10^{-2}	6.7×10^{-2}	6.6×10^{-2}	6.6×10^{-2}
δ^+	760	690	630	630
Re_θ	5.7×10^3	5.8×10^3	5.7×10^3	5.7×10^3
$\mathrm{Re}_{\theta i}$	2.5×10^3	2.6×10^3	2.5×10^3	2.5×10^3

Table 4. Mach 2.9 turbulent boundary layer: properties of the computational mesh, nondimensionalized using conditions at the reference station $x/\delta_0 = 100$.

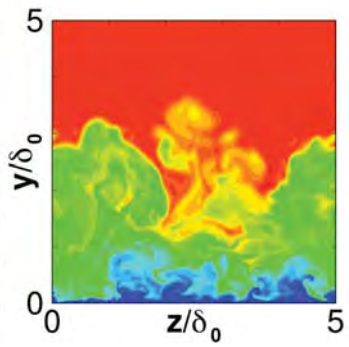

(a) End view: $x/\delta_0 = 100.0$ plane.

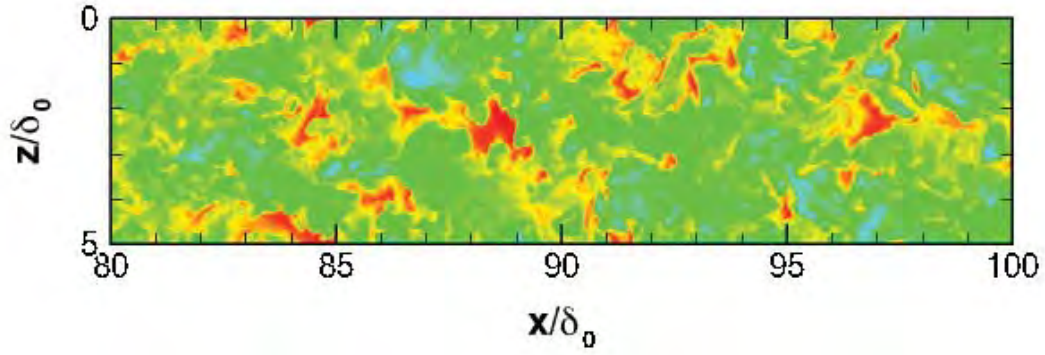

(b) Plan view: $y/\delta = 0.5$ plane.

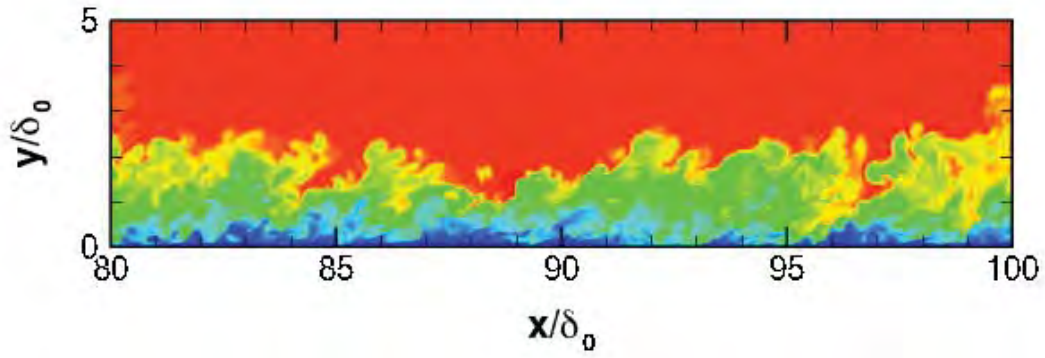

(c) Side view: $z/\delta_0 = 2.5$ plane.

Figure 1. Turbulent boundary layer at $M = 2.3$: contour plots of the instantaneous density (Grid 4). Contour range: $0.6 \leq \rho/\rho_\infty \leq 1.02$.

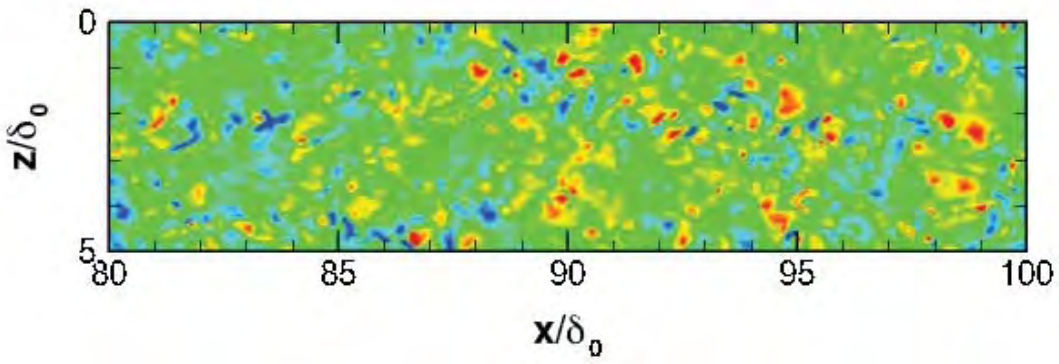

(a) Pressure, $y = 0$. Contour range: $0.134 \leq p/(\rho_\infty U_\infty^2) \leq 0.152$.

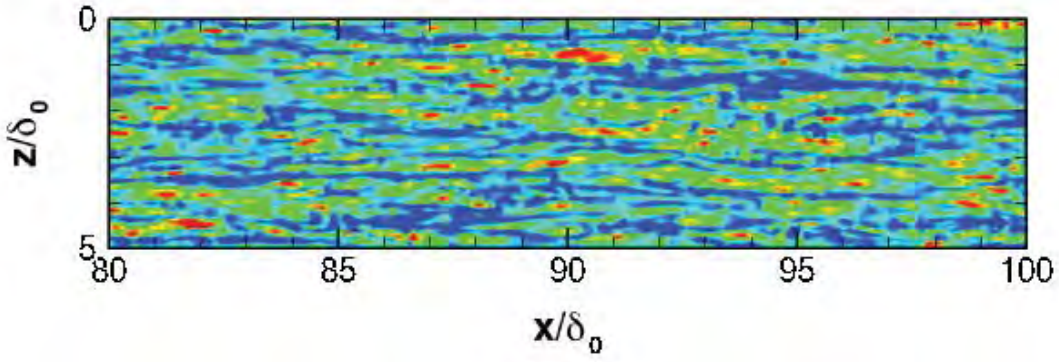

(b) Shear stress, $y = 0$. Contour range: $10 \leq \tau_w \, \delta_0/(\mu_\infty U_\infty) \leq 40$.

Figure 2. Turbulent boundary layer at $M = 2.3$: instantaneous contours of flow properties at the wall (Grid 4).

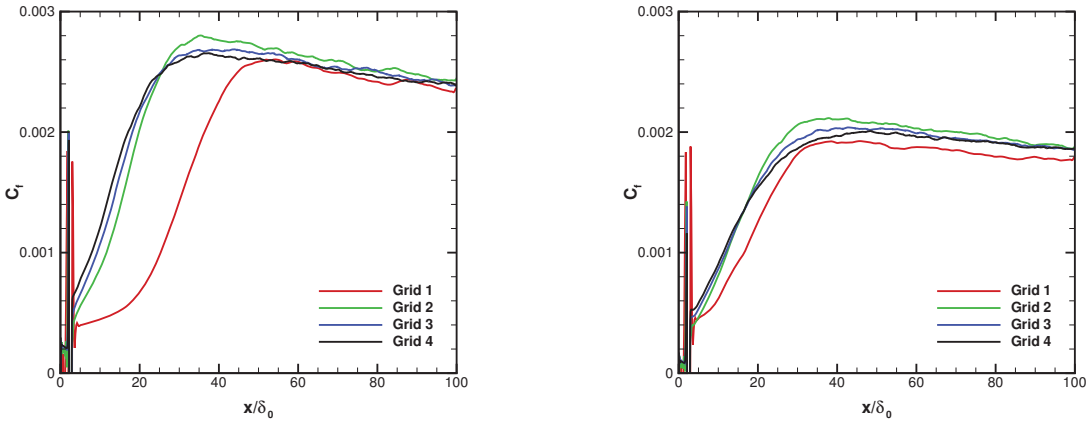

(a) $M = 2.3$. (b) $M = 2.9$.

Figure 3. Skin friction profiles, averaged over time and the spanwise coordinate.

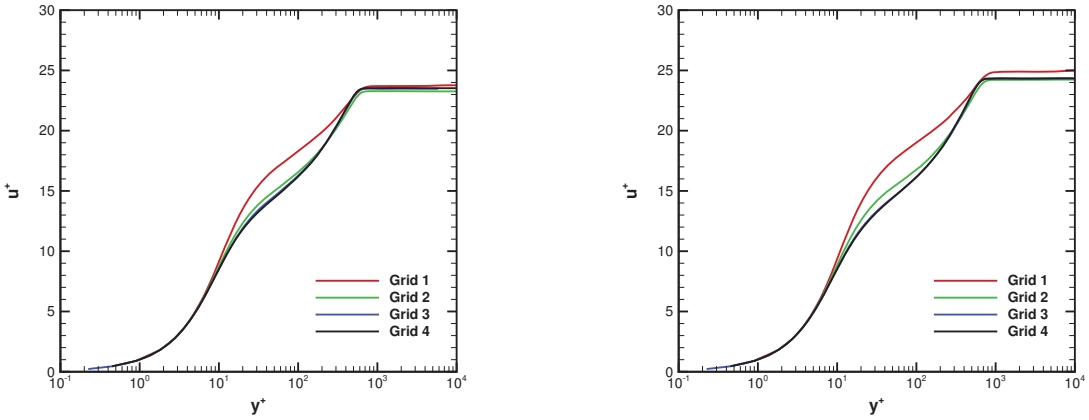

(a) $M = 2.3$, $\mathrm{Re}_{\theta i} = 2.0 \times 10^3$. (b) $M = 2.9$, $\mathrm{Re}_{\theta i} = 2.5 \times 10^3$.

Figure 4. Profiles of streamwise velocity, averaged over time and the spanwise coordinate, presented in van Driest transformed inner coordinates ($x/\delta_0 = 100$).

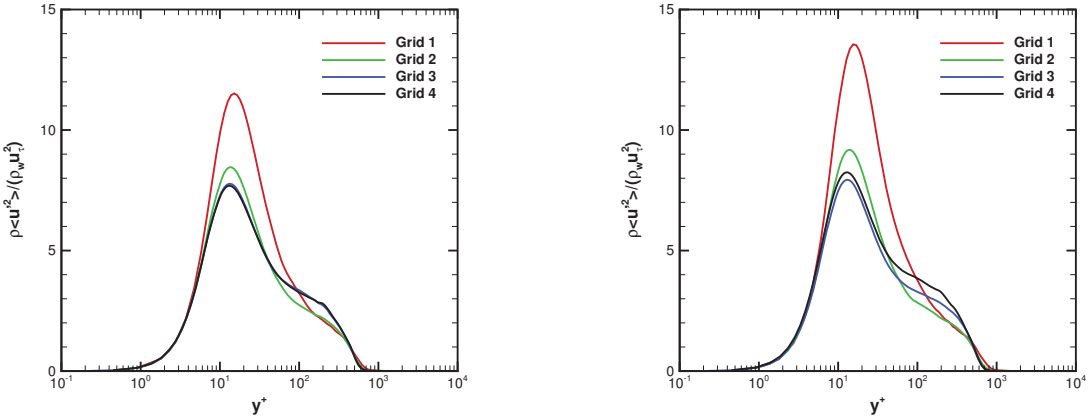

(a) $M = 2.3$, $\mathrm{Re}_{\theta i} = 2.0 \times 10^3$.

(b) $M = 2.9$, $\mathrm{Re}_{\theta i} = 2.5 \times 10^3$.

Figure 5. Profiles of Reynolds stress component $\overline{\rho}\,\widetilde{u'^2}/(\rho_w u_\tau^2)$ in inner coordinates ($x/\delta_0 = 100$).

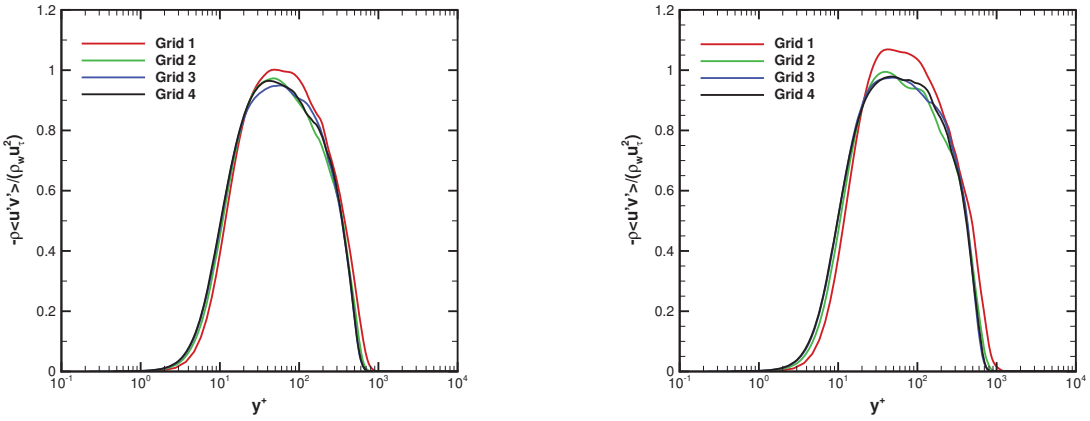

(a) $M = 2.3$, $\mathrm{Re}_{\theta i} = 2.0 \times 10^3$.

(b) $M = 2.9$, $\mathrm{Re}_{\theta i} = 2.5 \times 10^3$.

Figure 6. Profiles of Reynolds stress component $-\overline{\rho}\,\widetilde{u'v'}/(\rho_w u_\tau^2)$ in inner coordinates ($x/\delta_0 = 100$).

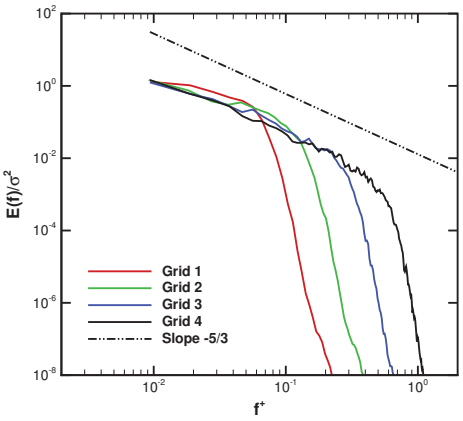

(a) Frequency spectrum, $M = 2.3$, $\mathrm{Re}_{\theta i} = 2.0 \times 10^3$.

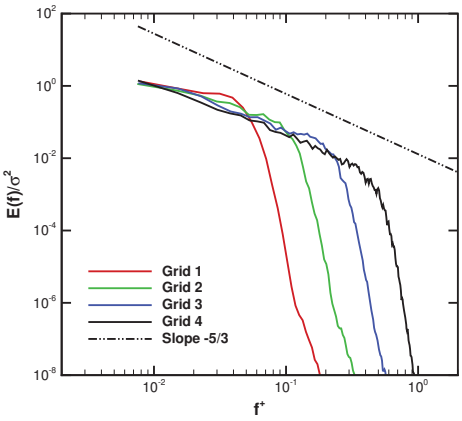

(b) Frequency spectrum, $M = 2.9$, $\mathrm{Re}_{\theta i} = 2.5 \times 10^3$.

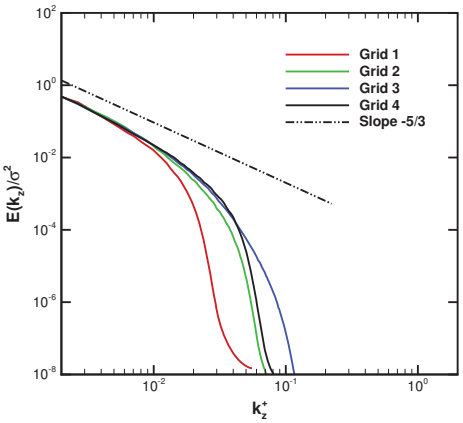

(c) Wavenumber spectrum, $M = 2.3$, $\mathrm{Re}_{\theta i} = 2.0 \times 10^3$.

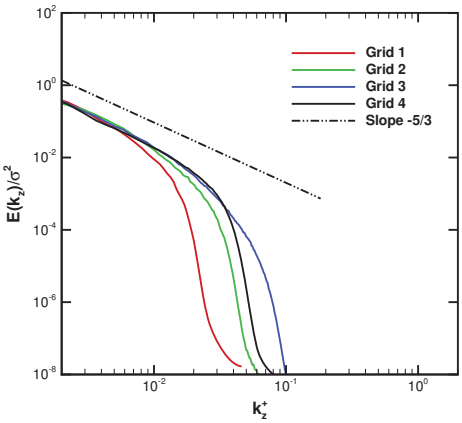

(d) Wavenumber spectrum, $M = 2.9$, $\mathrm{Re}_{\theta i} = 2.5 \times 10^3$.

Figure 7. Frequency and wavenumber spectra of mass flux fluctuations $(\rho u)'$ at $x/\delta_0 = 100$ and $y/\delta = 0.5$.

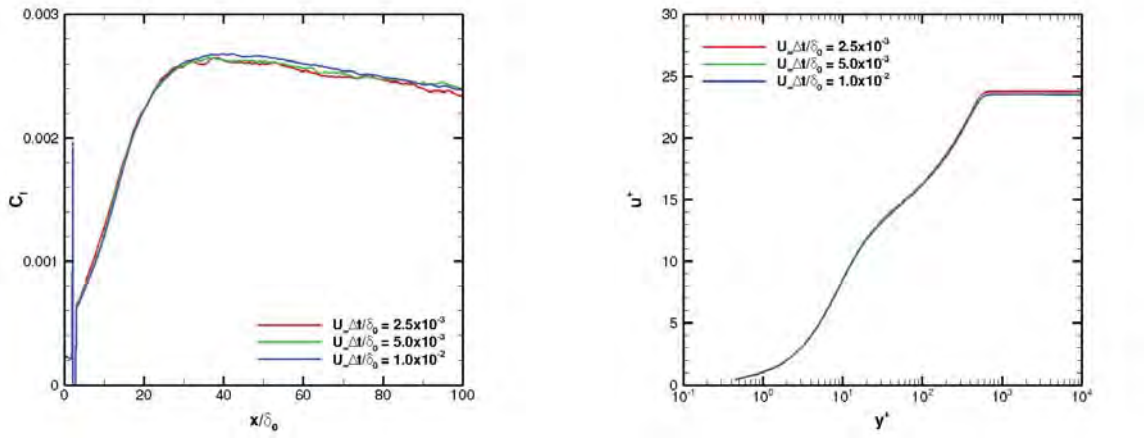

(a) Skin friction.

(b) Velocity profiles at $x/\delta_0 = 100$.

Figure 8. Effect of temporal resolution on turbulent boundary layer flow at $M = 2.3$, $\mathrm{Re}_{\theta i} = 2.0 \times 10^3$, Grid 4.

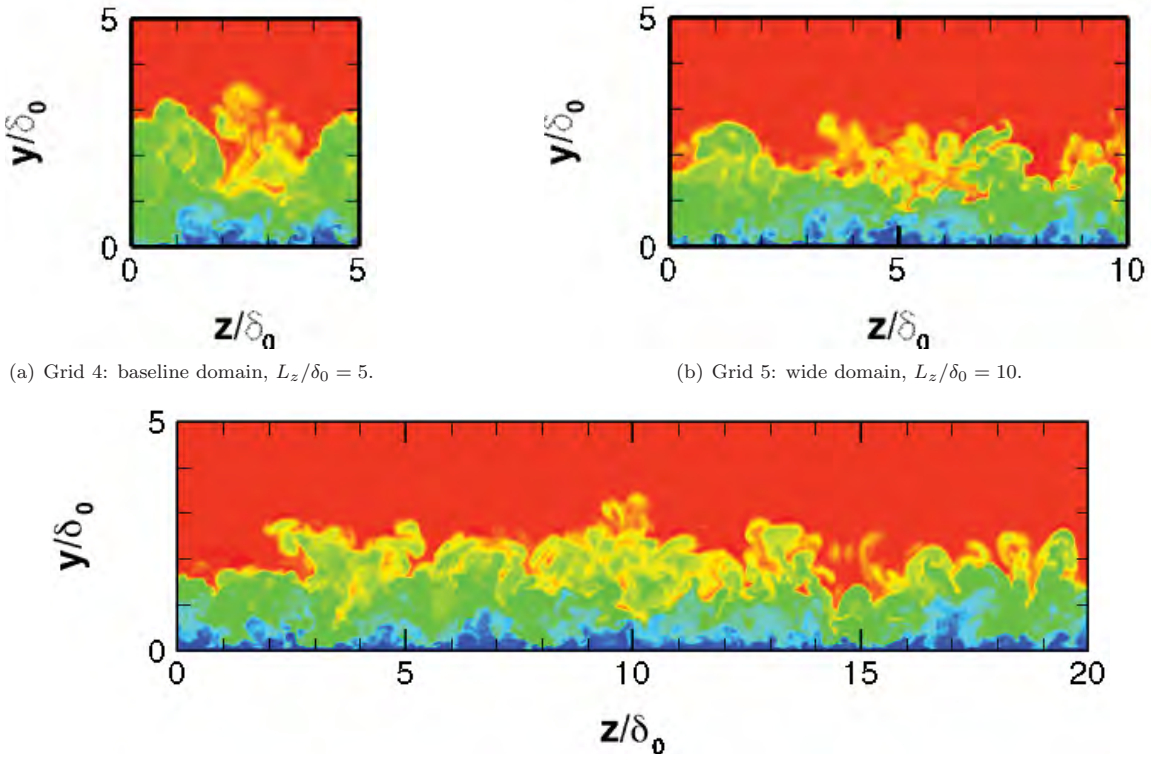

(a) Grid 4: baseline domain, $L_z/\delta_0 = 5$.

(b) Grid 5: wide domain, $L_z/\delta_0 = 10$.

(c) Grid 6: very wide domain, $L_z/\delta_0 = 20$.

Figure 9. Sample density contours in the $x/\delta_0 = 100$ plane (end view) illustrating the effect of domain width on turbulent boundary layer flow at $M = 2.3$, $\mathrm{Re}_{\theta i} = 2.0 \times 10^3$. Contour range: $0.6 \leq \rho/\rho_\infty \leq 1.02$.

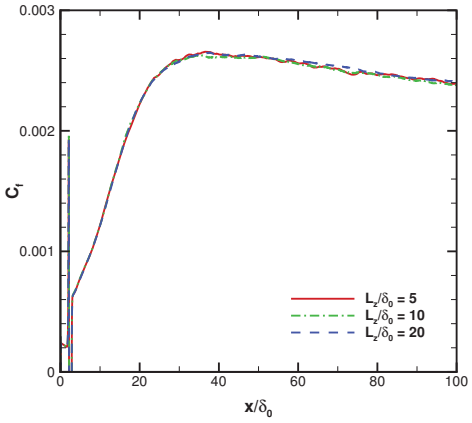

(a) Skin friction.

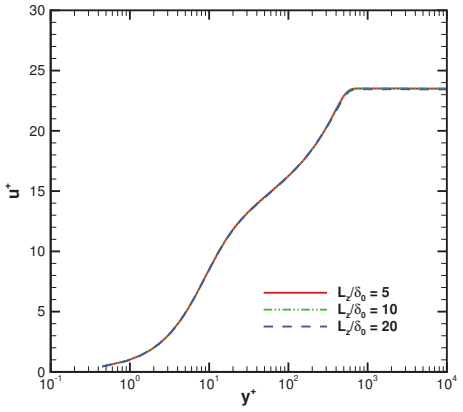

(b) Velocity profiles at $x/\delta_0 = 100$.

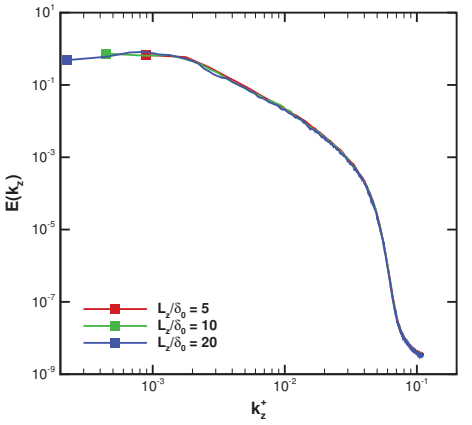

(c) Wavenumber spectra of mass flux at $x/\delta_0 = 100$, $y/\delta = 0.5$.

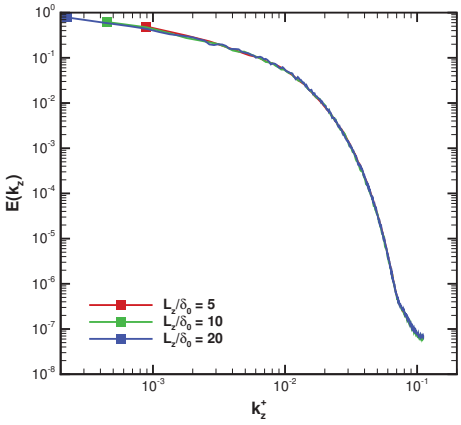

(d) Wavenumber spectra of wall pressure at $x/\delta_0 = 100$.

Figure 10. Effect of domain width on turbulent boundary layer flow at $M = 2.3$, $\mathrm{Re}_{\theta i} = 2.0 \times 10^3$, Grids 4–6.

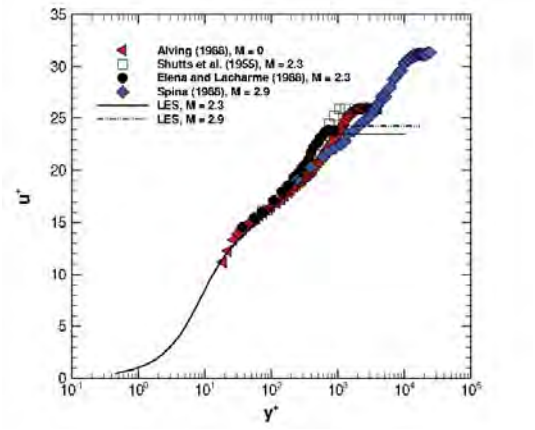

(a) Mean velocity profiles, with van Driest transformed inner coordinates.

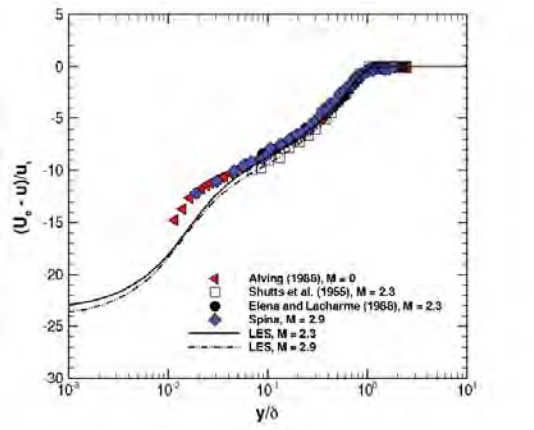

(b) Mean profiles, with van Driest transformed outer coordinates.

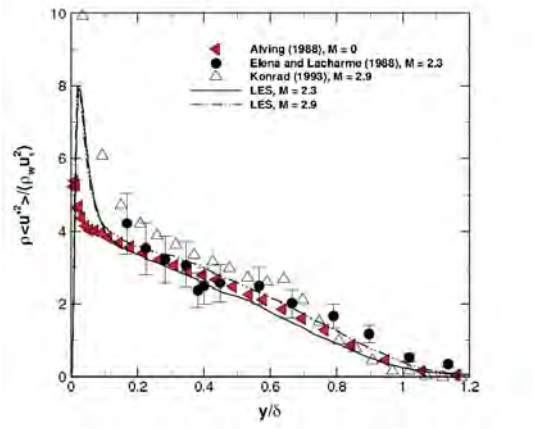

(c) Streamwise component of Reynolds normal stress.

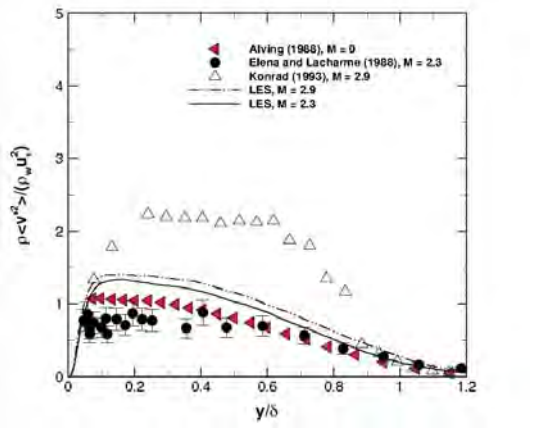

(d) Transverse component of Reynolds normal stress.

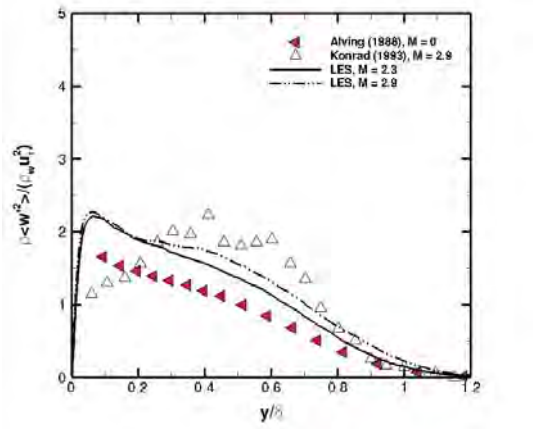

(e) Spanwise component of Reynolds normal stress.

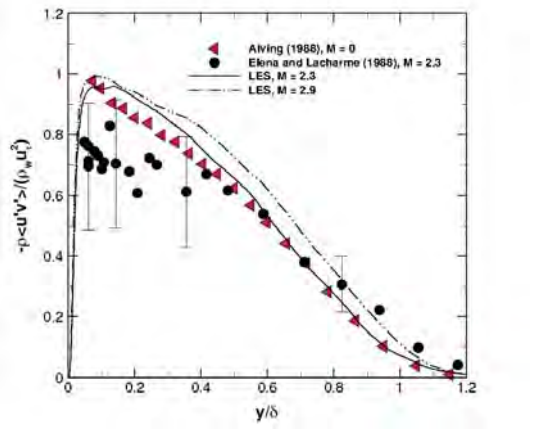

(f) Reynolds shear stress.

Figure 11. Comparison to experiment. Alving:[71] $M = 0$, $\mathrm{Re}_\theta = 5.0\times10^3$; **Shutts et al.:[61]** $M = 2.3$, $\mathrm{Re}_{\theta i} = 3.6\times10^3$, **Spina,[64] Konrad:[73]** $M = 2.9$, $\mathrm{Re}_{\theta i} = 3.6\times10^4$, **Éléna and Lacharme:[72]** $M = 2.3$, $\mathrm{Re}_{\theta i} = 2.6\times10^3$, **LES, Grid 4:** $M = 2.3$, 2.9, $\mathrm{Re}_{\theta i} = 2.0\times10^3$, 2.5×10^3.

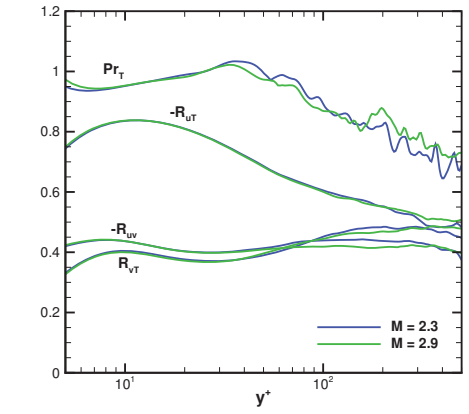

(a) Strong Reynolds analogy parameters.

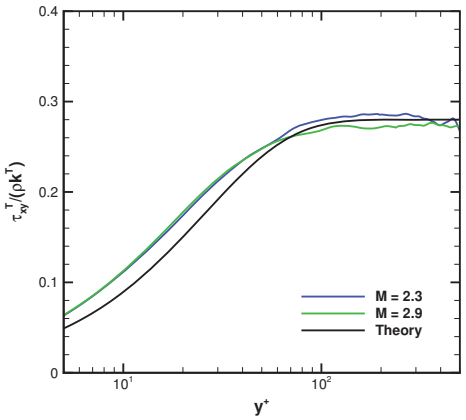

(b) Closure parameter $\tau_{xy}^T/(\rho k^T)$.

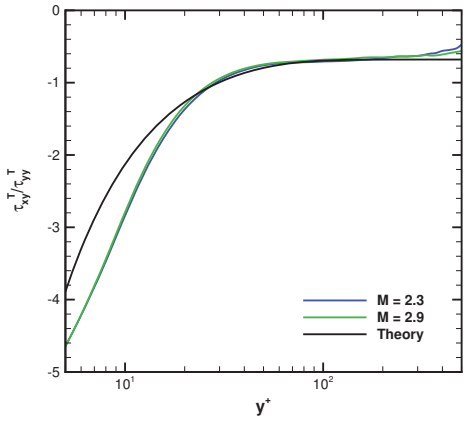

(c) Closure parameter τ_{xy}^T/τ_{yy}^T.

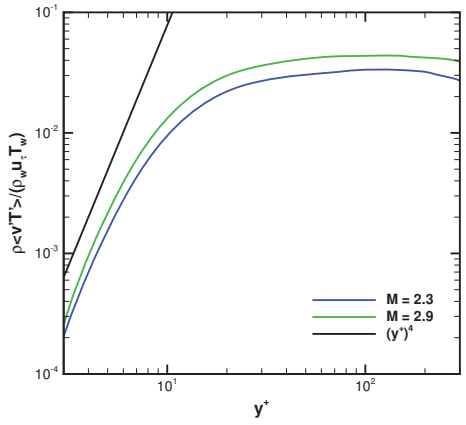

(d) Near-wall behavior of turbulent energy transport q_y^T.

Figure 12. Profiles of turbulence properties. Grid 4, flow conditions: $M = 2.3$, $\mathrm{Re}_{\theta i} = 2.0 \times 10^3$ **and** $M = 2.9$, $\mathrm{Re}_{\theta i} = 2.5 \times 10^3$**.**

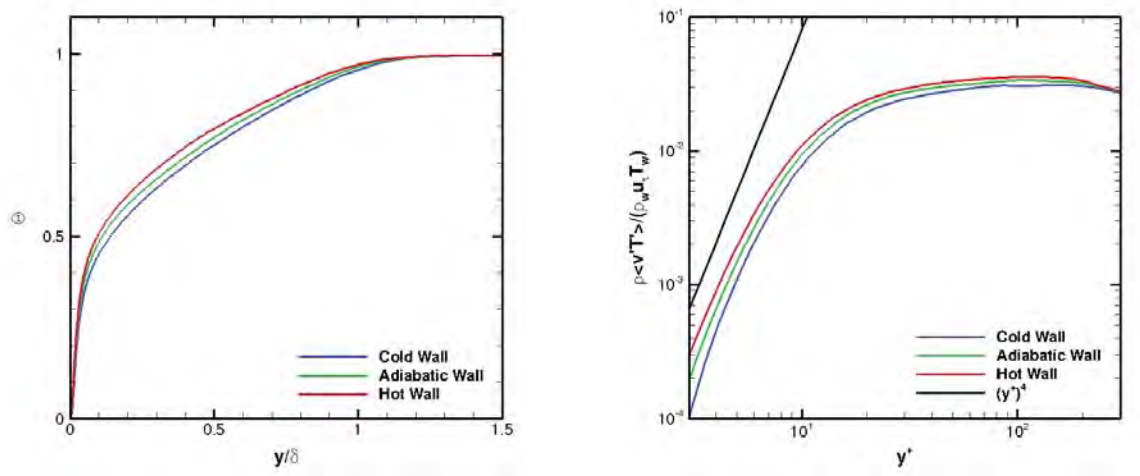

(a) Boundary layer profile of nondimensional temperature $\Theta = (T - T_w)/(T_e - T_w)$.

(b) Near-wall behavior of turbulent energy transport q_y^T.

Figure 13. Wall temperature effects at Mach 2.3, $M = 2.3$, $\mathrm{Re}_{\theta i} = 2.0 \times 10^3$. **Grid 4, wall temperatures:** $T_w = 303$ **K,** $T_w = 323$ **K, and** $T_w = 343$ **K.**

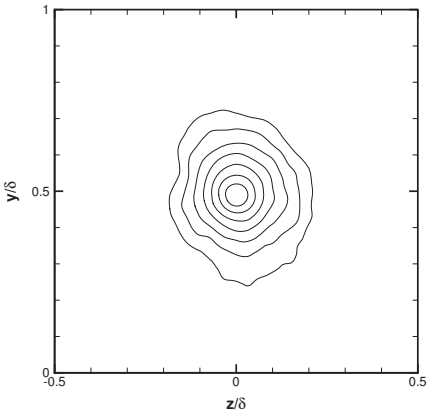

(a) End view, $x/\delta_0 = 100$ plane, $M = 2.3$, $\mathrm{Re}_{\theta i} = 2.0 \times 10^3$.

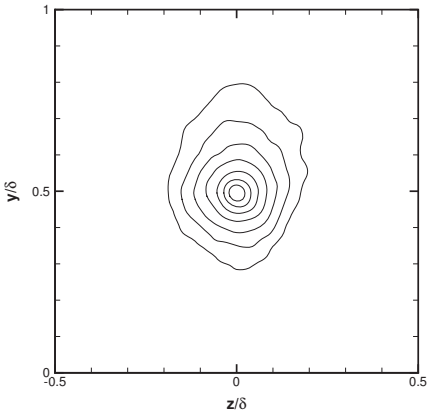

(b) End view, $x/\delta_0 = 100$ plane, $M = 2.9$, $\mathrm{Re}_{\theta i} = 2.5 \times 10^3$.

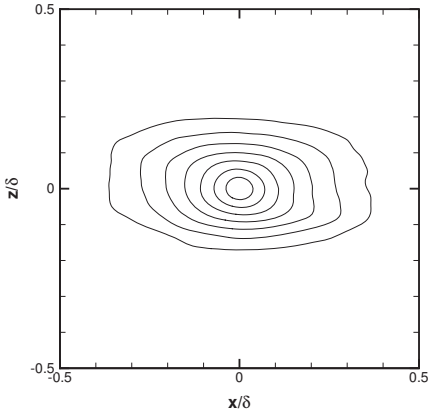

(c) Plan view, $y/\delta = 0.5$ plane, $M = 2.3$, $\mathrm{Re}_{\theta i} = 2.0 \times 10^3$.

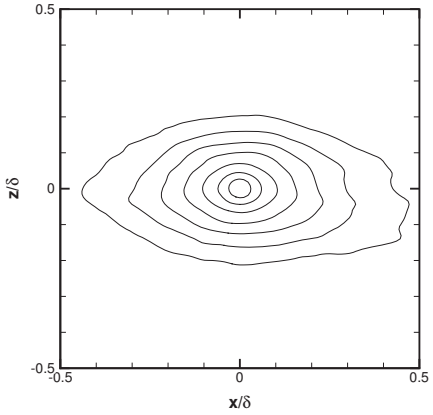

(d) Plan view, $y/\delta = 0.5$ plane, $M = 2.9$, $\mathrm{Re}_{\theta i} = 2.5 \times 10^3$.

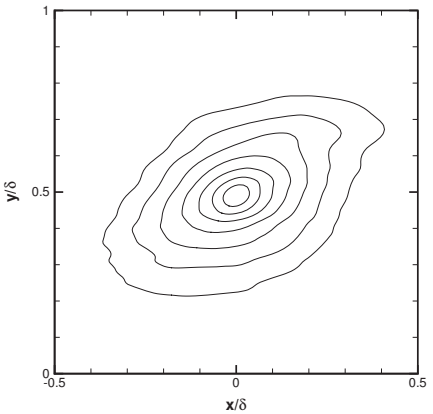

(e) Side view, $z/\delta_0 = 2.5$ plane, $M = 2.3$, $\mathrm{Re}_{\theta i} = 2.0 \times 10^3$.

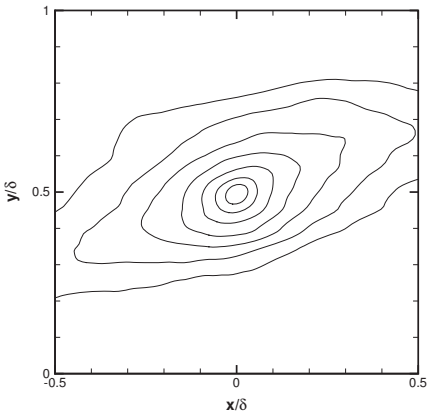

(f) Side view, $z/\delta_0 = 2.5$ plane, $M = 2.9$, $\mathrm{Re}_{\theta i} = 2.5 \times 10^3$.

Figure 14. Spatial correlations of streamwise mass flux ρu. Reference point: $x/\delta_0 = 100$, $y/\delta = 0.5$, $z/\delta_0 = 2.5$. Grid 4, correlation contours 0.3–0.9.

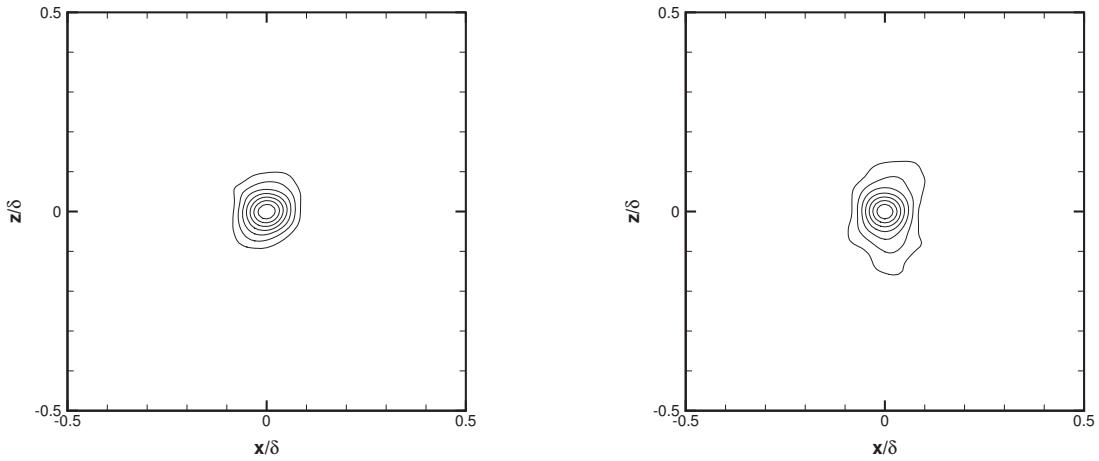

(a) Wall plane, $M = 2.3$, $\mathrm{Re}_{\theta i} = 2.0 \times 10^3$.

(b) Wall plane, $M = 2.9$, $\mathrm{Re}_{\theta i} = 2.5 \times 10^3$.

Figure 15. Spatial correlations of wall pressure fluctuations. Grid 4, correlation contours 0.3–0.9. Reference point: $x/\delta_0 = 100$, $y = 0$, $z/\delta_0 = 2.5$.

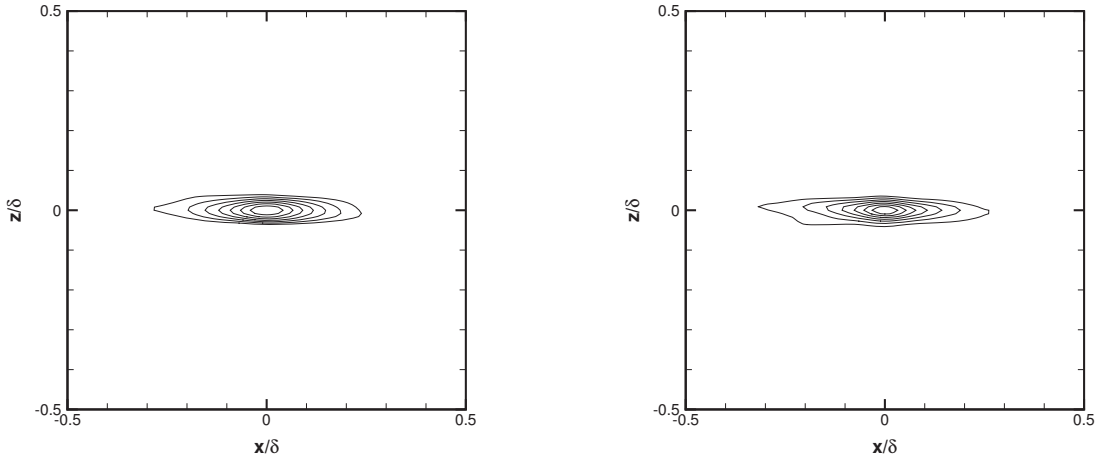

(a) Wall plane, $M = 2.3$, $\mathrm{Re}_{\theta i} = 2.0 \times 10^3$.

(b) Wall plane, $M = 2.9$, $\mathrm{Re}_{\theta i} = 2.5 \times 10^3$.

Figure 16. Spatial correlations of shear stress magnitude. Grid 4, correlation contours 0.3–0.9. Reference point: $x/\delta_0 = 100$, $y = 0$, $z/\delta_0 = 2.5$.

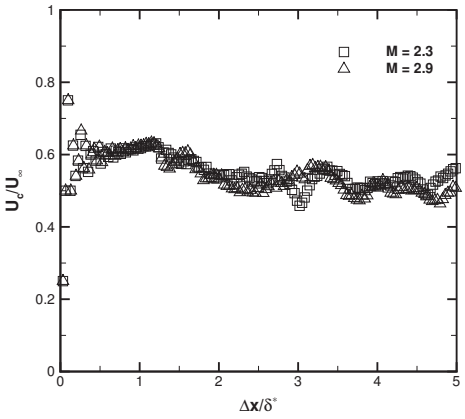

(a) Pressure fluctuations, $y = 0$.

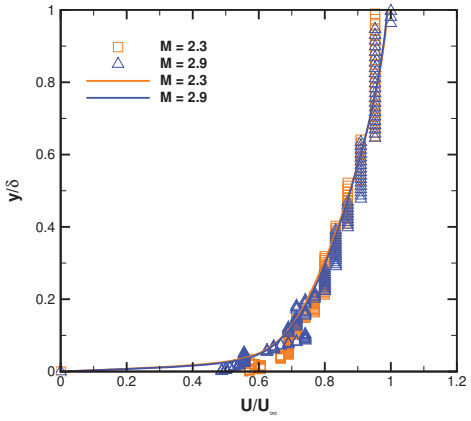

(b) Mass flux fluctuations, $\Delta x/\delta = 2.0$. Lines: mean velocity; symbols: convection velocity.

Figure 17. Convection velocities, Grid 4.

AIAA SciTech
5-9 January 2015, Kissimmee, Florida
53rd AIAA Aerospace Sciences Meeting

Compressible Turbulent Boundary Layer Simulations: Resolution Effects and Turbulence Modeling

Jonathan Poggie*
Air Force Research Laboratory, Wright-Patterson AFB, Ohio 45433-7512 USA

Direct numerical simulation (DNS) and high-fidelity, implicit large-eddy simulation (HFILES) were carried out for turbulent boundary layers at Mach 2.3 and 4.9. Transition to turbulence was promoted with an artificial body force trip. Two main projects were carried out in this work. First, the effects of spatial resolution on spectra and other flow statistics were examined for the baseline Mach 2.3 turbulent boundary layer flow. The finest grid in the spatial resolution study consisted of 3.3×10^{10} points, and maintained $\max(\Delta x_1^+, \Delta x_2^+, \Delta x_3^+) \leq 1$ everywhere. Examining velocity spectra in detail, HFILES was seen to converge seamlessly to DNS as the spatial resolution was increased. Further, turbulence statistics were found to be essentially independent of the domain width for values between two and eight times the maximum boundary layer thickness. Second, variations from the baseline flow conditions were considered, and the results compared to an algebraic model for the turbulent energy flux developed by R. Bowersox (J. Fluid Mech., vol. 633, pp. 61–70, 2009). An impressive match was obtained between the model and simulations, for a wide range of wall temperature and Mach number.

I. Introduction

This project aims to explore turbulent boundary layer flow in the context of direct numerical simulation (DNS), high-fidelity, implicit large-eddy simulation (HFILES), and Reynolds-averaged Navier-Stokes simulation (RANS). In particular, the present work focuses on assessing how well models at these different levels of approximation serve as tools for predicting the properties of turbulent boundary layer flow, and, given large-scale computing resources, whether high-resolution methods can be used in design.

Here DNS designates an approach where all significant turbulence length scales are resolved in the simulation. Implicit large-eddy simulation (ILES) is a general approach[1] in which the additional dissipation needed to account for the unresolved scales is provided directly by the numerical scheme. The terminology HFILES is intended to be more specific than ILES; the HFILES approach[2] uses high-order spatial differencing with filtering, and numerical dissipation is added only at the smallest spatial scales. In RANS, all turbulent fluctuations are modeled, and only the mean flow is computed. Intermediate levels of modeling, employing subgrid-scale models, are not considered here.

A. Turbulent Boundary Layer Physics

The structure of turbulence in compressible boundary layer flow cannot be considered well-understood, because neither experiments nor simulations can currently resolve the full range of space and time scales for conditions relevant for high-speed flight.[3–6] Thus, much of the understanding of turbulence in this regime comes from extrapolation of ideas developed for low-Reynolds-number, incompressible flow.

In the low-speed regime, coherent structures are believed to be the primary mechanism for the transport of mass, momentum, and energy across the boundary layer,[3] and for the entrainment of irrotational freestream fluid into the vortical boundary layer flow.[7,8] The inner part of the boundary layer ($y^+ < 100$) is characterized by alternating streaks of high and low speed fluid.[9] These streaks are persistent in space and time, and tend to be spaced about $\Delta z^+ \approx 100$ apart in the spanwise direction. The streaks have been observed to lift up

*Senior Aerospace Engineer, AFRL/RQHF. Associate Fellow AIAA.

from the wall, oscillate, and break up between $y^+ = 10$ and $y^+ = 30$. This inner layer burst cycle is believed to be the dominant mechanism for turbulence energy production in the boundary layer.[10]

Bulges are the dominant structure in the outer part of the boundary layer, from the beginning of the wake region to beyond the mean boundary layer edge ($y/\delta \approx 1.2$). The bulges are on the order of the boundary layer thickness in scale, and freestream fluid tends to penetrate close to the wall between the bulges. Studies of outer layer structure have found that a strong shear layer exists on the upstream side of these bulges, formed when high-speed freestream fluid impacts onto slow-moving fluid within the bulges.[11]

In supersonic flow, the large-scale structures have been studied using hotwires,[12–15] particle image velocimetry,[16] wall pressure transducers,[17] and flow visualization.[18,19] The primary effect of compressibility on turbulent boundary layers is the conversion of mechanical energy to heat through compression and viscous dissipation.[4,5] Near the wall, these factors cause the temperature to increase and the density to drop. The Reynolds number near the wall tends to decrease rapidly with increasing Mach number, a change that may have a strong effect on the turbulence structure in that region.[4,5,20]

If the fluctuating Mach number is small, Morkovin[21] proposed that the turbulence structure is similar to that of the incompressible case, with the primary difference being the property variation across the boundary layer. The principal support for this hypothesis is that a coordinate transform accounting for the fluid property variation succeeds in collapsing profiles of both mean velocity and turbulence statistics onto corresponding incompressible flow profiles.[4–6,22,23] When the fluctuating Mach number is larger, the turbulence structure could be significantly modified by compressible flow phenomena like eddy shocklets and sound radiation. Such effects have been documented for turbulent free shear layers.[24]

B. Compressible Turbulent Boundary Layer Simulations

A number of previous high-fidelity simulations (DNS and ILES) of compressible, wall-bounded flows[25–46] have been reported in the literature. Early simulations include studies by Coleman et al.[25,26] of channel flow. These studies focused on plane channels at Mach 1.5 and 3.0. Despite very strong property variations across the channel, the van Driest transformation[22] was found to collapse the data very well onto incompressible channel flow results. Direct compressibility effects were found to be very small.

The first direct numerical simulation of a supersonic turbulent boundary layer was carried out by Rai et al.[27] for a freestream Mach number of 2.25. The flow was spatially evolving, and tripped using a blowing and suction method. Again, scaling with local density was found to collapse the computational results onto incompressible flow data. Similar results were obtained later by Guarini et al.,[28] who carried out simulations of a turbulent boundary layer at Mach 2.5 using a mathematical model that assumed slow boundary layer growth in the streamwise direction.

Maeder et al.[29] expanded the Mach number range significantly, using a temporal approach to study boundary layers at Mach 3, 4.5, and 6. The results were generally consistent with local density scaling despite the higher Mach number range. Nonetheless, some deviation from the predictions of Morkovin's hypothesis was observed for the detailed turbulence statistics.

Urbin and Knight[30] adapted the rescaling-recycling technique[47] to supersonic flow to carry out simulations of turbulent boundary layer at Mach 3. Comparing an implicit large-eddy simulation approach to the Smagorinsky subgrid-scale model, they obtained nearly identical results with the two approaches. Rescaling and recycling were also used by Stolz and Adams[31] and Sagaut et al.,[34] who considered turbulent boundary layers at Mach 2.5 and 2.3, respectively.

With a spatially evolving approach, Rizzetta and Visbal[33] compared implicit large-eddy simulations to simulations with subgrid-scale models for a Mach 2.3 boundary layer, and again found little difference between the predictions of the different approaches.

Pirozzoli et al.[32] carried out simulations of a spatially evolving turbulent boundary layer at Mach 2.25. The boundary layer was tripped to turbulent flow using unsteady blowing and suction. The study again confirmed that direct compressibility effects are negligible for this Mach number range, and that a modified strong Reynolds analogy holds.

Pirozzoli's group has gone on to study Mach 2.0 boundary layers in detail.[37,44,46] Excellent comparison to incompressible flow DNS was obtained using Morkovin's scaling. They computed two-point correlations for large-scale structure shape, and the resulting structure angle compared well to the hotwire data of Spina.[48] They also compared spanwise and streamwise auto-correlation to experiment, and examined velocity-temperature correlation and turbulent Prandtl number. In their highest Reynolds number simulations,[46] in which $\delta^+ \approx 4000$, they observed a full decade of log-law in the mean velocity, a variation of peak

$\rho\overline{u'^2}/\tau_w$ with $\log\delta^+$, a clear $k^{-5/3}$ inertial subrange in spectra, and a k^{-1} range in the near-wall spectra. The group has also investigated wall pressure fluctuations.[40,45]

The research group of M. P. Martín has examined the effects of inflow conditions,[35,36] wall temperature,[39] Mach number,[41] and high enthalpy.[42] Further, Ringuette et al.[38] investigated coherent structures at Mach 3, and observed the long streamwise structures reported in the experiments of Ganapathisubramani et al.[49]

Lagha et al.[43] studied supersonic, turbulent boundary layer flows over a very large Mach number range (2.5–20), assuming ideal gas flow and employing the rescaling-recycling technique to generate the inflow. Real gas effects were not included because the main point of the study was to assess the effect of compressibility independent of these effects. Even over this large Mach number range, they found that the main turbulence statistics, when scaled by local density, were similar to the analogous incompressible statistics. The turbulent Mach number did not exceed 0.5 as the freestream Mach number was varied from 5 to 20.

Resolution and conditions reported for these various simulations of supersonic turbulent boundary layers are given in Table 1. Typical resolution recommendations[50,51] for wall-resolving large-eddy simulation are $50 \le \Delta x_1^+ \le 150$, $(\Delta x_2^+)_w < 1$, $15 \le \Delta x_3^+ \le 40$, and $\Delta t^+ < 1$. (The conventional inner variable scaling is used here: $\Delta t^+ = u_\tau^2 \Delta t/\nu_w$ and $(\Delta x_2^+)_w = u_\tau (\Delta x_2)_w/\nu_w$, where $u_\tau = \sqrt{\tau_w/\rho_w}$ is the friction velocity.) Corresponding recommendations for direct numerical simulation tighten the streamwise and spanwise resolution to the range $10 \le \Delta x_1^+ \le 20$ and $5 \le \Delta x_3^+ \le 10$. A wide range of spatial resolutions, spanning the range of LES and DNS, were reported for the studies listed in Table 1: $\Delta x_1^+ = 1.3$–59, $(\Delta x_2^+)_w = 0.1$–3.6, $\Delta x_3^+ = 1.2$–29. The grid resolution at the boundary layer edge $(\Delta x_2^+)_e$ has not been well documented. The reported domain width, relative to the maximum boundary layer thickness, has ranged over $L_3/\delta = 0.84$ to 3.8.

Because of the cost of such simulations, only limited spatial resolution studies have been carried out in these investigations of compressible turbulent boundary layer flows. Published resolution recommendations are a best estimate based on the available data. With the exception of the temporal simulation of Maeder et al.[29] at Mach 6 on a very small domain ($2.3\delta_0 \times 3.0\delta_0 \times 1.4\delta_0$), no study appears to have approached direct numerical simulation in the strictest sense, where the maximum mesh spacing in inner scaling is $\Delta\ell^+ \approx 1$.

To address this deficiency, the present study examined in detail the effects of spatial resolution on spectra and other flow statistics for a supersonic turbulent boundary layer flow at Mach 2.3 and $\delta^+ \approx 600$. The finest grid in the spatial resolution study consisted of 3.3×10^{10} points, and maintained $\max(\Delta x_1^+, \Delta x_2^+, \Delta x_3^+) \le 1$ everywhere on a domain with $L_3/\delta = 2.0$. Further, the effect of varying domain width between 2 and 8 local boundary layer thicknesses was examined. With this done, an additional project was carried out, comparing the results of simulations under different conditions to the algebraic energy flux model of Bowersox.[52,53]

II. Procedure

Supersonic turbulent boundary layer flows were explored using direct numerical simulation and high-fidelity, implicit large-eddy simulation. The numerical scheme was based on sixth-order compact spatial differences, second-order implicit time advancement, and eighth-order filtering. Rectangular grids with smooth stretching were employed, and transition from laminar to turbulent flow was promoted through a trip based on an artificial body force.

A. Physical Model

The calculations were carried out using the code HOPS (Higher Order Plasma Solver), developed by the author.[54–68] The code includes several physical models and numerical schemes. Here, the physical model consists of the perfect-gas, compressible-flow Navier-Stokes equations. The conservation of mass, momentum, and energy are expressed as:

$$\frac{\partial \rho}{\partial t} + \frac{\partial}{\partial x_j}\left(\rho u_j\right) = 0 \tag{1}$$

$$\frac{\partial}{\partial t}(\rho u_i) + \frac{\partial}{\partial x_j}\left(\rho u_j u_i - \Sigma_{ji}\right) = f_i \tag{2}$$

$$\frac{\partial \mathcal{E}}{\partial t} + \frac{\partial}{\partial x_j}\left(u_j \mathcal{E} - \Sigma_{ji} u_i + Q_j\right) = f_i u_i + S \tag{3}$$

where ρ is the gas density, u_i is its velocity, Σ_{ij} is the total stress tensor, $\mathcal{E} = \rho(\epsilon + u_i u_i/2)$ is the total fluid energy, ϵ is the internal energy, and Q_i is the heat flux. An optional body force f_i and energy source term S are included on the right hand side of the equations.

The total stress tensor Σ_{ij} is given by the usual constitutive equation for a Newtonian fluid, and the heat flux Q_i follows Fourier's heat conduction law:

$$\Sigma_{ij} = -p\delta_{ij} + \mu\left(\frac{\partial u_i}{\partial x_j} + \frac{\partial u_j}{\partial x_i}\right) - \frac{2}{3}\mu\frac{\partial u_k}{\partial x_k}\delta_{ij} \tag{4}$$

$$Q_i = -k\frac{\partial T}{\partial x_i} \tag{5}$$

where p is the pressure, μ is the viscosity, and k is the thermal conductivity. The transport coefficients were evaluated using the correlations given by White.[69] The working fluid (air) was assumed to be a calorically and thermally perfect gas: $\epsilon = c_v T$ and $p = \rho RT$, where T is the temperature, c_v is the specific heat, and R is the ideal gas constant.

B. Numerical Methods

The numerical approach was based on compact spatial differencing, filtering, and an implicit time-marching scheme. Employed in this manner as a perfect-gas, compressible-flow Navier-Stokes solver, the HOPS code is similar to the AFRL code FDL3DI.[70,71] A previous publication[67] showed good comparison between the HOPS and FDL3DI codes in a large-eddy simulation of a supersonic turbulent boundary layer flow. (See Pirozzoli[44] for alternative approaches, and for a general review of numerical methods for high-speed flows.)

The conservation laws were solved using an approximately-factored, implicit scheme, related to those developed by Beam and Warming[72] and Pulliam.[73] All calculations were carried out using double-precision arithmetic. Applying the standard transformation from physical coordinates x_i to grid coordinates ξ_i, the conservation equations (1)–(3) can be written in the form:

$$\frac{\partial \overline{U}}{\partial t} + \frac{\partial \overline{E}_j}{\partial \xi_j} = \frac{\partial \overline{E}_j^v}{\partial \xi_j} + \overline{S} \tag{6}$$

where the usual notation[74] is used. For example, $U = [\rho, \rho u_1, \rho u_2, \rho u_3, \mathcal{E}]^T$ is the the vector of dependent variables, E_i is a flux, $\overline{U} = U/J$, $\overline{E}_i = (\partial \xi_i/\partial x_j)E_j/J$, and J is the Jacobian of the grid transformation. The metrics were evaluated using the method of Thomas and Lombard.[75]

Writing Eq. (6) as $\partial \overline{U}/\partial t = R$, and discretizing in time, we have:

$$\frac{(1+\theta)\overline{U}^{n+1} - (1+2\theta)\overline{U}^{n} + \theta\overline{U}^{n-1}}{\Delta t} = R^{n+1} \tag{7}$$

where $\theta = 0$ for an implicit Euler scheme and $\theta = 1/2$ for a three point backward scheme. We introduce subiterations such that $\overline{U}^{n+1} \rightarrow \overline{U}^{p+1}$, with $\Delta\overline{U} = \overline{U}^{p+1} - \overline{U}^{p}$. The right hand side R^{n+1} is linearized in the standard thin layer manner. Collecting the implicit terms on the left hand side, and introducing approximate factoring and a subiteration time step $\Delta\hat{t}$ gives:

$$\mathcal{L}_1\mathcal{L}_2\mathcal{L}_3\ \Delta\overline{U} = -\frac{\Delta\hat{t}}{1+\theta}\left\{\frac{(1+\theta)\overline{U}^{p} - (1+2\theta)\overline{U}^{n} + \theta\overline{U}^{n-1}}{\Delta t} - R^{p}\right\} \tag{8}$$

where $\mathcal{L}_i$ is a derivative operator containing source and flux Jacobians. The implicit terms were evaluated using the scalar pentadiagonal formulation of Pulliam and Chaussee.[76] Equation (8) was solved at each subiteration, driving $\Delta\overline{U}$ to zero. The spatial derivatives on the left-hand-side are evaluated using second-order central differences, and the operators incorporate the implicit damping approach described by Pulliam.[73]

The spatial differencing scheme for the right-hand-side was based on compact differencing.[70,77,78] In one dimension, the finite difference approximation to the first derivative ϕ_i' is evaluated by solving a tridiagonal system of the form:

$$\alpha\phi_{i-1}' + \phi_i' + \alpha\phi_{i+1}' = a\,\frac{\phi_{i+1} - \phi_{i-1}}{2} + b\,\frac{\phi_{i+2} - \phi_{i-2}}{4} \tag{9}$$

where α, a, and b are constants chosen to give a certain order of accuracy and set of spectral properties for the scheme. Second derivatives were found by applying the first derivative operator twice. In the present work, a sixth-order scheme was used for interior points, dropping to fifth- and fourth-order approaching boundaries.

Numerical stability was enforced using a low-pass, Padé-type, non-dispersive spatial filter.[70,78] The filtering approach replaces the computed value ϕ_i at a particular node with a filtered value $\overline{\phi}_i$:

$$\alpha_f \overline{\phi}_{i-1} + \overline{\phi}_i + \alpha_f \overline{\phi}_{i+1} = \sum_{n=0}^{N} \frac{a_n}{2} (\phi_{i+n} + \phi_{i-n}) \tag{10}$$

where the constants α_f, a_0, ... a_N are chosen to give appropriate filter properties. The filter was applied to the solution vector, sequentially, in each of the three computational directions, following each sub-iteration in implicit time integration. The order of the filtering operation was permuted at each time step. For the computations presented here, an eighth-order filter with $\alpha_f = 0.40$ was employed for interior points. Near boundaries, the filter order was dropped in steps of 2, with no filtering of the boundary points. The filter coefficient was increased gradually to $\alpha_f = 0.49$ at the first point off the boundary.

The code's capabilities include the shock capturing method of Visbal and Gaitonde.[71] In this approach, a simple detector, based on a WENO smoothness criterion, is used to identify discontinuities, and the numerical scheme is reduced to a third-order upwind-biased Roe scheme for the cells in the vicinity of a shock. This feature was only employed for the Mach 4.9 turbulent boundary layer flow discussed in Sec. III.B.

In the implementation of the computer code, multi-level parallelism is exploited by using vectorization, multi-threading with OpenMP commands,[79] and multi-block decomposition implemented through MPI commands.[80] Typical runs on the largest grid were carried out by decomposing the domain into blocks of $141^3 \approx 2.8 \times 10^6$ points, each executed with an MPI task and up to eight OpenMP threads. Additional details on these aspects of the implementation were reported in an earlier paper.[61]

The largest computations (Grids 4 and 5, discussed below) were executed on 23040–46080 cores on the SGI ICE X supercomputer Spirit at AFRL, and on 46080–102400 cores on the Cray XE6 supercomputer Garnet at ERDC.

C. Flowfield

The present work investigated flat plate turbulent boundary layer flows. The baseline case was a flow at Mach 2.3, under conditions similar to those employed in several previous numerical investigations.[27,32,33,81] The flow conditions are listed in Table 2. The baseline case corresponds to the adiabatic wall temperature, $T_w = T_{aw}$ (see Sec. III.A). Additional calculations (see Sec. III.B) were carried out with different wall temperatures: $T_w = 0.52\,T_{aw}$ ($T_w = T_\infty$) and $T_w = 2.0\,T_{aw}$. A near-adiabatic wall case at Mach 4.9 was also considered; the conditions are listed in Table 3.

The notation used here is that x_1 is the coordinate in the streamwise direction, x_2 is the wall-normal coordinate, and x_3 is spanwise. In each case, the computational domain was a rectangular box, with the wall at the bottom ($x_2 = 0$) and periodic boundary conditions at the sides (x_3-direction). The size of the resolved region corresponds to $L_1 = 100\delta_0$ by $L_2 = 5\delta_0$ by $L_3 = 5\delta_0$, where δ_0 is the initial boundary layer thickness. A region of grid stretching (25 points) was added in the x_1- and x_2-directions to support the outflow boundary conditions at the top and the end of the domain. A small overlap region (5 points) in the x_3-direction was added to enforce periodicity.

The inflow boundary condition was provided by a similarity solution of the compressible, laminar boundary layer equations.[69] The inflow profiles used for each case are shown in Fig. 1. No-slip conditions were imposed on the flat-plate surface, with zero wall-normal pressure gradient.

Transition to turbulent flow was promoted using a body-force trip method.[82] An artificial body force f_i was added to the momentum equation (2), and its corresponding work $f_j u_j$ was added to the total energy equation (3). The magnitude of this body force was taken to be:

$$f = \frac{2D_c}{\pi \ell_1 \ell_2 \ell_3} \sin^2\left(\pi \frac{x_3 - X_3}{\ell_3}\right) \exp\left[-\left(\frac{x_1 - X_1}{\ell_1}\right)^2 - \left(\frac{x_2 - X_2}{\ell_2}\right)^2\right] \tag{11}$$

The smooth variation in the form of the trip function obviated the need for grid clustering around the trip, and the sinusoidal variation in the spanwise direction was found to promote more rapid transition.

(Previous work[67] used a force distribution for the trip that was triangular in the x_1-x_2-plane, and uniform in the spanwise direction.) The components of the force were:

$$\begin{aligned} f_1 &= f\cos\theta \\ f_2 &= f\sin\theta \\ f_3 &= 0 \end{aligned} \tag{12}$$

Typical parameters were chosen to be $X_1 = 2.5\,\delta_0$, $X_2 = 0$, $X_3 = 0$, $\ell_1 = 0.17\,\delta_0$, $\ell_2 = 0.01\,\delta_0$, $\ell_3 = 0.5\,\delta_0$, $\theta = 179$ deg, and $D_c = 1.5 \times 10^{-2}$. (Here δ_0 is the thickness of the laminar boundary layer imposed at the inflow boundary.) For this choice of parameters, only the $x_2 \geq 0$ half of the force magnitude distribution, Eq. (11), acts on the flow.

Each calculation was carried out with a nondimensional time step of $U_\infty \Delta t/\delta_0 = 5 \times 10^{-3}$, corresponding to a time step in inner units of $\Delta t^+ = 5 \times 10^{-2}$ for the baseline Mach 2.3 flow. A previous paper[68] showed that calculations employing a time step in this range are well resolved. An initial run to allow the solution to reach a statistically steady state was executed for at least 60000 time steps, that is, for $U_\infty T/\delta_0 = 300$ or three flow-through times for the domain. Statistics were recorded for at least 60000 additional iterations.

To minimize storage requirements for the larger computations, a limited subset of the data was recorded for statistical analysis. The plane $x_1/\delta_0 = 100$ was saved every 200 iterations, and a spanwise line at the boundary layer half-height ($x_1/\delta_0 = 100$, $x_2/\delta = 0.5$) was recorded for every time step. For the smaller calculations, data from the $x_2 = 0$ and $x_3/\delta_0 = 2.5$ planes were also saved.

D. Signal Analysis

To be consistent with experimental practice, the spectra and correlations were processed using the procedures described by Bendat and Piersol.[83] For the auto-spectra, the data were windowed and tapered with the Hanning window to avoid side-lobe leakage, and averaged using 50% overlap. For the auto-correlations, the data were windowed with no overlap, and zero-padded. Tapering and zero-padding were not used for periodic data in the present work, that is, for functions of the spanwise, x_3-direction.

To avoid aliasing, an analog low-pass filter, with a cut-off at the Nyquist frequency $f_c = 1/(2\Delta t)$, must be applied to experimental data before digitization. A stable numerical scheme obviates the need for this procedure in a simulation by suppressing small-scale oscillations. In general, the numerical results are over-resolved in time. For example, the time step for the baseline Mach 2.3 flow was $\Delta t^+ = 5.3 \times 10^{-2}$, so the Nyquist frequency in inner units was $f_c^+ = 9.4$, a region of the spectrum where there is almost no detectable energy.

For the temporal spectra and correlations, data were collected in windows of 10000 points, corresponding to $U_\infty T/\delta_0 = 50.0$. For the spanwise correlations and wavenumber spectra, the window size corresponded to the number of points in the span, less the 5 overlap points. Thus, the spanwise window size was 112–1126 points.

III. Results

Two main projects were carried out in this work. First, the effects of spatial resolution on spectra and other flow statistics were examined for the baseline Mach 2.3 turbulent boundary layer flow. This work is presented in Sec. III.A. Second, variations from the baseline flow conditions were considered, and the results compared to the turbulence model of Bowersox.[52] Results of this second project are reported in Sec. III.B.

A. Effects of Spatial Resolution

Table 2 shows the flow conditions for the calculations, and Tables 4–5 show the mesh size and spatial resolution of each grid. Grid 1 meets the requirements for wall-resolving implicit large-eddy simulation, and Grids 2–4 lie in a regime usually accepted as direct numerical simulation.[50] Grid 5 should correspond to direct numerical simulation in the strictest sense. Employing 3.3×10^{10} points, this grid maintains $\max(\Delta x_1^+, \Delta x_2^+, \Delta x_3^+) \leq 1$ everywhere. For comparison, the minimum value of the Kolmogorov length scale occurs at the wall, and has a value of $\eta^+ \approx 1.5$ (see Pope,[84] p. 287).

Figure 2 presents a sample of the solution obtained on Grid 5. The field of view corresponds to $95 \leq x_1/\delta_0 \leq 100$, $0 \leq x_2/\delta_0 \leq 5$, and $0 \leq x_3/\delta_0 \leq 5$. The local boundary layer thickness is about $\delta = 2.5\delta_0$,

so the field of view is a cube about 2δ on a side situated at the end of the resolved region of the mesh. At this high level of resolution, the solution looks remarkably like experimental laser scattering visualization of supersonic, turbulent boundary layer flows.[18,19,85] High-density, freestream fluid often penetrates close to the wall (as close as $x_2/\delta = 0.05$ here), and low-density boundary layer fluid is often ejected past the mean boundary layer edge (here as far as $x_2/\delta = 1.2$). A distinct, large-scale structure angle of about 45 deg is evident in the outer part of the the boundary layer, and a shallower angle of about 10 deg is apparent closer to the wall.

Figure 3 shows samples of the instantaneous density field in the $x_1/\delta_0 = 100$ plane for Grid 1 (HFILES) and Grid 5 (DNS). This view corresponds to the end-plane of the resolved region of the computational domain; flow is into the page. The effect of resolution is very apparent. Motions in the outer layer are highly smeared in the coarse grid case, whereas the fine grid captures the sharp vortical-irrotational interface of the viscous superlayer.[7]

Figure 4 shows the effect of spatial resolution on turbulent boundary layer profiles at $x_1/\delta_0 = 100$. Profiles of the mean streamwise velocity are shown in outer coordinates in Fig. 4a. These profiles are seen to collapse closely for Grids 2–5. Grid 1 appears to produce a transitional boundary layer flow. This is probably a result of slow streamwise development with the coarse streamwise resolution; better results would probably be obtained for this level of resolution on a longer streamwise domain.

Figure 4b shows mean velocity profiles in van Driest-transformed inner coordinates for Grids 3–5. Following Guarini et al.,[28] the composite inner layer profile of Reichardt[86] and Finley et al. is shown for comparison:

$$u^+ = C_1 \left(1 - e^{-x_2^+/\eta_1} - \frac{x_2^+}{\eta_1} e^{-b x_2^+} \right) + \frac{1}{\kappa} \ln(1 + \kappa x_2^+) + \frac{1}{\kappa} \left[(1 + 6\Pi) \left(\frac{x_2}{\delta} \right)^2 - (1 + 4\Pi) \left(\frac{x_2}{\delta} \right)^3 \right] \qquad (13)$$

Here $\eta_1 = 11$, $b = 33$, $C_1 = 7.1$, $\kappa = 0.41$, and $\Pi = 0.54$. Also shown are the experimental measurements of Éléna et al.[87] The discrepancy between computation and experiment is within the experimental uncertainty, which is about the size of the symbols on this plot.

Figure 4c shows profiles of the Reynolds normal stress $\rho\overline{u'^2}$ for the simulations ($M = 2.3$, $\mathrm{Re}_{\theta i} = 2.0 \times 10^3$, Grids 3–5) and the experiments of Alving[88] ($M \approx 0$, $\mathrm{Re}_\theta = 5.0 \times 10^3$), Éléna and Lacharme[87] ($M = 2.3$, $\mathrm{Re}_{\theta i} = 2.6 \times 10^3$), and Konrad[89] ($M = 2.9$, $\mathrm{Re}_{\theta i} = 3.6 \times 10^4$) . As expected for a plot in outer coordinates, the experimental data collapse approximately onto a common curve for $x_2/\delta > 0.2$. The computational results agree with this curve, within the reported experimental error.

Convergence of the Reynolds normal stress with grid resolution is illustrated in Fig. 4d, which shows the $\rho\overline{u_1'^2}$ profile in inner coordinates. Differences in the peak Reynolds stress are seen for Grids 1 and 2, but the data collapse nicely for Grids 3–5.

According to Corrsin and Kistler,[7] the viscous superlayer, or boundary between irrotational and turbulent fluid, is on the order of the Kolmogorov length scale in thickness. This small scale feature may thus be sensitive to numerical resolution near the boundary layer edge. Statistics characterizing the superlayer were analyzed to examine this possibility.

A density contour near the freestream value has often been used experimentally as a surrogate for the vortical-irrotational interface.[90] Here we examine the intermittency and probability density functions (PDFs) of the density. The PDF of density is bimodal in the outer part of the boundary layer, with a minimum at $\rho \approx 0.975\rho_\infty$. The intermittency was thus defined with this value as the threshold: $\gamma = P[\rho < 0.975\rho_\infty]$. In other words, the intermittency is the probability that the density is less than 97.5% of the freestream density.

The intermittency profile is shown in Fig. 5a. As found in previous studies,[7,11] the profile has the shape of an error function, or cumulative normal distribution. Thus the location of the superlayer has a normal (Gaussian) distribution, centered around $y/\delta = 0.9$ where $\gamma \approx 0.5$. The PDF for that station in the boundary layer is shown in Fig. 5b. Both the intermittency profile and the probability density function are seen to be relatively insensitive to grid resolution near the boundary layer edge. The statistics of superlayer location seem to be primarily fixed by large-scale boundary layer structures.

A comparison of the intermittency computed for Grid 5 to experimental data is shown in Fig. 5c. The experimental intermittency is derived from hotwire measurements[7,11,91] and from the vaporization boundary in condensate-enhanced Rayleigh scattering.[19] The shape of the curves is seen to be nearly identical. The differences between the results are primarily a result of the choice of threshold in computing intermittency. (There is no standard value in the literature for this threshold.)

Another way of characterizing intermittency is through the fractal dimension of the viscous superlayer.[90] The fractal dimension of an object embedded in a two-dimensional space can be efficiently estimated using the box-counting algorithm. Here a planar region is tiled with boxes of size r, and the number of boxes N that contain the boundary is counted. For a self-similar fractal, this number is $N(r) \propto r^{-D_2}$, where D_2 is the fractal dimension.

The fractal dimension can be viewed as a measure of the degree with which the fractal fills space; the value lies in the range $1 \leq D_2 < 2$. For a smooth, geometric shape, like a square, the fractal dimension is the same as the Euclidean dimension of the boundary: $D_2 = 1$. Through an argument based on dimensional analysis and Reynolds number independence, Sreenivasan et al.[92] predicted that $D_2 = 4/3$ for the boundary layer vortical-irrotational interface at high Reynolds number. This prediction has been corroborated by flow visualization experiments, with caveat that results obtained with a laser sheet thicker than the Kolmogorov scale tend display artificially low fractal dimension due to spatial averaging.

The box counting algorithm was applied to the $0.975\rho_\infty$ contour for the data on each of the grids. The results were averaged over about 300 realizations, and are shown on a log-log plot in Fig. 5d. The computational results are seen to lie on the predicted $-4/3$ slope for large scales, and change to -1 slope at small scale. This result is exactly as expected: the interface looks smooth when viewed on small scales. Interestingly, grid resolution in the range considered here has little effect on the fractal dimension at large scale. Filtering merely smooths out some of the small scale content.

A very strict test of spatial convergence of a turbulent flow simulation is comparison of computed velocity spectra on different grids.[25] A large body of spectral measurements in low-speed turbulent boundary layers is available in the literature. Since Morkovin's hypothesis[21] is expected to apply for $M = 2.3$, these data should be suitable for comparison to the present calculations. Saddoughi and Veeravalli[93] measured velocity spectra in a low Mach number, high Reynolds number turbulent boundary layer, and compared the results to a variety of experiments spaning the range $R_\lambda = 23$ to 3180 ($\mathrm{Re}_L = 79$ to 1.52×10^6). (Here R_λ is the Reynolds number based on the Taylor microscale, and $\mathrm{Re}_L = (k^T)^2/(\epsilon\nu) = 3R_\lambda^2/20$ is the turbulence Reynolds number.)

Pope[84] (pp. 232–234) proposed a semi-empirical model of the velocity spectrum of isotropic turbulence that is in excellent agreement with the experimental data presented by Saddoughi and Veeravalli. The energy spectrum function $E(\kappa)$ has the following properties. The integral over all wavenumbers $\kappa = 2\pi/\lambda$ is equal to the turbulent kinetic energy:

$$k^T = \int_0^\infty E(\kappa)\, d\kappa \tag{14}$$

and the second moment of the energy spectrum function is proportional to the dissipation:

$$\epsilon = 2\nu \int_0^\infty \kappa^2 E(\kappa)\, d\kappa \tag{15}$$

Pope's model has the following form:

$$\begin{aligned} E(\kappa) &= C\, \epsilon^{2/3} \kappa^{-5/3}\, f_L(\kappa L)\, f_\eta(\kappa\eta) \\ f_L(\kappa L) &= \left[\frac{\kappa L}{\sqrt{(\kappa L)^2 + c_L}} \right]^{5/3+p_0} \\ f_\eta(\kappa\eta) &= \exp\left(-\beta \left\{ \left[(\kappa\eta)^4 + c_\eta^4 \right]^{1/4} - c_\eta \right\} \right) \end{aligned} \tag{16}$$

where $p_0 = 2$, $C = 1.5$, and $\beta = 5.2$. The remaining constants c_L and c_η are determined for a given Reynolds number by satisfying Eqs. (14)–(15). For the present work, these values were obtained numerically using integration of the spectra with the trapezoidal rule, and applying quasi-Newton iteration to solve the resulting two nonlinear equations for c_L and c_η. Figure 6a shows the model $E(\kappa)$ spectrum for different values of the turbulence Reynolds number Re_L. (Note that $\kappa L = \kappa\eta\, \mathrm{Re}_L^{3/4}$.)

The corresponding one-dimensional, longitudinal spectrum (see Pope,[84] pp. 226–227) can be determined from the following integral:

$$E_{11}(\kappa_1) = \int_{\kappa_1}^\infty \frac{E(\kappa)}{\kappa} \left(1 - \frac{\kappa_1^2}{\kappa^2} \right) d\kappa \tag{17}$$

This integral was evaluated for the model spectrum using the trapezoidal rule, and is plotted in Fig. 6b. The flat spectrum at low wavenumber in Fig. 6b is a result of aliasing in the conversion from the three-dimensional

spectrum to one-dimensional spectrum. Under the assumption of isotropy, the spectra $E_{11}(\kappa_1)$ and $E_{33}(\kappa_3)$, which will be examined below, have the same form.

Computational results on the different grids were compared to Pope's model spectrum. To convert the computational results to the appropriate nondimensional variables, integrals of the following form were evaluated for each spectrum:

$$k^T = \frac{3}{2}\int_0^\infty E_{11}(\kappa_1)\, d\kappa_1$$
$$\epsilon = 15\nu \int_0^\infty \kappa_1^2 E_{11}(\kappa_1)\, d\kappa_1 \tag{18}$$

Data from local conditions were employed in all the calculations. For the temporal spectra, Taylor's hypothesis was applied to convert frequency to streamwise wavenumber: $\kappa_1 = 2\pi f/U_c$. For the present flow, $U_c \approx 0.5\, u_1$ was found to provide a good match between the temporal spectra and the spanwise wavenumber spectra at $x_2/\delta = 0.5$.

Figure 7 shows the effect of spatial resolution in the computations on velocity spectra extracted at $x_1/\delta_0 = 100$, $x_2/\delta = 0.5$. In these plots, the wavenumber corresponding to the local Kolmogorov scale is $\kappa_i\eta = 2\pi \approx 6$. The black line is Pope's model spectrum. Based on Eq. (18), the Taylor microscale Reynolds number is $R_\lambda \approx 70$ and the turbulent Reynolds number is $\mathrm{Re}_L \approx 800$.

Results are presented for the spanwise wavenumber spectrum $E_{33}(\kappa_3)$ in Fig. 7a. As the spanwise grid resolution decreases from $\Delta x_3^+ = 10$ on Grid 2 to $\Delta x_3^+ = 1$ on Grid 5, the computational spectra converge smoothly to Pope's model spectrum. At lower frequencies there is agreement between all the curves, but at higher frequencies, the effect of spatial filtering is evident at a rapid drop-off in the magnitude of the spectrum on the coarser grids. Similar trends were observed by Rizzetta and Visbal[33] in a comparison of their wavenumber spectra to those of the better-resolved computation of Rai et al.[27] (See Fig. 7 of Ref. 33.)

Results are presented for the temporal spectrum $E_{11}(\kappa_1)$ in Fig. 7b. For the temporal domain, the computational spectra are again seen to converge to a close match to Pope's model spectrum as resolution is increased. In particular, smooth convergence and agreement at low wavenumber are seen for Grids 2–5. Results of marginal quality are obtained on Grid 1; this may be a result of the transitional state of this case (see Fig. 4a).

Additional calculations were carried out, maintaining the resolution of Grid 3, but varying the domain width over the range $L_3/\delta_0 = 5$, 10, 15, corresponding to $L_3/\delta = 2$, 4, 8, where δ_0 is the initial boundary layer thickness and δ is the local boundary layer thickness at $x_1/\delta_0 = 100$. Figure 8 shows samples of the instantaneous density field in the $x_1/\delta_0 = 100$ plane for each of the three cases. There is no qualitative difference between the cases. Further, the boundary layer thickness is the same, as are boundary layer profiles. (The plots are omitted for brevity; see Poggie.[68]).

Figure 9 shows the effect of varying domain width on the spanwise wavenumber spectra and the temporal spectra. (Compare with Fig. 7.) The spanwise wavenumber spectra (Fig. 9a) collapse perfectly at high wavenumber, and the only effect of additional domain width is to extend the spectrum at low wavenumber. Capturing this long-wavelength content in the spanwise direction may be of interest in the simulation of unsteady separation,[94] and warrants additional work. The temporal spectra (Fig. 9b) are indistinguishable on the three grids.

Figure 10 shows the effect of domain width on the auto-correlation of velocity R_{11}. The spanwise auto-correlation of velocity $R_{11}(x_3)$ (Fig. 10a) is quite small at the maximum spanwise separation: $R_{11} < 0.05$ for $x_3 = \delta$ on the baseline grid, and it is negligible on the wider grids. The temporal correlations $R_{11}(t)$ are indistinguishable on the three grids.

To summarize, basic turbulence statistics were converged for a grid resolution of $\Delta x_1^+ \le 10$, $(\Delta x_2^+)_w < 1$, $(\Delta x_2^+)_e \le 10$, $\Delta x_3^+ \le 10$. The requirements for of the velocity spectra are more stringent, perhaps $\Delta x_1^+ \le 2$, $(\Delta x_2^+)_w < 1$, $(\Delta x_2^+)_e \le 2$, $\Delta x_3^+ \le 1$ for strict convergence. A domain width of twice the maximum boundary layer thickness seen to be adequate, but probably should be considered the minimum acceptable width.

B. Turbulence Models, Wall Temperature, and Mach Number

A second project was undertaken to explore turbulent boundary layer physics in the context of turbulence modeling. Of particular interest was the turbulent energy flux, and the ability to accurately predict heat transfer rates. To explore a range of conditions relevant to high-speed flight, calculations were carried out at Mach 2.3 for different wall temperatures: $T_w = 0.52\, T_{aw}$, $1.0\, T_{aw}$, and $2.0\, T_{aw}$, and at Mach 4.9 for

$T_w = 0.93\,T_{aw}$. Dimensional flow conditions for the Mach 2.3 adiabatic wall case are given in Table 2; only the wall temperature was varied for the remaining supersonic cases. Flow conditions for the hypersonic Mach 4.9 case are listed in Table 3. Grid resolution was maintained at a level close to the Grid 3 case discussed in Sec. III.A. Details are given in Table 6.

Before comparing to the turbulence model, we examine the HFILES results over the range of flow conditions. Figure 11a shows profiles of the mean streamwise velocity in van Driest transformed[22] inner coordinates. As expected, there is reasonably good collapse in these coordinates for the inner region of the profile. Figure 11b shows profiles of the Reynolds normal stress $\rho\overline{u_1'^2}$ in outer coordinates. Again, relatively good collapse is obtained, supporting Morkovin's hypothesis.[21] Overall, the level of collapse of the data is similar to that obtained in previous studies of Mach number[41,43] and wall temperature[39] effects.

The two near-adiabatic wall cases, $M = 2.3$, $T_w/T_{aw} = 1.0$, $\delta^+ = 560$ and $M = 4.9$, $T_w/T_{aw} = 0.93$, $\delta^+ = 730$, had nearly matching Reynolds numbers. Thus a comparison of these two cases isolates the effects of Mach number alone. To this end, Fig. 12 shows correlations for these two cases. Figures 12a and 12c show correlations of the streamwise mass flux in an end-view plane ($x_1/\delta_0 = 90$), and Figs. 12b and 12d show pressure correlations at the wall ($x_2 = 0$). The change in Mach number has a relatively small effect. The correlation contours look very similar, with perhaps a slight reduction in length scale for the higher Mach number case.

The results of the simulations were compared to the turbulence model of Bowersox,[52,53] implemented in a boundary layer solver. This model emphasizes internal energy as the coupling mechanism between the kinematic and thermodynamic fluctuations. For simplicity in the present description of the model, we assume an ideal gas and ignore the difference between Reynolds-averaged and Favre-averaged variables. In the Reynolds-averaged equations of motion (see Gatski and Bonnet,[6] Sec. 3.3–3.4 and Smits and Dussauge,[5] Sec. 3.2), the two moments that require closure models are the turbulent energy flux $q_i^T = \rho\overline{h'u_i'}$ and the Reynolds stress $\tau_{ij}^T = -\rho\overline{u_i'u_j'}$.

First we consider the algebraic model for the energy flux. In the Bowersox model, the transport equation of the energy flux $\theta_i^T = \rho\overline{e'u_i'}$ was simplified to:

$$\begin{aligned} a_{ik}\theta_k^T &= b_i \\ a_{ik} &= \left[\frac{1}{\tau_\theta} + \frac{R}{C_v}\frac{\partial u_m}{\partial x_m}\right]\delta_{ik} + \frac{\partial u_i}{\partial x_k} \\ b_i &= \tau_{ik}^T\left(\frac{\partial h}{\partial x_k} - \frac{1}{\rho}\frac{\partial p}{\partial x_k}\right) + \frac{1}{\rho}\left(\tau_{kl}^T\frac{\partial u_l}{\partial x_k}\right)\frac{\partial p}{\partial x_i}\tau_e \end{aligned} \tag{19}$$

Here, $\tau_\theta = \sigma_\theta\tau_u$ and $\tau_e = \sigma_e\tau_u$ are time scales. For a boundary layer flow, Eq. (19) reduces to:

$$\begin{aligned} \theta_1^T &= \tau_{12}^T\frac{\partial h}{\partial x_2}\tau_\theta - \tau_{22}^T\frac{\partial h}{\partial x_2}\frac{\partial u_1}{\partial x_2}\tau_\theta^2 \\ \theta_2^T &= \tau_{22}^T\frac{\partial h}{\partial x_2}\tau_\theta \end{aligned} \tag{20}$$

For the present work, adjustable constant in the time scale $\tau_\theta = \sigma_\theta\tau_u$ taken to be $\sigma_\theta = 0.28/\gamma$. The turbulence time scale was defined to be $\tau_u = k^T/\epsilon$ as in the k–ϵ model,[95] and estimated as:

$$\tau_u = \frac{a_1/C_\mu}{\partial u_1/\partial x_2} \tag{21}$$

where $a_1 = 0.28$ and $C_\mu = 0.09$. At the present level of approximation, we use Eq. (20) to find θ_i^T, and find the turbulent energy flux as $q_i^T = \gamma\theta_i^T$.

As part of the approximation leading to Eq. (19), the following relation was used:

$$\rho C_v\overline{T'^2} = -2\,\tau_{22}^T\left(\frac{\partial h}{\partial x_2}\right)^2\tau_\theta\tau_e \tag{22}$$

where the time scale $\tau_e = \sigma_e\tau_u$ was computed using $\sigma_e = 0.72/\gamma$ and Eq. (21).

For simplicity, the Reynolds shear stress was computed using a traditional eddy viscosity model:

$$\tau_{12}^T = \mu^T\frac{\partial u_1}{\partial x_2} \tag{23}$$

The turbulent viscosity had the following form in the inner region:

$$\mu_i^T = \rho \left[\kappa x_2 \left(1 - e^{-x_2^+/A^+}\right)\right]^2 \left|\frac{\partial u_1}{\partial x_2}\right| \tag{24}$$

where $\kappa = 0.41$ and $A^+ = 26.0$. This is a mixing length model, employing the van Driest damping function.[22] In the outer region, the turbulent viscosity had the form:

$$\mu_o^T = \frac{C_C\, \rho U_e \delta_k^*}{1 + C_K\, (x_2/\delta)^{n_K}} \tag{25}$$

where $\delta_k^* = \int_0^\infty (1 - u_1/U_\infty)\, dx_2$ is the kinematic displacement thickness. Here $C_C = 0.018$, $C_K = 1.2$, and $n_K = 6.0$. Equation (25) corresponds to the Clauser[96] model with the Klebanoff[97] intermittency correction. A Klebanoff-type blending was used to smoothly merge Eqs. (24)-(25) at height of $x_2 = (C/\kappa)(U_e/u_\tau)\delta^*$. The Reynolds normal stress τ_{22}^T was computed from:

$$\frac{\tau_{12}^T}{\tau_{22}^T} = -\frac{C}{1 - e^{-x_2^+/A^+}} \tag{26}$$

where $C = 0.68$ and $A^+ = 26.0$.

A comparison of the predictions of the simulations and the turbulence model is given in Figs. 13–16. Figure 13 shows the mean streamwise velocity profiles in outer coordinates. Agreement between the two approaches is seen to be excellent in all cases. A similar level of agreement is seen in plots (Fig. 14) of the Reynolds shear stress $-\rho\overline{u_1' u_2'}$. Relative to the simulations, the turbulence model is seen to produce slightly lower values of the peak Reynolds stress.

The core of the Bowersox model is the prediction of the turbulent energy flux through the reduced form of the energy flux transport equation (19). Results for the streamwise and spanwise components of the energy flux are presented in Figs. 15–16 .

Figure 15 compares the streamwise turbulent energy flux $\rho\overline{u_1' T'}$ predicted by the large-eddy simulations to that predicted by the Bowersox model. For the cold wall case (Fig. 15a), this quantity is positive near the wall, but changes sign in the outer part of the boundary layer. For higher wall temperatures (Figs. 15b-d), $\rho\overline{u_1' T'} \leq 0$ across the whole profile.

A change of sign is also seen in the corresponding profiles of the transverse turbulent energy flux $\rho\overline{u_2' T'}$ (Figure 16). For the cold wall case (Figure 16a), the transverse energy flux is negative near the wall, and positive near the boundary layer edge. For the remaining cases, we find $\rho\overline{u_2' T'} \geq 0$ over the whole profile.

Figure 17 shows the intensity of temperature fluctuations $(\rho\overline{T'^2})^{1/2}$. The turbulence model employed Eq. (22) to predict this quantity. Interestingly, two maxima are present in these profiles. One occurs close to the wall, and the other near the boundary layer edge. The two peaks are most prominent in the cold-wall case.

It is impressive how well the algebraic energy flux model matches the large-eddy simulations for such low Reynolds numbers, and for such a wide range of wall temperatures. Even when there are quantitative differences, the curves match qualitatively. In particular, similar maxima and minima are present.

IV. Conclusions

Direct numerical simulations (DNS) and high-fidelity, implicit large-eddy simulations (HFILES) were carried out for turbulent boundary layers at Mach 2.3 and 4.9. Transition to turbulence was promoted with an artificial body force trip. Two main projects were carried out in the work reported here.

First, the effects of spatial resolution on spectra and other flow statistics were examined for a Mach 2.3, adiabatic wall, turbulent boundary layer flow. Examining velocity spectra in detail, HFILES was seen to converge seamlessly to DNS as the spatial resolution was increased. Further, turbulence statistics were found to be essentially independent of the domain width for values between two and eight times the maximum boundary layer thickness.

Second, variations from the baseline flow conditions were considered, and the results compared to an algebraic model for the energy flux developed by R. Bowersox. An impressive match was obtained between the model and simulations, for a wide range of wall temperature and Mach number.

Acknowledgments

This project was sponsored in part by the Air Force Office of Scientific Research, under LRIR Task 14RQ18COR monitored by I. Leyva. It was also supported by grants of High Performance Computing time from the Department of Defense Supercomputing Resource Centers at the Air Force Research Laboratory, the Army Research Laboratory, and the Army Engineer Research and Development Center, provided under a Department of Defense, High-Performance Computation Modernization Program Frontier Project.

The work presented in Sec. III.A was carried out in collaboration with N. Bisek and R. Gosse under the Frontier Project. The work presented in Sec. III.B was carried out in collaboration with R. Bowersox under AFOSR sponsorship.

References

[1]Boris, J. P., Grinstein, F. F., Oran, E. S., and Kolbe, R. L., "New Insights into Large Eddy Simulation," *Fluid Dynamics Research*, Vol. 10, No. 4–6, 1992, pp. 199–228.

[2]Visbal, M. R. and Rizzetta, D. P., "Large-Eddy Simulation on Curvilinear Grids Using Compact Differencing and Filtering Schemes," *Journal of Fluids Engineering*, Vol. 124, No. 4, 2002, pp. 836–847.

[3]Robinson, S. K., "Coherent Motions in the Turbulent Boundary Layer," *Annual Review of Fluid Mechanics*, Vol. 23, 1991, pp. 601–639.

[4]Spina, E. F., Smits, A. J., and Robinson, S. K., "The Physics of Supersonic Turbulent Boundary Layers," *Annual Review of Fluid Mechanics*, Vol. 26, 1994, pp. 287–319.

[5]Smits, A. J. and Dussauge, J.-P., *Turbulent Shear Layers in Supersonic Flow*, Springer, New York, 2nd ed., 2006.

[6]Gatski, T. B. and Bonnet, J.-P., *Compressibility, Turbulence and High Speed Flow*, Elsevier, Amsterdam, 2nd ed., 2013.

[7]Corrsin, S. and Kistler, A. K., "Free-Stream Boundaries of Turbulent Flow," Technical Report NACA-TR-1244, National Advisory Committee for Aeronautics, January 1955.

[8]Hussain, A. K. M. F., "Coherent Structures – Reality and Myth," *Physics of Fluids*, Vol. 26, No. 10, 1983, pp. 2816–2850.

[9]Kline, S. J., Reynolds, W. C., Schraub, F. A., and Runstadler, P. W., "The Structure of Turbulent Boundary Layers," *Journal of Fluid Mechanics*, Vol. 30, 1967, pp. 741–773.

[10]Offen, G. R. and Kline, S. J., "A Proposed Model of the Bursting Process in Turbulent Boundary Layers," *Journal of Fluid Mechanics*, Vol. 70, 1975, pp. 209–228.

[11]Kovasznay, L. S. G., Kibens, V., and Blackwelder, R. F., "Large-Scale Motion in the Intermittent Region of a Turbulent Boundary Layer," *Journal of Fluid Mechanics*, Vol. 41, 1970, pp. 283–325.

[12]Owen, F. K. and Horstman, C. C., "On The Structure of Hypersonic Turbulent Boundary Layers," *Journal of Fluid Mechanics*, Vol. 53, 1972, pp. 611–636.

[13]Spina, E. F. and Smits, A. J., "Organized Structures in a Compressible, Turbulent Boundary Layer," *Journal of Fluid Mechanics*, Vol. 182, 1987, pp. 85–109.

[14]Spina, E. F., Donovan, J. F., and Smits, A. J., "On the Structure of High-Reynolds-Number Supersonic Turbulent Boundary Layers," *Journal of Fluid Mechanics*, Vol. 222, 1991, pp. 293–327.

[15]Smith, D. R. and Smits, A. J., "Simultaneous Measurement of Velocity and Temperature Fluctuations in the Boundary Layer of a Supersonic Flow," *Experimental Thermal and Fluid Science*, Vol. 7, No. 3, 1993, pp. 221–229.

[16]Tichenor, N. R., Humble, R. A., and Bowersox, R. D. W., "Response pf a Hypersonic Turbulent Boundary Layer to Favorable Pressure Gradients," *Journal of Fluid Mechanics*, Vol. 722, 2013, pp. 187–213.

[17]Beresh, S. J., Henfling, J. F., Spillers, R. W., and Pruett, B. O. M., "Fluctuating Wall Pressures Measured Beneath a Supersonic Turbulent Boundary Layer," *Physics of Fluids*, Vol. 23, 2011, pp. 075110.

[18]Smith, M. W. and Smits, A. J., "Visualization of the Structure of Supersonic Turbulent Boundary Layers," *Experiments in Fluids*, Vol. 18, 1995, pp. 288–302.

[19]Poggie, J., Erbland, P. J., Smits, A. J., and Miles, R. B., "Quantitative Visualization of Compressible Turbulent Shear Flows using Condensate-Enhanced Rayleigh Scattering," *Experiments in Fluids*, Vol. 37, 2004, pp. 438–454.

[20]Bradshaw, P., "Compressible Turbulent Shear Layers," *Annual Review of Fluid Mechanics*, Vol. 9, 1977, pp. 33–52.

[21]Morkovin, M. V., "Effects of Compressibility on Turbulent Flows," *Méchanique de la Turbulence*, edited by A. Favre, CNRS, Paris, France, 1962, pp. 367–380.

[22]van Driest, E. R., "On the Turbulent Flow Near a Wall," *Journal of the Aeronautical Sciences*, Vol. 23, 1956, pp. 1007–1011.

[23]Smits, A. J., Spina, E. F., Alving, A. E., Smith, R. W., Fernando, E. M., and Donovan, J. F., "A Comparison of the Turbulence Structure of Subsonic and Supersonic Boundary Layers," *Physics of Fluids*, Vol. 1, No. 11, 1989, pp. 1865–1875.

[24]Papamoschou, D., "Evidence of Shocklets in a Counterflow Supersonic Shear Layer," *Physics of Fluids*, Vol. 7, 1995, pp. 233–235.

[25]Coleman, G. N., Kim, J., and Moser, R. D., "A Numerical Study of Turbulent Supersonic Isothermal-Wall Channel Flow," *Journal of Fluid Mechanics*, Vol. 305, 1995, pp. 159–183.

[26]Huang, P. G., Coleman, G. N., and Bradshaw, P., "Compressible Turbulent Channel Flows: DNS Results and Modelling," *Journal of Fluid Mechanics*, Vol. 305, 1995, pp. 185–218.

[27]Rai, M. M., Gatski, T. B., and Erlebacher, G., "Direct Simulation of Spatially Evolving Compressible Turbulent Boundary Layers," AIAA Paper 95-583.

[28]Guarini, S. E., Moser, R. D., Shariff, K., and Wray, A., "Direct Numerical Simulation of a Supersonic Turbulent Boundary Layer at Mach 2.25," *Journal of Fluid Mechanics*, Vol. 414, 2000, pp. 1–33.

[29]Maeder, T., Adams, N. A., and Kleiser, L., "Direct Simulation of Supersonic Turbulent Boundary Layers by an Extended Temporal Approach," *Journal of Fluid Mechanics*, Vol. 429, 2001, pp. 187–216.

[30]Urbin, G. and Knight, D., "Large-Eddy Simulation of a Supersonic Boundary Layer Using an Unstructured Grid," *AIAA Journal*, Vol. 39, No. 7, 2001, pp. 1288–1295.

[31]Stolz, S. and Adams, N. A., "Large-eddy Simulation of High-Reynolds-Number Supersonic Boundary Layers Using the Approximate Deconvolution Model and a Rescaling and Recycling Technique," *Physics of Fluids*, Vol. 15, No. 8, 2003, pp. 2398–2412.

[32]Pirozzoli, S., Grasso, F., and Gatski, T. B., "Direct Numerical Simulation and Analysis of a Spatially Evolving Supersonic Turbulent Boundary Layer at $M = 2.25$," *Physics of Fluids*, Vol. 16, No. 3, 2004, pp. 530–545.

[33]Rizzetta, D. P. and Visbal, M. R., "Large-Eddy Simulation of Supersonic Boundary-Layer Flow by a High-Order Method," *International Journal of Computational Fluid Dynamics*, Vol. 18, No. 1, 2004, pp. 15–27.

[34]Sagaut, P., Garnier, E., Tromeur, E., Larchevêque, L., and Labourasse, E., "Turbulent Inflow Conditions for Large-Eddy Simulation of Compressible Wall-Bounded Flows," *AIAA Journal*, Vol. 42, No. 3, 2004, pp. 469–477.

[35]Xu, S. and Martin, M. P., "Assessment of Inflow Boundary Conditions for Compressible Turbulent Boundary Layers," *Physics of Fluids*, Vol. 16, No. 7, 2004, pp. 2623–2639.

[36]Martín, M. P., "Direct Numerical Simulation of Hypersonic Turbulent Boundary Layers. Part 1. Initialization and Comparison with Experiments," *Journal of Fluid Mechanics*, Vol. 570, 2007, pp. 347–364.

[37]Pirozzoli, S., Bernardini, M., and Grasso, F., "Characterization of Coherent Vortical Structures in a Supersonic Turbulent Boundary Layer," *Journal of Fluid Mechanics*, Vol. 613, 2008, pp. 205–231.

[38]Ringuette, M. J., Wu, M., and Martín, M. P., "Coherent Structures in Direct Numerical Simulation of Turbulent Boundary Layers at Mach 3," *Journal of Fluid Mechanics*, Vol. 594, 2008, pp. 59–69.

[39]Duan, L., Beekman, I., and Martín, M. P., "Direct Numerical Simulation of Hypersonic Turbulent Boundary Layers. Part 2. Effect of Wall Temperature," *Journal of Fluid Mechanics*, Vol. 655, 2010, pp. 419–445.

[40]Bernardini, M. and Pirozzoli, S., "Wall Pressure Fluctuations beneath Supersonic Turbulent Boundary Layers," *Physics of Fluids*, Vol. 23, 2011, pp. 085102.

[41]Duan, L., Beekman, I., and Martín, M. P., "Direct Numerical Simulation of Hypersonic Turbulent Boundary Layers. Part 3. Effect of Mach Number," *Journal of Fluid Mechanics*, Vol. 672, 2011, pp. 245–267.

[42]Duan, L., Beekman, I., and Martín, M. P., "Direct Numerical Simulation of Hypersonic Turbulent Boundary Layers. Part 4. Effect of high enthalpy," *Journal of Fluid Mechanics*, Vol. 684, 2011, pp. 25–59.

[43]Lagha, M., Kim, J., Eldredge, J. D., and Zhong, X., "A Numerical Study of Compressible Turbulent Boundary Layers," *Physics of Fluids*, Vol. 23, 2011, pp. 015106.

[44]Pirozzoli, S., "Numerical Methods for High-Speed Flows," *Annual Review of Fluid Mechanics*, Vol. 43, 2011, pp. 163–194.

[45]Di Marco, A., Camussi, R., Bernardini, M., and Pirozzoli, S., "Wall Pressure Coherence in Supersonic Turbulent Boundary Layers," *Journal of Fluid Mechanics*, Vol. 732, 2013, pp. 445–456.

[46]Pirozzoli, S. and Bernardini, M., "Probing High-Reynolds Number Effects in Numerical Boundary Layers," *Physics of Fluids*, Vol. 25, 2013, pp. 021704.

[47]Lund, T. S., Wu, X., and Squires, K. D., "Generation of Turbulent Inflow Data for Spatially-Developing Boundary Layer Simulations," *Journal of Computational Physics*, Vol. 140, 1998, pp. 233–258.

[48]Spina, E. F., *Organized Structures in a Supersonic Turbulent Boundary Layer*, Ph.D. Dissertation, Princeton University, Princeton NJ, October 1988.

[49]Ganapathisubramani, B., Clemens, N. T., and Dolling, D. S., "Large-Scale Motions in a Supersonic Turbulent Boundary Layer," *Journal of Fluid Mechanics*, Vol. 556, 2006, pp. 271–282.

[50]Georgiadis, N. J., Rizzetta, D. P., and Fureby, C., "Large-Eddy Simulation: Current Capabilities, Recommended Practices, and Future Research," *AIAA Journal*, Vol. 48, No. 8, 2010, pp. 1772–1784.

[51]Choi, H. and Moin, P., "Grid-Point Requirements for Large Eddy Simulation: Chapman's Estimates Revisited," *Physics of Fluids*, Vol. 24, 2012, pp. 011702.

[52]Bowersox, R. D., "Extension of Equilibrium Turbulent Heat Flux Models to High-Speed Shear Flows," *Journal of Fluid Mechanics*, Vol. 633, 2009, pp. 61–70.

[53]Bowersox, R. D. W. and North, S. W., "Algebraic Turbulent Energy Flux Models for Hypersonic Shear Flows," *Progress in Aerospace Sciences*, Vol. 46, 2010, pp. 49–61.

[54]Poggie, J. and Gaitonde, D. V., "Electrode Boundary Conditions in Magnetogasdynamic Flow Control," AIAA Paper 2002-0199.

[55]Sternberg, N. and Poggie, J., "Plasma-Sheath Transition in the Magnetized Plasma-Wall Problem for Collisionless Ions," *IEEE Transactions on Plasma Science*, Vol. 32, No. 6, 2004, pp. 2217–2226.

[56]Poggie, J., "Numerical Exploration of Flow Control with Glow Discharges," AIAA Paper 2004-2658.

[57]Poggie, J. and Sternberg, N., "Transition from the Constant Ion Mobility Regime to the Ion-Atom Charge-Exchange Regime for Bounded Collisional Plasmas," *Physics of Plasmas*, Vol. 12, No. 023502, 2005.

[58]Poggie, J., "Computational Studies of High-Speed Flow Control with Weakly-Ionized Plasma," AIAA Paper 2005-0784.

[59]Poggie, J., "Numerical Simulation of Direct Current Glow Discharges for High-Speed Flow Control," *Journal of Propulsion and Power*, Vol. 24, No. 5, 2008, pp. 916–922.

[60]Poggie, J., "Discharge Modeling for Flow Control Applications," AIAA Paper 2008-1357.

[61]Poggie, J., "Control of Shock-Wave / Boundary-Layer Interaction Using Volumetric Energy Deposition," AIAA Paper 2008-1090.

[62]Poggie, J., "High-Order Compact Difference Methods for Glow Discharge Modeling," AIAA Paper 2009-1047.

[63]Poggie, J., "Compact Difference Methods for Discharge Modeling in Aerodynamics," AIAA Paper 2009-3908.

[64]Poggie, J., "Role of Charged Particle Inertia in Pulsed Electrical Discharges," AIAA Paper 2010-1195.

[65]Poggie, J., "High-Order Numerical Methods for Electrical Discharge Modeling," AIAA Paper 2010-4632.

[66]Poggie, J., Adamovich, I., Bisek, N., and Nishihara, M., "Numerical simulation of nanosecond-pulse electrical discharges," *Plasma Sources Science and Technology*, Vol. 22, 2013, pp. 015001.

[67]Poggie, J., Bisek, N. J., Leger, T., and Tang, R., "Implicit Large-Eddy Simulation of a Supersonic Turbulent Boundary Layer: Code Comparison," AIAA Paper 2014-0423, 2014.

[68]Poggie, J., "Large-Scale Structures in Implicit Large-Eddy Simulation of Compressible Turbulent Flow," AIAA Paper 2014-3328, June 2014.

[69]White, F. M., *Viscous Fluid Flow*, McGraw-Hill, New York, 2nd ed., 1991.

[70]Visbal, M. R. and Gaitonde, D. V., "On the Use of Higher-Order Finite-Difference Schemes on Curvilinear and Deforming Meshes," *Journal of Computational Physics*, Vol. 181, 2002, pp. 155–185.

[71]Visbal, M. R. and Gaitonde, D. V., "Shock Capturing Using Compact-Differencing-Based Methods," AIAA Paper 2005-1265.

[72]Beam, R. and Warming, R., "An Implicit Factored Scheme for the Compressible Navier-Stokes Equations," *AIAA Journal*, Vol. 16, No. 4, 1978, pp. 393–402.

[73]Pulliam, T. H., "Implicit Finite-Difference Simulations of Three-Dimensional Compressible Flow," *AIAA Journal*, Vol. 18, No. 2, 1980, pp. 159–167.

[74]Hoffmann, K. A. and Chiang, S. T., *Computational Fluid Dynamics*, Engineering Educational System, Wichita KS, 4th ed., 2000.

[75]Thomas, P. D. and Lombard, C. K., "Geometric Conservation Law and Its Application to Flow Computations on Moving Grids," *AIAA Journal*, Vol. 17, No. 10, 1979, pp. 1030–1037.

[76]Pulliam, T. H. and Chaussee, D. S., "A Diagonal Form of an Implicit Approximate-Factorization Algorithm," *Journal of Computational Physics*, Vol. 39, 1981, pp. 347–363.

[77]Lele, S. K., "Compact Finite Difference Schemes with Spectral-Like Resolution," *Journal of Computational Physics*, Vol. 103, 1992, pp. 16–42.

[78]Gaitonde, D. V. and Visbal, M. R., "High-Order Schemes for Navier-Stokes Equations: Algorithm Implementation into FDL3DI," Technical Report AFRL-VA-WP-TR-1998-3060, Air Force Research Laboratory, Wright-Patterson Air Force Base, Ohio, August 1998.

[79]Chandra, R., Dagum, L., Kohr, D., Maydan, D., McDonald, J., and Menon, R., *Parallel Programming in OpenMP*, Academic Press, San Diego, 2001.

[80]Gropp, W., Lusk, E., and Skjellum, A., *Using MPI: Portable Parallel Programming with the Message-Passing Interface*, The MIT Press, Cambridge, MA, 2nd ed., 1999.

[81]Bisek, N. J., Rizzetta, D. P., and Poggie, J., "Plasma Control of a Turbulent Shock Boundary-Layer Interaction," *AIAA Journal*, Vol. 51, No. 8, 2013, pp. 1789–1804.

[82]Mullenix, N. J., Gaitonde, D. V., and Visbal, M. R., "Spatially Developing Supersonic Turbulent Boundary Layer with a Body-Force Based Method," *AIAA Journal*, Vol. 51, No. 8, 2013, pp. 1805–1819.

[83]Bendat, J. S. and Piersol, A. G., *Random Data: Analysis and Measurement Procedures*, J. Wiley, New York, 2nd ed., 1986.

[84]Pope, S. B., *Turbulent Flows*, Cambridge University Press, Cambridge, UK, 2000.

[85]Smith, D. R., Poggie, J., Konrad, W., and Smits, A. J., "Visualization of the Structure of Shock Wave Turbulent Boundary Layer Interactions using Rayleigh Scattering," AIAA Paper 91-0651.

[86]Reichardt, H., "Vollständige Darstellung der turbulenten Geschwindigkeitsverteilung in glatten Leitungen," *Zeitschrift für Angewandte Mathematik und Mechanik*, Vol. 31, No. 7, 1951, pp. 208–219.

[87]Éléna, M. and Lacharme, J. P., "Experimental Study of a Supersonic Turbulent Boundary Layer Using a Laser Doppler Anemometer," *Journal Mécanique Théorique et Appliquée*, Vol. 7, 1988, pp. 175–190.

[88]Alving, A. E., *Boundary Layer Relaxation from Convex Curvature*, Ph.D. dissertation, Princeton University, Princeton NJ, 1988.

[89]Konrad, W., *A Three-Dimensional Supersonic Turbulent Boundary Layer Generated by an Isentropic Compression*, Ph.D. Dissertation, Princeton University, Princeton NJ, 1993.

[90]Poggie, J., *Quantitative Flow Visualization Applied to the Study of Compressible Turbulent Flow*, Master's thesis, Princeton University, June 1991.

[91]Selig, M. S., Andreopoulos, J., Muck, K. C., Dussauge, J. P., and Smits, A. J., "Turbulence Structure in a Shock Wave / Turbulent Boundary-Layer Interaction," *AIAA Journal*, Vol. 27, No. 7, 1989, pp. 862–869.

[92]Sreenivasan, K. R., Ramshankar, R., and Meneveau, C., "Mixing, Entrainment and Fractal Dimensions of Surfaces in Turbulent Flows," *Proceedings of the Royal Society of London A*, Vol. 421, No. 1860, 1989, pp. 79–108.

[93]Saddoughi, S. G. and Veeravalli, S. V., "Local Isotropy in Turbulent Boundary Layers at High Reynolds Number," *Journal of Fluid Mechanics*, Vol. 268, 1994, pp. 333–372.

[94]Poggie, J., Bisek, N. J., Kimmel, R. L., and Stanfield, S. A., "Spectral Characteristics of Separation Shock Unsteadiness," *AIAA Journal*, 2014, Accepted for publication. DOI: 10.2514/1.J053029.

[95]Jones, W. P. and Launder, B. E., "The Prediction of Laminarization with a two-equation model of turbulence," *International Journal of Heat and Mass Transfer*, Vol. 15, No. 2, 1972, pp. 301–314.

[96]Clauser, F. H., "The Turbulent Boundary Layer," *Advances in Applied Mechanics*, Vol. 4, 1956, pp. 1–51.

[97]Klebanoff, P., "Characteristics of turbulence in a boundary layer with zero pressure gradient." Technical Report NACA-TR-1247, National Advisory Council for Aeronautics, January 1955.

Reference	M_∞	$\mathrm{Re}_{\theta i}$	δ^+	T_w/T_{aw}	L_3/δ	Δx_1^+	$(\Delta x_2^+)_w$	$(\Delta x_2^+)_e$	Δx_3^+
Coleman et al.[25,26]	1.5–3.0					17–39	0.1–0.2		10–24
Rai et al.[27]	2.3			1.0	3.8	27	0.95		10
Guarini et al.[28]	2.5	850		1.0		8.9	0.48	7.8	5.9
Urbin and Knight[30]	3.0			1.0	0.87–3.5	11–56	0.9–1.7		3.1–26
Maeder et al.[29]	3.0–6.0	500–1200		0.95–0.96	0.84–1.4	1.3–2.9	~ 0.4		1.2–2.2
Stolz and Adams[31]	2.5	2200–4900		1.1		41–59	2.7–3.6		21–29
Pirozzoli et al.[32]	2.3	2300		1.0	2.1	15	1.1		6.6
Rizzetta and Visbal[33]	2.3	1900		1.0	3.8	84	0.9		22
Sagaut et al.[34]	2.3				1.4	50	1.0		18
Xu and Martin[35]	4.0				1.4	13	0.12	570	4.8
Martin[36]	3.0–6.0		330–400	1.0	1.7–2.3	7.2–8.0	~ 0.3		2.7–3.0
Pirozzoli et al.[37]	2.0	860	360	1.0	2.9	4.5	0.95	4.1	4.5
Ringuette et al.[38]	2.9–3.0		330–480		2.2–2.3	8.0–9.3			3.0–5.8
Duan et al.[39]	5.0	1500	390–800	0.18–1.0	1.8–2.6	7.4–7.8	0.30–0.33		2.8–3.0
Duan et al.[41]	0.3–12	1500–1600	380-570		2.4–2.9	6.8–8.4	0.10–0.30		2.3–3.1
Lagha et al.[43]	2.5–20		300–340	1.0	2	8	0.30	11	3
Lagha et al.[43]	5.0		380	0.47–5.4					
Pirozzoli et al.[44,46]	2.0	720–16000	250–4000	1.0		5.2–6.5	0.7–0.9	6.5–17	4.5–5.9

Table 1. Resolution and conditions reported in the literature for ILES and DNS of supersonic turbulent boundary layers.

Parameter	Value
δ_0	0.610 mm
U_∞	588 m/s
p_∞	23.8 kPa
T_∞	170 K
T_w	323 K
M	2.25
$U_\infty \delta_0 / \nu_\infty$	1.5×10^4

Table 2. Flow conditions for Mach 2.3 turbulent boundary layer.

Parameter	Value
δ_0	4.00 mm
U_∞	795 m/s
p_∞	4.98 kPa
T_∞	65.5 K
T_w	321 K
M	4.9
$U_\infty \delta_0 / \nu_\infty$	1.9×10^5

Table 3. Flow conditions for Mach 4.9 turbulent boundary layer.

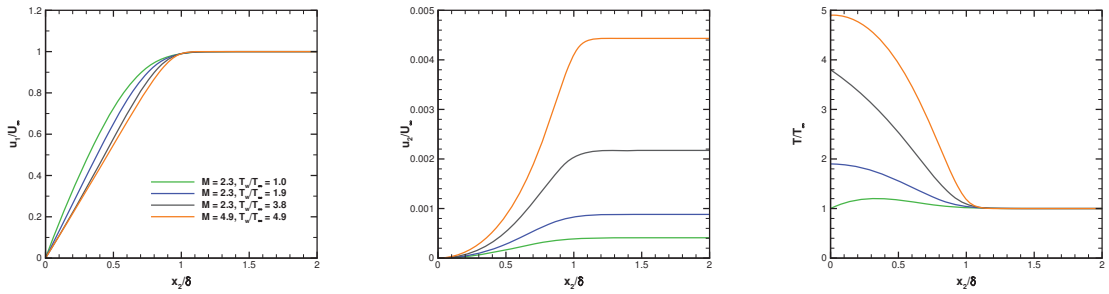

(a) Streamwise velocity. (b) Wall-normal velocity. (c) Temperature.

Figure 1. Laminar boundary layer profiles used for inflow boundary conditions. Flow conditions correspond to Tables 2–3, with varying wall temperature.

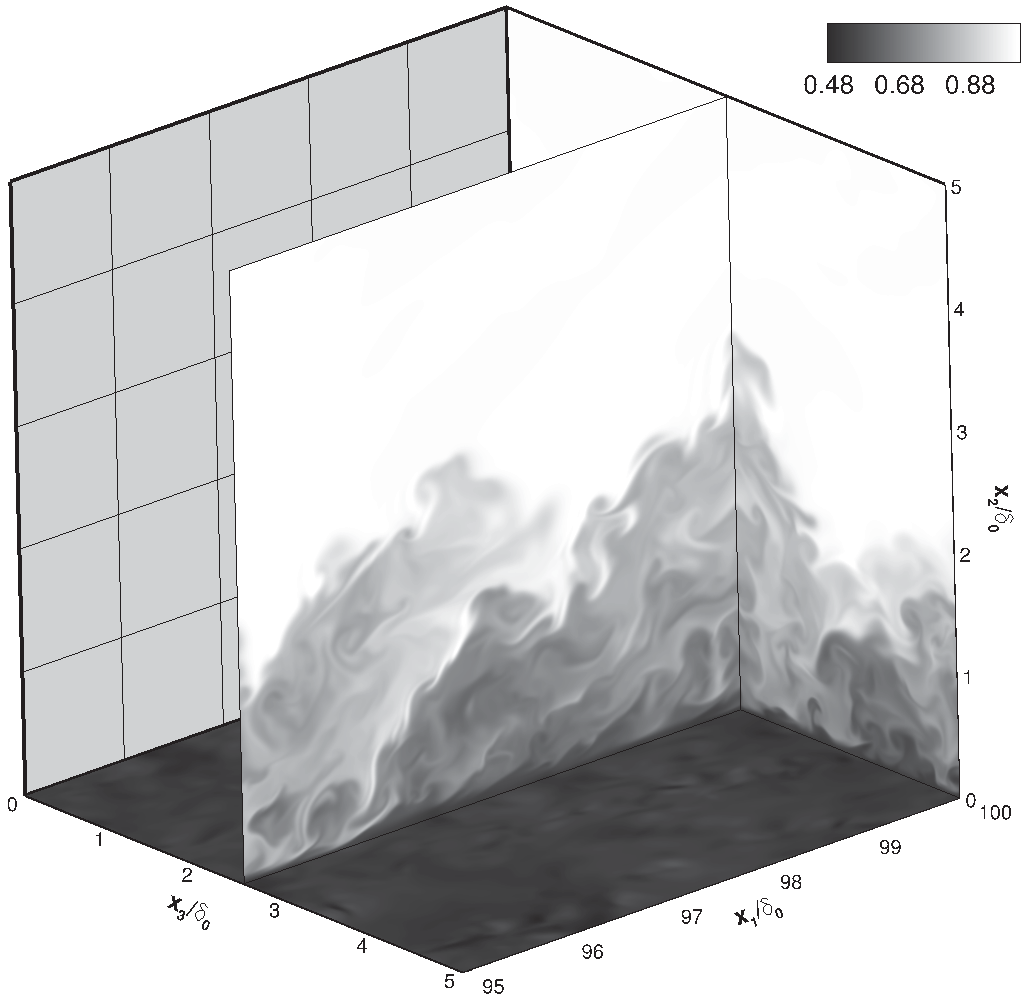

Figure 2. Sample density field ρ/ρ_∞ for the turbulent boundary layer at $M = 2.3$ on Grid 5 ($\Delta x_1^+ = 1$, $\Delta x_2^+ = 0.9$, $\Delta x_3^+ = 1$.). The field of view is a cube with side of about 2δ. Local conditions at $x_1/\delta_0 = 100$: $\mathrm{Re}_{\theta i} = 2000$, $C_f = 2.3 \times 10^{-3}$, $\delta^+ = 570$.

Grid	N_1	N_2	N_3	N	L_1/δ_0	L_2/δ_0	L_3/δ_0
1	526	151	130	1.0×10^7	100	5	5
2	2278	1277	117	3.4×10^8	100	5	5
3	4026	276	255	2.8×10^8	100	5	5
3W	4026	276	505	5.6×10^8	100	10	5
3VW	4026	276	1005	1.1×10^9	100	20	5
4	11287	1277	568	8.2×10^9	100	5	5
5	22548	1277	1131	3.3×10^{10}	100	5	5

Table 4. Properties of the computational meshes for $M = 2.3$, $T_w = T_{aw}$ cases.

Grid	M_∞	$\mathrm{Re}_{\theta i}$	δ^+	T_w/T_{aw}	L_3/δ	Δx_1^+	$(\Delta x_2^+)_w$	$(\Delta x_2^+)_e$	Δx_3^+
1	2.3	1900	640	1.0	2.0	45	0.9	19	9
2	2.3	2000	560	1.0	2.0	10	0.9	0.9	10
3	2.3	2000	560	1.0	2.0	6	0.5	9	5
3W	2.3	2000	560	1.0	4.0	6	0.5	9	5
3VW	2.3	2000	570	1.0	8.0	6	0.5	9	5
4	2.3	2000	570	1.0	2.0	2	0.9	0.9	2
5	2.3	2000	570	1.0	2.0	1	0.9	0.9	1

Table 5. Resolution and conditions for present simulations with $M = 2.3$, $T_w = T_{aw}$, nondimensionalized using conditions at the reference station $x_1/\delta_0 = 100$.

M	T_w/T_{aw}	$\mathrm{Re}_{\theta i}$	δ^+	L_3/δ	Δx_1^+	$(\Delta x_2^+)_w$	Δx_3^+
2.3	0.52	3500	1200	2.2	14	0.5	11
2.3	1.0	2000	560	2.0	6	0.5	5
2.3	2.0	1000	250	2.0	2	0.2	2
4.9	0.93	4000	750	2.8	11	0.4	9

Table 6. Properties of the computational mesh for different cases, nondimensionalized using conditions at the reference station $x_1/\delta_0 = 100$. For each case the size of the mesh was $4026 \times 276 \times 255$ for a total of 2.8×10^8 points.

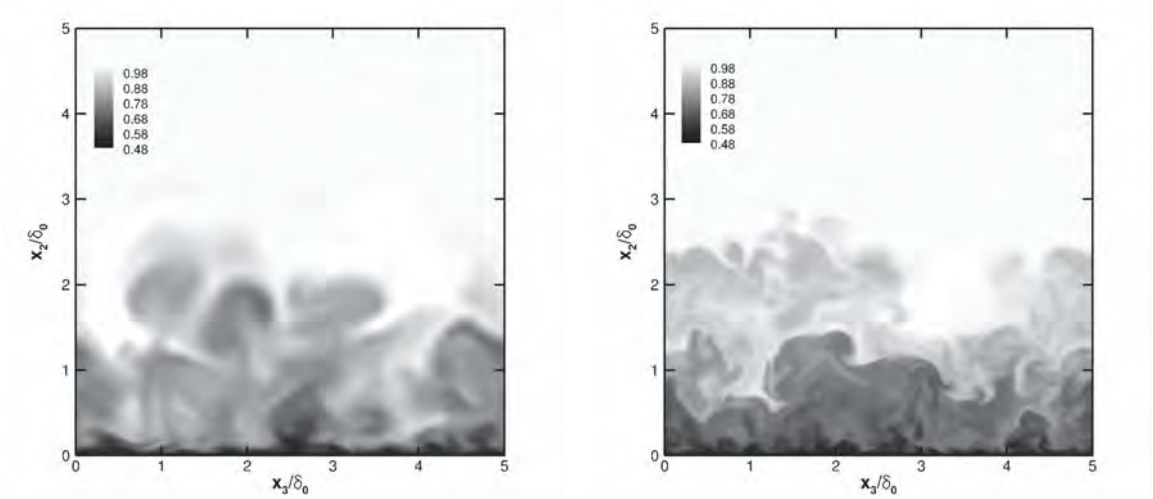

(a) Grid 1: $\Delta x_1^+ = 45$, $\Delta x_2^+ = 0.9 - 19$, $\Delta x_3^+ = 9$.

(b) Grid 5: $\Delta x_1^+ = 1$, $\Delta x_2^+ = 0.9$, $\Delta x_3^+ = 1$.

Figure 3. Sample density fields (ρ/ρ_∞) in the $x_1/\delta_0 = 100$ plane for the turbulent boundary layer at $M = 2.3$.

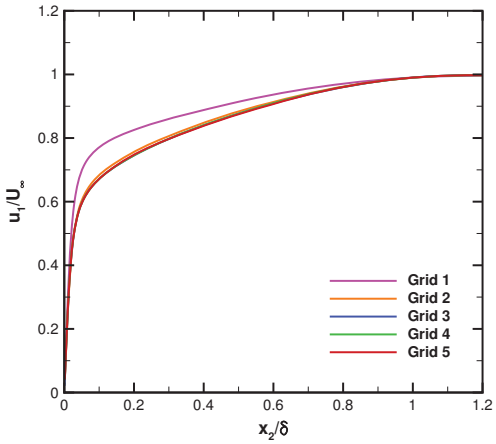

(a) Mean velocity profile, outer coordinates.

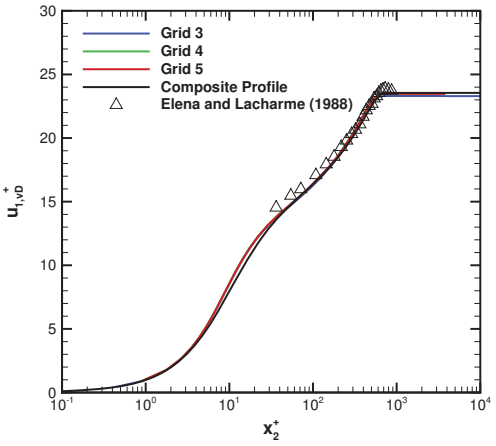

(b) Mean velocity profile, inner coordinates.

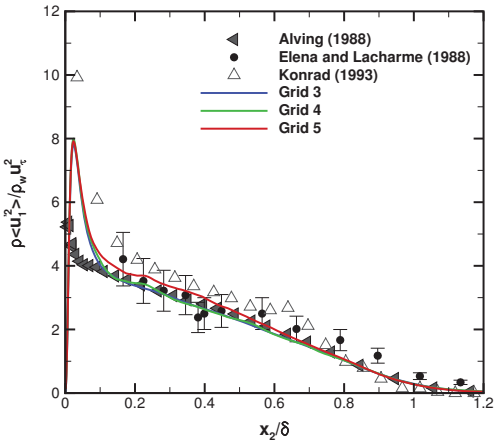

(c) Reynolds normal stress, outer coordinates.

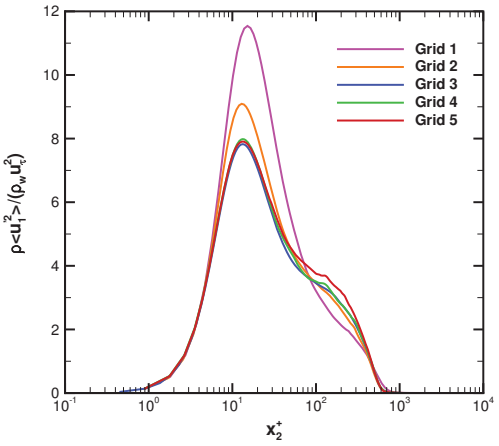

(d) Reynolds normal stress profile, inner coordinates.

Figure 4. Effect of spatial resolution on boundary layer profiles.

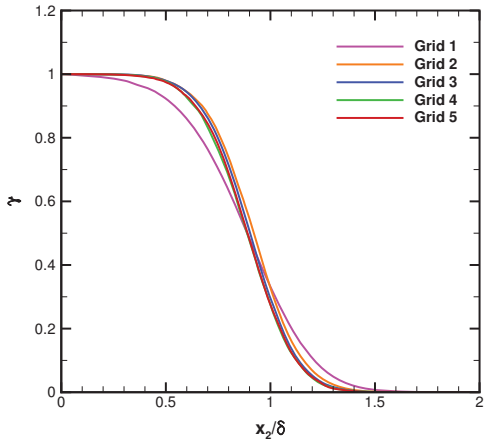

(a) Intermittency profiles through the boundary layer (threshold $0.975\rho_\infty$).

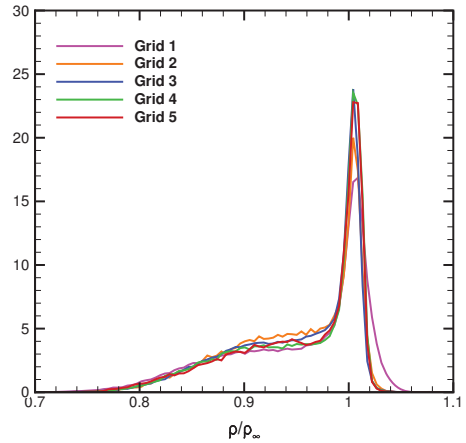

(b) Probability density function of density at $y/\delta = 0.9$.

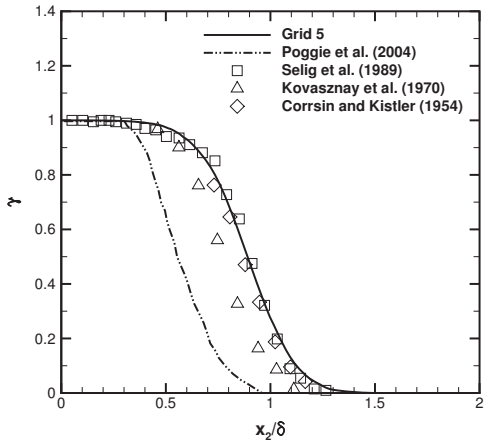

(c) Computed intermittency profile compared to hotwire measurements[7,11,91] and condensate-enhanced Rayleigh scattering data.[19]

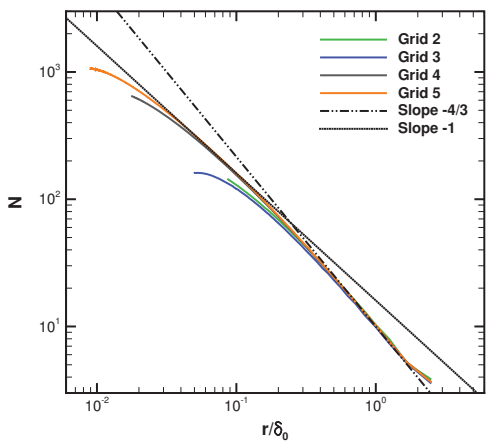

(d) Boxcounting algorithm applied to $0.975\rho_\infty$ contour.

Figure 5. Effect of spatial resolution on intermittency of the density field.

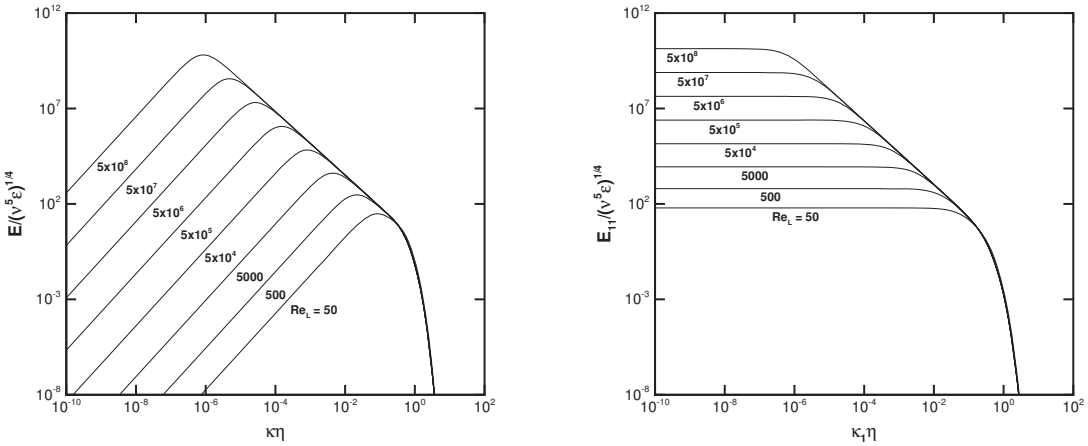

(a) Three-dimensional spectrum. (b) Longitudinal one-dimensional spectrum.

Figure 6. Pope's model spectrum[84] for isotropic turbulence.

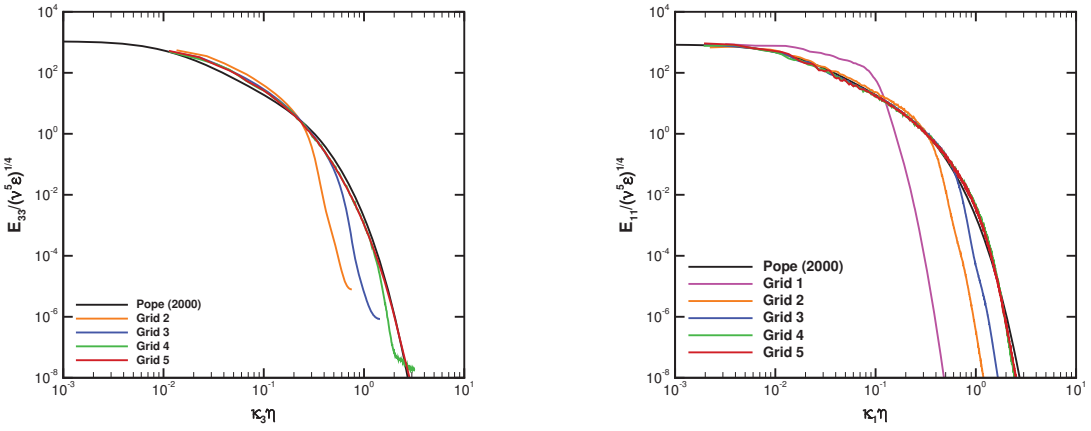

(a) Longitudinal spectrum $E_{33}(\kappa_3)$. (b) Longitudinal spectrum $E_{11}(\kappa_1)$.

Figure 7. Effect of spatial resolution on spectra at $x_1/\delta_0 = 100$, $x_2/\delta = 0.5$ for the turbulent boundary layer at $M = 2.3$. The wavenumber corresponding to the Kolmogorov length scale is $\kappa_i\eta = 2\pi \approx 6$.

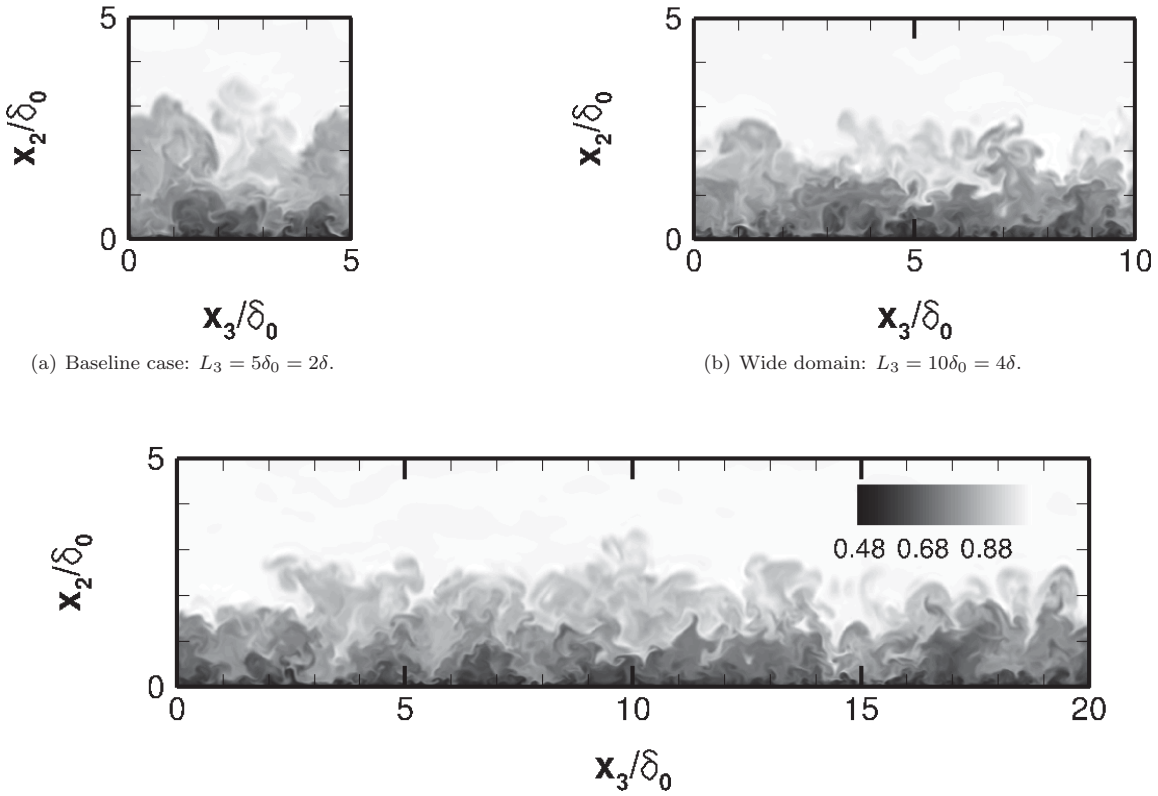

(a) Baseline case: $L_3 = 5\delta_0 = 2\delta$.

(b) Wide domain: $L_3 = 10\delta_0 = 4\delta$.

(c) Very wide domain: $L_3 = 20\delta_0 = 8\delta$.

Figure 8. Effect of domain width: sample density fields (ρ/ρ_∞) in the $x_1/\delta_0 = 100$ plane for the turbulent boundary layer at $M = 2.3$.

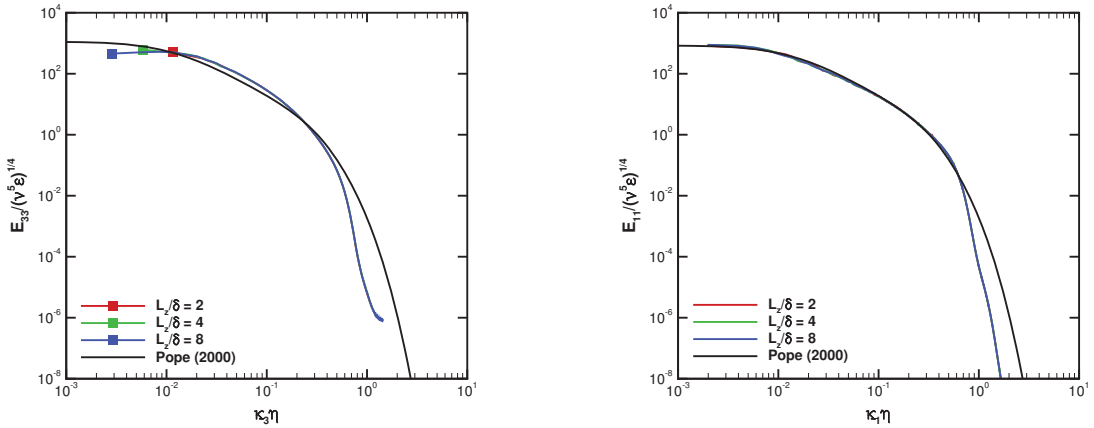

(a) Longitudinal wavenumber spectrum $E_{33}(\kappa_3)$.

(b) Longitudinal temporal spectrum $E_{11}(\kappa_1)$.

Figure 9. Effect of domain width on velocity spectra at $x_1/\delta_0 = 100$, $x_2/\delta = 0.5$ for the turbulent boundary layer at $M = 2.3$. The wavenumber corresponding to the Kolmogorov length scale is $\kappa_i\eta = 2\pi \approx 6$.

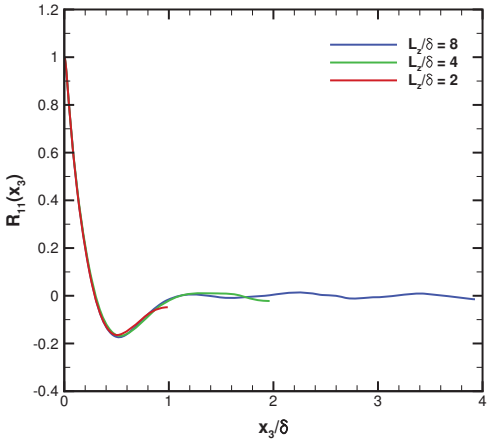

(a) Transverse spatial correlation $R_{11}(x_3)$.

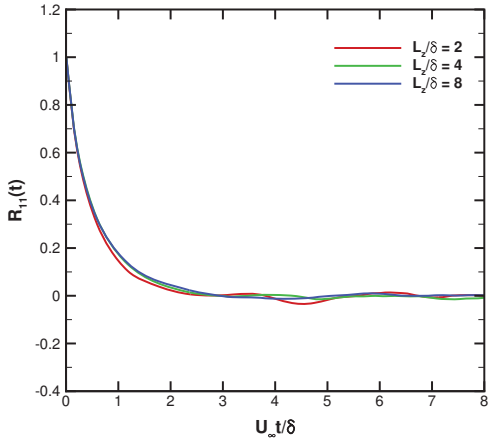

(b) Temporal correlation $R_{11}(t)$.

Figure 10. Effect of domain width on velocity correlations at $x_1/\delta_0 = 100$, $x_2/\delta = 0.5$ for the turbulent boundary layer at $M = 2.3$.

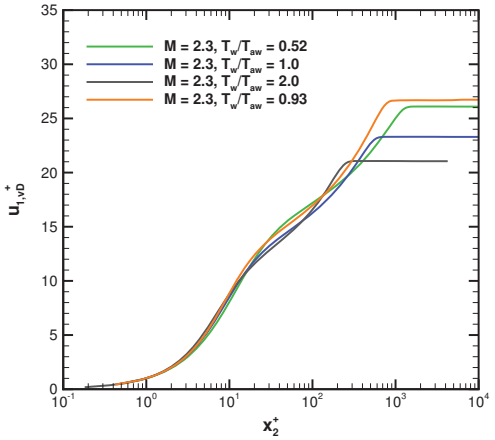

(a) Mean velocity profiles in van Driest transformed inner coordinates.

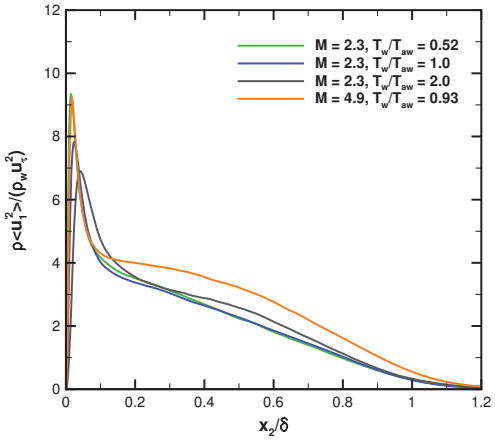

(b) Reynolds normal stress profiles in outer coordinates.

Figure 11. Test of van Driest[22] and Morkovin[21] scaling.

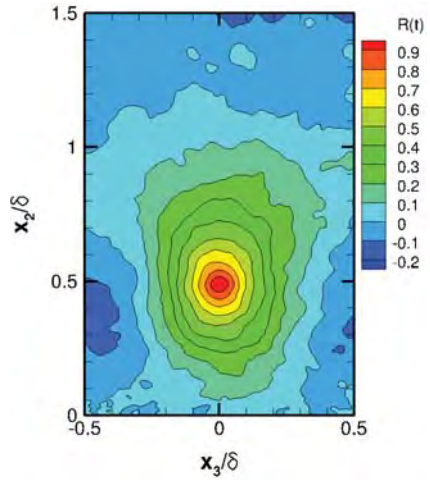

(a) Streamwise mass flux correlations in end plane $x_1/\delta_0 = 90$. $M = 2.3$, $T_w/T_{aw} = 1.0$, $\delta^+ = 560$. Reference point: $(90\delta_0, 0.5\delta, 2.5\delta_0)$.

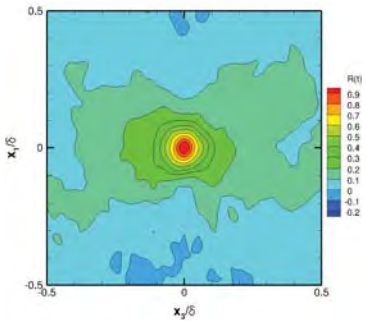

(b) Wall pressure correlations. $M = 2.3$, $T_w/T_{aw} = 1.0$, $\delta^+ = 560$. Reference point: $(90\delta_0, 0, 2.5\delta_0)$.

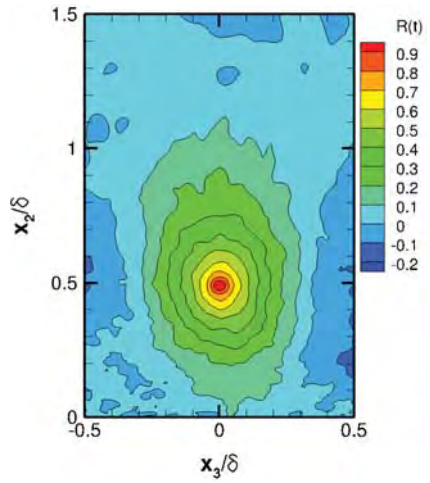

(c) Streamwise mass flux correlations in end plane $x_1/\delta_0 = 90$. $M = 4.9$, $T_w/T_{aw} = 0.93$, $\delta^+ = 730$. Reference point: $(90\delta_0, 0.5\delta, 2.5\delta_0)$.

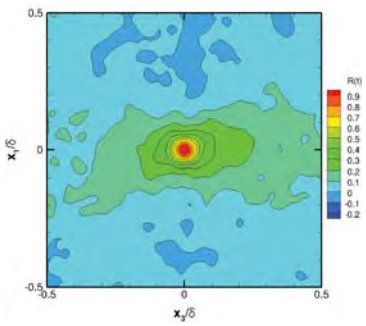

(d) Wall pressure correlations. $M = 4.9$, $T_w/T_{aw} = 0.93$, $\delta^+ = 730$. Reference point: $(90\delta_0, 0, 2.5\delta_0)$.

Figure 12. Spatial correlations: Mach number effect.

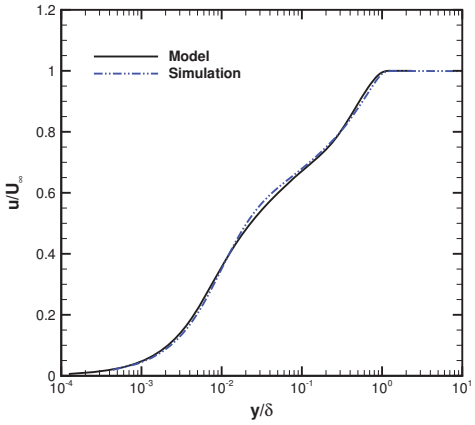

(a) $M = 2.3$, $T_w/T_{aw} = 0.52$, $\delta^+ = 1200$.

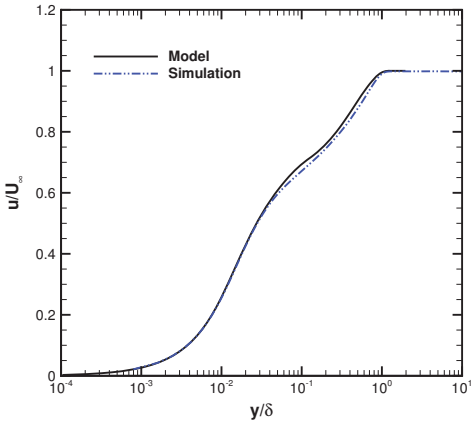

(b) $M = 2.3$, $T_w/T_{aw} = 1.0$, $\delta^+ = 560$.

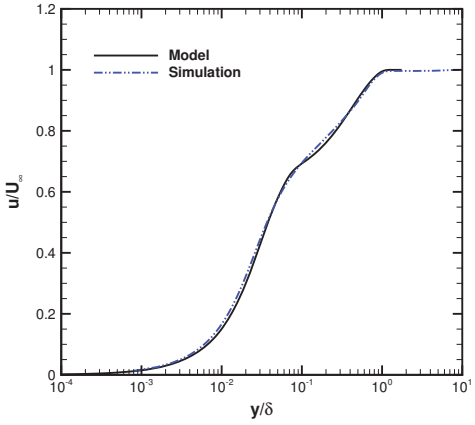

(c) $M = 2.3$, $T_w/T_{aw} = 2.0$, $\delta^+ = 250$.

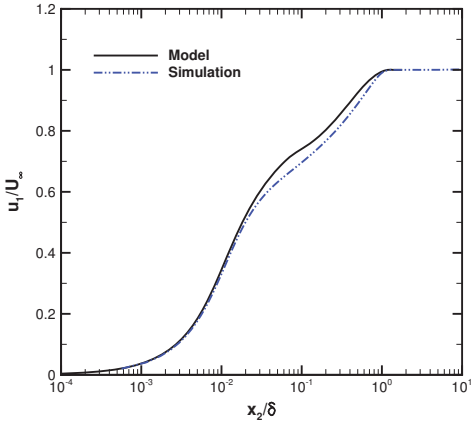

(d) $M = 4.9$, $T_w/T_{aw} = 0.93$, $\delta^+ = 730$.

Figure 13. Profiles of mean streamwise velocity.

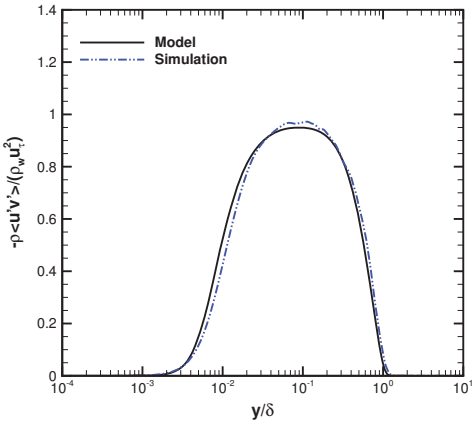

(a) $M = 2.3$, $T_w/T_{aw} = 0.52$, $\delta^+ = 1200$.

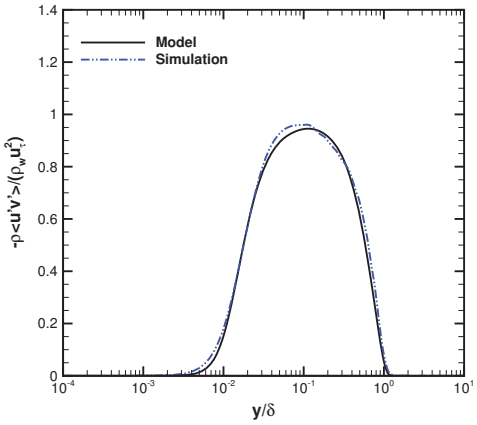

(b) $M = 2.3$, $T_w/T_{aw} = 1.0$, $\delta^+ = 560$.

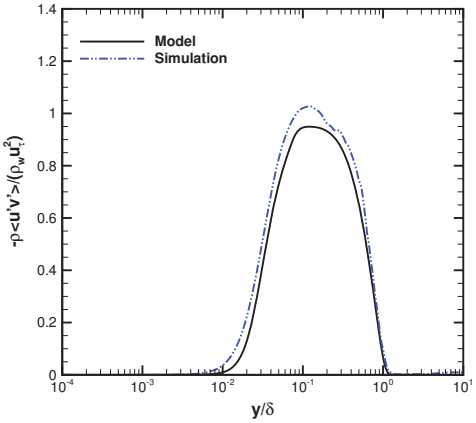

(c) $M = 2.3$, $T_w/T_{aw} = 2.0$, $\delta^+ = 250$.

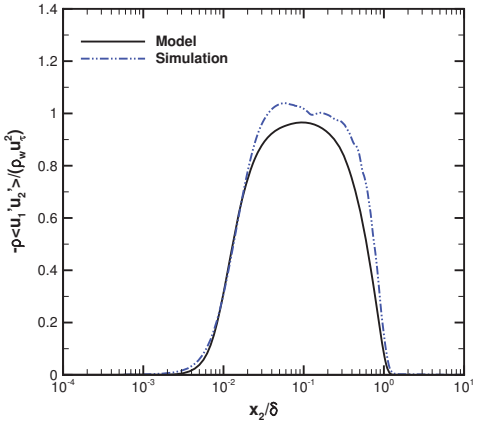

(d) $M = 4.9$, $T_w/T_{aw} = 0.93$, $\delta^+ = 730$.

Figure 14. Profiles of Reynolds shear stress.

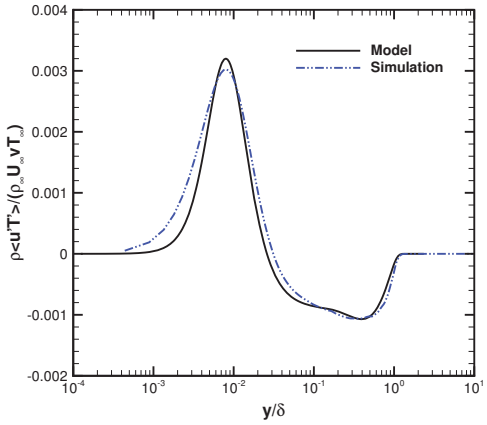

(a) $M = 2.3$, $T_w/T_{aw} = 0.52$, $\delta^+ = 1200$.

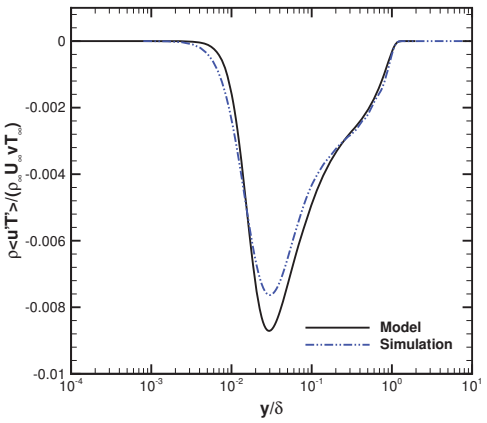

(b) $M = 2.3$, $T_w/T_{aw} = 1.0$, $\delta^+ = 560$.

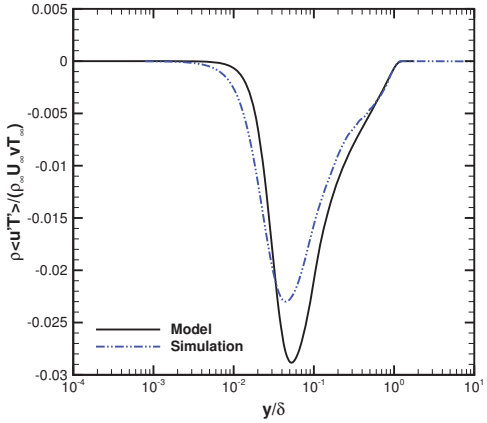

(c) $M = 2.3$, $T_w/T_{aw} = 2.0$, $\delta^+ = 250$.

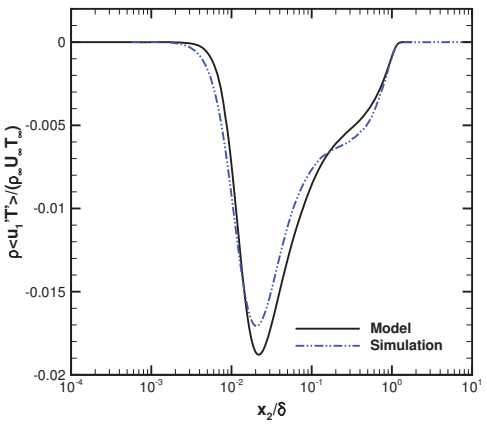

(d) $M = 4.9$, $T_w/T_{aw} = 0.93$, $\delta^+ = 730$.

Figure 15. Streamwise turbulent energy flux.

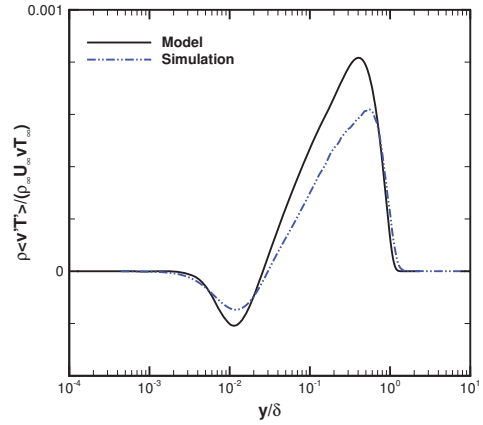

(a) $M = 2.3$, $T_w/T_{aw} = 0.52$, $\delta^+ = 1200$.

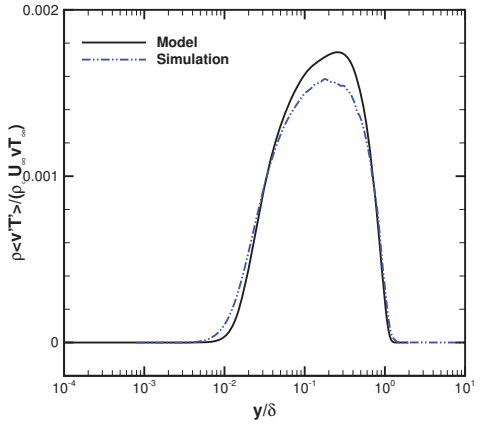

(b) $M = 2.3$, $T_w/T_{aw} = 1.0$, $\delta^+ = 560$.

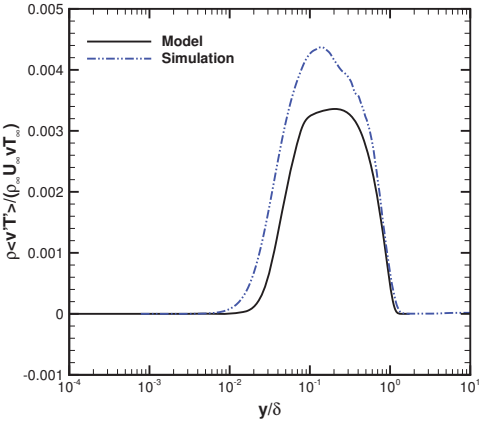

(c) $M = 2.3$, $T_w/T_{aw} = 2.0$, $\delta^+ = 250$.

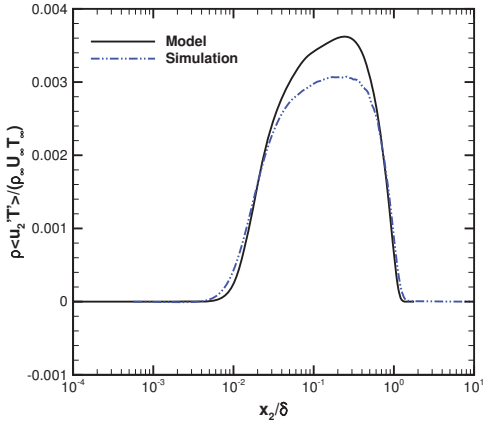

(d) $M = 4.9$, $T_w/T_{aw} = 0.93$, $\delta^+ = 730$.

Figure 16. Transverse turbulent energy flux.

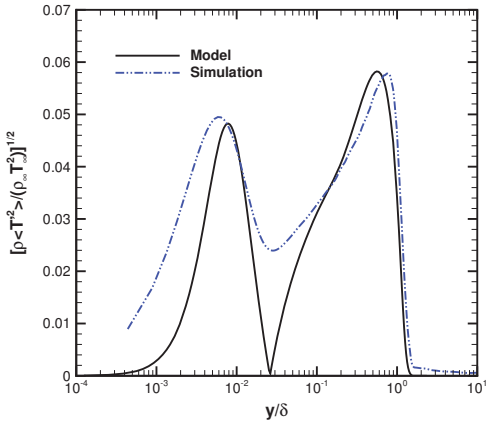

(a) $M = 2.3$, $T_w/T_{aw} = 0.52$, $\delta^+ = 1200$.

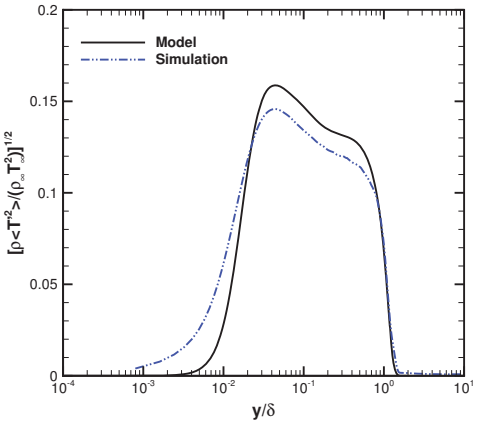

(b) $M = 2.3$, $T_w/T_{aw} = 1.0$, $\delta^+ = 560$.

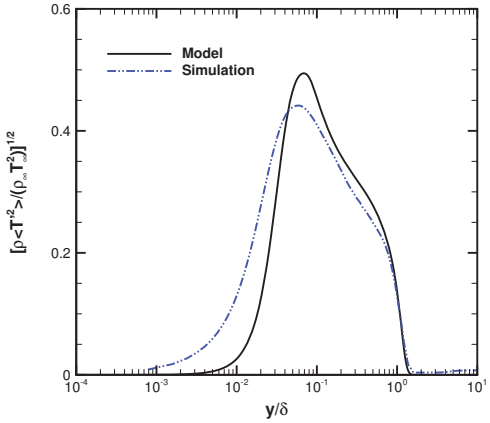

(c) $M = 2.3$, $T_w/T_{aw} = 2.0$, $\delta^+ = 250$.

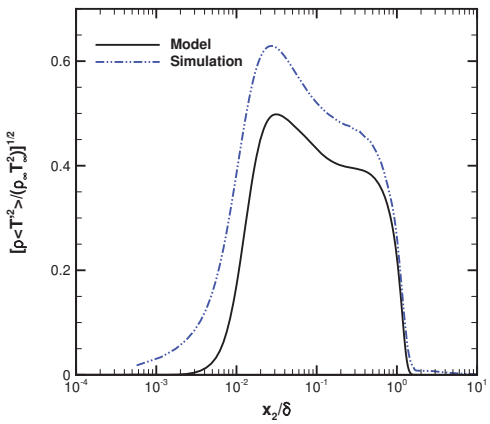

(d) $M = 4.9$, $T_w/T_{aw} = 0.93$, $\delta^+ = 730$.

Figure 17. Temperature fluctuations.

APPENDIX B
CORNER FLOWS

AIAA SciTech
13-17 January 2014, National Harbor, Maryland
52nd Aerospace Sciences Meeting

52nd AIAA Aerospace Sciences Meeting

High-Order Implicit Large-Eddy Simulations of Supersonic Corner Flow

Nicholas J. Bisek*

Air Force Research Laboratory, Wright-Patterson AFB, OH, 45433-7512, USA

Large-eddy simulations are used to investigate a supersonic wall-bounded turbulent corner flow. Solutions are obtained using a high-fidelity time-implicit numerical scheme and an implicit large-eddy simulation approach. The inclusion of the sidewall leads to the development of a corner core flow which grows in size as the flow progresses downstream. A grid resolution study, with over a billion cells for the fine grid, is performed and both mean and time-accurate statistics are analyzed. The solutions are compared to a spanwise-periodic flat-plate turbulent boundary layer developed at the same conditions and yield similar results when measured sufficiently far from the corner. Two-point autocorrelations verify that the domain's cross-sectional area is sufficient to de-correlate the corner core flow front eh turbulent equilibrium boundary-layer developed on each of the adjoining flat-plate walls. In addition, triple products are collected and demonstrate that the corner-dominated flow is significantly different from the rest of the domain.

Nomenclature

c_f	= skin-friction coefficient, $(2\,\mu_w/Re_\ell)\frac{\partial\,u}{\partial\,s}\big\vert_w$, where s is the wall normal direction
E	= total specific energy
$\mathbf{F}, \mathbf{G}, \mathbf{H}$	= inviscid vector fluxes
$\mathbf{F}_v, \mathbf{G}_v, \mathbf{H}_v$	= viscous vector fluxes
J	= transformation Jacobian
ℓ	= geometry length
M	= Mach number
p	= nondimensional static pressure
Re	= Reynolds number, $\rho_\infty\,u_\infty\,\ell/\mu_\infty$
t	= nondimensional time
T	= nondimensional static temperature
$\mathbf{U}$	= conserved variable vector
u, v, w	= nondimensional Cartesian velocity components in the x, y, z directions
x, y, z	= streamwise, normal, and spanwise directions in nondimensional Cartesian coordinates
y^+	= nondimensional wall distance normalized by local inner scales, $u_\tau\,\rho_w\,y/\mu_w$
δ	= boundary-layer thickness, $0.99\,u_\infty$
ξ, η, ζ	= computational coordinates
θ	= compressible boundary-layer momentum thickness, $\int_0^\infty \frac{\rho\,u}{\rho_\infty\,u_\infty}\left(1-\frac{u}{u_\infty}\right)\,\mathrm{d}y$
μ	= dynamic viscosity
ρ	= nondimensional density
τ_{ij}	= components of the viscous stress tensor
Subscript	
w	= wall
∞	= freestream

*Research Aerospace Engineer, AFRL/RQHF. Senior Member AIAA.

I. Introduction

Large-scale computing resources have seen steadily growth over the past several decades. The increased capacity has allowed computational researchers to explore a wide range of problems, including full-vehicle simulations,[1] tightly-coupled multi-disciplinary scenarios,[2] and even fully-resolved spatial and temporal canonical problems.[3] As such, recent research has strived towards both larger parametric studies and higher-fidelity computations in order understand both the fundamental flow physics and its general application to scenarios that extend beyond unit-sized problems (in both geometric and fluid dynamic complexities). While many aspects in the broad discipline of fluid dynamics have benefited from the buildup in computational resources, one area that has seen substantial growth is the use of large eddy simulations (LES) for supersonic flows. With many of today's supercomputing systems providing users with more than one peta floating-point operations per second (PFLOPS), LES are routinely being used to investigating three-dimensional flows with more than 10^7 grid points. In addition, the increased spatial resolution has allowed some LES research to replace subgrid-scale (SGS) closure models with higher-order numerical methods to achieve the necessary dissipation inherit to the numerical scheme.

While solving for all spatial and temporal scales via direct numerical simulation (DNS) of nominal flight vehicles at flight conditions is still beyond the reach of current computational resources, implicit LES or 'DNS-like' simulations (i.e., computations that do not use a SGS model to dissipate energy, yet have adequate resolution and high-order metrics to accurately resolve most spatial scales), have been used to study reduced problems, including shock impingement on a turbulent boundary layer (SBLI),[4–10] as illustrated in Fig. 1. While these works have shed light into the fundamental mechanisms responsible for the SBLI, a common physical phenomenon encountered in high-speed flight, the computational studies have assumed a spanwise homogeneity in the solution domain to reduce the computational requirements to a level reflective of the resources available.

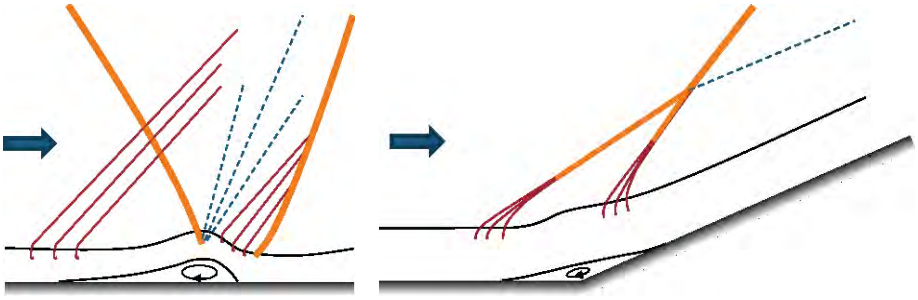

(a) Oblique impinging shock. (b) Flow over a compression corner.

Figure 1. Canonical (unit) problems developed to study SBLI.

Like the SBLI phenomenon, the streamwise corner flow is of vital importance to many applications, like the wing fuselage junction and rectangular ducts for internal flow paths, which for air-breathing SCRAM-jets may also contain a series of SBLIs. The corner flow is dominated by a strong three-dimensional inviscid-viscous interaction and has been studied numerically for several decades. One of the first inviscid calculations of a streamwise supersonic corner was performed in the 1970's by Shankar.[11] A few years later, the first Reynolds-averaged Navier-Stokes (RANS) were carried out by Hung and McCormack[12] for a fully turbulent flow, and by Shang *et al.*[13] which included a transition model. The RANS solutions showed that even the relatively simply turbulence models used were able to reasonably capture many of the bulk properties, (i.e., surface pressure and embedded shock positions), though the results could not predict unsteady properties. More recently, a detached eddy simulation (DES) by Garnier[14] investigated the corner flow as part of a larger effort to study its influence on a turbulent SBLI (which was also present in the computation). In addition, a recent LES of an SBLI by Hadjadj,[15] examined the influence of slip side-walls versus a periodic sidewall boundary condition. While slip walls are a limiting scenario, the results both from Garnier's DES[14] and Hadjadj's LES[15] showed that both the corner flow and slip sidewall had a significant influence on the bulk flow features and the accompanying SBLI. Their efforts suggest that the sidewall boundary-layer present in many configurations can be an important factor that should not be excluded from the computation. Likewise, similar observations have been seen in recent experiments by Burton and Babinsky[16] and Babinsky *et al.*[17]

The focus of the present work was to develop a methodology for generating a supersonic turbulent corner flow using a high-fidelity implicit LES approach and to investigate the effects of spatial accuracy on the solution. Two-point autocorrelations were performed to better understand the influence the symmetric boundary condition has on the computational domain. In addition, the solutions obtained were compared to previous work[10] which investigated the same flow but for a spanwise-periodic computational domain. The addition of the second viscous wall in the current work allowed for a detailed investigation of the influence the corner has on the rest of the flow.

II. Method

Flow-field results are obtained using a time-accurate three-dimensional compressible Navier-Stokes solver known as FDL3DI,[18] which has been widely used in previous calculations for both steady and unsteady, subsonic and supersonic flows.[19–25]

A. Governing Equations

The governing equations are transformed from Cartesian coordinates into a general time-dependent curvilinear coordinate system that is recast in strong conservation-law form:

$$\frac{\partial\,\mathbf{U}}{\partial\,t}+\frac{\partial\,(\mathbf{F}-\mathbf{F}_v)}{\partial\,\xi}+\frac{\partial\,(\mathbf{G}-\mathbf{G}_v)}{\partial\,\eta}+\frac{\partial\,(\mathbf{H}-\mathbf{H}_v)}{\partial\,\zeta}=\mathbf{S}_c \tag{1}$$

where t is the time and ξ, η, and ζ are the computational coordinates. The solution vector and vector fluxes (both inviscid and viscous) are:

$$\mathbf{U}=\frac{1}{J}\begin{bmatrix}\rho\\ \rho\,u\\ \rho\,v\\ \rho\,w\\ \rho\,E\end{bmatrix},\ \mathbf{F}=\frac{1}{J}\begin{bmatrix}\rho\,U\\ \rho\,u\,U+\xi_x\,p\\ \rho\,v\,U+\xi_y\,p\\ \rho\,w\,U+\xi_z\,p\\ \rho\,E\,U+\xi_{x_i}u_i\,p\end{bmatrix},\ \mathbf{F}_v=\frac{1}{Re\,J}\begin{bmatrix}0\\ \xi_{x_i}\,\tau_{i1}\\ \xi_{x_i}\,\tau_{i2}\\ \xi_{x_i}\,\tau_{i3}\\ \xi_{x_i}\,(u_j\tau_{ij}-q_i)\end{bmatrix} \tag{2}$$

and

$$U=\xi_t+\xi_{x_i}u_i,\quad V=\eta_t+\eta_{x_i}u_i,\quad W=\zeta_t+\zeta_{x_i}u_i,\quad E=\frac{T}{(\gamma-1)\ M_\infty^2}+\frac{1}{2}u_i^2 \tag{3}$$

where u, v, and w are the Cartesian velocity components, ρ is the density, p is the pressure, T is the temperature, and γ is the specific heat ratio and is 1.4 for air. J is the transformation Jacobian, $\partial(\xi,\eta,\zeta,t)/\partial(x,y,z,t)$.[26] Note that the formulas for $\mathbf{G}$, $\mathbf{G}_v$, $\mathbf{H}$, and $\mathbf{H}_v$ are similar to those specified in Eqn. (2).

The source vector, $\mathbf{S}_c$, on the right side of Eqn. (1), is typically set to zero, but has nonzero values at specific locations within the domain to transition the flow to fully turbulent. This work using the counter-flow force bypass transition method developed by Mullenix *et al.*[27] for supersonic flows, since the method uses a broad-band disturbance to transition the flow, it does not introduce any discrete frequencies into the domain.

All length scales are nondimensionalized by the reference length, ℓ, and all dependent variables are normalized by their respective reference values, expect for pressure, which is nondimensionalized by $\rho_\infty u_\infty^2$. The perfect gas relationship and Sutherland law for the molecular viscosity were employed with a reference temperature of 110.3 K for Sutherland's molecular viscosity.

B. The Numerical Method

For this extended abstract, time-accurate solutions to Eqn. (1) were obtained numerically by the implicit approximately-factored finite-difference algorithm of Beam and Warming,[28] employing Newton-like subiterations,[29] which has evolved as an efficient tool for generating solutions to a wide variety of complex fluid flow problems, and may be written as follows:

$$\left[\frac{1}{J}+\left(\frac{2\Delta t}{3}\right)\delta_{\xi 2}\left(\frac{\partial\mathbf{F}^p}{\partial\boldsymbol{Q}}-\frac{1}{Re}\frac{\partial\mathbf{F}_v^p}{\partial\boldsymbol{Q}}\right)\right]J\times\left[\frac{1}{J}+\left(\frac{2\Delta t}{3}\right)\delta_{\eta 2}\left(\frac{\partial\mathbf{G}^p}{\partial\boldsymbol{Q}}-\frac{1}{Re}\frac{\partial\mathbf{G}_v^p}{\partial\boldsymbol{Q}}\right)\right]J\times$$

$$\left[\frac{1}{J}+\left(\frac{2\Delta t}{3}\right)\delta_{\zeta 2}\left(\frac{\partial \mathbf{H}^p}{\partial \boldsymbol{Q}}-\frac{1}{Re}\frac{\partial \mathbf{H}_v^p}{\partial \boldsymbol{Q}}\right)\right]\Delta \boldsymbol{Q}=-\left(\frac{2\Delta t}{3}\right)\left[\left(\frac{1}{2\Delta t}\right)\left(\frac{3\boldsymbol{Q}^p-4\boldsymbol{Q}^n+\boldsymbol{Q}^{n-1}}{J}\right)\right]$$
$$+\delta_{\xi 6}\left(\mathbf{F}^p-\frac{1}{Re}\mathbf{F}_v^p\right)+\delta_{\eta 6}\left(\mathbf{G}^p-\frac{1}{Re}\mathbf{G}_v^p\right)+\left[\delta_{\zeta 6}\left(\mathbf{H}^p-\frac{1}{Re}\mathbf{H}_v^p\right)-\mathbf{S}_c^p\right] \tag{4}$$

Equation (4) is employed to advance the solution in time, such that $\boldsymbol{Q}^{p+1}$ is the $p+1$ approximation to $\boldsymbol{Q}$ at the $n+1$ time level $\boldsymbol{Q}^{n+1}$, and $\Delta \boldsymbol{Q}=\boldsymbol{Q}^{p+1}-\boldsymbol{Q}^p$. For $p=1$, $\boldsymbol{Q}^p=\boldsymbol{Q}^n$. Second-order-accurate backward-implicit time differencing was used to obtain temporal derivatives.

The implicit segment of the algorithm (left-hand side of Eqn. (4)), incorporates second-order-accurate centered differencing for all spatial derivatives, and utilizes nonlinear artificial dissipation[30] to augment stability. For simplicity, the dissipation terms are not shown in Eqn. (4). Efficiency is enhanced by solving this implicit portion of the factorized equations in diagonalized form.[31] Unfortunately, the temporal accuracy can be degraded when the diagonal form is used, so subiterations are employed within each time step to minimize any degradation of the temporal solution. Any deterioration of the solution caused by use of artificial dissipation and by lower-order spatial resolution of implicit operators is also reduced by subiterating the time advancement. Three subiterations per time step were applied throughout this work to preserve second-order temporal accuracy.

The compact difference scheme is employed on the right-hand side of Eqn. (4). It is based upon the pentadiagonal system of Lele,[32] and is capable of attaining spectral-like resolution. This is achieved through the use of a centered implicit difference operator with a compact stencil, thereby reducing the associated discretization error. For the present computations, a sixth-order tridiagonal subset of Lele's system is utilized, which is illustrated here in one spatial dimension as:

$$\frac{1}{3}\left(\frac{\partial \mathbf{F}}{\partial \xi}\right)_{i-1}+\left(\frac{\partial \mathbf{F}}{\partial \xi}\right)_i+\frac{1}{3}\left(\frac{\partial \mathbf{F}}{\partial \xi}\right)_{i+1}=\frac{14}{9}\left(\frac{\mathbf{F}_{i+1}-\mathbf{F}_{i-1}}{2}\right)+\frac{1}{9}\left(\frac{\mathbf{F}_{i+2}-\mathbf{F}_{i-2}}{4}\right) \tag{5}$$

The scheme has been adapted by Visbal and Gaitonde[33] as an implicit iterative time-marching technique, applicable for unsteady vortical flows, and has been used to obtain the spatial derivative of any scalar, flow variable, metric coefficient, or flux component. It is used in conjunction with a low-pass Padé-type non-dispersive spatial filter developed by Gaitonde et al.,[34] which has been shown to be superior to the use of explicitly added artificial dissipation for maintaining both stability and accuracy on stretched curvilinear meshes.[33] The filter is applied to the solution vector sequentially in each of the three computational directions following each subiteration, and is implemented in one dimension as:

$$\alpha_f \hat{\boldsymbol{Q}}_{i-1}+\hat{\boldsymbol{Q}}_i+\alpha_f \hat{\boldsymbol{Q}}_{i+1}=\sum_{n=0}^{4}\frac{a_n}{2}(\boldsymbol{Q}_{i+n}+\boldsymbol{Q}_{i-n}) \tag{6}$$

where $\hat{\boldsymbol{Q}}$ designates the filtered value of $\boldsymbol{Q}$. The filtering operation is a post-processing technique, applied to the evolving solution in order to regularize features that are captured, but poorly resolved. On uniform grids, the filtering procedures preserve constant functions while completely eliminating the odd-even mode decoupling.[23,35] Equation (6) represents a one-parameter family of eighth-order filters, where numerical values for the a_n's may be found in Ref. 18. The filter coefficient α_f is a free adjustable parameter which may be selected for specific applications, where $\mid \alpha_f \mid < 0.5$. The value of α_f determines sharpness of the filter cutoff and has been set to 0.30 for the present simulations.

C. The LES Approach

In the LES approach, physical dissipation at the Kolmogorov scale is not represented, thereby allowing for less spatial resolution and a savings in computational resources. For non-dissipative numerical schemes, without use of SGS models, this leads to an accumulation of energy at high mesh wave numbers, and ultimately to numerical instability. Traditionally, explicitly added SGS models are then employed as a means to dissipate this energy. In the present methodology, the effect of the smallest fluid structures is accounted for by a high-fidelity implicit large-eddy simulation (HFILES) technique, which has been successfully utilized for a number of turbulent and transitional computations. The present HFILES approach was first introduced by Visbal et al.[35,36] as a formal alternative to conventional methodologies, and is predicated upon the high-order compact differencing and low-pass spatial filtering schemes, without the inclusion of additional

SGS modeling. This technique is similar to monotonically integrated large-eddy simulation (MILES)[37] in that it relies upon the numerical solving procedure to provide the dissipation that is typically supplied by conventional SGS models. Unlike MILES however, dissipation is contributed by the aforementioned high-order Padé-type low-pass filter only at high spatial wavenumbers where the solution is poorly resolved. This provides a mechanism for the turbulence energy to be dissipated at scales that cannot be accurately represented on a given mesh system, in a fashion similar to subgrid modeling. For purely laminar flows, filtering may be required to maintain numerical stability and preclude a transfer of energy to high-frequency spatial modes due to spurious numerical events. The HFILES methodology thereby permits a seamless transition from large-eddy simulation to direct numerical simulation as the resolution is increased. In the HFILES approach, the unfiltered governing equations may be employed, and the computational expense of evaluating subgrid models, which can be substantial, is avoided. This procedure also enables the unified simulation of flow-fields where laminar, transitional, and turbulent regions simultaneously coexist.

It should also be noted that the HFILES technique may be interpreted as an approximate deconvolution SGS model,[38] which is based upon a truncated series expansion of the inverse filter operator for the unfiltered flow-field equations. Mathew *et al.*[39] have shown that filtering provides a mathematically consistent approximation of unresolved terms arising from any type of nonlinearity. Filtering regularizes the solution, and generates virtual subgrid model terms that are equivalent to those of approximate deconvolution.

III. Supersonic Turbulent Corner

In the current work, the supersonic flow transitioned from laminar to turbulent on each of the two adjoining flat plates. This scenario is necessary for the development of a fully-turbulent corner boundary layer flow, which can then be used to facilitate coupled analysis of turbulent corner flow over various geometries, such as a SBLI initiated by the inclusion of a compression corner or an impinging shock.

The flow in the present simulations is consistent with previous studies by Rai *et al.*,[4] Rizzetta and Visbal,[40] Pirozzoli and Grasso,[6] and Bisek *et al.*,[10] which investigated supersonic flow on a flat plate at Mach 2.25, with the notable exception that the present effort includes a second wall, while all previous studies assumed spanwise-periodic boundary conditions. In addition, the previous studies employed an extrapolated upper boundary condition to accommodate the growing boundary-layer, whereas the the current work employed symmetric boundary conditions for the boundaries opposite both of the walls, as seen in Fig. 2. The inclusion of the second wall and accompanying symmetry boundary conditions makes the current work representative of an isolator section of a scram-jet flow path.

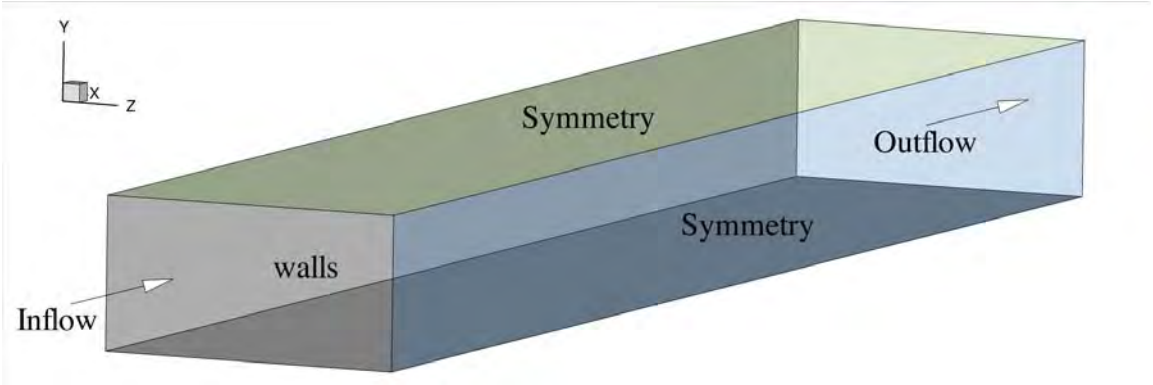

Figure 2. Cartoon of the boundary conditions for supersonic flow over a corner.

The inflow boundary prescribed in this work was developed in two steps. First, a solution to the compressible laminar boundary-layer equations[41] was used to specify the boundary-layer profile on each wall, with the boundary-layer height scaled to the reference length, $\ell = 6.096 \times 10^{-4}$ m, and freestream conditions applied outside the boundary-layer. Near the corner junction (i.e., y, $z < 1$), a wall-distance-weighted average (from both walls), was used to smoothly transition the prescribed flow between the two flat-plate compressible laminar boundary-layer profiles. Next, this initial laminar solution was evolved for a streamwise

distance of $50\,\ell$, which allowed the profile to adjust to a steady-state solution. Note that only minor changes where observed (primarily near the corner). A solution slice was extracted at $x = 50\,\ell$ plane and rescaled so the boundary-layer height above each plate was approximately equal to the reference length, ℓ. This plane was used as the incoming laminar inflow.

An extrapolated boundary-condition was used at the outflow boundary. Along the wall surface, a no-slip velocity boundary condition was imposed with an isothermal wall set to the nominal adiabatic wall temperature. The surface pressure was computed by enforcing a zero wall-normal derivative to third-order spatial accuracy. The reference conditions for the case are listed in Table 1, which were based on a 1955 experiment by Shutts *et al.* (Case 55010501).[42]

Table 1. Flow conditions for Mach 2.25 air flow over a flat plate.

Parameter	Value	
M	2.249	
u_∞	588	m/s
T_∞	169	K
T_w	322	K
p	23,830	Pa
Re/m	2.5×10^7	m^{-1}
Re_θ	2930-5300	

The necessary reference conditions for the nondimensional fluid code FDL3DI were $\ell = 6.096 \times 10^{-4}$ m, $u_\infty = 588$ m/s, M= 2.249, and $Re_\ell = 15,240$. These values were identical to the ones used in the spanwise-periodic simulations previously studied.[10] In the analysis of the results that follow, the solution flow variables were decomposed into time-mean and fluctuating components (i.e., $u = \bar{u} + u'$, where u' is the fluctuating component). Time-average and time-dependent data were collected for five flow-through times (unless otherwise noted), where one flow-through time is defined as the time for the freestream flow to traverse the resolved portion of computational domain. Solutions were obtained using a nondimensional time-step, $\Delta t = 0.002$, which results in $\Delta t^+ = Re_\ell(\frac{u_\tau}{u_\infty})^2(\frac{u_\infty\, t}{\ell}) = 0.076$ at the end of the resolved streamwise domain ($x = 80\,\ell$).

A. Grid Development

Using the parameters listed in Table 1, a computational domain was developed to support LES using the guidelines recommended by Georgiadis *et al.*[43] As previously mentioned, the reference length, ℓ, was set to the incoming boundary-layer height (i.e., $\ell = \delta_{x=0}$ away from the corner), and a Cartesian coordinate system was established with its origin corresponding to the upstream corner location of the computational domain. The streamwise extent of the domain was approximately $130\,\ell$, although the last $50\,\ell$ was stretched to dissipate any structures before reaching the extrapolated exit boundary condition. Figure 3 shows both side and head-on views of the grid. Note that only 1/5 of the coarse grid points are included for clarity.

The streamwise grid distribution starts at $x = 0\,\ell$ with a spacing of $\Delta x = 0.2\,\ell$. As seen in the $x-y$ view in Fig. 3(a), the streamwise grid spacing was monotonically refined from the leading edge to $x = 2\,\ell$ using 30 points. The $x = 2\,\ell$ location corresponded to the start of the highly-refined grid needed to accommodate the bypass-transition method developed by Mullenix *et al.*[27] The refined section was $1.0\,\ell$ long and contained 101 uniformly-spaced points. The grid points were monotonically coarsened from $x = 3\,\ell$ to $x = 5\,\ell$ using 40 additional points. From $x = 5\,\ell$ to $x = 80\,\ell$ a constant streamwise grid spacing of $\Delta x = 0.15\,\ell$ was used for the coarse grid. Finally, the grid was monotonically coarsened for the last $50\,\ell$ using 54 points. Note that grid stretching was not allowed to exceed 10% between subsequent grid points. As such, the coarse grid contained 725 streamwise points.

The bypass-transition region developed for the coarse grid was found to have sufficient resolution to support the trip process, so the refined grids were primarily refined in the constant region (i.e., $5\ell \le x \le 80\ell$). As such, the medium resolution grid had a constant spacing of $\Delta x = 0.1\,\ell$ between $5\,\ell \le x \le 80\,\ell$ and had a total of 977 streamwise points once the various transition regions were adjusted to accommodate the finer

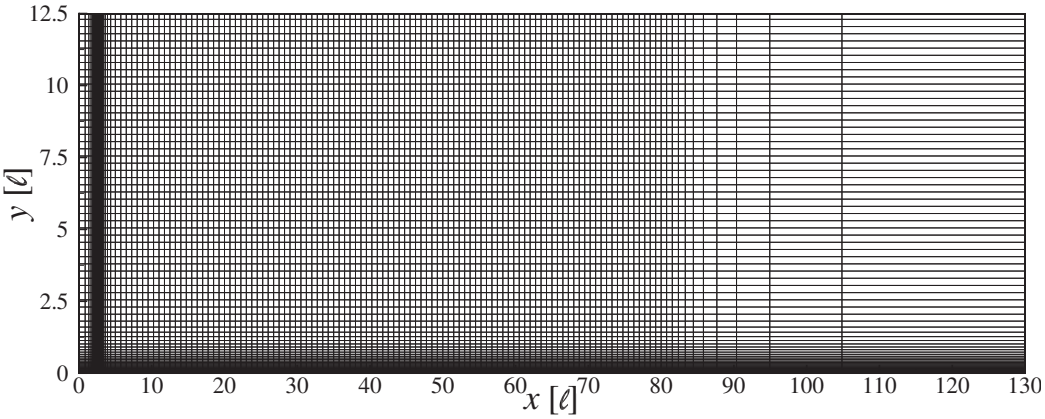

(a) $x - y$ (side) view.

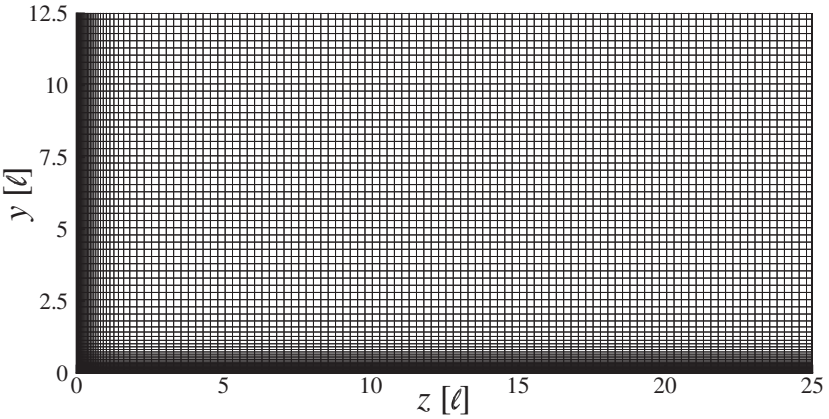

(b) $y - z$ (front) view.

Figure 3. Schematic of the computational domain.

grid. The fine resolution grid has a constant spacing of $\Delta x = 0.075\,\ell$ between $5\,\ell \leq x \leq 80\,\ell$ and a total of 1235 streamwise points.

The grid spacing for both wall-normal directions (i.e., the y and z directions), was developed in a similar manner to facilitate the development of the fully-turbulent boundary-layer profiles on both walls. Grid spacing in the normal direction was specified at the wall boundary such that $y_w^+ < 1$. The grid was monotonically stretched using a hyperbolic tangent expansion and 145 points until $y = 2\,\ell$ (i.e., $\Delta y = 0.003\,\ell$ at $y = 0$ and $\Delta y = 0.05\,\ell$ at $y = 2\,\ell$). A constant grid spacing of $\Delta y = 0.05\,\ell$ was used from $y = 2\,\ell$ to $y = 12.5\,\ell$.

The grid spacing in the spanwise direction was specified at the wall boundary such that $z_w^+ < 1$, then monotonically stretched using a hyperbolic tangent expansion using 145 points until $z = 2\ell$ (i.e., $\Delta z = 0.003\ell$ at $z = 0$ and $\Delta z = 0.05\,\ell$ at $z = 2\,\ell$). The rest of the grid distribution used a constant grid spacing of $\Delta z = 0.05\,\ell$ from $z = 2\,\ell$ to $z = 25\,\ell$.

As seen in $y - z$ view in Fig. 3(b), this approach resulted in the majority of the grid points being located within each boundary-layer, yet the grid distribution still provided high resolution outside the boundary layer to accommodate acoustic disturbances as they travelled through the inviscid core flow and where reflected back into the domain by the symmetry planes ($\Delta y^+ = \Delta z^+ \approx 11$, for $y > 2\,\ell$ and $z > 2\,\ell$ for the coarse resolution grid). The coarse grid contained 355 points in the $y-$direction and 605 points in the $z-$direction for a total of 156×10^6 points.

The medium resolution had 1.5 times the resolution of the coarse grid in both the y and z directions. The grid contained 473 points the y-direction with 193 points for the first $2\,\ell$ (i.e., $\Delta y = 0.00225\,\ell$ at $y = 0$ and $\Delta y = 0.0375\,\ell$ for $y \geq 2\,\ell$). Likewise, the medium grid had 805 streamwise points with 193 points in the

first $2.05\,\ell$ (i.e., $\Delta z = 0.00225\,\ell$ at $z = 0$ and $\Delta y = 0.0375\,\ell$ for $z \geq 2.05\,\ell$), for a total of 372×10^6 points. The fine grid had twice the resolution of the coarse grid in both the y and z directions, so it required 709 points in the $y-$direction and 1209 points in the $z-$direction, for a total of 1059×10^6 points.

A five-point overlap was used to decompose the grid onto the processors to maintained high-order differencing and filtering between computational blocks. The coarse grid carried out the simulation using 3000 processors, the medium grid with 4860 processors, and the fine grid used 13440 processors. It is important to note that it was necessary to use high core-counts in order to fit the problem in memory and obtain results in a reasonable wall time. That said, using so many processors simultaneously generates additional complexities, like data management and potential system latency issues during the message-passing and I/O subroutines. As such, great care was taken to ensure the simulations ran at a very high efficiency, resulting in very minimal ($\approx 6\%$), performance degradation for the fine grid simulation compared to the coarse grid.

While the concept of grid independence does not exist for LES,[44] it is possible to show that some of the time-mean quantities converge, or approach convergence, with adequate resolution. This occurs because grid refinement allows for finer features to be captured, thus changing the instantaneous data, while bulk quantities that are time-averaged, and less sensitive to the behavior of the fine structures, should converge. Note that some statistics, such as the those characteristic of the viscous super-layer, would not be adequately captured expect in true DNS, where all the length and time scales are fully resolved everywhere in the flow. The grids used in the current work have similar resolution to the flat-plate portion of the 'coarse', 'medium', and 'fine' grids used in previous work by Bisek *et al.*[10] In that work, the turbulent equilibrium boundary-layer was achieved at $x = 60\,\ell$ with a Reynolds number momentum-thickness, $Re_\theta = 2000$.

B. Features of the Instantaneous Flow

Figure 4 plots instantaneous iso-surfaces of the incompressible Q-criterion[45] ($\mathrm{Q}_{\mathrm{criterion}} = \frac{1}{2}\left[\Omega^2 - \mathbf{S}^2\right] = 1$), colored by the u-velocity. The Q-criterion is the second invariant of the velocity gradient tensor, which compares the vorticity, Ω, to the strain-rate, $\mathbf{S}$. The Q-criterion is commonly used to highlight organized structures in turbulence, especially for wall-bounded turbulent flows where the large streamwise velocity gradient can hide vorticity due to vortex motion if vorticity magnitude iso-surfaces were used in its place. The figure also includes a slice of the instantaneous nondimensional pressure contours (grey-scale), at $x = 80\ell$ to highlight the acoustic radiation being generated by the turbulent boundary-layer as it evolves.

The location of the counter-flow trip (i.e., the bypass-transition method), is apparent at the beginning of each the sub-figures in Fig. 4, as seen as blue structures. The strength of the counter-flow trip model was controlled through a scalar, $D_c = 5.5$, as described by Mullenix *et al.*,[27] which was less than the $D_c = 6.1$ value used in the previous flat plate simulations[10] for a similar flow. A lower value was selected because the inclusion of the second wall aided in transition. It is important to note the bypass-transition trip was excluded from the corner region (i.e., $y < 1.25\,\ell$ or $z < 1.25\,\ell$), to ensure that the transition process in the corner flow was not driven by the counter-flow body force trip. In addition, it was unclear how the lower momentum corner flown would react when the model's momentum addition.

The disturbances introduced by the trip grow along each flat plate wall until they have convected a sufficient distance downstream ($\approx 10 - 40\,\ell$ from the trip), to have grown enough to transition to a fully turbulent flow. As the transitional flow travels downstream, the turbulent structures spread and convect into the corner, which aids in its transition to a turbulence state. As expected, and as seen in previous work,[10] the refined grids transition sooner since the additional resolution supported a larger range of scales.

A close investigation of of the instantaneous pressure slice shown in the subplots of Fig. 4 shows a lot of δ-scale structures, which is particularly obvious in Fig. 4(a), since the sub-figure does not have as many small scales hair-pin iso-surface structures to mask the strong pressure gradients near the boundary-layer edge. Likewise, the greyscale pressure contours at the $x = 80\,\ell$ plane shows a lot of fine-scale acoustic disturbances traveling in the inviscid core region of the flow for each scenario.

C. Features of the Time-Mean Flow

Time-average statistics were collected for ten flow-through times on the coarse grid. Note one flow-through time is defined as the time for the freestream flow to traverse the resolved portion of the computational domain (i.e., one flow-through time required 40,000 iterations since the resolved streamwise domain was $80\,\ell$ long and a nondimensional time-step $\Delta t = 0.002$ was used). Figure 5(a) shows surface contours of the time-mean skin-friction coefficient, c_f, and a $y - z$ slice at $x = 80\,\ell$ highlighting the boundary-layer

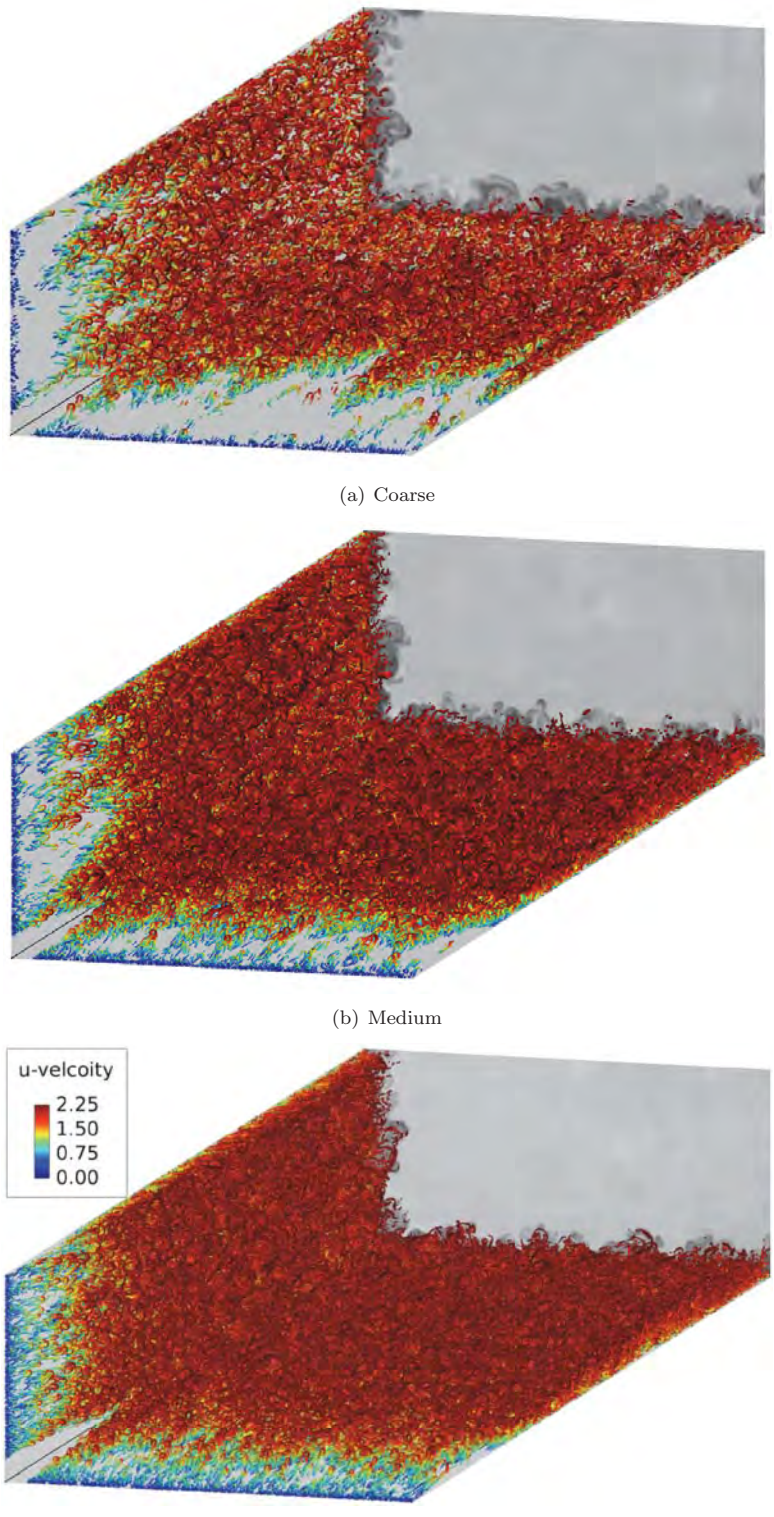

(a) Coarse

(b) Medium

(c) Fine

Figure 4. Instantaneous iso-surfaces of the Q-criterion colored by the u-velocity and a slice of pressure contours at $x = 80\,\ell$ for Mach 2.25 turbulent air over a corner. Note the solution for $x < 3\,\ell$ was excluded for clarity.

thickness, δ. In addition, Fig. 5 includes line plots of the skin-friction coefficient at select locations on both walls, which have been averaged over three different time lengths for the coarse grid.

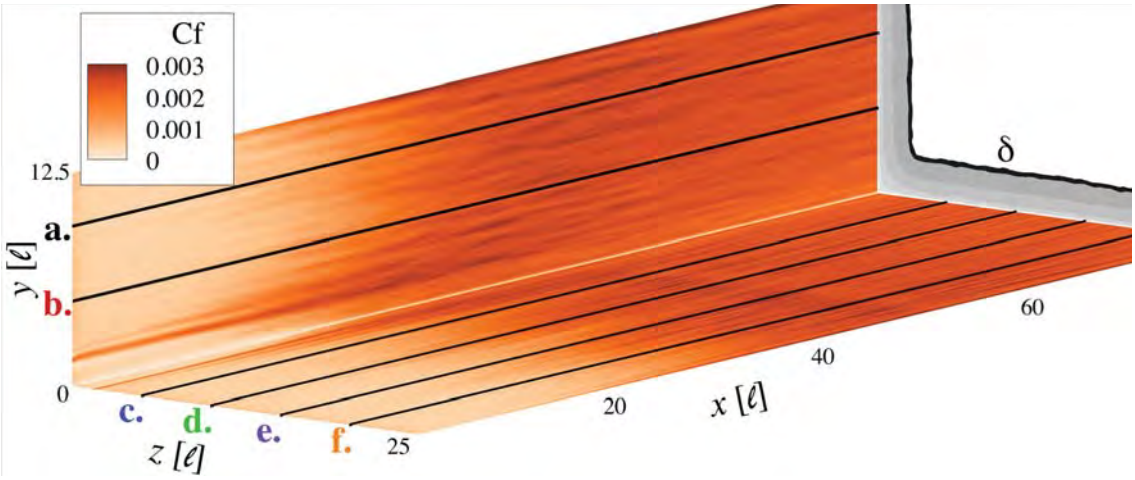

(a) Averaged over 5 flow-through times.

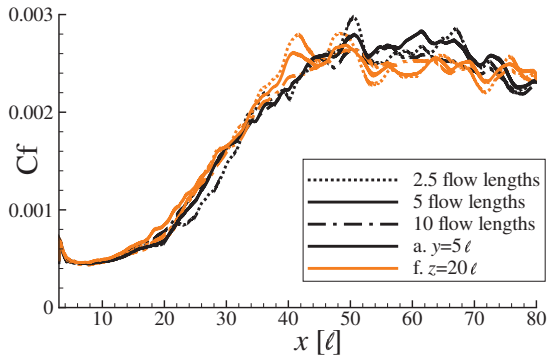

(b) Lines **a** ($y = 5\,\ell$) and **f** ($z = 20\,\ell$) for various time-averages.

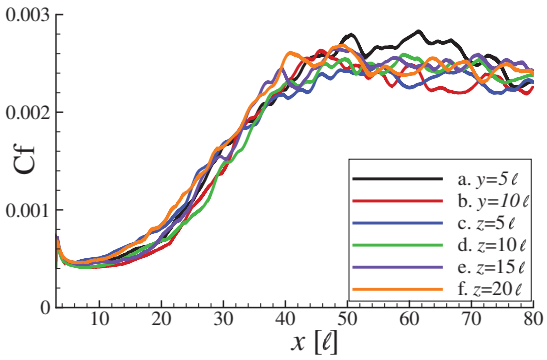

(c) Time-mean from 5 flow-through times.

Figure 5. Surface contours of the time-mean skin-friction coefficient, c_f, and an $x - y$ slice identifying the boundary-layer thickness, δ, at $x = 80\,\ell$ for various time-averages and specific wall locations on the coarse grid.

A close examination of the Fig. 5(b) shows minor differences in the solutions with the most noticeable changes observed between the time-mean solutions collected from 2.5 and 5 flow-through times, respectively. While averaging the solution over five addition flow-through times further refined the resulting profiles, the slight changes in the solutions could not warrant the large increase in computational cost. As such, the time-averaged results from 5 flow-through times was considered to be sufficient and the remaining analysis and time-mean results are based on 5 flow-through times of data. Figure 5(c) shows that the skin-friction profile was very similar for a majority of both plate surfaces. Note that a close examination of Fig. 5(a) shows that while the majority of the flow is represented by lines **a.** to **f.**, transition begins closer to the trip near the corner (due to the introduction of a spanwise instability, since the counter-flow trip was sharply turned off near the corner).

As seen in Fig. 6, the incoming laminar flow is disturbed by the counter-flow trip (centered at $x = 2.5\,\ell$). The trip was strong enough to produce a small separated region (not shown), which rapidly recovers back to a positive skin-friction coefficient value (i.e., the flow reattached as it adjusts from the trip). In the same region, the trip-induced separation generated broadband small-scale instabilities which grew nonlinearly as the flow convects downstream. The transitioning flow approached the theoretical curve for equilibrium turbulence near $x \sim 40\,\ell$ for the coarse grid. The theoretical curves in the figure correspond to the laminar compressible Blasius solution[41] and the turbulent correlation of White and Christoff.[41] From Fig. 6 it is clear that the medium and fine grid solutions start transiting the flow about the same distance downstream

from the trip, though the fine grid solution has a slightly steeper curve and reaches the theoretical curve for an equilibrium turbulent boundary-layer sooner.

Since the fine solution transitioned slightly sooner, it achieved a slighter higher Reynolds number based on the boundary-layer momentum thickness, Re_θ, by the end of the computational domain. Similar behavior was observed in previous, spanwise-periodic, work,[10] where the solution from the higher resolution scenario was slightly different compared to the coarse grid. Note that while the boundary-layer momentum thickness was higher for the two higher resolution scenarios, all three grids had a boundary-layer thickness, $\delta \approx 2.4\,\ell$ at $x = 80\,\ell$.

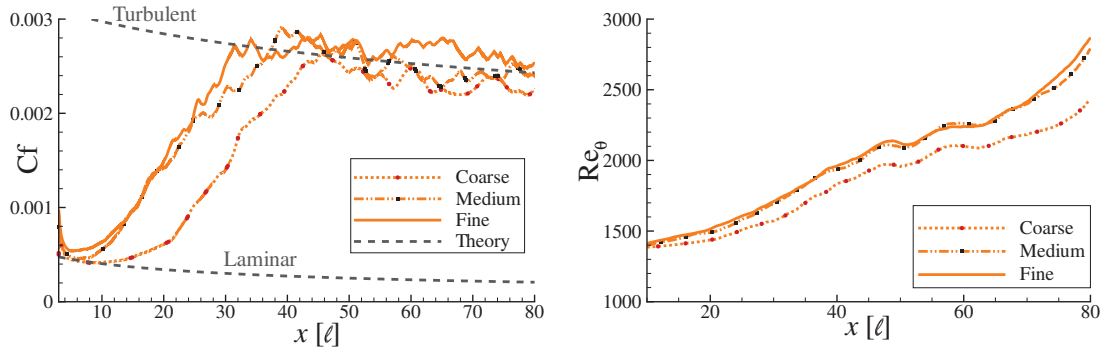

(a) Skin-friction coefficient.

(b) Reynolds number based on the boundary-layer momentum-thickness.

Figure 6. Time-mean skin-friction coefficient, c_f, and Reynolds number based on the boundary-layer momentum-thickness, Re_θ, for various grids and theoretical correlations along line f ($z = 20\,\ell$).

The streamwise velocity profile was transformed using the van Driest transformation.[46] The transformed streamwise velocity was nondimensionalized by the wall friction velocity, $u^+ = u_{\mathrm{vD}}/u_\tau$, where u_τ is the wall friction velocity. The profiles were plotted versus the nondimensional inner length scale $y^+ = y\,\rho_w\,u_\tau/\mu_w$ (for the bottom-wall plots) and $z^+ = z\,\rho_w\,u_\tau/\mu_w$ (for the side-wall plots). Figure 7 plots the van Driest transformed velocity in the near-wall region at $x = 60\,\ell$ from previous spanwise-averaged solutions[10] and computational results from Rai *et al.*[4] In addition to the experimental measurements by Shutts *et al.*,[42] experiment data by Elena and LaCharme[47] is included. Their data was collected under similar flow conditions using Laser Doppler Velocimetry (LDV) and Hot-Wire Anemometry (HWA).

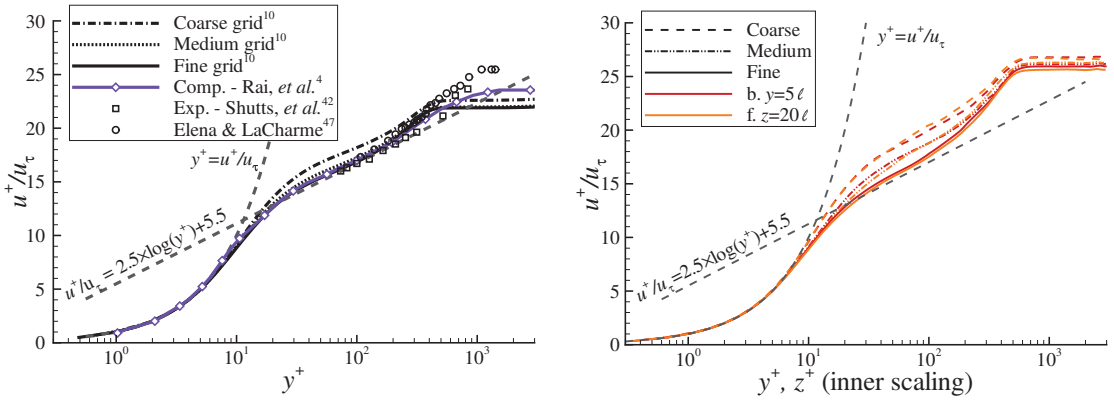

(a) Span-averaged results from previous work at $x = 60\,\ell$.[10]

(b) Locations **b** ($y = 5\,\ell$) and **f** ($z = 20\,\ell$) for various grids.

Figure 7. Time-mean streamwise velocity profiles using the Van Driest transform and normalized by the friction velocity at $x = 80\,\ell$.

Figure 7(b) shows the wall-normal profiles at $x = 80\ell$, $y = 5\ell$ and $z = 20\ell$, respectively for the three grids (note the locations correspond with the end of each line identified in Fig. 5(a)). The numerical solutions

are in good agreement with both the inner layer and logarithmic profiles, although the results from the coarse grid slightly over-predicted the expected solution within the logarithm region. This is indicative of an under-resolved grid or a solution that has not yet achieved equilibrium turbulence. Note that the coarse grid solution has developed to a slightly different equilibrium turbulent boundary-layer since the boundary-layer momentum thickness is lower for the coarse grid compared to the medium and fine grids.

Figure 8(a) shows additional profiles of the van Driest transformed streamwise velocity from the fine grid. As expected, the results were consistent with those observed in Fig. 5(c), namely, that the wall-normal profiles on both walls (away from the corner) achieve very similar results. This observation was further strengthened by span-averaging the time-mean profiles over select ranges on both walls. On the bottom wall, the profiles were averaged from $z = 5\,\ell$ to $z = 20\,\ell$ and on the sidewall from $y = 5\,\ell$ to $y = 10\,\ell$. Figure 8(b) shows that the two range-averaged profiles are almost identical suggesting that large regions on both flat plates behave like flat-plate boundary-layers with no influence from the symmetry boundary-condition or the corner-dominated flow.

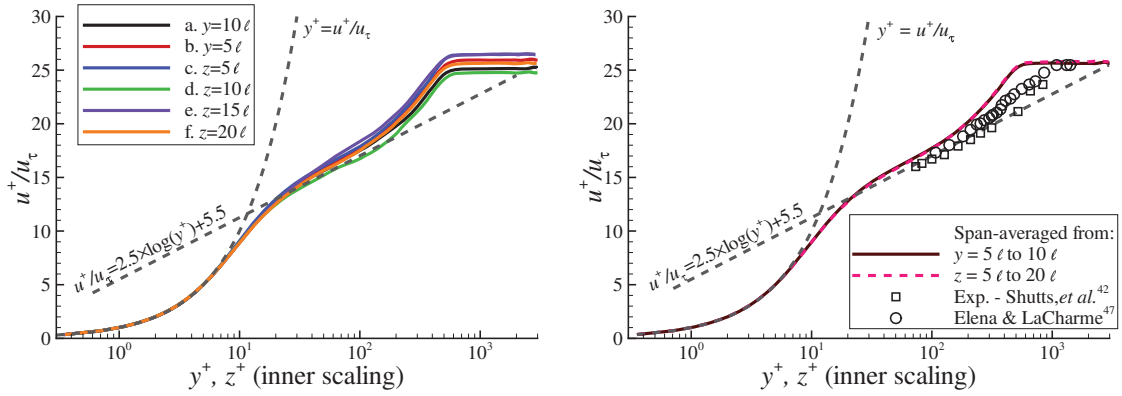

(a) Time-mean profiles at specific locations on the fine grid. (b) Span-averaged over selection regions for the fine grid.

Figure 8. Mean streamwise Van Driest transform velocity profiles normalized by the friction velocity at $x = 80\ell$.

The fluctuating velocity components normalized by the friction velocity for the Reynolds stress profile is shown in Fig. 9 for the near-wall region. Unfortunately, the experimental data by Shutts *et al.*[42] did not include fluctuating measurements, so these results are compared to the incompressible experiment of Karlson and Johansson,[48] which were made using LDV techniques for $Re_\theta = 2420$. This comparison is consistent with previous work by Rizzetta and Visbal,[40] who demonstrated that this assumption was valid because the compressibility effects are not strong for this flow.

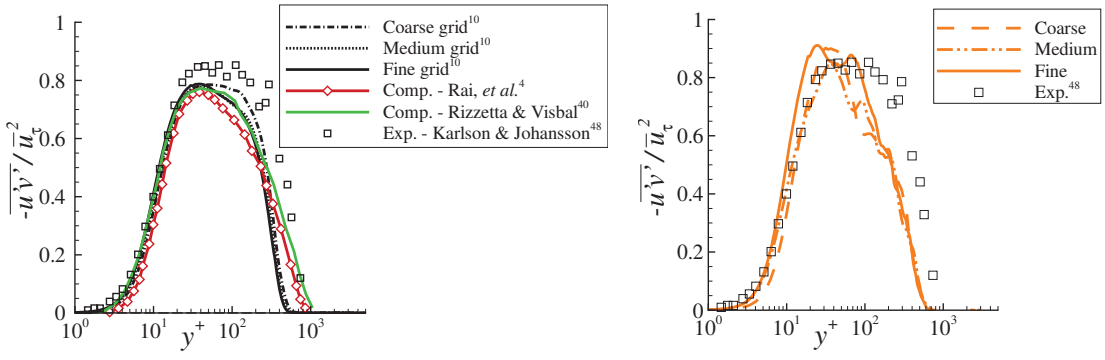

(a) Span-averaged results from previous work at $x = 60\,\ell$.[10] (b) Location **f** ($z = 20\,\ell$) for various grids.

Figure 9. Time-mean Reynolds stress profile versus distance from the wall normalized by inner scales at $x = 80\,\ell$.

As seen in Fig. 9(a) the previously collected span-averaged results[10] agree very closely with other com-

putations and the experimental values. Figure 9(b) shows that the current solution profiles deviate slightly at the edge of the semi-log region ($y^+ \approx 100$), but the overall shape and magnitude are in good agreement with the results and measurements. While the plot was not shown in the current work for brevity, the span-average Reynolds stress profile from $z = 5\,\ell$ to $z = 20\,\ell$ was smoother than the specific location curve show in Fig. 9(b). In addition, the span-averaged profile more closely matched the experimental values near $y^+ \approx 100$, a result consistent with the observations seen in Fig. 8(b). In addition, Fig. 9(b) shows the three grids yield similar profiles. Figure 10 plots the individual velocity components versus distance from the wall.

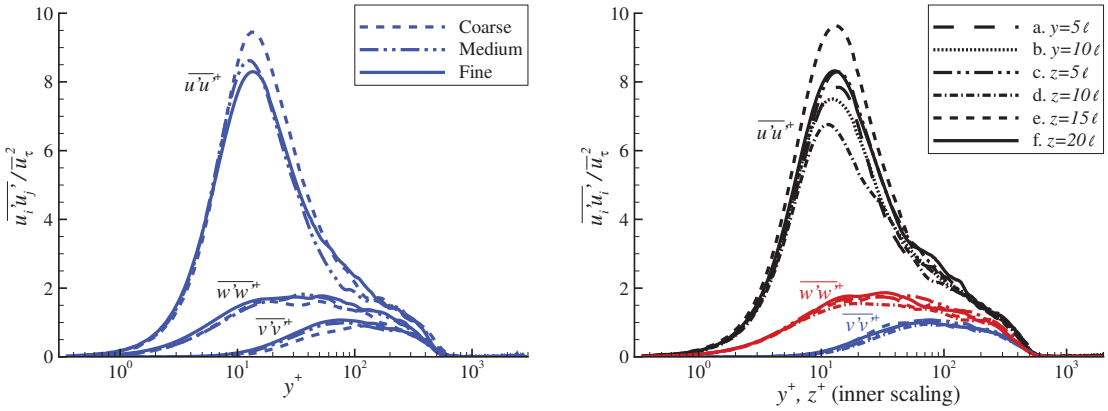

(a) Location **c** ($z = 5\,\ell$) for various grids.

(b) Various locations for the fine grid.

Figure 10. Time-mean fluctuating velocity component profiles versus distance from the wall normalized by inner scales at $x = 80\,\ell$.

As seen in Fig. 10, the normal and spanwise velocity fluctuation profiles are very similar for the various grids, whereas the streamwise fluctuations show a larger variation in magnitude. This is due, in part, to the fairly high normal and spanwise resolution for all three grids, whereas the streamwise resolution was much coarser, as seen in Table 2. The large variations observed in the streamwise component in Fig. 10(b) also implies that the time-mean solution may benefit from a longer sampling time.

Table 2. Grid resolution normalized by inner scaling at $x = 80\,\ell$.

Grid	$\Delta\, s^+$	x_w^+	y_w^+	y_δ^+	z_w^+	z_δ^+
Coarse	224.1	33.6	0.67	11.2	0.67	11.2
Medium	227.1	22.7	0.51	8.5	0.51	8.5
Fine	235.1	17.6	0.35	5.9	0.35	5.9

D. Features of the Time-Accurate Flow

Figure 11 shows the instantaneous time-history of the turbulent kinetic energy (TKE) at various locations in the boundary-layer at the end of resolved portion of the domain. The time-accurate data was collected for 5 flow lengths every 50 iterations. The TKE is computed by summing the velocity components and multiplying by a half (i.e., TKE $= 0.5 \times [u + v + w]$). As seen in the figure, the magnitude of instantaneous TKE increases with boundary-layer thickness, while the deviation decreases. Outside the boundary-layer ($z^+ = 1000$), the instantaneous deviation is significantly deduced, especially compared to the TKE at the boundary-layer edge ($z^+ = 500$).

From the time-history, one-dimensional spectra of the instantaneous pressure and TKE were computed. The power spectral density (PSD) was computed at specific locations by multiplying the instantaneous fluctuating quantities with a Hanning window for a segment of the data set. The data set was multiplied by the Hanning window to suppress side-lobe leakage,[49] with the window pre-multiplied by $\sqrt{8/3}$ to account for the low-frequency bias introduced by using the window. Next, a discrete Fourier transform of the windowed

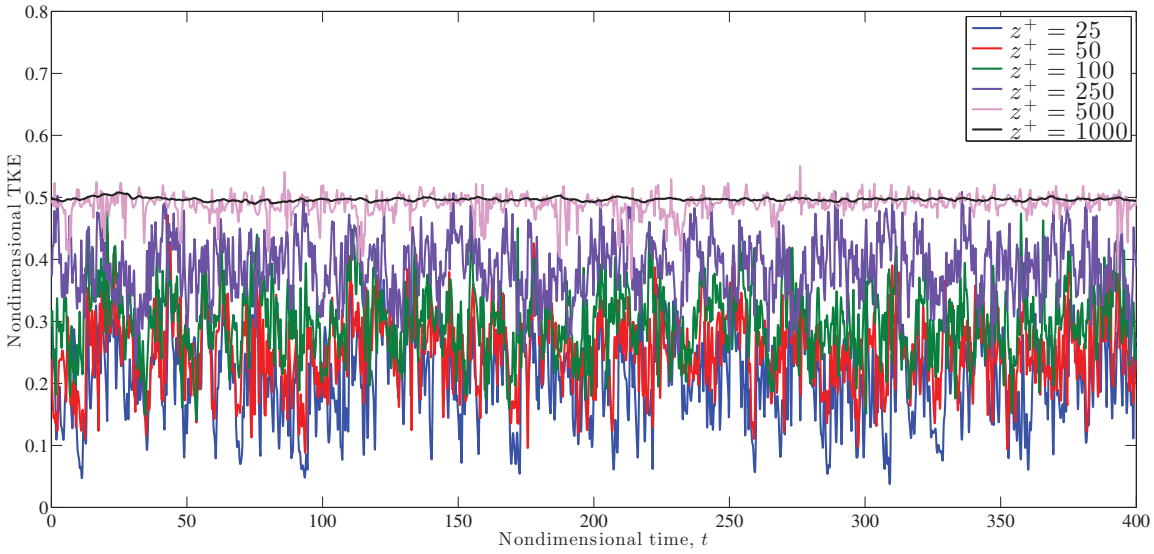

Figure 11. Time history of the turbulent kinetic energy at the location b ($x = 80\,\ell$, $y = 10\,\ell$) for the fine grid.

data was performed and the square of the Fourier transform solution (including the imaginary component), was normalizing by the length of the windowed signal. Note that in previous spanwise periodic studies,[10] the signal was further improved by span-averaging the results. Figure 12 plots the PSD of pressure and TKE versus normalized frequency for the different grids and at various locations in the boundary-layer.

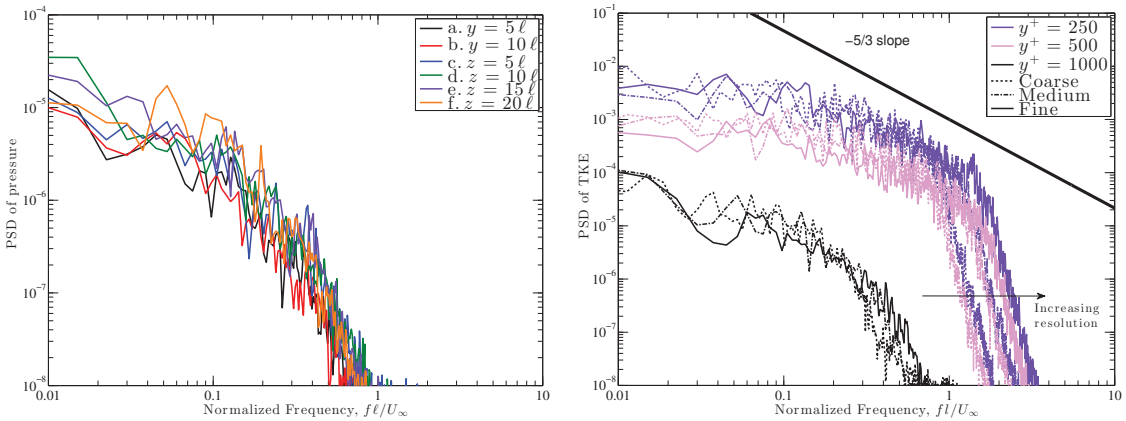

(a) PSD of wall pressure at several locations for the fine grid.

(b) PSD of TKE at location **e** ($z = 15\,\ell$).

Figure 12. Power spectral density of turbulent kinetic energy and pressure at $x = 80\ell$, using 5 Hanning windows with a 50% overlap.

As seen in Fig. 12(a), the PSD of wall pressure was very similar at several locations along both walls. In addition, the results are consistent with the PSD of pressure computed at a similar Re_θ in previous work,[50] though the previous work had a much longer time-history and sampling window. This suggests the surface pressure away from the corner was consistent with an equilibrium turbulent flat-plate boundary-layer.

Figure 12(b) showed increased resolution allowed the LES to capture a larger portion of the inertial subrange (as indicated by the region with a $-5/3$ slope). As expected, the magnitude of the PSD was lower at the boundary-layer edge compared to the profile collected at approximately half the boundary-layer height. Outside the boundary-layer, the PSD of TKE does not clearly show a $-5/3$ region and the shape and magnitude are consistent with the PSD of pressure at the same location (not shown for brevity). This is

because the PSD of TKE outside the boundary-layer is driven by acoustic disturbances and is not reflective of a turbulent equilibrium boundary-layer. Figure 12 shows the solutions for all three grids are consistent, implying that even the coarse grid has sufficient resolution for the LES. In addition, Fig. 12 shows the profiles are free of any discrete frequencies which may be present in other bypass-transition methods.

In addition to spectra, two-point autocorrelations were computed to ensure the symmetric boundary-conditions used in the simulation were sufficiently far from the corner-dominated flow. The standard two-point autocorrelations along a line in each of the spanwise and normal direction were computed:

$$R_{u_i,u_j} = \frac{\overline{u_i' \, u_j'}}{\sqrt{\overline{u_i'^2} * \overline{u_j'^2}}} \quad \text{for each spanwise point } i \tag{7}$$

where u_i' and u_j' are the fluctuating component of the streamwise velocity at grid points i and j, respectfully. The over-bar indicates the time-mean of the instantaneous fluctuations was computed. A perfectly correlated solution would have a value of one, while a perfectly un-correlated solution has a value of zero. A negative value means the two points are still correlated, but the fluctuations are going in opposite directions. Figure 13 plots the two-point autocorrelations for both pressure and TKE fluctuations as a function of the distance from either the spanwise or normal symmetry boundary locations, respectively.

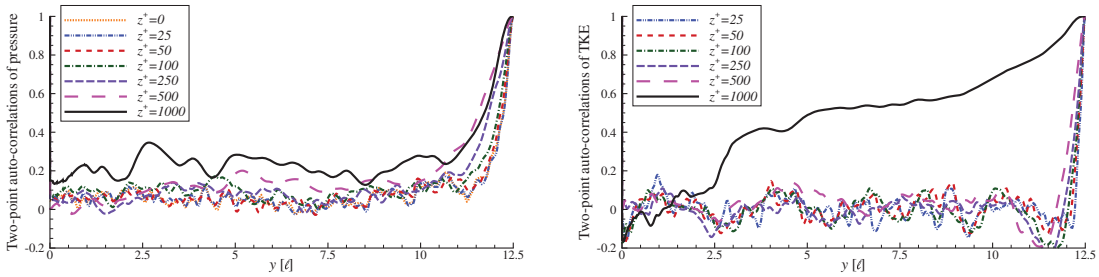

(a) Pressure at the $x-z$ symmetry boundary for the fine grid.

(b) TKE at the $x-z$ symmetry boundary for the fine grid.

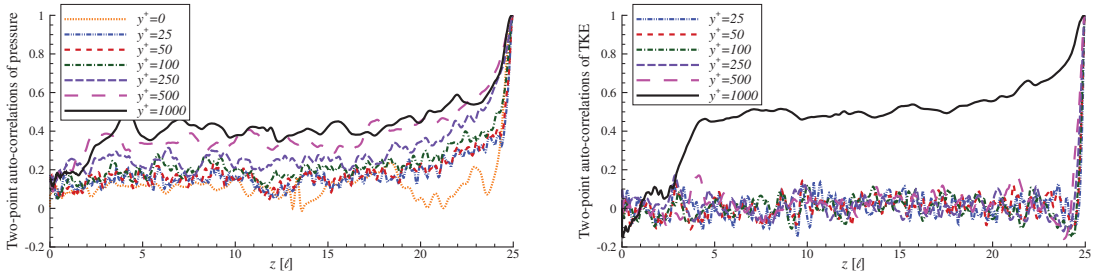

(c) Pressure at the $x-y$ symmetry boundary for the fine grid.

(d) TKE at the $x-y$ symmetry boundary for the fine grid.

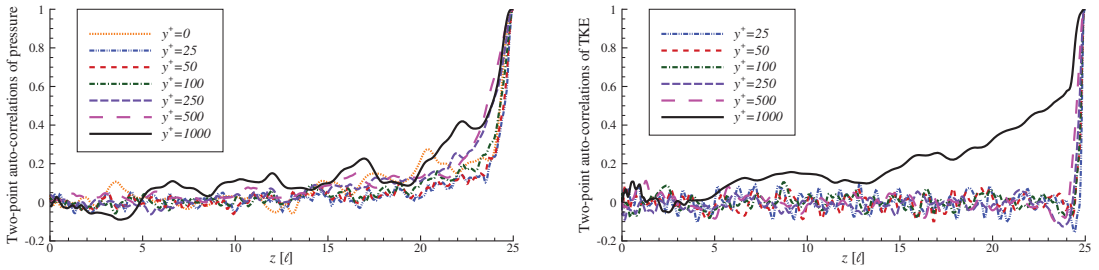

(e) Pressure at the $x-y$ symmetry boundary for the coarse grid.

(f) TKE at the $x-y$ symmetry boundary on the coarse grid.

Figure 13. Two-point autocorrelations of the turbulent kinetic energy and pressure fluctuations versus distance from the symmetry plane for the fine grid (a - d) and the coarse grid (e and f).

As seen for the fine grid solutions in Figs. 13(a)-13(d), pressure required a wider domain to de-correlate from the symmetry boundary, expect outside the boundary-layer (i.e., $y^+ = 1000$). Here, the two-point

autocorrelations for both TKE and pressure are very similar, because the velocity fluctuations in the inviscid core flow coincide with acoustic perturbations, a feature already observed in Fig. 12(b). Likewise, it is important to recall that while the magnitude of the two-point autocorrelations appears large outside the boundary-layer, the standard deviation of the TKE fluctuations is very small, as seen in Fig. 11.

The resultant TKE profiles in the inviscid region are quite different between the fine grid (Fig. 13(d)) and the coarse grid (Fig. 13(f)). This is because the very high span and normal resolution used for the fine grid was able to carry more of the acoustic noise generated at the boundary-layer edge due to the strong inviscid-viscous interactions. As listed in Table 2 the grid spacing in the inviscid flow for the fine grid is $y_\delta^+ = z_\delta^+ = 5.9$, whereas $y_\delta^+ = z_\delta^+ = 11.2$ for the coarse grid. As a result of the filtering procedure used, the coarse grid simulation removes more, under-resolved (higher-order), data (i.e., acoustic noise), from the solution. This conclusion, can also be drawn by looking at the two-point autocorrelations for pressure between the two grids (Figs. 13(c) and 13(e)). For the lower resolution coarse grid, the pressure correlations quickly fall to anear zero over $5\,\ell$, whereas the curves remain higher for a greater length in the fine grid results.

IV. Details in the Corner

While the majority of the flow exhibits the features of, and agrees with, the theoretical and experimental values of a flat-plate boundary-layer, the presence of the second viscous wall causes the solution to digress from the quasi-spanwise homogeneous wall-bounded solution near the corner. Figure 14 shows the time-mean average of the triple product of the velocity components, with the near-zero contours excluded for clarity. Note that away from the corner (in the boundary-layer on each wall), the small contours seen will continue to shrink and eventually disappear with a longer sampling period. This is because the average spanwise velocity, $\bar{w}$, on the bottom wall (i.e., near $y = 0\,\ell$), tends toward zero for a span-wise periodic flat-plate boundary-layer. Likewise, the average normal velocity, $\bar{v}$, on the side wall (i.e., near $z = 0\,\ell$), tends to zero for the same reason. However, the large negative-valued contours seen in the corner ($y < 2.5\,\ell$, $z < 2.5\,\ell$), will remain in Fig. 14, since the cross-velocity components are non-zero, though the peak magnitude will remain small since the streamwise velocity, $\bar{u}$, is small in the corner due to the strong viscous effects present.

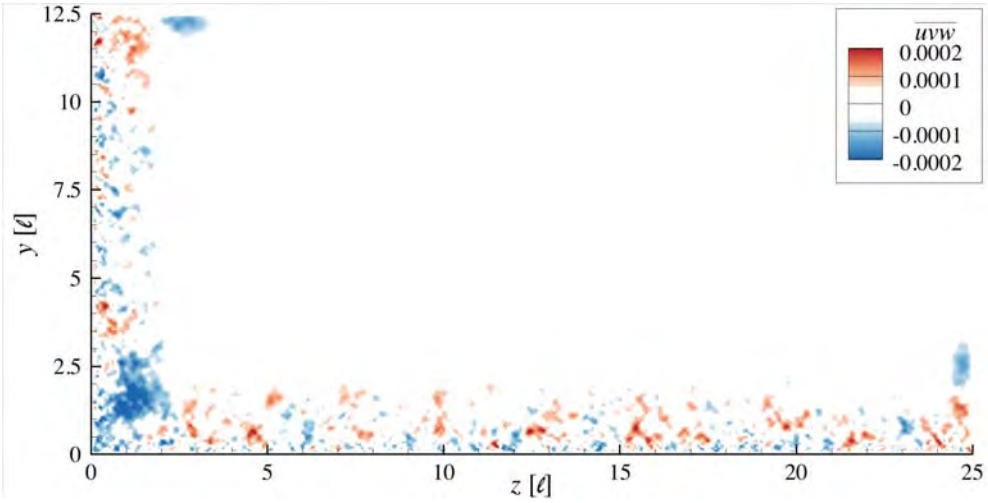

Figure 14. Contour slice of the triple correlation of the velocity components at $x = 80\,\ell$ for the fine grid.

Figure 15 shows the surface pressure in the corner near the end of the resolved domain ($x = 65\,\ell$ to $80\,\ell$). As seen in the figure, the pressure in the corner is higher than the adjoining plates. Near the end of the domain, the pressure rises more dramatically as the corner flow grows in size. This growth coincides with a less-full streamwise velocity profile, as seen by comparing the u-velocity profiles in Figs. 16(a) and 16(f), and makes the corner flow more susceptible to separation and the onset of a corner vortex. Note that in the present work, the corner did not separate.

Figure 16 shows line plots of the three velocity components versus distance from the bottom wall at

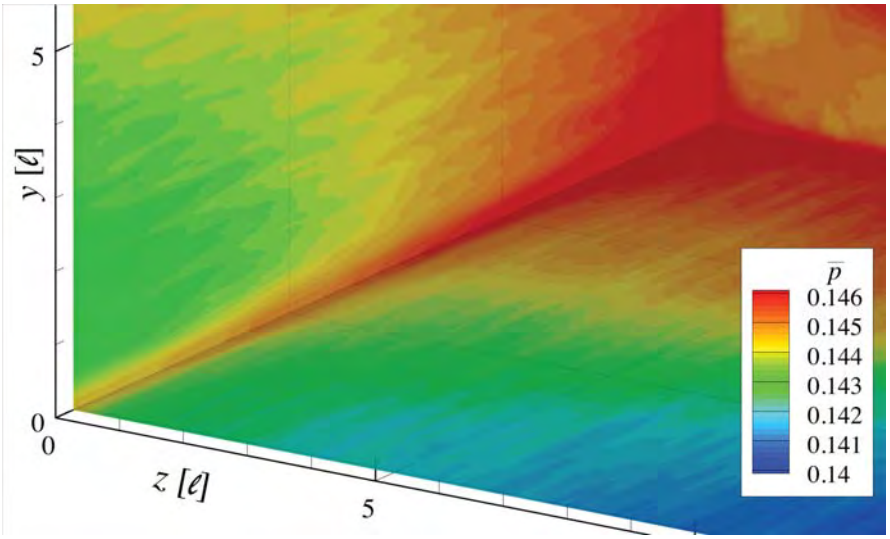

Figure 15. Nondimensional surface pressure contours from $x = 65\,\ell$ to $80\,\ell$ for the fine grid.

several locations along the bottom plate. As seen in the Fig. 16(a), the streamwise velocity is about 70% of its inviscid value inside the corner core flow, though by $z = 2\,\ell$ (Fig. 16(d)), its peak has increased to the inviscid limit by the edge of the boundary-layer. Likewise, by $z = 2.5\,\ell$ (Fig. 16(f)) the streamwise component of the boundary-layer has relaxed into a turbulent equilibrium profile.

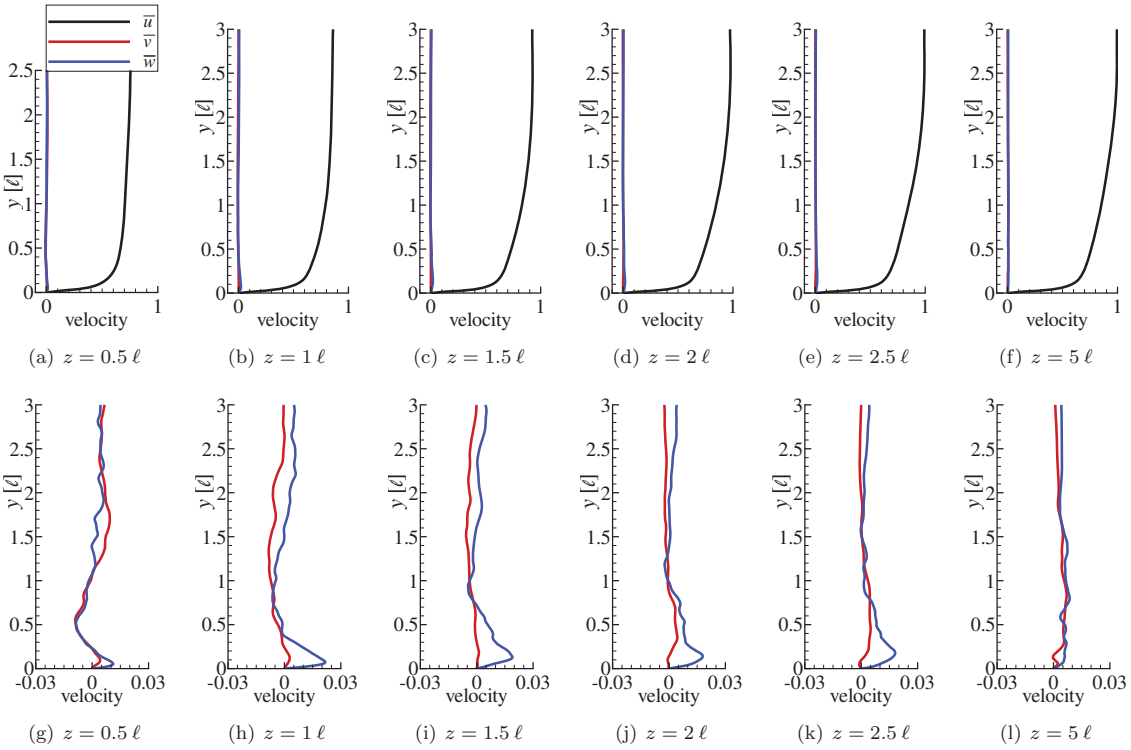

(a) $z = 0.5\,\ell$ (b) $z = 1\,\ell$ (c) $z = 1.5\,\ell$ (d) $z = 2\,\ell$ (e) $z = 2.5\,\ell$ (f) $z = 5\,\ell$

(g) $z = 0.5\,\ell$ (h) $z = 1\,\ell$ (i) $z = 1.5\,\ell$ (j) $z = 2\,\ell$ (k) $z = 2.5\,\ell$ (l) $z = 5\,\ell$

Figure 16. Line plots of the time-mean velocity components at $x = 80\,\ell$ for fine grid.

A close examination of the spanwise and normal velocity components in Fig. 16(g) shows a large region of reverse flow for both the normal and spanwise velocity components near $y = 0.5\,\ell$, which is the same distance from the corner as the spanwise location where the profiles were collected (i.e., Fig. 16(g) is at $z = 0.5\,\ell$). This flow feature corresponds to a weak vortex pair forming along the edge of the two slip surfaces originating from the corner. It is interesting to note that the spanwise velocity, $\bar{w}$, had a noticeable positive value a short distance from the surface for each profile to $z = 2.5\,\ell$. This outward velocity is the result of the corner boundary-layer flow growing and shows how the spanwise velocity in the boundary-layer profile is significantly different from the nominal flat-plate profile, like that observed in Fig. 16(l).

Figure 17 show the average density multiple by the average product of two components of the velocity fluctuations. As expected, the normal velocity component is important in the bottom wall boundary-layer (Fig. 17(a)), whereas the spanwise velocity component is important on the sidewall boundary-layer (Fig. 17(b)). Figure 17(d) reiterates the conclusions drawn from Fig. 14, since the small fluctuations observed in the two flat-plate boundary layers tend towards zero, whereas the fluctuations in the corner will remain non-zero. It is important to note that the magnitude of the average fluctuations in the corner is consistent with the mean triple product of the velocity components shown in Fig. 14. This shows that the fluctuations from the product of the cross-derivatives may be as important as the mean quantities themselves in the corner-dominated region. It also suggests that a simple flat-plate wall model would incorrectly predict the Reynolds stress when applied in a corner-dominated region of the flow.

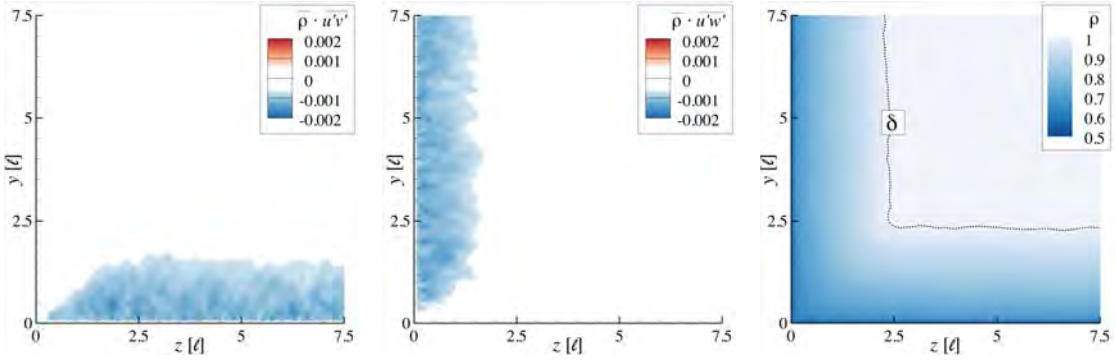

(a) Density times streamwise and normal velocity fluctuations

(b) Density times streamwise and spanwise velocity fluctuations.

(c) Density and a line indicating the boundary-layer thickness, δ.

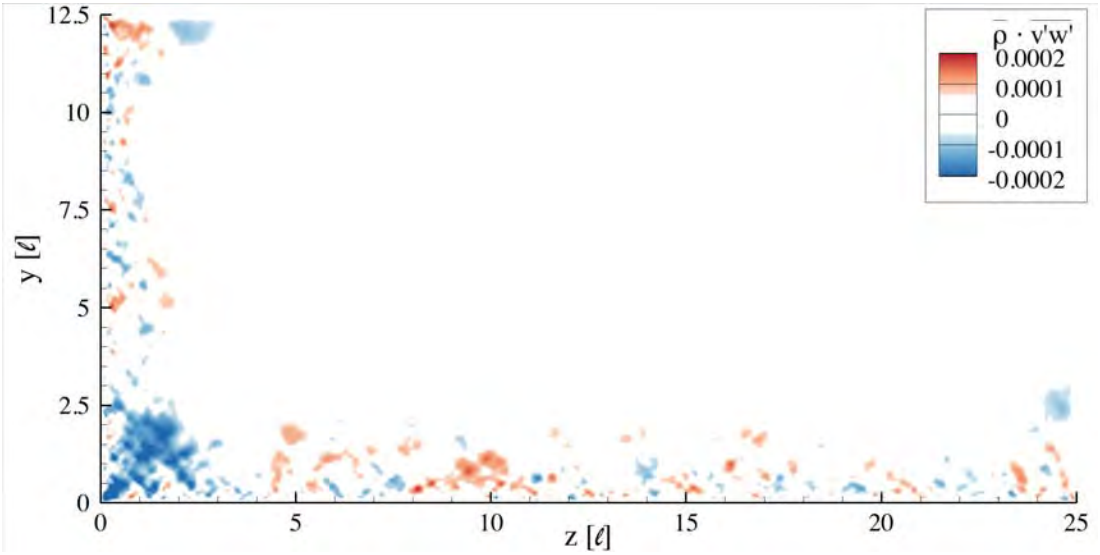

(d) Density times normal and spanwise velocity fluctuations.

Figure 17. Time-mean velocity component correlation contours at $x = 80\,\ell$ for the fine grid.

V. Conclusions

High-order implicit large-eddy simulations were used to investigate a supersonic wall-bounded turbulent corner flow. Solutions are obtained using a high-fidelity time-implicit numerical scheme and an implicit large-eddy simulation approach. The inclusion of the sidewall led to the development of a corner core flow which grew in size as the flow traveled downstream. A computational domain was developed with symmetric boundary-conditions for the boundaries opposite the adjoining walls. The resolved portion of the computational domain was $80\delta_0$ long, $25\delta_0$ wide, and $12.5\delta_0$ tall, where δ_0 is the incoming boundary-layer height. A grid resolution study, with the fine grid containing over 10^9 points, was performed and both mean and time-accurate statistics were collected. The solutions were compared to a spanwise-periodic flat-plate turbulent boundary layer developed at the same conditions. The resultant profiles were similar when compared at locations far from the corner. Two-point autocorrelations indicate that the both the span and normal dimensions of the domain were sufficient to de-correlate the symmetric boundary condition used in the calculations. In addition, the highly-resolved fine-grid was found to have sufficient resolution to support almost all the acoustic noise generated by the strong inviscid-viscous interactions present in the simulation. Triple products were collected and demonstrated the importance of resolving the corner-dominated flow without a closure model. In particular, the results showed that the magnitude of the fluctuations of the cross-velocity components in the corner was similar to the triple product of the mean velocity components in that same region.

Acknowledgments

The author would like to thank J. Poggie for his useful conservations regarding this research. This work was sponsored, in part, by the Air Force Office of Scientific Research under grant number LRIR 12RB01COR monitored by Dr. J. Schmisseur, AFOSR/RSA. Computational resources were supported by a grant of supercomputer time from the U.S. Department of Defense Supercomputing Resource Center at the U.S. Army Engineer Research and Development Center, Vicksburg, MS and the Air Force Research Laboratory, Wright-Patterson Air Force Base, OH.

References

[1]Graves, R. E., "Characterization of the Relative Aerodynamic Uncertainity Budget of an Energy-Efficiency Aircraft Design Change," AIAA Paper 2013-0906, 2013.

[2]Bisek, N. J., Gosse, R. C., and Poggie, J., "Computational Study of Impregnated Ablator for Improved Magnetohydrodynamic Heat Shield," *Journal of Spacecraft and Rockets*, Vol. 50, No. 5, 2013, pp. 927–936, doi:10.2514/1.39032.

[3]Lele, S. K., "Direct Numerical Simulation of Compressible Free Shear Flows," AIAA Paper 1989-0374, 1989.

[4]Rai, M. M., Gatski, T. B., and Erlebacher, G., "Direct Simulation of Spatially Evolving Compressible Turbulent Boundary Layers," AIAA Paper 1995-583, 1995.

[5]Adadms, N. A., "Direct simulation of the turbulent boundary layer along a compression ramp at M = 3 and Re_θ = 1685," *Journal of Fluid Mechanics*, Vol. 420, No. 1, 2000, pp. 47–83.

[6]Pirozzoli, S., Grasso, F., and Gatski, T. B., "Direct Numerical Simulation and Analysis of a Spatially Evolving Supersonic Turbulent Boundary Layer at M=2.25," *Physics of Fluids*, Vol. 16, No. 3, March 2004, pp. 530–545.

[7]Wu, M. and Pino Martin, M., "Direct Numerical Simulation of Supersonic Turbulent Boundary Layer Over a Compression Ramp," *AIAA Journal*, Vol. 45, No. 4, April 2007, pp. 879–889.

[8]M., R., Wu, M., and Pino Martin, M., "Low Reynolds Number Effects in a Mach 3 Shock/Turbulent Boundary-Layer Interaction," *AIAA Journal*, Vol. 46, No. 7, July 2008, pp. 1884–1887.

[9]Priebe, S. and Pino Martín, M., "Low-Frequency Unsteadiness in the DNS of a Compression Ramp Shockwave and Turbulent Boundary Layer Interaction," AIAA Paper 2010-108, 2010.

[10]Bisek, N. J., Rizzetta, D. P., and Poggie, J., "Plasma Control of a Turbulent Shock Boundary-Layer Interaction," *AIAA Journal*, Vol. 51, No. 8, 2013, pp. 1789–1804, doi:10.2514/1.J052248.

[11]Shankar, V., "Numerical solutions for inviscid supersonic corner flows," AIAA Paper 1975-0221, 1975.

[12]Hung, C. and MacCormack, R. W., "Numerical solution of a three-dimensional shock wave and turbulent boundary-layer interaction," AIAA Paper 1978-0161, 1978.

[13]Shang, J. S., Hanky, W. L., and Petty, J. S., "Three-Dimensional Supersonic Interacting Turbulent Flow along a Corner," *AIAA Journal*, Vol. 17, No. 7, July 1978, pp. 706–713.

[14]Garnier, E., "Simulated Detached Eddy Simulation of three-dimensional shock/boundary layer interaction," *Shock Waves*, Vol. 19, 2009, pp. 479–486.

[15]Hadjadj, A., "Large-Eddy Simulation of Shock/Boundary-Layer Interaction," *AIAA Journal*, Vol. 50, No. 12, December 2012, pp. 2919–2927.

[16]Burton, D. M. F. and Babinsky, H., "Corner Separation Effects for Normal Shock Wave/Turbulent Boundary Layer Interactions in Rectangular Channels," *Journal of Fluid Mechanics*, Vol. 707, September 2012, pp. 287–306.

[17]Babinsky, H., Oorebeek, J., and Cottingham, T. G., "Corner Effects in Reflecting Oblique Shock-Wave/Boundary Layer Interactions," AIAA Paper 2013-859, 2013.

[18]Gaitonde, D. and Visbal, M. R., "High-order Shcemes for Navier-Stokes Equations: Algortithm and Implementaiton into FDL3DI," Tech. rep., Air Force Research Laboratory, August 1998, AFRL-VA-WP-TR-1998-3060.

[19]Visbal, M. R., "Computational Study of Vortex Breakdown on a Pitching Delta Wing," AIAA Paper 1993-2974, 1993.

[20]Gordnier, R. E. and Visbal, M. R., "Numerical Simulation of Delta-Wing Roll," *Aerospace Science and Technology*, Vol. 2, No. 6, September 1998, pp. 347–357.

[21]Visbal, M. R., Gaitonde, D. V., and Gogineni, S., "Direct Numerical Simulation of a Forced Transitional Plane Wall Jet," AIAA Paper 1998-2643, 1998.

[22]Rizzetta, D. P., Visbal, M. R., and Blaisdell, G. A., "Application of a High-Order Compact Difference Scheme to Large-Eddy and Direct-Numerical Simulation," AIAA Paper 1999-3714, 1999.

[23]Morgan, P. E., Rizzetta, D. P., and Visbal, M. R., "High-Order Numerical Simulation of Turbulent Flow over a Wall-Mounted Hump," *AIAA Journal*, Vol. 44, No. 2, February 2006, pp. 239–251.

[24]Garmann, D. J. and Visbal, M. R., "Implicit LES Computations for a Rapidly Pitching Plate," AIAA Paper 2010-4282, 2010.

[25]White, M. D. and Visbal, M. R., "High Fidelity Analysis of Aero-Optical Interaction with Compressible Boundary Layers," AIAA Paper 2010-4496, 2010.

[26]Anderson, D., Tannehill, J., and Pletcher, R., *Computational Fluid Mechanics and Heat Transfer*, 1984, McGraw-Hill.

[27]Mullenix, N. J., Gaitonde, D. V., and Visbal, M. R., "A Plasma-Actuator-Based Method to Generate a Supersonic Turbulent Boundary Layer Inflow Condition for Numerical Simulation," AIAA Paper 2011-3556, 2011.

[28]Beam, R. and Warming, R., "An Implicit Factored Scheme for the Compressible Navier-Stokes Equations," *AIAA Journal*, Vol. 16, No. 4, April 1978, pp. 393–402.

[29]Gordnier, R. E. and Visbal, M. R., "Numerical Simulation of Delta-Wing Roll," AIAA Paper 1993-544, 1993.

[30]Jameson, A., Schmidt, W., and Turkel, E., "umerical Solutions of the Euler Equations by Finite Volume Methods Using Runge-Kutta Time Stepping Schemes," AIAA Paper 1981-1259, 1981.

[31]Pulliam, T. H. and Chaussee, D. S., "A Diagonal Form of an Implicit Approximate-Factorization Algorithm," *Journal of Computational Physics*, Vol. 39, No. 2, Febuary 1981, pp. 347–363.

[32]Lele, S., "Compact Finite Difference Schemes with Spectral-like Resolution," *Journal of Computational Physics*, Vol. 103, 1992, pp. 16–42.

[33]Visbal, M. R. and Gaitonde, D. V., "High-Order-Accurate Methods for Complex Unsteady Subsonic Flows," *AIAA Journal*, Vol. 37, No. 10, October 1999, pp. 1231–1239.

[34]Gaitonde, D., Shang, J. S., and Young, J. L., "Practical Aspects of High-Order Accurate Finite-Volume Schemes for Electromagnetics," AIAA Paper 1997-363, 1997.

[35]Visbal, M. R. and Rizzetta, D. P., "Large-Eddy Simulation on Curvilinear Grids Using Compact Differencing and Filtering Schemes," *Journal of Fluids Engineering*, Vol. 124, 2002, pp. 836–847.

[36]Visbal, M. R., Morgan, P. E., and Rizzetta, D. P., "An Implicit LES Approach Based on High-Order Compact Differencing and Filtering Schemes," AIAA Paper 2003-4098, 2003.

[37]Fureby, C. and Grinstein, F. F., "Monotonically Integrated Large Eddy Simulation," *AIAA Journal*, Vol. 37, No. 5, May 1999, pp. 544–556.

[38]Stoltz, S. and Adams, N. A., "An Approximate Deconvolution Procedure for Large-Eddy Simulation," *Physics of Fluids*, Vol. 11, No. 7, July 1999, pp. 1699–1701.

[39]Mathew, J., Lechner, R., Foysi, H., Sesterhenn, J., and Friedrich, R., "An Explicit Filtering Method for Large Eddy Simulation of Compressible Flows," *Physics of Fluids*, Vol. 15, No. 8, August 2003, pp. 2279–2289.

[40]Rizzetta, D. P. and Visbal, M. R., "Large-Eddy Simulation of Supersonic Boundary-Layer Flow by a High-Order Method," *International Journal of Computational Fluid Dynamics*, Vol. 18, No. 1, January 2004, pp. 15–27.

[41]White, F. M., *Viscous Fluid Flow, 3rd Ed.*, 2006, McGraw Hill.

[42]Fernholz, H. H. and Finley, P. J., "A Critical Compilation of Compressible Turbulent Boundary Layer Data," Tech. rep., 1977, AFARDograph No. 223, Case 55010501.

[43]Georgiadis, N. J., Rizzetta, D. P., and Fureby, C., "Large-Eddy Simulation: Current Capabilites, Recommended Practices, and Future Research," *AIAA Journal*, Vol. 48, No. 8, August 2010, pp. 1772–1784.

[44]Ghosal, S., "Mathematical and Physical Constraints on Large-Eddy Simulation of Turbulence," *AIAA Journal*, Vol. 37, No. 4, 1999, pp. 425–433.

[45]Jeong, J. and Hussain, F., "On the Identification of a Vortex," *Journal of Fluid Mechanics*, Vol. 285, 1995, pp. 69–94.

[46]van Driest, E. R., "On the Turbulent Flow Near a Wall," *Journal of the Aeronautical Sciences*, Vol. 23, 1956, pp. 1007–1011.

[47]Elena, M. and LaCharme, J. P., "Experimental Study of a Supersonic Turbulent Boundary Layer Using Laser Doppler Anemometer," *Journal de Mécanique Théorique et Appliquée*, Vol. 7, 1988, pp. 175–190.

[48]Karlson, R. I. and Johansson, T. G., "LDV Measurements of Higher-Order Moments of Velocity Fluctuations in a Turbulent Boundary Layer," Proceedings from the 3rd International Symposium on Applications of Laser Anemometry to Fluid Mechanics, (Instituto Superior Tecnico, Lisbon, Portugal), 1986.

[49]Bendat, J. S. and Piersol, A. G., *Random Data, 2nd Ed.*, 1986, John Wiley & Sons.

[50]Bisek, N. J. and Poggie, J., "Large-Eddy Simulations of Separated Supersonic Flow with Plasma Control," AIAA Paper 2013-528, 2013.

AIAA Aviation
22-26 June 2015, Dallas, TX
22nd AIAA Computational Fluid Dynamics Conference

Supersonic Corner Flow Predictions using the Quadratic Constitutive Relation

Timothy Leger,* Nicholas Bisek, † and Jonathan Poggie ‡
U.S. Air Force Research Laboratory, Wright-Patterson Air Force Base, OH 45433-7512, USA

A series of Reynolds Average Navier-Stokes simulations are performed for a supersonic, wall-bounded, turbulent corner flow. These are compared to a high order, implicit, Large-Eddy Simulation for the same geometry and flow conditions. Since the LES results were obtained for a low Reynolds number, near the boundary of the validity for the turbulence models, the comparison of results with the two approaches was qualitative. Inclusion of the Quadratic Constitutive Relation in the Reynolds Average Navier-Stokes simulation results in significant improvement in qualitative agreement with the Large Eddy Simulation, specifically the presence of secondary flow (a counter rotating vortex pair). The range of valid values for the constant in the Quadratic Constitutive Relation formulation is explored. Additionally, the effects on this range from different turbulence models and momentum thickness Reynolds number for the corner are also examined. These effects of the Quadratic Constitutive Relation are explored using both the finite-difference fluid solver OVERFLOW, and the the finite-volume fluid solver US3D. The results indicate that the Quadratic Constitutive Relation term directly affects the strength of the vortex pair in the secondary flow and that its influence appears directly dependent on all the aforementioned parameters.

Nomenclature

M	Mach number
Re/m	Unit Reynolds number
Re_θ	Momentum thickness Reynolds number
p	Pressure
T	Temperature
ρ	Density
u	Streamwise velocity
v	Normal velocity
w	Spanwise velicity
l	Reference length
x	Streamwise distance
y	Wall-normal/spanwise distance
z	Spanwise distance
δ	Boundary layer thickness, 0.99 u_∞
θ	Boundary layer momentum thickness
τ	Reynolds-stress tensor
S	Strain-rate tensor
μ	Dynamic viscosity
k	Turbulent kinetic energy
δ_{ij}	Kronecker delta
O_{ij}	Anti-symmetric rotation tensor

*Research Scientist, Ohio Aerospace Institute, Senior Member AIAA, timothy.leger.ctr@us.af.mil
†Research Aerospace Engineer, AFRL/RQHF, Senior Member AIAA
‡Senior Aerospace Engineer, AFRL/RQHF, Associate Fellow AIAA

C_{cr}	QCR constant
L^*	Distance of vortex core from corner
α	Angle of vortex core from nearest wall
Cf	Skin-friction coefficient

Superscripts

$+$	Inner coordinates
$-$	Time mean
$\prime$	Fluctuations
t	Turbulent
QCR	Quadratic Constitutive Relation

Subscripts

∞	Freestream
w	Wall
1	First cell off the wall
t	Turbulent

I. Introduction

Corners are a common feature in the design of both internal and external aerodynamic configurations. In turbulent flows, the anisotropy of turbulence causes such corners to generate secondary flow. Prandtl was the first to document this and in 1926 he classified it as secondary flow of the second kind.[1] This secondary flow, which is driven by turbulence and will be referred to as corner flow here, is characterized by a pair of counter rotating vortices which transfer momentum from the mean flow into the corner. While corner flows are relatively weak, being only 1 - 3% of the freestream velocity, they have a significant effect on wall shear stress and heat transfer in the corner.[2]

For external corners, such as the junction between a wing and fuselage, this results in interference drag.[3] In internal flows, such as rectangular ducts and isolators, corner flows significantly distort the primary flow field,[4] which may lead to "unstart" conditions in airbreathing engine flowpaths.[5] In addition, corner flows can have a significant effect on the behavior of Shock Boundary Layer Interaction (SBLI).[6] It is therefore important to gain a better understanding of and improve predictions of corner flow effects for the design and development of future air vehicles.

Detailed investigations of corner flow go back half a century. A summary of the early RANS simulations and experimental measurements is provided by Demuren and Rodi.[7] These early RANS simulations failed to predict any secondary flow. Due to the difficulty in making such measurements, only a few experiments of corner flow have been reported since.[8–10] However, there has been a renewed interest in experimental measurement of corner flow using non-intrusive techniques. Recently, Morajkar[11] reported on stereo particle image velocimetry (SPIV) measurements of a Mach 2.75 flow in a low aspect ratio rectangular channel. By using SPIV, the three components of the velocity field were measured instantaneously, at three cross-section planes, and analyzed to study the formation of corner flow and its effect on the mean flow field. Results showed that vortices form in the corner and then convect into the mean flow.

Concurrently, the increase in computational power over the past two decades has resulted in several Direct Numerical Simulations (DNS) and Large-Eddy Simulations (LES) being used to further investigate corner flow.[12–18] While DNS captures all motions contained in the flow, and is thus recognized as the most precise simulation method available for turbulent flows, it is extremely computationally expensive. As such, it is only used for very low Reynolds numbers and makes some assumptions about the state of the turbulent flow.[19] LES models require less computational expense, but lacks resolution of the smallest scale motions. Although not as restrictive as DNS, LES calculations are also limited in the maximum Reynolds numbers that can be effectively simulated.

One of the first DNS of a square duct was performed by Gavrilakis,[12] which confirmed that secondary flow results from the anistropy of turbulence. Gavrilakis also discovered a second, very weak pair of counter rotating vorticies in the corner, below those characterizing the main secondary flow. As Garvrilakis reports, this second vortex pair had not been reported in any experiment, but since they are so weak, small, and

close to the corner, they would be extremely difficult to measure. Madabhushi and Vanka[13] appear to have been the first to perform an LES of a square duct. Along with providing mean flow properties and turbulent statistics, this simulations demonstrated that LES is capable of capturing the turbulence driven secondary flow in a corner. Kajishma and Miyake[14] performed LES calculations for fully developed turbulent flow in a square duct and reported that the secondary flow was produced as a consequence of the delicate imbalance between the gradient of the turbulent stress and that of the corresponding pressure very near the walls of the corner. Huser and Biringen[15] performed a DNS of a square duct and through a quadrant analysis of the fluctuations determined that the mean secondary flow in the corner was related to the burst and ejection of turbulent structures near the wall. Xu and Pollard[16] investigated a square annular duct using LES and reported that the secondary flow counter rotating vortex pair was predicted symmetrically around the convex 90 degree corner along with a weaker counter rotating vortex pair symmetrically located in the concave 90 degree corner. Huijnen et al.[17] investigated the effect of subgrid scale models in LES calculations of a square duct. They concluded that the Smagorinsky model significantly over-predicted shear at wall, which negatively influenced the prediction of secondary flow. Joung et al.[18] performed DNS calculations of a square duct and used a quadrant analysis of the fluctuations to characterize the mean secondary flow in an attempt to describe the mechanism by which secondary flow is generated. They reported that the sweep and ejection events dominated in regions of local maximum and minimum shear stress respectively.

While these simulations have added to the knowledge about corner flow, LES and DNS are still too computationally expensive for design work, as the computational timestep required is too small for rapid turn around. Instead, RANS simulations, along with hybrid methods based on RANS, such as Detached Eddy Simulations (DES), are almost exclusively used for design work. However, it should be possible to use the insights gained by higher fidelity calculations to improve the results of RANS simulations. One such improvement for RANS models, at least with regards to corner flow, is the Quadratic Constitutive Relation (QCR).[20] While QCR alleviates the most often cited flaw with RANS calculations (i.e. turbulence models based on linear eddy-viscosity models), it does introduce another constant which must be set. The objectives of this paper is to explore the range of valid values for this constant and determine if it can be tuned using results from higher fidelity simulations. To aid in this effort, results from the LES simulation of Bisek[21] are included for qualitative comparison. In addition, the effect on this range from different turbulence models and various Reynolds momentum number in the corner are also examined. Finally, the effects of QCR are compared between finite-difference and finite-volume numerical schemes.

II. Approach

II.A. Numerical Method

For this work, two different RANS solvers were utilized, US3D (version RC22.8) and OVERFLOW (version 2.2g). US3D is a cell-centered, finite-volume, solver for the non-equilibrium, compressible Navier-Stokes equations on unstructured grids, and was developed at the University of Minnesota.[22] Inviscid fluxes are evaluated using the modified Steger-Warming flux vector splitting scheme developed by MacCormack and Candler.[23] This modified Steger-Warming method utilizes a pressure-dependent weighting function to switch smoothly from a low-dissipation scheme in regions of low gradients to the original Steger-Warming scheme when a large-pressure gradient is detected across a face (such as for a strong shock). This is combined with a MUSCL reconstruction[24] at the faces to achieve second order spatial accuracy. Diffusive fluxes are computed using a second-order scheme, in which the gradients are calculated using a deferred correction approach similar to that of Nompelis et al.,[22,25,26] MacCormack and Candler,[23,27] and Kim et al.[28] Weighted least square fits are then used to calculate the viscous fluxes from the second order accurate gradients.

Solutions in US3D are driven to a steady state convergence using backward Euler time stepping, which is fully implicit, but only first order accurate. Future time level fluxes are approximated by linearizing the fluxes about the current time level using exact flux Jacobians. The data-parallel line relaxation (DPLR) method, based on the Gauss-Seidel line relaxation method of MacCormack,[29] is then employed to solve the resulting linear system. To improve performance on parallel systems, the DPLR method replaces the Gauss-Seidel sweeps with a series of line relaxation sweeps.[30] Overall, the DPLR method has high parallel efficiency and good convergence characteristics, particularly when solving large compressible flow problems. For closure, the Spalart-Allmaras turbulence model is used with a correction for compressibility by Catrix and Aupoix (SA-Catrix).[31]

OVERFLOW is a well-validated, finite-difference, time-marching, implicit Navier-Stokes solver for struc-

tured and overset grids. It was developed as a joint effort between NASA's Johnson Space Flight and Ames Research Centers. The solver has numerous options, but those exercised for this work include the following. To accelerate the solution, grid sequencing and multigrid options[32] were enabled with two grid levels and 300 iterations per level. Central differencing was used for the right hand side Euler terms, along with the ARC3D diagonalized Beam-Warming scalar pentadiagonal scheme[33] on the left hand side. Local time-stepping was used with a CFL range of 2.5 to 100. For some of the simulations, the lower end of the CFL range was reduced to 0.5 to help with convergence. All other solver options were left at their default values.

Three of the turbulence models available in OVERFLOW were used for this work; Spalart-Allmaras without the trip term (SA-noft2),[34] Menter's Shear Stress Transport model with Sarkar compressibility correction (SST),[35,36] and the k-ω model of Wilcox.[37] For the SST and k-ω two equation turbulence models, the Diagonally Dominant Alternating Direction Implicit (DDADI) implementation[38] was utilized.

II.B. Flow Conditions

The flow conditions utilized for this work are given in Table 1, and are based on a 1955 experiment by Shutts et al.,[39] case 55010501. They are consistent with those used by Bisek[21] to perform an LES of supersonic turbulent corner flow at Mach 2.25, with two exceptions. First, the LES simulations were performed for a two-to-one corner while the RANS simulations are for a one-to-one corner. Second, the walls of the corner in the LES simulation were treated as isothermal with a fixed temperature of 320 K, which is close to the adiabatic temperature of the flat plate. This was done to help stability of the LES simulation. In the RANS simulations presented here, the walls of the corner were treated as purely adiabatic.

Table 1. Flow Conditions used for Mach 2.25 Supersonic Turbulent Corner Simulations.

Parameter	Value	
M	2.249	
Re/m	23.6 x 10^6	m^{-1}
u_∞	584.96	m/s
ρ_∞	4.615	kg/m^3
P_∞	22.29	kPa
T_∞	168.29	K
Re_θ	2,000 - 6,000	

III. Flat Plate Study

Before investigating corner flow with the RANS solvers, a series of flat plate simulations were first performed. The primary purpose of these simulations was to investigate the behavior of the available turbulence models at the relatively low momentum Reynolds number achieved in the LES simulation. First, it was necessary to determine if these models could produce an appropriate turbulent boundary layer profile. This was an initial concern because the turbulence models were calibrated for much higher Reynolds numbers than investigated here. Secondly, once a reasonable turbulent boundary layer was obtained, it was of interest to determine how it compared with experimental measurements,[39,40] as well as results from higher-order simulations for the same flow conditions.[41–43]

III.A. Grid

In order to determine the minimum grid requirements, a grid independence study for the flat plate was performed. For convenience of comparison, the same non-dimensional geometry length, representative of the incoming laminar boundary layer thickness, l = 6.096 x 10^{-4} m of Bisek[21] was used. The 2-D flat plate domain was constructed in the $x-z$ plane, as required by OVERFLOW to use the 2-D boundary condition, and was 200 l long by 12.5 l high. This length allowed a turbulent boundary layer to develop to a Re_θ of just over 3,000 for all turbulence models. The coarse grid was constructed first, with 32 cells in the plate normal direction, z. Point clustering near the wall was achieved in the normal direction using a hyperbolic tangent function. The initial normal spacing near the plate surface, Δz_1, was adjusted till a $z_1^+ \lesssim 1$ was

achieved, while the initial spacing at the upper part of the boundary was left unspecified. For US3D, Δz_1 was determined to be 6.0 x 10^{-3} l, while for OVERFLOW, it was 3.7 x 10^{-3} l. The factor of nearly two difference is due primarily to the fact that the simulation data is computed based on the cell-center location in US3D and the node location in OVERFLOW. This grid clustering yielded approximately 20 cells in the boundary layer region, which is the minimum requirement for turbulence models without wall functions.[44]

To alleviate issues with the weak shock that forms at the plate leading edge, the streamwise cell spacing was broken into two parts. In the portion of the domain from 10 to 200 l, 190 cells were used with uniform spacing, where as the first 10 l of the domain contained 32 cells. These were clustered using a hyperbolic tangent function, with the initial spacing at the inlet unspecified and the initial spacing at the other end set to match the adjacent streamwise domain spacing. The coarse 2-D grid plane is shown in Fig. 1, with only the first 40 l of the streamwise domain for clarity.

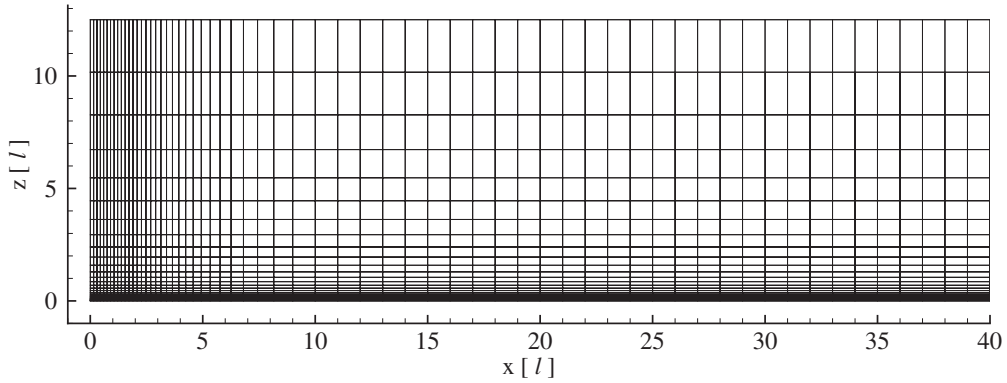

Figure 1. Streamwise $(x-z)$ View of the Coarse Plate Grid, with Only the First 40 l of the Domain Shown for Clarity.

The completed 2-D grids were created by extruding the 2-D grid plane in the y direction. Since US3D is a finite volume solver, the grid was extruded by a single cell l wide, resulting in a grid 222 by 1 by 32 cells. For OVERFLOW, three planes are required, so it was extruded by two cells, each cell being l wide, resulting in a grid 222 by 2 by 32 cells. The medium grids were constructed from the coarse grids using a cubic spline algorithm to double the number of cells in both the x and z dimensions, while maintaining the cell distribution. Fine grids were then generated from the medium grids using the same procedure. A second set of medium grids were constructed to investigate turbulence model behavior at higher Re_θ. These were generated by extending the initial medium grids to 2,000 l in the streamwise direction using the constant spacing at the end of the initial grids.

III.B. Boundary Conditions

For the US3D simulations, supersonic inflow and outflow boundary conditions were applied at the inlet and outlet respectively. An adiabatic wall boundary condition was applied at the flat plate surface, $z = 0$, with an initial temperature of 320 K. To improve convergence, the upper portion of the domain opposite the plate, $z = 12.5\ l$, was also set as an inlet boundary condition with freestream conditions specified. Symmetry boundary conditions were applied in the periodic direction, y.

In the OVERFLOW simulations, the inlet was set to a freestream boundary conditions while the outlet was set to a purely extrapolated outflow boundary condition. A viscous adiabatic wall boundary condition, based on pressure extrapolation, was applied to the flat plate surface at $z = 0$. At the upper portion of the domain opposite the plate, $z = 12.5\ l$, a freestream boundary condition was used. A 2D boundary condition was applied to the center y plane. To support transition of the flow, a laminar region (with zero production in the turbulence model) was specified for the first 10 l of the domain from the inlet.

III.C. Results

For each solution, the momentum thickness was calculated along the streamwise direction and the velocity profile was extracted where $Re_\theta \approx 2{,}000$. Fig. 2 shows this extracted profile for the coarse, medium, and

fine grids from OVERFLOW with the SA-noft2, k-ω, and SST turbulence models, along with US3D for the SA-Catrix turbulence model. From these plots, it can been seen that grid independence has been achieved by the medium grid for each scenario.

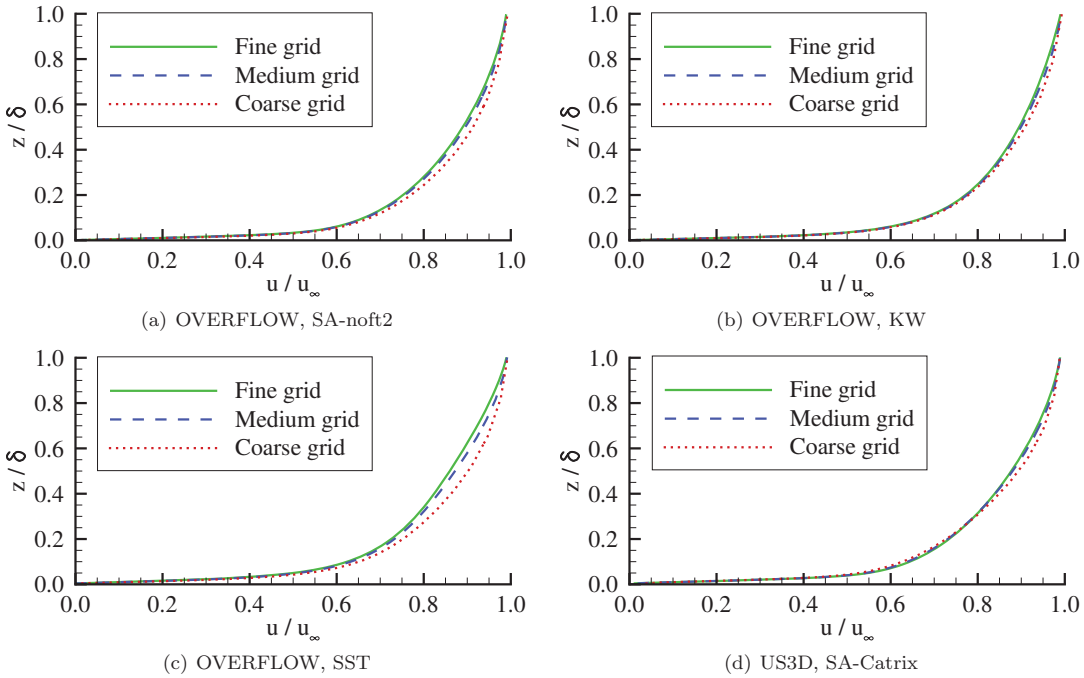

(a) OVERFLOW, SA-noft2 (b) OVERFLOW, KW

(c) OVERFLOW, SST (d) US3D, SA-Catrix

Figure 2. Normalized Streamwise Velocity Profiles at Re_θ of 2,000.

Fig. 3(a) shows the extracted velocity profiles from each of the medium grids where Re_θ was approximately 2,000. Included for comparison is the turbulent boundary layer profile from the medium grid of the LES simulation by Bisek.[21] While a turbulent profile is obtained by the turbulence models for this low Re_θ, there is a noticeably difference between the results of the different RANS models. Additionally, none of turbulent model profiles predict results consistent with the LES results. Fig. 3(b) shows the same velocity profiles, but with the RANS profiles extracted where Re_θ was 20,000. At this higher Re_θ, the results from the different turbulence models collapse on top of each other and also agree more favorably with the low Re_θ LES results. This demonstrates that the turbulence models, although capable of generating a turbulent boundary layer at such low Re_θ, are clearly tuned for higher Re_θ.

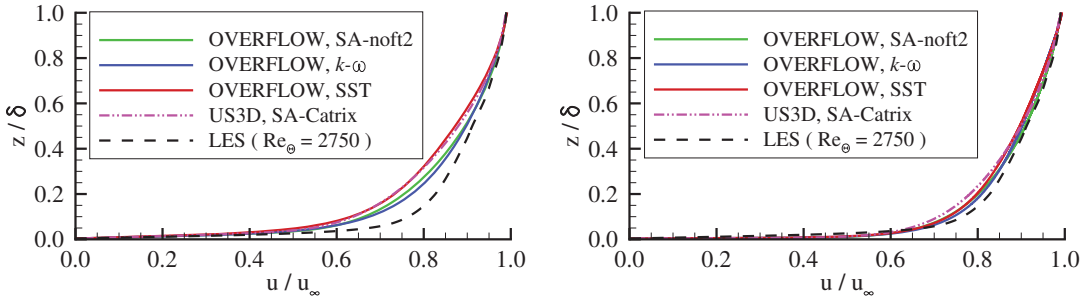

(a) $Re_\theta = 2,000$ (b) $Re_\theta = 20,000$

Figure 3. Normalized Streamwise Velocity Profiles for Different Turbulence Models Using Medium Grids.

The van Driest transformation was applied to the extracted profiles from the medium grids at Re_θ of 2,000 and the results are shown in Fig. 4. Included in Fig. 4 are results from Rai et al.,[41] Rizzetta and Visbal,[42] and Bisek et al.,[43] which were performed using high-order techniques to investigate development of

the same turbulent boundary layer. Also included in Fig. 4 are the experimental measurements of Shutts et al.,[39] along with those from Elena and LaCharme.,[40] which were collected for similar flow conditions using Laser Doppler Velocimetry (LDV) and Hot-Wire Anemometry (HWA). It is clear to see from this figure that the results from the turbulence models, even at such low Re_θ, agree more favorably with results obtained from higher-order simulations and experimental measurements when normalized by the variable density (in compressible flow).

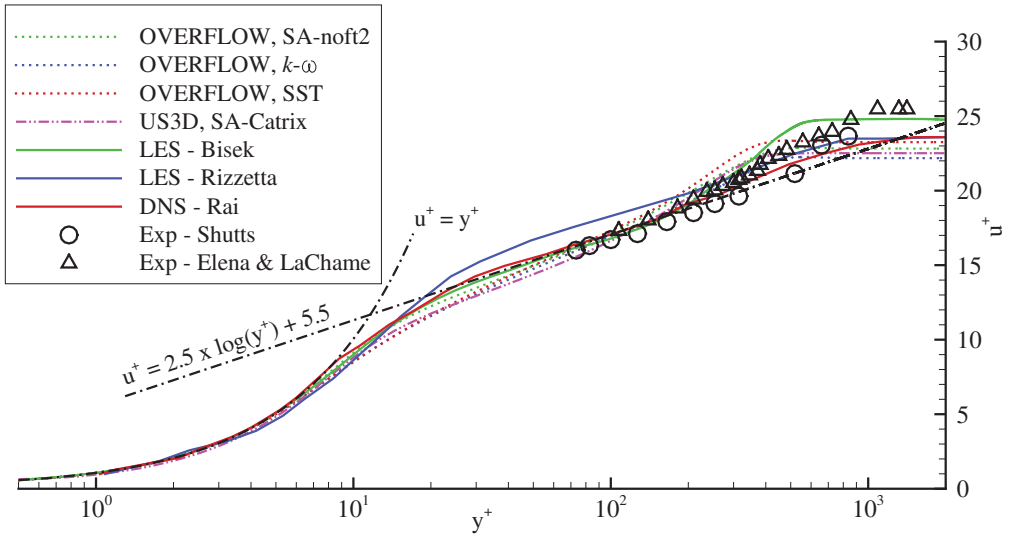

Figure 4. Comparison of Turbulent Boundary Layers from Medium Grids using Van Driest Transformation.

IV. Corner Flow in a Quarter Duct

IV.A. Reference LES Calculations

One aspect of the current work was to determine if RANS simulations involving corner flow could be improved by tuning the C_{cr1} constant in the QCR term. An LES by Bisek was used as reference, and thus drove the range of momentum Reynolds numbers to be investigated.[21] In his calculations, a high-fidelity time-accurate, three-dimensional, compressible, nondimensionalized Navier-Stokes solver (FDL3DI)[45,46] was used to simulate supersonic turbulent boundary-layer flow near a 90° corner. The simulation was performed using sixth-order centered implicit-difference operator in conjunction with a low-pass, Padé-type, non-dispersive eighth-order spatial filter. The filter regularizes poorly-resolved features at the grid scale and generates virtual SGS model terms that are equivalent to those of an approximate deconvolution.[47] Three grids of increasing resolution were used in the study, with the fine grid having a maximum spatial resolution of $\Delta x^+ = 17.6$ in the streamwise direction. In the wall normal directions, $\Delta y_w^+ = \Delta z_w^+ = 0.35$ at the wall, which was stretched to $\Delta y^+ = \Delta z^+ = 5.9$ at the boundary-layer edge. This resolution was maintained throughout the inviscid core for a total of 1.1×10^9 points. The coarse grid used half the resolution in all three-directions, while the medium grid had 1.5 times the resolution of the coarse grid.

The original LES study showed that the first moments had converged within the running-mean time collected ($\approx$ 200 eddy turn-over times based on the boundary-layer height and edge velocity), but that higher-moments, like secondary flow, required more iterations to converge. Since the medium and fine grids yielded similar turbulent equilibrium flows, the medium grid was run for an addition 1200 eddy turn-over times to further converge the second moments. Fig. 5 shows planar contours of the mean cross-velocity ($\overline{u \cdot v}$), and the mean fluctuations ($\overline{u' \cdot v'}$) at a streamwise station with a Reynolds number momentum thickness of approximately 2,500 from the medium grid. Two main conclusions can be reached from the results. First, the corner flow clearly shows two counter-rotating vortices indicative of secondary motion which confirms the results by Madabhushi and Vanka that LES can capture secondary motion. And second,

that the magnitude of the cross-velocity fluctuations is on the same order as the mean cross-velocities. As seen in the figures, the vortex pair appears to be nearly symmetric across the 45° bi-sector, although even more samples are desired to further refine the resultant contours and remove the finest-scale fluctuations seen along each sidewall. Since the RANS results assume the fluctuations of individual velocity components are zero (i.e., $\overline{v'} = \overline{w'} = 0$), direct comparison between RANS and the LES is ill-advised and the comparisons of features, such as the location of the vortex center, should be taken with caution, but might be used to indicate the strength of the QCR term.

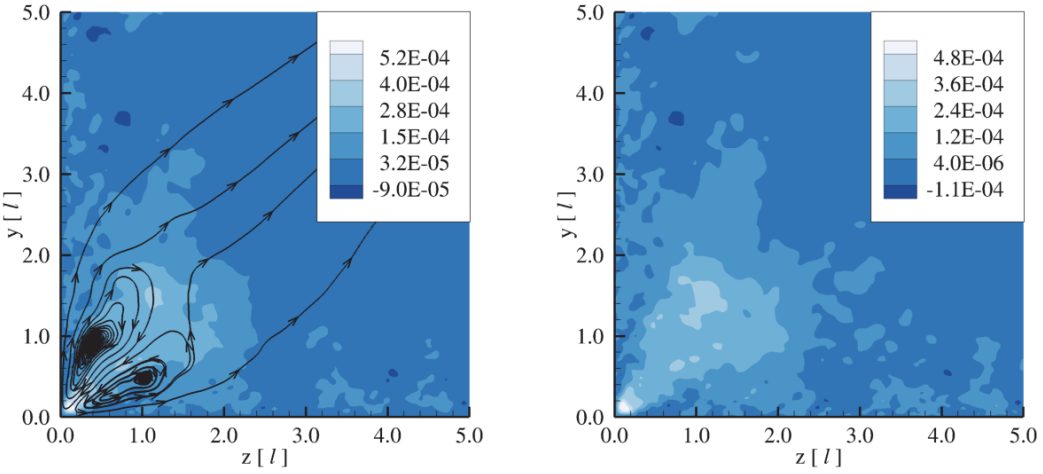

(a) Average Cross Velocity Magnitude, $(\overline{v \cdot w})/(u_\infty^2)$

(b) Cross Velocity Fluctuations, $(\overline{v' \cdot w'})/(u_\infty^2)$

Figure 5. Cross Velocity Components from the LES Calculation[21] on the Medium Grid for Re_θ = 2500 in the Near Corner Region, with Cross Velocity Streamlines to Highlight the Vortex Pair Associated with Secondary Flow.

IV.B. Grid

To investigate corner flow, one quarter of a one-to-one duct was simulated. Grids for the quarter duct were developed in a similar manner to those from the flat plate grids, with a resolved domain size of 12.5 l by 12.5 l, and 200 l long. As with the flat plate, this length allowed the boundary layer away from the corner to develop to a Re_θ of just over 3,000 for all turbulence models and a grid independence study was performed. The coarse grid was constructed first, with the same streamwise spacing as the flat plate (clustered towards the inlet from 1 to 10 l, with constant spacing there after). For convenience, the corner was set to be along the line $y = z = 0$. From the corner to $y = z = l$, 22 cells were used on each wall with clustering via a hyperbolic tangent function, such that at the corner the same initial spacing as in the flat plate was used, and at $y = z = l$, a spacing of 0.2 l was set. From $y = z = l$ to $y = z = 3$ l, 10 cells were used on each wall with constant spacing. From $y = z = 3$ l to $y = z = 12.5$ l, 16 additional cells were used along each wall and clustered using a hyperbolic tangent function, with the spacing at $y = z = 3$ l set to 0.2 l and left unconstrained at $y = z = 12.5$ l. A downstream view of the resulting grid is show in Fig. 6. The clustering from the corner to $y = z = 3$ l was chosen to best capture the counter rotating vortex pair associated with secondary flow. From DNS and LES results reported in the literature, this counter rotating vortex pair is expected to be on the size of the turbulent boundary layer thickness, which for the current flow conditions is between 2.5 and 3 l. This resulted in a coarse grid which was 222 by 48 by 48 cells or 511,488 cells total. The medium grid was constructed from the coarse grid using a cubic spline algorithm to double the number of cells in each direction while maintaining the original distribution. Fine grids were then generated from the medium grids using the same procedure.

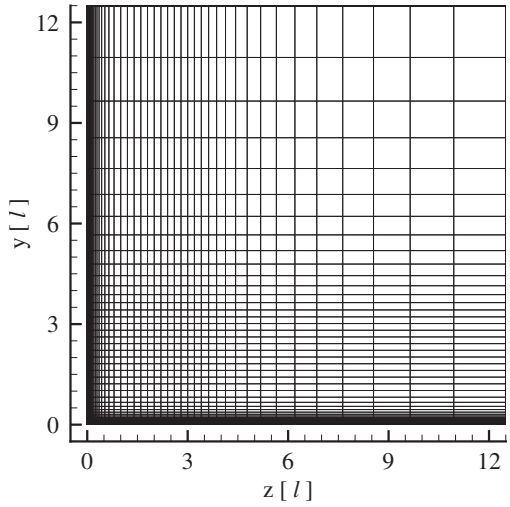

Figure 6. Downstream $(y-z)$ View of the Coarse Corner Grid.

IV.C. Boundary Conditions

For the US3D simulations, supersonic inflow and outflow boundary conditions were applied at the inlet and outlet respectively. An adiabatic wall boundary condition was applied at the two walls, $y = 0$ and $z = 0$, with an initial temperature of 320 K. Symmetry boundary conditions were applied opposite the walls, at $y = 12.5\ l$ and $z = 12.5\ l$. Unfortunately, this symmetry condition resulted in a weak shock, formed at the start of the wall, being reflected onto the boundary layer and limiting convergence. To remedy this and obtain results with US3D, the boundaries opposite the walls were changed to a freestream boundary condition.

In the OVERFLOW simulations, the inlet was set to a freestream boundary conditions while the outlet was set to a purely extrapolated outflow boundary condition. A viscous adiabatic wall boundary condition, based on pressure extrapolation, was applied at the two walls, $y = 0$ and $z = 0$. Symmetry boundary conditions were applied opposite the walls, at $y = 12.5\ l$ and $z = 12.5\ l$. To support transition of the flow, a laminar region (with zero production in the turbulence model) was specified for the first $10\ l$ of the domain from the inlet.

IV.D. Quadratic Constitutive Relation

The failure of early RANS simulations to predict secondary flow in rectangular ducts and channels can be traced back to the Boussinesq approximation used in their formulation. This approximation states that the turbulent Reynolds-stress tensor, τ_{ij}^t, is linearly proportional to the strain-rate tensor, S_{ij}, by the eddy-viscosity, μ_t, which is calculated by the turbulence model.

$$\tau_{ij}^t = 2\mu_t \left(S_{ij} - \frac{1}{3}\frac{\partial u_k}{\partial x_k}\delta_{ij} \right) - \frac{2}{3}\rho k \delta_{ij} \tag{1}$$

$$S_{ij} = \frac{1}{2}\left(\frac{\partial u_i}{\partial x_j} + \frac{\partial u_j}{\partial x_i}\right) \tag{2}$$

Note that the last term in the Boussinesq approximation is typically ignored when used with turbulence models for which k is not readily available, such as Spalart-Allmaras.

However from DNS and LES results, the turbulent Reynolds-stress tensor is known to be anisotropic for some flows, including corner flow.[12] One approach to account for this, known as Algebraic Stress Models (ASM), is to discard the Boussinesq approximation and calculate the turbulent Reynolds stresses directly using nonlinear constitutive relations.[37] Unfortunately these models often have unpleasant mathematical

behavior, resulting in multiple solutions or even singularities that limit any numerical solvers robustness and stability.[48]

As an alternative, Spalart proposed the Quadratic Constitutive Relation (QCR) in 2000, to more easily account for the anisotropic, non-linear Reynolds-stress behavior in corner flow.[20] To obtain a nonlinear Reynolds-stress tensor, an additional term is added to the Boussinesq approximation:

$$\tau_{ij}^{t,QCR} = \tau_{ij}^{t} - C_{cr1}(O_{ik}\tau_{jk}^{t} + O_{jk}\tau_{ik}^{t}) \tag{3}$$

where τ_{ij}^{t} is the Boussinesq approximation and the term O_{ij} is an anti-symmetric normalized rotation tensor defined as:

$$O_{ij} = \frac{(\partial u_i/\partial x_j) - (\partial u_j/\partial x_i)}{\sqrt{(\partial u_m/\partial x_n)(\partial u_m/\partial x_n)}} \tag{4}$$

Note that the summation convention is used in equations 3 and 4, with i and j as free indices, and k, m, and n as repeated indices (see Appendix for details). Spalart recommended a value of 0.3 for the constant C_{cr1}, but also stated that this value was calibrated in the outer region of a simple boundary layer by requiring a fair level of anisotropy, $\overline{u'^2} > \overline{w'^2} > \overline{v'^2}$ (the streamwise, spanwise, and wall-normal Reynolds stresses, respectively). While QCR uses only one of many possible quadratic combinations of strain and vorticity, it does reproduce secondary flow quite well as shown in Fig. 7. In a recent article,[49] Spalart suggested the constant C_{cr1} could be varied, but also reported that values below 0.2 suppressed the QCR effect while values above 0.35 tended to cause instabilities, along with unphysical vortices in the boundary layer. A significant advantage of QCR is that it can be used with any turbulence model that normally makes use of the Boussinesq approximation.

In 2013, an additional term was added to the QCR formulation:[50]

$$\tau_{ij}^{t,QCR} = \tau_{ij}^{t} - C_{cr1}(O_{ik}\tau_{jk}^{t} + O_{jk}\tau_{ik}^{t}) - C_{cr2}\mu_t\sqrt{2S_{mn}^{*}S_{mn}^{*}}\delta_{ij} \tag{5}$$

$$S_{ij}^{*} = S_{ij} - \frac{1}{3}\frac{\partial u_k}{\partial x_k}\delta_{ij} \tag{6}$$

This additional term is related to a proposal by Wilcox and Rubeson[51] and is found in many Algebraic Reynolds Stress models. Once again, the summation convention is used, where k, m, and n are repeated indices. The recommended value for the constant C_{cr2} is 2.5. Following the notation of the NASA Langley Research Center turbulence modeling website,[52] this variant is known as QCR2013, while the original version by Spalart is referred to as QCR2000. Note that if the turbulence model employed provides k, then this new term is redundant with the $-2\rho k\delta_{ij}/3$ term in the Boussinesq approximation, and the latter should be used instead. However, it has been reported that this new term can lead to unstable results in finite volume solvers,[53] especially grids with mixed elements.[50] For such situations, C_{cr2} should be set to zero, as corner flow is dominated by the C_{cr1} term.

OVERFLOW includes QCR2000, but the current release of US3D does not include either form of QCR. For simplicity, the QCR2000 formulation was selected and added to US3D so results from a finite volume solver could be included in this work.

IV.E. Analysis Procedure

For the results presented from this point forward, the following procedure was used to extract $y - z$ planes from the 3D corner simulations. First, a 2D slice of the solution was taken along the $z = 6.2\ l$ streamline to obtain the momentum thickness along the streamwise direction away from the corner. This location was chosen for two reasons. First, it corresponds to the third grid line away from the symmetry boundary condition in the coarse grid. Since a factor of 2 was used to refine the grids in each direction, this location is consistent for all three levels of refinement. Second, the location is sufficient far from both the symmetry boundary condition and corner, such that the flow is as close as possible to a flat-plate boundary layer. Fig. 8 shows profiles just upstream of the outlet for the medium grid from OVERFLOW with the SA-noft2 turbulence model and C_{cr1} set to 0.3. From this figure, the corner effects appear to only extend 2 l away from the corner. By $z = 5\ l$, corner effects no longer influence the turbulent boundary layer. This 2D slice was used to calculate Re_θ along the streamline direction.

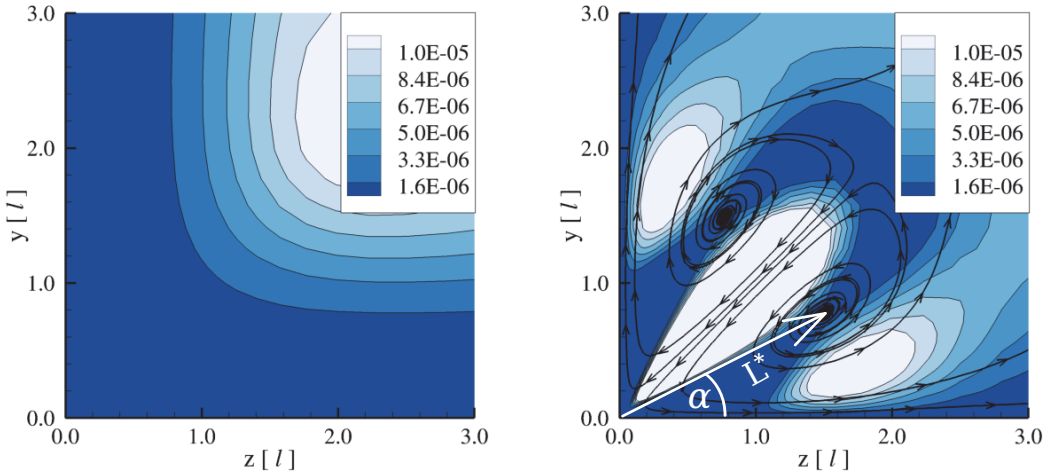

(a) QCR off, $C_{cr1} = 0.0$ (b) QCR on, $C_{cr1} = 0.3$

Figure 7. Effects of Quadratic Constitutive Relation(QCR), Contours of $(v \cdot w)/(u_\infty^2)$ and Cross Velocity Streamlines in the Near Corner Region from OVERFLOW using SA-noft2 and Medium Grid at Re_θ of 2,000.

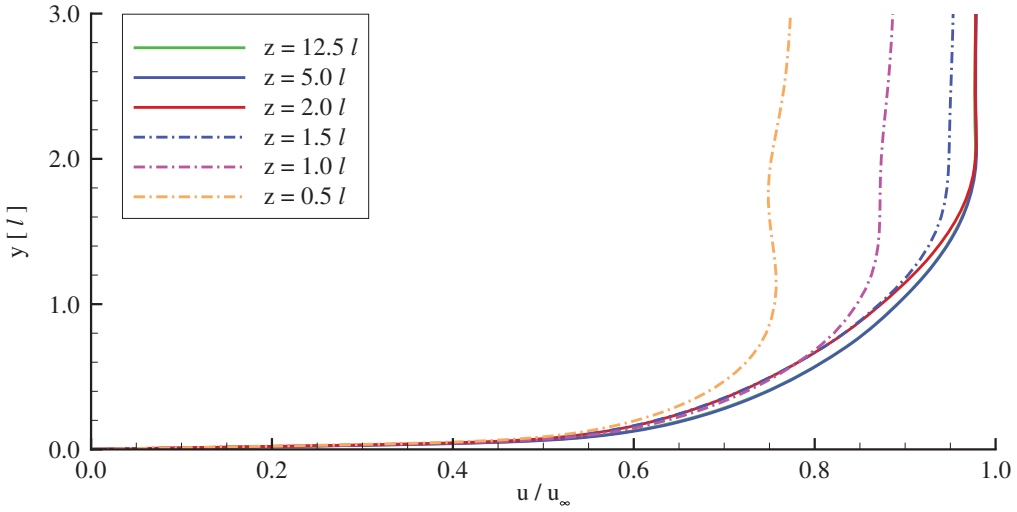

Figure 8. Correlation of Streamwise Velocity Profile with Distance from Corner, OVERFLOW with SA-noft2 and $C_{cr1} = 0.3$ for Medium Grid just Upstream of the Outlet.

Several methods were tried in order to determine the location of the counter rotating vortex pair(s). Tecplot 360$^{\text{TM}}$ [54] was used for the visualization of the results, which includes MIT's Fluid Feature Extraction toolkit.[55] Unfortunately, the Vorticity Vector method in the toolkit failed to detect any secondary flow vortex cores and the Velocity Gradient Eigenmodes method in the toolkit produced inconsistent results. This may be due to the vortices being too weak for proper detection. Instead, the easiest and most reliable method for finding the vortex pairs was found to be plotting contours of $(v \cdot w)/(u_\infty^2)$ and using this to identify seed locations for streamlines of the cross flow velocity. From these streamlines, the center of the lower vortex core from the main vortex pair was identified and quantified by the angle, α, and distance from the corner, L^*, as illustrated in Fig. 7(b).

It is interesting to note that through the use of these cross velocity streamlines, a second, and much

smaller, pair of counter rotating vortices was discovered in the very near corner. However, this smaller vortex pair was noted to rotate in the opposite direction as compared with the main vortex pair. These are shown in Fig. 9 for the solution from OVERFLOW with the SA-noft2, and this feature was also observed in all the scenarios considered in this study, as long as the grid was sufficiently resolved and the QCR constant was high enough to generate the main vortex pair typically associated with secondary flow. This result was also reported by Gavrilakis[12] in his DNS, but using the same cross velocity streamlines with the fine grid LES from Bisek[21] failed to detect them. The mechanism allowing this second pair of vortices to exist is still unknown and its not clear from the simulations if they are real or merely an artifact of the numerical approach.

To determine the strength of the vortex pairs, Tecplot 360$^{\mathrm{TM}}$ was used to calculate the vorticity, helicity, and swirl, but none of these quantities showed nearly as much change in solution contours in the vicinity near the vortex pair as the cross flow velocity magnitude $(v \cdot w)/(u_\infty^2)$. However, Divergence of Velocity in the plane $(\nabla \cdot V = \partial v/\partial y + \partial w/\partial z)$ did, and hence, is used along with the magnitude of the cross velocity in the following analysis. Fig. 10 shows contour plots of the divergence of velocity for the solution from OVERFLOW with the SA-noft2 turbulence model, C_{cr1} set to 0.3, on the medium grid at Re_θ of 2,000.

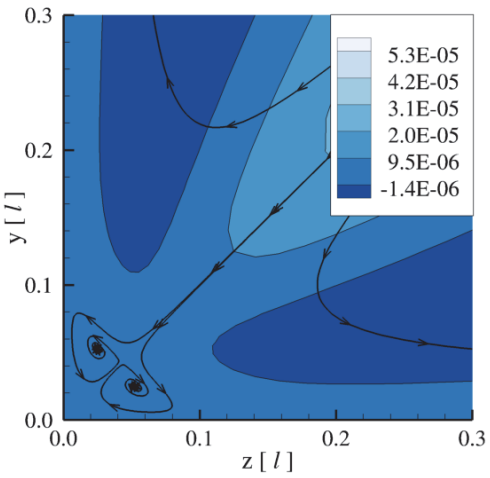

Figure 9. Close up View of Near Corner Region, Contours of $(v \cdot w)/(u_\infty^2)$ and Cross Velocity Streamlines from OVERFLOW using SA-noft2 with C_{cr1} = 0.3 and Medium Grid at Re_θ of 2,000.

IV.F. Grid Refinement with QCR

A grid independence study was performed to determine the maximum cell size which could be used while not significantly changing the solution. This was performed for all four turbulence model scenarios, with C_{cr1} set to the recommended value of 0.3. Planes where Re_θ equaled 2,000 were extracted and contours of $(v \cdot w)/(u_\infty^2)$ plotted as shown in Fig. 11. In these plots, the fine grid results are shown as flood contours, the medium grid results are given as solid contour lines, and the coarse grid results are shown with dashed contour lines. It is important to note that the contour levels are from the fine grid and that the contour range between grid refinement levels did not match exactly. From this figure, the results for the OVERFLOW solutions appear to be converged between the fine and medium grids.

IV.G. QCR and Turbulence Models

As mentioned earlier, one of the strengths of QCR is that it can be used with any turbulence model that makes use of the Boussinesq approximation. However, one finding from this current study is that different turbulence models, when used with QCR, produce different results. It is important to note that SST and SA-Catrix turbulence models incorporate compressibility corrections while the SA-noft2 and k-ω do not. In Fig. 12, planes at Re_θ of 2,000 are shown from the medium grid, with C_{cr1} set to 0.3, for each of the turbulence models. Once again, contour plots of $(v \cdot w)/(u_\infty^2)$ are shown along with streamlines of the cross

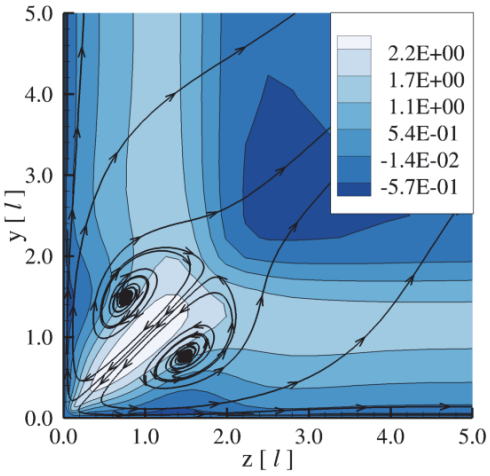

(a) Divergence of Velocity, $\nabla \cdot V$

Figure 10. Contour Plot of the Velocity Divergence from OVERFLOW, with the SA-noft2 Turbulence Model, C_{cr1} = 0.3, on the Medium Grid at Re_θ of 2,000.

velocity. An interesting observation from this plot is the similarity between the k-ω, SST, and SA-Catrix simulations, in the bulge of the contour lines away from the corner above the vortex pair. This is not too surprising for the k-ω and SST models, as the SST model near surfaces is based on the k-ω model. Also observed is that this contour line away from the corner is slightly less concave in the SST results, and more convex in the SA-Catrix results, compared with the k-ω results.

For these plots, the seed points for the six streamlines were kept the same. This allows for a few interesting trends between the turbulence models to be observed. First, the core of the vortex pair in the k-ω, SST, and SA-Catrix results appears to be tighter than in the SA-noft2 results. Looking at the middle streamline on either side of the corner bisect, the k-ω results show more of the momentum from the vortex pair being directed along the walls than in both the SA-noft2 and SA-Catrix results, while in the SST results, the momentum is directed back along the diagonal.

IV.H. Valid Range of the QCR Constant and Effects of Re_θ

One of the main objectives of this work was to determine if an LES solution could be used to tune the constant C_{cr1} in a QCR enabled RANS model, and thus obtain a better RANS result for corner flow. However, a more fundamental outcome is determining a valid range of C_{cr1} values for which a feasible result can be obtained. For simplicity, the definition of a good result used here is one which shows a single vortex pair of significant size. The formation of the very small vortex pair in the viscous sublayer is not counted toward this definition. Tables 2 and 3 give the total number of vortex pairs, including those in the viscous sublayer, detected using cross velocity streamlines for each scenario. It should be noted that for each of the results listed in Tables 2 and 3, the previously mentioned small pair of counter rotating vortices in the near corner, viscous sub-region were present. The determination of a valid range for the QCR constant is further complicated by the effects of different turbulence models when used with QCR, as has been illustrated, along with effects of Re_θ, which will be demonstrated as well.

During exploration of the C_{cr1} range, it was discovered that values too low failed to produce any detectable vortex pair and values too high produced extra vortex pairs in the near corner region. These additional vortex pairs were much smaller than the main pair and were mostly located along the walls for moderately high values of C_{cr1}, as shown in Fig. 13(a). However, as C_{cr1} was increased further, an additional and much larger vortex pair, formed about the main vortex pair, as shown in Fig. 13(b). Simulations with values of C_{cr1} at and beyond this became unstable and failed to converge.

Fig. 14 shows the distance from the corner to the core center of the main vortex, L^*, with changes in the strength of QCR via C_{cr1}. The general trend from this figure is that increases in C_{cr1} cause the vortex pair

Table 2. Total Number of Vortex Pairs Detected Using Cross Velocity Streamlines for OVERFLOW Results.

	$Re_\theta = 2,000$			$Re_\theta = 2,500$			$Re_\theta = 3,000$		
C_{cr1}	SA-noft2	k-ω	SST	SA-noft2	k-ω	SST	SA-noft2	k-ω	SST
0.10	2	1	1	2	2	4	2	2	2
0.15	2	2	2	-	-	-	-	-	-
0.20	2	2	2	2	2	4	2	2	2
0.25	2	2	2	-	-	-	-	-	-
0.30	2	2	2	2	2	4	2	2	4
0.35	2	2	2	-	-	-	-	-	-
0.40	3	2	2	3	3	4	2	2	4
0.45	3	2	3	-	-	-	-	-	-
0.50	3	3	3	3	3	5	3	3	5
0.55	3	3	3	-	-	-	-	-	-
0.60	3	3	5	4	3	7	5	4	6
0.65	4	3	-	-	-	-	-	-	-

Table 3. Total Number of Vortex Pairs Detected Using Cross Velocity Streamlines for US3D Results.

	$Re_\theta = 2,000$	$Re_\theta = 2,500$	$Re_\theta = 3,000$
C_{cr1}	SA-Catrix	SA-Catrix	SA-Catrix
0.10	1	1	1
0.20	2	2	2
0.30	2	2	2
0.40	2	2	2
0.50	3	3	3
0.60	3	3	4
0.70	4	4	5

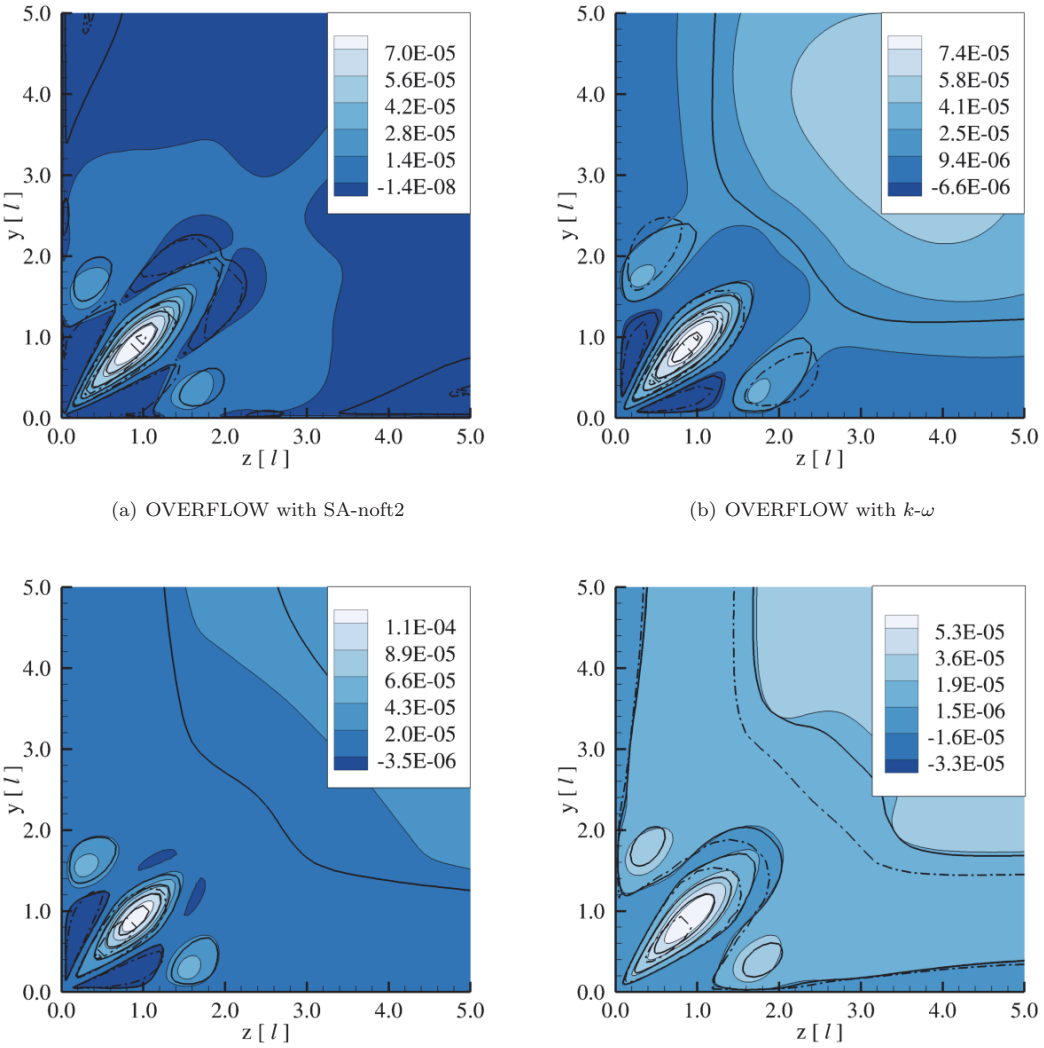

(a) OVERFLOW with SA-noft2

(b) OVERFLOW with k-ω

(c) OVERFLOW with SST

(d) US3D with SA-Catrix

Figure 11. Effects of Grid Resolution on Quadratic Constitutive Relation with $C_{cr1} = 0.3$, Contours of $(v \cdot w)/(u_\infty^2)$. (Flood is fine grid, solid line is medium grid, dash-dot line is coarse grid)

to move closer towards the corner, thus, strengthening the vortex pair and the corner flow effects. Another trend from this figure is that the vortex core moves away from the corner with increased momentum Reynolds number, indicating that the vortex grows as it develops downstream. Note that the slopes of the different turbulence models for each particular Re_θ appear to match, with the exception of the SA-noft2 for Re_θ of 2,000. Additionally, the slopes for Re_θ of 2,000 and 2,500 are very similar, but not as steep as that for Re_θ of 3,000. Another observation from this figure is a difference in sensitivity to changes in the momentum Reynolds number by the different turbulence models. For a particular C_{cr1} value, the SST shows less of an increase in L^* with increased Re_θ than the SA-noft2 and k-ω turbulence models. Also included in this figure is the LES results from the medium grid ($Re_\theta = 2750$) calculation. Since the vortex pair from the LES simulation is not perfectly symmetrical about the corner bisect, the length from both of the vortex cores to the corner are shown in the figure. While the trend with increased C_{cr1} values is towards the LES values, the QCR results never quite reach those of the LES simulation with stable values of C_{cr1}. Thus the vortex distance from the corner is not a quantity which QCR can be adjusted or tuned in order to match the LES

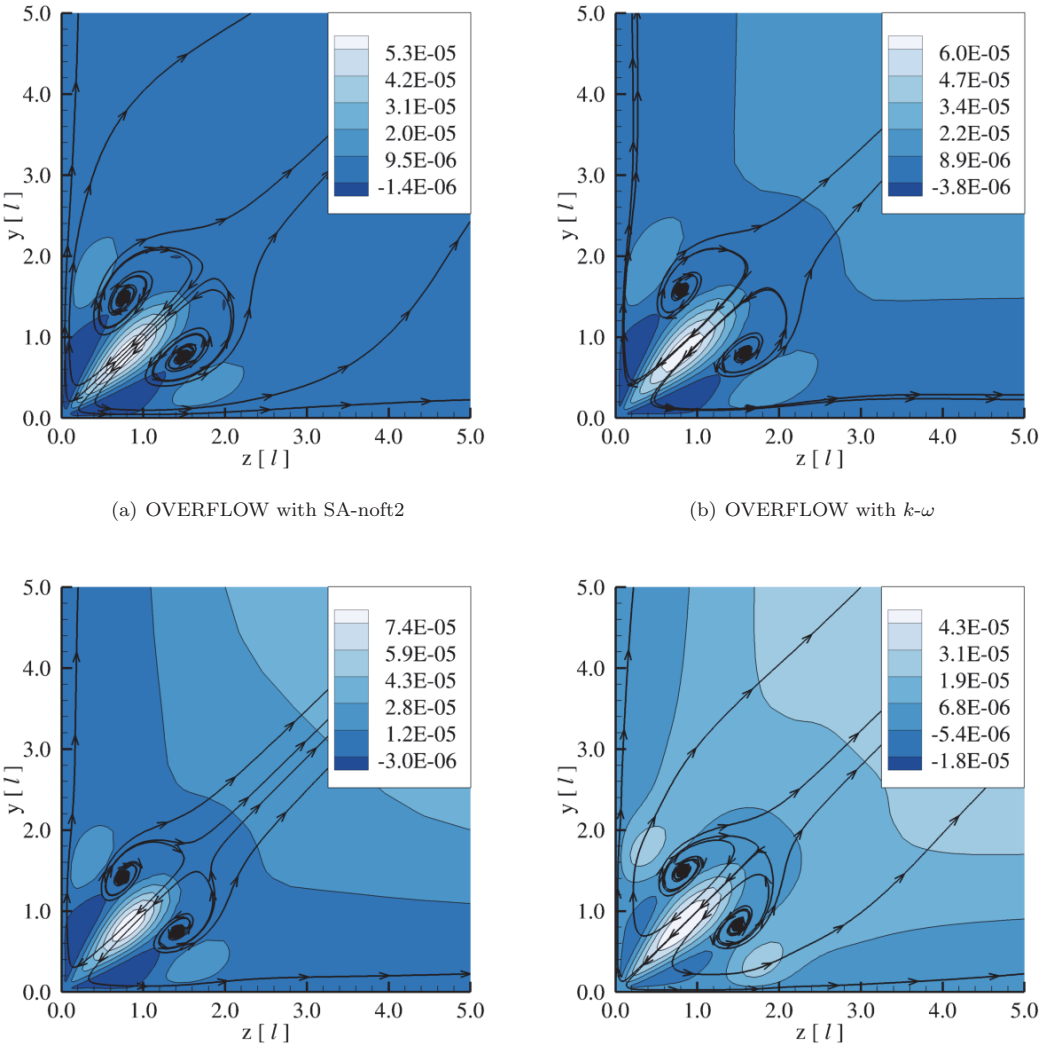

(a) OVERFLOW with SA-noft2

(b) OVERFLOW with k-ω

(c) OVERFLOW with SST

(d) US3D with SA-Catrix

Figure 12. Effects of Turbulence Model with Quadratic Constitutive Relation and $C_{cr1} = 0.3$ on Medium Grids, Contours of $(v \cdot w)/(u_\infty^2)$ with Cross Velocity Streamlines.

results.

The angle between the vortex core and the closest wall, α, with changes in the strength of QCR via C_{cr1} is given in Fig. 15. A general trend from this figure is that increases in C_{cr1} moves the vortex core closer to the wall. Changes in the momentum Reynolds number, as well as the use of different turbulence models, appears to have much less of an effect on the angle, α, than observed for L^*, with a maximum variation of around three degrees. Also observed from this figure for Re_θ of 2,000 is an inflection point around C_{cr1} of approximately 0.2. As with the previous figure, the LES results from the medium grid (Re_θ = 2750) calculation are included. Once again, since the vortex pair from the LES simulation is not perfectly symmetrical about the corner bisect, the angle from both of the vortex cores to the closest wall are shown in the figure. While the trend with increased C_{cr1} values is towards the LES values, only some of the turbulence model and Re_θ combinations come close to the LES results, and only for the highest C_{cr1} values for which a converged solution could be obtained. Hence the angle of the vortex core from the closest wall is not a quantity which QCR can be adjusted to match with the LES results, and given the previous result, shows

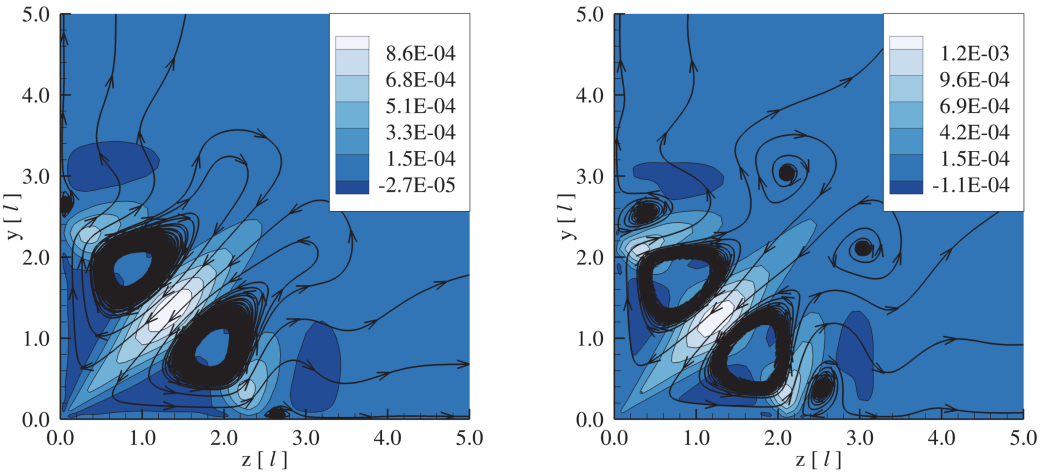

(a) $C_{cr1} = 0.5$ (b) $C_{cr1} = 0.6$

Figure 13. Effects of C_{cr1} Being Too High, Contours of $(v \cdot w)/(u_\infty^2)$ and Cross Velocity Streamlines in the Near Corner Region from OVERFLOW using SA-noft2 and Medium Grid at Re_θ of 3,000.

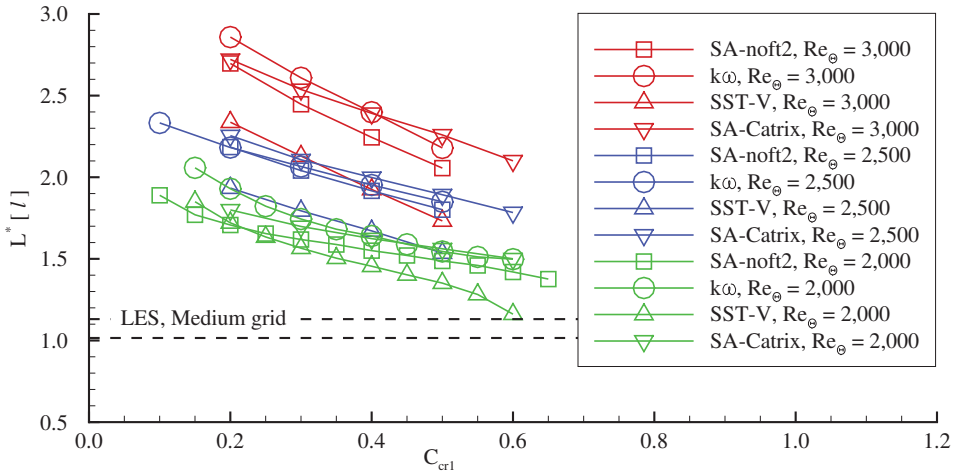

Figure 14. Effect of QCR Constant on Distance of Vortex Core from Corner for Re_θ of 2,000 (green symbols), 2,500 (blue symbols), and 3,000 (red symbols) using the Medium Grids.

that QCR cannot be tuned to reproduce the vortex locations of the LES calculation.

Fig. 16 shows the maximum velocity divergence, $\nabla \cdot V$, along the corner bisect in the corner region, for a range of C_{cr1} values. The general trend is that the divergence of velocity increases as C_{cr1} increases, with what appears to be an inflection point around C_{cr1} of 0.3. Also included in this figure is the LES result from the medium grid ($Re_\theta = 2750$) calculation. Results from Re_θ of 2,500 and 3,000 appear to collapse onto one another with the exception of the SA-Catrix results. It is interesting to note that at Re_θ of 2,000, the SA-noft2 results are below the LES result up till a C_{cr1} of 0.4, while the other turbulence models are well above the LES result for all the C_{cr1} values used. Since the trend for k-ω with increased C_{cr1} at Re_θ of 2,000 differs from that at Re_θ of 2,500 and 3,000, as well as the trends for the other turbulence models for all three Re_θ values, it is questionable whether the k-ω turbulence model is valid at a Re_θ of 2,000. Further more, this difference in trends for the k-ω is only visible in the divergence of velocity. For an Re_θ of 2,000,

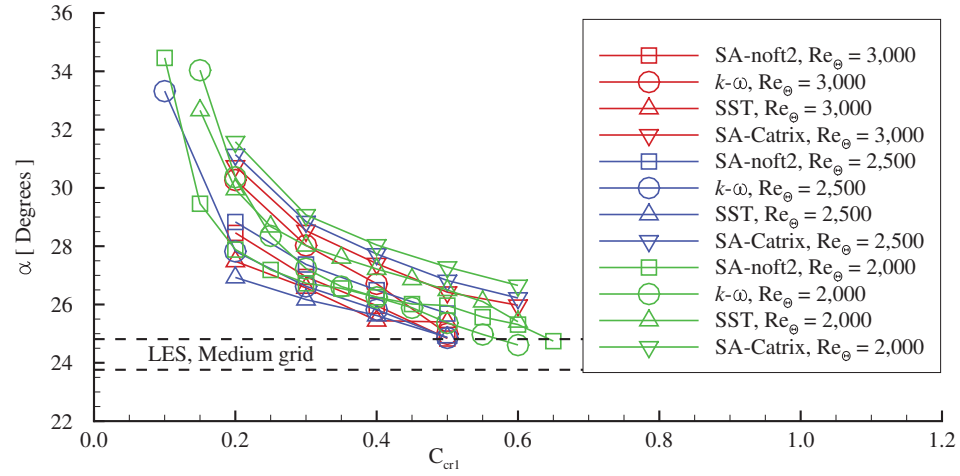

Figure 15. Effect of QCR Constant on Angle of Vortex Core from Nearest Wall for Re_θ of 2,000 (green symbols), 2,500 (blue symbols), and 3,000 (red symbols) using the Medium Grids.

the SA-noft2 results have an inflection point around C_{cr1} of 0.4, while the k-ω results appear to have an inflection point around 0.5. An inflection point may also exist for the SST results at Re_θ of 2,000 near C_{cr1} of 0.55, but difficulty was encountered in obtaining a converged solution for higher C_{cr1} values above 0.6 with the SST turbulence model. Contrary to this, the SA-Catrix results show no such inflection point. Since none of the results for the two higher Re_θ values reach that from the LES calculation, the maximum velocity divergence does not appear to be a quantity for which QCR can be tuned to match.

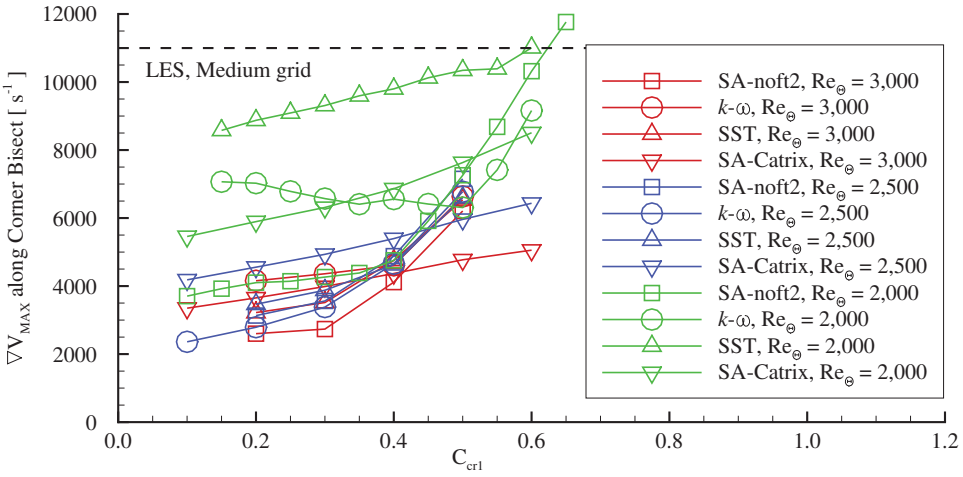

Figure 16. Effect of QCR Constant on Maximum Divergence of Velocity along Corner Bisect for Re_θ of 2,000 (green symbols), 2,500 (blue symbols), and 3,000 (red symbols) using the Medium Grids.

A plot of the maximum cross velocity magnitude, normalized by the freestream velocity, with respect to C_{cr1} is given in Fig. 17. Again, the LES result from the medium grid (Re_θ = 2750) calculation is included for comparison. The QCR results appear to collapse on top of one another, indicating that cross velocity is independent of turbulence model and Re_θ, and approach an asymptotic value as C_{cr1} is increased. Interestingly, this asymptotic value seems close to that obtained from the LES result. However, since this asymptotic limit is never reached by the QCR results, this is yet another quantity for which QCR can not

be tuned to match.

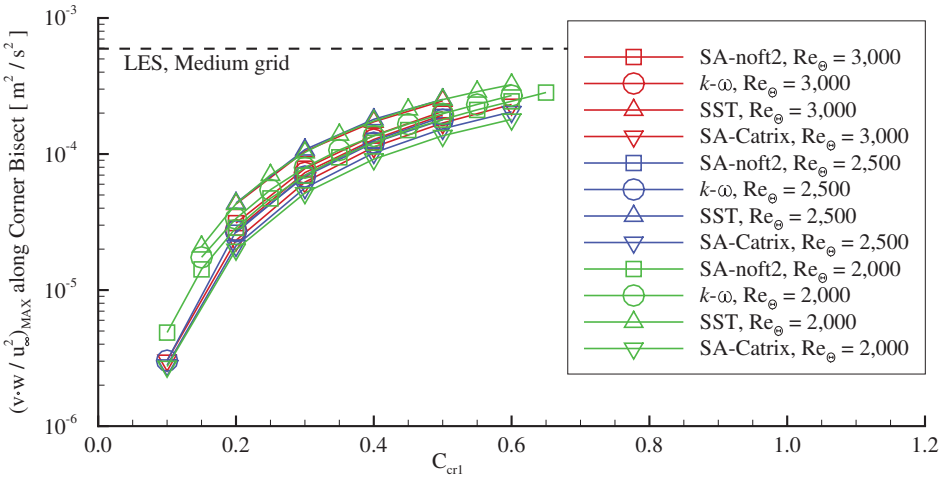

Figure 17. Effect of QCR Constant on Maximum Cross Velocity along Corner Bisect for Re_θ of 2,000 (green symbols), 2,500 (blue symbols), and 3,000 (red symbols) using the Medium Grids.

Fig. 18 shows the effect of C_{cr1} on the corner temperature. Note that for C_{cr1} of zero, QCR is disabled and thus no corner flow is captured by the RANS simulation. As expected, the general trend from this figure is an increased heating of the corner with higher values of C_{cr1}. This increased heating does not appear to be significantly influenced by the turbulence model used, nor Re_θ, and appears to become linear after C_{cr1} of 0.3. In addition, the SA-Catrix and SST results are approximately one and a half degrees higher than those from the other two turbulence models up til a C_{cr1} value of 0.3. Beyond this, results from the different turbulence models and Re_θ appear to merge, with the exception of the SA-Catrix for Re_θ defining a slightly higher corner temperature and the Re_θ of 2,000 results defining a slightly lower corner temperature. The difference in corner temperature between C_{cr1} of zero (QCR disabled) and the recommended value of 0.3 is approximately 5 K, but since Fig. 16 and 17 show C_{cr1} could be as high as 0.5, the temperature change in the corner could be as high as 20 K.

The effect of C_{cr1} on wall temperature in the near corner region, at Re_θ of 2,000 is shown in Fig. 19. From these figures, the increase corner heating is within 1.5 to 2 l of the corner, and the lines appear to cross at around 1.5 l for all cases. The main effect of increasing C_{cr1}, as was shown in Fig. 18, is to increase the temperature in the near corner region. In addition, this figures shows oscillations in the temperature profile along the wall. These occur at around C_{cr1} values of 0.5, 0.6, 0.4, and 0.6 for the SA-noft2, k-ω, SST, and SA-Catrix turbulence models respectively, and is likely due to the extra vortex pairs which form at such high C_{cr1} values. The SA-Catrix turbulence model also shows slightly higher temperatures overall.

Fig. 20 shows the effects of C_{cr1} on skin friction in the near corner region, at Re_θ of 2,000. Once again, oscillations in the skin friction are obvious, but start at values of C_{cr1} below those where oscillations in the wall temperature are observed, and vanish after approximately 4 l. The skin friction values cross at around 1.4 l for the SA-noft2, k-ω, and SA-Catrix results, and around 1.2 l for the SST results with the exception of C_{cr1} at 0.6. In the region from the corner to this crossing point, higher values of C_{cr1} produce increased skin friction, with an approximate increase of 10% for C_{cr1} of 0.6 compared to C_{cr1} of 0 (QCR disabled). Also included in these figures are the LES results from the medium grid (Re_θ = 2750) calculation. In the very near corner region, the skin friction from the LES calculation rises quickly over a very short distance, and the higher C_{cr1} values appear to capture this. However, the higher values of C_{cr1} also produce additional vortex pairs along the wall which show up as oscillations in skin friction immediately following this rapid rise. Thus, QCR appears to be tunable in order to capture the quick rise of skin friction in the near the corner region, but not the peak value.

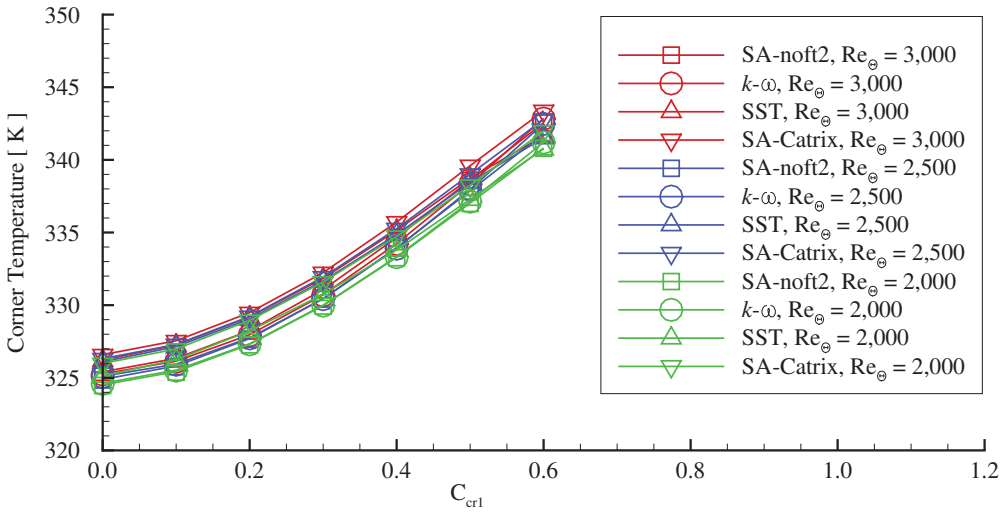

Figure 18. Effect of QCR Constant on Corner Temperature for Re_θ of 2,000 (green symbols), 2,500 (blue symbols), and 3,000 (red symbols) using Medium Grids.

V. Conclusions

A series of Reynolds Average Navier-Stokes (RANS) simulations were performed using two different flow solvers, OVERFLOW and US3D, for supersonic, wall bounded, turbulent corner flow. The ability of both flow solvers, along with four different turbulence models, to produce a turbulent boundary layer at the relatively low momentum thickness Reynolds number typical of LES calculations was verified. However, the turbulent boundary layer profiles produced at Re_θ of 2,000 were noticeably different for each of the turbulence models as well as from the LES calculation. At an Re_θ of 20,000 though, the profiles from the other turbulence models collapsed and agreed favorably with the lower Re_θ LES trend. This demonstrated that the four turbulence models used for this work, while capable of generating a turbulent boundary layer, are clearly tuned for higher Re_θ.

For the corner flow, one quarter of a one-to-one duct was simulated using geometry and flow conditions very similar to a set of high fidelity LES calculations done by Bisek. Use of the Quadratic Constitutive Relation (QCR) in the RANS flow solvers was shown to significantly improve the results and more closely match the LES calculation. This was primary through the production of counter rotating pairs of vortices in the corner, which are indicative of corner flow. To determine a valid range for the C_{cr1} constant in the QCR formulation, RANS simulations were performed with different values of this constant. In addition, the behavior of different turbulence models along with that at three different momentum Reynolds numbers was explored.

The distance from the corner to the main vortex pair core, L^*, along with the angle from the core to the closest wall, α, were calculated for each case. From this, it was determined that increasing C_{cr1} results in the vortex core moving in towards the corner and out towards the walls. The angle of vortex core from the closest wall, α, appeared to be independent of turbulence model and Re_θ, with a maximum difference of approximately three degrees. However for L^*, increases in Re_θ pushed the vortex further away from the corner, but the results were, for the most part, independent of the turbulence model used. When compared with the LES calculations, it appears that QCR can not be tuned to match the position of the vortex pair.

To determine the strength of the corner flow, the maximum divergence of velocity and maximum cross velocity magnitude along the corner bisect were used. As C_{cr1} was increased, the maximum divergence of velocity also increased. Results from Re_θ of 2,500 and 3,000 appear to collapse upon one another. Since the results for these two higher Re_θ do not reach the maximum velocity divergence from the LES medium grid calculation, this appears to be a quantity for which QCR can not be tuned to match. The maximum cross velocity magnitude also increased as C_{cr1} was increased, and appeared to approach an asymptotic limit.

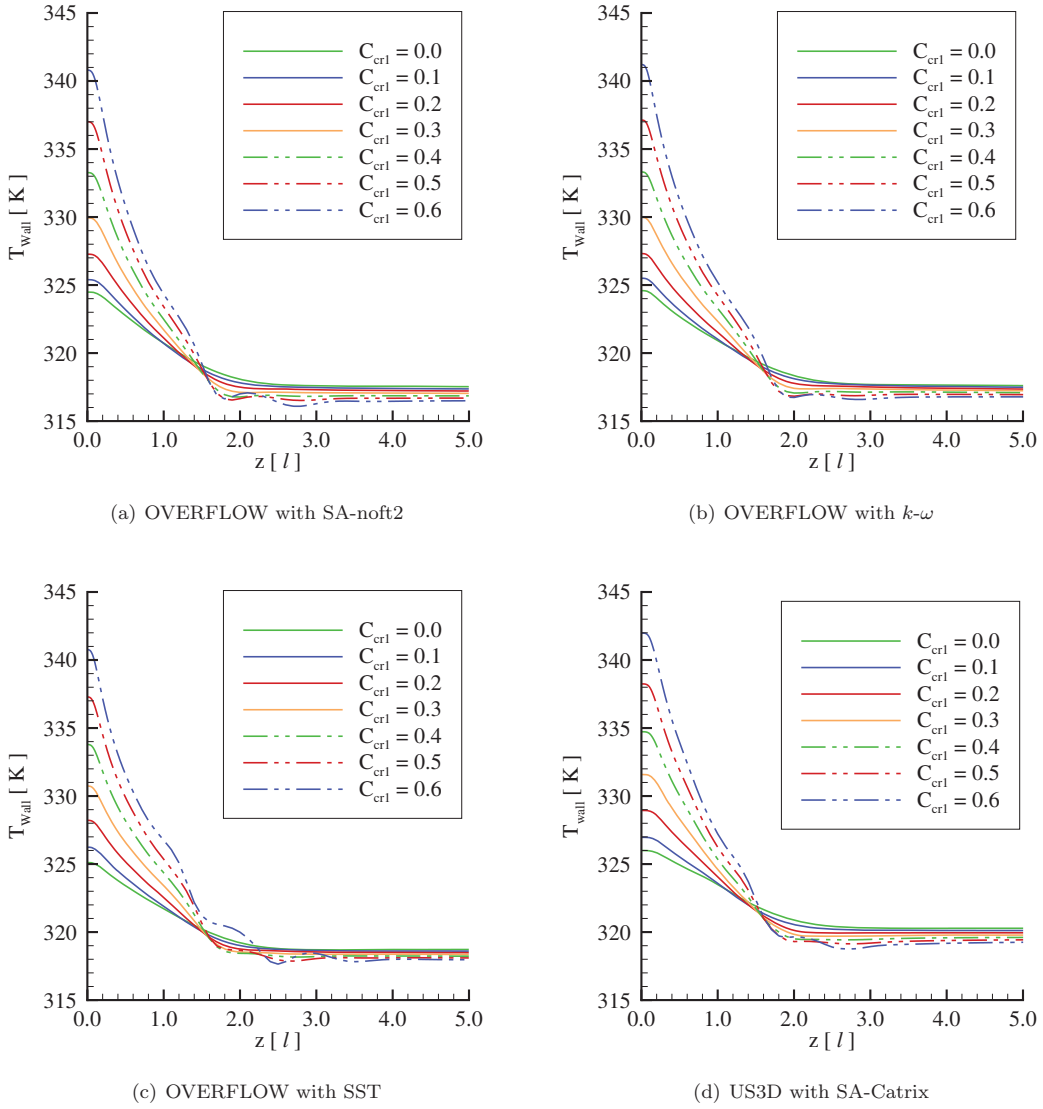

(a) OVERFLOW with SA-noft2

(b) OVERFLOW with k-ω

(c) OVERFLOW with SST

(d) US3D with SA-Catrix

Figure 19. Effects of C_{cr1} on Wall Temperature with the Medium Grids for Re_θ of 2,000.

However this limit is below the maximum cross velocity from the LES medium grid calculation, and is thus another quantity for which QCR can not be tuned to match. Since the maximum cross velocity results with QCR collapsed to the same curve, it indicates that this quantity is independent of turbulence model and Re_θ.

Since an adiabatic wall condition was used for the RANS simulations, the temperature at the corner was also examined to determine the strength of the corner flow. As C_{cr1} was increased, so was the temperature at the corner, with the behavior appearing to be linear after C_{cr1} of 0.3. It was also observed that different turbulence models and changes in Re_θ had little to no effect on the corner temperature. The difference in corner temperature between QCR with C_{cr1} at the recommended value of 0.3, and that without QCR, was approximately 5 K.

Looking at skin friction and temperature along the wall in the near corner region, oscillations were observed for high values of C_{cr1}. These oscillations were stronger and more noticeable in the skin friction than in the wall temperature. At a distance of approximately 4 l from the corner, oscillations in both skin

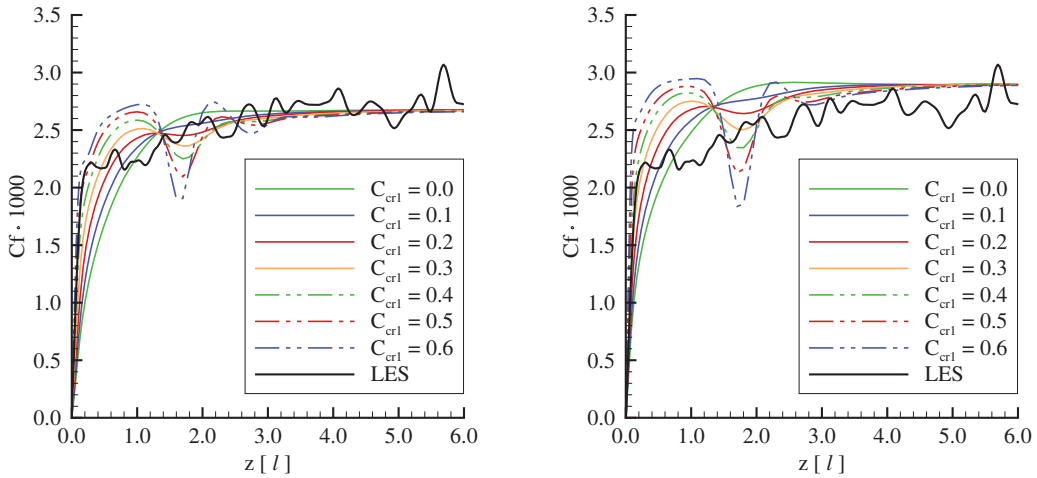

(a) OVERFLOW with SA-noft2

(b) OVERFLOW with k-ω

(c) OVERFLOW with SST

(d) US3D with SA-Catrix

Figure 20. Effects of C_{cr1} on Skin Friction with the Medium Grids for Re_θ of 2,000.

friction and wall temperature were no longer noticeable. These oscillations are likely due to the additional vortex pairs which form along the wall at the higher C_{cr1} values. Thus, QCR appears to be tunable in order to capture the quick rise of skin friction in the near the corner region, but not the peak value.

VI. Appendix

For brevity in the QCR equations, the summation convention was used, in which repeated indices (those which appear twice in the same term) are summed over. It is also important to note that the diagonal terms of the anti-symmetric rotation tensor, O_{xx}, O_{yy}, and O_{zz}, are zero. Thus when expanded, the QCR2000 formulation becomes:

$$\tau_{xx}^{t,QCR} = \tau_{xx}^{t} - 2 \cdot C_{cr1} \left(-O_{yx}\tau_{yx}^{t} - O_{zx}\tau_{zx}^{t} \right) \tag{A-1}$$

$$\tau_{xy}^{t,QCR} = \tau_{yx}^{t,QCR} = \tau_{yx}^{t} - C_{cr1}\left(-O_{zy}\tau_{zx}^{t} - O_{zx}\tau_{zy}^{t} + O_{yx}(\tau_{xx}^{t} - \tau_{yy}^{t})\right) \tag{A-2}$$

$$\tau_{xz}^{t,QCR} = \tau_{zx}^{t,QCR} = \tau_{zx}^{t} - C_{cr1}\left(O_{zy}\tau_{yx}^{t} - O_{yx}\tau_{zy}^{t} + O_{zx}(\tau_{xx}^{t} - \tau_{zz}^{t})\right) \tag{A-3}$$

$$\tau_{yy}^{t,QCR} = \tau_{yy}^{t} - 2 \cdot C_{cr1}\left(O_{yx}\tau_{yx}^{t} - O_{zy}\tau_{zy}^{t}\right) \tag{A-4}$$

$$\tau_{yz}^{t,QCR} = \tau_{zy}^{t,QCR} = \tau_{zy}^{t} - C_{cr1}\left(O_{zx}\tau_{yx}^{t} + O_{yx}\tau_{zx}^{t} + O_{zy}(\tau_{yy}^{t} - \tau_{zz}^{t})\right) \tag{A-5}$$

$$\tau_{zz}^{t,QCR} = \tau_{zz}^{t} - 2 \cdot C_{cr1}\left(O_{zx}\tau_{zx}^{t} + O_{zy}\tau_{zy}^{t}\right) \tag{A-6}$$

and the anti-symmetric rotation tensor terms are:

$$O_{yx} = \frac{(\partial v/\partial x) - (\partial u/\partial y)}{\sqrt{\left(\frac{\partial u}{\partial x}\right)^2 + \left(\frac{\partial u}{\partial y}\right)^2 + \left(\frac{\partial u}{\partial z}\right)^2 + \left(\frac{\partial v}{\partial x}\right)^2 + \left(\frac{\partial v}{\partial y}\right)^2 + \left(\frac{\partial v}{\partial z}\right)^2 + \left(\frac{\partial w}{\partial x}\right)^2 + \left(\frac{\partial w}{\partial y}\right)^2 + \left(\frac{\partial w}{\partial z}\right)^2}} \tag{A-7}$$

$$O_{zx} = \frac{(\partial w/\partial x) - (\partial u/\partial z)}{\sqrt{\left(\frac{\partial u}{\partial x}\right)^2 + \left(\frac{\partial u}{\partial y}\right)^2 + \left(\frac{\partial u}{\partial z}\right)^2 + \left(\frac{\partial v}{\partial x}\right)^2 + \left(\frac{\partial v}{\partial y}\right)^2 + \left(\frac{\partial v}{\partial z}\right)^2 + \left(\frac{\partial w}{\partial x}\right)^2 + \left(\frac{\partial w}{\partial y}\right)^2 + \left(\frac{\partial w}{\partial z}\right)^2}} \tag{A-8}$$

$$O_{zy} = \frac{(\partial w/\partial y) - (\partial v/\partial z)}{\sqrt{\left(\frac{\partial u}{\partial x}\right)^2 + \left(\frac{\partial u}{\partial y}\right)^2 + \left(\frac{\partial u}{\partial z}\right)^2 + \left(\frac{\partial v}{\partial x}\right)^2 + \left(\frac{\partial v}{\partial y}\right)^2 + \left(\frac{\partial v}{\partial z}\right)^2 + \left(\frac{\partial w}{\partial x}\right)^2 + \left(\frac{\partial w}{\partial y}\right)^2 + \left(\frac{\partial w}{\partial z}\right)^2}} \tag{A-9}$$

Acknowledgments

This project was funded in part by AFOSR contract LRIR task 14RQ18COR, monitored by Dr. I. Leyva, AFOSR/RTE. The authors wish to thank the Air Force Research Laboratory Department of Defense Supercomputing Resource Center for computer time and Prof. G. Candler for the use of the US3D solver. Additional computer hours were provided under a DoD HPCMP Frontier Project (Dr. R. Gosse, Principal Investigator).

References

[1]Prandtl, L., "Turbulent Flow," Tech. Rep. NACA TM 435, September 1926.

[2]Demuren, O., "Calculation of Turbulence-Driven Secondary Motion in Ducts with Arbitrary Cross-Section," *AIAA Journal*, Vol. 29, No. 4, 1991, pp. 531–537.

[3]Gand, F., Deck, S., Brunet, V., and Sagaut, P., "Flow Dynamics Past a Simplified Wing Body Junction," *Physics of Fluids*, Vol. 22, No. 11, 2010, Paper 115111.

[4]Davis, D. O. and Gessner, F. B., "Further Experiments on Supersonic Turbulent Flow Development in a Square Duct," *AIAA Journal*, Vol. 27, No. 8, 1989, pp. 1023–1030.

[5]Valdivia, A., Yuceil, K. B., Wagner, J. L., Clemens, N. T., and Dolling, D. S., "Control of Supersonic Inlet-Isolator Unstart Using Active and Passive Vortex Generators," *AIAA Journal*, Vol. 52, No. 6, 2014, pp. 1207–1218.

[6]Burton, D. M. and Babinsky, H., "Corner Separation Effects for Normal Shock Wave/Turbulent Boundary Layer Interactions in Rectangular Channels," *Journal of Fluid Mechanics*, Vol. 707, 2012, pp. 287–306.

[7]Demuren, A. O. and Rodi, W., "Calculation of Turbulence-Driven Secondary Motion in Non-Circular Ducts," *Journal of Fluid Mechanics*, Vol. 140, 1984, pp. 189–222.

[8]Nezu, I., Nakagawa, H., and Tominaga, A., "Secondary Currents in a Straight Channel Flow and the Relation to its Aspect Ratio," *Turbulent Shear Flows 4*, edited by L. J. S. Bradbury, D. F., B. E. Launder, F. W. Schmidt, and J. H. Whitelaw, Springer, Berlin, 1985, pp. 246–260.

[9]Niederschulte, M. A., *Turbulent Flow Through a Rectangular Channel*, Ph.D. thesis, University of Illinois at Urbana, Champaign, IL, 1989.

[10]Cheesewright, R., McGrath, G., and Perry, D., "LDA Measurements of Turbulent Flow in a Duct of Square Cross Section at Low Reynolds Number," Aeronautical Engineering Department Report ER 1011, Queen Mary Westfield College, University of London, London, England, 1990.

[11]Morajkar, R. R., Driscoll, J. F., and Gamba, M., "Experimental Study of Supersonic Turbulent Corner Flow Evolution in a Low Aspect Ratio Rectangular Channel," AIAA Paper 2015-0542.

[12]Gavrilakis, S., "Numerical Simulation of Low-Reynolds-Number Turbulent Flow Through a Straight Square Duct," *Journal of Fluid Mechanics*, Vol. 244, 1992, pp. 102–129.

[13]Madabhushi, R. K. and Vanka, S. P., "Large Eddy Simulation of Turbulence-Driven Secondary Flow in a Square Duct," *Physics of Fluids A*, Vol. 3, No. 11, 1991, pp. 2734–2748.

[14]Kajishima, T. and Miyake, Y., "A Discussion on Eddy Viscosity Models on the Basis of the Large Eddy Simulation of Turbulent Flow in a Square Duct," *Computers and Fluids*, Vol. 21, No. 2, 1992, pp. 151–161.

[15]Huser, A. and Biringen, S., "Direct Numerical Simulation of Turbulent Flow in a Square Duct," *Journal of Fluid Mechanics*, Vol. 257, 1993, pp. 65–95.

[16]Xu, H. and Pollard, A., "Large Eddy Simulation of Turbulent Flow in a Square Annular Duct," *Physics of Fluids*, Vol. 13, No. 11, 2001, pp. 3321–3337.

[17]Huijnen, V., Somers, L. M. T., Baert, R. S. G., and de Goey, L. P. H., "Validation of the LES Approach in Kiva-3V on a Square Duct Geometry," *International Journal For Numerical Methods in Engineering*, Vol. 64, No. 7, 2005, pp. 907–919.

[18]Joung, Y., Choi, S., and Choi, J., "Direct Numerical Simulation of Turbulent Flow in a Square Duct: Analaysis of Secondary Flows," *Journal of Engineering Mechanics*, Vol. 133, No. 2, 2007, pp. 213–221.

[19]Lauder, B. E., "Phehenomenological modeling: Present ... and future?" *Whither Turbulence? Turbulence at the Crossroads*, edited by J. L. Lumley, Vol. 357 of *Lecture Notes in Physics*, Springer, Berlin, 1990, pp. 357–439.

[20]Spalart, P. R., "Strategies for Turbulence Modelling and Simulations," *International Journal of Heat and Fluid Flow*, Vol. 21, 2000, pp. 252–263.

[21]Bisek, N. J., "High Order Implicit Large-Eddy Simulations of a Supersonic Corner," AIAA Paper 2014-0588.

[22]Nompelis, I., Dryna, T., and Candler, G., "Development of a Hybrid Unstructured Implicit Solver for the Simulation of Reacting Flows over Complex Geometries," AIAA Paper 2004-2227.

[23]MacCormack, R. and Candler, G., "The Solution of the Navier-Stokes Equations Using Gauss Seidel Line Relaxation," *Computers and Fluids Journal*, Vol. 17, No. 1, 1989, pp. 135150.

[24]Hirsch, C., *Numerical Computations of Internal and External Flows*, Wiley, New York, NY, 1991.

[25]Nompelis, I., Dryna, T., and Candler, G., "A Parallel Unstructured Implicit Solver for the Simulation of Reacting Flow Simulation," AIAA Paper 2005-4867.

[26]Nompelis, I., *Computational Study of Hypersonic Double-Cone Experiments for Code Validation*, Ph.D. thesis, University of Minnesota, Minneapolis, MN, 2004.

[27]Candler, G. and MacCormack, R., "The Computation of Hypersonic Ionized Flows in Chemical and Thermal Nonequilibrium," *Journal of Thermophysics and Heat Transfer*, Vol. 5, No. 3, 1991, pp. 266273.

[28]Kim, S. E., Makaroy, B., and Caraeni, D., "A Multi-Dimensional Linear Reconstruction Scheme for Arbitrary Unstructured Grids," AIAA Paper 2003-3990.

[29]MacCormack, R., "Current Status of the Numerical Solutions of the NavierStokes Equations," AIAA Paper 1985-0032.

[30]Wright, M., Candler, G., and Bose, D., "Data-Parallel Line Relaxation Method for the NavierStokes Equations," *AIAA Journal*, Vol. 36, No. 9, 1998, pp. 16031609.

[31]Catrix, S. and Aupoix, B., "Density Corrections for Turbulence Models," *Aerospace Science and Technology*, Vol. 4, 2000, pp. 1–11.

[32]Jespersen, D. C., Pulliam, T. H., and Buning, P. G., "Recent Enhancements to OVERFLOW (Navier-Stokes Code)," AIAA Paper 1997-0644.

[33]Pulliam, T. H. and Chaussee, D. S., "A Diagonalized Form of the an Implicit Approximate Factorization Algorithm," *Journal of Computational Physics*, Vol. 39, No. 2, 1981, pp. 347–363.

[34]Eca, L., Hoekstra, M., Hay, A., and Pelletier, D., "A Manufactured Solution for a Two-Dimensional Steady Wall-Bounded Incompressible Turbulent Flow," *International Journal of Computational Fluid Dynamics*, Vol. 21, No. 3, 2007, pp. 175–188.

[35]Menter, F. R., "Improved Two-Equation k-omega Turbulence Models for Aerodynamic Flows," Tech. Rep. NASA TM 103975, October 1992.

[36]Sarkar, S., Erlebacher, G., Hussaini, M. Y., and Kreiss, H. O., "The Analysis and Modeling of Dilatational Terms in Compressible Turbulence," *Journal of Fluid Mechanics*, Vol. 227, 1991, pp. 473–493.

[37]Wilcox, D. C., *Turbulence Modeling for CFD*, DCW Industries, La Canada, CA, 3rd ed., 2006.

[38]Klopfer, G. H., Hung, C. M., Van der Wijngaart, R. F., and Onufer, J. T., "A Diagonalized Diagonal Dominant Alternating Direction Implicit (D3ADI) Scheme and Subiteration Correction," AIAA Paper 1998-2824.

[39]Shutts, W. H., Hartwig, W. H., and Weiler, J. E., "Final Report on Turbulent Boundary Layer and Skin Friction Measurements on a Smooth, Thermally Insulated Flat Plate at Supersonic Speeds," *A Critical Compilation of Compressible Turbulent Boundary Layer Data*, edited by H. H. Fernolz and P. J. Finley, AGARD Report AGARD-AG-223, NATO Advisory Group for Aerospace Research and Development, London, England, June 1977, pp. 5501–A–1–5501–C–2.

[40]Elena, M. and LaCharme, J. P., "Experimental Study of a Supersonic Turbulent Boundary Layer Using Laser Doppler Anemometer," *Journal de Mécanique Théorique et Appliquée*, Vol. 7, 1998, pp. 175–190.

[41]Rai, M. M., Gatski, T. B., and Erlebacher, G., "Direct Simulation of Spatially Evolving Compressible Turbulent Boundary Layers," AIAA Paper 1995-0583.

[42]Rizzetta, D. P. and Visbal, M. R., "Large-Eddy Simulation of Supersonic Boundary-Layer Flow by a High-Order Method," *International Journal of Computational Fluid Dynamics*, Vol. 18, No. 1, 2004, pp. 15–27.

[43]Bisek, N. J., Rizzetta, D. P., and Poggie, J., "Plasma Control of a Turbulent Shock Boundary-Layer Interaction," *AIAA Journal*, Vol. 51, No. 8, 2013, pp. 1789–1804.

[44]Kalitzin, G., Medic, G., Iaccarino, G., and Durbin, P., "Near-wall behavior of RANS turbulence models and implications for wall functions," *Journal of Computational Physics*, Vol. 204, 2005, pp. 265–291.

[45]Gaitonde, D. and Visbal, M. R., "High-order Schemes for Navier-Stokes Equations: Algorithm and Implementation into FDL3DI," Tech. rep., Air Force Research Laboratory, 1998, AFRL-VA-WP-TR-1998-3060.

[46]Visbal, M. R. and Gaitonde, D. V., "High-Order-Accurate Methods for Complex Unsteady Subsonic Flows," *AIAA Journal*, Vol. 37, No. 10, 1999, pp. 1231–1239, doi:10.2514/2.591.

[47]Stoltz, S. and Adams, N. A., "An Approximate Deconvolution Procedure for Large-Eddy Simulation," *Physics of Fluids*, Vol. 11, No. 7, 1999, pp. 1699–1701, doi:10.1063/1.869867.

[48]Speziale, C. G., "Comparison of Explicit and Traditional Algebraic Stress Models of Turbulence," *AIAA Journal*, Vol. 35, No. 9, 1997, pp. 1506–1509.

[49]Spalart, P. R. and Garbaruk, A. ansd Strelets, M., "RANS Solutions in Couette Flow with Streamwise Vorticies," *International Journal of Heat and Fluid Flow*, Vol. 49, 2014, pp. 128–134.

[50]Mani, M., Babcock, D. A., Winkler, C. M., and Spalart, P. R., "Predictions of a Supersonic Turbulent Flow in a Square Duct," AIAA Paper 2013-0860.

[51]Wilcox, D. C. and Rubesin, M. W., "Progress in Turbulence Modeling for Complex Flow-Fields Including Effects of Compressibility," Tech. Rep. NASA-TP-1517, 1980.

[52]Rumsey, C., "Turbulence Modeling Resource," http://turbmodels.larc.nasa.gov, NASA Langley Research Center, Hampton, VA, [retrieved 9 APR 2014].

[53]Dandois, J., "Improvement of Corner Flow Prediction Using the Quadratic Constitutive Relation," *AIAA Journal*, Vol. 52, No. 12, 2014, pp. 2795–2806.

[54]Amtec Engineering Inc., *Tecplot 360 User's Manual, Version 2013 R1*, Amtec Engineering, Incorporated, 2013.

[55]Kenwright, D. N. and Haimes, R., "Automatic Vortex Core Detection," *IEEE Computer Graphics and Applications, IEEE Computer Society*, Vol. 18, No. 4, 1998, pp. 70–74.

APPENDIX C
SHOCK BOUNDARY-LAYER INTERACTION

AIAA Aviation
16-20 June 2014, Atlanta, GA
7th AIAA Theoretical Fluid Mechanics Conference

Detached-Eddy Simulation of a Reattaching Shear Layer in Compressible Turbulent Flow

Tim Leger* and Jonathan Poggie †

U.S. Air Force Research Laboratory, Wright-Patterson Air Force Base, OH 45433-7512, USA

Simulations of a Mach 2.9 turbulent shear layer in a back-step/ramp configuration were performed using both Reynolds Averaged Navier Stokes (RANS) and Detached Eddy Simulation (DES) methods. The results from these simulation are compared with experimental measurements including shear layer and reattaching boundary layer profile surveys, along with surface pressure and skin friction on the reattachment ramp.

Nomenclature

P	Pressure
T	Temperature
M	Mach number
Re/m	Unit Reynolds number
u	Velocity
ρ	Density
R	Reattachment location
μ	Dynamic viscosity
ν	Kinematic viscosity
f	Function
$\tilde{d}$	DES modified distance/length scale
d	Distance
c	Constant
r	Length scale ratio
C_{DES}	DES constant
Δ	Maximum cell dimension
δ	Boundary layer thickness
δ^*	Boundary layer displacement thickness
θ	Boundary layer momentum thickness
H	Boundary layer shape factor
x	Streamwise distance from the step corner
y	Vertical distance from the step corner
z	Spanwise distance
$x*$	Distance along the ramp
$y*$	Distance normal to the ramp
D	Step height = 25.4 mm
y^+	Dimensionless wall distance
τ	Shear stress
c_f	Skin friction coefficient
Ψ	Low Reynolds number correction
κ	von Karman constant

*Research Scientist, Ohio Aerospace Institute, AIAA Member, timothy.leger.ctr@us.af.mil
†Senior Aerospace Engineer, AFRL/RQHF, Associate Fellow AIAA

Subscript

o	Stagnation
∞	Freestream
w	Wall
s	Sutherlands's law
k	Keye's law
t	Turbulent
l	Laminar
d	Delayed

I. Introduction

The separation and reattachment of compressible turbulent shear layers plays a key role in the design and performance of supersonic and hypersonic flight vehicles. This includes several practical problems, such as fatigue failure due to heating and pressure fluctuations,[1,2] control surface problems associated with unsteady flow over stalled airfoils,[3] and mixing of fuel with air in scramjet engines.[4] Although numerous experiments with various geometries have been conducted to study this phenomena, the involved physics of shear layer reattachment and the developing flow following reattachment are still not fully understood, especially for turbulent, compressible flows.[5] Making measurements of such flows is very challenging, particularly with regards to time-resolved quantities. As a result, numerical simulations have become a valuable tool for predicting such phenomena during early design phases, along with investigating the fundamental flow structure and acquiring a better understanding of the key flow physics involved.

During preliminary design work of hypersonic and supersonic vehicles, RANS models provide a relatively quick and robust way to obtain the major mean flow features upon which early design decisions are often based. However RANS models, by their very nature, can not provide information about the instantaneous flowfield or unsteady flow phenomena[6] such as shear layer separation and reattachment. The Detached-Eddy Simulation (DES) method can provide the next level of fidelity in the design process.[7,8] While DES requires a significantly larger amount of computational resources compared to a RANS simulation, it is still several orders of magnitudes less than higher fidelity approaches such as Direct Numerical Simulation (DNS) in which all turbulent scales are resolved, especially when it comes to simulation run times. In the DES approach, the bulk of the flow is modeled with a Large Eddy Simulation (LES), so large scale turbulence is resolved. However in the near wall regions of the flow, where the resolution requirements of LES quickly become prohibitive,[9] a RANS model with turbulence closure is utilized,[10] greatly reducing the computational cost compared to a full LES calculation.

In the work presented here, simulations are performed for a reattaching turbulent free shear layer using both steady state RANS and unsteady DES approaches, with a comparison conducted between the results and experimental measurements. For the DES work, simulations with both the Delayed Detached Eddy Simulation (DDES) and Improved Delayed Detached Eddy Simulation (IDDES) methods are performed. All simulations utilize the Spalart-Allmaras turbulence model, but the RANS simulations incorporate dissipative shock capturing numerics, while the DES simulations employ low dissipation numerics. Unstructured grids consisting of purely hexahedron cells are used for all simulations.

The motivation for performing these simulations is as a stepping stone to simulating the experiment of Poggie,[11–13] in which blowing ports were used to control the shear layer and its reattachment on the ramp. To this end, the 3D grid used for the RANS, DDES, and IDDES simulations is 9 ports wide in the spanwise direction and includes geometry for the blowing ports. However for the simulations, the blowing ports are effectively turned off by setting their boundary conditions to the same as the plate/cavity floor which they are part of.

II. Reference Experiment

For this work, the thoroughly documented experiment of Baca[14,15] is utilized. The experiment was conducted in the Princeton University 8 inch by 8 inch high Reynolds number, blow down, supersonic wind tunnel. Figure 1 illustrates the basic geometry and flows involved for the experiment. The test model was constructed from brass, and consisted of a wedge-shaped plate with a cavity, 25.4 mm deep and 61.9 mm

long, followed by a 160 mm long 20 degree ramp. Although the model was bolted to the tunnel walls and thus spanned the entire test section, the cavity and ramp were only 152.4 mm wide, with a 25.4 mm inset between them and the tunnel walls on both sides to prevent effects from the tunnel wall boundary layers. Aerodynamic fences were attached to the portion of the ramp which extended above the cavity to help ensure two dimensionality of the redeveloping boundary layer and flow.

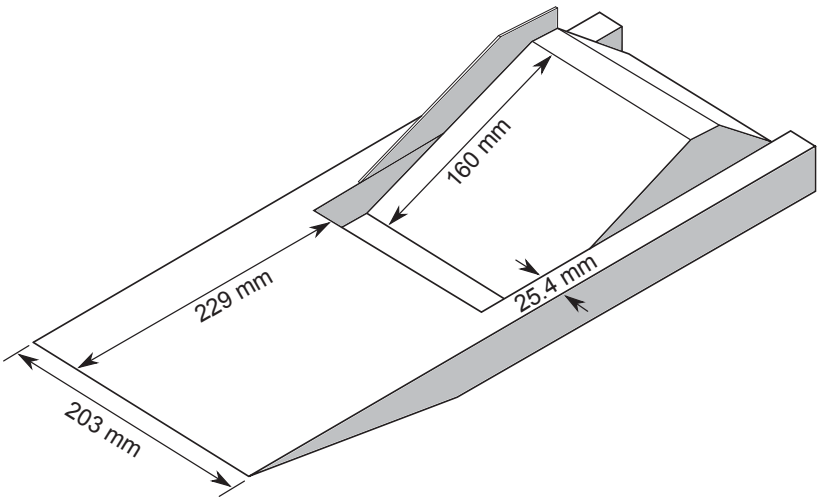

(a) Illustration of the experimental model with one aerodynamic fence removed

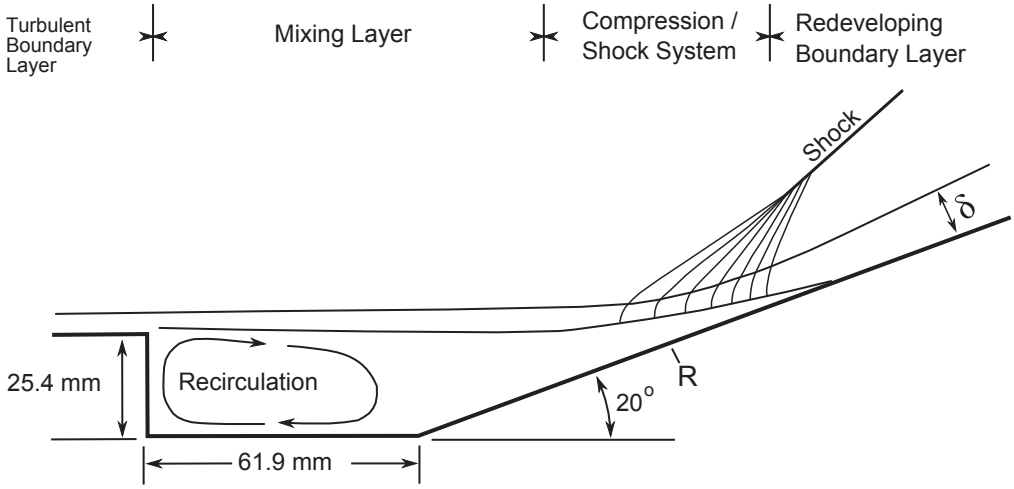

(b) Cross section of the mean flow field

Figure 1. Experimental Configuration (Adapted from Baca[14])

Nominal flow conditions for the experiment were $P_o = 0.689$ MPa $\pm$ 1%, $T_o = 258$ K $\pm$ 4%, $M_\infty = 2.92$ $\pm$ 0.015, $U_\infty = 572$ m/s $\pm$ 2%, $\rho_\infty = 0.77$ kg/m^3, $T_\infty = 95$ K $\pm$ 4 %, Re/m = 67E6/m $\pm$ 4%, with air as the working fluid. Measurements from surface thermocouples on the model indicated that the model surface was essentially adiabatic, $T_w/T_o = 1.03$. Surface measurements[14,15] along the cavity and ramp included static pressure via pressure taps and skin friction via Preston tubes. In addition, several profile surveys of the shear layer and re-developing boundary layer were taken, including pressure and total temperature via

a Pitot tube. Skin friction along the ramp was both measured using Preston tubes and extrapolated from wake fits to the profile surveys.

Poggie[11] extended this experiment by adding two spanwise rows of blowing ports, to explore the effect of disturbances on the unsteadiness of the shock system. One row of blowing ports was located 12.7 mm upstream of the step and the other located 12.7 mm downstream of the step on the cavity floor. Each row was 101.6 mm long and consisted of 33 ports, 1.6 mm in diameter and spaced 3.175 mm apart from one another. Air was supplied to the ports from a stagnation tank with a stagnation pressure and stagnation temperature the same as the nominal flow conditions in the tunnel. The ratio of mass flux through the port to the freestream mass flux was on the order of $\frac{\rho_p u_p}{\rho_\infty u_\infty} = 0.07$, with the momentum flux ratio on the order of $\frac{\rho_p u_p^2}{\rho_\infty u_\infty^2} = 0.04$, and a velocity ratio of $\frac{u_p}{u_\infty} = 0.6$.

III. Approach

III.A. Numerical Model

Simulations were carried out using US3D, a well-validated, cell-centered, finite-volume, solver for the solution of the non-equilibrium, compressible Navier-Stokes equations on unstructured grids, developed at the University of Minnesota.[16] For the steady state RANS simulations, the modified Steger-Warming flux vector splitting scheme of MacCormack and Candler[17] is used to evaluate the the inviscid fluxes, along with MUSCL reconstruction[18] at the faces to achieve second order spatial accuracy. The modified Steger-Warming method uses a pressure-dependent weighting function to switch smoothly from a low-dissipation method in regions of low gradients to the original Steger-Warming scheme when a large-pressure gradient is detected across a face (such as for a strong shock). Diffusive fluxes are computed using a second-order scheme, in which the gradients are computed using a deferred correction approach similar to that of Nompelis et al.,[16,19,20] MacCormack and Candler,[17,21] and Kim et al.[22] Weighted least square fits are used to calculate the viscous fluxes from second order accurate gradients.

RANS solutions are driven to a steady state convergence using a backward Euler time stepping, which is fully implicit, but only first order accurate. Future time level fluxes are approximated by linearizing the fluxes about the current time level using exact flux Jacobian. The data-parallel line relaxation (DPLR) method, based on the Gauss-Seidel line relaxation method of MacCormack,[23] is then employed to solve the resulting linear system. To improve performance on parallel systems, the DPLR method replaces Gauss-Seidel sweeps with a series of line relaxation sweeps.[24] Overall, the DPLR method has high parallel efficiency and good convergence characteristics, particularly when solving large compressible flow problems.

The shock capturing scheme used to evaluate the fluxes in the steady state RANS simulations, while very good at capturing shocks, is too dissipative to resolve unsteady turbulence. To overcome this problem, symmetric flux evaluations are often used, as they contain no dissipation. Unfortunately, such methods are unstable in the presence of strong gradients, such as shock waves. For the unsteady DES results presented here, a hybrid flux scheme is used, which combines a sixth order accurate symmetric flux evaluation with the dissipative portion of the shock-capturing modified Steger-Warming flux vector splitting scheme.[25] This approach allows for a large range of turbulent scales to be resolved without excessive dissipation. Stability in the presence of strong shock waves is maintained by the use of a Ducros switch. To advance the DES solution in time, a second order implicit Crank-Nicolson scheme is utilized.

US3D is designed for high enthalpy high temperature flows, such as those encountered in hypersonic flight or shock tunnels. In contrast, the experiment simulated here has a rather low enthalpy flow, with a static inlet temperature of 95 K. While US3D has an option to use Sutherlands viscosity law (with 2% error for temperatures down to 170 K), a modified viscosity model, blended with Keyes low temperature viscosity law was employed:[26]

$$\mu = \begin{cases} \mu_s = 1.4858\text{x}10^{-6} \cdot T^{\frac{3}{2}}/(T + 110.4), & T > 100 \text{ K} \\ f_\mu \cdot \mu_s + (1 - f_\mu)\mu_k, & 100 \text{ K} \leq T \leq 88.8 \text{ K} \\ \mu_k = 1.488\text{x}10^{-6} \cdot \sqrt{T}/(1 + 122.1\text{x}10^{-\frac{5}{T}}/T), & T < 88.8 \text{ K} \end{cases} \quad (1)$$

Where T is the static temperature, μ is the dynamic viscosity, μ_s is the dynamic viscosity from Sutherlands law, μ_k is the dynamic viscosity from Keyes law, and f_μ is the blending function, given by:

$$f_\mu = (T - 88.8)/11.2 \tag{2}$$

The standard Spalart-Allmaras (SA) turbulence closure model with trip term[27] and corrections for compressible flow by Catris and Aupoix[28] was used for all simulations. For the DES work, simulations with both the Delayed Detached Eddy Simulation (DDES) and Improved Delayed Detached Eddy Simulation (IDDES) methods were performed. In the DES approach, the switch between RANS and LES modes in the domain is based on a modified distance function, which is evaluated at each cell, every iteration:

$$\tilde{d} = \min(d_w, C_{DES}\Delta) \tag{3}$$

Where d_w is the distance from the cell center to the closest wall, C_{DES} is the DES constant 0.65 from Ref.,[29] and Δ is the largest cell dimension. The modified distance, $\tilde{d}$, is then used in the turbulence model calculation for the length scale in place of the distance to the nearest wall. This modification results in RANS being utilized for cells in which the turbulent length scale is less than or equal to the maximum cell dimension (primarily near walls), and LES in regions of domain where the grid is refined enough to support it.

Since the DES technique is dependent on cell size, the switch over from RANS to LES can easily occur in undesirable regions of the domain, where the LES approach is not correct. Without corrections, extreme care must be taken in grid generation and refinement to ensure the switch from RANS to LES occurs at the edge of the boundary layer. To make DES easier to use, modifications for certain situations have been developed and those employed in the current work are briefly discussed.

The first of these is the low Reynolds number correction, which accounts for the low Reynolds number terms in the original SA turbulence model. These terms use the ratio of eddy and molecular viscosities to determine proximity to walls. In the LES mode of DES, the subgrid eddy viscosity decreases with reduced cell size and lower Reynolds number. As a result, the DES model can mis-interpret situations with small cells as being in proximity to a wall and excessively lower the eddy viscosity, relative to the ambient velocity and length scales, in the turbulence model. To overcome this, a low Reynolds number correction term, Ψ, was derived by Spalart[30] for the original SA model:

$$\Psi^2 = \min\left[10^2, \frac{1 - \frac{c_{b1}}{c_{w1}\kappa^2 f_w^*}[f_{t2} + (1 - f_{t2})f_{v2}]}{f_{v1}\max(10^{-10}, 1 - f_{t2})}\right] \tag{4}$$

The DES modified distance function is then modified as follows to incorporate this correction term.

$$\tilde{d} = \min(d_w, \Psi C_{DES}\Delta) \tag{5}$$

In equation 4, all the terms are the same as in the original SA model, with the exception of f_w^*, which acts as a limit value for the f_w function in the SA model and is assigned the value of 0.424. The correction term Ψ takes on a value between 1, for a subgrid eddy viscosity higher than $\sim 10\nu$ (i.e. inactive), and 10, for significantly low values of subgrid eddy viscosity, thus delaying the switch from RANS to LES mode.

Another situation in which the DES model can inappropriately switch from RANS to LES mode is due to Modeled Stress Depletion (MSD), which can result from excessive grid refinement. In this case, the grid cells near the wall are small enough to trigger the switch from RANS to LES well within the boundary layer, where the grid is not refined enough to support the resolved velocity fluctuations internal to the boundary layer (i.e. LES content). As a result, the eddy viscosity and therefore the modeled Reynolds stress is reduced without any sizable resolved stress to restore the balance.[31] Mentor and Kuntz[32] developed a function for the SST turbulence model to identify boundary layers and delay the switch from RANS to LES in those regions. Their function makes use of the ratio between the internal length scale of the k-ω turbulence model and the distance to the wall. Unfortunately the SA model does not employ an internal length scale, so Spalart extended the method of Mentor and Kuntz to the SA model by using the ratio of the model length scale to the wall distance:[30]

$$r_d = \frac{\nu_t + \nu_l}{\sqrt{U_{i,j}U_{i,j}}\kappa^2 d_w^2} \tag{6}$$

Equation 6 equals 1 in the logarithmic layer and gradually falls to zero towards the edge of the boundary layer. This is then used in the following delay function, which is 1 above the boundary layer (where $r_d \ll 1$) and 0 elsewhere:

$$f_d = 1 - \tanh([8r_d]^3) \tag{7}$$

The DES modified distance function is then redefined as:

$$\tilde{d} = d_w - f_d \max(0, d_w - \Psi C_{DES}\Delta) \tag{8}$$

This modification is known as the Delayed Detached Eddy Simulation method or DDES.

Shur et al.[33] extended the DDES method by adding a Wall-Modelled LES (WMLES) capability, which is only active when turbulent content exists, and behaves as DDES otherwise. This modification is known as the Improved Delayed Detached Eddy Simulation or IDDES method. For this method, the DES modified distance function is redefined as:

$$\tilde{d} = \tilde{f}_d(1 + f_e)d_w + (1 + \tilde{f}_d)\Psi C_{DES}\Delta \tag{9}$$

Equation 9 is basically a blended function between the RANS length scale and the WMLES length scale. The function $\tilde{f}_d$ is used to blend the DDES and WMLES length scales together:

$$\tilde{f}_d = \max\{(1 - f_d), f_b\} \tag{10}$$

The term f_b in equation 10 provides rapid switching of the model from RANS mode to LES mode and is defined as:

$$f_b = \min\{2\exp(-9\alpha^2), 1.0\}, \quad \alpha = 0.25 - \frac{d_w}{\Delta} \tag{11}$$

In equation 9, f_e, is aimed at preventing an excessive reduction of the RANS Reynolds stresses in the interaction region of the RANS and LES modes, and is defined as:

$$f_e = \max\{(f_{e1} - 1), 0\}\Psi f_{e2} \tag{12}$$

The function f_{e1} provides a predefined (dependent only on the grid) value for the RANS component of the WMLES length scale and is defined as:

$$f_{e1}\left(\frac{d_w}{\Delta}\right) = \begin{cases} 2\exp\left(-11.09\alpha^2\right), & \alpha \geq 0 \\ 2\exp\left(-9.0\alpha^2\right), & \alpha < 0 \end{cases} \tag{13}$$

Function f_{e2} controls the intensity of the RANS component and is defined as:

$$f_{e2} = 1 - \max\left(f_{dt}, f_{dl}\right) \tag{14}$$

Where f_{dt} and f_{dl} are the turbulent and laminar delay functions respectively, and r_{dt} and r_{dl} are the turbulent and laminar components respectively of the model length scale to the wall distance ratio:

$$\begin{aligned} f_{dt} &= \tanh\left[\left(c_t^2 r_{dt}\right)^3\right], \quad r_{dt} = \frac{\nu_t}{\kappa^2 d_w^2 \max\left\{\left[\sum_{ij}(\partial u_i/\partial x_j)^2\right]^{\frac{1}{2}}, 10^{-10}\right\}} \\ f_{dl} &= \tanh\left[\left(c_l^2 r_{dl}\right)^{10}\right], \quad r_{dl} = \frac{\nu_l}{\kappa^2 d_w^2 \max\left\{\left[\sum_{ij}(\partial u_i/\partial x_j)^2\right]^{\frac{1}{2}}, 10^{-10}\right\}} \end{aligned} \tag{15}$$

In equations 15, the terms c_t and c_l are model constants which depend on the RANS model used and for the work presented here are 1.63 and 3.55 respectively.

There is no indication from the available experimental measurements where the flow over the wedge becomes turbulent. To account for transition of the boundary layer, a steady state 2D RANS simulation was performed for the inlet conditions on a flat plate. A trip was set 100 mm from the leading edge using the trip term in the SA turbulence model. Boundary layer profiles were extracted at several locations along the plate and compared to the experimental boundary layer profile taken 25.4 mm upstream of the step (designated as station 10 in the experiment). At a distance of approximately 240 mm from the leading edge, the simulation profile was in good agreement with the experimentally measured profile at station 10. This extracted boundary layer profile was then used as the inlet condition for all simulations of the cavity.

III.B. Grid Generation

Unstructured grids consisting of purely hexahedral cells were utilized for all simulations. As mentioned, the transition location for the turbulent boundary layer on the wedge could not be determined from the experimental measurements, thus a 2D steady state RANS simulation was performed on a flat plate to obtain a proper inlet condition for the cavity. The grid for this flat plate simulation had a domain 500 mm long, 50.8 mm tall, and 0.5 mm wide with 1,000 cells in the streamwise direction and 128 cells in the normal direction. Cells were clustered along the plate surface using a hyperbolic tangent function and the initial grid spacing was adjusted until the maximum y^+ was approximately unity, or $\Delta y_1 = 3.5\text{e-}3$ mm.

For the cavity, 2D grids were first used in a iterative process with RANS simulations to help define the domain and refine the grid before extrusion in the spanwise direction to form the 3D grid. The domain of the first 2D grids extended from 25.4 mm upstream of the cavity to the end of the ramp in the streamwise direction and from 25.4 mm above the plate at the inlet to roughly 75 mm above the ramp at the outlet in the normal direction. To allow transients an easier path to exit, the domain was extended at the inlet to 50.8 mm above the plate and the outlet extended to roughly 130 mm above the ramp. The streamwise domain was also extended to include part of the relief/expansion at the end at the ramp from the experiment, to help the outlet boundary condition by slightly weakening the shock structure present there.

The final domain/grid can be broken down into three main sections as shown in figure 2; before the step with a dimension of 195 x 128 cells (green), after the step and above the cavity/shear layer with a dimension of 1785 x 128 cells (red), and the region after the step below the shear layer with a dimension of 1785 x 160 cells (blue). For ease of reference, the step corner was chosen as the streamwise/normal origin for the cavity grids. Cells were clustered in the grid using a hyperbolic tangent function and initial grid spacing or Δy_1. Along the plate, an initial grid spacing normal to the wall of 3.5e-3 mm was used to obtain a maximum y^+ of approximately unity. In a similar fashion, initial grid spacings normal to the surfaces of 2.0e-2 mm at the start of the cavity floor, 5.0e-3 mm along the ramp, and 1.0e-2 mm at the end of the relief were used. In the streamwise direction, 50 cells were clustered within a 2.4 mm distance either side of the step, using a cell spacing at the step of 3.75e-3 mm. Similarly, 50 cells in the streamwise direction were clustered within a 2.4 mm distance either side of the joint between the ramp and relief with a cell spacing distance of 4.0e-2 mm at the joint. Along the joining line between the upper and lower grids aft of the step, clustering was also used to spread the grid slightly and help convergence of the shear layer. The initial normal spacing between the two regions near the step was 3.75e-3 mm, but widened to 4.0e-2 mm just after the start of the ramp, and increased to 3.0e-1 mm at the outlet to help diffuse the shock and prevent it from oscillating/jumping to nearby cells. At the outlet, cells in the last half of the relief section are stretched so that the last cell has a spacing of 2.0 mm from the outlet. In a similar manner, to help dissipate any transients before they reach the boundary, cells are stretched in last two thirds of the top domain in the normal direction with a final distance to the boundary of 4.0 mm. Lastly, grid lines were forced to be perpendicular along the cavity floor, ramp, and relief surfaces by subdividing the grids and curving the the lines defining these regions as necessary.

The streamwise cell spacing in the unstretched regions was kept as close as possible to 0.15875 mm, which corresponds to the DES rule of thumb of 1/20 the boundary layer thickness,[30] with $\delta = 3.175$ mm. This value for the boundary layer thickness was chosen based on the follow reasons. While the incoming boundary layer thickness at the inlet is 2.88 mm, it grows to 3.28 mm just before the step. In addition, the interest in simulating this case is to explore the control of the shear layer by a series of blowing ports, which have a spanwise spacing of 3.175 mm. Thus for practicality, the spacing in the spanwise direction will be some equal division of this dimension. In DES, it is advisable to keep the streamwise and spanwise spacings as close as possible to one another, as the direction of shear forces are not known a priori. Since the spanwise spacing of the blowing ports is well within the boundary layer heights approaching the cavity, it is reasonable to use it as the basis for both the streamwise and spanwise grid spacing. The 3D grid was generated from the 2D grid by extruding it 28.575 mm in the spanwise direction. This was done using 180 uniformly distributed cells, giving a spanwise grid spacing $\Delta z = 0.15875$ mm. The completed 3D grid contains 98,105,760 cells.

III.C. Boundary Conditions

Symmetry boundary conditions were used in the spanwise direction for the 2D flat plate case. At the inlet, a supersonic inflow condition was applied, along with a supersonic outflow condition at the outlet and top of the domain. Along the plate surface, an isothermal wall condition with a temperature of 265.7 K was

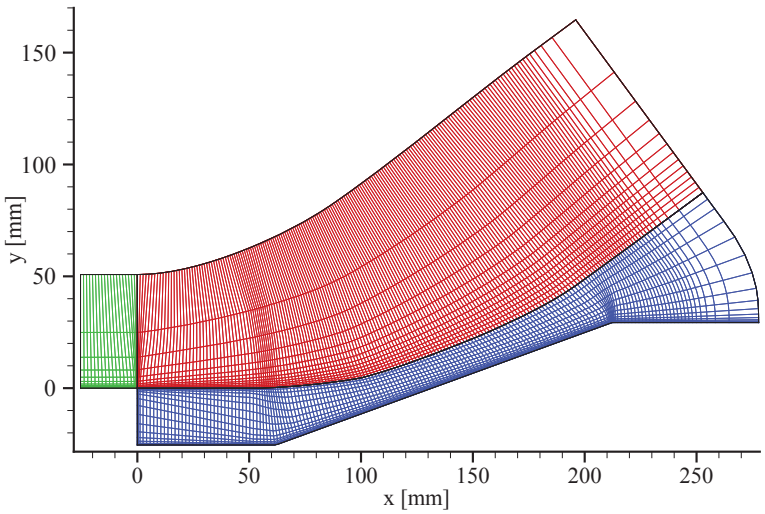

Figure 2. Grid with Main Sections Highlighted (Every tenth grid line shown for clarity)

used. The simulation was initialized using freestream conditions, $u_\infty = 572$ m/s, $\rho_\infty = 0.77$ kg/m^3, and T = 95 K. The boundary layer profile extracted from the flat plate case was used as the inflow condition for the cavity cases by setting the ghost cells connected to the inflow boundary to the values extracted as the boundary layer profile.

A 2D RANS simulation of the cavity was run to serve as an initial solution for the 3D RANS cavity cases. For this simulation, symmetry boundary conditions in the spanwise direction were used along with supersonic outflow conditions at the outlet and top of the domain. Along the bottom domain (plate, step, cavity floor, ramp, and relief), an isothermal wall condition with a temperature of 265.7 K was applied. The converged solution was applied to 3D cavity as an initialization condition in the spanwise direction.

The same boundary conditions from the 2D cavity grid was used for the 3D cavity grid, with the exception of periodic boundary conditions being applied in the spanwise direction. Both the DDES and IDDES simulation were started from the converged RANS simulation using the 3D cavity grid.

IV. Results

IV.A. Inflow Boundary Layer Profile

Before proceeding to the cavity geometry, a 2D flat plate cases was run to obtain an appropriate boundry layer profile for the inlet. The plate was 500 mm long with a trip applied 100 mm downstream of the leading edge. Several boundary layer profiles were extracted from the converged simulation and compared with the reported experimentally measured profiles. Baca[14,15] reports the experimental boundary layer thickness, displacement thickness, and momentum thickness at three locations upstream of the step, 25.4 mm, 12.7 mm, and 2.54 mm (corresponding to station 10, 15, and 19 in the experiment). It was determined that at 140 mm from the trip, the boundary layer profile along the flat plate simulation most closely matched that reported in the experiment at 25.4 mm upstream of the step (station 10). Table 1 gives a comparison of extracted boundary layer profiles from the simulation using this alignment with experimentally determined values.

While no experimental profile surveys are available at the 2.54 mm or 12.7 mm locations upstream of the step, one is available at the 25.4 mm locations. Figure 3 shows a comparison of the velocity, density, and temperature profiles between the experiment and the extracted boundary layer from the flat plate simulation at 140 mm downstream of the trip.

Table 1. Comparison of Extrapolated Boundary Layer Properties with Experimentally Measured Values at Three Locations Upstream of the Step Based on Alignment at Station 10

	25.4 mm (Station 10)		12.7 mm (Station 15)		2.54 mm (Station 19)	
	RANS	EXP	RANS	EXP	RANS	EXP
δ	2.797 mm	2.88 mm	2.956 mm	3.28 mm	3.100 mm	3.28 mm
δ^*	0.943 mm	0.89 mm	0.998 mm	1.01 mm	1.043 mm	1.02 mm
θ	0.173 mm	0.17 mm	0.185 mm	0.19 mm	0.194 mm	0.20 mm
H	5.44	5.2	5.40	5.3	5.38	5.1

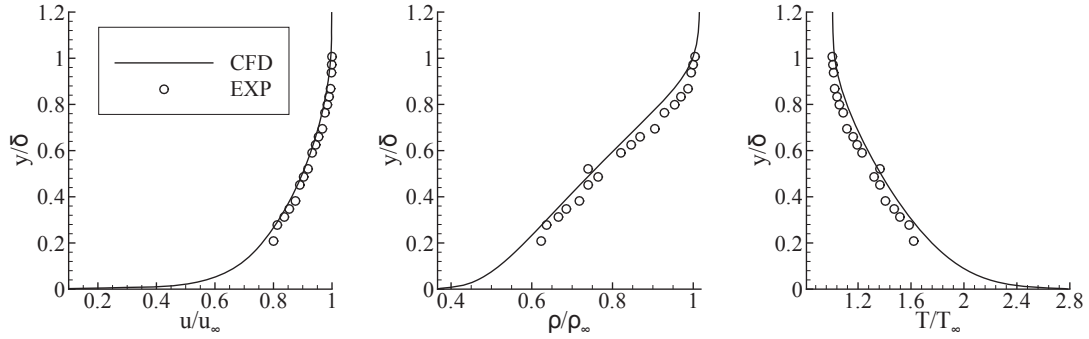

(a) Velocity (b) Density (c) Temperature

Figure 3. Comparison of Experimentally Measured and Extracted Boundary Layer Profiles

IV.B. General Flow Features

A density contour plot of the spanwise centerline plane from the 3D RANS simulation is shown in figure 4. For simplicity, the streamwise and normal directions in this and future contour plots, have been non-dimensionalized by the step height D, which is 25.4 mm. As highlighted in figure 4, the simulation reproduces the major flow features observed in the experiment. At the corner of the step, the turbulent boundary layer detaches, creating a free shear layer over the cavity. As this free shear layer reattaches along the ramp, it forms a shock system, and flow is entrained into the cavity near this reattachment location. Also present in the simulation, but not in the experiment, is an expansion fan which forms off the corner of the step. This is believed to be caused by either modeling the upper domain as an outflow condition instead of the actual tunnel wall, or more likely, a result of only modeling a slice of the cavity geometry in the spanwise direction. As will be shown in the DES results, three dimensionality effects tend to increase the pressure in the cavity.

The converged 3D RANS solution was used to initialize both the DDES and IDDES simulations. It was also used to determine the characteristic flow through time, defined as the time it takes a freestream particle to traverse the domain, which was calculated as 0.748 milliseconds. Using 50,000 iterations per this characteristic time gives a fixed time step of 14.96 nanoseconds, resulting in a CFL of 2.346 with the grid and implicit time integration scheme used. The DDES and IDDES simulations were run for 3 characteristic flow through times to wash out initial transients, after which statistics were collected using every 100th iteration (or 1.496 microseconds) for an additional 2 characteristic flow through times. Contour plots of the instantaneous density at the spanwise centerline plane for the DDES and IDDES simulations after 5 characteristic flow through times are shown in figure 5.

In figure 5, the turbulent structures supported by the DES methods are readily apparent compared to the RANS results. By taking the gradient of the instantaneous density, as shown in figure 6, a "psuedo Schlieren" is created, which makes the shear layer, turbulent structures, and shock system easier to identify. The turbulent structures form as the shear layer begins to separate at approximately x/D of 1.5. Also visible in figure 6 are accoustic waves above the shear layer as it begins to separate, along with those reflected in the region between the reattachment shock and the redeveloping boundary layer. Comparing the DES results, the separated shear layer in the DDES simulation appears to grow more rapidly than in the IDDES simulation. Along the ramp, the IDDES simulation appears to contains larger turbulent structures than the

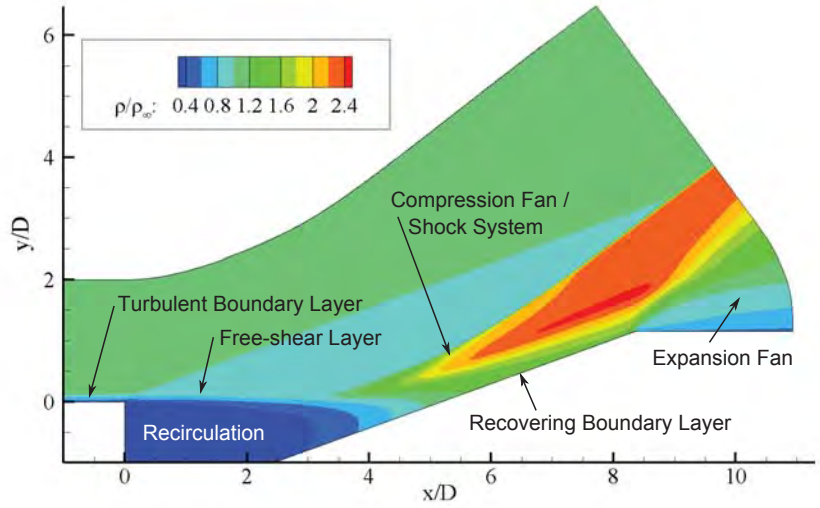

Figure 4. Density Contours of the Spanwise Centerline Plane from the 3D RANS Simulation with Major Flow Features Identified

DDES simulation. This is likely explained by the primary difference between the two methods. Recall that the IDDES method switches from DDES mode to a Wall Modeled LES mode when turbulent structures exist near the wall. Thus as the turbulent structures created by the separating shear layer impact the ramp, the IDDES simulation switches from DDES mode to WMLES mode, thus allowing more turbulent structures to exist along the ramp than in the DDES simulation.

IV.C. Cavity Flow

As previously mentioned, several measured profile surveys of the shear layer above the cavity and the boundary layer along the ramp are available from the experiment. Profiles were extracted from each of three 3D simulations for comparison with a number of these experimentally measured profile surveys. For ease of reference, the locations of these profiles are shown in figure 7. As previously noted, the streamwise and normal directions have been non-dimensionalized by the step height, D=25.4 mm, with the origin at the step corner.

Instantaneous values from the DES simulations along the spanwise centerline plane were sampled at every 1.496 microseconds for two characteristic flow through times (or 1.496 milliseconds). These samples were then time averaged, from which the required profiles were then extracted. In the RANS simulation, the profiles were extracted along the same spanwise centerline plane using the converged solution. Figure 8 shows a comparison of normalized velocity for the extracted profiles from the simulations with the experimental measurements at four locations. The results match closely with those reported by others who have simulated the same experiment.[34–36] In all four profiles, the DES simulations closely match one another and are in closer agreement to the experimental measurements. For the first three profiles from the step corner, the DES simulations show much sharper changes in velocity near the shear layer than the RANS results.

For both the RANS and DES results, the vertical location of the shear layer is underpredicted. An assumption of the homogeneity in the spanwise direction may be the cause of this issue. It has been shown that three dimensional effects can play a significant role in flow separation, even when extensive steps are taken in the experiment to ensure some level of two dimensionality.[37] While aerodynamic fences were placed on either side of the ramp in the experiment, the interaction of the reattaching shear layer with the fences was not modeled in the current simulations, instead a periodic boundary condition was used in the spanwise direction. It is also possible that the spanwise width used in the simulations was not wide enough to adequately capture the largest spanwise flow features associated with the recirculation region in the cavity. Despite the mismatch in the vertical location of the shear layer, the spreading rate of the shear layer is captured quite accurately by the DES simulations, more so than in the RANS simulation.

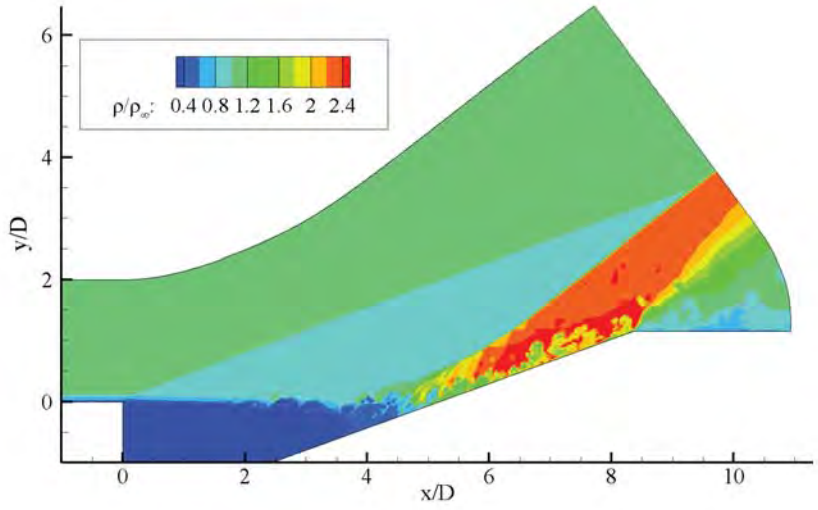

(a) DDES

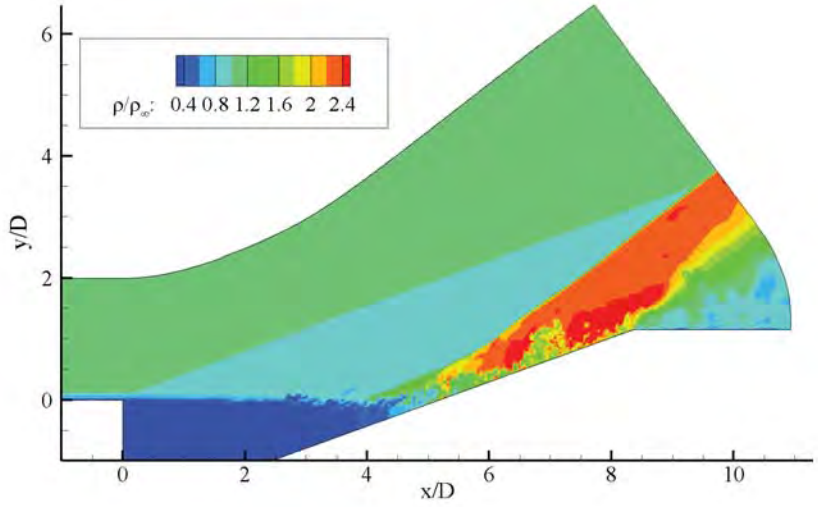

(b) IDDES

Figure 5. Contour Plots of the Instantaneous Density at the Spanwise Centerline Plane After 5 Characteristic Flow Through Times for the DES Methods

Figure 9 gives a comparison of the experimentally measured normalized pressure profiles to those extracted from the simulations. The results of the simulations are not in good agreement with the experimental measurements. This is not surprising, as the simulation shows a significantly lower pressure in the cavity compared with the experiment, as evident by the expansion fan seen in the density contour plots of the simulations and not in the experiment.

IV.D. Reattachment Ramp

Predictions of the normalized velocity and static pressure profiles along the reattachment ramp are shown in figures 10 and 11. These results are once again in good agreement to those reported by others who have simulated the same experiment.[34–36] The DES results show a much closer match to the experimentally measured profiles, both for the normalized velocity and pressure, than the RANS results. From figure 10,

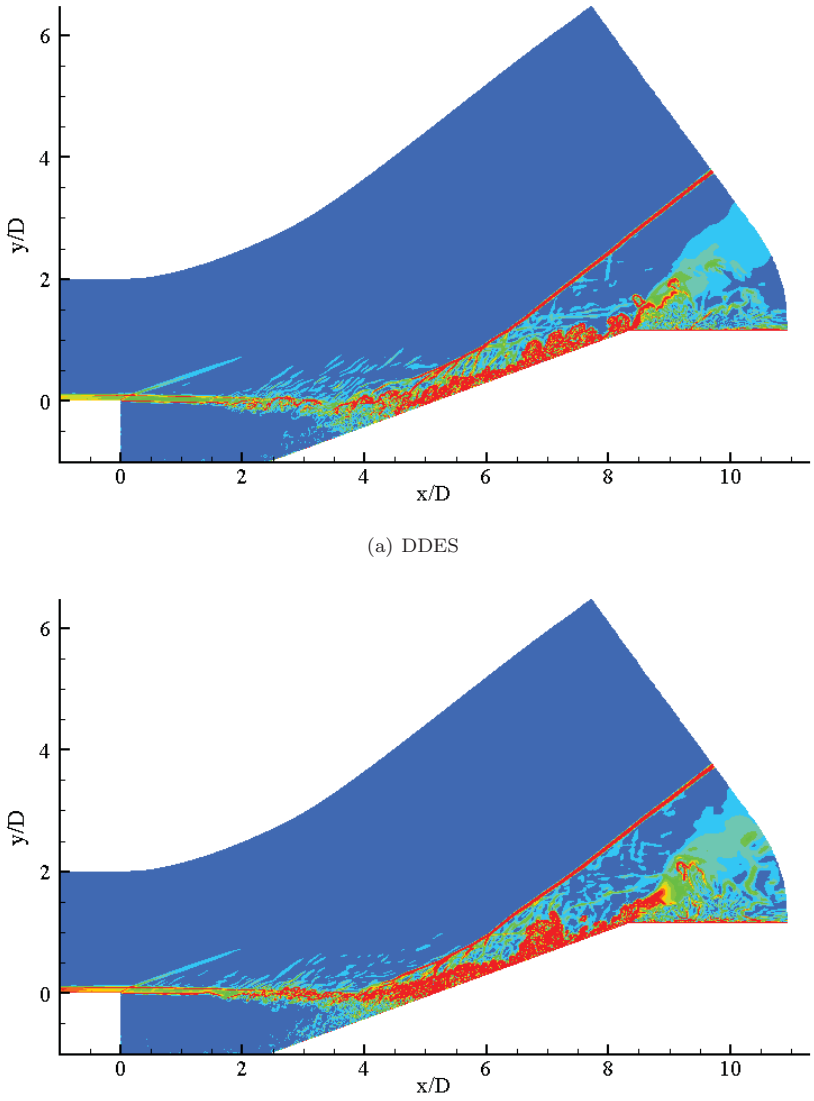

(a) DDES

(b) IDDES

Figure 6. Contours of the Instantaneous Density Gradient at the Spanwise Centerline Plane After 5 Characteristic Flow Through Times for the DES Methods

the ability of the DES methods to correctly predict the boundary layer recovery rate following separation, especially in the inner part of the boundary layer, is quite noticeable when compared to the RANS simulation.

Normalized wall pressure along the reattachment ramp from the simulations is compared with experimental pressure tap measurements in figure 12. Once again, the results are in good agreement with those reported by others who have simulated the same experiment.[34–36] The DES simulation have converged to almost the exact same values and are in very good agreement with the experimental measurments. For the RANS simulation, the increase in predicted wall pressure occurs well upstream of that predicted by the DES simulations and experimental measurements. Additionally for the RANS simulation, the final wall pressure takes longer to reach and is below that of the DES simulations and experimental measurements.

Skin friction predictions along the reattachment ramp are compared with experimental measures via both Preston tubes and wake fits to profile surveys in figure 12. Considering the uncertainty associated with skin

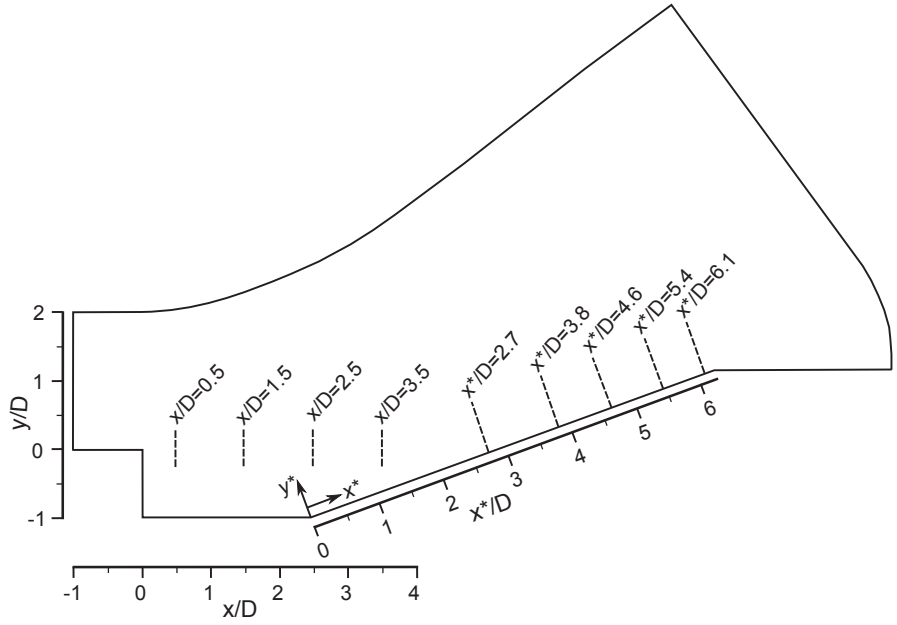

Figure 7. Location of Profile Surveys

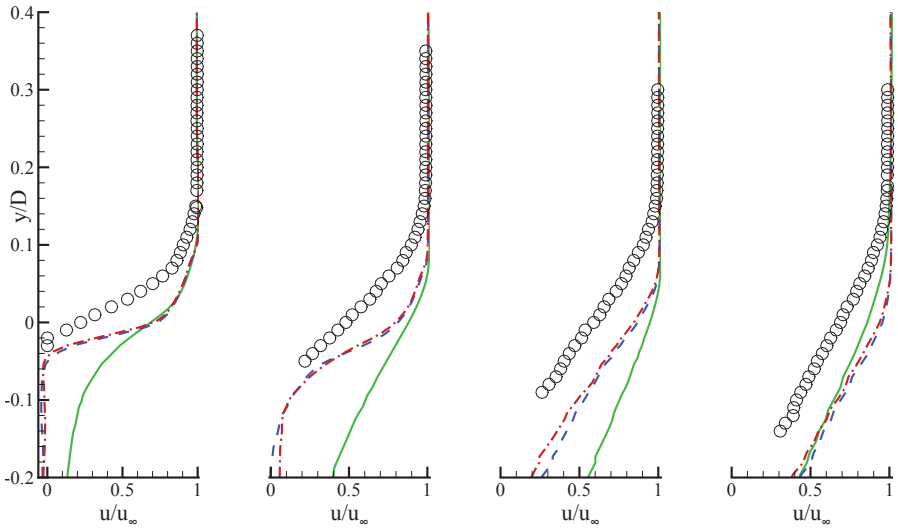

(a) x/D=0.5 (b) x/D=1.5 (c) x/D=2.5 (d) x/D=3.5

Figure 8. Comparison of Experimentally Measured and Extracted Normalized Cavity Velocity Profiles (RANS solid green line, DDES blue dashed line, IDDES red dash-dot line, Experiment open circles)

friction measurements, the RANS simulations are in good agreement with the experiment. While the DES simulations are in better agreement with the first two experimental points, the results quickly fall off and diverge away from the expected trend.

A possibility reason for this behavior is given in figure 14, which is a plot of the y^+ values along the reattachment ramp. When developing the 3D grid, which was extruded form the 2D grid, the wall normal spacing along the ramp was adjusted to give a y^+ value of approximately unity for the RANS simulations along the ramp until the reattachment point. The wall normal spacing along the ramp after the reattachment location was not adjusted further because the redeveloping boundary layer, and thus the y^+ value in this

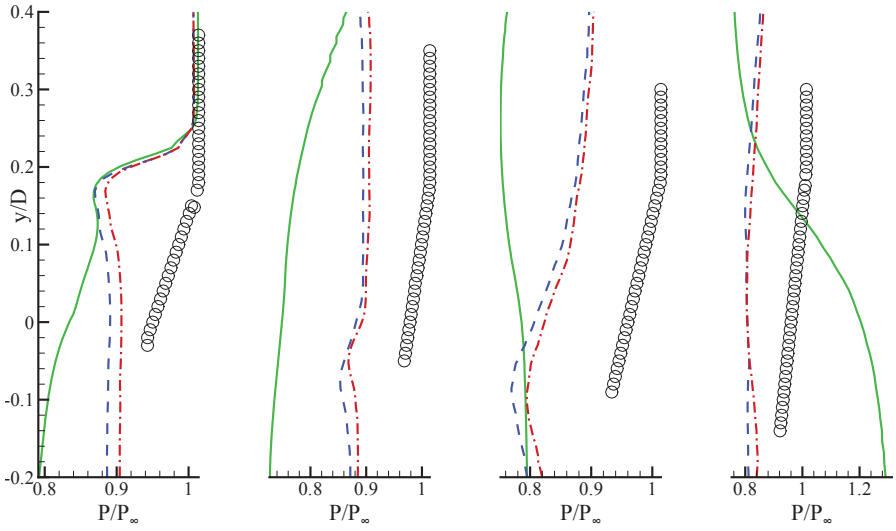

(a) x/D=0.5 (b) x/D=1.5 (c) x/D=2.5 (d) x/D=3.5

Figure 9. Comparison of Experimentally Measured and Extracted Normalized Cavity Pressure Profiles (RANS solid green line, DDES blue dashed line, IDDES red dash-dot line, Experiment open circles)

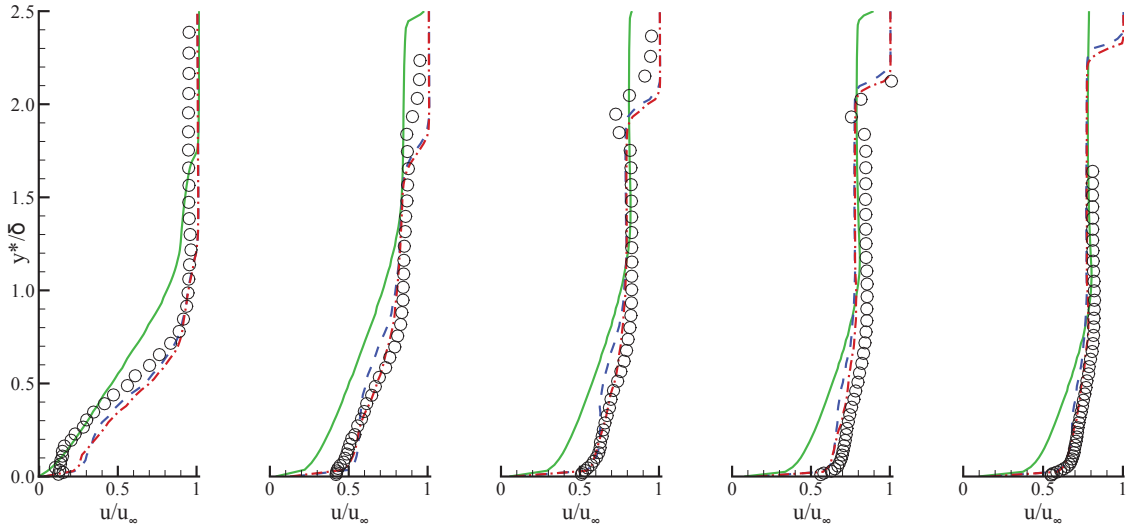

(a) x*/D=2.7 (b) x*/D=3.8 (c) x*/D=4.6 (d) x*/D=5.4 (e) x*/D=6.1

Figure 10. Comparison of Experimentally Measured and Extracted Normalized Ramp Velocity Profiles (RANS solid green line, DDES blue dashed line, IDDES red dash-dot line, Experiment open circles)

region, was expected to be incorrect in the RANS simulation. However, the DES simulations appear to more sensative to wall normal spacing than the RANS simulations. This is due to the fact that unlike the RANS simulations, the DES simulations are able to predict the redevelopment of the boundary layer after reattachment much better and as a result require a finer normal grid spacing in this region of the ramp.

The reattachment location was approximated as the point where the skin friction crosses zero on the ramp. From this, the reattachment point was calculated as x*/D=2.74 for RANS, x*/D=2.27 for DDES, x*/D=2.33 for IDDES. Compared with the reported x*/D=2.66 for the experiment, the DES simulations show a significantly early reattachment of the shear layer, while the RANS simulation is fairly close. The

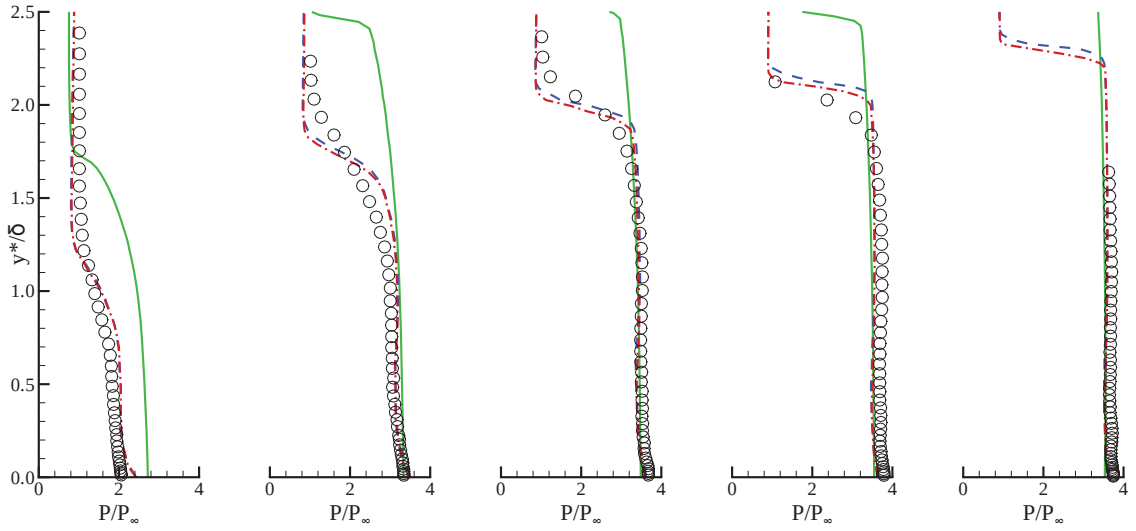

Figure 11. Comparison of Experimentally Measured and Extracted Normalized Ramp Pressure Profiles (RANS solid green line, DDES blue dashed line, IDDES red dash-dot line, Experiment open circles)

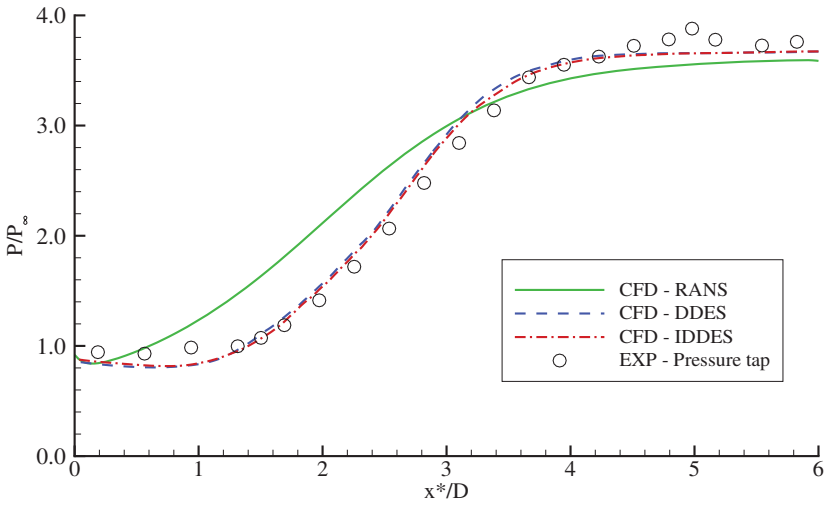

Figure 12. Normalized Wall Pressure Along the Reattachment Ramp

ability of the DES simulations to predict the reattachment location may be hindered by the wall normal spacing just discussed.

Contour plots of the instantaneous normalized density and shear stress along the ramp for the DES simulations are given figures 15 and 16. Comparing the contours between the DDES and IDDES simulations, the IDDES shows smaller, more refined structures. This is most noticeable in the shear stress contour plots, where the IDDES simulation shows fine streaks downstream of reattachment, starting at approximately x*/D=4, while the DDES simulations shows much thicker streaks in this region. This is not surprising, as IDDES simulation is acting as a Wall-Modeled LES in this region. Coincidently, this region also corresponds with the role off of the skin friction results for the DES simulation and a bend in the y^+ plots for all three simulations.

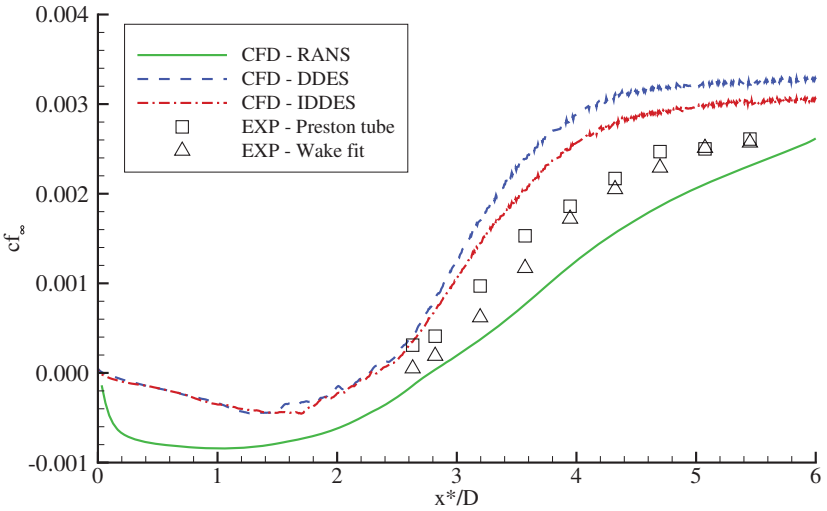

Figure 13. Skin Friction Along the Reattachment Ramp

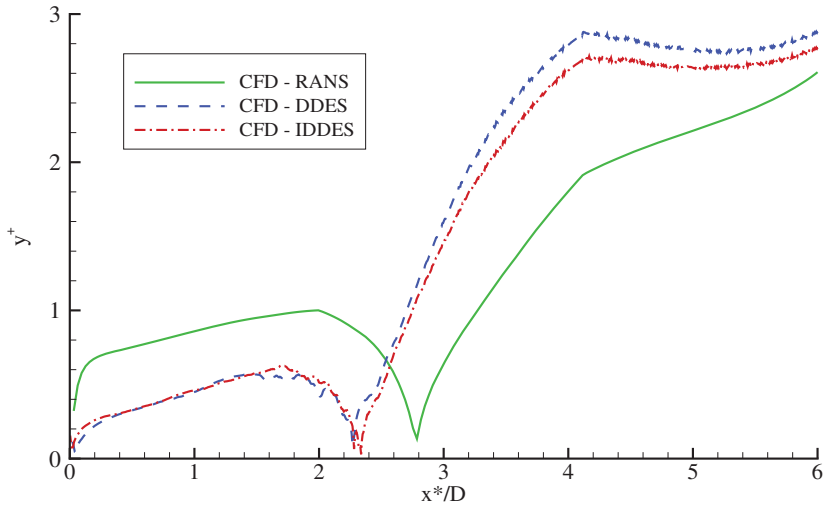

Figure 14. Dimensionless Wall Distance along the Reattachment Ramp

IV.E. Future Work

Additional work is planned to address the short comings observed in the simulation results. First, the normal grid spacing along the reattachment ramp will be adjusted so that y^+ for all three simulations is at or below unity. To address the difference between the simulations and the experiment in the cavity wall pressure, more of the experimental domain will be included in the computaional domain. While ambitious, this will be accomplished by creating a new 3D grid which extends from the tunnel wall to the centerline plane in the spanwise direction. A symmetry boundary condition will be used along the spanwise centerline plane. By including the cavity side wall and lip in the spanwise direction, more of the three dimensional nature of the experiment will be modelled and hopefully will elliminate the expnsion fan eminating from the step corner in the simulations. If this can be accomplished, it should allow the blowing ports in the cavity floor to have a more noticeable and proper effect on the reattachment shock and associate wall pressure along the reattachment ramp.

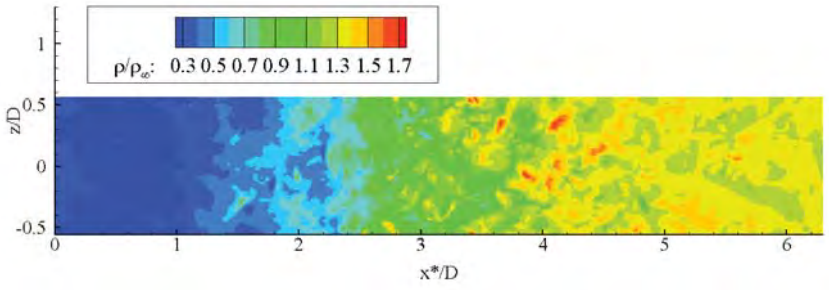

(a) DDES

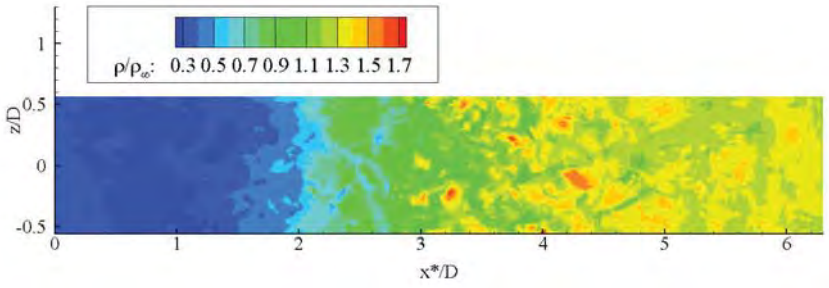

(b) IDDES

Figure 15. Contour Plot of Normalized Density Along the Reattachment Ramp

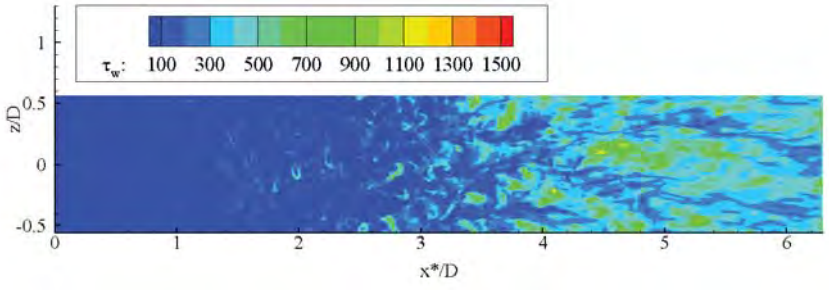

(a) DDES

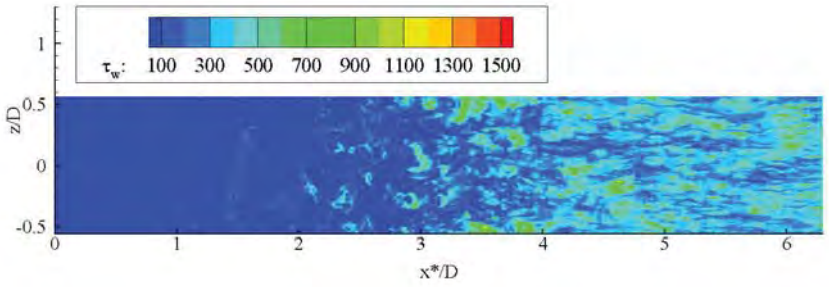

(b) IDDES

Figure 16. Contour Plot of Shear Stress Along the Reattachment Ramp

Acknowledgments

This project was funded in part by AFOSR contract LRIR 12RB01COR, monitored by Dr. J. Schmisseur, AFOSR/RTE. The authors wish to thank the Air Force Research Laboratory Department of Defense

Supercomputing Resource Center for computer time and Prof. G. Candler for the use of the US3D solver. Additional computer hours were provided under a DoD HPCMP Project (Dr. R. Gosse, Principal Investigator). The authors also thank Dr. D. Peterson, Dr. R. Gosse, and Dr. N. Bisek for their helpful and insightful discussions on performing these calculations.

References

[1]Zuchowski, B., Wittman, R., Leung, K., and Favela, J., "Structural Response and Service Life Prediction Concerns in the Design of Hypersonic Flight Vehicle Hot Structure," AIAA Paper No. 2013-1457.

[2]Poggie, J., Bisek, N. J., Kimmel, R. L., and Stanfield, S. A., "Spectral Characteristics of Separation Shock Unsteadiness," *AIAA Journal*, In Press, 2014.

[3]Wiese, D. P. and Annaswamy, A. M., "Adaptive Control of a Generic Hypersonic Vehicle," AIAA Paper No. 2013-4515.

[4]Peterson, D. M., Hagenmaier, M., and Carter, C. D., "Hybrid Reynolds-Averaged and Large-Eddy Simulations of a Supersonic Cavity Flameholder," AIAA Paper No. 2013-2483.

[5]Smits, A. J. and Dussauge, J. P., *Turbulent Shear Layers in Supersonic Flow*, AIP Press, New York, NY, 2nd ed., 2006.

[6]Leger, T. J. and Poggie, J., "Computational Analysis of Shock Wave Turbulent Boundary Layer Interaction," AIAA Paper No. 2014-0951.

[7]Peterson, D. M. and Candler, G. V., "Hybrid Reynolds-Averaged and Large-Eddy Simulation of Normal Injection Into a Supersonic Crossflow," *Journal of Propulsion and Power*, Vol. 26, No. 3, 2010, pp. 533–544.

[8]Spalart, P. R., "Detached-Eddy Simulation," *Annual Review of Fluid Mechanics*, Vol. 41, 2009, pp. 181–202.

[9]Piomelli, U. and Balaras, E., "Wall-Layer Models for Large-Eddy Simulations," *Annual Review of Fluid Mechanics*, Vol. 34, 2002, pp. 349–374.

[10]Mockett, C., *A Comprehensive Study of Detached-Eddy Simulation*, University of Berlin, Berlin, 2009.

[11]Poggie, J., *On the Control of a Compressible, Reattaching Shear Layer*, Ph.D. thesis, Princeton University, Princeton, NJ, 1995.

[12]Poggie, J. and Smits, A. J., "Shock Unsteadiness in a Reattaching Shear Layer," *Journal of Fluid Mechanics*, Vol. 429, 2001, pp. 155–185.

[13]Poggie, J. and Smits, A. J., "Large-Scale Structures in a Compressible Mixing Layer Over a Cavity," *AIAA Journal*, Vol. 41, No. 4, 2014, pp. 2410–2419.

[14]Baca, B. K., *An Experimental Study of the Reattachment of a Free Shear Layer in Compressible Turbulent Flow*, Master's thesis, Princeton University, Princeton, NJ, 1981.

[15]Settles, G. S., Williams, D. R., Baca, B. K., and Bogdonoff, S. M., "Reattachment of a Compressible Turbulent Free Shear Layer," *AIAA Journal*, Vol. 20, No. 1, 1982, pp. 60–67.

[16]Nompelis, I., Dryna, T., and Candler, G., "Development of a Hybrid Unstructured Implicit Solver for the Simulation of Reacting Flows over Complex Geometries," AIAA Paper No. 2004-2227.

[17]MacCormack, R. and Candler, G., "The Solution of the Navier-Stokes Equations Using GaussSeidel Line Relaxation," *Computers and Fluids Journal*, Vol. 17, No. 1, 1989, pp. 135150.

[18]Hirsch, C., *Numerical Computations of Internal and External Flows*, Wiley, New York, NY, 1991.

[19]Nompelis, I., Dryna, T., and Candler, G., "A Parallel Unstructured Implicit Solver for the Simulation of Reacting Flow Simulation," AIAA Paper No. 2005-4867.

[20]Nompelis, I., *Computational Study of Hypersonic Double-Cone Experiments for Code Validation*, Ph.D. thesis, University of Minnesota, Minneapolis, MN, 2004.

[21]Candler, G. and MacCormack, R., "The Computation of Hypersonic Ionized Flows in Chemical and Thermal Nonequilibrium," *Journal of Thermophysics and Heat Transfer*, Vol. 5, No. 3, 1991, pp. 266273.

[22]Kim, S. E., Makaroy, B., and Caraeni, D., "A Multi-Dimensional Linear Reconstruction Scheme for Arbitrary Unstructured Grids," AIAA Paper No. 2003-3990.

[23]MacCormack, R., "Current Status of the Numerical Solutions of the NavierStokes Equations," AIAA Paper No. 1985-0032.

[24]Wright, M., Candler, G., and Bose, D., "Data-Parallel Line Relaxation Method for the NavierStokes Equations," *AIAA Journal*, Vol. 36, No. 9, 1998, pp. 16031609.

[25]Subareddy, P. K. and Candler, G. V., "A Fully Discrete, Kinetic Energy Consistent Finite-Volume Scheme for Compressible Flow," *Journal of Computational Physics*, Vol. 228, 2009, pp. 1347–1364.

[26]Yoder, D. A., *Wind-US Users Guide*, The NPARC Alliance, NASA Glenn Research Center, Ohio, Mar 2012, pp. 314.

[27]Spalart, P. R. and Allmaras, S. R., "A One Equation Turbulence Model for Aerodynamic Flows," AIAA Paper No. 1992-0439.

[28]Catris, S. and Aupoix, B., "Density Corrections for Turbulence Models," *Aerospace Science Technology*, Vol. 4, 2000, pp. 1–11.

[29]Forsythe, J. and Woodson, S., "Unsteady CFD Calculations of Abrupt Wing Stall Using Detached-Eddy Simulation," AIAA Paper No. 2003-0594.

[30]Spalart, P. R., Deck, S., Shur, M. L., and Squires, K. D., "A New Version of detached-Eddy Simulation, Resistant to Ambiguous Grid Densities," *Theoretical Computational Fluid Dynamics*, Vol. 20, 2006, pp. 181–195.

[31]Spalart, P. R., Jou, W. H., Strelets, M., and Allmaras, S. R., "Comments on the Feasibility of LES for Wings, and on a Hybrid RANS/LES Approach," *Proceedings of the First AFOSR International Conference on DNS/LES*, Greyden Press, Ruston, LA, 1997.

[32]Menter, F. R. and Kuntz, M., "Adaption of Eddy-Viscosity Turbulence Models to Unsteady Separated Flow Behind Vehicles," Springer, Monterey, CA, 2004.

[33]Shur, M. L., Spalart, P. R., Strelets, M. K., and Travin, A. K., "A Hybrid RANS-LES Approach with Delayed-DES and Wall-modelled LES Capabilities," *International Journal of Heat and Fluid Flow*, Vol. 29, 2008, pp. 1638–1649.

[34]Horstman, C. C., Settles, G. S., Williams, D. R., and Bogdonoff, S. M., "A Reattaching Free Shear Layer in Compressible Turbulent Flow," *AIAA Journal*, Vol. 20, No. 1, 1982, pp. 79–85.

[35]Fan, C. T., Tian, M., Edwards, J. R., Hassan, H. A., and Baurle, R. A., "Validation of a Hybrid Reynolds-Averaged / Large-eddy Simulation Method for Simulating Cavity Flameholder Configurations," AIAA Paper No. 2001-2929.

[36]Quinlan, J. R., McDaniel, J. C., and Baurle, R. A., "Simulations of a Wall-Bounded Flow using a Hybrid LES/RAS Approach with Turbulence Recycling," AIAA Paper No. 2012-3285.

[37]Oliver, A. B., Lillard, R. P., Schwing, A. M., Blaisdell, G. A., and Lyrintzis, A. S., "Assessment of Turbulent Shock-Boundary Layer Interaction Computations Using the OVERFLOW Code," AIAA Paper No. 2007-0104.

AIAA Aviation
16-20 June 2014, Atlanta, GA
44th AIAA Fluid Dynamics Conference

High-Order Implicit Large-Eddy Simulations of a Supersonic Corner Flow over a Compression Ramp

Nicholas J. Bisek*

Air Force Research Laboratory, Wright-Patterson AFB, OH, 45433-7512, USA

Large-eddy simulations were performed for a Mach 2.25 turbulent airflow as it travels over a 24° compression ramp in the presence of a sidewall. Two flat plates were joined perpendicular to each other to form the corner with each plate having sufficient computational extent to developed an equilibrium turbulent boundary layer profile far from the corner junction. The turbulent flow on each plate propagated into the corner and aided in its transition. On the bottom plate, the turbulent equilibrium boundary-layer flow traveled over a 24° compression ramp which lead to an unsteady oblique shock and subsequent separation bubble. At the same time, the inclusion of the sidewall led to the development of a corner vortex and an increasingly three-dimensional shock front. The complex corner flow included a nodal attachment point and separation vortex that traveled along the sidewall with the oblique shock. Theses features interacted with the sidewall turbulent boundary-layer, forming a smaller, swept, separation bubble. The solutions were obtained using a high-fidelity time-implicit numerical scheme and an implicit large-eddy simulation approach. Time mean and instantaneous flow quantities were collected and evaluated. The results were compared with a spanwise periodic scenario performed at the same conditions. In both scenarios, the mean flow separated upstream of the compression ramp, but in the current scenario the separation length varied significantly with distance from the sidewall. Since separation length correlates with the unsteady frequency of the shock boundary-layer interaction, the inclusion of the sidewall not only yielded a highly three-dimensional shock system, but also changed the local frequency of the unsteady shock boundary-layer interaction.

Nomenclature

c_f	= skin-friction coefficient, $(2\,\mu_w/Re_\ell)\frac{\partial\,u}{\partial\,s}\big\vert_w$, where s is the wall normal direction
E	= total specific energy
$\mathbf{F}, \mathbf{G}, \mathbf{H}$	= inviscid vector fluxes
$\mathbf{F}_v, \mathbf{G}_v, \mathbf{H}_v$	= viscous vector fluxes
J	= transformation Jacobian
ℓ	= geometry length
M	= Mach number
p	= nondimensional static pressure
Re	= Reynolds number, $\rho_\infty\,u_\infty\,\ell/\mu_\infty$
t	= nondimensional time
T	= nondimensional static temperature
$\mathbf{U}$	= conserved variable vector
u, v, w	= nondimensional Cartesian velocity components in the x, y, z directions
x, y, z	= streamwise, normal, and spanwise directions in nondimensional Cartesian coordinates
y^+	= nondimensional wall distance normalized by local inner scales, $u_\tau\,\rho_w\,y/\mu_w$
δ	= boundary-layer thickness, $0.99\,u_\infty$
ξ, η, ζ	= computational coordinates
θ	= compressible boundary-layer momentum thickness, $\int_0^\infty \frac{\rho\,u}{\rho_\infty\,u_\infty}\left(1-\frac{u}{u_\infty}\right)\,\mathrm{d}y$

*Research Aerospace Engineer, AFRL/RQHF. Senior Member AIAA.

μ = dynamic viscosity
ρ = nondimensional density
τ_{ij} = components of the viscous stress tensor

Subscript
w = wall
∞ = freestream

I. Introduction

Investigations of supersonic turbulent flows have been a widely studied field since the late 1940's. Of late, there has been a particular emphasis on turbulent shock boundary layer interaction (SBLI), since the separated flow that exists under the shock foot generates localized fatigue loading which can lead to premature failure of the structure.[1] In addition, recent work by Poggie *et al.*,[2] has shown that the separation behaves like a frequency-selective amplifier for both high-fidelity simulations, wind-tunnel experiments, and flight tests across a range of Mach and Reynolds numbers.

Since SBLI typically occurs in the inlet - isolator sections of a high-speed air-breathing vehicle, any upstream disturbances could be amplified and damage to downstream subsystems or effect fuel mixing and decreased engine performance. While direct numerical simulation (DNS) of nominal flight vehicles at flight conditions is still beyond the reach of current computational resources, DNS-like large-eddy simulations (LES) (i.e., computations that do not rely on a subgrid stress model to dissipate energy), have been used to study simplified problems,[3–11] as illustrated in Fig. 1. The unit scenarios shown in Fig. 1 allow researchers to replicate the physical mechanisms at a computational tractable scale so that they might better understand and predict flow behavior, develop low-order models to mimic system, and explore ways of either controlling or leveraging the potentially-detrimental flow feature.

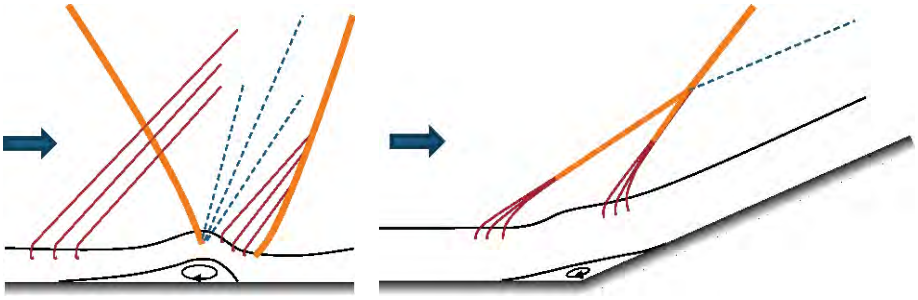

(a) Oblique impinging shock. (b) Flow over a compression ramp.

Figure 1. Canonical (unit) problems developed to study SBLI.

While there have been several spanwise homogenous simulations investing SBLI's, few LES have investigated the effects of the sidewall boundary layer. This is due, in part, to the significant increase in computational resources needed to conduct a large-scale LES have only become available in the last few years and the added complexity of including the sidewall makes the numerical investigation much more challenging (both in scale, grid generation, and the corresponding analysis). That said, Morgan *et al.*[12] recently performed an LES a constant area rectangle duct flow, which included all four walls. In the work, the Mach 1.6 turbulent flow choked and a normal shock train formed in the duct. While the starting location of the shock-train disagreed with the accompanying experiment, the subsequent shock-system agreed well with measurements.

Unfortunately, some wind-tunnels configurations and internal flow paths on flight-vehicles have finite span, and, as such, the sidewall could significantly influence the mean flow. This behavior has been seen in both computations[13] and wind tunnel studies.[14–16] The current work explores the influence the sidewall has on the SBLI, as seen in Fig. 2, by using high-fidelity, high-resolution ILES. The time-mean and time-accurate results were also compared with the spanwise periodic solutions.[11]

In the results to follow, the inclusion of the sidewall boundary layer led to the development of a corner

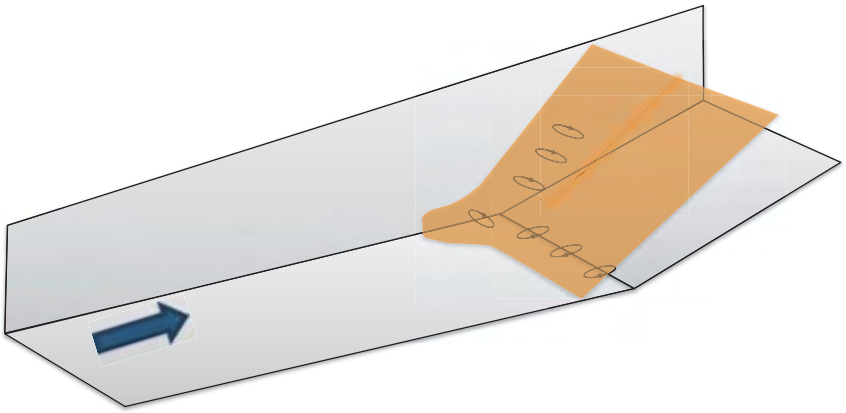

Figure 2. Cartoon of flow over a compression ramp near a sidewall

separation which appeared upstream of the midspan oblique-shock induced separation. Compression waves emanated from the corner separation, traveled along both walls, and relaxed the local pressure gradient, which delayed separation near the corner junction, but lead to a slightly larger separation length away from the corner. Near the midspan, the separation length was consistent with the spanwise periodic solution.[11]

On the sidewall, the compression waves caused the flow to slow, which thickened the boundary layer and lead to a large intermittent zone. A separation vortex also formed in the compression ramp corner junction and traveled along the sidewall with the oblique shock. This interaction lead to a clearly observed λ-shock system and a separation bubble near the trailing foot which weakened with streamwise distance.

II. Method

Flow-field results are obtained using a time-accurate three-dimensional compressible Navier-Stokes solver known as FDL3DI,[17] which has been widely used in previous calculations for both steady and unsteady, subsonic and supersonic flows.[18–24]

A. Governing Equations

The governing equations are transformed from Cartesian coordinates into a general time-dependent curvilinear coordinate system that is recast in strong conservation-law form:

$$\frac{\partial \mathbf{U}}{\partial t} + \frac{\partial (\mathbf{F} - \mathbf{F}_v)}{\partial \xi} + \frac{\partial (\mathbf{G} - \mathbf{G}_v)}{\partial \eta} + \frac{\partial (\mathbf{H} - \mathbf{H}_v)}{\partial \zeta} = \mathbf{S}_c \tag{1}$$

where t is the time and ξ, η, and ζ are the computational coordinates. The solution vector and vector fluxes (both inviscid and viscous) are:

$$\mathbf{U} = \frac{1}{J}\begin{bmatrix} \rho \\ \rho\, u \\ \rho\, v \\ \rho\, w \\ \rho\, E \end{bmatrix}, \quad \mathbf{F} = \frac{1}{J}\begin{bmatrix} \rho\, U \\ \rho\, u\, U + \xi_x\, p \\ \rho\, v\, U + \xi_y\, p \\ \rho\, w\, U + \xi_z\, p \\ \rho\, E\, U + \xi_{x_i} u_i\, p \end{bmatrix}, \quad \mathbf{F}_v = \frac{1}{Re\, J}\begin{bmatrix} 0 \\ \xi_{x_i}\, \tau_{i1} \\ \xi_{x_i}\, \tau_{i2} \\ \xi_{x_i}\, \tau_{i3} \\ \xi_{x_i}\, (u_j \tau_{ij} - q_i) \end{bmatrix} \tag{2}$$

and

$$U = \xi_t + \xi_{x_i} u_i, \quad V = \eta_t + \eta_{x_i} u_i, \quad W = \zeta_t + \zeta_{x_i} u_i, \quad E = \frac{T}{(\gamma - 1)\ M_\infty^2} + \frac{1}{2} u_i^2 \tag{3}$$

where u, v, and w are the Cartesian velocity components, ρ is the density, p is the pressure, and T is the temperature. J is the transformation Jacobian, $\partial(\xi, \eta, \zeta, t)/\partial(x, y, z, t)$.[25] Note that the formulas for $\mathbf{G}$, $\mathbf{G}_v$, $\mathbf{H}$, and $\mathbf{H}_v$ are similar to those specified in Eqn. (2).

The source vector, $\mathbf{S}_c$, on the right side of Eqn. (1), is typically set to zero, but has nonzero values at specific locations within the domain to transition the flow to fully turbulent. The source vector corresponds with the counter-flow force bypass transition method developed by Mullenix *et al.*[26] for supersonic flows since the method uses a broad-band disturbance to transition the flow.

All length scales are nondimensionalized by the reference length, ℓ, and all dependent variables are normalized by their respective reference values, expect for pressure, which is nondimensionalized by $\rho_\infty u_\infty^2$. The perfect gas relationship and Sutherland law for the molecular viscosity were employed with a reference temperature of 110.3 K for Sutherland's molecular viscosity.

B. The Numerical Method

Time-accurate solutions to Eqn. (1) were obtained numerically by the implicit approximately-factored finite-difference algorithm of Beam and Warming,[27] employing Newton-like subiterations,[28] which has evolved as an efficient tool for generating solutions to a wide variety of complex fluid flow problems, and may be written as follows:

$$\left[\frac{1}{J}+\left(\frac{2\Delta t}{3}\right)\delta_{\xi 2}\left(\frac{\partial \mathbf{F}^p}{\partial \boldsymbol{Q}}-\frac{1}{Re}\frac{\partial \mathbf{F}_v^p}{\partial \boldsymbol{Q}}\right)\right] J\times\left[\frac{1}{J}+\left(\frac{2\Delta t}{3}\right)\delta_{\eta 2}\left(\frac{\partial \mathbf{G}^p}{\partial \boldsymbol{Q}}-\frac{1}{Re}\frac{\partial \mathbf{G}_v^p}{\partial \boldsymbol{Q}}\right)\right] J\times$$
$$\left[\frac{1}{J}+\left(\frac{2\Delta t}{3}\right)\delta_{\zeta 2}\left(\frac{\partial \mathbf{H}^p}{\partial \boldsymbol{Q}}-\frac{1}{Re}\frac{\partial \mathbf{H}_v^p}{\partial \boldsymbol{Q}}\right)\right]\Delta \boldsymbol{Q}=-\left(\frac{2\Delta t}{3}\right)\left[\left(\frac{1}{2\Delta t}\right)\left(\frac{3\boldsymbol{Q}^p-4\boldsymbol{Q}^n+\boldsymbol{Q}^{n-1}}{J}\right)\right]$$
$$+\delta_{\xi 6}\left(\mathbf{F}^p-\frac{1}{Re}\mathbf{F}_v^p\right)+\delta_{\eta 6}\left(\mathbf{G}^p-\frac{1}{Re}\mathbf{G}_v^p\right)+\left[\delta_{\zeta 6}\left(\mathbf{H}^p-\frac{1}{Re}\mathbf{H}_v^p\right)-\mathbf{S}_c^p\right] \tag{4}$$

Equation (4) is employed to advance the solution in time, such that $\boldsymbol{Q}^{p+1}$ is the $p+1$ approximation to $\boldsymbol{Q}$ at the $n+1$ time level $\boldsymbol{Q}^{n+1}$, and $\Delta \boldsymbol{Q}=\boldsymbol{Q}^{p+1}-\boldsymbol{Q}^p$. For $p=1$, $\boldsymbol{Q}^p=\boldsymbol{Q}^n$. Second-order-accurate backward-implicit time differencing was used to obtain temporal derivatives.

The implicit segment of the algorithm (left-hand side of Eqn. (4)), incorporates second-order-accurate centered differencing for all spatial derivatives, and utilizes nonlinear artificial dissipation[29] to augment stability. For simplicity, the dissipation terms are not shown in Eqn. (4). Efficiency is enhanced by solving this implicit portion of the factorized equations in diagonalized form.[30] Unfortunately, the temporal accuracy can be degraded when the diagonal form is used, so subiterations are employed within each time step to minimize any degradation of the temporal solution. Any deterioration of the solution caused by use of artificial dissipation and by lower-order spatial resolution of implicit operators is also reduced by subiterating the time advancement. Three subiterations per time step were applied throughout this work to preserve second-order temporal accuracy.

The compact difference scheme is employed on the right-hand side of Eqn. (4). It is based upon the pentadiagonal system of Lele,[31] and is capable of attaining spectral-like resolution. This is achieved through the use of a centered implicit difference operator with a compact stencil, thereby reducing the associated discretization error. For the present computations, a sixth-order tridiagonal subset of Lele's system is utilized, which is illustrated here in one spatial dimension as:

$$\frac{1}{3}\left(\frac{\partial \mathbf{F}}{\partial \xi}\right)_{i-1}+\left(\frac{\partial \mathbf{F}}{\partial \xi}\right)_i+\frac{1}{3}\left(\frac{\partial \mathbf{F}}{\partial \xi}\right)_{i+1}=\frac{14}{9}\left(\frac{\mathbf{F}_{i+1}-\mathbf{F}_{i-1}}{2}\right)+\frac{1}{9}\left(\frac{\mathbf{F}_{i+2}-\mathbf{F}_{i-2}}{4}\right) \tag{5}$$

The scheme has been adapted by Visbal and Gaitonde[32] as an implicit iterative time-marching technique, applicable for unsteady vortical flows, and has been used to obtain the spatial derivative of any scalar, flow variable, metric coefficient, or flux component. It is used in conjunction with a low-pass Padé-type non-dispersive spatial filter developed by Gaitonde et al.,[33] which has been shown to be superior to the use of explicitly added artificial dissipation for maintaining both stability and accuracy on stretched curvilinear meshes.[32] The filter is applied to the solution vector sequentially in each of the three computational directions following each subiteration, and is implemented in one dimension as:

$$\alpha_f\,\hat{\boldsymbol{Q}}_{i-1}+\hat{\boldsymbol{Q}}_i+\alpha_f\,\hat{\boldsymbol{Q}}_{i+1}=\sum_{n=0}^{4}\frac{a_n}{2}(\boldsymbol{Q}_{i+n}+\boldsymbol{Q}_{i-n}) \tag{6}$$

where $\hat{\boldsymbol{Q}}$ designates the filtered value of $\boldsymbol{Q}$. The filtering operation is a post-processing technique, applied to the evolving solution in order to regularize features that are captured, but poorly resolved. On uniform grids, the filtering procedures preserve constant functions while completely eliminating the odd-even mode decoupling.[22,34] Equation (6) represents a one-parameter family of eighth-order filters, where numerical values for the a_n's may be found in Ref. 17. The filter coefficient α_f is a free adjustable parameter which may be selected for specific applications, where $\mid \alpha_f \mid < 0.5$. The value of α_f determines sharpness of the filter cutoff and has been set to 0.40 for the present simulations.

The spatial filter associated with the high-order compact scheme may produce spurious oscillations (i.e., Gibbs phenomenon), in the vicinity of strong shocks, which can be detrimental to the solver's stability and introduce numerical error in the solution. To address this issue, a 3$^{\text{rd}}$ order Roe scheme[35] with the van Albada flux limiter[36] was employed near shocks. This hybrid approach was developed, and successfully used, in previous work for a supersonic turbulent compression-corner.[4,11] During each sub-iteration of the solver, the shock location was identified by the pressure gradient detector developed by Swanson and Turkel:[37]

$$\phi = \frac{|p_{i+1} - 2\,p_i + p_{i-1}|}{(1-\omega)\,(|p_{i+1} - p_{i-1}|) + \omega\,(p_{i+1} + 2\,p_i + p_{i-1})}, \quad \begin{cases} \phi > 0.05, & \text{Roe scheme} \\ \phi \leq 0.05, & \text{compact scheme} \end{cases} \tag{7}$$

where p_i is the pressure at grid point i in the specified direction, and ω is a constant that can be varied from 0.5 to 1.0, for this work $\omega = 0.5$. Once the shock was located, a 5-point stencil was established around the shock, and the inviscid fluxes from the Roe scheme were substituted for the existing compact solutions within the stencil. Because of the upwind nature of the Roe flux-difference scheme, the filtering technique was not used where the Roe flux was applied. Figure 3 shows instantaneous Mach contours and the computational grid modified to show where the Roe scheme replaces the high-order compact scheme.

(a) Mach contours (b) Grid corresponding to the compact stencil

Figure 3. Planar slice of the instantaneous Mach contours with the shock-capturing stencil for Mach 2.25 flow over a 24° ramp.

As a result of the hybrid approach, the high-order compact scheme captures the fine-scale structures in the shock-free regions of the turbulent flow, while the Roe scheme accurately simulates the flow near the shock. Due to the high sensitivity of the shock detector, the Roe scheme was not employed in the boundary-layer and was only applied in the inviscid region of the flow, as shown in Fig. 3(b).

C. The LES Approach

In the LES approach, physical dissipation at the Kolmogorov scale is not represented, thereby allowing for less spatial resolution and a savings in computational resources. For non-dissipative numerical schemes, without use of subgrid-scale (SGS) models, this leads to an accumulation of energy at high mesh wave numbers, and ultimately, numerical instability. Traditionally, explicitly added SGS models are then employed to dissipate this energy. In the present methodology, the effect of the smallest fluid structures is accounted for by a high-fidelity implicit large-eddy simulation (HFILES) technique, which has been successfully utilized for a number of turbulent and transitional computations. The present HFILES approach was first introduced by Visbal *et al.*[34,38] as a formal alternative to conventional methodologies, and is predicated upon the

high-order compact differencing and low-pass spatial filtering schemes, without the inclusion of additional SGS modeling. This technique is similar to monotonically integrated large-eddy simulation (MILES)[39] since it relies upon the numerical solving procedure to provide the dissipation that is typically supplied by conventional SGS models. Unlike MILES however, dissipation is contributed by the aforementioned high-order Padé-type low-pass filter which only operates on high spatial wavenumbers where the solution is poorly resolved. This provides a mechanism for the turbulence energy to be dissipated at scales that cannot be accurately represented on a given mesh system, in a fashion similar to subgrid modeling. The HFILES methodology thereby permits a seamless transition from LES to DNS as the resolution is increased. In the HFILES approach, the unfiltered governing equations are employed, so the computational expense of evaluating subgrid models, which can be substantial, is avoided. This procedure also enables the unified simulation of flow-fields where laminar, transitional, and turbulent regions coexist.

It should also be noted that the HFILES technique may be interpreted as an approximate deconvolution SGS model,[40] which is based upon a truncated series expansion of the inverse filter operator for the unfiltered flow-field equations. Mathew *et al.*[41] have shown that filtering provides a mathematically consistent approximation of unresolved terms arising from any type of nonlinearity. Filtering regularizes the solution, and generates virtual subgrid model terms that are equivalent to those of approximate deconvolution.

III. Supersonic Turbulent Corner Flow

In the present computation, the supersonic flow transitioned from laminar to turbulent separately on each of the two flat plates. The approach was necessary for the development of a fully-turbulent boundary layer flow including the corner. The flat-plate flow is consistent with previous studies by Rai *et al.*,[42] Rizzetta and Visbal,[43] Pirozzoli and Grasso,[44] and Bisek *et al.*,[11] which investigated supersonic flow on a spanwise periodic flat plate at the same Mach 2.25 conditions. An extrapolated boundary condition was used for the exit and the upper faces of the domain to accommodate the growing boundary-layer and oblique shock system. Grid stretching (i.e., a buffer-layer[6]), was used near the upper and exit boundaries to transfer the energy to higher spatial wave-numbers, where the spatial filter removed it from the computation.

The inflow boundary prescribed in this work is identical to the approach used for the turbulent corner flow previously studied[45] and was developed in two steps. First, a solution to the compressible laminar boundary-layer equations[46] was used to specify the boundary layer profile on each wall, with the boundary-layer height scaled to the reference length, ℓ, and freestream conditions applied outside the boundary-layer. Near the corner (i.e., $y < 1\,\ell$ and $z < 1\,\ell$), a wall-distance weighted-average smoothly transitioned the prescribed flow between the two flat-plate compressible laminar boundary-layer profiles. This initial laminar solution was evolved for a streamwise distance of $50\,\ell$, which allowed the profile to adjust to a steady-state solution. Only minor changes where observed in the flow quantities (primarily very near the corner junction). A solution slice was extracted at the $x = 50\,\ell$ plane and rescaled so the boundary-layer height above each plate was approximately equal to ℓ and used as the incoming laminar inflow.

The laminar inflow transitioned to turbulent using a counter-flow trip model consistent with previous work.[45] The trip model was centered at $x = 2.5\,\ell$, had a 4:1 length to height ratio, and maximum height of 0.003ℓ. The strength of the trip model was controlled through a scalar, $D_c = 5.5$, as described by Mullenix *et al.*,[26] which was less than the $D_c = 6.1$ value used in the previous spanwise-periodic simulations.[11] A lower trip strength was selected because the inclusion of the second wall and higher grid resolution both aided in transition. The disturbances introduced by the trip grew as they convected and eventually transitioned to a fully turbulent flow ($\approx 20\,\ell$ from the trip model). The trip model was not applied near the corner (i.e., $y < 1.25\,\ell$ or $z < 1.25\,\ell$), to ensure that the model did not drive the transition process in the near-corner region. As such, turbulent structures above each flat plate spread into the near-corner region and aided in its transition.

Along both wall surfaces, a no-slip velocity boundary condition was imposed with an isothermal wall set to the nominal adiabatic wall temperature. The surface pressure was computed by enforcing a zero wall-normal derivative to third-order spatial accuracy. A symmetric boundary condition was used to specify the midspan spanwise boundary. Reference conditions are listed in Table 1, which were based on a 1955 experiment by Shutts *et al.* (Case 55010501).[47] Figure 4 illustrates the boundary conditions used.

The necessary reference conditions for the nondimensional fluid code FDL3DI[17] were $\ell = 6.096 \times 10^{-4}$ m, $u_\infty = 588$ m/s, M= 2.249, and $Re_\ell = 15,240$. Solutions were obtained using a nondimensional time-step, $\Delta t = 0.001$, which results in $\Delta t^+ = Re_\ell \left(\frac{u_\tau}{u_\infty}\right)^2 \left(\frac{u_\infty\, t}{\ell}\right) = 0.035$ in the fully developed equilibrium turbulent

Table 1. Flow conditions for Mach 2.25 air flow over a flat plate.

Parameter	Value	
M	2.249	
u_∞	588	m/s
T_∞	169	K
T_w	322	K
p	23,830	Pa
Re/m	2.5×10^7	m^{-1}
Re_θ	2930-5300	

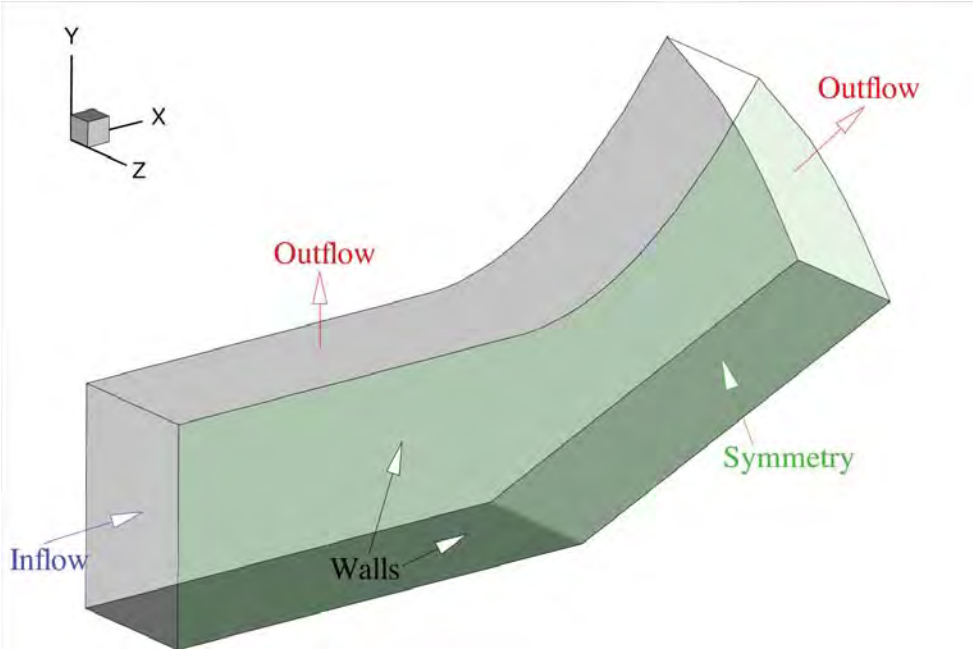

Figure 4. Boundary conditions for supersonic corner flow over a 24° ramp.

boundary-layer flow. This time step is 1/2 the time step used in the previous corner simulations[45] and 1/5 the time step for the spanwise periodic study,[11] but was necessary for numerical stability due to the highly three-dimensional corner-dominated shock system. In the analysis of the results that follow, the solution flow variables were decomposed into time-mean and fluctuating components (i.e., $u = \bar{u} + u'$, where u' is the fluctuating component).

A. Grid Development

Using the parameters listed in Table 1, a computational domain was developed to support LES based on previous experience and the guidelines recommended by Georgiadis *et al.*[48] As previously mentioned, the reference length, ℓ, was set to the incoming boundary-layer height (i.e., $\ell = \delta_{x=0}$ away from the corner junction), and a Cartesian coordinate system was established with its origin corresponding to the upstream corner location of the computational domain. The streamwise extent of the domain was approximately $155\,\ell$, although the last $50\,\ell$ was stretched to dissipate unsteady structures before reaching the extrapolated exit boundary condition. The 24° compression ramp was located at $x = 85\,\ell$. Figure 5 shows both side and top-down views of the grid. Note that only 1/20 of the grid points were included for clarity.

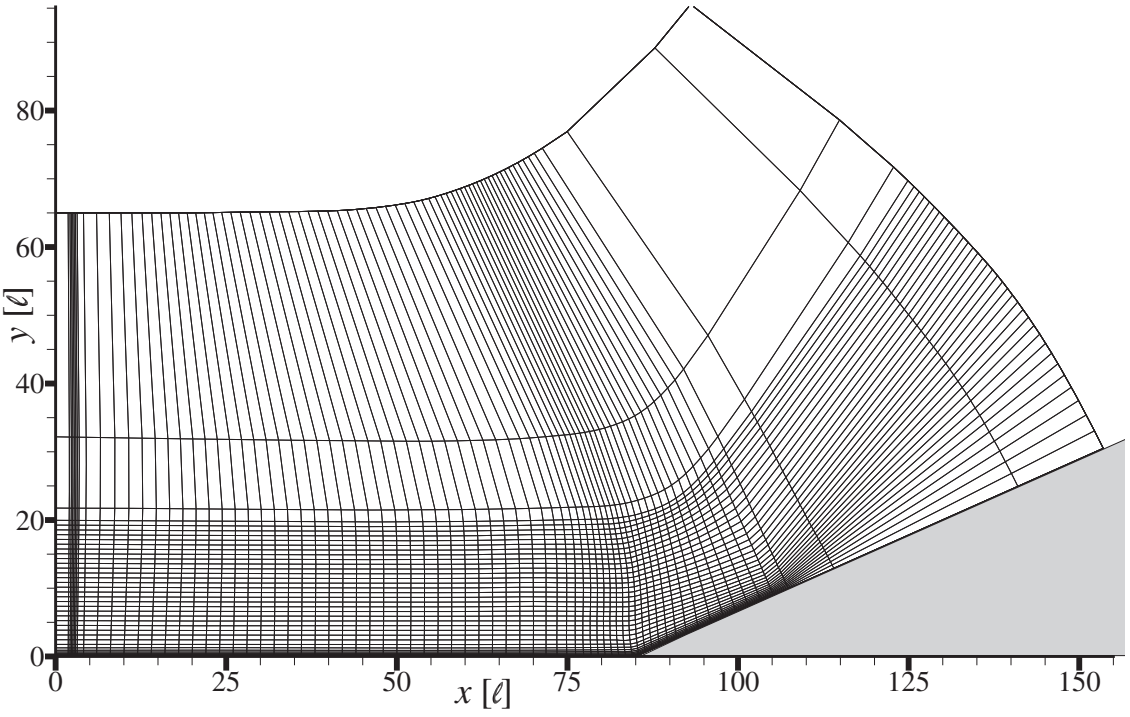

(a) $x - y$ (side) view.

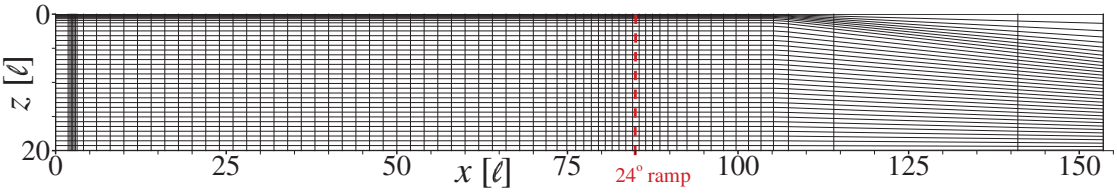

(b) $x - z$ (top-down) view.

Figure 5. Schematic of the computational domain.

Previous results[45] for Mach 2.25 flow in a 2:1 corner indicated that corner-core region extended into the domain about $3\,\ell$ at $x = 80\,\ell$. At the same streamwise location, two-point correlations of the fluctuations of the turbulent kinetic energy and pressure showed the symmetry boundary de-correlated $\approx 5\,\ell$ from the symmetry plane. In order to have sufficient spanwise space to de-correlate both the core-corner flow and the midspan symmetry boundary condition, while keeping the computational domain within a computationally achievable size, the half-span domain was set to $20\,\ell$. The sidewall was also resolved for $20\,\ell$ in the normal (y) direction, so that the interaction between the sidewall and the swept oblique shock was well resolved above the interaction. From the spanwise periodic results,[11] the span-averaged separation length was $\approx 11\,\ell$ for an upstream boundary layer thickness, $\delta = 1.8\,\ell$. According to a recent RANS study[49]investigating the influence spanwise extent on separation length in the presence of a corner, a full span domain of $40\,\ell$ should yield a large aspect ratio scenario and a quasi-2D midspan separation if the resultant midspan separation length and incoming boundary-layer thickness are consistent with the spanwise periodic results.

The development of the grid upstream of the compression ramp was consistent with previous work for supersonic flow in the presence of a corner.[45] Near the compression ramp compression ramp, grid development was based on previous compression ramp simulations.[11] The streamwise grid distribution starts at $x = 0\,\ell$ with a spacing of $\Delta x = 0.2\,\ell$. As seen in Fig. 5, the streamwise grid spacing was monotonically refined from the leading edge to $x = 2\,\ell$ using 30 points. The $x = 2\,\ell$ location corresponded to the start

of the highly-refined region needed to accommodate the bypass-transition source. This refined section was $1.0\,\ell$ long and contained 101 uniformly-spaced points. The grid points were monotonically coarsened from $x = 3\,\ell$ to $x = 5\,\ell$ using 40 additional points. From $x = 5\,\ell$ to $x = 70\,\ell$ a constant streamwise grid spacing of $\Delta x = 0.1\,\ell$ was used. The streamwise spacing up to this point is identical with the 'fine' grid used in the spanwise periodic study.[11]

From $x = 70\,\ell$ to $80\,\ell$, the streamwise spacing monotonically decreased to $\Delta x = 0.05\,\ell$, so the compression ramp region had a higher streamwise resolution. A constant streamwise spacing of $\Delta\xi = 0.05\,\ell$ was used from $x = 80\,\ell$ to $x = 95\,\ell$ (note the spacing is displayed in computational streamwise direction, ξ, due to the compression ramp). From $x = 95\,\ell$ to $x \approx 110\,\ell$ the streamwise monotonically relaxed back to $\Delta\xi = 0.10\,\ell$. Finally, the grid was monotonically coarsened over the last $\sim 50\,\ell$ using 53 points for a total 1405 streamwise points. Note grid stretching was not allowed to exceed 10% between subsequent grid points.

The grid spacing for both wall-normal directions was developed in a similar manner to facilitate the development of the turbulent equilibrium boundary-layer profiles on both walls. Grid spacing in the normal direction was specified at the wall boundary such that $y_w^+ < 1$. The grid was monotonically stretched using a hyperbolic tangent expansion and 188 points until $y = 2\,\ell$ (i.e., $\Delta y = 0.0025\,\ell$ at $y = 0$ and $\Delta y = 0.035\,\ell$ at $y = 2\,\ell$). A constant grid spacing of $\Delta y = 0.035\,\ell$ was used from $y = 2\,\ell$ to $y = 20.095\,\ell$. From $y = 20.095\,\ell$ to $65\,\ell$ the grid was monotonically coarsened using 50 additional points, for a total of 755 normal points.

Consistent with the y direction, grid spacing in the spanwise direction was specified at the wall boundary such that $z_w^+ < 1$. The grid was monotonically stretched using a hyperbolic tangent expansion and 188 points until $z = 2\,\ell$ (i.e., $\Delta z = 0.0025\,\ell$ at $z = 0$ and $\Delta z = 0.035\,\ell$ at $z = 2\,\ell$). A constant grid spacing of $\Delta z = 0.035\,\ell$ was used from $z = 2\,\ell$ to $z = 20.095\,\ell$, requiring a total of 705 spanwise points. As such, the resolved portion of the half-span ILES domain was approximately $110\,\ell$ long, $20\,\ell$ wide and $20\,\ell$ tall and contained a total of 749×10^6 points.

A close investigation of the streamwise stretched region of Fig. 5 ($x > 110\,\ell$), shows that grid spacing normal to both walls grew. This grid stretching was performed to allow the high-order filter to further dissipate turbulent structures as they propagate towards the exit boundary. Note wall normal grid stretching in this streamwise stretched region of the computational domain was not required for either the spanwise periodic compression ramp simulations[11] or the supersonic corner flow study.[45] However, the inclusion of both the compression ramp and the corner on such a highly refined grid allowed the amplified turbulent structures to persist far into the stretched region. This behavior was primarily observed near the corner junction and was detrimental for the exit boundary condition prior to the grid stretching modification.

A five-point overlap was used to decompose the grid onto the processors to maintain high-order differencing and filtering between computational blocks. Each side of the decomposed block contained 55 points, which allowed for optimal computational performance due to memory cache and loop lengths. The simulation was run using 5880 MPI tasks and typically used 4 OPENMP threads to greatly reduce turnaround time. It is worth noting that this particularly simulation experienced super-linear performance when run using 4 threads on the DoD HPCMP AFRL/Spirit system, compared with 1, 2 or 8 threads, due to better memory layout and improved MPI staging.

B. Features of the Instantaneous Flow

Using Fig. 2 to orientate the view, Fig. 6 plots instantaneous iso-surfaces of the incompressible Q-criterion[50] ($\mathrm{Q}_{\mathrm{criterion}} = \frac{1}{2}\left[\Omega^2 - \mathbf{S}^2\right] = 1$), colored by the u-velocity for the half-span simulation near the 24° compression ramp. The Q-criterion is the second invariant of the velocity gradient tensor, which compares the vorticity, Ω, to the strain-rate, $\mathbf{S}$. The Q-criterion is commonly used to highlight organized structures in turbulence, especially for wall-bounded turbulent flows where the large streamwise velocity gradient masks structures due to vorticity. An iso-surface of nondimensional pressure, $p = 1.1$, is also included to highlight the three-dimensional shock front. The pressure iso-surface was restricted to preclude it from going into the boundary layer for clarity. Although partially blocked by the semi-transparent shock iso-surface, the back plane in the figure shows the instantaneous nondimensional pressure gradient magnitude contours (grey-scale) at the end of the resolved domain. These contours highlight both the acoustic radiation emanating from the turbulent boundary-layer flow and clearly illustrate the shock-structure.

As the turbulent boundary-layer flow traveled toward the compression ramp, the flow's sharp turning angle resulted in the formation of an oblique shock above the boundary layer. Two shock feet that correspond to the separation point and reattachment of the separated flow are illustrated by the upstream moving (dark-blue colored) iso-surfaces along the midspan symmetry plane on the right side of the image and are similar

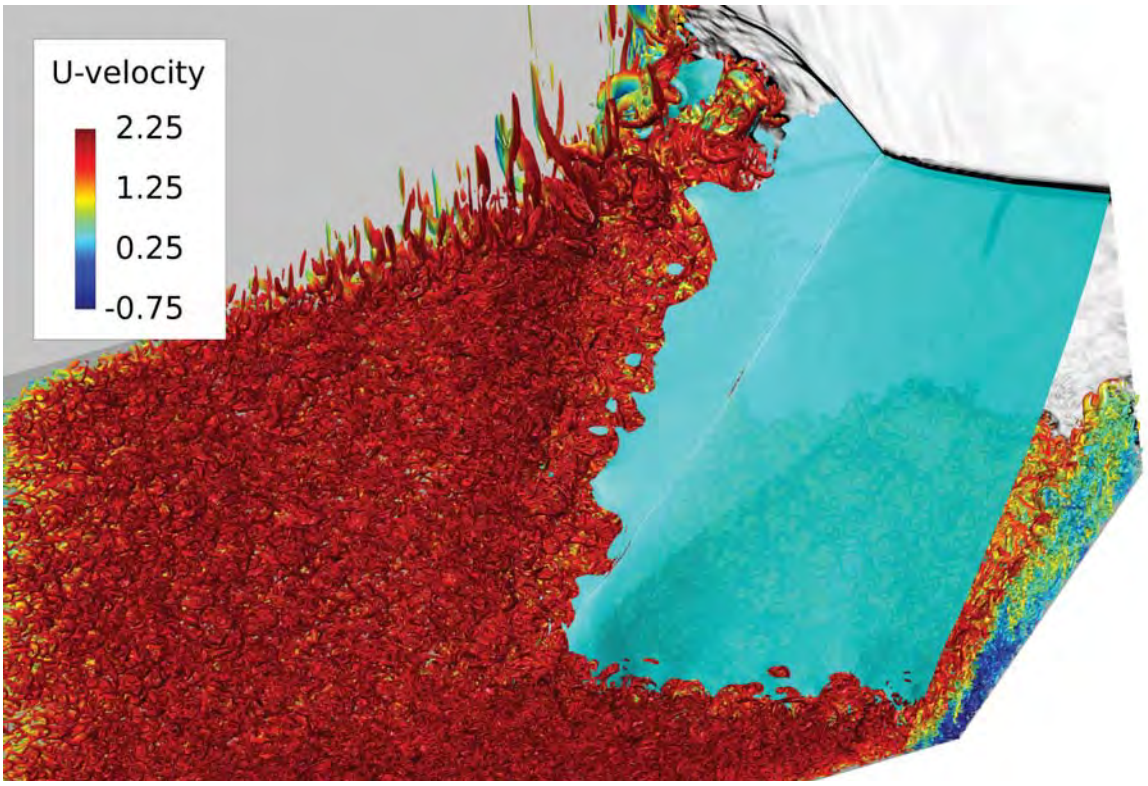

Figure 6. Instantaneous iso-surfaces of the Q-criterion colored by the u-velocity for Mach 2.25 turbulent airflow over a 24° compression-ramp near a corner.

to the cartoon sketched in Fig. 1(b). This behavior gives rise to the well-known λ-shock structure. The shock front primarily oscillated in the streamwise direction. The large-scale, low-frequency portion of this oscillation is commonly referred to as a *breathing* motion.[51] The post-shock flow expanded as it travels downstream, eventually reattaching about $5-10\ell$ downstream of the compression ramp.

As the oblique shock propagated away from the compression ramp, the sidewall turbulent boundary-layer also interacted with the shock. This interaction lead to a strongly three-dimensional shock front and also created a λ-shock structure above the sidewall, as seen in the planar contours of pressure gradient magnitude at the end of the domain. A highly non-uniform shock surface was observed near both boundary-layers but is much smoother where the inviscid core flow interacts with the oblique shock system. The shock surface also showed a kink in Fig. 6 where the spanwise shock front merged with the sidewall oblique shock. The shock surface kink traveled toward the midspan symmetry plane as the flow moves downstream due to the growth of the sidewall boundary layer. Note the sidewall turbulent boundary-layer flow (and corresponding iso-surface structures) did not exist along the entire sidewall surface due to lack of resolution for $y > 20\,\ell$, as discussed in the grid development section. As such, the interaction between the top edge of the developed turbulent sidewall boundary-layer and the oblique sidewall shock near the downstream edge of the resolved domain was exaggerated as the turbulent structures grew and was quickly dissipate due to lack of grid resolution.

While Fig. 6 contains a lot of details, the fast-moving iso-surfaces near the boundary-layer edge mask the flow features near the surface, particularly near the juncture of the corner and the compression ramp. Fig. 7 shows the same Q-criterion = 1 iso-surfaces as Fig. 6, but only includes surfaces where the streamwise velocity is less than $1/4 u_\infty$. As seen in the instantaneous streamwise slice at the end of the resolved domain, the post-shock flow was highly non-uniform. In particular, very large-scale structures ($> \delta$ scale) exist along the span and sidewall, though the sidewall boundary-layer is dominated by the λ-shock structure. In the core-corner region ($y < 3\,\ell$ and $z < 3\,\ell$), the structures are much smaller ($\approx \delta$-scale), though the

entire contour slice shows acoustic radiation. Note a strong acoustic wave situated parallel to the sidewall and perpendicular to the spanwise oblique shock decayed in strength as it traveled toward the midspan symmetry plane on the right side of the image.

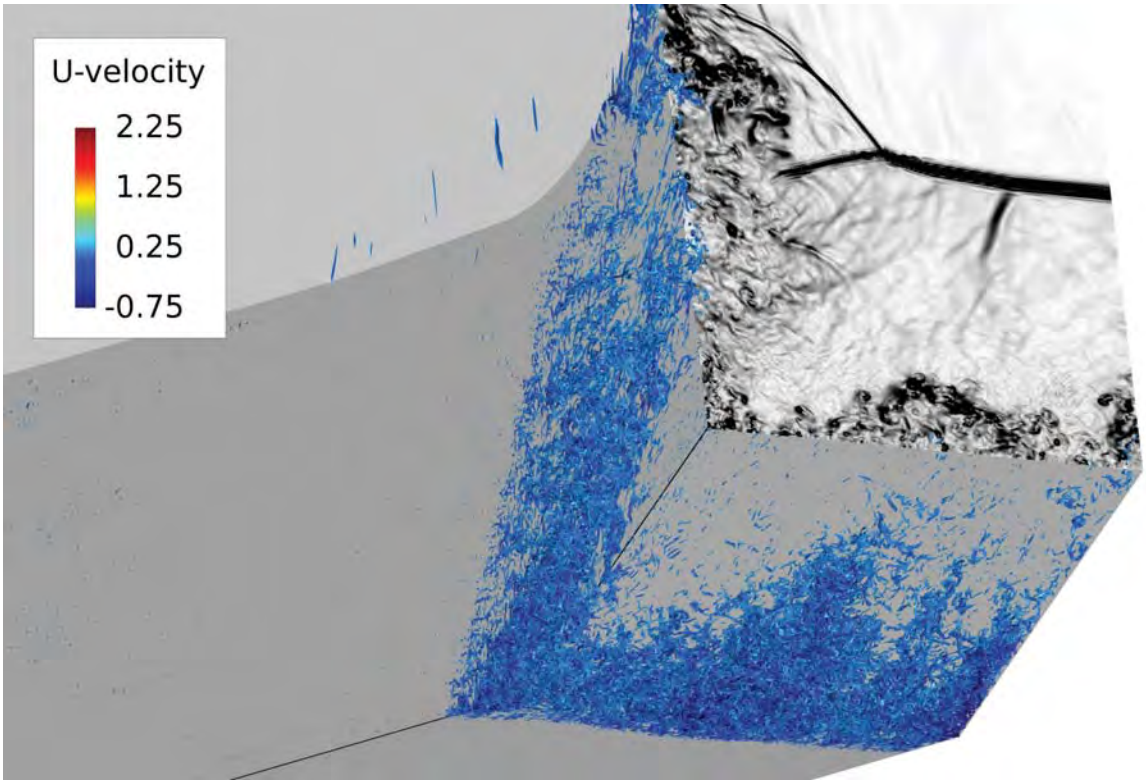

Figure 7. Planar contours of the instantaneous pressure gradient magnitude and iso-surfaces of the Q-criterion where $u < 0.25u_\infty$ colored by the u-velocity for Mach 2.25 turbulent airflow over a 24° compression-ramp near a corner .

The iso-surfaces of Q-criterion in Fig. 7 shows a large region of highly clustered, slow moving or reverse flow structures that exists between the legs of the sidewall λ-shock, although the structures appear smaller and more sparsely populated near the upstream foot. This behavior is different from the flow traveling over the bottom wall, which abruptly exhibits a large number of upstream moving structures giving the flow a distinct separation location. Note the structures near the juncture of the corner and compression ramp reach the farthest upstream, thought they disappear (the flow has reattached) soon after the start of the compression ramp. This corner separation emitted compression waves, which travel along both walls. These waves locally reduce the pressure gradient, which delayed local separation. The compression ramp limited this effect on the bottom wall due to the formation of a normally two-dimensional shock front, whereas the sidewall boundary-layer was unimpeded to interact with the compression waves upstream of the oblique shock interaction. As such, the sidewall boundary-layer thickened upstream of the interaction which lead to sparse pockets of separated flow and a less pronounced SBLI.

Figure 8 shows the instantaneous surface pressure contours at the same time instance as Figs. 6 and 7. As seen in the figure, the spanwise shock front was largely uniform on the bottom plate, though lower pressure contours were prevalent near the juncture of the corner and compression ramp . Reattachment, highlighted by the yellow-orange contours was much less distant and had a larger spanwise variation.

C. Features of the Time-Mean Flow

Flow transients convected out of the domain for 225,000 iterations before the mean and time-accurate solutions were collected. This corresponds to about 2 flow-through lengths since the resolved portion was

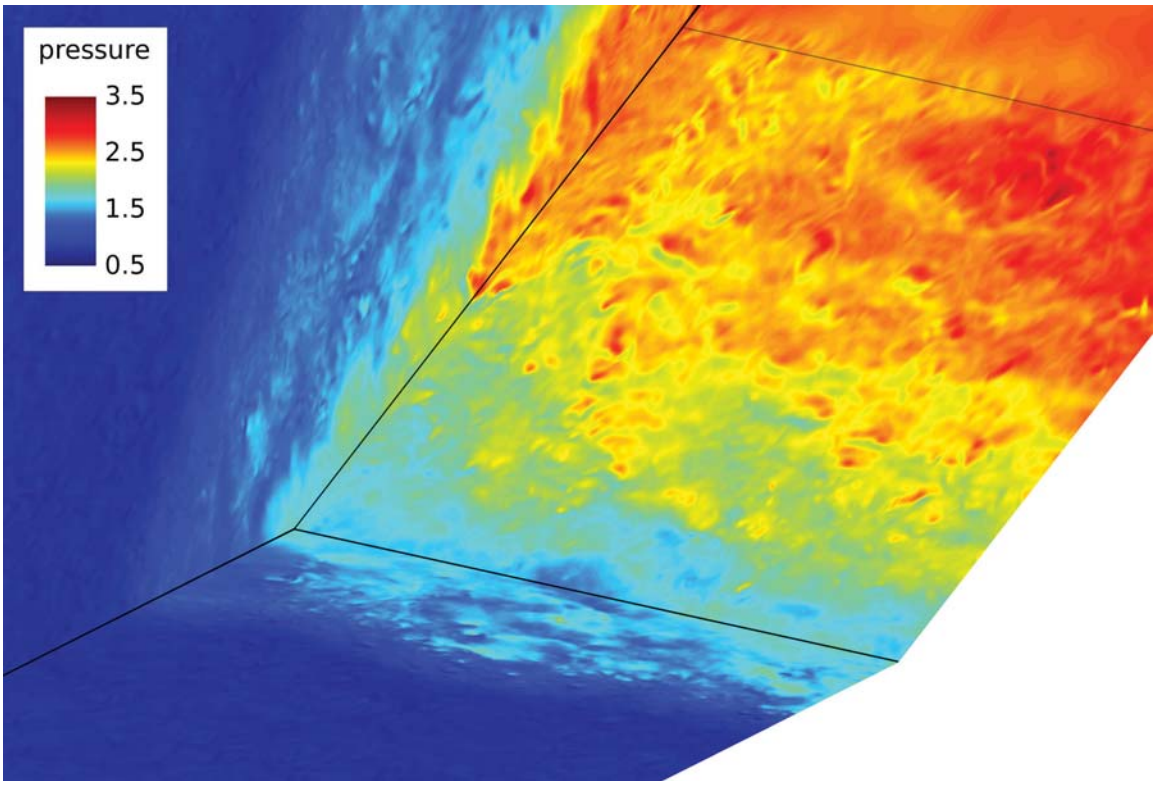

Figure 8. Instantaneous nondimensional surface pressure contours for Mach 2.25 turbulent airflow over a 24° compression-ramp.

$\approx 110\,\ell$ long and a nondimensional time-step $\Delta t = 0.001$ was used. Mean and time-accurate statistics were developed from five additional flow-through times. Previous work on both the corner flow[45] and spanwise homogenous compression ramp[11] indicate that a sampling length of 5 flow-though times was sufficient to converge mean quantities, though higher-order statistics would require additional samples. In addition, it is important to note that the solutions presented were not span-averaged since a homogenous direction does not exist.

To ensure the flow upstream of the compression ramp was in turbulent equilibrium, streamwise velocity profiles were exacted from the mean solution and transformed using the van Driest transformation.[52] The transformed streamwise velocity was nondimensionalized by the wall friction velocity, u_τ. The profiles were plotted versus the nondimensional inner length scale, $y^+ = y\,\rho_w\,u_\tau/\mu_w$ (for the lines normal to the bottom-wall) and $z^+ = z\,\rho_w\,u_\tau/\mu_w$ (for the side-wall). Figure 9(a) plots the van Driest transformed velocity for the near-wall region on both flat plates. It also includes previous spanwise-averaged solutions,[11] computational results from Rai *et al.*,[42] and experimental measurements by Shutts *et al.*,[47] and Elena and LaCharme.[53] The latter was collected at conditions similar to the experiment by Shutts *et al.*.[47]

As seen in the figure, the flow above each wall has developed into an equilibrium turbulent boundary layer. Fig. 9(b) shows Reynolds stress profiles at the same streamwise location ($x = 60\,\ell$). As seen in the figure, the streamwise component shows more variation than the other directions, though all the line plots show consistent behavior. As such, the upstream flow appears to be in turbulent equilibrium and exhibits little variation in mean quantities away from the corner.

Figure 10 shows a three-dimensional view of the mean skin-friction contours, c_f, while Fig. 11 includes planar views and results from the spanwise periodic simulation.[11] Since the compression ramp for the spanwise periodic case was located at $x = 75\,\ell$, compared to $x = 85\,\ell$ in the current scenario, the x-axis has been adjusted to account for the ramp in Fig. 11 ($x* = x - x_{\text{ramp corner}}$). As seen in the figures, a large separation bubble occurs on the bottom plate both upstream and downstream of the compression

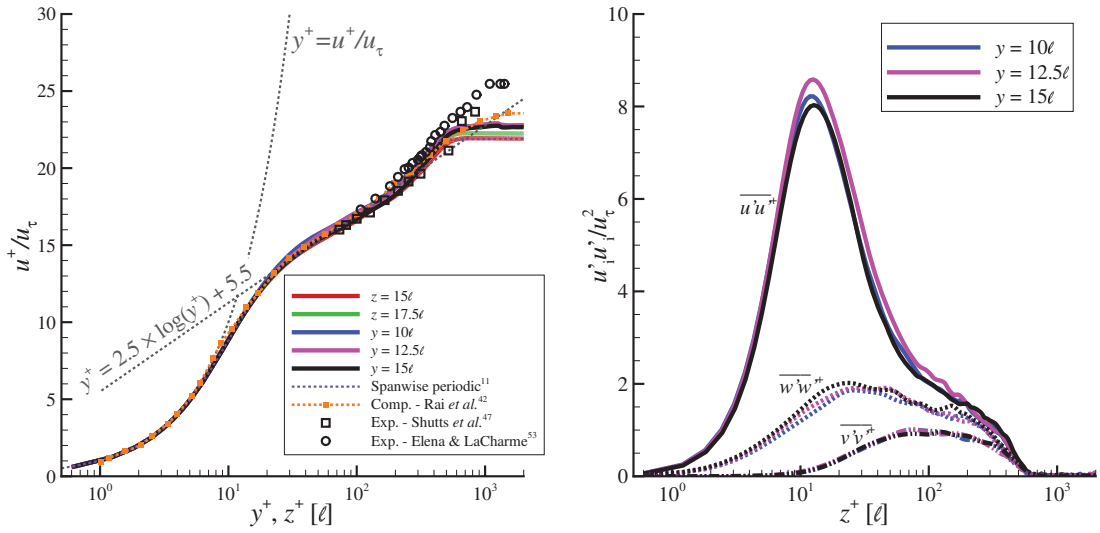

(a) Van Driest transformed streamwise velocity

(b) Reynolds stress profiles

Figure 9. Time-mean streamwise velocity profiles using the Van Driest transform and Reynolds Stress normalized by the friction velocity.

ramp. Along the sidewall, the oblique shock interacted with the turbulent flow which lead to a time-mean separation, though the separation length is not as long in the streamwise direction and weakened with distance from the bottom wall. The black lines in Fig. 11 correspond to $c_f = 0$.

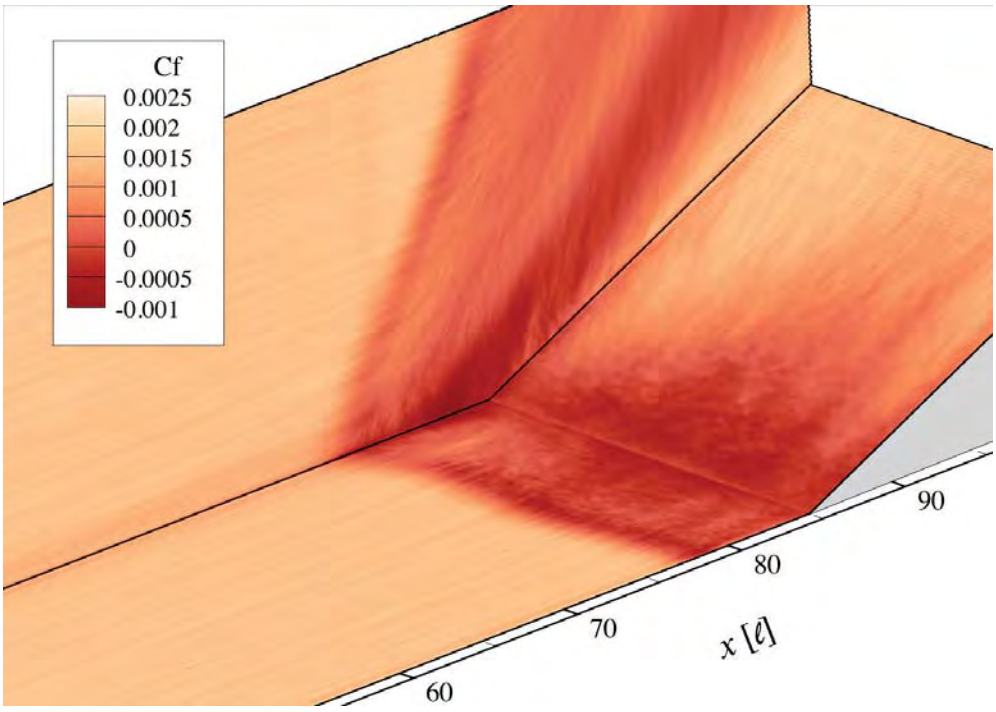

Figure 10. Surface contours of the time-mean skin-friction coefficient.

.

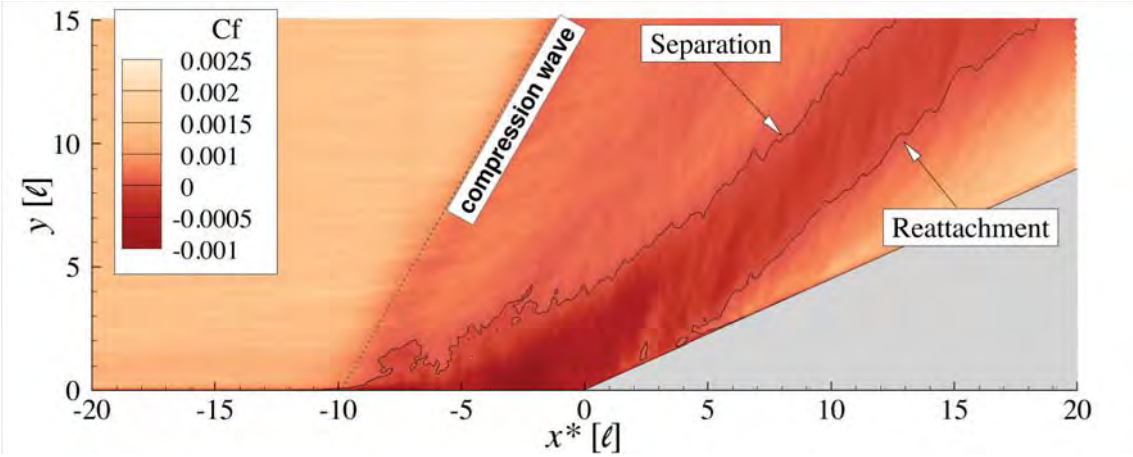

(a) Current results (side view)

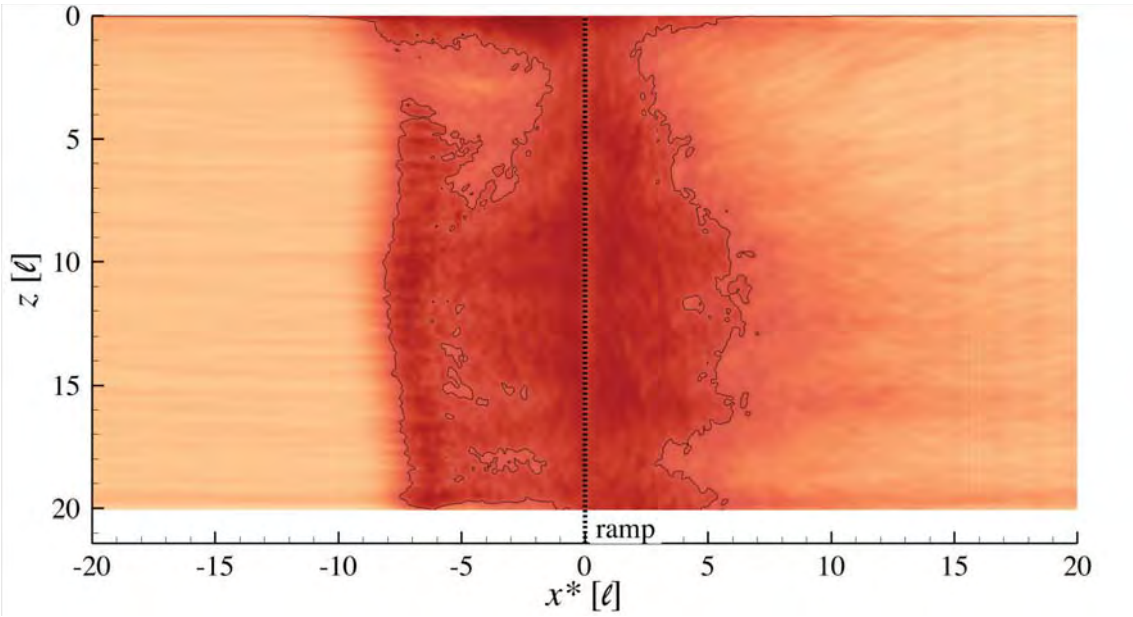

(b) Current results (top-down view)

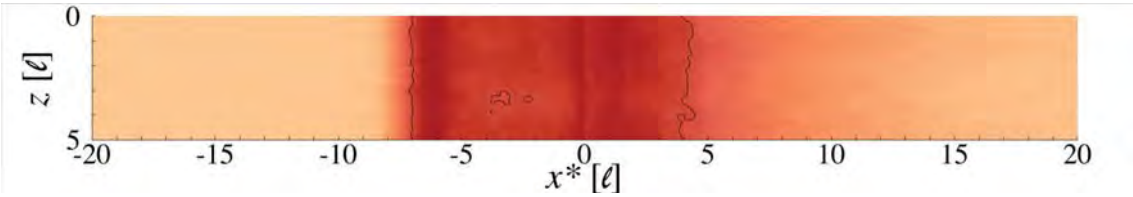

(c) Previous spanwise periodic results[11]

Figure 11. Surface contours of the time-mean skin-friction coefficient.

The weakened sidewall separation was anticipated since the corner separation produced compression waves, which emitted along the sidewall and allowed the sidewall boundary-layer to start to adjust prior to its iteration with the oblique shock. At the same time, a separation vortex, which originated upstream of the juncture of the corner and compression ramp, travel with the sidewall shock and weakened it by spreading apart the λ-shock feet. Given enough streamwise extent and distance from the bottom compression ramp, the sidewall boundary layer may remain attached in the time mean solution.

A comparison of Fig. 11(b) and 11(c) shows the streamwise separation length varies significantly for the scenario with a sidewall. The flow remains mostly attached near the corner ($l_{\text{sep}} \approx 4\ell$ at $z = 3\ell$), then rapidly separates to its maximum extent ($l_{\text{sep}} \approx 13.5\,\ell$ at $z = 10\,\ell$), before gradually relaxing to a length consistent with the spanwise periodic solution[11] ($l_{\text{sep}} \approx 11\,\ell$ for $z > 15\,\ell$). Note the boundary layer thickness δ and Reynolds number based on momentum thickness Re_θ were slightly larger for the corner flow configuration compared to the spanwise periodic scenario due to the compression ramp being located farther downstream ($Re_\theta = 2000$ for the spanwise periodic scenario, $Re_\theta = 2500$ for the scenario with a sidewall).

As previously mentioned, the spanwise separation length was not uniform across the span, particularly near the corner due to the core-corner separation, which occurred about $4\,\ell$ upstream of the maximum spanwise separation. This feature was partially due to the separation vortex which has a nodal attachment point located on the bottom plate, as seen in the black colored velocity streamlines in Fig. 12.

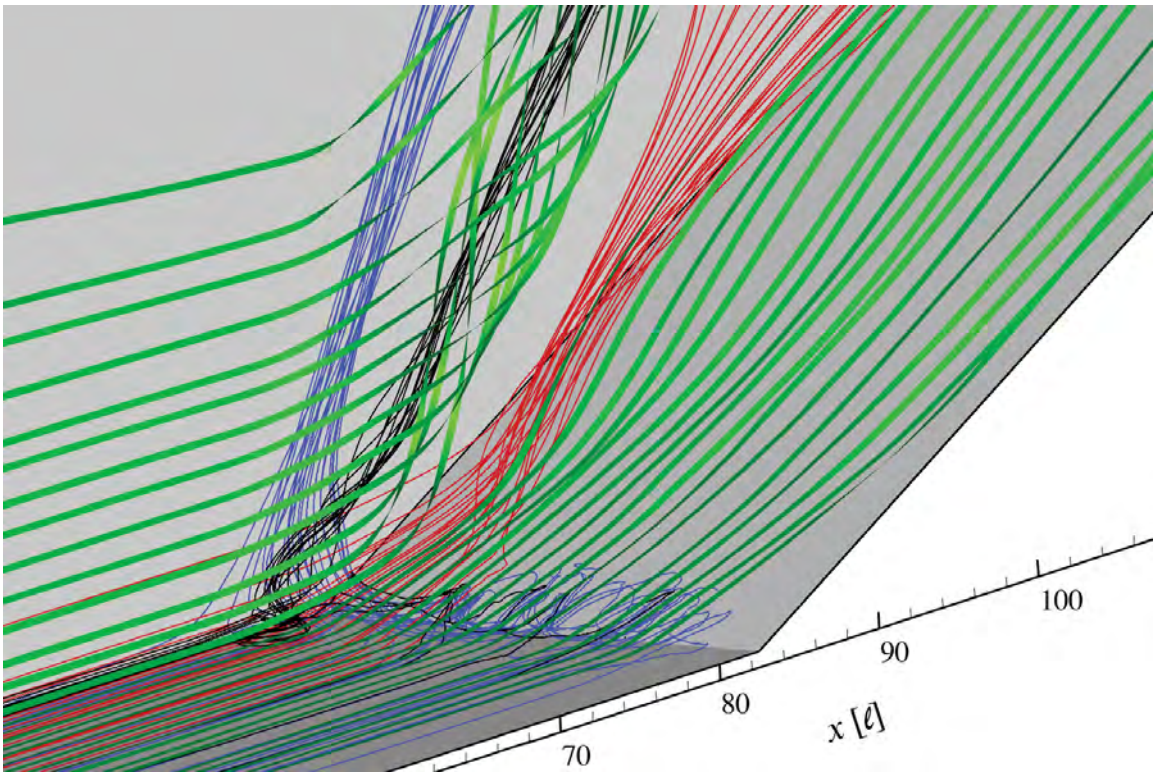

Figure 12. Streamlines of the time-mean velocity comments for Mach 2.25 flow over a 24° compression ramp in the presence of a sidewall.

.

Blue streamlines highlight the bottom wall separation bubble which exhibited a spanwise velocity component that pulled mass from the compression-ramp-induced separation toward the sidewall. Most of this flow turned slightly upstream and back to the right so it could traveled with the sidewall compression waves which emanated from the leading corner separation. However, some of the flow turned left (back towards the symmetry plane) and aided in the development of a nodal attachment point and subsequent separation vortex. The separation vortex was entrained by the sidewall oblique shock and moved along the edge of the sidewall boundary-layer. The formation of the nodal attachment point and separation vortex is consistent

with a sharp-fin interaction, except the nodal attachment point formed on the sidewall in the Mach 4 RANS simulation.[54] The difference in the nodal attachment location may be due to a number of different reasons including: a lack of resolution or the wall model used in the RANS study; a difference in geometries due to the inclusion of a upstream sidewall; or the result of the lower freestream Mach and Reynolds numbers in the current work.

The green streamlines in Fig. 12 where populated from the upstream inviscid flow (near the boundary-layer edge). As seen in the figure, the lines travel over the bottom wall separation and remain largely unaffected by its presence, whereas the sidewall streamlines bend due the compression waves and were entrained into the large separation vortex. Some of the flow near the corner ramp was accelerated around the nodal attachment point as it expanded back into the core-corner region downstream of the corner-ramp junction (as illustrated by the red streamlines). Since the separation vortex entrained most of the sidewall flow, the red streamlines expand primarily along the sidewall in the post-shock core-corner region.

Figure 13 shows planar contours of the mean streamwise velocity the corner-ramp junction. The contour slices were clipped for $u > 0.975u_\infty$ for clarity. The first three slices correspond to $x = 50\,\ell$, $60\,\ell$, and $70\,\ell$, which are all upstream of the unsteady oblique shock front. At these locations the boundary-layer appears smooth and reflective of a turbulent equilibrium corner flow, with the boundary-layer height, δ, growing with downstream distance. By $x = 75\,\ell$, which is just upstream of the spanwise oblique shock front, $\delta \approx 2.2\,\ell$, and a Reynolds number momentum thickness, $Re_\theta \approx 2500$. In the spanwise periodic scenario,[11] the compression ramp was located at $x = 75\,\ell$ and at $x = 60\,\ell$, $\delta = 1.8\,\ell$ and $Re_\theta = 2000$.

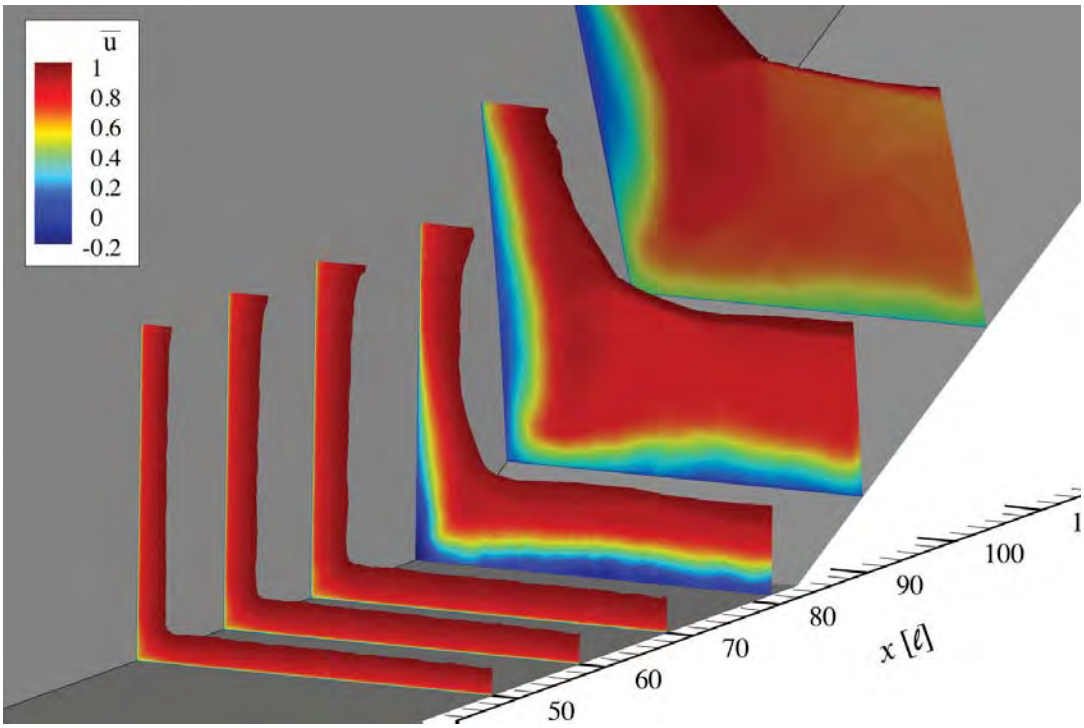

Figure 13. Planar contours of time-mean streamwise u velocity for Mach 2.25 flow over a 24° compression ramp in the presence of a sidewall.

.

As the flow travels through the oblique shock, the core-corner separates first, which develops an asymmetric corner profile and leads to a nonuniform boundary-layer thickness across the span. Further downstream, the core-corner velocity has become much lower and the outer edge of the slices are dominated by a the oblique shock system. At the last streamwise station, the bottom wall appears fairly uniform since the oblique shock has moved far from the wall. On the sidewall, the oblique shock interacted with the boundary-layer, though the separation vortex as weakened its strength, as seen in by the large region of the low velocity flow in the sidewall boundary-layer.

In a previous study of Mach 2.25 turbulent flow in a corner,[45] profiles of the mean Reynolds stress illustrated non-zero contours in the core-corner region of the domain. More importantly, the magnitude of these quantities was on the same order as the product of the mean velocity components. This behavior was also observed in the first three planar slices in Figs. 14(a) and 14(b).

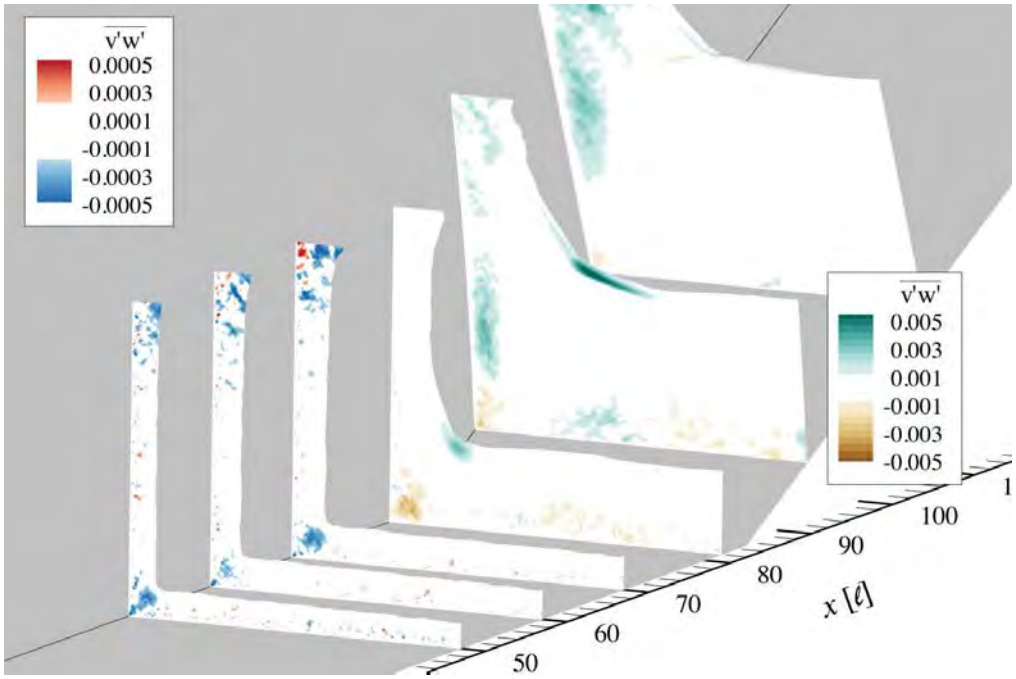

(a) $\overline{v'w'}$

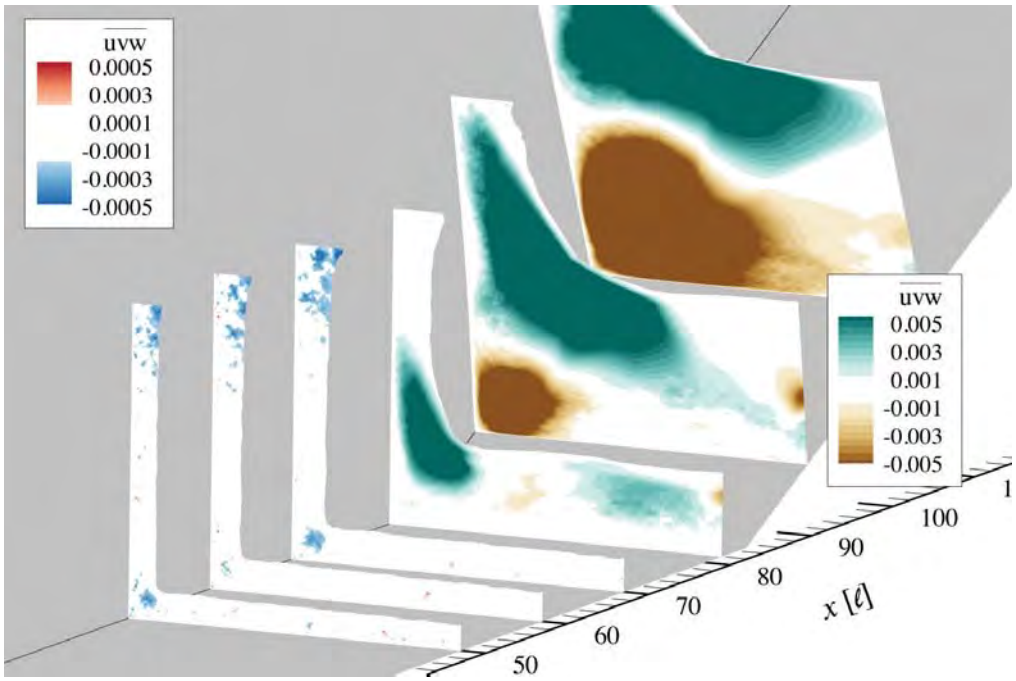

(b) $\overline{uvw}$

Figure 14. Planar contours of various Reynolds stresses.

Downstream of the compression ramp, the planar contours become increasing complicated due to the flow's sharp turning angle from the compression ramp and corresponding three-dimensional oblique shock system. In addition, the separation acts as a frequency selective amplifier for perturbations with frequencies higher the fundamental frequency associated with the separation.[2] Recall, the fundamental frequency of the separation bubble is a function of the separation length and incoming boundary layer edge velocity, so the bubble amplifies a large range of frequencies and provides the system with strong normal and spanwise components. As seen in Figs. 14 and 15, the post-shock flow is initially dominated by normal velocity fluctuations as it responds to the compression ramp. However, a spanwise component also becomes prevalent due the rotation the separation vortex and the growth of the sidewall boundary-layer interaction as the flow progresses downstream.

Upstream of the shock system, non-zero values for the streamwise and spanwise velocity components exist on the sidewall, while the bottom wall has non-zero streamwise and normal velocities, as seen in Fig. 15. These results correspond with an equilibrium turbulent boundary-layer. After the shock, the velocity fluctuations are amplified by both the shock and the separation. The bottom wall shows considerable non-zero fluctuations within the 4th planar slice, which corresponds with the mean separation zone. These fluctuations relax in the last two stations as the flow drives towards its post-shock turbulent equilibrium state. It is worth noting these fluctuations should tend toward zero with sufficient samples since the region contains both positive and negative values, whereas the sidewall fluctuations will persist since they are a result of the geometric change.

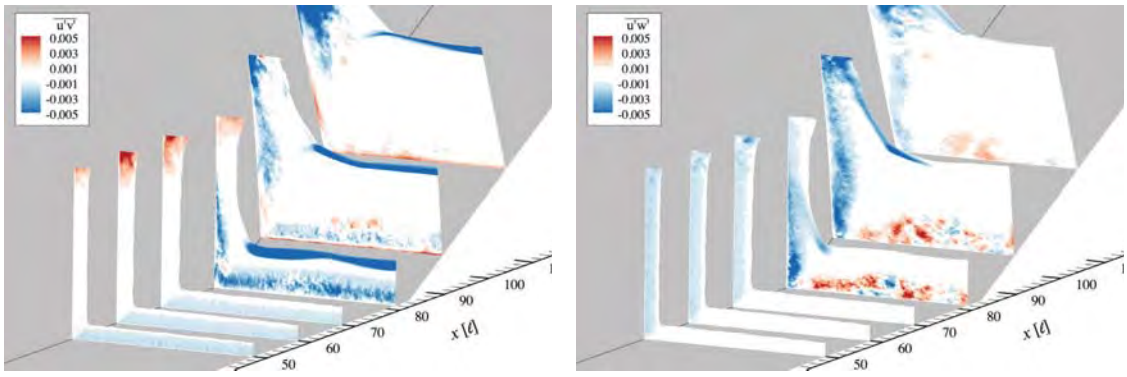

(a) $\overline{u'v'}$ (b) $\overline{u'w'}$

Figure 15. Planar contours of various Reynolds stresses.

D. Features of the Time-Accurate Flow

Due to the large size of the computational domain, it is not practical to collect time-accurate data for the entire domain. Instead, time-accurate statistics were only collected at discrete locations. Samples were taken in the corner core-flow region, along 4 streamwise-orientated surface lines located on the bottom (z) wall away from both the core-corner flow and the symmetry plane, and at various heights and locations in both wall boundary-layers. The line samples were collected upstream and through the bottom wall shock separation point to analyze the shock unsteadiness, while the other points were used to verify the incoming turbulent profiles were in equilibrium and analyze the post-shock flow. Table 2 lists the probe locations, with Fig. 16 illustrating their positions in the computation domain. A total 216 point probes and 4 line probes where used. Each line probe contained 200 continuous streamwise points. The probe data was collected every 100 iterations, which corresponds to a sampling frequency of approximately 10 MHz based on the time step and reference parameters listed.

Figure 17 shows the power spectral density (PSD) of the turbulent kinetic energy (TKE) at various locations in each flat-plate boundary-layer upstream of the shock iteration. The time-accurate history was collected for approximately 5 flow lengths (500,000 iterations). From the time-history, one-dimensional spectra was computed by multiplying the instantaneous fluctuating quantities with a Hanning window for a segment of the data set. The data set was multiplied by the Hanning window to suppress side-lobe leakage,[55] with the window pre-multiplied by $\sqrt{8/3}$ to account for the low-frequency bias introduced by

Table 2. Probe locations of Mach 2.25 flow over a 24° compression ramp in the presence of a sidewall.

Desciption	Location			Color
	x [ℓ]	y^* [ℓ]	z [ℓ]	(in Fig. 16)
core-corner	60, 75, 80, 85, 90, 95	0.5, 1, 1.5, 2, 2.5	0.5, 1, 1.5, 2, 2.5	black
y-wall boundary layer	60, 75, 80, 85, 90, 95	12.5	0, 0.5, 1, 1.5, 2, 2.5	pink
z-wall boundary layer	60, 75, 80, 85, 90, 95	0, 0.5, 1, 1.5, 2, 2.5	12.5	purple
z-wall surface lines	70 to 82.5,	0	10	red
z-wall surface lines	70 to 82.5,	0	12.5	blue
z-wall surface lines	70 to 82.5,	0	15	orange
z-wall surface lines	70 to 82.5,	0	17.5	green

* distance above the surface (displacement due to the compression ramp not included)

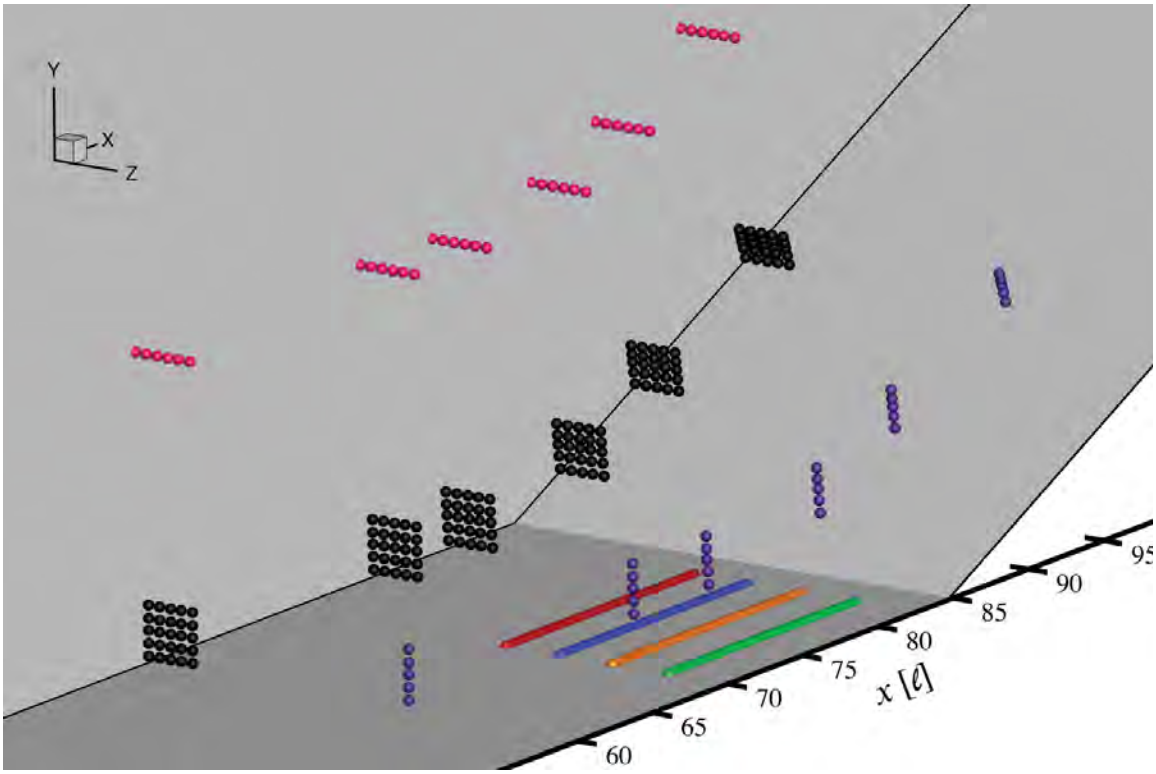

Figure 16. Locations of the sampling probes for the time-accurate data collection.

.

using the window. The discrete Fourier transform of the windowed data was performed and the square of the Fourier transform solution (including the imaginary component), was normalized by the length of the windowed signal to develop the PSD of the signal. The Welsh method,[55] with five overlapping segments, was used to further reduce the noise in the signal by averaging the five resultant PSD curves at each probe location.

As seen in the Fig. 17, the curves are very similar above both sidewalls and in the core-corner region. All three of the streamwise locations in Fig. 17(a), including the corner region probe, show the simulation has had sufficient streamwise distance to develop a turbulent equilibrium boundary-layer profile and adequate

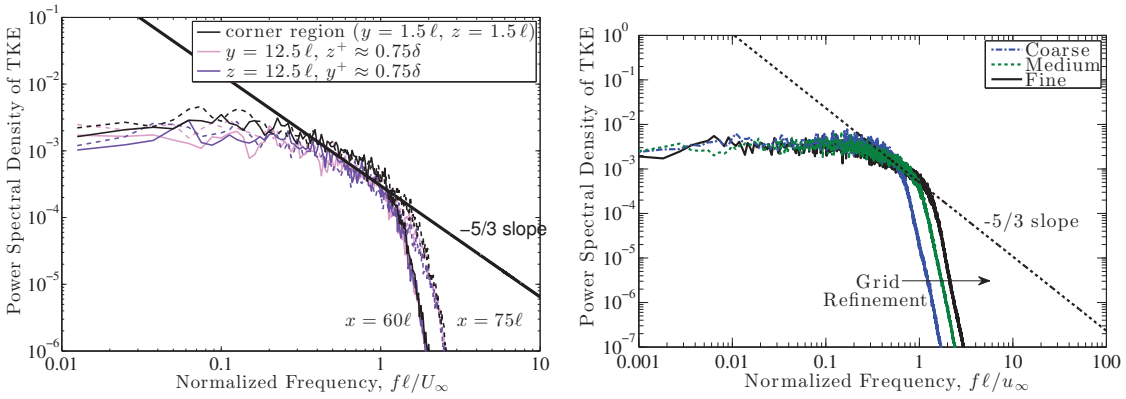

(a) $x = 60\,\ell$ (solid) and $x = 75\,\ell$ (dashed)

(b) Previous spanwise periodic results[11] at $x = 60\,\ell$

Figure 17. Power spectral density of the turbulent kinetic energy above both walls and in the core-corner for the current simulation at approximately $0.75\,\delta$**.**

resolution to capture a portion of the inertial subrange of the turbulent kinetic energy, as highlighted by the $^{-5}/_{3}$ slope line. The lines at the downstream location, $x = 75\,\ell$, have a larger inertial subrange because the flow has had more streamwise distance to developed and, thus, has a slightly thicker boundary-layer and a slightly higher momentum thickness Reynolds number. As seen in Fig. 17(b) previous LES[11] also captured a portion of the inertial subrange, with the finer grid capturing a large region due to increased resolution and because the higher resolution allowed transition to occur earlier which resulted in a larger δ and Re_θ at the same streamwise location. The signal also appeared slightly smoother, especially for the lower frequencies, since the lines in Fig. 17(b) were span-averaged plots and had a longer sampling time-history due to the larger computational time step used in that study ($\Delta\,t = 0.005$ in the spanwise periodic simulations compared to $\Delta\,t = 0.001$ in the current simulation).

Time-accurate data from the 4 line probes located on the surface was used to develop a PSD of pressure at each streamwise location. Solutions from discrete streamwise points on the $z = 12.5\,\ell$ line (i.e., the purple points in Fig. 16), are shown in Fig. 18(b). The streamwise locations are both upstream and downstream of the mean separation, which occurred near $x \approx 76\,\ell$ at $z = 12.5\,\ell$ based on skin-friction, c_f, in Fig: 11(b). As seen in the chart, the low frequencies have little energy upstream of the separation, then suddenly have significant energy as the flow travels through the separated shock foot. This is because the shock unsteadiness has a large-scale, low-frequency motion, which corresponds to a Strouhal number of 0.03 based on the local mean separation length. This behavior was consistent with the spanwise periodic SBLI[11] shown in Fig. 18(a) which had a separation location near $x = 67\,\ell$. Downstream of the separation, the energy spreads into higher frequencies as the turbulent flow starts to readjust and the low-frequency content is not as prevalent.

Fig. 18(c) shows the PSD of pressure on the sidewall at the $y = 12.5\,\ell$ discrete points. Unfortunately, a line of probes was not collected on the sidewall, but from the discrete points, the flow experiences a rapidly increase in energy content. This behavior appears similar to the upstream and downstream curves seen on the bottom wall in Fig. 18(b), but it is important to note that all the the displayed probe locations were upstream of the mean separation. Instead PSD of the sidewall point probes show the rapid increase in total energy as the sidewall boundary-layer grew as it responded to the compression waves emitted from the corner separation, as illustrated in Fig. 11(a).

IV. Conclusions

High-order implicit large-eddy simulations were used to investigate a supersonic wall-bounded turbulent corner flow over a 24° compression ramp. Solutions were obtained using a high-fidelity time-implicit numerical scheme and an implicit large-eddy simulation approach. The inclusion of the sidewall led to the development of a corner core-flow, which grew in size as the flow traveled downstream. A half-span computational domain was developed with a symmetric boundary-condition opposite to the sidewall. The resolved portion of the computational domain was $110\delta_0$ long, $20\delta_0$ wide, and $20\delta_0$ tall, where δ_0 is the

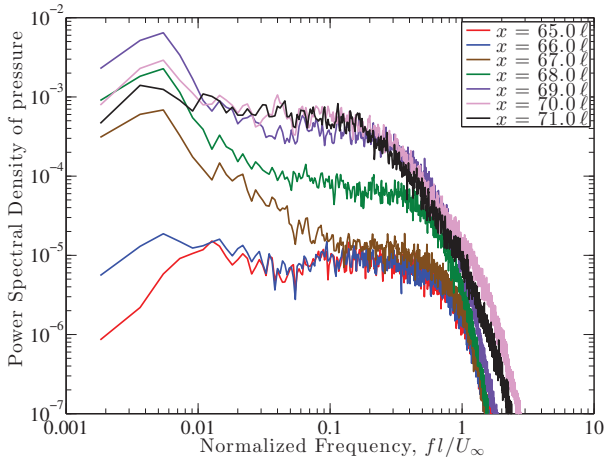

(a) Previous spanwise periodic results[11] with the compression ramp at $x = 75\,\ell$

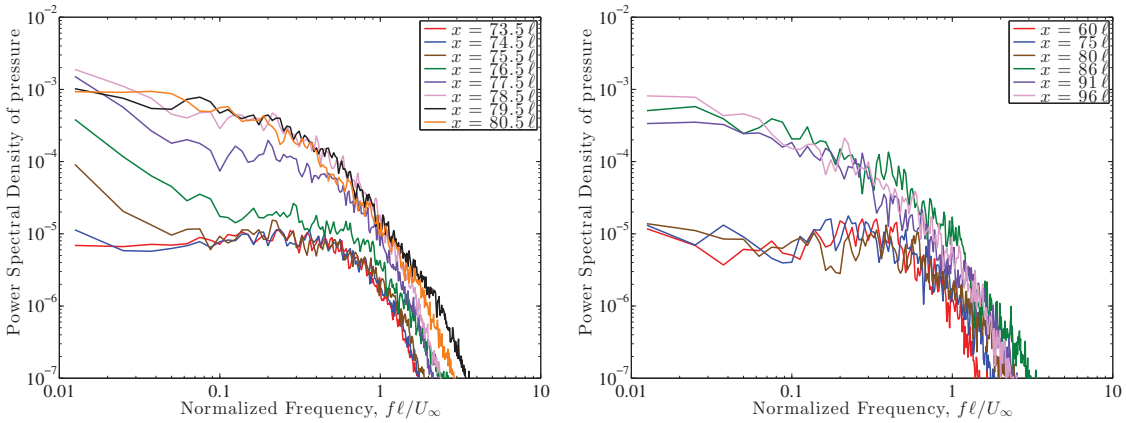

(b) bottom wall ($z = 12.5\,\ell$)

(c) sidewall ($y = 12.5\,\ell$)

Figure 18. Power spectral density of wall pressure using 5 Hanning windows with a 50% overlap.

incoming boundary-layer height. A grid with 748×10^6 points was developed with sufficient resolution to support the high-fidelity high-resolution implicit large eddy simulation. Both time-mean and time-accurate statistics were collected for $t^+ = 500$. The solutions were compared to spanwise-periodic compression-ramp simulations developed at the same conditions. The resultant profiles were similar when compared a near the symmetry plane, though the inclusion of the sidewall lead to a slightly larger separated boundary-layer interaction on the compression ramp and a highly three-dimensional shock front. In addition, the presence of the sidewall boundary-layer lead to the development of a separation vortex, which had a nodal attachment point located just upstream of the juncture between the compression-ramp and corner.

Triple products were collected and demonstrated the importance of resolving the corner-dominated flow without a closure model. In particular, the results showed that the magnitude of the fluctuations of the cross-velocity components in the corner was similar to the product of the mean velocity components for the flow upstream of the shock interaction. Downstream of the shock boundary-layer interaction the highly three-dimensional flow contained λ-shock system which dominated the sidewall boundary-layer profile. The separation vortex caused the legs of the sidewall λ-shock to spread with streamwise distance, effectively diminishing the strength of the sidewall SBLI which lead to a smaller time-mean separation with streamwise distance. Time-accurate data showed the bottom wall SBLI was consistent with the spanwise periodic scenario, though the corner vortex and accompanying compression waves allowed the sidewall boundary-layer to adjust to the sidewall oblique shock in a more gradual manner.

Acknowledgments

The author would like to thank J. Poggie for his useful conversations regarding this research. This work was sponsored, in part, by the Air Force Office of Scientific Research under grant number LRIR 12RB01COR monitored by Dr. J. Schmisseur, AFOSR/RSA. Computational resources were provided through a grant of supercomputer time from the U.S. Department of Defense High Performance Computing Modernization Program at the Air Force Research Laboratory, Wright-Patterson Air Force Base, OH.

References

[1]Blevins, R. D., Holehouse, I., and Wentz, K. R., "Thermoacoutsic Loads and Fatigue of Hypersonic Vehicle Skin Panels," *Journal of Aircraft*, Vol. 30, No. 6, 1993, pp. 971–978.

[2]Poggie, J., Bisek, N. J., Kimmel, R. L., and Stanfield, S., "Spectral Characteristics of Separation Shock Unsteadiness," AIAA Paper 2013-3203, 2013.

[3]Adadms, N. A., "Direct simulation of the turbulent boundary layer along a compression ramp at M = 3 and Re_θ = 1685," *Journal of Fluid Mechanics*, Vol. 420, No. 1, 2000, pp. 47–83.

[4]Rizzetta, D. P., Visbal, M. R., and Gaitonde, D. V., "Large-Eddy Simulation of Supersonic Compression-Ramp Flow by a High-Order Method," *AIAA Journal*, Vol. 39, No. 12, December 2001, pp. 2283–2292.

[5]Garnier, E. and Sagaut, P., "Large Eddy Simulation of Shock/Boundary-Layer Interaction," *AIAA Journal*, Vol. 20, No. 10, October 2002, pp. 1935–1944.

[6]Pirozzoli, S. and Grasso, F., "Direct Numerical Simulation of Impinging Shock Wave/Turbulent Boundary Layer Interaction at M=2.25," *Physics of Fluids*, Vol. 18, No. 065113, 2006, pp. 1–17.

[7]Wu, M. and Pino Martin, M., "Direct Numerical Simulation of Supersonic Turbulent Boundary Layer Over a Compression Ramp," *AIAA Journal*, Vol. 45, No. 4, April 2007, pp. 879–889.

[8]M., R., Wu, M., and Pino Martin, M., "Low Reynolds Number Effects in a Mach 3 Shock/Turbulent Boundary-Layer Interaction," *AIAA Journal*, Vol. 46, No. 7, July 2008, pp. 1884–1887.

[9]Priebe, S. and Pino Martín, M., "Low-Frequency Unsteadiness in the DNS of a Compression Ramp Shockwave and Turbulent Boundary Layer Interaction," AIAA Paper 2010-108, 2010.

[10]Muppidi, S. and Mahesh, K., "DNS of Unsteady Shock Boundary Layer Interaction," AIAA Paper 2011-724, 2011.

[11]Bisek, N. J., Rizzetta, D. P., and Poggie, J., "Plasma Control of a Turbulent Shock Boundary-Layer Interaction," *AIAA Journal*, Vol. 51, No. 8, 2013, pp. 1789–1804, doi:10.2514/1.J052248.

[12]Morgan, B., Duraisamy, K., and Lele, S. K., "Large-Eddy Simulations of a Normal Shock Train in a Constant-Area Isolator," *AIAA Journal*, Vol. 52, No. 3, March 2014, pp. 539–558.

[13]A., H., "Large-Eddy Simulation of Shock/Boundary-Layer Interaction," *AIAA Journal*, Vol. 50, No. 12, 2012, pp. 2919–2927, doi: 10.2514/1.J051786.

[14]Reda, D. C. and Murphy, J. D., "Shock Wave/Turbulent Boundary-Layer Interactions in Rectangular Channels," *AIAA Journal*, Vol. 11, 1973, pp. 139–140.

[15]Burton, D. M. F. and Babinsky, H., "Corner Separation Effects for Normal Shock Wave/Turbulent Boundary Layer Interactions in Rectangular Channels," *Journal of Fluid Mechanics*, Vol. 707, September 2012, pp. 287–306.

[16]Babinsky, H., Oorebeek, J., and Cottingham, T. G., "Corner Effects in Reflecting Oblique Shock-Wave/Boundary Layer Interactions," AIAA Paper 2013-859, 2013.

[17]Gaitonde, D. and Visbal, M. R., "High-order Shcemes for Navier-Stokes Equations: Algortithm and Implementaiton into FDL3DI," Tech. rep., Air Force Research Laboratory, August 1998, AFRL-VA-WP-TR-1998-3060.

[18]Visbal, M. R., "Computational Study of Vortex Breakdown on a Pitching Delta Wing," AIAA Paper 1993-2974, 1993.

[19]Gordnier, R. E. and Visbal, M. R., "Numerical Simulation of Delta-Wing Roll," *Aerospace Science and Technology*, Vol. 2, No. 6, September 1998, pp. 347–357.

[20]Visbal, M. R., Gaitonde, D. V., and Gogineni, S., "Direct Numerical Simulation of a Forced Transitional Plane Wall Jet," AIAA Paper 1998-2643, 1998.

[21]Rizzetta, D. P., Visbal, M. R., and Blaisdell, G. A., "Application of a High-Order Compact Difference Scheme to Large-Eddy and Direct-Numerical Simulation," AIAA Paper 1999-3714, 1999.

[22]Morgan, P. E., Rizzetta, D. P., and Visbal, M. R., "High-Order Numerical Simulation of Turbulent Flow over a Wall-Mounted Hump," *AIAA Journal*, Vol. 44, No. 2, February 2006, pp. 239–251.

[23]Garmann, D. J. and Visbal, M. R., "Implicit LES Computations for a Rapidly Pitching Plate," AIAA Paper 2010-4282, 2010.

[24]White, M. D. and Visbal, M. R., "High Fidelity Analysis of Aero-Optical Interaction with Compressible Boundary Layers," AIAA Paper 2010-4496, 2010.

[25]Anderson, D., Tannehill, J., and Pletcher, R., *Computational Fluid Mechanics and Heat Transfer*, 1984, McGraw-Hill.

[26]Mullenix, N. J., Gaitonde, D. V., and Visbal, M. R., "A Plasma-Actuator-Based Method to Generate a Supersonic Turbulent Boundary Layer Inflow Condition for Numerical Simulation," AIAA Paper 2011-3556, 2011.

[27]Beam, R. and Warming, R., "An Implicit Factored Scheme for the Compressible Navier-Stokes Equations," *AIAA Journal*, Vol. 16, No. 4, April 1978, pp. 393–402.

[28]Gordnier, R. E. and Visbal, M. R., "Numerical Simulation of Delta-Wing Roll," AIAA Paper 1993-544, 1993.

[29]Jameson, A., Schmidt, W., and Turkel, E., "umerical Solutions of the Euler Equations by Finite Volume Methods Using Runge-Kutta Time Stepping Schemes," AIAA Paper 1981-1259, 1981.

[30]Pulliam, T. H. and Chaussee, D. S., "A Diagonal Form of an Implicit Approximate-Factorization Algorithm," *Journal of Computational Physics*, Vol. 39, No. 2, Febuary 1981, pp. 347–363.

[31]Lele, S., "Compact Finite Difference Schemes with Spectral-like Resolution," *Journal of Computational Physics*, Vol. 103, 1992, pp. 16–42.

[32]Visbal, M. R. and Gaitonde, D. V., "High-Order-Accurate Methods for Complex Unsteady Subsonic Flows," *AIAA Journal*, Vol. 37, No. 10, October 1999, pp. 1231–1239.

[33]Gaitonde, D., Shang, J. S., and Young, J. L., "Practical Aspects of High-Order Accurate Finite-Volume Schemes for Electromagnetics," AIAA Paper 1997-363, 1997.

[34]Visbal, M. R. and Rizzetta, D. P., "Large-Eddy Simulation on Curvilinear Grids Using Compact Differencing and Filtering Schemes," *Journal of Fluids Engineering*, Vol. 124, 2002, pp. 836–847.

[35]Roe, P. L., "Approximate Riemann Solvers, Parameter Vectors, and Difference Schemes," *Journal of Computational Physics*, Vol. 43, No. 2, 1981, pp. 357–372.

[36]van Albada, G. D., van Leer, B., and Roberts, W. W., J., "A Comparative Study of Computational Methods in Cosmic Gas Dynamics," *Astronomy and Astrophysics*, Vol. 108, April 1982, pp. 76–84.

[37]Swanson, R. C. and Turkel, E., "On Central-Difference and Upwind Schemes," *Journal of Computational Physics*, Vol. 101, No. 2, August 1992, pp. 292–306.

[38]Visbal, M. R., Morgan, P. E., and Rizzetta, D. P., "An Implicit LES Approach Based on High-Order Compact Differencing and Filtering Schemes," AIAA Paper 2003-4098, 2003.

[39]Fureby, C. and Grinstein, F. F., "Monotonically Integrated Large Eddy Simulation," *AIAA Journal*, Vol. 37, No. 5, May 1999, pp. 544–556.

[40]Stoltz, S. and Adams, N. A., "An Approximate Deconvolution Procedure for Large-Eddy Simulation," *Physics of Fluids*, Vol. 11, No. 7, July 1999, pp. 1699–1701.

[41]Mathew, J., Lechner, R., Foysi, H., Sesterhenn, J., and Friedrich, R., "An Explicit Filtering Method for Large Eddy Simulation of Compressible Flows," *Physics of Fluids*, Vol. 15, No. 8, August 2003, pp. 2279–2289.

[42]Rai, M. M., Gatski, T. B., and Erlebacher, G., "Direct Simulation of Spatially Evolving Compressible Turbulent Boundary Layers," AIAA Paper 1995-583, 1995.

[43]Rizzetta, D. P. and Visbal, M. R., "Large-Eddy Simulation of Supersonic Boundary-Layer Flow by a High-Order Method," *International Journal of Computational Fluid Dynamics*, Vol. 18, No. 1, January 2004, pp. 15–27.

[44]Pirozzoli, S., Grasso, F., and Gatski, T. B., "Direct Numerical Simulation and Analysis of a Spatially Evolving Supersonic Turbulent Boundary Layer at M=2.25," *Physics of Fluids*, Vol. 16, No. 3, March 2004, pp. 530–545.

[45]Bisek, N. J., "High-Order Implicit Large-Eddy Simulations of Supersonic Corner Flow," AIAA Paper 2014-0588, 2014.

[46]White, F. M., *Viscous Fluid Flow, 3rd Ed.*, 2006, McGraw Hill.

[47]Fernholz, H. H. and Finley, P. J., "A Critical Compilation of Compressible Turbulent Boundary Layer Data," Tech. rep., 1977, AFARDograph No. 223, Case 55010501.

[48]Georgiadis, N. J., Rizzetta, D. P., and Fureby, C., "Large-Eddy Simulation: Current Capabilites, Recommended Practices, and Future Research," *AIAA Journal*, Vol. 48, No. 8, August 2010, pp. 1772–1784.

[49]Benek, J., Suchyta, C., and Babinsky, "The Effect of Tunnel Size on Incident Shock Boundary Layer Interaction Experiments," AIAA Paper 2013-0862, 2013.

[50]Jeong, J. and Hussain, F., "On the Identification of a Vortex," *Journal of Fluid Mechanics*, Vol. 285, 1995, pp. 69–94.

[51]Dolling, D. S., "Unsteady Phenomena in Shock Wave/Boundary Layer Interaction," Tech. rep., Advisory Group for Aerospace Research & Development, May 1993, Special Course on Shock-Wave/Boundary-Layer Interaction in Supersonic and Hypersonic Flows, AGARD-R-792, pp. 4-1–4-46.

[52]van Driest, E. R., "On the Turbulent Flow Near a Wall," *Journal of the Aeronautical Sciences*, Vol. 23, 1956, pp. 1007–1011.

[53]Elena, M. and LaCharme, J. P., "Experimental Study of a Supersonic Turbulent Boundary Layer Using Laser Doppler Anemometer," *Journal de Mécanique Théorique et Appliquée*, Vol. 7, 1988, pp. 175–190.

[54]Gaitonde, D. and Shang, J. S., "The Structure of a Turbulent Double-Fin Interaction at Mach 4," AIAA Paper 1994-2810, 1994.

[55]Bendat, J. S. and Piersol, A. G., *Random Data,* 2^{nd} *Ed.*, 1986, John Wiley & Sons.

AIAA SciTech
5-9 January 2015, Kissimmee, Florida
53rd AIAA Aerospace Sciences Meeting

Spectral Scaling in a Supersonic Reattaching Shear Layer

Tim Leger* and Jonathan Poggie †
U.S. Air Force Research Laboratory, Wright-Patterson Air Force Base, OH 45433-7512, USA

Simulations of a Mach 2.9 turbulent shear layer in a back-step/ramp configuration are performed using Improved Delayed Detached Eddy Simulations (IDDES) techniques. For this configuration, the separation point of the turbulent boundary layer is essentially fixed at the edge of the back-step, with the point of reattachment allowed to move freely along the ramp. The influence of boundary layer thickness at separation on the reattachment shock system is explored. Power spectra from the surface pressure fluctuations along the ramp are used to characterize the unsteady reattachment shock system and attempts are made to correlate the data through scaling.

Nomenclature

P	Pressure
T	Temperature
M	Mach number
Re/m	Unit Reynolds number
u	Velocity
ρ	Density
μ	Dynamic viscosity
ν	Kinematic viscosity
f	Function
$\tilde{d}$	DES modified distance/length scale
d	Distance
c	Constant
r	Length scale ratio
C_{DES}	DES constant
Δ	Maximum cell dimension
δ	Boundary layer thickness
δ^*	Boundary layer displacement thickness
θ	Boundary layer momentum thickness
H	Boundary layer shape factor
x	Streamwise distance from the step corner
y	Vertical distance from the step corner
z	Spanwise distance
x^*	Distance along the ramp
D	Step height = 25.4 mm
y^+	Dimensionless wall distance
Ψ	Low Reynolds number correction
κ	von Karman constant
R	Correlation of Pressure
σ	RMS of pressure fluctuations

*Research Scientist, Ohio Aerospace Institute, AIAA Member, timothy.leger.ctr@us.af.mil
†Senior Aerospace Engineer, AFRL/RQHF, Associate Fellow AIAA

Subscript

0	Baseline case
1	Start of the ramp
2	End of the ramp
o	Stagnation
∞	Freestream
w	Wall
t	Turbulent
l	Laminar
d	Delayed
G	Grid
R	Reattachment
SEP	Separation

I. Introduction

The separation and reattachment of compressible turbulent shear layers plays a key role in the design and performance of supersonic and hypersonic flight vehicles. This includes several practical problems, including fatigue failure due to heating and pressure fluctuations,[1,2] control surface problems associated with unsteady flow over stalled airfoils,[3] and mixing of fuel with air in scramjet engines.[4] Although numerous experiments and simulations with various geometries have been conducted to study this phenomenon, the majority of this research has focused on the unsteadiness of the separation shock, with little emphasis on the reattachment shock.

Shen et al.[5] made measurements of wall pressure fluctuations in the reattachment region of a supersonic free shear layer formed by a backward facing step. While the overall behavior was found to be similar in scale and magnitude to that in compression ramp flows, the unsteady characteristics of the shock reattachment were substantially different. In particular, less of the spectral content was concentrated at low frequencies and no characteristic intermittent pressure signal was observed. Similar features have been observed in measurements of other supersonic flows near unsteady reattachment.[6–8]

Poggie et al.[9] extended this work by investigating the influence of disturbances in the incoming boundary layer on the unsteadiness of the reattachment shock system through steady air injection in the vicinity of separation. The effects were dramatic, with substantial increases in the intensity of pressure fluctuations and amplitude of the shock motion. Power spectra of the ramp pressure fluctuations exhibited a distinct shift to lower frequencies. The spectra were also shown to collapse onto a common curve in non-dimensional coordinates based on a length scale and a convection velocity, derived from two-point cross-correlations. Comparison of the data with the theory of Plotkin[10] proved to be a reasonable fit to the separation shock motion in the shear layer. It was concluded that shock motion in the reattaching shear layer is primarily due to organized flow structures in the incoming turbulent flow.

In the work presented here, influences on the unsteadiness of the reattaching shear layer shock system are investigated using Improved Delayed Detached Eddy Simulation (IDDES) techniques. The baseline case is constructed to match the configuration of Shen et al.[5] A second case, with double the boundary layer thickness just upstream of the separation point or $2\delta_0$, is also performed and compared with the baseline case. The unsteady surface pressure along the ramp for both cases is analyzed using power spectra. Attempts are made to correlate the spectra from both these cases with each other.

II. Reference Experiment

The baseline configuration is based on a set of experiments performed in the Princeton University 204 mm by 204 mm high Reynolds number, blow down, supersonic wind tunnel. Figure 1 illustrates the basic geometry and flow involved. The test model was constructed from brass, and consisted of a wedge-shaped plate with a cavity, 25.4 mm deep and 61.9 mm long, followed by a 160 mm long 20 degree ramp. Although the model was bolted to the tunnel walls and thus spanned the entire test section, the cavity and ramp were only 152.4 mm wide, with a 25.4 mm inset between them and the tunnel walls on both sides to mitigate

effects from the tunnel side wall boundary layers. Aerodynamic fences were attached to the portion of the ramp which extended above the cavity to help ensure two dimensionality of the mean flow.

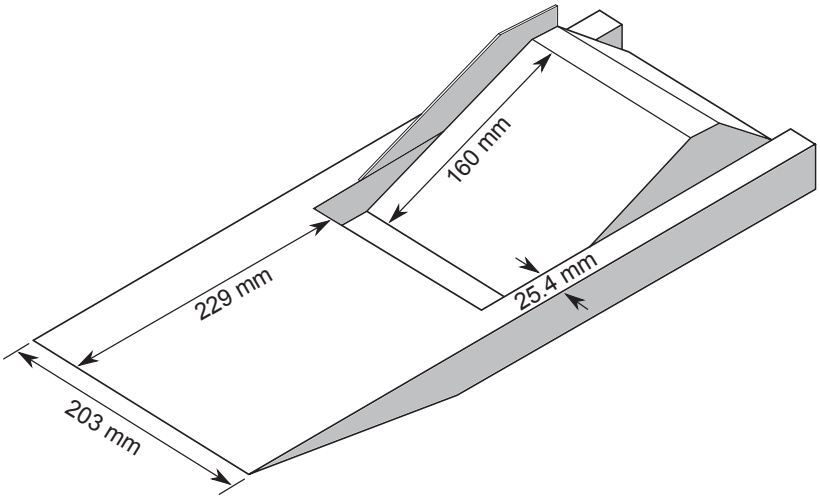

(a) Illustration of the experimental model with one aerodynamic fence removed

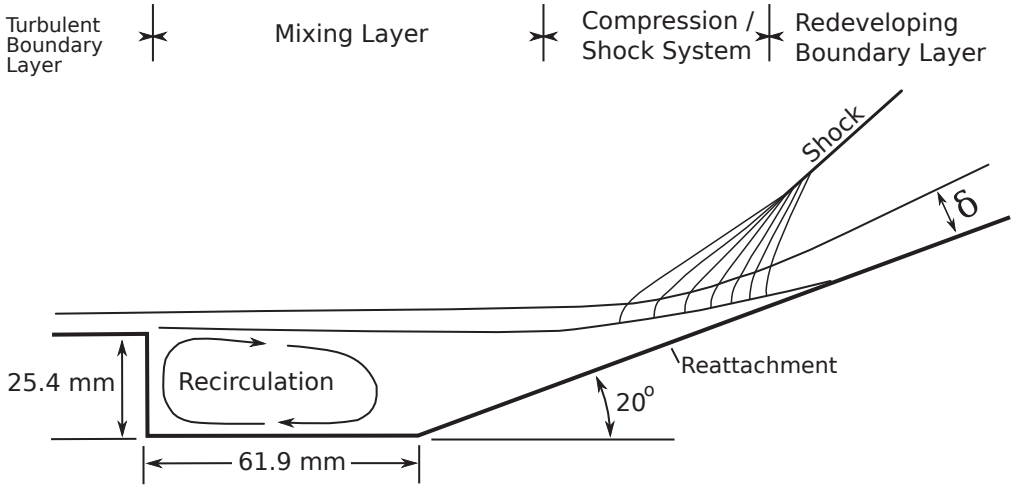

(b) Cross section of the mean flow field

Figure 1. Experimental Configuration (Adapted from Baca[11])

Surveys of the flow field and basic properties were initially performed by Baca et al.,[11,12] with additional work later by Hayakawa et al.,[13] and Shen et al.[5] Nominal flow conditions were $P_o = 0.689$ MPa $\pm$ 1%, T_o = 258 K $\pm$ 4%, $M_\infty = 2.92 \pm 0.015$, $U_\infty = 572$ m/s $\pm$ 2%, $\rho_\infty = 0.77$ kg/m^3, $T_\infty = 95$ K $\pm$ 4 %, Re/m = 67E6/m $\pm$ 4%, with air as the working fluid. Measurements from surface thermocouples on the model indicated that the model surface was essentially adiabatic, $T_w/T_o = 1.03$.

III. Approach

III.A. Numerical Model

Simulations were carried out using US3D, a well-validated, cell-centered, finite-volume, solver for the solution of the non-equilibrium, compressible Navier-Stokes equations on unstructured grids, developed at the University of Minnesota.[14] To provide a good starting point for the IDDES simulations, a steady state RANS simulation is first performed. For these steady state RANS calculations, the modified Steger-Warming flux vector splitting scheme of MacCormack and Candler[15] is used to evaluate the the inviscid fluxes, along with MUSCL reconstruction[16] at the faces to achieve second order spatial accuracy. The modified Steger-Warming method uses a pressure-dependent weighting function to switch smoothly from a low-dissipation method in regions of low gradients to the original Steger-Warming scheme when a large-pressure gradient is detected across a face (such as for a strong shock). Diffusive fluxes are computed using a second-order scheme, in which the gradients are computed using a deferred correction approach similar to that of Nompelis et al.,[14,17,18] MacCormack and Candler,[15,19] and Kim et al.[20] Weighted least square fits are used to calculate the viscous fluxes from second order accurate gradients.

The RANS solutions are driven to a steady state convergence using a backward Euler time stepping, which is fully implicit, but only first order accurate. Future time level fluxes are approximated by linearizing the fluxes about the current time level using exact flux Jacobian. The data-parallel line relaxation (DPLR) method, based on the Gauss-Seidel line relaxation method of MacCormack,[21] is then employed to solve the resulting linear system. To improve performance on parallel systems, the DPLR method replaces Gauss-Seidel sweeps with a series of line relaxation sweeps.[22] Overall, the DPLR method has high parallel efficiency and good convergence characteristics, particularly when solving large compressible flow problems.

The shock capturing scheme used to evaluate the fluxes in the steady state RANS simulations, while very good at capturing shocks, is too dissipative to resolve unsteady turbulence. To overcome this problem, symmetric flux evaluations are often used, as they contain no dissipation. Unfortunately, such methods are unstable in the presence of strong gradients, such as shock waves. For the unsteady IDDES results presented here, a hybrid flux scheme was used, which combines a fourth order accurate symmetric flux evaluation with the dissipative portion of the shock-capturing modified Steger-Warming flux vector splitting scheme.[23] This approach allows for a large range of turbulent scales to be resolved without excessive dissipation. Stability in the presence of strong shock waves is maintained by adding dissipative fluxes via a Ducros shock sensor switch.[24] To advance the IDDES solution in time, a second order implicit Crank-Nicolson scheme is utilized.

The standard Spalart-Allmaras (SA) turbulence closure model with trip term[25] and corrections for compressible flow by Catris and Aupoix[26] was used for all simulations. In the DES approach, the switch between RANS and LES modes in the domain is based on a modified distance function, which is evaluated at each cell, every iteration:

$$\tilde{d} = \min(d_w, C_{DES}\Delta) \tag{1}$$

Where d_w is the distance from the cell center to the closest wall, C_{DES} is the DES constant 0.65 from Ref.,[27] and Δ is the largest cell dimension. The modified distance, $\tilde{d}$, is then used in the turbulence model calculation for the length scale in place of the distance to the nearest wall. This modification results in RANS being utilized for cells in which the turbulent length scale is less than or equal to the maximum cell dimension (primarily near walls), and LES in regions of domain where the grid is refined enough to support it.

Since the DES technique is dependent on cell size, the switch over from RANS to LES can easily occur in undesirable regions of the domain, where the LES approach is not correct. Without corrections, extreme care must be taken in grid generation and refinement to ensure the switch from RANS to LES occurs at the edge of the boundary layer. To make DES easier to use, modifications for certain situations have been developed and those employed in the current work are briefly discussed.

The first of these is the low Reynolds number correction, which accounts for the low Reynolds number terms in the original SA turbulence model. These terms use the ratio of eddy and molecular viscosities to determine proximity to walls. In the LES mode of DES, the subgrid eddy viscosity decreases with reduced cell size and lower Reynolds number. As a result, the DES model can misinterpret situations with small cells as being in the proximity of a wall and excessively lower the eddy viscosity, relative to the ambient velocity and length scales. To overcome this, a low Reynolds number correction term, Ψ, was derived by Spalart[28] for the original SA model:

$$\Psi^2 = \min\left[10^2, \frac{1 - \frac{c_{b1}}{c_{w1}\kappa^2 f_w^*}[f_{t2} + (1 - f_{t2})f_{v2}]}{f_{v1}\max(10^{-10}, 1 - f_{t2})}\right] \tag{2}$$

The DES modified distance function is then modified as follows to incorporate this correction term.

$$\tilde{d} = \min(d_w, \Psi C_{DES}\Delta) \tag{3}$$

In equation 2, all the terms are the same as in the original SA model, with the exception of f_w^*, which acts as a limit value for the f_w function in the SA model and is assigned the value of 0.424. The correction term Ψ takes on a value between 1, for a subgrid eddy viscosity higher than $\sim 10\nu$ (i.e. inactive), and 10, for significantly low values of subgrid eddy viscosity, thus delaying the switch from RANS to LES mode.

Another situation in which the DES model can inappropriately switch from RANS to LES mode is due to Modeled Stress Depletion (MSD), which can result from excessive grid refinement. In this case, the grid cells near the wall are small enough to trigger the switch from RANS to LES well within the boundary layer, where the grid is not refined enough to support the resolved velocity fluctuations internal to the boundary layer (i.e. LES content). As a result, the eddy viscosity and therefore the modeled Reynolds stress is reduced without any sizable resolved stress to restore the balance.[29] Mentor and Kuntz[30] developed a function for the SST turbulence model to identify boundary layers and delay the switch from RANS to LES in those regions. Their function makes use of the ratio between the internal length scale of the k-ω turbulence model and the distance to the wall. Unfortunately the SA model does not employ an internal length scale, so Spalart extended the method of Mentor and Kuntz to the SA model by using the ratio of the model length scale to the wall distance:[28]

$$r_d = \frac{\nu_t + \nu_l}{\sqrt{U_{i,j}U_{i,j}}\kappa^2 d_w^2} \tag{4}$$

Equation 4 equals 1 in the logarithmic layer and gradually falls to zero towards the edge of the boundary layer. This is then used in the following delay function, which is 1 above the boundary layer (where $r_d \ll 1$) and 0 elsewhere:

$$f_d = 1 - \tanh([8r_d]^3) \tag{5}$$

The DES modified distance function is then redefined as:

$$\tilde{d} = d_w - f_d \max(0, d_w - \Psi C_{DES}\Delta) \tag{6}$$

This modification is known as the Delayed Detached Eddy Simulation method or DDES.

Shur et al.[31] extended the DDES method by adding a Wall-Modelled LES (WMLES) capability, which is only active when turbulent content exists, and behaves as DDES otherwise. This modification is known as the Improved Delayed Detached Eddy Simulation or IDDES method. For this method, the DES modified distance function is redefined as:

$$\tilde{d} = \tilde{f}_d(1 + f_e)d_w + (1 + \tilde{f}_d)\Psi C_{DES}\Delta \tag{7}$$

Equation 7 is basically a blended function between the RANS length scale and the WMLES length scale. The function $\tilde{f}_d$ is used to blend the DDES and WMLES length scales together:

$$\tilde{f}_d = \max\{(1 - f_d), f_b\} \tag{8}$$

The term f_b in equation 8 provides rapid switching of the model from RANS mode to LES mode and is defined as:

$$f_b = \min\{2\exp(-9\alpha^2), 1.0\}, \quad \alpha = 0.25 - \frac{d_w}{\Delta} \tag{9}$$

In equation 7, f_e, is aimed at preventing an excessive reduction of the RANS Reynolds stresses in the interaction region of the RANS and LES modes, and is defined as:

$$f_e = \max\{(f_{e1} - 1), 0\}\Psi f_{e2} \tag{10}$$

The function f_{e1} provides a predefined (dependent only on the grid) value for the RANS component of the WMLES length scale and is defined as:

$$f_{e1}\left(\frac{d_w}{\Delta}\right) = \begin{cases} 2\exp\left(-11.09\alpha^2\right), & \alpha \geq 0 \\ 2\exp\left(-9.0\alpha^2\right), & \alpha < 0 \end{cases} \tag{11}$$

Function f_{e2} controls the intensity of the RANS component and is defined as:

$$f_{e2} = 1 - \max\left(f_{dt}, f_{dl}\right) \tag{12}$$

Where f_{dt} and f_{dl} are the turbulent and laminar delay functions respectively, and r_{dt} and r_{dl} are the turbulent and laminar components respectively of the model length scale to the wall distance ratio:

$$\begin{aligned} f_{dt} &= \tanh\left[\left(c_t^2 r_{dt}\right)^3\right], \;\; r_{dt} = \frac{\nu_t}{\kappa^2 d_w^2 \max\left\{\left[\sum_{ij}(\partial u_i/\partial x_j)^2\right]^{\frac{1}{2}}, 10^{-10}\right\}} \\ f_{dl} &= \tanh\left[\left(c_l^2 r_{dl}\right)^{10}\right], \;\; r_{dl} = \frac{\nu_l}{\kappa^2 d_w^2 \max\left\{\left[\sum_{ij}(\partial u_i/\partial x_j)^2\right]^{\frac{1}{2}}, 10^{-10}\right\}} \end{aligned} \tag{13}$$

In equations 13, the terms c_t and c_l are model constants which depend on the RANS model used and for the work presented here are 1.63 and 3.55 respectively.

III.B. Grid Generation

Unstructured grids consisting of purely hexahedral cells are utilized for all simulations. To obtain an appropriate turbulent boundary layer profile for the inlet of the cavity, a 2D steady state RANS simulation was performed for a flat plate. The plate was 1.016 m long by 50.8 mm high by 0.5 mm wide and consisted of 6400 cells in the streamwise direction, 128 cells in the normal direction, and was one cell wide. Cells were clustered along the plate surface using a hyperbolic tangent function and the initial grid spacing was adjusted until the maximum y^+ along the wall was approximately unity, or $\Delta y_1 = 3.5\text{e-}3$ mm.

The domain for the cavity grid extends from 25.4 mm upstream of the step to 60.5 mm downstream of the ramp. At the inlet, the domain is 50.8 mm tall, to allow transients an easier path to exit, and at the end of the ramp, the upper boundary is roughly 75 mm above the ramp. The relief section at the end of the ramp is longer than in the test article, but was included in the domain to help improve stability of the outlet boundary condition. The upper boundary of the domain at the outlet is approximately 130 mm above the relief surface. The grid/domain can be broken down into three main sections as shown in figure 2; before the step with a dimension of 190 x 128 cells (green), after the step and above the cavity/shear layer with a dimension of 1780 x 128 cells (red), and the region after the step below the shear layer with a dimension of 1780 x 160 cells (blue). For ease of reference, the step corner was chosen as the streamwise/normal origin for the cavity grids.

Streamwise cell spacing in the unstretched regions of the grid was held as close as possible to 0.15875 mm, which corresponds to 1/20 of the expected baseline boundary layer thickness ($\delta_G = 3.175$ mm).[28] Cells were clustered in the grid using a hyperbolic tangent function and initial grid spacing or Δy_1. Along the plate, an initial grid spacing normal to the wall of 3.5e-3 mm was used to obtain a maximum y^+ of approximately unity. In a similar fashion, initial grid spacings normal to the surfaces of 1.0e-2 mm at the start of the cavity floor, 1.6e-3 mm along the ramp, and 1.0e-2 mm at the end of the relief were used. In the streamwise direction, 25 cells were clustered within a 3.2 mm distance either side of the step, using a cell spacing at the step of 3.75e-3 mm. Similarly, 30 cells in the streamwise direction were clustered within a 8 mm distance either side of the joint between the cavity floor and the start of the ramp, and 28 cells were clustered in a region 2.8 mm either side of the joint between the end of the ramp and start of the relief section. Along the joining line between the upper and lower grids aft of the step, clustering was also used to spread the grid slightly and help convergence of the shear layer. The normal spacing between the two regions near the step was 4.0e-2 mm just after the start of the ramp, and increased to 3.0e-1 mm at the outlet to help diffuse the shock and prevent it from oscillating/jumping to nearby cells. At the outlet, cells in the last half of the relief section are stretched so that the last cell has a spacing of 2.7 mm from the outlet. In a

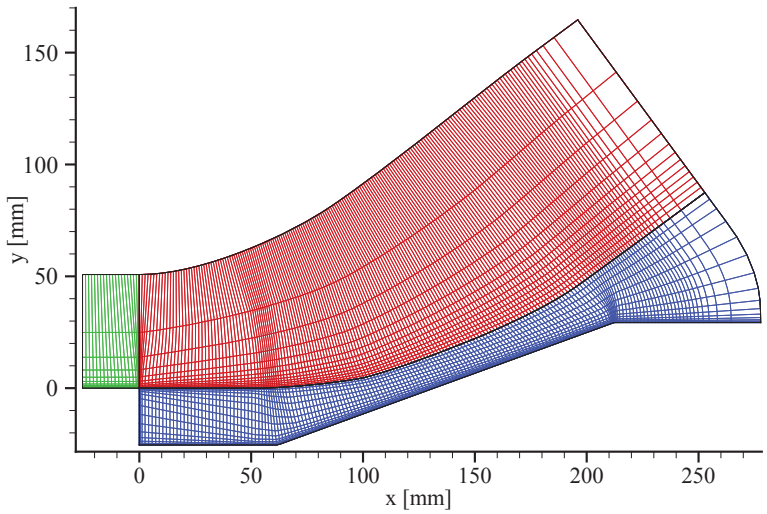

Figure 2. Grid for the Baseline Case with Main Sections Highlighted (Every tenth grid line shown for clarity)

similar manner, to help dissipate any transients before they reach the boundary, cells are stretched in last two thirds of the top domain in the normal direction with a final distance to the boundary of 4.0 mm. Grid lines were then forced to be perpendicular along the cavity floor, ramp, and relief surfaces by subdividing the grids and curving the the lines defining these regions as necessary. These individual grid sections were also smoothed using a Steger-Sorenson algorithm with orthogonality at the walls and equal angles between adjacent grids as boundary conditions. Finally, the 3D grid was formed by extruding this 2D grid in the streamwise direction by 38.1 mm, using a cell spacing of 0.15875 mm, resulting in a modeled domain one quarter the width of the test article ramp and containing 128,870,400 cells.

III.C. Boundary Conditions

From the available experimental data, the transition of the boundary layer is know to occur within the first 30 mm of the wedge from the leading edge.[5] However, all turbulence models, including Spalart-Allmaras, are know to inaccurately predict the location of transition on their own and it is highly recommended that a fixed transition point be specified with their use.[25] Thus to account for transition and obtain a proper turbulent boundary layer profile for the cavity inlet, a 2D steady state RANS simulations was performed for a 1.016 m long flat plate. Transition was set at 25 mm from the leading edge of the plate using the Spalart-Allmaras trip term. This transition location was chosen based on being within the first 30 mm of the plate while being far enough from the leading edge to still achieve good convergence. Symmetry boundary conditions were specified in the spanwise direction, along with supersonic inflow and outflow at the inlet and outlet respectively. Along the plate surface, an isothermal wall condition with a temperature of 265.7 K was used. The simulation was initialized using freestream conditions, $u_\infty = 572$ m/s, $\rho_\infty = 0.77$ kg/m^3, and T = 95 K.

Several boundary layer profiles were extracted from the converged 2D flat plate solution and the boundary layer thickness, displacement thickness, and momentum thicken were calculated at each location. For these calculations, the boundary layer thickness was defined as 99% of the freestream velocity. These were then compared with the experimentally determined values 2.54 mm upstream of the step (designated as station 19 in the experiment). The closest match, based on momentum thickness, was found to be approximately 257.81 mm from the plate leading edge. Momentum thickness was used as the matching quantity between the simulation and experiment, as it is an integrated value across the entire boundary layer and thus contains the least amount of localized measurement error. The boundary layer profile 22.86 mm upstream of this location (corresponding to the cavity inlet based on alignment at station 19), was then extracted and used as the inlet condition for the baseline, δ_0 cavity case. A comparison of the properties for the extracted boundary layers with the experimentally determined ones is given in Table 1 and 2.

Table 1. Comparison of Extrapolated Boundary Layer Properties with Experimentally Measured Values at 25.4 mm Upstream of Step (Station 10)

	δ	δ^*	θ	H
Exp. Baca[11]	2.88 mm	0.89 mm	0.17 mm	5.24 mm
RANS, δ_0	3.02 mm	0.98 mm	0.18 mm	5.41 mm
RANS, $2\delta_0$	6.37 mm	1.98 mm	0.37 mm	5.32 mm

Table 2. Comparison of Extrapolated Boundary Layer Properties with Experimentally Measured Values at 2.54 mm Upstream of Step (Station 19)

	δ	δ^*	θ	H
Exp. Baca[11]	3.28 mm	1.02 mm	0.20 mm	5.10 mm
RANS, δ_0	3.29 mm	1.07 mm	0.20 mm	5.41 mm
RANS, $2\delta_0$	6.62 mm	2.05 mm	0.39 mm	5.32 mm

For the thick boundary layer case, the boundary layer thickness at 260.35 mm from the leading edge (corresponding to the step in the baseline case) was first calculated and doubled. Next, the boundary layer profile at several locations along the flat plate were extracted until the closest match to this doubled boundary layer thickness was found, or 554.67 mm from the plate leading edge. The boundary layer 25.4 mm upstream of this location (corresponding to the inlet of the cavity) was then extracted and used as the inlet profile for the thick boundary layer, $2\delta_0$ case. A comparison of the estimated properties for both boundary layer cases at the step is given in Table 3.

For the cavity cases, a periodic boundary condition was used in the spanwise direction. The cavity inlet was set as a supersonic boundary condition with a specified boundary layer profile. The top domain was also set as a supersonic inflow boundary condition, but with freestream conditions. A supersonic outflow condition was used for the outlet. An isothermal wall condition, with a temperature of 265.7 K, was used for the plate, step wall, cavity floor, ramp, and relief surfaces.

IV. Results

IV.A. General Flow Features

Figure 3 shows a density contour plot of the spanwise centerline plane from the converged RANS simulation for the baseline case. For simplicity, the streamwise and normal directions in this and future contour plots, have been non-dimensionalized by the step height D, which is 25.4 mm. As highlighted in figure 3, the simulation reproduces the major flow features observed in the experiment. At the corner of the step, the turbulent boundary layer detaches, creating a free shear layer over the cavity. As this free shear layer reattaches along the ramp, the change in the flow direction forms a shock system, and flow is en-trained into the cavity near this reattachment location.

The estimated separation length and boundary layer thickness at reattachment from the RANS solutions are shown in Table 4. Reattachment was determined by where the shear stress along the ramp crossed zero. To estimate the boundary layer thickness, the velocity profile from the spanwise centerline slice was extracted along a 25.4 mm long line, perpendicular to the ramp,starting at reattachment. Since the velocity profile in this region does not reach 99% of the freestream velocity due the weak expansion fan off the step, the boundary layer thickness was determined as the height where the velocity reached 99% of the maximum

Table 3. Estimated Boundary Layer Properties at the Step.

	δ	δ^*	θ	H
RANS, δ_0	3.32 mm	1.08 mm	0.20 mm	5.41 mm
RANS, $2\delta_0$	6.64 mm	2.06 mm	0.39 mm	5.32 mm

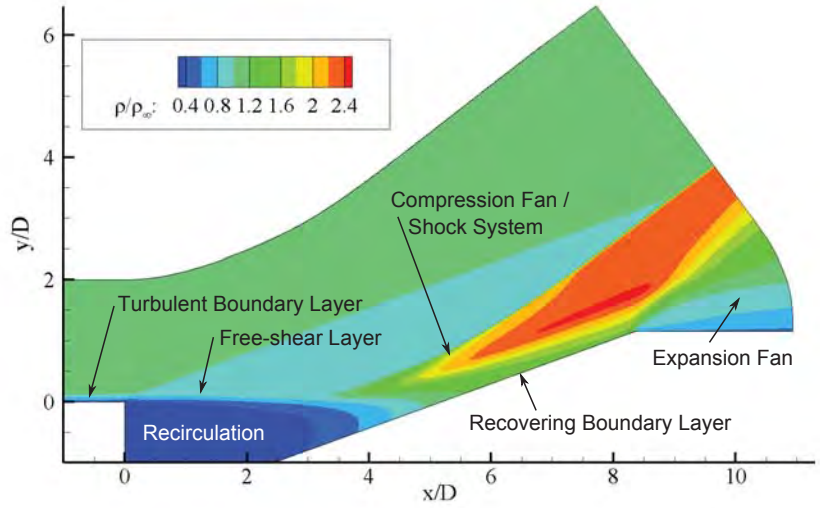

Figure 3. Density Contours of the Spanwise Centerline Plane from the 3D RANS Simulation with Major Flow Features Identified

profile velocity.

Table 4. Estimates of Separation Length and Boundary Layer Thickness at Reattachment from the RANS Simulations

	L_{SEP}	δ_R
Exp. Baca[11]	126.34 mm	10.40 mm
RANS, δ_0	128.57 mm	15.56 mm
RANS, $2\delta_0$	142.27 mm	20.46 mm

As mentioned earlier, converged RANS solutions are used to start the IDDES simulations. The baseline RANS solution was also used to determine the characteristic flow through time, defined as the time it takes a freestream particle to traverse the domain, which was calculated as 0.748 milliseconds. Using 50,000 iterations per this characteristic time gives a fixed time step of 14.96 nanoseconds. This time step was chosen for the simulations because it results in a maximum CFL number of around unity in the regions of interest, i.e. the shear layer and reattachment region of the ramp.[28] IDDES simulations for both the baseline and thick boundary layer case were run for four characteristic flow through times to wash out transients. A contour plots of the instantaneous density at the spanwise centerline plane after these four characteristic flow through times is shown in figure 4.

In figure 4, the turbulent structures supported by the IDDES method are readily apparent compared to the RANS result for the baseline case. By plotting the magnitude of the two dimensional spatial gradient of the instantaneous density, a "psuedo Schlieren" image is created as shown in figure 5, which makes the shear layer, turbulent structures, and shock system easier to identify. Turbulent structures form as the shear layer begins to transition, however the location at which this becomes visible is different for the two cases. In the baseline case, structures appear to begin at x/D of 2, while in the thick boundary layer case, they become visible at x/D of 1. This is most likely due to the streamwise grid resolution relative to the initial shear layer thickness in each case. Also visible in figure 5 are acoustical waves, which emanate from the shear layer as it begins to transition. This is because the convective Mach number for the shear layer is slightly greater than one. These acoustical waves are also seen to emanate from the redeveloping boundary layer after reattachment and reflect off the reattachment shock before being dissipated by the expansion fan.

After washing out the initial transients, the simulations were continued for another eight characteristic flow through times. During this time, the instantaneous solution in each cell on the ramp and along the spanwise centerline plane were stored at each iteration. Two-point auto-correlations were performed in the spanwise direction using the collected pressure history along the ramp.

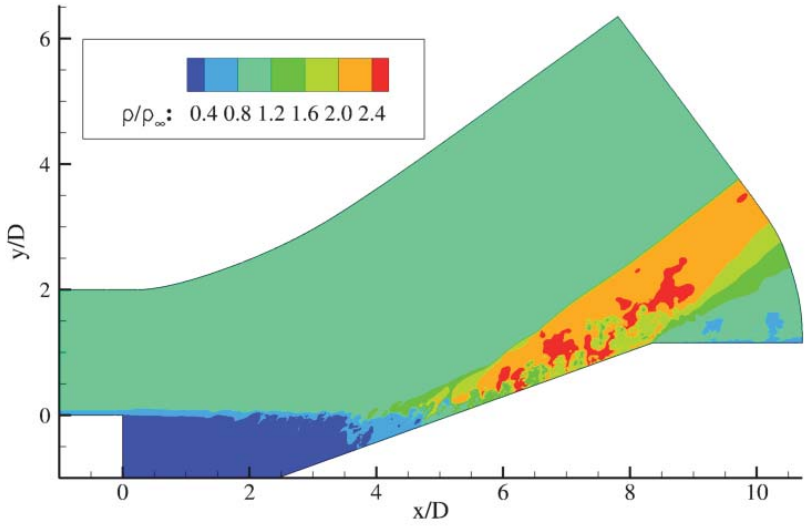

(a) Baseline Case

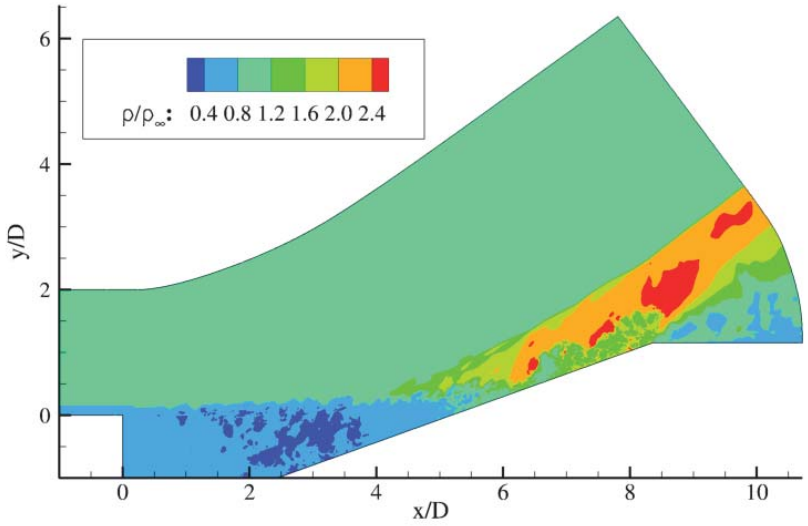

(b) Thick Boundary Layer Case

Figure 4. Contour Plots of the Instantaneous Density at the Spanwise Centerline Plane After Four Characteristic Flow Through Times

$$R_{p_i,p_j} = \frac{\overline{p'_i p'_j}}{\sqrt{\overline{p'^2_i} \cdot \overline{p'^2_j}}} \tag{14}$$

$$R_{p_j} = \frac{1}{kdm} \sum_{i=1}^{kdm} R_{p_{[i-kdm/2],p_j}} \tag{15}$$

Equation 14 is performed at every location, i, along the spanwise line and j is the fixed location on the line about which the correlation is performed. Additionally, p'_i and p'_j are the pressure fluctuations

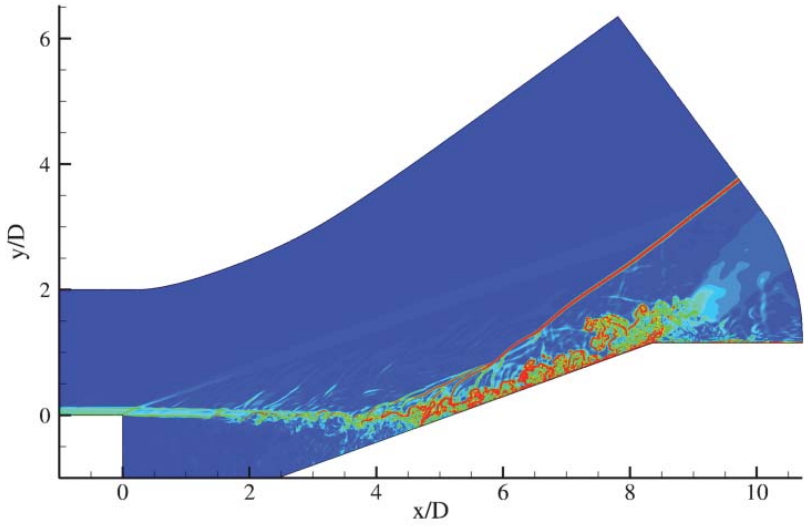

(a) Baseline Case

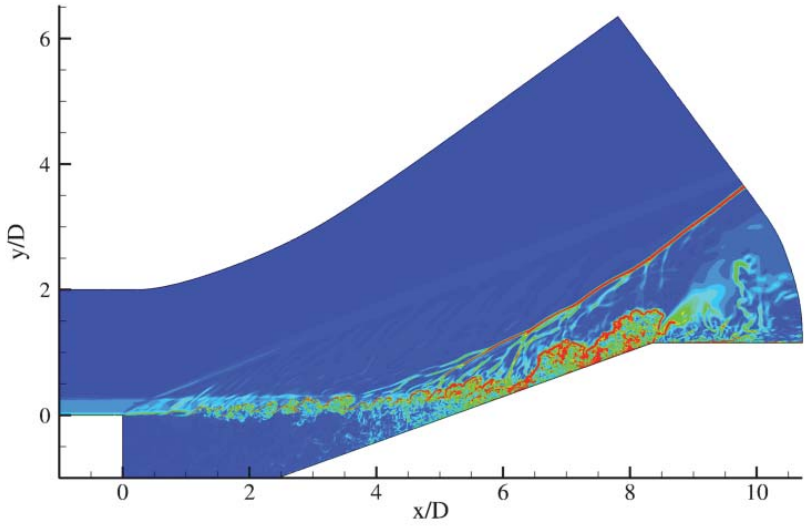

(b) Thick Boundary Layer Case

Figure 5. Contours of the Instantaneous Density Spatial Gradient Magnitude at the Spanwise Centerline Plane After Four Characteristic Flow Through Times

at locations i and j respectfully, with kdm being the number of locations in the spanwise line. Perfectly correlated locations will have a value of one while perfectly uncorrelated locations will have a value of zero. A negative value means the locations are still correlated, but the fluctuations are in opposite directions. Figure 6 gives the two-point auto-correlation for both cases at three streamwise locations, taken about the spanwise centerline. The three streamwise locations are; x^*=56.5 mm which is near reattachment for the baseline case, x^*=78.9 mm which is near reattachment for the thick boundary layer case, and x^*=125.3 mm which is downstream of reattachment for both cases. In these figures, the solutions show asymmetry (more severe in the the thick boundary layer case), which indicate a greater number of characteristic flow through times are needed in order to obtain good statistics. However, these figures also show the solutions to be

correlated within a spanwise width of $4\delta_G$. Thus to improve the statistical and spectral analysis with the obtained data, the pressure history along 3 streamlines on the ramp, each $4\delta_G$ apart from one another, were extracted and processed separately. The results from each of these streamlines were then averaged together, thus effectively producing results representative of 24 flow through times.

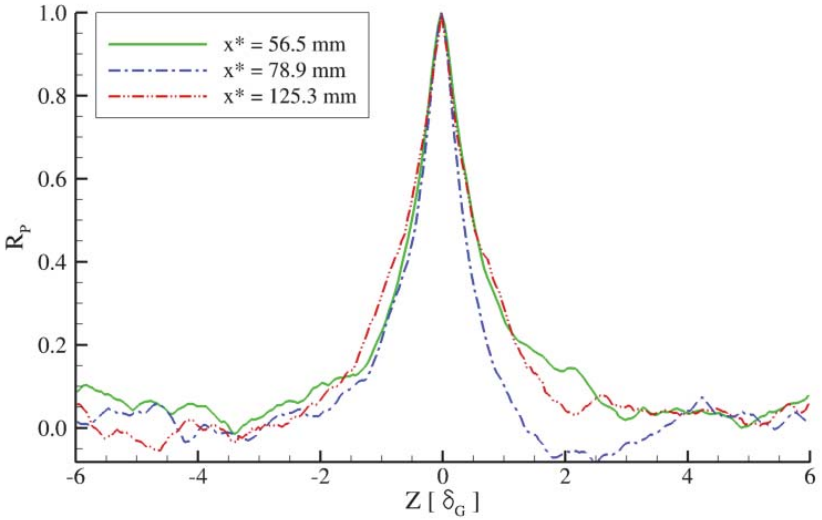

(a) Baseline Case

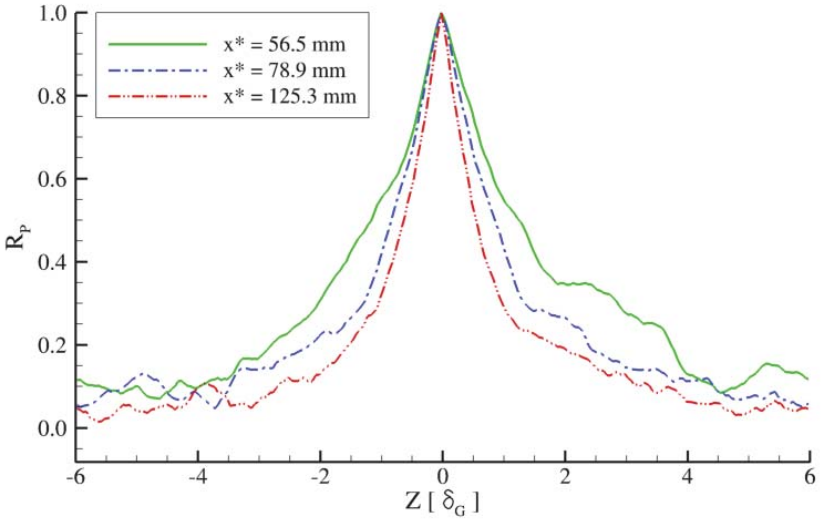

(b) Thick Boundary Layer Case

Figure 6. Two-point Auto-correlations of Ramp Wall Pressure about the Spanwise Centerline for Three Streamwise Locations

To obtain estimates of the reattachment location and associated boundary layer thickness from the IDDES simulations, the stored instantaneous solutions along ramp and spanwise centerline plane were time averaged. The velocity near the ramp at three spanwise slices (each $4\delta_G$ apart from one another) was extracted and averaged together, from which the reattachment location was estimated as the location where the velocity crossed zero. Next, the velocity profile at this location was extracted along a 25.4 mm long line from the

time averaged spanwise centerline plane and the boundary layer thickness was estimated as the distance above the ramp where the velocity normal to the ramp reached 99% of the maximum profile velocity. The reattachment location and boundary layer thickness calculated from this process are given in Table 5.

Table 5. Estimates of Separation Length and Boundary Layer Thickness at Reattachment from the IDDES Simulations

	L_{SEP}	δ_R
Exp. Baca[11]	126.34 mm	10.40 mm
IDDES, δ_0	115.00 mm	10.10 mm
IDDES, $2\delta_0$	136.00 mm	15.60 mm

IV.B. Statistical Analysis

The mean wall pressure distribution along the ramp, normalized by the freestream pressure, for both the baseline and thick boundary layer cases is given in figure 7(a). Also included in this figure is the experimental pressure tap measurements of Baca. For the baseline case, the pressure rises monotonically from roughly 85% of the freestream at the start of the ramp, to a constant value approximately 3.6 times freestream downstream of the primary oblique shock. The thick boundary layer case starts with a pressure slightly greater than the freestream and then gradually rises to approximately the same value as the baseline case, just before the end of the ramp. In figure 7(b), the same pressure distributions have been plotted using a scaled, non-dimensional ramp distance of $(x^* - x_R^*)/\delta_R$ and a normalized pressure of $(p - p_1)/(p_2 - p_1)$, where p_1 and p_2 are the pressure at the start and end of the ramp respectively. From this figure, the scaling collapses the data quite nicely, including the experimental pressure tap measurements of Baca.

Figure 8(a) shows the standard deviation of the wall pressure fluctuation, $\sigma_p = (\overline{p'^2})^{1/2}$, along the ramp normalized by the freestream pressure for both cases. The baseline case shows an initial rise in fluctuations for the first quarter of the ramp to 15% of freestream pressure, followed by a steeper rise which peaks near reattachment at roughly 50% of the freestream pressure, and then gradually drops downstream to approximately 15% of freestream. For the thick boundary layer case, a similar although flattened curve is also visible. In the thick boundary layer case, the initial rise in fluctuations is longer and gradual, followed by a plateau, and then a gradual drop to 20% of the freestream pressure. In figure 8(b), the same standard deviation of the wall pressure fluctuations has been plotted using a scaled, non-dimensional ramp distance of $(x^* - x_R^*)/\delta_R$ and a normalized pressure fluctuation of $(\sigma - \sigma_1)/(\sigma_{Max} - \sigma_1)$, where σ_1 and σ_{Max} are the RMS pressure fluctuation at start of the step and the maximum RMS pressure fluctuation respectively. From this figure, the scaling collapses the data reasonably well.

IV.C. Spectral Analysis

Figure 9(a) gives the auto-spectra in dimensional form for the pressure fluctuations at x^*=125.3 mm. To obtain these spectra, 49 Hanning windows with half window overlaps were used. For both cases, the signal has a broad-band energy content, with a single hump around 0.7 MHz. The spectrum in the thick boundary layer case is shifted upwards, indicating an increase in the pressure fluctuations intensity. Features in the spectra for the thick boundary layer case also exhibit a shift to the left (in particular, the bump near 0.7 MHz), indicating a decrease in characteristic frequency. In figure 9(b), the same spectral data has been plotted in a scaled form. The frequency was non-dimensionalized by the separation length and freestream velocity, while the spectrum was scaled by the mean square of pressure fluctuations, $\overline{p'^2}$ and the time scale δ_R/U_∞. This collapses the data fairly well, and in particular, the hump in the spectrum become lined-up.

Cross correlation of the pressure signals at x^*=125.3 mm with Δx=1.5875 mm is shown in figure 10(a). A short distance between locations was taken to reduce error caused by a limited pressure time history. An estimate of the convection velocity, U_c, was obtained by dividing the distance between locations, Δx, by the peak correlation time. For the baseline case, U_c was determined to be 484.6 m/s, while for the thick boundary layer case, it was 429.9 m/s. Figure 10(b) shows the same cross correlation, but with the time scaled by U_∞/δ_R. This scaling results in the correlation time peaks becoming aligned.

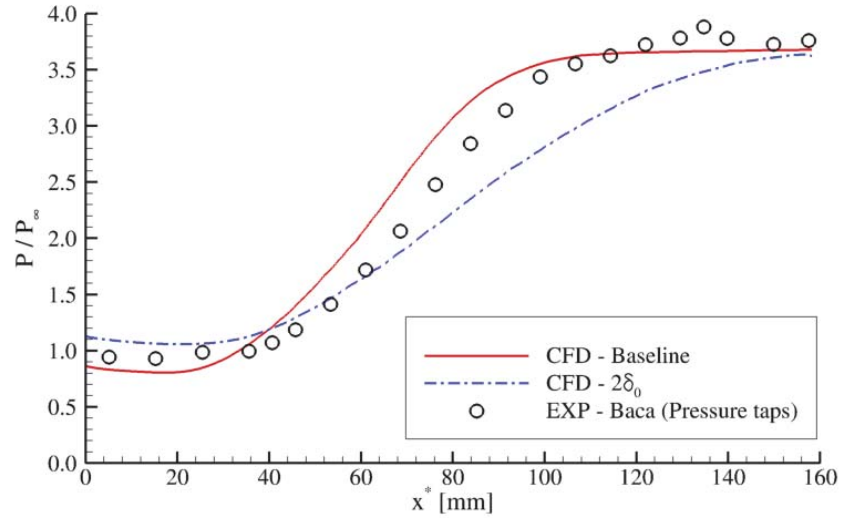

(a) Unscaled, Dimensional Ramp Distance

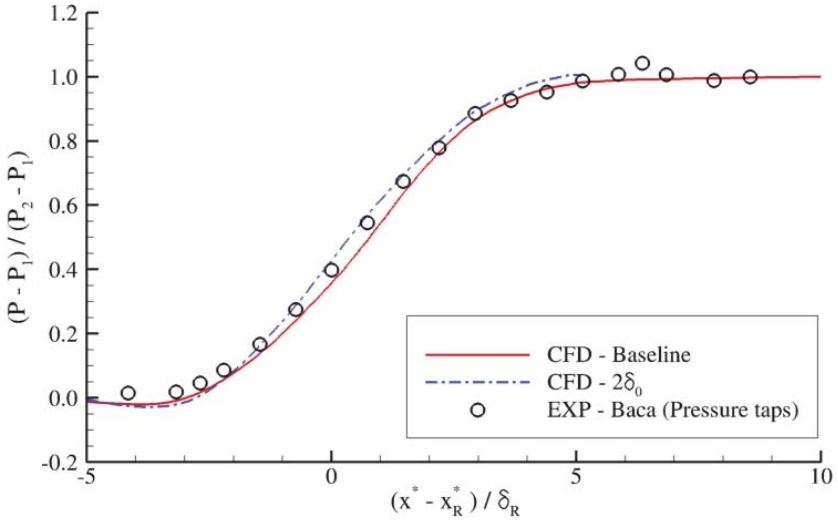

(b) Scaled, Non-dimensional Pressure and Ramp Distance

Figure 7. Mean Pressure Distribution along the Ramp

V. Conclusions

Simulations of a Mach 2.9 turbulent shear layer in a back-step/ramp configuration were performed using Improved Delayed Detached Eddy Simulations (IDDES) techniques. The influence of boundary layer thickness at separation on the reattachment shock system was explored. In general, the thicker boundary layer resulted in a longer separation length and thicker reattachment boundary layer. From statistics of the pressure history along the ramp, the thicker boundary layer also produced a 30% reduction in the magnitude of pressure fluctuations. The statistics were shown to partially collapse with a scaling based on the reattachment location and associated boundary layer thickness. Power spectra of the surface pressure along the ramp showed an increase in the pressure fluctuation intensity along with a shift to lower characteristic

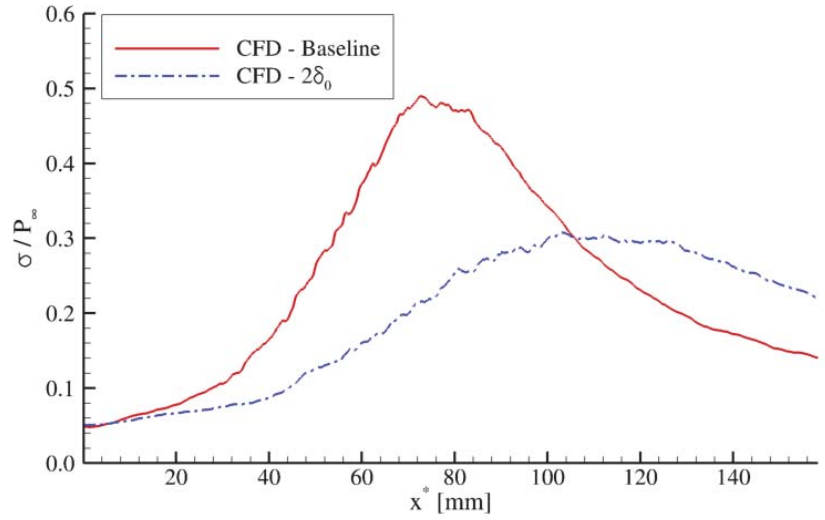

(a) Unscaled, Dimensional Ramp Distance

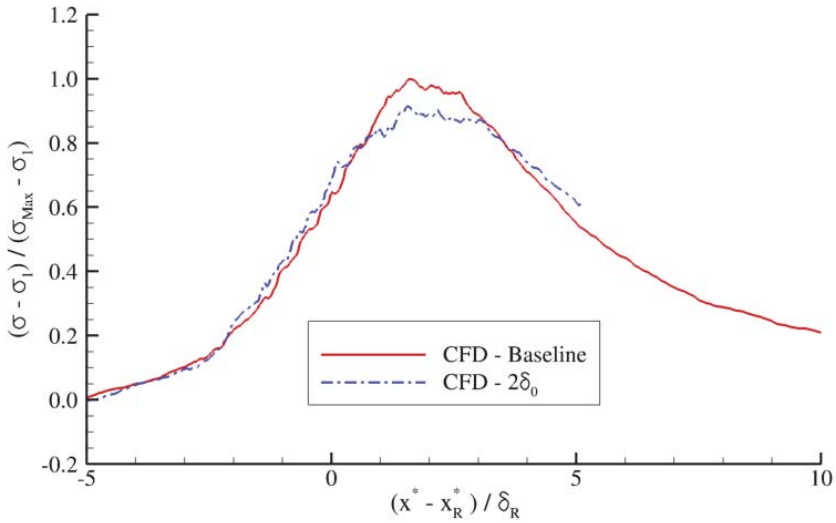

(b) Scaled, Non-dimensional Fluctuation and Ramp Distance

Figure 8. Standard Deviation of Wall Pressure Fluctuations along the Ramp

frequencies. The power spectra were also shown to collapse by scaling the frequency, based on the separation length and freestream velocity, and the spectrum, based on the mean square of pressure fluctuations and the time scale δ_R/U_∞. A cross correlation at x^*=125.3 mm was performed and the results used to estimate the convection velocity. The convection velocity for the thick boundary layer case was approximately 11% less than the baseline case.

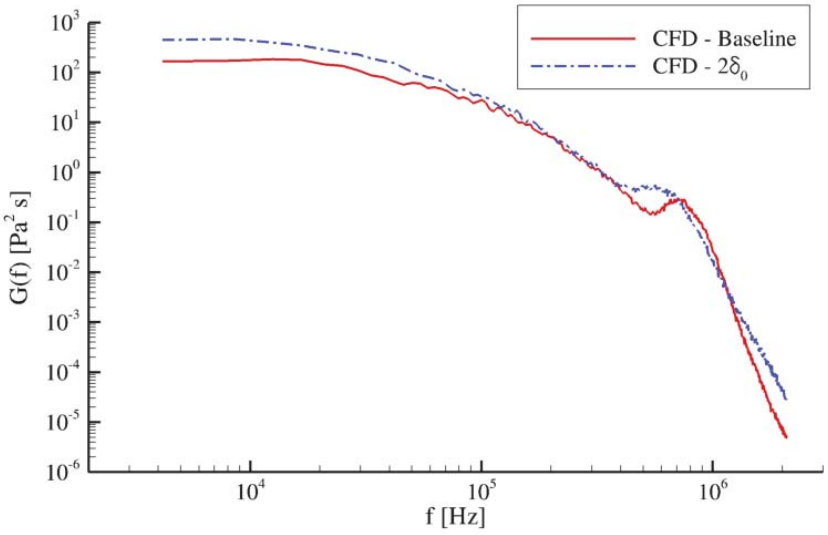

(a) Unscaled, Dimensional Energy and Frequency

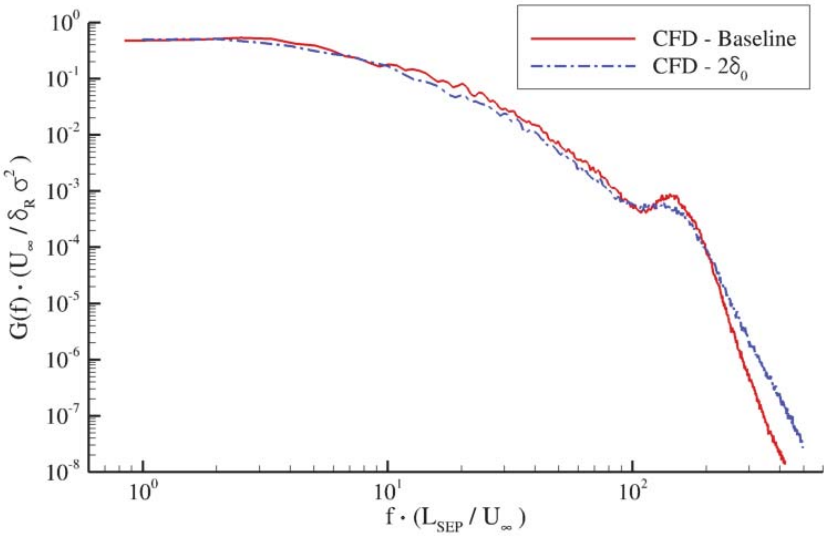

(b) Scaled, Non-dimensional Energy and Frequency

Figure 9. Auto-Spectra of Ramp Wall Pressure Fluctuations at x^*=125.3 mm

Acknowledgments

This project was funded in part by AFOSR contract LRIR task 14RQ18COR, monitored by Dr. I. Leyva, AFOSR/RTE. The authors wish to thank the Air Force Research Laboratory Department of Defense Supercomputing Resource Center for computer time and Prof. G. Candler for the use of the US3D solver. Additional computer hours were provided under a DoD HPCMP Frontier Project (Dr. R. Gosse, Principal Investigator). The authors also thank Dr. D. Peterson, Dr. R. Gosse, and Dr. N. Bisek for their helpful and insightful discussions on performing these calculations.

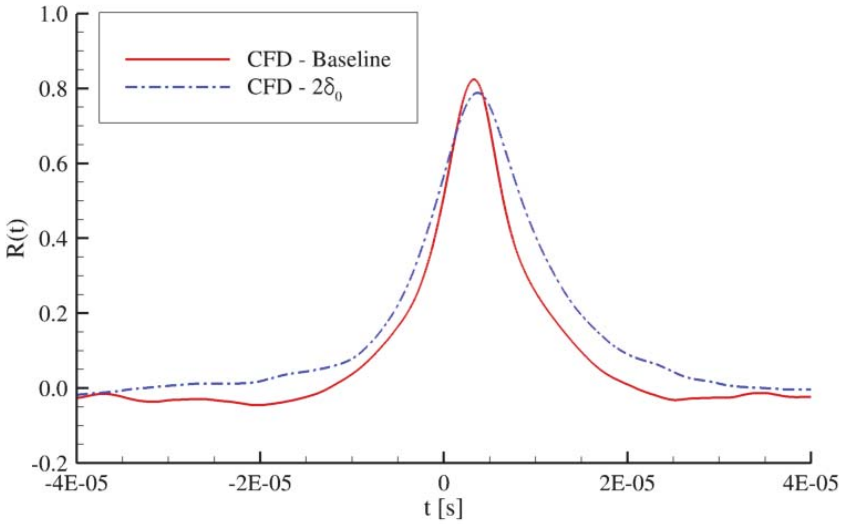

(a) Unscaled, Dimensional Time

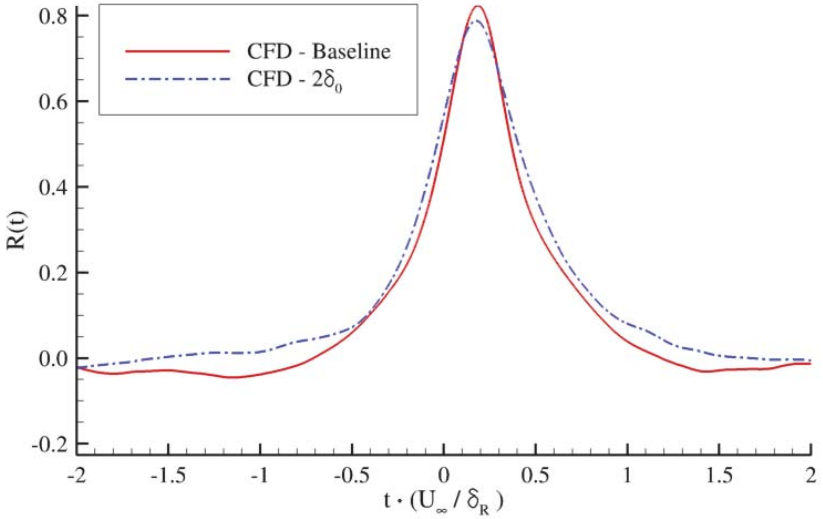

(b) Scaled, Non-dimensional Time

Figure 10. Cross Correlation of Ramp Wall Pressure Fluctuations at x^*=125.3 mm with Δx=1.5875 mm

References

[1]Zuchowski, B., Wittman, R., Leung, K., and Favela, J., "Structural Response and Service Life Prediction Concerns in the Design of Hypersonic Flight Vehicle Hot Structure," AIAA Paper No. 2013-1457.

[2]Poggie, J., Bisek, N. J., Kimmel, R. L., and Stanfield, S. A., "Spectral Characteristics of Separation Shock Unsteadiness," *AIAA Journal*, In Press, 2014.

[3]Wiese, D. P. and Annaswamy, A. M., "Adaptive Control of a Generic Hypersonic Vehicle," AIAA Paper No. 2013-4515.

[4]Peterson, D. M., Hagenmaier, M., and Carter, C. D., "Hybrid Reynolds-Averaged and Large-Eddy Simulations of a Supersonic Cavity Flameholder," AIAA Paper No. 2013-2483.

[5]Shen, Z. H., Smith, D. R., and Smits, A. J., "Wall Pressure Fluctuations in the Reattachment Region of a Supersonic Free Shear Layer," *Journal of Experimental Fluids*, Vol. 14, 1993, pp. 10–16.

[6]Dolling, D. S. and Murphy, M. T., "Unsteadiness of the Separation Shock Wave Structure in a Supersonic Compression Ramp Flowfield," *AIAA Journal*, Vol. 21, No. 12, 1983, pp. 1628–1634.

[7]Selig, M. S., Andreopoulos, J., Muck, K. C., Dussauge, J. P., and Smits, A. J., "Turbulence Structure in a Shock Wave/Turbulent Boundary-Layer Interaction," *AIAA Journal*, Vol. 27, No. 7, 1989, pp. 862–869.

[8]Thomas, F. O., Putnam, C. M., and Chu, H. C., "On the Mechanism of Unsteady Oscillation in Shock Wave/Turbulent Boundary Layer Interaction," *Experiments in Fluids*, Vol. 18, 1994, pp. 69–81.

[9]Poggie, J. and Smits, A. J., "Shock Unsteadiness in a Reattaching Shear Layer," *Journal of Fluid Mechanics*, Vol. 429, 2001, pp. 155–185.

[10]Plotkin, K. J., "Shock Wave Oscillation Driven by Turbulent Boundary-Layer Fluctuations," *AIAA Journal*, Vol. 13, No. 8, 1975, pp. 1036–1040.

[11]Baca, B. K., *An Experimental Study of the Reattachment of a Free Shear Layer in Compressible Turbulent Flow*, Master's thesis, Princeton University, Princeton, NJ, 1981.

[12]Settles, G. S., Williams, D. R., Baca, B. K., and Bogdonoff, S. M., "Reattachment of a Compressible Turbulent Free Shear Layer," *AIAA Journal*, Vol. 20, No. 1, 1982, pp. 60–67.

[13]Hayakawa, K., Smits, A. J., and Bogdonoff, S. M., "Turbulence Measurements in a Compressible Reattaching Shear Layer," *AIAA Journal*, Vol. 22, No. 7, 1984, pp. 889–895.

[14]Nompelis, I., Dryna, T., and Candler, G., "Development of a Hybrid Unstructured Implicit Solver for the Simulation of Reacting Flows over Complex Geometries," AIAA Paper No. 2004-2227.

[15]MacCormack, R. and Candler, G., "The Solution of the Navier-Stokes Equations Using GaussSeidel Line Relaxation," *Computers and Fluids Journal*, Vol. 17, No. 1, 1989, pp. 135150.

[16]Hirsch, C., *Numerical Computations of Internal and External Flows*, Wiley, New York, NY, 1991.

[17]Nompelis, I., Dryna, T., and Candler, G., "A Parallel Unstructured Implicit Solver for the Simulation of Reacting Flow Simulation," AIAA Paper No. 2005-4867.

[18]Nompelis, I., *Computational Study of Hypersonic Double-Cone Experiments for Code Validation*, Ph.D. thesis, University of Minnesota, Minneapolis, MN, 2004.

[19]Candler, G. and MacCormack, R., "The Computation of Hypersonic Ionized Flows in Chemical and Thermal Nonequilibrium," *Journal of Thermophysics and Heat Transfer*, Vol. 5, No. 3, 1991, pp. 266273.

[20]Kim, S. E., Makaroy, B., and Caraeni, D., "A Multi-Dimensional Linear Reconstruction Scheme for Arbitrary Unstructured Grids," AIAA Paper No. 2003-3990.

[21]MacCormack, R., "Current Status of the Numerical Solutions of the NavierStokes Equations," AIAA Paper No. 1985-0032.

[22]Wright, M., Candler, G., and Bose, D., "Data-Parallel Line Relaxation Method for the NavierStokes Equations," *AIAA Journal*, Vol. 36, No. 9, 1998, pp. 16031609.

[23]Subareddy, P. K. and Candler, G. V., "A Fully Discrete, Kinetic Energy Consistent Finite-Volume Scheme for Compressible Flow," *Journal of Computational Physics*, Vol. 228, 2009, pp. 1347–1364.

[24]Ducros, F., Ferrand, V., Nicoud, F., Darracq, D., Gacherieu, and Poinsot, T., "Large-Eddy Simulation of the Shock/Turbulence Interaction," *Journal of computational Physics*, Vol. 152, 1999, pp. 517–549.

[25]Spalart, P. R. and Allmaras, S. R., "A One Equation Turbulence Model for Aerodynamic Flows," AIAA Paper No. 1992-0439.

[26]Catris, S. and Aupoix, B., "Density Corrections for Turbulence Models," *Aerospace Science Technology*, Vol. 4, 2000, pp. 1–11.

[27]Forsythe, J. and Woodson, S., "Unsteady CFD Calculations of Abrupt Wing Stall Using Detached-Eddy Simulation," AIAA Paper No. 2003-0594.

[28]Spalart, P. R., Deck, S., Shur, M. L., and Squires, K. D., "A New Version of detached-Eddy Simulation, Resistant to Ambiguous Grid Densities," *Theoretical Computational Fluid Dynamics*, Vol. 20, 2006, pp. 181–195.

[29]Spalart, P. R., Jou, W. H., Strelets, M., and Allmaras, S. R., "Comments on the Feasibility of LES for Wings, and on a Hybrid RANS/LES Approach," *Proceedings of the First AFOSR International Conference on DNS/LES*, Greyden Press, Ruston, LA, 1997.

[30]Menter, F. R. and Kuntz, M., "Adaption of Eddy-Viscosity Turbulence Models to Unsteady Separated Flow Behind Vehicles," Springer, Monterey, CA, 2004.

[31]Shur, M. L., Spalart, P. R., Strelets, M. K., and Travin, A. K., "A Hybrid RANS-LES Approach with Delayed-DES and Wall-modelled LES Capabilities," *International Journal of Heat and Fluid Flow*, Vol. 29, 2008, pp. 1638–1649.

AIAA SciTech
5-9 January 2015, Kissimmee, Florida
53rd AIAA Aerospace Sciences Meeting

53th AIAA Aerospace Sciences Conference

Sidewall Interaction of a Supersonic Flow over a Compression Ramp

Nicholas J. Bisek*

Air Force Research Laboratory, Wright-Patterson AFB, OH, 45433-7512, USA

High-order implicit large-eddy simulations were used to investigate Mach 2.25 turbulent airflow as it traveled over a 24° compression corner in the presence of both sidewalls. The bottom plate was sufficiently wide such that an equilibrium turbulent boundary-layer profile developed far from both corner junctions. The turbulent equilibrium boundary-layer flow traveled over a 24° compression ramp which lead to an unsteady oblique shock and subsequent separation bubble. At the same time, the inclusion of the sidewall lead to the development of a corner vortex and an increasingly three-dimensional shock front. The complex corner flow includes a nodal attachment point and separation vortex which traveled along the sidewall consistent with a fin-junction interaction. A glancing shock boundary-layer interaction occurred along each sidewall which included a separation bubble downstream of the shock front. The full span results were compared with a spanwise symmetric scenario which exhibited a different mean surface pressure profile near the midspan due to the symmetry boundary. Time-accurate results throughout the shock interaction region were collected an analyzed. The solutions show that the shock front exhibited low-frequency streamwise oscillations, even along the sidewalls.

Nomenclature

c_f	= skin-friction coefficient, $(2\,\mu_w/Re_\ell)\frac{\partial\,u}{\partial\,s}\big\vert_w$, where s is the wall normal direction
E	= total specific energy
$\mathbf{F}, \mathbf{G}, \mathbf{H}$	= inviscid vector fluxes
$\mathbf{F}_v, \mathbf{G}_v, \mathbf{H}_v$	= viscous vector fluxes
J	= transformation Jacobian
ℓ	= geometry length
M	= Mach number
p	= nondimensional static pressure
q	= nondimensional heat flux
Re	= Reynolds number, $\rho_\infty\,u_\infty\,\ell/\mu_\infty$
t	= nondimensional time
T	= nondimensional static temperature
$\mathbf{U}$	= conserved variable vector
u, v, w	= nondimensional Cartesian velocity components in the x, y, z directions
x, y, z	= streamwise, normal, and spanwise directions in nondimensional Cartesian coordinates
y^+	= nondimensional wall distance normalized by local inner scales, $u_\tau\,\rho_w\,y/\mu_w$
δ	= boundary-layer thickness, $0.99\,u_\infty$
ξ, η, ζ	= computational coordinates
θ	= compressible boundary-layer momentum thickness, $\int_0^\infty \frac{\rho\,u}{\rho_\infty\,u_\infty}\left(1-\frac{u}{u_\infty}\right)\,\mathrm{d}y$
μ	= dynamic viscosity
ρ	= nondimensional density
τ_{ij}	= components of the viscous stress tensor

*Research Aerospace Engineer, AFRL/RQHF. Senior Member AIAA.

Subscript

w	= wall
∞	= freestream

I. Introduction

Turbulent shock boundary-layer interactions (SBLI) are a common phenomenon for supersonic aerodynamics. For example, SBLI typically occurs in high-speed inlets as the incoming air is rapidly slowed and vectored into the combustor. Unfortunately, the SBLI can be problematic since each interaction inflicts an adverse pressure gradient on the boundary-layer which can lead to localized flow separation. Not only does separation reduce the inlet's inviscid core flow, which limits engine performance, but the separated region has been shown to contain a low-frequency unsteadiness that generates localized fatigue loading and can lead to premature failure of the structure.[1] In addition, recent work by Poggie *et al.*,[2] has shown that the separated region behaves like a broadband amplifier for both high-fidelity simulations, wind-tunnel experiments, and flight tests across a range of Mach and Reynolds numbers. As such, upstream disturbances could be amplified as they travel through the SBLI region and damage to downstream subsystems, or even lead to an engine "un-start" event.

These detrimental consequences have renewed the interest in studying SBLI, not only to better understand the underpinning fluid dynamics, but to predict and potentially control its behavior. Of late, there have been many studies of the SBLI, both experimental and computational using the state-of-the-art in computing resources. Due to the strict grid and time-scale requirements of direct numerical simulation (DNS), which requires the computation to have sufficient resolution to support all scales present in the flow, including the Kolmogorov length scales, large-eddy simulations (LES) are a popular approach for investigating these flows.

In LES, direct simulation is used to compute all the larger, well-resolved, fluid scales. Since fluid dynamics can cause these structures to grow or decrease in size, the corresponding turbulent kinetic energy can transfer in either direction in the spectrum (from small-scale to larger scale and visa-versa). In LES, it is assumed that the smallest resolved structures exist in the inertial sub-range of the turbulent kinetic energy spectrum, and that these structures are essentially homogeneous and isotropic. As such, energy at the smallest resolved scale can only cascade down to smaller scales (i.e., dissipate), an effect which is modeled using a subgrid-scale (SGS) model or by numerical dissipate inherit to the scheme. This assumption allows LES users to benefit from less stringent grid requirements, while still obtaining highly-resolved physically-accurate results. The LES approach has been used to study several SBLI unit-problems, including an oblique impinging shock or flow over a compression corner.[3–11] However, even these simplified unit problems require very large computational grids and computing resources, which has restricted the aforementioned studies to ignore sidewall effects by utilizing spanwise-periodic boundary conditions.

Unfortunately, the aerodynamics on a typical high-speed vehicle are more complicated than the traditional spanwise-periodic unit problems since most inlets have either circular or rectangle cross-sections. This leads to additional complexities, especially near the corner junction regions, where the adverse pressure gradient present in the boundary layer is subjected to higher viscous effects from the adjoining wall. As a result, the core-corner flow tends to separate upstream of the midspan SBLI thereby facilitating a highly three-dimensional shock front and a glancing shock interaction along the sidewall.[12] It is very challenging to experimentally interrogate many of the unsteady features in the near corner region, so some computational studies have been used to supplement the investigation of the corner effects. However, due to the enormous grids required to capture all the fine-scale structures present in just a LES of a turbulent corner, almost all computational research has had to relied on Reynolds-averaged Navier-Stokes (RANS),[13–15] although recent work by Garner used Detached Eddy Simulations (DES)[16] to investigate SBLI in the presence of a sidewall.

Fortunately, supercomputer capabilities continue to grow at an exponential rate, which has allowed computational researchers to simulate larger and more complex configurations. Recently, Morgan *et al.*[17] performed an LES for a constant area rectangle duct flow, which included all four walls. In the work, the Mach 1.6 turbulent flow choked and a normal shock train formed in the duct. While the starting location of the shock-train disagreed with the accompanying experiment, the subsequent shock-system agreed well with measurements.

Wind-tunnels also have a finite span and the sidewall flow can directly influence the midspan flow, as seen in both computations[18,19] and experiments.[12,20–22] The effects of the SBLI in the presence of a sidewall was

recently studied using a high-order implicit LES,[23] though the simulation assumed a spanwise symmetric boundary at the midspan to reduce the computational expense. The results showed the development of a separation vortex near the sidewall junction similar to a fin-juncture interaction. Interesting, the shock front relaxed near the midspan and closely resembled the spanwise-periodic solution.[11] However, that scenario only allowed even-mode spanwise waves to exist and did not allow the two corner separations to exist independent of each other. The following study explores the final case, where the full-span domain is simulated. Figure 1 illustrates a few of the scenarios that could not exist in the spanwise symmetric case.

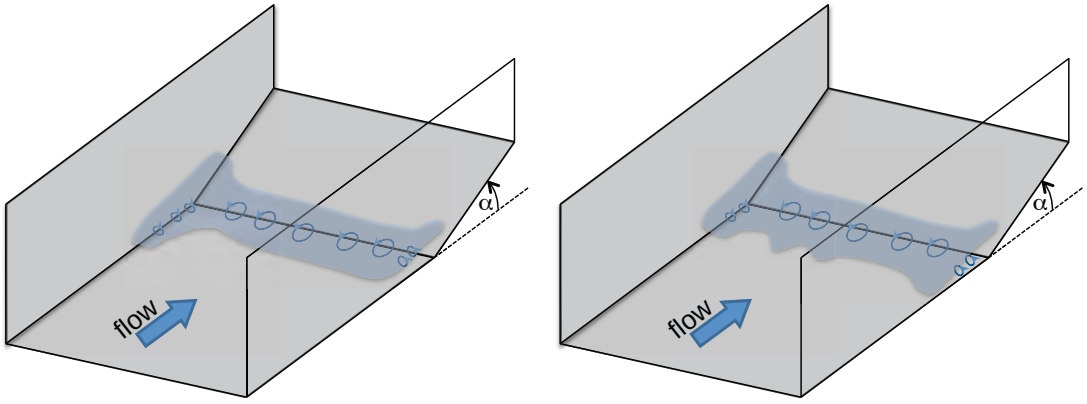

(a) One wall with upstream separation (b) Odd-mode spanwise traveling waves

Figure 1. Cartoons of supersonic flow over a finite-span compression corner α with both sidewalls.

The following results show that it is necessary to conduct the full-span simulation since the previous half-span scenario[23] used a midspan symmetry boundary condition which lead to an artificial strengthening of the upstream boundary-layer and a delayed separation location. Likewise, the previous spanwise-periodic scenario[11] was not able to support the complex corner separation vortex and glancing shock interaction. It also under-predicted the separation bubble length compared to the current results, so the low-frequency oscillations associated with the separation bubble were at a higher frequency than the current results.

II. Method

Flow-field results were obtained using a time-accurate three-dimensional compressible Navier-Stokes solver known as FDL3DI,[24] which has been widely used in previous calculations for both steady and unsteady, subsonic and supersonic flows.[25–31]

A. Governing Equations

The governing equations are transformed from Cartesian coordinates into a general time-dependent curvilinear coordinate system that is recast in strong conservation-law form:

$$\frac{\partial \mathbf{U}}{\partial t} + \frac{\partial \left(\mathbf{F} - \mathbf{F}_v\right)}{\partial \xi} + \frac{\partial \left(\mathbf{G} - \mathbf{G}_v\right)}{\partial \eta} + \frac{\partial \left(\mathbf{H} - \mathbf{H}_v\right)}{\partial \zeta} = \mathbf{S}_c \tag{1}$$

where t is the time and ξ, η, and ζ are the computational coordinates. The solution vector and vector fluxes (both inviscid and viscous) are:

$$\mathbf{U} = \frac{1}{J}\begin{bmatrix} \rho \\ \rho\, u \\ \rho\, v \\ \rho\, w \\ \rho\, E \end{bmatrix}, \quad \mathbf{F} = \frac{1}{J}\begin{bmatrix} \rho\, U \\ \rho\, u\, U + \xi_x\, p \\ \rho\, v\, U + \xi_y\, p \\ \rho\, w\, U + \xi_z\, p \\ \rho\, E\, U + \xi_{x_i} u_i\, p \end{bmatrix}, \quad \mathbf{F}_v = \frac{1}{Re\, J}\begin{bmatrix} 0 \\ \xi_{x_i}\, \tau_{i1} \\ \xi_{x_i}\, \tau_{i2} \\ \xi_{x_i}\, \tau_{i3} \\ \xi_{x_i}\left(u_j \tau_{ij} - q_i\right) \end{bmatrix} \tag{2}$$

and

$$U = \xi_t + \xi_{x_i} u_i, \quad V = \eta_t + \eta_{x_i} u_i, \quad W = \zeta_t + \zeta_{x_i} u_i, \quad E = \frac{T}{(\gamma - 1)\ M_\infty^2} + \frac{1}{2} u_i^2 \tag{3}$$

where u, v, and w are the Cartesian velocity components, ρ is the density, p is the pressure, and T is the temperature. J is the transformation Jacobian, $\partial(\xi, \eta, \zeta, t)/\partial(x, y, z, t)$.[32] Note that the formulas for $\mathbf{G}$, $\mathbf{G}_v$, $\mathbf{H}$, and $\mathbf{H}_v$ are similar to those specified in Eqn. (2).

The source vector, $\mathbf{S}_c$, on the right side of Eqn. (1), is typically set to zero, but has nonzero values at specific locations within the domain to transition the flow to fully turbulent. This work uses the counter-flow force bypass transition method developed by Mullenix *et al.*[33] for supersonic flows since the method uses a broad-band disturbance to transition the flow, it does not introduce any discrete frequencies into the domain.

All length scales are nondimensionalized by the reference length, ℓ, and all dependent variables are normalized by their respective reference values, expect for pressure, which is nondimensionalized by $\rho_\infty u_\infty^2$. The perfect gas relationship and Sutherland law for the molecular viscosity were employed with a reference temperature of 110.3 K for Sutherland's molecular viscosity.

B. The Numerical Method

Time-accurate solutions to Eqn. (1) were obtained numerically by the implicit approximately-factored finite-difference algorithm of Beam and Warming,[34] employing Newton-like subiterations,[35] which has evolved as an efficient tool for generating solutions to a wide variety of complex fluid flow problems, and may be written as follows:

$$\begin{aligned}
&\left[\frac{1}{J} + \left(\frac{2\Delta t}{3}\right)\delta_{\xi 2}\left(\frac{\partial \mathbf{F}^p}{\partial \boldsymbol{Q}} - \frac{1}{Re}\frac{\partial \mathbf{F}_v^p}{\partial \boldsymbol{Q}}\right)\right] J \times \left[\frac{1}{J} + \left(\frac{2\Delta t}{3}\right)\delta_{\eta 2}\left(\frac{\partial \mathbf{G}^p}{\partial \boldsymbol{Q}} - \frac{1}{Re}\frac{\partial \mathbf{G}_v^p}{\partial \boldsymbol{Q}}\right)\right] J \times \\
&\left[\frac{1}{J} + \left(\frac{2\Delta t}{3}\right)\delta_{\zeta 2}\left(\frac{\partial \mathbf{H}^p}{\partial \boldsymbol{Q}} - \frac{1}{Re}\frac{\partial \mathbf{H}_v^p}{\partial \boldsymbol{Q}}\right)\right] \Delta \boldsymbol{Q} = -\left(\frac{2\Delta t}{3}\right)\left[\left(\frac{1}{2\Delta t}\right)\left(\frac{3\boldsymbol{Q}^p - 4\boldsymbol{Q}^n + \boldsymbol{Q}^{n-1}}{J}\right)\right] \\
&\quad + \delta_{\xi 6}\left(\mathbf{F}^p - \frac{1}{Re}\mathbf{F}_v^p\right) + \delta_{\eta 6}\left(\mathbf{G}^p - \frac{1}{Re}\mathbf{G}_v^p\right) + \left[\delta_{\zeta 6}\left(\mathbf{H}^p - \frac{1}{Re}\mathbf{H}_v^p\right) - \mathbf{S}_c^p\right]
\end{aligned} \tag{4}$$

Equation (4) is employed to advance the solution in time, such that $\boldsymbol{Q}^{p+1}$ is the $p+1$ approximation to $\boldsymbol{Q}$ at the $n+1$ time level $\boldsymbol{Q}^{n+1}$, and $\Delta \boldsymbol{Q} = \boldsymbol{Q}^{p+1} - \boldsymbol{Q}^p$. For $p = 1$, $\boldsymbol{Q}^p = \boldsymbol{Q}^n$. Second-order-accurate backward-implicit time differencing was used to obtain temporal derivatives. For simplicity, the dissipation terms are not shown in Eqn. (4).

The left-hand side of Eqn. (4) represents the implicit segment of the algorithm. It incorporates second-order-accurate centered differencing for all spatial derivatives and nonlinear artificial dissipation[36] to augment stability. Computational efficiency was improved by solving this implicit portion of the factorized equations in diagonalized form.[37] The temporal accuracy can be degraded when employing the diagonal form, so subiterations are used within each time step to minimize any degradation of the temporal solution. Note any deterioration of the solution caused by use of artificial dissipation or from the lower-order spatial resolution of implicit operators is also reduced by sub-iterating the time advancement. Three subiterations per time step were applied throughout this work to preserve second-order temporal accuracy.

The compact difference scheme is employed on the right-hand side of Eqn. (4). It is based upon the pentadiagonal system of Lele,[38] and is capable of attaining spectral-like resolution. This is achieved through the use of a centered implicit difference operator with a compact stencil, which reduces the associated discretization error. For the present computations, a sixth-order tridiagonal subset of Lele's system[38] is utilized, which in one spatial dimension is:

$$\frac{1}{3}\left(\frac{\partial \mathbf{F}}{\partial \xi}\right)_{i-1} + \left(\frac{\partial \mathbf{F}}{\partial \xi}\right)_i + \frac{1}{3}\left(\frac{\partial \mathbf{F}}{\partial \xi}\right)_{i+1} = \frac{14}{9}\left(\frac{\mathbf{F}_{i+1} - \mathbf{F}_{i-1}}{2}\right) + \frac{1}{9}\left(\frac{\mathbf{F}_{i+2} - \mathbf{F}_{i-2}}{4}\right) \tag{5}$$

The scheme was been adapted into FDL3DI by Visbal and Gaitonde[39] as an implicit iterative time-marching technique, applicable for unsteady vortical flows, and has been used to obtain the spatial derivative of any scalar, flow variable, metric coefficient, or flux component. It is used in conjunction with a low-pass Padé-type non-dispersive spatial filter developed by Gaitonde et al.,[40] which has been shown to be superior to the use of explicitly added artificial dissipation for maintaining both stability and accuracy on

stretched curvilinear meshes.[39] The filter is applied to the solution vector sequentially in each of the three computational directions following each subiteration, and is implemented in one dimension as:

$$\alpha_f \hat{\boldsymbol{Q}}_{i-1} + \hat{\boldsymbol{Q}}_i + \alpha_f \hat{\boldsymbol{Q}}_{i+1} = \sum_{n=0}^{4} \frac{a_n}{2} (\boldsymbol{Q}_{i+n} + \boldsymbol{Q}_{i-n}) \tag{6}$$

where $\hat{\boldsymbol{Q}}$ designates the filtered value of $\boldsymbol{Q}$. The filtering operation is a post-processing technique, applied to the evolving solution in order to regularize features that are captured, but poorly resolved. On uniform grids, the filtering procedures preserve constant functions while completely eliminating the odd-even mode decoupling.[29,41] Equation (6) represents a one-parameter family of eighth-order filters with numerical values for a_n listed in Ref. 24. The filter coefficient α_f is a free adjustable parameter which may be selected for specific applications, where $\mid \alpha_f \mid < 0.5$. The value of α_f determines sharpness of the filter cutoff and was set to 0.45 for the present simulation.

The spatial filter associated with the high-order compact scheme may produce spurious oscillations in the vicinity of strong shocks, which can be detrimental to the solver's stability and create numerical error in the solution. To address this issue, a 3rd order Roe scheme[42] with the van Albada flux limiter[43] was employed near shocks. This hybrid approach was developed, and successfully used, in previous work for a supersonic turbulent compression-corner.[11,23,44] During each sub-iteration of the solver, the shock location was identified by the pressure gradient detector developed by Swanson and Turkel:[45]

$$\phi = \frac{|p_{i+1} - 2\,p_i + p_{i-1}|}{(1-\omega)\,(|p_{i+1} - p_{i-1}|) + \omega\,(p_{i+1} + 2\,p_i + p_{i-1})}, \quad \begin{cases} \phi > 0.05, & \text{Roe scheme} \\ \phi \leq 0.05, & \text{compact scheme} \end{cases} \tag{7}$$

where p_i is the pressure at grid point i in the specified direction, and ω is a constant that can be varied from 0.5 to 1.0, and was set to $\omega = 0.5$ for the present simulation. As such, the Roe scheme was not employed in the boundary-layer and only applied in the inviscid region of the flow. Once the shock was located, a 5-point stencil was established around the shock, and the inviscid fluxes from the Roe scheme were substituted for the existing compact solutions within the stencil. Because of the upwind nature of the Roe flux-difference scheme, the filtering technique was not used in those regions. As a result of the hybrid approach, the high-order compact scheme captures the fine-scale structures in the shock-free regions of the turbulent flow, while the Roe scheme accurately simulates the flow near the shock.

III. Supersonic Turbulent Corner Flow

In the present simulation, supersonic flow transitioned from laminar to turbulent separately on each of the three flat plates. The approach was necessary for the development of a fully-turbulent boundary layer flow including the corner regions. The turbulent boundary-layer flow away from each corner was consistent with previous studies by Rai *et al.*,[3] Rizzetta and Visbal,[46] Pirozzoli and Grasso,[5] and Bisek *et al.*,,[11] which studied a spanwise-periodic flow at the same freestream conditions. An extrapolated boundary condition was employed at the exit and the upper faces of the computational domain to accommodate the growing boundary-layer and oblique shock system. Grid stretching (i.e., a buffer layer[6]), was also used outside the resolved portion of the domain, near both the upper and exit boundaries, to transfer the energy to higher spatial wave-numbers, where the spatial filter removed it from the computation. This technique regularized the flow in the under-resolved regions of the domain which prevented spurious reflections at the domain boundaries.

The inflow boundary used in this work was identical to the approach used for the turbulent corner flow previously studied[47] and was developed in two steps. First, a solution to the compressible laminar boundary-layer equations[48] was used to specify the boundary-layer profile above each flat-plate. The boundary-layer height was scaled to the reference length $\ell = \delta_{x=0} = 6.096 \times 10^{-4}$ m and freestream conditions applied outside the boundary-layer. Near each corner junction (i.e., $y < 1\,\ell$, $z < 1\,\ell$ and $y < 1\,\ell$, $z > 39\,\ell$), a wall-distance-weighted average from the two adjoining walls was used to smoothly transition the prescribed flow between the two flat-plate compressible laminar boundary-layer profiles. This initial laminar solution was evolved for a streamwise distance of $50\,\ell$, which allowed the profile to relax to its new steady-state. Only minor differences were observed in the flow quantities from the prescribed inflow and the solution at $x = 50\,\ell$, with the largest variations occurring very near the core-corner. A solution slice was extracted at the $x = 50\,\ell$ plane and set as the incoming laminar inflow condition.

Along each flat plate (i.e., wall surface), a no-slip velocity boundary condition was imposed with an isothermal wall set to the nominal adiabatic wall temperature. The surface pressure was computed by enforcing a zero wall-normal derivative to third-order spatial accuracy. The reference conditions for the supersonic flat-plate turbulent boundary-layer are listed in Table 1 and were based on a 1955 experiment by Shutts *et al.* (Case 55010501).[49] Figure 2 illustrates the boundary conditions used in the present study. In some of the discussion that follows, the 'left wall' is located on the $z = 0\,\ell$ plane and the 'right wall' corresponds with $z = 40\,\ell$. The 'bottom wall' or 'compression ramp' corresponds with $y = 0\,\ell$ plane and also includes the 24° compression ramp.

Table 1. Flow conditions for Mach 2.25 air flow over a flat plate.

Parameter	Value	
M	2.249	
u_∞	588	$^{m}/_{s}$
T_∞	169	K
T_w	322	K
p_∞	23,830	Pa
Re/m	2.5×10^7	m^{-1}
Re_θ	2930-5300	

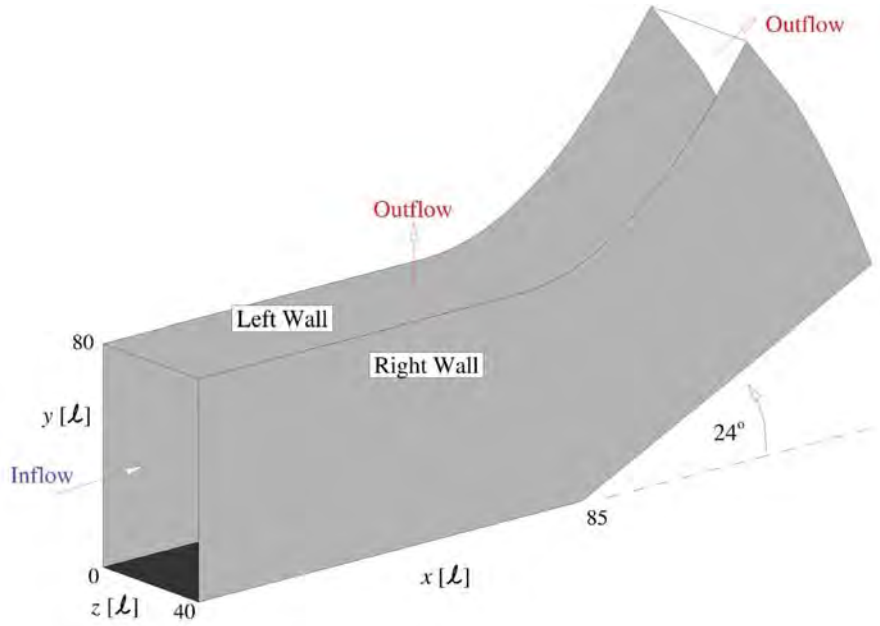

Figure 2. Boundary conditions for supersonic corner flow over a 24° ramp.

The laminar inflow was rapidly transitioned to turbulent using a counter-flow trip model. The trip model was similar to previous work,[23,47] but has been modified following the procedure described by Poggie.[50] Specifically, Poggie suggested two modifications to improve the counter-flow bypass transition process. First, the counter-flow force model was prescribed using a Gaussian profile instead of the right-triangle specified by Mullenix *et al.*,[33] with the length and height of the Gaussian profile similar the dimensions of the original triangle. This modification significantly reduced the streamwise grid spacing needed to support the body-force model without leading to numerical instability.

The second improvement advocated spanwise variation, similar to work by Aubard *et al.*[51] In the current simulation, this was accomplished by modifying the counterflow body-force strength using a Sine function

in the spanwise direction, with one period per $\delta_{x=0} = \ell$. The spanwise variation enhanced spanwise mixing which moved transition forward. As a result of these changes, the strength of the trip model, controlled through a scalar D_c was lowered from 5.5 in the previous half-span calculations[23] to 0.015 here. It is important to note that the bypass-transition trip was excluded from the two corner regions (i.e., $y < 1.25\,\ell$ and $z < 1.25\,\ell$ or $y < 1.25\,\ell$ and $z > 38.75\,\ell$), to ensure that the transition process in the corner was not directly driven by the trip model. As a result, disturbances introduced by the trip grow along each flat-plate wall until they have convected a sufficient distance downstream ($\approx 15\,\ell$ from the trip), to transition to a fully turbulent flow. As the transitional flow traveled farther downstream, the turbulent structures convect into the corner which aided in its transition. In this simulation, the flow appeared to be fully turbulent across the entire domain by $x = 50\,\ell$.

The necessary reference conditions for the nondimensional fluid code FDL3DI[24] were $\ell = 6.096 \times 10^{-4}$ m, $u_\infty = 588$ m/s, M= 2.249, and $Re_\ell = 15,240$. Solutions were obtained using a nondimensional time-step, $\Delta t = 0.00125$, which resulted in $\Delta t^+ = u_\tau^2/\nu_w\,\Delta t = 0.01$ based on the friction velocity in the fully developed equilibrium turbulent boundary-layer flow away from any corner. This time step is slightly larger than that used in the half-span simulations[23] ($\Delta t = 0.001$), but less than the time step used in the previous corner-only simulations[47] ($\Delta t = 0.002$). Note the present calculation used one-forth the time step compared to the spanwise-periodic simulations[11] ($\Delta t = 0.005$). The smaller time step was needed to ensure numerical stability because of the highly three-dimensional shock front compared with the *quasi* two-dimensional shock in the spanwise-periodic simulations.[11] In the analysis of the results that follow, the solution flow variables were decomposed into time-mean and fluctuating components (i.e., $\phi = \bar{\phi} + \phi'$, where ϕ' is the fluctuating component of variable ϕ).

A. Grid Development

A computational domain was developed to support the LES based on previous work[23] and the guidelines recommended by Georgiadis *et al.*[52] As previously mentioned, the reference length, ℓ, was set to the incoming boundary-layer height (i.e., $\ell = \delta_{x=0}$ away from the corner), and a Cartesian coordinate system was established with its origin corresponding to the incoming corner junction. The grid used in this work was similar to the half-span simulation,[23] but was modified in several ways to increase the solution fidelity.

First, the stretched (buffer) regions were extended to further regularize unsteady structures before reaching the outflow boundaries. This change negated the need for grid stretching to occur in both wall normal directions in the stretched regions, which was needed in the previous half-span simulation.[23] Second, the streamwise resolution in the trip region was reduced since it was no longer required by the improved trip model. These grid points were shifted downstream to increase the streamwise resolution in the vicinity of the compression ramp. Third, previous results[23,47] showed the resolution within the inviscid core flow was finer than required by the LES, especially when compared with the resolution in the rest of the domain, so the resolution in this region was slightly reduced. Finally, the resolved portion of the LES domain in the y-direction was extended from $y = 20\,\ell$ to $y = 40\,\ell$ to increase the resolution around the glancing SBLI. Figure 3 shows both side and downstream views of the current grid. Note that only 1/20th of the grid points were included for clarity.

The streamwise grid distribution used a constant spacing of $\Delta x = 0.1\,\ell$ from the origin to $x = 60\,\ell$. The grid spacing was monotonically refined from $x = 60\,\ell$ to $x = 75\,\ell$ using 320 points. A constant spacing of $\Delta\xi = 0.05\,\ell$ was used from $x = 75\,\ell$ to $x = 95\,\ell$. Note the spacing is specified in computational coordinates to account for the 24° compression ramp at $x = 85\,\ell$. The grid was monotonically stretched from $x = 95\,\ell$ to $x = 100\,\ell$ using 65 points. A constant spacing of $\Delta\xi = 0.1\,\ell$ was used from $x = 100\,\ell$ to $x = 110\,\ell$. Finally, the grid was monotonically coarsened over $130\,\ell$ using 50 more points for a total of 1461 streamwise points.

The grid spacing for both wall-normal directions (i.e., the y and z directions), was developed in an identical manner to facilitate the development of the fully-turbulent boundary-layer profiles on three walls. Grid spacing in the normal direction was specified at the wall boundary such that $y_w^+ < 1$. The grid was monotonically stretched with a hyperbolic tangent expansion function and 190 points until $y = 2\,\ell$ (i.e., $\Delta y = 0.0025\,\ell$ at $y = 0$ and $\Delta y = 0.04\,\ell$ at $y = 2\,\ell$). A constant grid spacing of $\Delta y = 0.04\,\ell$ was used from $y = 2\,\ell$ to $y = 40\,\ell$. From $y = 40\,\ell$ to $y = 78\,\ell$ (at $x = 0\,\ell$ plane), the grid was monotonically coarsened using 48 additional points for a total of 1188 normal points. The equilibrium turbulent boundary layer height *delta* was approximately $2.25\,\ell$ at $x = 60\,\ell$ and approximately $2.5\,\ell$ just upstream of the SBLI.

Consistent with the y direction, grid spacing in the spanwise direction was specified at the wall boundary such that $z_w^+ < 1$. The grid was monotonically stretched using 190 points until $z = 2\,\ell$ (i.e., $\Delta z = 0.0025\,\ell$

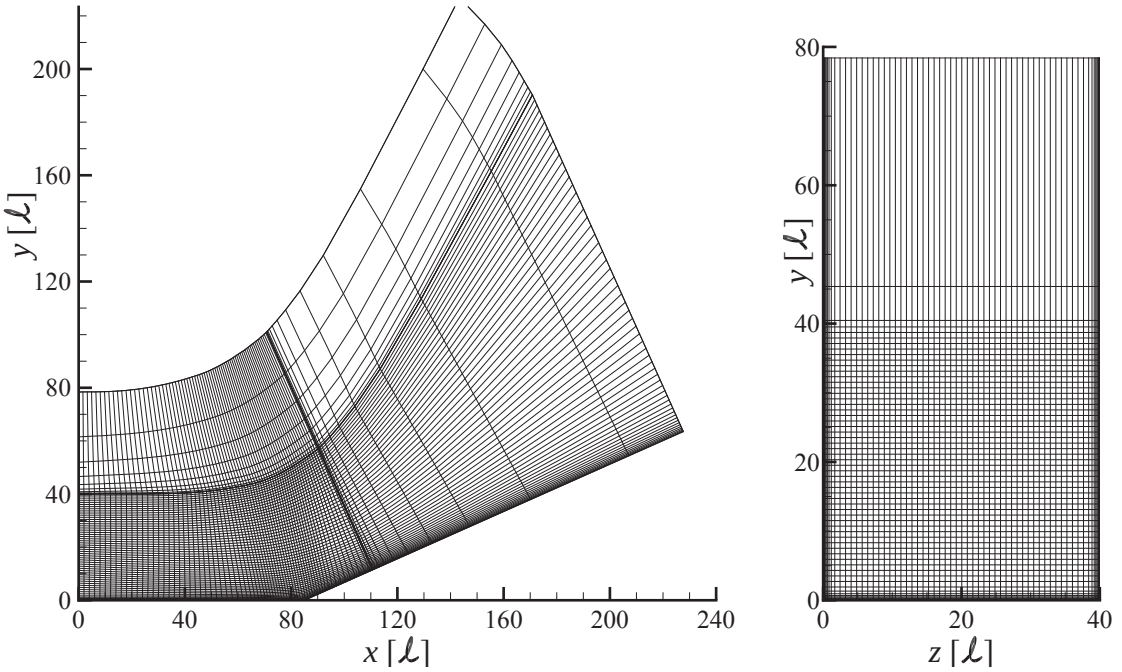

(a) Side view.

(b) Downstream view at the inflow

Figure 3. Schematic of the computational domain.

at $z = 0$ and $\Delta z = 0.04\,\ell$ at $z = 2\,\ell$). A constant grid spacing of $\Delta z = 0.04\,\ell$ was used from $z = 2\,\ell$ to $z = 38\,\ell$. Identical to the left wall, the right wall required 190 additional points which were monotonically refined (i.e., $\Delta z = 0.04\,\ell$ at $z = 38\,\ell$ and $\Delta z = 0.0025\,\ell$ at $z = 40$), for a total of 1279 spanwise points.

As a result of the prescribed resolution, the computational domain had a grid-spacing based on inner units of $\Delta x^+ = 11.5$, $\Delta y_w^+ = 0.58$, $\Delta z^+ = 9.2$ at the wall and $\Delta x^+ = 11.5$, $\Delta y^+ = 9.2$, $\Delta z^+ = 9.2$ at the boundary layer edge. This resolution was maintained throughout the inviscid core. Recent calculations by Poggie[53] show that this level of resolution (11-1-9) could be constituted as *effective* direct numerical simulation (DNS), but since the domain does not have a constant 1-1-1 spacing everywhere it is labeled as a LES in this work. All total, the resolved portion of the LES domain was approximately $110\,\ell$ long, $40\,\ell$ wide and $40\,\ell$ tall for a total of 2.22×10^9 points. Note that grid stretching was not allowed to exceed 8% between subsequent grid points.

A five-point overlap was used to decompose the grid onto the parallel processors to maintained high-order differencing and filtering between computational blocks. Total computational efficiency of the current simulation was improved compared to previous studies[23,47] by reducing the number of five-point overlaps. This was accomplished by increasing the size of each decomposed block so each side of the block contained 96 points (56 points per side were used in the previous half-span calculation[23]). The increased block size also improved computational performance due to better memory cache management and improved vectorization since the vector lengths were increased. However, increasing the number of grid points per block (i.e., per MPI task), also meant there was more computational work per task (i.e., a significant increase in walltime per iteration). Fortunately, the potential walltime increase was negated by using OPENMP threads to assist with the computational work per MPI task. As such, the size of the domain was carefully developed such that each block was identical and each loop length was a multiple of the number of threads to be used. The current simulation was carried out using 2912 MPI tasks and either 4, 6, 8, 12 OPENMP threads on the DoD AFRL DSRC *Lightning* supercomputer, which has 24 processors per node. Linear to super-linear speed-up was observed using any number of the aforementioned threads, but most of the iterations were carried out using 6 threads due to availability of the compute nodes and since each 24 processor node was composed of 2 12 processor chips with 1 numa node per chip. Due to the very large size of the computational domain,

a parallel I/O framework was used to significantly reduce the walltime associated with both reading and writing the restart and solution files. Careful adjustment of the Lustre filesystem environment parameters reduced the I/O time of the 250GB restart file from 30 minutes to 3 minutes.

B. Features of the Instantaneous Flow

Figure 4 shows results from a typical solution time in the fluid domain. The image plots instantaneous iso-surfaces of the incompressible Q-criterion[54] ($Q_{criterion} = \frac{1}{2}\left[\Omega^2 - \mathbf{S}^2\right] = 1$), colored by the u-velocity over half the domain. The Q-criterion is the second invariant of the velocity gradient tensor, which compares the vorticity, Ω, to the strain-rate, $\mathbf{S}$. The Q-criterion is commonly used to highlight organized structures in turbulence, especially for wall-bounded turbulent flows where stronger streamwise velocity gradients can mask structure due to vorticity. Wall pressure contours highlight the three-dimensional shock footprint, especially near reattachment on the ramp wall. The figure also includes a slice of the instantaneous nondimensional pressure gradient magnitude contours (grey-scale), near the downstream end of the resolved domain. This contour slice highlights both the acoustic radiation emanating from the turbulent boundary-layer and the shock-structure of the sidewall glancing shock interaction.

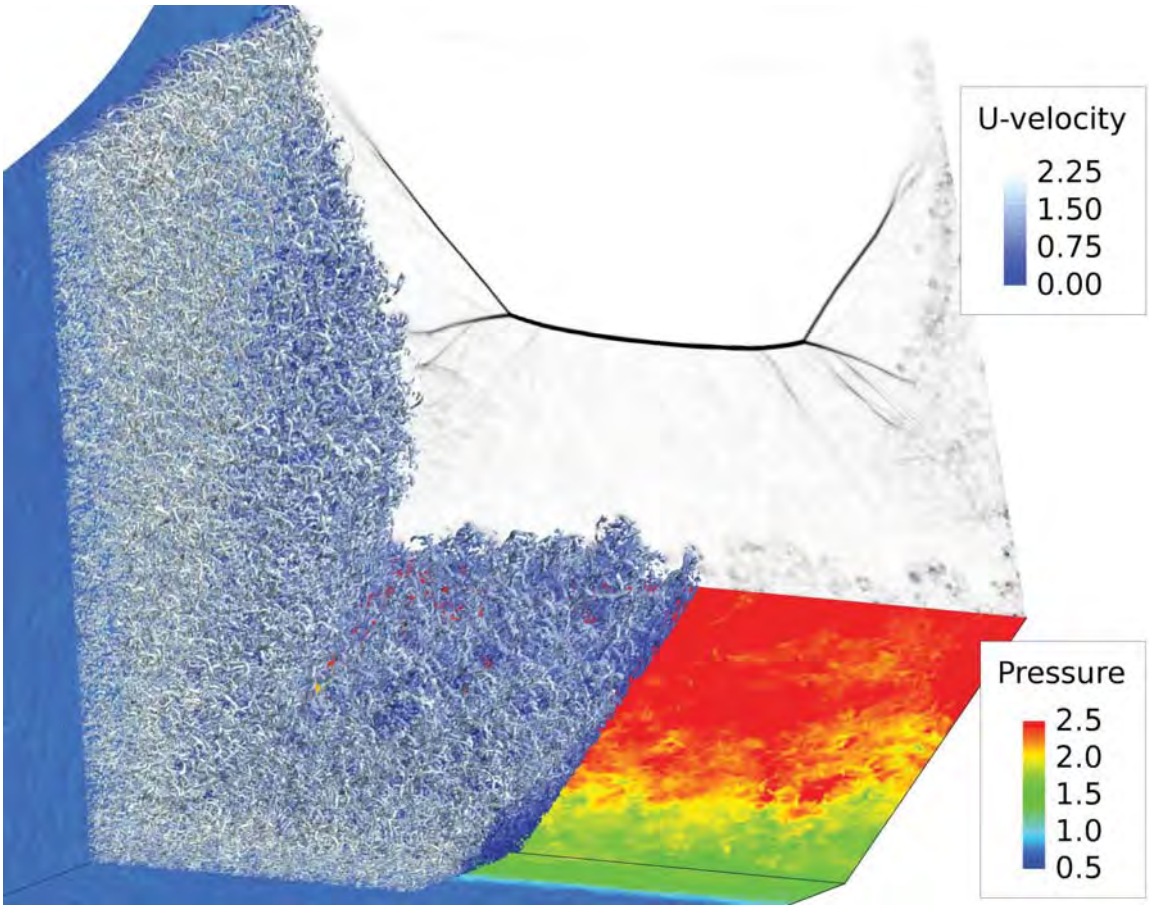

Figure 4. Instantaneous iso-surfaces of the Q-criterion over half the span falsely colored by the u-velocity for Mach 2.25 turbulent airflow over a 24° compression-ramp between two sidewalls. The figure also includes surface pressure contours (colored) and a streamwise slice of pressure gradient magnitude (gray-scale).

Due to the size of the solution domain only a small portion of the resolved domain is included in the figure (i.e. $60\,\ell < x < 110\,\ell$, $y < 40\,\ell$). Even with this significant reduction in scope, the data set was too large to visualize using standard visualization tools, so Fig. 4 was created by only using 1/8 of the actual resolution (i.e., only every other point in each direction was used). Still, the image provides tremendous

detail and insight into the flow. A turbulent boundary-layer flow has developed on each wall, as seen by the turbulent Q-criterion iso-surface structures (which were excluded from the image upstream of $x = 74\,\ell$ and for $z > 20\,\ell$ for brevity). Note these restrictions were also needed to allow the image to be generated within the limitations the high-performance visualization computer's capabilities.

As the turbulent flow travels toward the compression corner, the flow's sharp turning angle resulted in the formation of an oblique shock above the boundary-layer. Two shock feet form that correspond to the separation point and reattachment of the separated flow along the bottom wall. This behavior gives rise to the well-known λ-shock structure. A similar λ-shock structure exists above each of the two sidewalls, which is clearly seen in the gray-scale pressure gradient magnitude contour slice. The incident shock along the sidewall coincides with a glancing SBLI.[12] However, the flow does not immediately separate under the leading foot, but rather, separates at a farther downstream distance due to the presence of a corner-induced separation vortex. The second foot (reattachment shock), is also evident in the image, with the separation vortex existing between the two legs of the λ-shock system, as it traveled along the sidewall similar to a sharp fin interaction.

Due to the turbulent inflow, the shock front oscillated primarily in the streamwise direction. The large-scale, low-frequency portion of this oscillation is commonly referred to as a *breathing* motion.[55] Along the bottom plate, the post-shock flow expands as it travels downstream, eventually reattaching about $4 - 10\ell$ downstream of the 24° compression ramp.

Figure 5 shows a several instantaneous surface pressure contours, some of which are similar to those illustrated in Fig. 1. The images in Fig. 5 show a top-down view and were selected to portray several of the anti-symmetric scenarios that exist in the full-span time-accurate simulation. Most of these scenarios could not exist in the half-span simulation since the symmetry boundary condition was used at the midspan.[23]

As seen in Fig.5, the flow is almost always anti-symmetric across the midspan, however a few prevailing observations can be drawn from the figures. Downstream of reattachment (yellow-red contours), there were bands of lower pressure flow (yellow) near each sidewall that move toward the midspan. The inward-turning sidewall flow was due to the sidewall boundary-layer growth and the lifted sidewall-traveling separation vortex from the glancing shock interaction. The flow had a large time-mean streamwise separation zone (green) on the bottom plate, but pockets of attached flow (yellow) existed in the time-accurate results. Finally, whenever the corner separation moved significantly upstream, separation is delayed in the region next to it. This is because the corner separation generates compression waves which move radially outward from the leading separation point. The nearby boundary-layer responded to the waves by developing a slightly fuller profile which delays separation on the bottom wall. The sidewall developed a glancing shock-boundary layer interaction, but the interaction was not strong enough to cause the sidewall flow to immediately separate along the incident shock front.

IV. Features of the Time-Mean Flow

Flow transients were convected out of the domain for 300,000 iterations before the mean and time-accurate solutions were collected. This corresponded to about 5 flow lengths since the resolved portion was $\approx 110\,\ell$ long and a nondimensional time-step $\Delta t = 0.002$ was used for the first 260,000 iterations. The timestep was lowered to $\Delta t = 0.00125$ for the last 40,000 iterations of the transients calculation. Mean and time-accurate statistics were developed from additional 1.6×10^6 iterations (about 18 additional flow lengths or $t = 2000$). Previous work on both the corner flow[47] and spanwise homogenous compression ramp[11] show that a sampling length of about 5 flow lengths ($t = 500$), was sufficient to converge mean quantities, though higher-order statistics required additional samples. It is important to note that the solutions presented here can not be span-averaged since a homogenous direction does not exist.

To ensure the flow upstream of the compression ramp was in turbulent equilibrium, streamwise velocity profiles were exacted from the mean solution and transformed using the van Driest transformation.[56] The transformed streamwise velocity was nondimensionalized by the wall friction velocity, u_τ. The profiles were plotted versus the nondimensional inner length scale, $y^+ = y\,\rho_w\,u_\tau/\mu_w$ (for the lines normal to the bottom-wall) and $z^+ = (z - z_w)\,\rho_w\,u_\tau/\mu_w$ (for either side-wall). Figure 6(a) plots the van Driest transformed velocity for the near-wall region above each flat plate. It also includes previous spanwise-averaged solutions,[11] computational results from Rai *et al.*,[3] and experimental measurements by Shutts *et al.*,[49] and Elena and LaCharme.[57] The latter was collected at conditions similar to the experiment by Shutts *et al.*.[49]

Fig. 6(b) shows Reynolds stress profiles at the same streamwise location ($x = 70\,\ell$). The streamwise

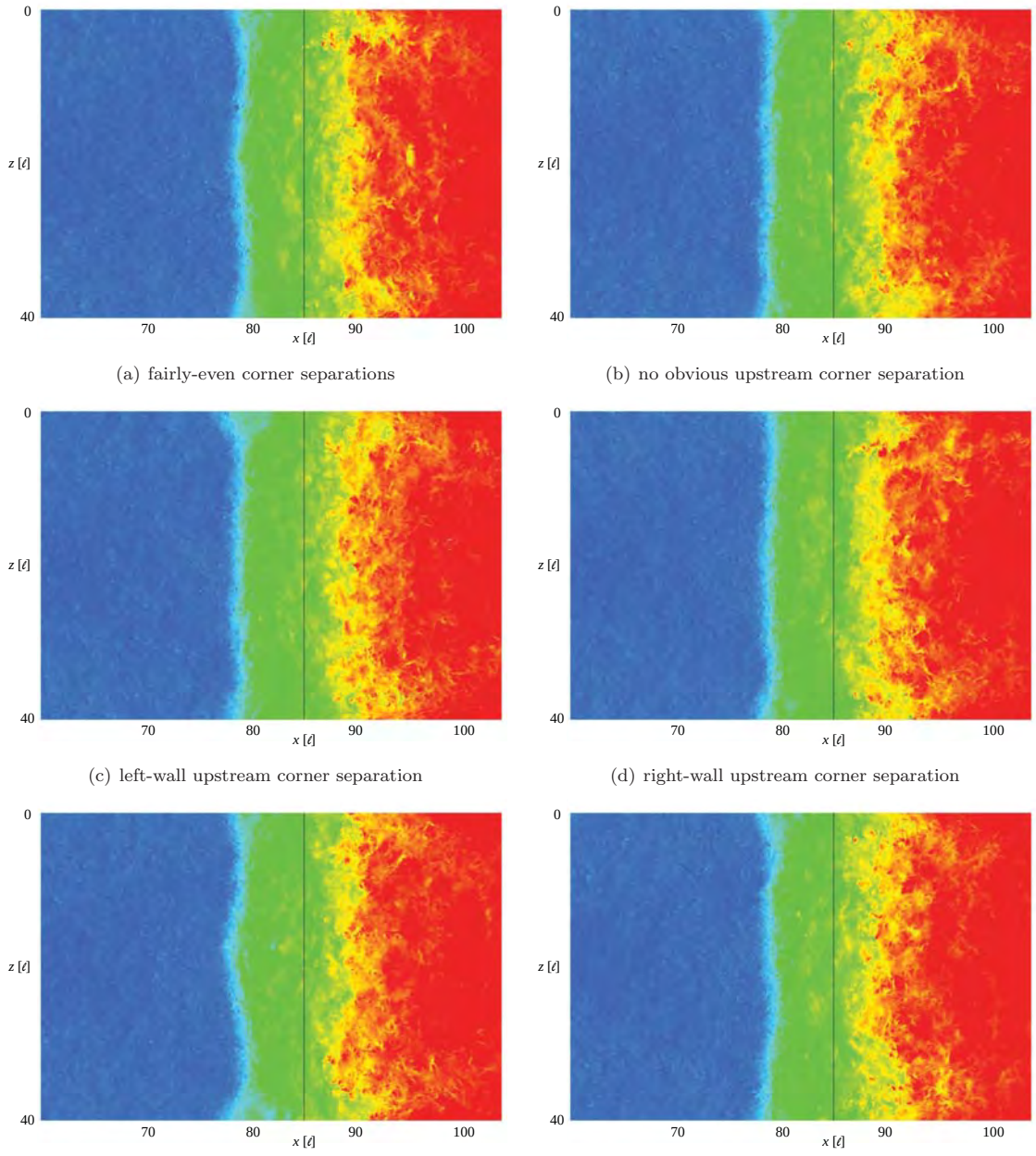

(a) fairly-even corner separations

(b) no obvious upstream corner separation

(c) left-wall upstream corner separation

(d) right-wall upstream corner separation

(e) fairly-even mode spanwise waves across the separation front

(f) odd-mode spanwise waves across the separation front

Figure 5. Select instantaneous surface pressure contours with the solid black line indicating the compression corner at $x = 85\,\ell$. Flow is from left to right. ($x - z$ top-down view)

component of the Reynolds stress shows more variation than the other directions, though all the lines have very consistent behavior. Additional locations along all three walls produced similar results and have been excluded for brevity. From these results, the flow upstream of the shock interaction was consistent with a turbulent equilibrium boundary-layer.

Figure 7 shows contours of skin-friction coefficient from a topdown view from the current full-span, half-span,[23] and spanwise-periodic simulations.[11] As previously mentioned the current results were averaged over $t = 2000$ iterations, but were essentially the same as the results obtained for $t = 1000$ which were been

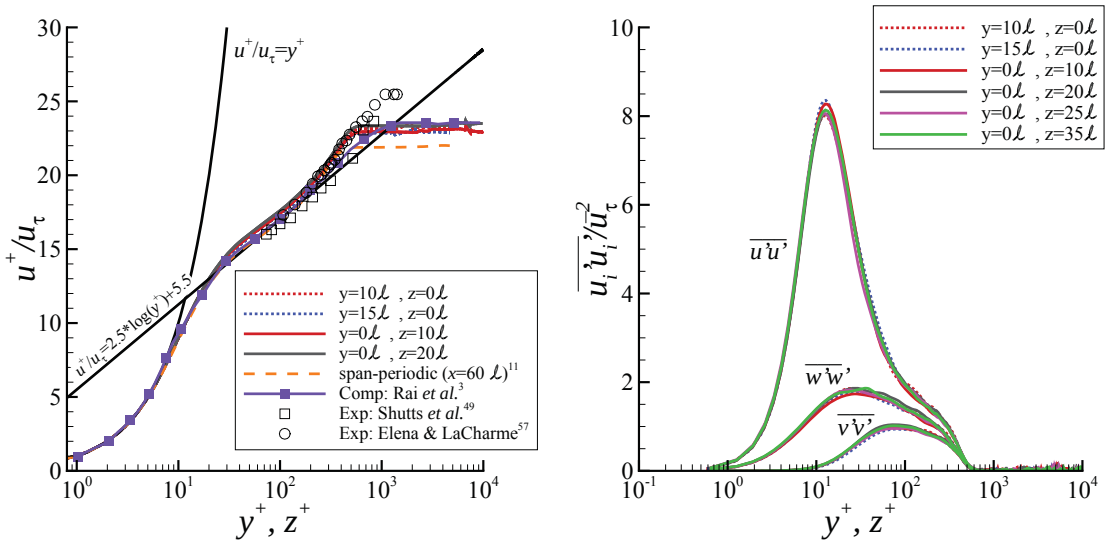

(a) Van Driest transformed streamwise velocity

(b) Reynolds stress profiles from the left and bottom walls

Figure 6. Time-mean streamwise velocity profiles using the Van Driest transform and Reynolds Stress normalized by the friction velocity at $x = 70\,\ell$.

excluded for brevity. Since the compression ramp for the spanwise-periodic case[11] was located at $x = 75\,\ell$, compared to $x = 85\,\ell$ in the full-span and half-span[23] scenarios, the x-axis has been adjusted to account for the ramp location ($x* = x - x_{\text{ramp corner}}$). From the figures, it is clear a large separation bubble ($c_f < 0$), which existed on each bottom plate, both upstream and downstream of the 24° ramp. The black lines in Fig. 7 correspond to $c_f = 0$.

While the solutions appear qualitatively similar, several differences were observed between the full-span, half-span, and periodic simulation. The most obvious was the presence of a separation vortex which originated near the sidewall juncture and kept the mean flow attached in that region (i.e., a nodal attachment point). In Fig. 7(c), the streamwise separation location moved downstream slightly near the midspan, such that the separation location near the spanwise symmetry plane very closely resembled the spanwise-periodic results in Fig. 7(b). This behavior was originally anticipated because the spanwise domain was very wide relative to the incoming boundary-layer thickness δ and the separation length ℓ_{sep}. As such, it was expected that the flow would be *quasi* two-dimensional near the midspan symmetry plane and yield results in that region consistent with the spanwise-periodic scenario.[19,23]

A comparison between the full-span and half-span scenarios shows the presence of the same nodal attachment point and subsequent separation vortex near each sidewall. However, Fig. 7(a) shows the separation location moving upstream as the flow approaches the spanwise center in the full-span simulation results. This behavior was inconsistent with the half-span scenario results previously discussed. The difference was result to several factors. First, the full-span scenario allows both odd and even spanwise modes to exist. This change lead to different time-accurate flow patterns already seen and discussed in the instantaneous surface pressure contours of Fig. 5. This allowed spanwise waves to travel through the midspan instead of being reversed at the midspan symmetry boundary. Whereas, in the half-span scenario the waves slowed and were reversed at the midspan which lead to an artificial increase in the boundary-layer thickness near the symmetry plane, even upstream of separation.

Figure 8 shows contour plots of the boundary-layer thickness $\delta = 0.99u_\infty$ at $x = 73\,\ell$ for the full-span and half-span scenarios. The slice location $x = 73\,\ell$ was approximately one δ upstream of the time-mean compression ramp separation location. As seen in the figure, the symmetry scenario shows a slightly thicker ($\sim 15\%$) boundary-layer near the symmetry plane which was not seen in the full span profile in Fig. 8(b). The thicker boundary-layer coincides with a fuller velocity profile.

Figure 9 shows streamwise velocity profiles versus the normal distance from the wall. The distance has been normalized by the local boundary-layer thickness δ. The lines were extracted from various stations

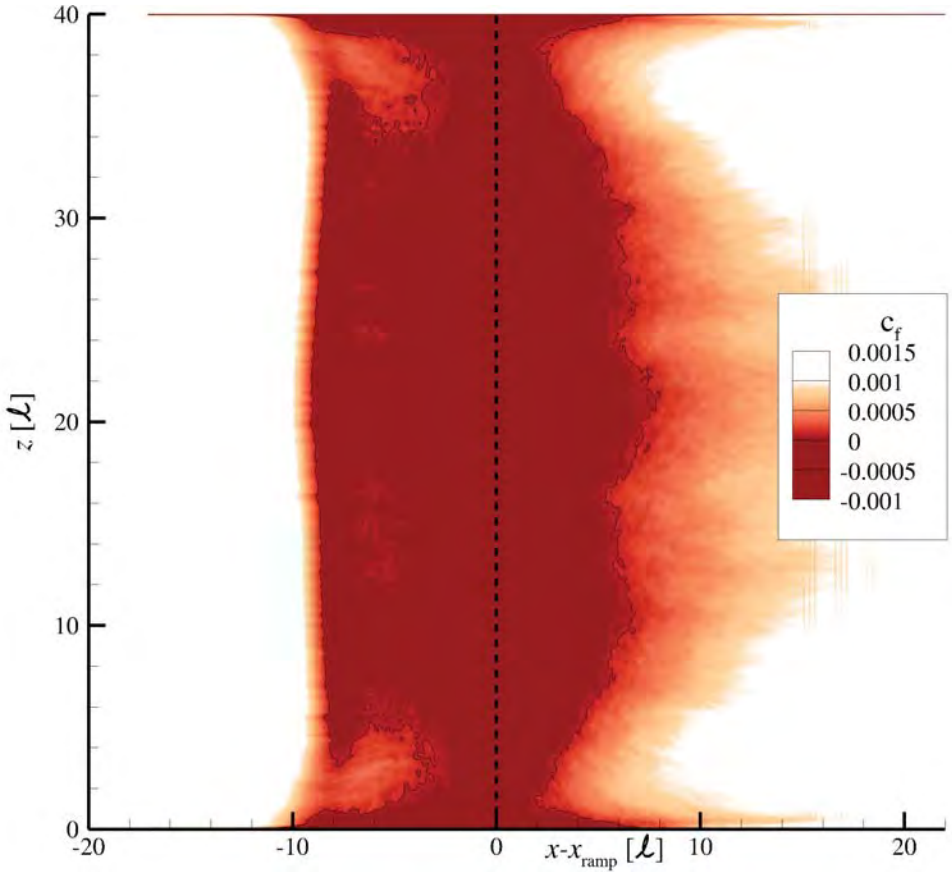

(a) Current results

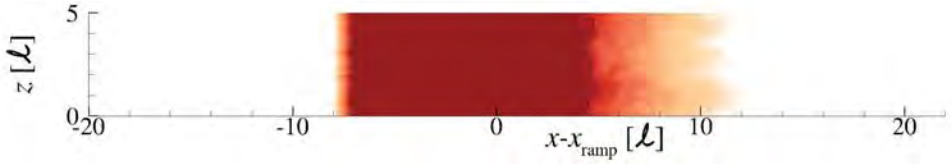

(b) Previous spanwise-periodic results[11]

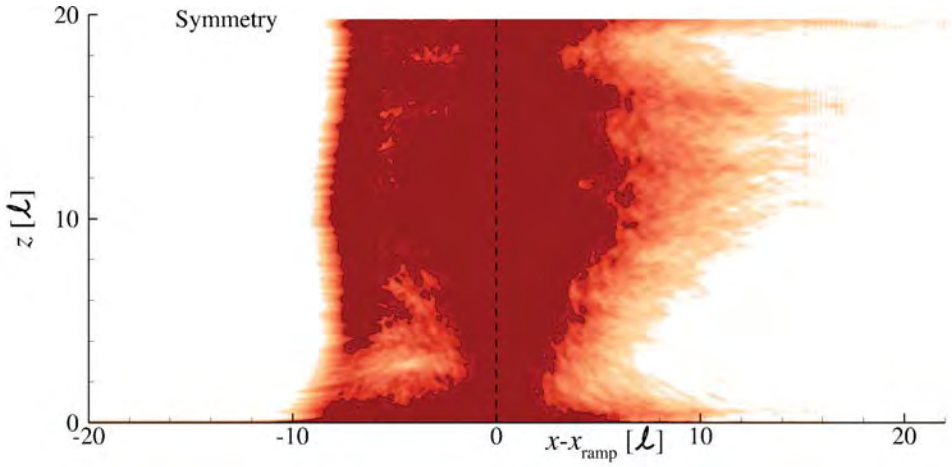

(c) Previous half-span results[23]

Figure 7. Surface contours of the time-mean skin-friction coefficient (top-down view).

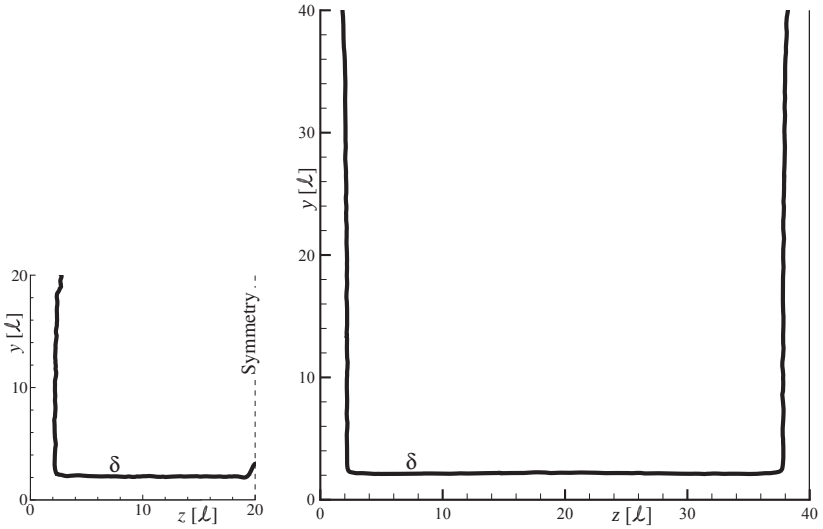

(a) Half-span results[23] (b) Current results

Figure 8. Planar contour of the time-mean streamwise velocity $u = 99\%u_\infty$ to identify the boundary-layer thickness δ (downstream view).

along the walls for both the full-span and the previously computed half-span scenario.[23] As seen in the figure, the profiles were very similar everywhere except for the half-span scenario at its symmetry plane ($z = 20\,\ell$), which is denoted with open diamond symbols. The fuller profile delayed separation near the mid-span symmetry plane. Note that in both scenarios the midspan flow was not directly influenced by the upstream corner separation compression waves due to large width of the domain as seen in Figs. 7(a) and 7(c). This aspect of the flow was consistent with theory suggested by Benek *et al.*,[19] but the results clearly show the spanwise separation front was not two-dimensional in the midspan region either, so the assumption that the solution in that region woudl be similar to a spanwise-periodic scenario was incorrect. Likewise, the separation length at the midspan of the full-span scenario was approximately 20% greater than the spanwise-periodic results. Since the low-frequency motion of the shock front is related to the separation length, the spanwise-periodic results predict higher shock oscillation frequencies compared to those seen in the current full-span simulation.

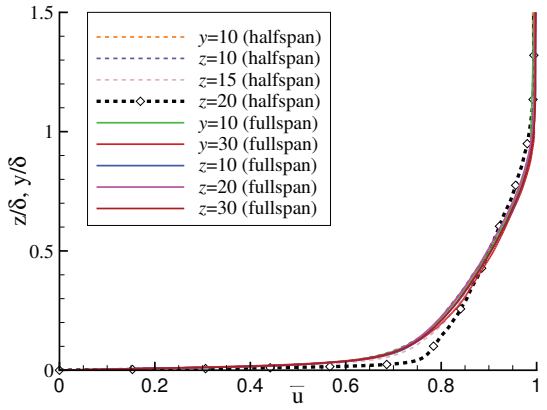

Figure 9. Line plots of time-mean streamwise velocity u at various locations normal to the wall at $x = 73\,\ell$ for both the full-span and the previously computed half-span scenario.[23]

Figure 10 plots skin-friction contours along both side walls for the full-span and for the one sidewall in

the previously computed half-span simulation.[23] While the surface skin-friction contours were noticeably different near the midspan in Fig. 7, the sidewall profiles appear very similar between the two scenarios. This was expected because the development of the sidewall boundary-layer was identical between the half-span and full-span cases. Note the half-span scenario was only resolved to support LES to $y = 20\,\ell$, so the unsteady flow above it was under-resolved and excluded from Fig. 10(c)

The faint, nearly vertical, line seen in the full-span sidewall skin-friction contours (i.e., Figs. 10(a) and 10(b)), near $x = 85\,\ell$, $y = 20\,\ell$, was the result of the upstream trip model and the highly three-dimensional shock interaction system present in that region of the flow. The trip used a local body-force to transition the flow to turbulence. This process also produced a weak acoustic waves which originated from the laminar boundary-layer edge, directly above the trip location ($x = 2.5\ell$). Since the fluid code used a non-dissipative high-order scheme and the inviscid core region of the domain was very highly resolved (i.e., *effective* DNS[53]), the acoustic waves from the sidewall trips persisted through the domain and interact with the opposite sidewall boundary-layer near that location. By coincidence, the leading foot of the glancing SBLI also traveled through that location.

The interaction between the acoustic waves and the glancing incident shock front was further complicated by the presence of the separation vortex which has a nodal attachment point near each corner, as seen in Fig. 11. The separation vortex is colored by black lines and originated on the compression ramp surface, upstream of the ramp. The sidewall compression wave (which corresponds to the leading foot of the sidewall glancing shock system), emanated from the corner separation and is colored with blue lines. As seen in the figure, the separation vortex entrains mass flow from the sidewall boundary-layer. It also captured some of the mass flow that traveled into the bottom-plate separation bubble. The trip-generated acoustic waves distort and slightly bend versus distance from the bottom wall as they travel near the highly three-dimensional shock system before impinging with the opposite sidewall. While the trip-induced acoustic waves are not desired in the simulation, they yield results similar to those produced by small imperfections in the surfaces of wind tunnels and flight vehicles. Note the acoustics waves from the bottom plate trip do not interact with the SBLI system since the highly stretched upper domain wall allowed them to travel directly out the back of the domain without reflecting.

Along either sidewall, the glancing oblique shock interacted with the turbulent flow which eventually lead to a time-mean separation and reattachment. This λ-shock system was evident in the pressure gradient magnitude contour discussed slice in Fig. 4. The sidewall separation vortex traveled at a shallow angle relative to the wall, so the contour slice captured both the size of the vortex core and both the separation and reattachment feet associated with glancing shock system. Note in the pressure gradient magnitude slice of Fig. 4, the side-wall separation foot was farther from the ramp surface, whereas the reattachment foot appeared closer to the ramp.

The cross-sectional area of the separation vortex was also seen in Fig. 12, which shows an iso-surface of time-mean density ($\bar{\rho} = 1.5$), along with some time-mean velocity streamlines, and a few planar contours of density. The right sidewall surface was removed to show the vortex core. As seen in the figure, the separation vortex has a low density core, whereas the post-shock density in the core-corner was quite high. High density corresponded with high pressure in that region which turned the velocity vectors inward, as illustrated by the red streamlines in Fig. 11.

Accounting for the flow's turning angle (due to the ramp), the mean separation length along each sidewall can also be computed. Table 2 lists the separation length at various locations on all three walls, based on time-mean skin friction contours of Figs. 7(a), 10(a), and 10(b). As seen in the table, the separation length on the sidewall was much less than the separation length on the bottom plate. This is due, in part, to the effects of the core-corner separation, the ambiguity of defining separation and reattachment along constant streamlines in the presence of a glancing SBLI, and that the sidewall separation was due to the separation vortex and not the incident shock in the glancing SBLI.

As previously discussed, separation near either of the two-wall junctions almost always occurred upstream of the separation location on the bottom plate. As a result of this phenomenon, the region generated weak conical compression waves which radiate outward along both walls. Due to the geometric limitations and the production of a separation vortex, these compression waves do not influence much of the bottom wall SBLI. However, the same geometric conditions allow these waves to travel along each sidewalls. The compression waves were not strong enough to cause the sidewall boundary-layer to immediately separate in the time-mean analysis, but the compression waves do correspond with the incident shock (leading foot) of the sidewall λ-shock system.

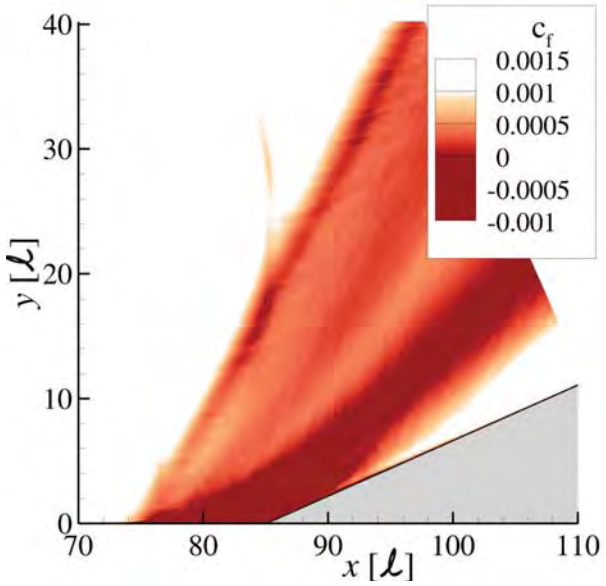

(a) Left wall ($z = 0\,\ell$)

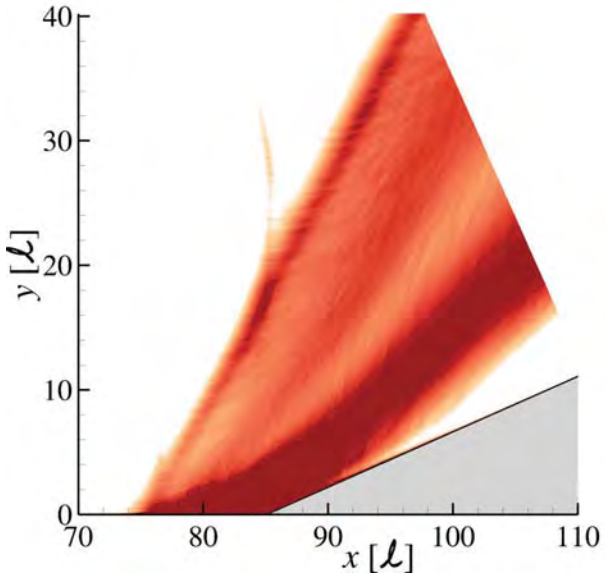

(b) Right wall ($z = 40\,\ell$)

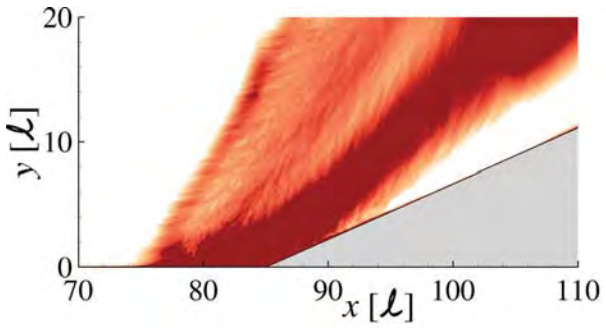

(c) Previous left wall ($z = 0\,\ell$)[23]

Figure 10. Surface contours of the time-mean skin-friction coefficient ($x - y$ side view).

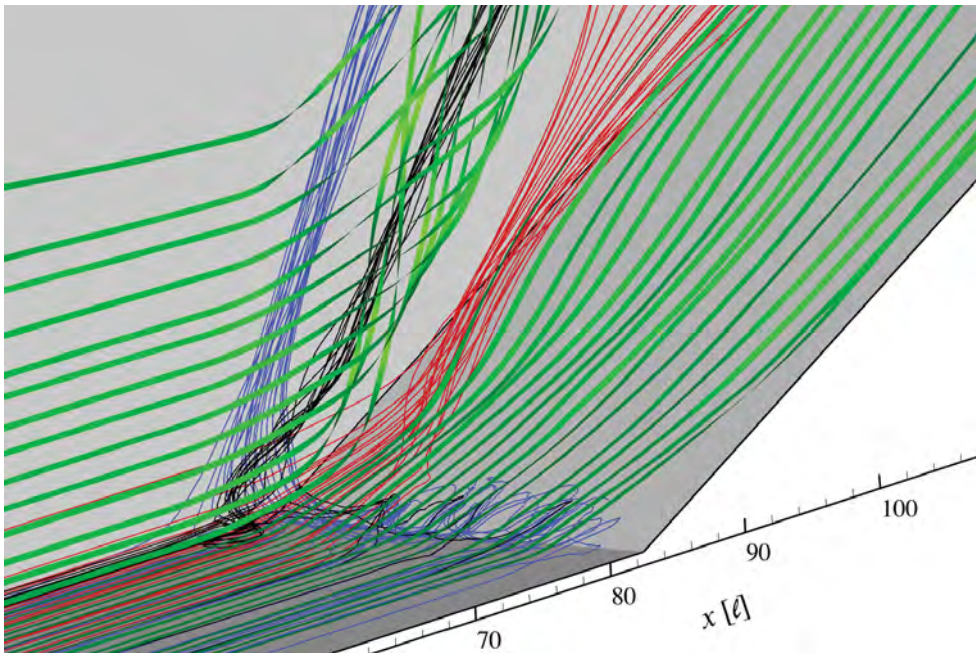

Figure 11. Time-mean velocity streamlines for Mach 2.25 flow over a 24° compression ramp near the left sidewall.

.

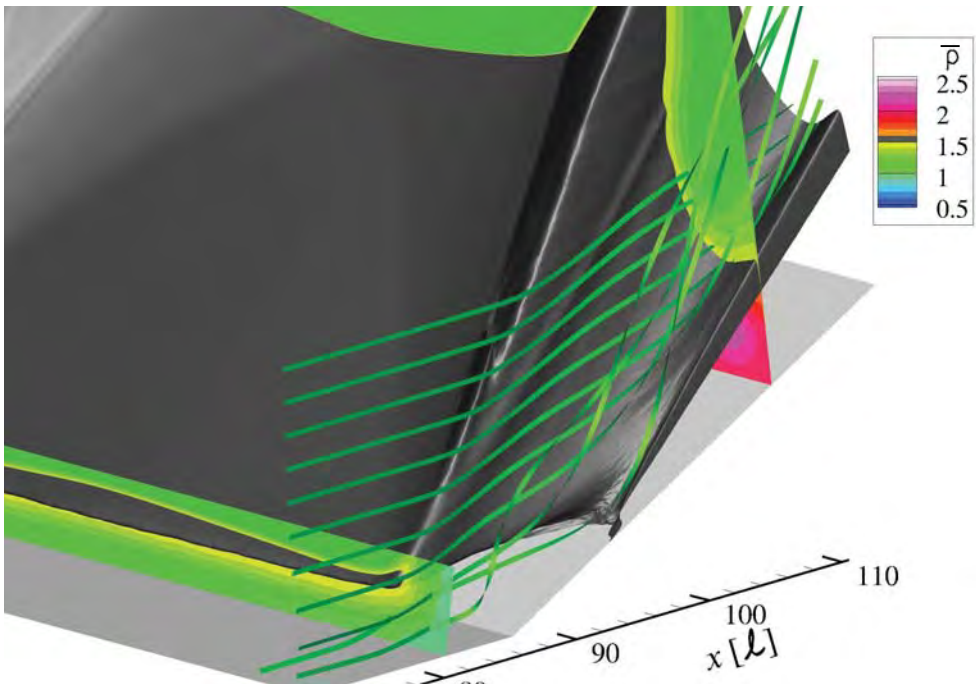

Figure 12. Time-mean planar contours of density and an iso-surface of constant density ($\bar{\rho} = 1.5$), along with velocity streamlines for Mach 2.25 flow over a 24° compression ramp near the right sidewall.

.

Table 2. Separation length at various locations for the full span compression corner.

Plate / Wall	Separation	Reattachment	Separation length, ℓ_{sep}
$z = 5\,\ell$	$x = 76.8\,\ell$, $y = 0\,\ell$	$x = 89.0\,\ell$, $y = 1.8\,\ell$	$12.9\,\ell$
$z = 10\,\ell$	$x = 76.5\,\ell$, $y = 0\,\ell$	$x = 91.5\,\ell$, $y = 2.9\,\ell$	$15.3\,\ell$
$z = 15\,\ell$	$x = 76.4\,\ell$, $y = 0\,\ell$	$x = 91.0\,\ell$, $y = 2.7\,\ell$	$14.8\,\ell$
$z = 20\,\ell$	$x = 75.9\,\ell$, $y = 0\,\ell$	$x = 92.4\,\ell$, $y = 3.3\,\ell$	$16.8\,\ell$
$z = 25\,\ell$	$x = 76.1\,\ell$, $y = 0\,\ell$	$x = 91.3\,\ell$, $y = 2.8\,\ell$	$15.5\,\ell$
$z = 30\,\ell$	$x = 76.5\,\ell$, $y = 0\,\ell$	$x = 90.9\,\ell$, $y = 2.6\,\ell$	$14.6\,\ell$
$z = 35\,\ell$	$x = 76.8\,\ell$, $y = 0\,\ell$	$x = 88.9\,\ell$, $y = 1.7\,\ell$	$12.2\,\ell$
$z = 0\,\ell$	$x = 92.3\,\ell$, $y = 10\,\ell$	$x = 102.6\,\ell$, $y = 14.6\,\ell$	$11.3\,\ell$
$z = 40\,\ell$	$x = 92.3\,\ell$, $y = 10\,\ell$	$x = 102.5\,\ell$, $y = 14.6\,\ell$	$11.2\,\ell$

V. Features of the Time-Accurate Flow

Solutions from the time-accurate domain were collected from a subset of the resolved portion of the computational domain, specifically in the vicinity of the compression ramp ($65\,\ell < x < 110\,\ell$, $y <\sim 50\,\ell$). Even with this large reduction in computation area, the remaining grid still included over 1.3×10^9 points. Since a large number of time-accurate samples were needed to analyze the flow and the exact regions of interest were unknown *a priori*, the time-accurate sampling domain was reduced by an additional 98% by sub-sampling the domain onto 6 sparse grids listed in Table 3. The dimensions are listed as i, j, k points since grid point clustering was used to develop the actual grid. For reference, sparse grids 1-3 correspond with each of the three walls from $x = 50\,\ell$ to $x = 110\,\ell$ and $y \leq 40\,\ell$.

Table 3. Grid dimensions for sparse data sampling from the full-span compression corner simulation.

Grid	i-direction			j-direction			k-direction		
	start	end	skip	start	end	skip	start	end	skip
1	510	1410	1	1	3	1	1	1279	1
2	510	1410	1	1	1141	1	1	3	1
3	510	1410	1	1	1141	1	1277	1279	1
4	660	730	10	1	1141	6	1	1279	6
5	730	830	5	1	1141	2	1	1279	2
6	830	1410	2	1	1141	2	1	1279	2

In addition to sub-sampling, the time-accurate data was written with single precision, even though the calculations were performed using double-precision arithmetic. Time-accurate data was collected from the domain every 40 iterations ($\Delta t = 0.05$) for 80,000 iterations, to explore the flow's high frequency content and every 160 iterations ($\Delta t = 0.2$) for 1.6×10^6 iterations to quantify the flow's lower frequency features. As a result of these various data sampling decisions, the total disk-space need to store the time-accurate results was approximately 35TB (which represents a large but manageable amount of storage). Note that over 125PB of storage would have been needed if the complete data set had been saved.

Figure 13 shows the power spectral density (PSD) of the turbulent kinetic energy (TKE) at various locations upstream of the ramp and subsequent shock system. As previously mentioned, the high-frequency time-accurate history was collected for 80,000 iterations, which corresponds to approximately 1 flow length. From the time-history, one-dimensional spectra were computed by multiplying the instantaneous fluctuating quantities with a Hanning window for each segment of the data set. The Hanning window suppresses side-lobe leakage,[58] but the windowed datum was also multiplied by $\sqrt{8/3}$ to account for the low-frequency bias introduced by using the window. The discrete Fourier transform of the windowed data was performed and the square of the Fourier transform solution (including the imaginary component), was normalized by the

length of the windowed signal to develop the PSD of the signal. The Welsh method,[58] with 50% overlapping windows, was used to further reduce the noise in the signal by averaging the resultant PSD curves at each probe location. The PSD of TKE was computed by summing the PSD of each velocity component: PSD of TKE = PSD(u) + PSD(v) + PSD(w).

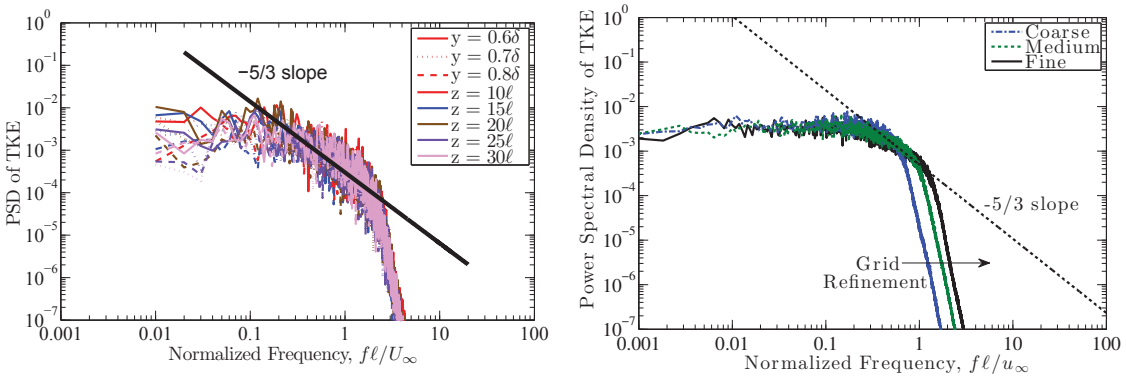

(a) Current results at $x = 70\,\ell$

(b) Previous spanwise-periodic results[11] at $x = 60\,\ell$

Figure 13. Power spectral density of the turbulent kinetic energy at several locations in the boundary-layer δ upstream of the shock boundary-layer interaction.

As seen in the Fig. 13(a), all the curves are very similar and show the simulation had sufficient streamwise distance to develop into a turbulent equilibrium boundary-layer profile and adequate resolution to capture a portion of the inertial subrange of the turbulent kinetic energy, as highlighted by the $-5/3$ slope line. Figure 13(b) shows results from a previous spanwise-periodic LES[11] which also captured a portion of the inertial subrange, with the fine grid capturing a larger portion of the inertial subrange due to increased resolution and because the higher resolution allowed transition to occur earlier which resulted in a larger δ and Re_θ at the sampling station. The current simulation had more resolution than the fine grid from the previous spanwise-periodic LES[11] and was collected at a station farther downstream, so its momentum thickness was larger and had a longer inertial subrange. The signal from the previous scenario appears smoother in Fig. 13(b) since the lines were span-averaged and because it had a significantly longer sampling time-history.

Figure 14 illustrates where several streamwise surface pressure lines were extracted relative to the time-mean skin-friction contours previously shown. The lines correspond to $z = 0.5\,\ell,\ 1\,\ell,\ 5\,\ell,\ 10\,\ell,\ 15\,\ell,\ 20\,\ell$ on the plate with the compression ramp and $y = 0.5\,\ell,\ 1\,\ell,\ 10\,\ell,\ 15\,\ell,\ 20\,\ell$ on the sidewall. The data was sampled at a slightly lower rate ($\Delta\, t = 0.2$), since the focus was lower frequency shock oscillations. From these data sets, higher moments and spectra were developed following the same procedure as outlined for the PSD of TKE curves.

Figure 15 plots both the root mean square (rms) and the skewness (skw) of wall pressure (p_w) along the aforementioned streamwise lines near the left wall junction with the bottom wall. In addition, the accompanying sub-figures include the PSD of wall pressure at selected locations which correspond to various peaks in the rms and skewness plots. The rms plot shows two peaks upstream of the compression ramp which is the result of the streamwise trace being influenced by / traveling through the separation vortex and nodal attachment previously discussed.

As previously mentioned, the core-corner flow does not have the same characteristics as a single plate SBLI due to the effect of the second wall. But, as seen in the figures, the results were very similar regardless of trace studied. The two traces closer to the corner ($y,\ z = 0.5\,\ell$) indicate the flow separated and had a strong low-frequency component by $x = 74\ell$, as seen in Figs. 15(b) and 15(f). The corner separation actually started very near to the corner juncture and sweeps downstream, as seen in Fig. 16. This was consistent with the results in the two other surface traces studied in Fig. 15 which shows that the separation front had moved about $1.5\,\ell$ downstream to $x = 75.6\,\ell$.

Results more typical of a *quasi* two-dimensional SBLI are shown in Fig. 17 which shows lines extracted from the bottom plate, away from either sidewall. The PSD sub-plots of Fig. 17 show the curves were outside the influence of the core-corner flow and look very similar (i.e., $5 \geq z \leq 35\,\ell$). In each of those curves there was essentially no low frequency energy present upstream of separation as indicated by the red lines

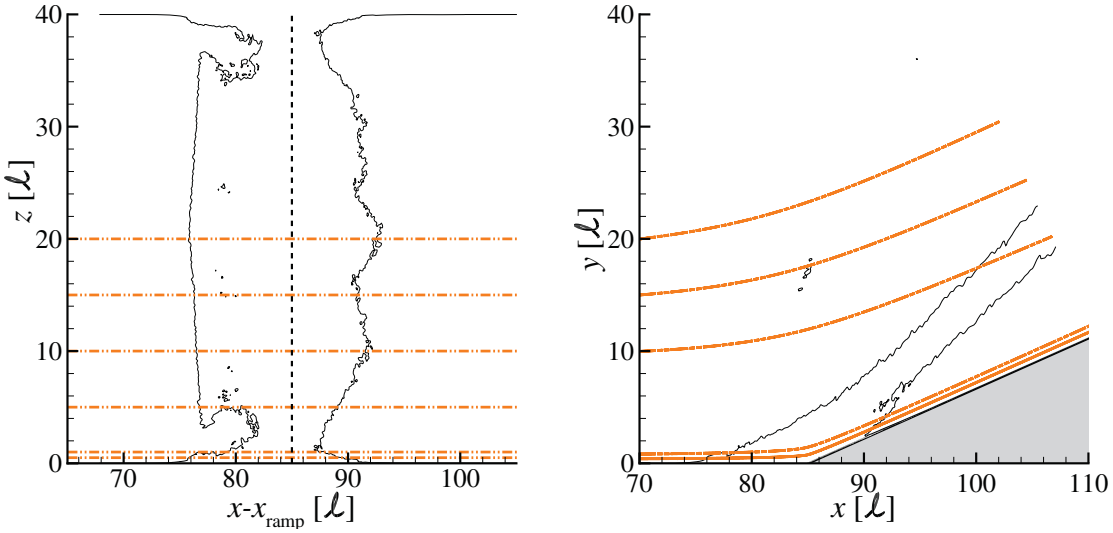

(a) $x - z$ top-down view

(b) $x - y$ side-down view

Figure 14. Outline of the time-mean zero skin-friction coefficient $c_f = 0$ and lines (orange) corresponding to the following surface pressure analysis. Flow is from left to right.

($x = 74\,\ell$). A small distance downstream, the PSD figures show a large increase in low frequency energy, which corresponds with peaks in the rms and skew of the signal. This low frequency oscillation occurs at a frequency close to 0.03 when scaled by the separation length and is consistent with observations made by Poggie *et al.*[2] Further downstream, energy from the lowest frequencies dissipates and the total energy of the system increases due to the shock. Near reattachment (indicated by the purple lines) the curves look similar to the pre-shock system, expect the total energy has increased and the curve at the higher frequencies is elongated since the system has not had sufficient distance to relax back to a new homogeneous equilibrium state.

Away from the core-corner flow but along the sidewalls, the sidewall flow does eventually separate. But it occurred downstream of the leading λ foot and only separated just upstream of the downstream λ foot, as seen in the surface plots of skin-friction in Fig. 10. Extracting a few surface lines at $y = \eta = 10\,\ell$ from each sidewall and $y = \eta = 15\,\ell,\ 20\,\ell$ from the left ($z = 0\,\ell$) wall, the higher moments and PSD of wall pressure were computed and shown in Fig. 18.

The results are similar to those seen in Fig. 17. Along the sidewall, the upstream flow appears consistent with the flow along the other two walls, in that it exhibits no low frequency content. Likewise, as the flow moves downstream, the PSD shows a rapid increase in energy at the lower frequencies, at locations that corresponds with the leading foot of the sidewall λ-shock structure. The leading foot corresponds with the side-wall oblique shock, but unlike the flow upstream of the compression corner, the flow does not separate underneath the it, as seen in Fig. 10. The flow did not separate because it was turned by a glancing oblique shock system with a turning angle of 65.6° which gave rise to a *glancing* shock boundary-layer interaction.[59] Still, the sidewall oblique shock front exhibited a low frequency oscillation, which exist at the same frequencies as those measured in the core-corner separation in Fig. 15(h).

As previously mentioned, the separation vortex, which originated from a nodal attachment point upstream of the compression ramp also travels along the sidewall at an angle of 44°. The separation vortex exists between the λ-shock feet and moved away from the sidewall surface with downstream distance. However, the vortex was strong enough to cause part of the boundary-layer to separate, though only over a small streamwise distance relative to the width of the λ-shock feet. Interestingly, a close examination of the PSD curves in this separation bubble did not find any clear evidence of low frequency oscillations. This suggests that the vortex-induced separation on the sidewall was nearly stationary.

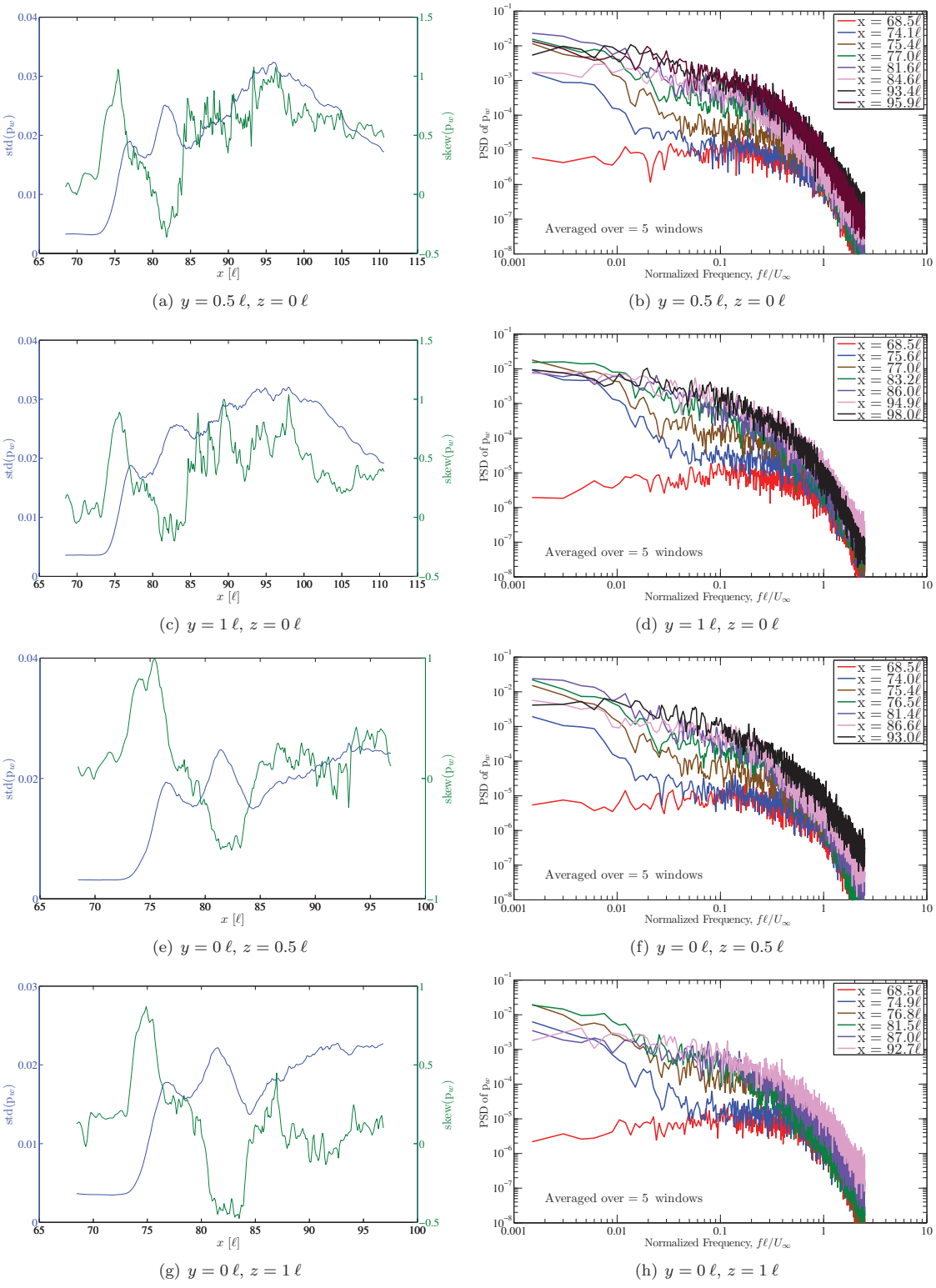

(a) $y = 0.5\,\ell$, $z = 0\,\ell$ (b) $y = 0.5\,\ell$, $z = 0\,\ell$

(c) $y = 1\,\ell$, $z = 0\,\ell$ (d) $y = 1\,\ell$, $z = 0\,\ell$

(e) $y = 0\,\ell$, $z = 0.5\,\ell$ (f) $y = 0\,\ell$, $z = 0.5\,\ell$

(g) $y = 0\,\ell$, $z = 1\,\ell$ (h) $y = 0\,\ell$, $z = 1\,\ell$

Figure 15. Root mean square, skewness, and the power spectral density of surface pressure at several streamwise and spanwise locations on the plate near the left side-wall and 24° compression ramp junction.

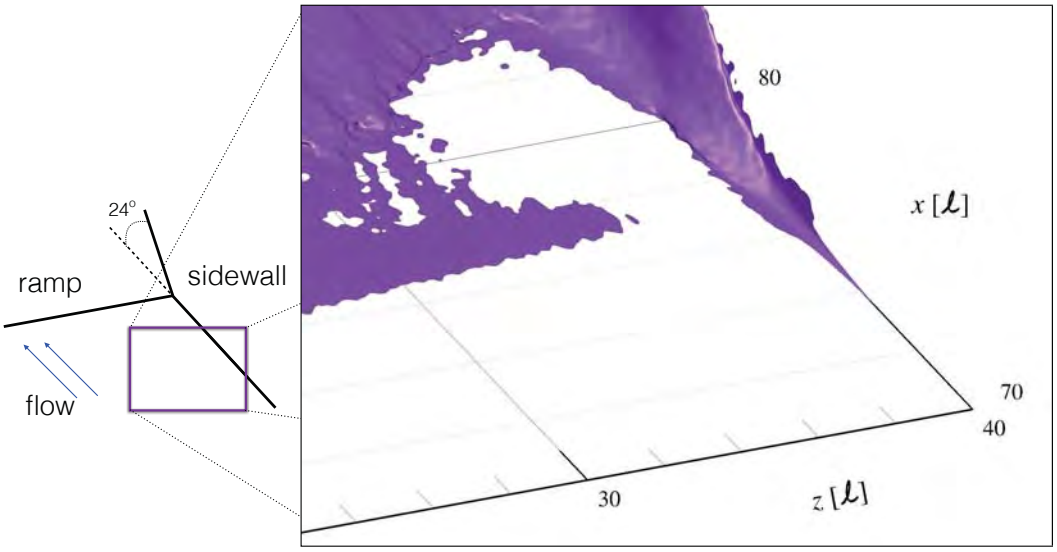

Figure 16. Iso-surface of $\bar{u} = 0$ near the right sidewall junction and the 24° compression ramp. The iso-surfaces very near to the wall ($< 10^{-3}$) have been excluded to highlight the core-corner separation front.

VI. Conclusions

A high-fidelity implicit large-eddy simulation was performed for a Mach 2.25 turbulent boundary-layer flow over a 24° compression ramp with both sidewalls. The domain was sufficiently wide to prevent the core-corner separation from influencing the midspan system. The simulation was compared with previously computed large eddy simulations at the same conditions, including both a spanwise-periodic scenario and a half-span scenario. The resultant flow was qualitatively similar to the two previous scenarios, though inclusion of both sidewall boundary-layers yielded a very three-dimensional corner flow not seen in the spanwise-periodic case. The half-span scenario was performed using a symmetry boundary condition at the midspan. It showed noticeably differences near the midspan compared to the current full-span results. The were a number of reasons for the discrepancy, but most notably was that the half-span scenario only allowed even-mode spanwise traveling waves to exist. This lead to an artificial growth of the midspan boundary-layer, a fuller velocity profile, and delayed separation near the midspan in the half-span simulation. Both the previous half-span and current full-span results show the domain was sufficiently wide to de-correlate the midspan flow from the core-corner, but the current results also show that the flow was still highly three-dimensional, even near the midspan so the resultant shock structure and its behavior in that region could not be replicated with a spanwise-periodic simulation.

Inclusion of both sidewall boundary-layers lead to the development of a highly three-dimensional shock front. This included a separation vortex which originated near each sidewall junction, upstream of the compression ramp. As was previously observed in the half-span scenario, the core-corner flow separated upstream of the midspan shock boundary-layer interaction. The compression ramp induced bow shock and the corner separation both exhibited a low frequency oscillation, consistent with Plotkin's theoretical work. In addition, the corner separation generated a compression wave which traveled along the sidewall. The sidewall boundary-layer responded to the *glancing* oblique shock, but the flow did not separate directly downstream of the incident shock (leading foot of the sidewall λ-shock system), due to its low turning-angle. However, the aforementioned separation vortex traveled along the sidewall between the λ-shock feet and had sufficient strength to cause the time-mean sidewall flow to separate just upstream of the reattachment foot. The vortex-induced separation bubble did not exhibit the low frequency oscillation seen at the other shock-induced separation locations.

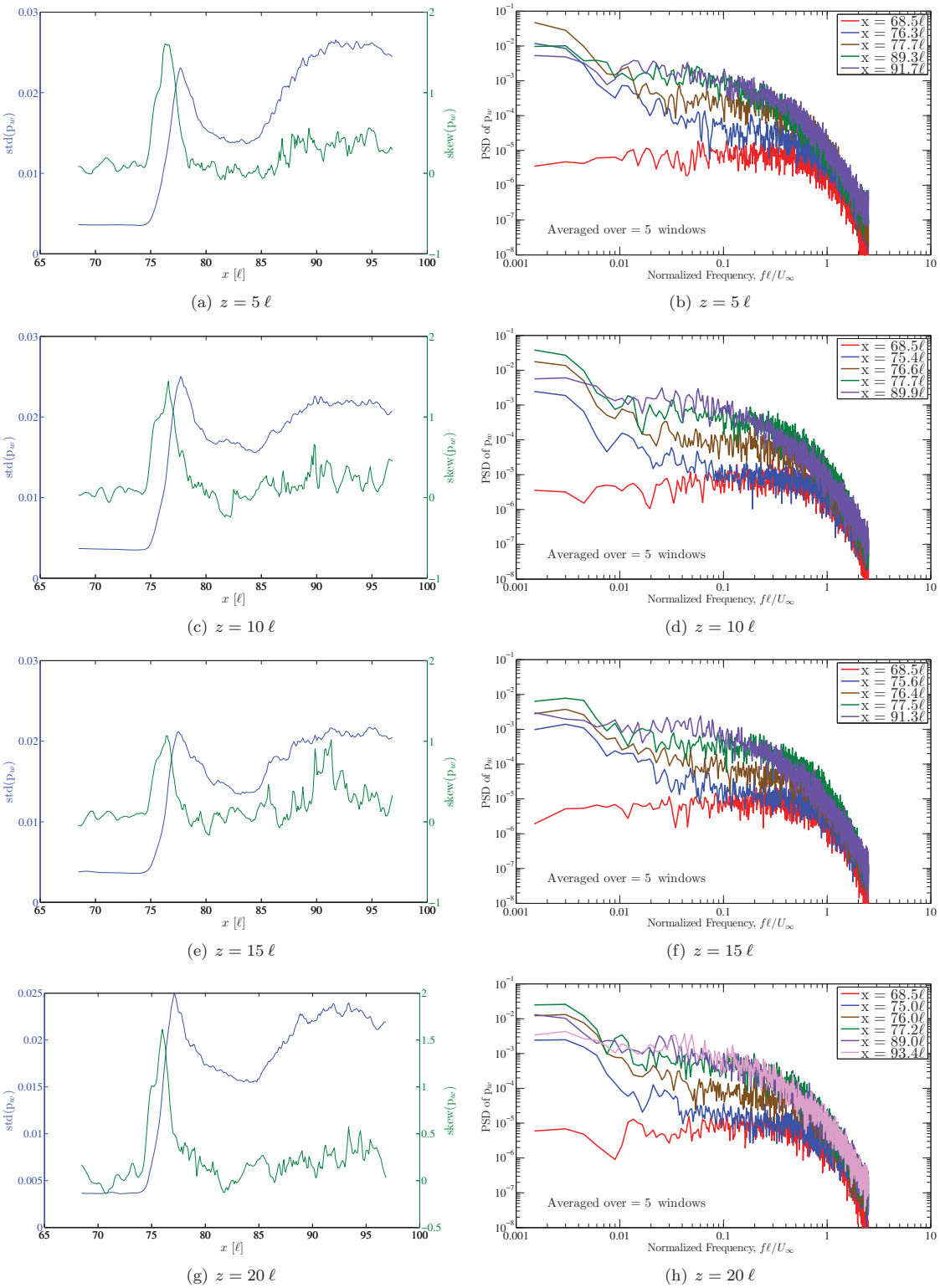

(a) $z = 5\,\ell$ (b) $z = 5\,\ell$

(c) $z = 10\,\ell$ (d) $z = 10\,\ell$

(e) $z = 15\,\ell$ (f) $z = 15\,\ell$

(g) $z = 20\,\ell$ (h) $z = 20\,\ell$

Figure 17. Root mean square, skewness, and the power spectral density of surface pressure at several streamwise and spanwise locations on the plate with the 24° compression ramp.

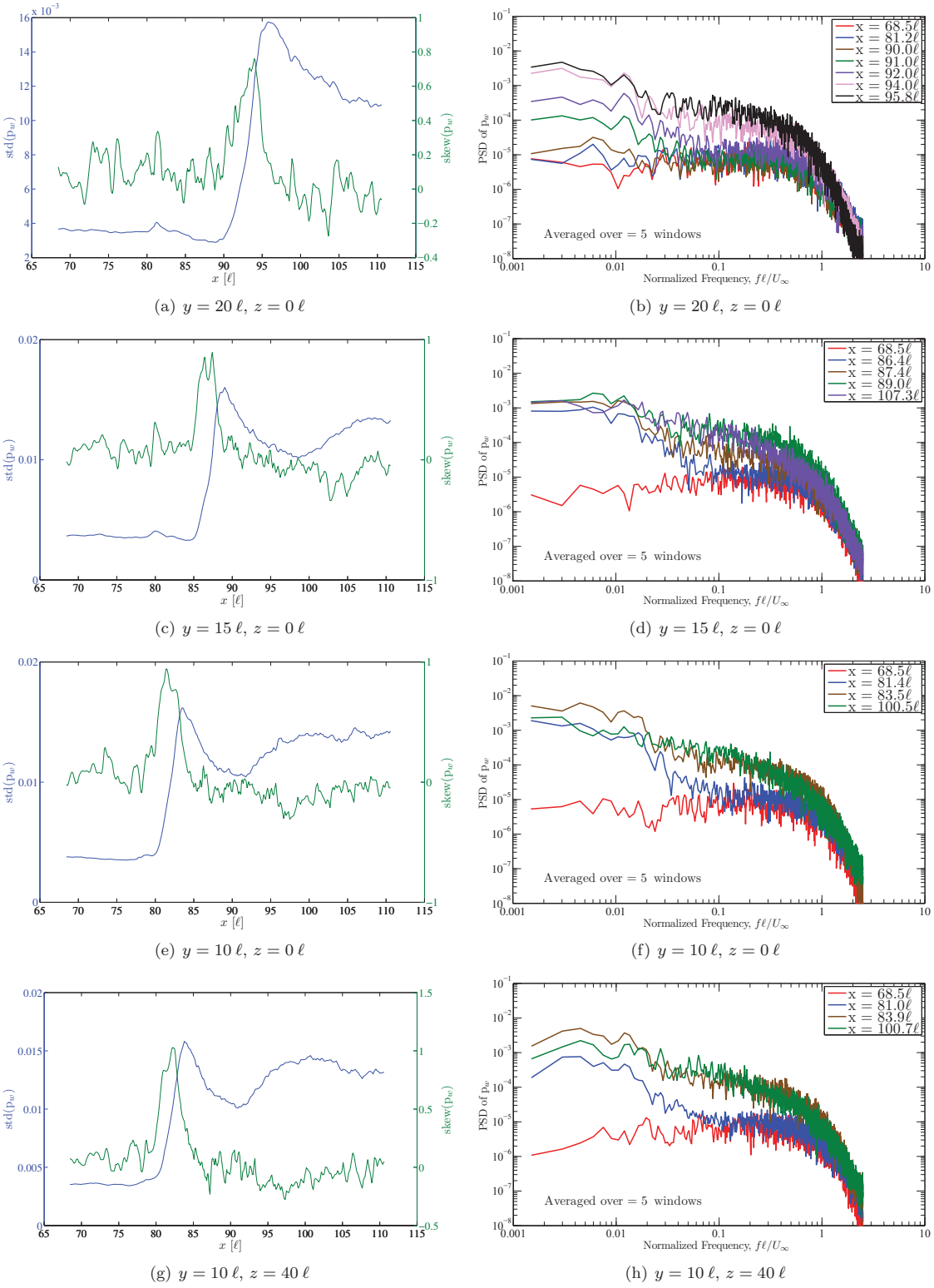

(a) $y = 20\,\ell$, $z = 0\,\ell$ (b) $y = 20\,\ell$, $z = 0\,\ell$

(c) $y = 15\,\ell$, $z = 0\,\ell$ (d) $y = 15\,\ell$, $z = 0\,\ell$

(e) $y = 10\,\ell$, $z = 0\,\ell$ (f) $y = 10\,\ell$, $z = 0\,\ell$

(g) $y = 10\,\ell$, $z = 40\,\ell$ (h) $y = 10\,\ell$, $z = 40\,\ell$

Figure 18. Root mean square, skewness, and the power spectral density of surface pressure at several streamwise and spanwise locations on the sidewall plates adjoining a 24° compression ramp for Mach 2.25 flow.

Acknowledgments

The author would like to thank J. Poggie for his useful conversations regarding this research. This work was sponsored, in part, by the Air Force Office of Scientific Research under grant number LRIR 14RQ18COR monitored by Dr. I. Leyva, AFOSR/RSA. The computational resources were supported by a grant of supercomputer time from the U.S. Department of Defense Supercomputing Resource Center at the Air Force Research Laboratory, Wright-Patterson Air Force Base, OH.

References

[1]Blevins, R. D., Holehouse, I., and Wentz, K. R., "Thermoacoutsic Loads and Fatigue of Hypersonic Vehicle Skin Panels," *Journal of Aircraft*, Vol. 30, No. 6, 1993, pp. 971–978.

[2]Poggie, J., Bisek, N. J., Kimmel, R. L., and Stanfield, S., "Spectral Characteristics of Separation Shock Unsteadiness," *AIAA Journal*, 2014, pp. 1–15.

[3]Rai, M. M., Gatski, T. B., and Erlebacher, G., "Direct Simulation of Spatially Evolving Compressible Turbulent Boundary Layers," AIAA Paper 1995-583, 1995.

[4]Adadms, N. A., "Direct simulation of the turbulent boundary layer along a compression ramp at M = 3 and Re_θ = 1685," *Journal of Fluid Mechanics*, Vol. 420, No. 1, 2000, pp. 47–83.

[5]Pirozzoli, S., Grasso, F., and Gatski, T. B., "Direct Numerical Simulation and Analysis of a Spatially Evolving Supersonic Turbulent Boundary Layer at M=2.25," *Physics of Fluids*, Vol. 16, No. 3, March 2004, pp. 530–545.

[6]Pirozzoli, S. and Grasso, F., "Direct Numerical Simulation of Impinging Shock Wave/Turbulent Boundary Layer Interaction at M=2.25," *Physics of Fluids*, Vol. 18, No. 065113, 2006, pp. 1–17.

[7]Wu, M. and Pino Martin, M., "Direct Numerical Simulation of Supersonic Turbulent Boundary Layer Over a Compression Ramp," *AIAA Journal*, Vol. 45, No. 4, April 2007, pp. 879–889.

[8]M., R., Wu, M., and Pino Martin, M., "Low Reynolds Number Effects in a Mach 3 Shock/Turbulent Boundary-Layer Interaction," *AIAA Journal*, Vol. 46, No. 7, July 2008, pp. 1884–1887.

[9]Priebe, S. and Pino Martín, M., "Low-Frequency Unsteadiness in the DNS of a Compression Ramp Shockwave and Turbulent Boundary Layer Interaction," AIAA Paper 2010-108, 2010.

[10]Muppidi, S. and Mahesh, K., "DNS of Unsteady Shock Boundary Layer Interaction," AIAA Paper 2011-724, 2011.

[11]Bisek, N. J., Rizzetta, D. P., and Poggie, J., "Plasma Control of a Turbulent Shock Boundary-Layer Interaction," *AIAA Journal*, Vol. 51, No. 8, 2013, pp. 1789–1804, doi:10.2514/1.J052248.

[12]Dickman, C. C., "Glancing Interaction with a Turbulent Boundary Layer," Tech. rep., Cranfield College of Aeronautics, Cranfield, U.K., June 1976, AFOSR-76-3006.

[13]Shang, J. S., Hankey, W. L., and Petty, J. S., "Three-Dimensional Supersonic Interacting Turbulent Flow along a Corner," *AIAA Journal*, Vol. 17, No. 7, 1978, pp. 706–713.

[14]Gaitonde, D. and Shang, J. S., "The Structure of a Turbulent Double-Fin Interaction at Mach 4," AIAA Paper 1994-2810, 1994.

[15]Oliver, A. B., Lillard, R. P., Schwing, A. M., Blaisdell, G. A., and S., L. A., "Assessment of Turbulent Shock-Boundary Layer Interaction Computations Using the OVERFLOW Code," AIAA Paper 2007-0104, 2007.

[16]Garnier, E., "Stimulated Detached Eddy Simulation of Three-Dimensional Shock/Boundary-Layer Interaction," *Shock Waves*, Vol. 19, September 2009, pp. 479–486.

[17]Morgan, B., Duraisamy, K., and Lele, S. K., "Large-Eddy Simulations of a Normal Shock Train in a Constant-Area Isolator," *AIAA Journal*, Vol. 52, No. 3, March 2014, pp. 539–558.

[18]A., H., "Large-Eddy Simulation of Shock/Boundary-Layer Interaction," *AIAA Journal*, Vol. 50, No. 12, 2012, pp. 2919–2927, doi: 10.2514/1.J051786.

[19]Benek, J., Suchyta, C., and Babinsky, H., "The Effect of Tunnel Size on Incident Shock Boundary Layer Interaction Experiments," AIAA Paper 2013-862, 2013.

[20]Reda, D. C. and Murphy, J. D., "Shock Wave/Turbulent Boundary-Layer Interactions in Rectangular Channels," *AIAA Journal*, Vol. 11, 1973, pp. 139–140.

[21]Burton, D. M. F. and Babinsky, H., "Corner Separation Effects for Normal Shock Wave/Turbulent Boundary Layer Interactions in Rectangular Channels," *Journal of Fluid Mechanics*, Vol. 707, September 2012, pp. 287–306.

[22]Babinsky, H., Oorebeek, J., and Cottingham, T. G., "Corner Effects in Reflecting Oblique Shock-Wave/Boundary Layer Interactions," AIAA Paper 2013-859, 2013.

[23]Bisek, N. J., "High-Order Implicit Large-Eddy Simulations of a Supersonic Corner Flow over a Compression Ramp," AIAA Paper 2014-3335, 2014.

[24]Gaitonde, D. and Visbal, M. R., "High-order Shcemes for Navier-Stokes Equations: Algortithm and Implementaiton into FDL3DI," Tech. rep., Air Force Research Laboratory, August 1998, AFRL-VA-WP-TR-1998-3060.

[25]Visbal, M. R., "Computational Study of Vortex Breakdown on a Pitching Delta Wing," AIAA Paper 1993-2974, 1993.

[26]Gordnier, R. E. and Visbal, M. R., "Numerical Simulation of Delta-Wing Roll," *Aerospace Science and Technology*, Vol. 2, No. 6, September 1998, pp. 347–357.

[27]Visbal, M. R., Gaitonde, D. V., and Gogineni, S., "Direct Numerical Simulation of a Forced Transitional Plane Wall Jet," AIAA Paper 1998-2643, 1998.

[28]Rizzetta, D. P., Visbal, M. R., and Blaisdell, G. A., "Application of a High-Order Compact Difference Scheme to Large-Eddy and Direct-Numerical Simulation," AIAA Paper 1999-3714, 1999.

[29]Morgan, P. E., Rizzetta, D. P., and Visbal, M. R., "High-Order Numerical Simulation of Turbulent Flow over a Wall-Mounted Hump," *AIAA Journal*, Vol. 44, No. 2, February 2006, pp. 239–251.

[30]Garmann, D. J. and Visbal, M. R., "Implicit LES Computations for a Rapidly Pitching Plate," AIAA Paper 2010-4282, 2010.

[31]White, M. D. and Visbal, M. R., "High Fidelity Analysis of Aero-Optical Interaction with Compressible Boundary Layers," AIAA Paper 2010-4496, 2010.

[32]Anderson, D., Tannehill, J., and Pletcher, R., *Computational Fluid Mechanics and Heat Transfer*, 1984, McGraw-Hill.

[33]Mullenix, N. J., Gaitonde, D. V., and Visbal, M. R., "A Plasma-Actuator-Based Method to Generate a Supersonic Turbulent Boundary Layer Inflow Condition for Numerical Simulation," AIAA Paper 2011-3556, 2011.

[34]Beam, R. and Warming, R., "An Implicit Factored Scheme for the Compressible Navier-Stokes Equations," *AIAA Journal*, Vol. 16, No. 4, April 1978, pp. 393–402.

[35]Gordnier, R. E. and Visbal, M. R., "Numerical Simulation of Delta-Wing Roll," AIAA Paper 1993-544, 1993.

[36]Jameson, A., Schmidt, W., and Turkel, E., "umerical Solutions of the Euler Equations by Finite Volume Methods Using Runge-Kutta Time Stepping Schemes," AIAA Paper 1981-1259, 1981.

[37]Pulliam, T. H. and Chaussee, D. S., "A Diagonal Form of an Implicit Approximate-Factorization Algorithm," *Journal of Computational Physics*, Vol. 39, No. 2, Febuary 1981, pp. 347–363.

[38]Lele, S., "Compact Finite Difference Schemes with Spectral-like Resolution," *Journal of Computational Physics*, Vol. 103, 1992, pp. 16–42.

[39]Visbal, M. R. and Gaitonde, D. V., "High-Order-Accurate Methods for Complex Unsteady Subsonic Flows," *AIAA Journal*, Vol. 37, No. 10, October 1999, pp. 1231–1239.

[40]Gaitonde, D., Shang, J. S., and Young, J. L., "Practical Aspects of High-Order Accurate Finite-Volume Schemes for Electromagnetics," AIAA Paper 1997-363, 1997.

[41]Visbal, M. R. and Rizzetta, D. P., "Large-Eddy Simulation on Curvilinear Grids Using Compact Differencing and Filtering Schemes," *Journal of Fluids Engineering*, Vol. 124, 2002, pp. 836–847.

[42]Roe, P. L., "Approximate Riemann Solvers, Parameter Vectors, and Difference Schemes," *Journal of Computational Physics*, Vol. 43, No. 2, 1981, pp. 357–372.

[43]van Albada, G. D., van Leer, B., and Roberts, W. W., J., "A Comparative Study of Computational Methods in Cosmic Gas Dynamics," *Astronomy and Astrophysics*, Vol. 108, April 1982, pp. 76–84.

[44]Rizzetta, D. P., Visbal, M. R., and Gaitonde, D. V., "Large-Eddy Simulation of Supersonic Compression-Ramp Flow by a High-Order Method," *AIAA Journal*, Vol. 39, No. 12, December 2001, pp. 2283–2292.

[45]Swanson, R. C. and Turkel, E., "On Central-Difference and Upwind Schemes," *Journal of Computational Physics*, Vol. 101, No. 2, August 1992, pp. 292–306.

[46]Rizzetta, D. P. and Visbal, M. R., "Large-Eddy Simulation of Supersonic Boundary-Layer Flow by a High-Order Method," *International Journal of Computational Fluid Dynamics*, Vol. 18, No. 1, January 2004, pp. 15–27.

[47]Bisek, N. J., "High-Order Implicit Large-Eddy Simulations of Supersonic Corner Flow," AIAA Paper 2014-0588, 2014.

[48]White, F. M., *Viscous Fluid Flow, 3rd Ed.*, 2006, McGraw Hill.

[49]Fernholz, H. H. and Finley, P. J., "A Critical Compilation of Compressible Turbulent Boundary Layer Data," Tech. rep., 1977, AFARDograph No. 223, Case 55010501.

[50]Poggie, J., "Large-Scale Structures in Implicit Large-Eddy Simulation of Compressible Turbulent Flows," AIAA Paper 2014-3328, 2014.

[51]Aubard, G., Gloerfelt, X., and Robinet, J.-C., "Large-Eddy Simulation of Broadband Unsteadiness in a Shock/Boundary-Layer Interaction," *AIAA Journal*, Vol. 51, No. 10, 2013, pp. 2395–2409.

[52]Georgiadis, N. J., Rizzetta, D. P., and Fureby, C., "Large-Eddy Simulation: Current Capabilites, Recommended Practices, and Future Research," *AIAA Journal*, Vol. 48, No. 8, August 2010, pp. 1772–1784.

[53]Poggie, J., "DNS of Supersonic Turbulent Boundary Layers: Effects of Resolution and Comparison to Models," To be presented at the 53rd AIAA Aerospace Sciences Conference, Kissimmee, Florida, Jan., 2015.

[54]Jeong, J. and Hussain, F., "On the Identification of a Vortex," *Journal of Fluid Mechanics*, Vol. 285, 1995, pp. 69–94.

[55]Dolling, D. S., "Unsteady Phenomena in Shock Wave/Boundary Layer Interaction," Tech. rep., Advisory Group for Aerospace Research & Development, May 1993, Special Course on Shock-Wave/Boundary-Layer Interaction in Supersonic and Hypersonic Flows, AGARD-R-792, pp. 4-1–4-46.

[56]van Driest, E. R., "On the Turbulent Flow Near a Wall," *Journal of the Aeronautical Sciences*, Vol. 23, 1956, pp. 1007–1011.

[57]Elena, M. and LaCharme, J. P., "Experimental Study of a Supersonic Turbulent Boundary Layer Using Laser Doppler Anemometer," *Journal de Mécanique Théorique et Appliquée*, Vol. 7, 1988, pp. 175–190.

[58]Bendat, J. S. and Piersol, A. G., *Random Data,* 2^{nd} *Ed.*, 1986, John Wiley & Sons.

[59]Paynter, G. C., "Analysis of Weak Glancing Shock/Boundary-Layer Interactions," *Journal of Aircraft*, Vol. 17, No. 3, 1982, pp. 160–166.

LIST OF SYMBOLS, ABBREVIATIONS, AND ACRONYMS

ACRONYM	DESCRIPTION
AFOSR	Air Force Office of Scientific Research
AFOSR/RSA	Aerothermodynamics Department
AFRL	Air Force Research Laboratory
AFRL/RQ	Aerospace Systems Directorate
AFRL/RQHF	Hypersonic Sciences Branch
ARL	Army Research Laboratory
DES	Detached-eddy simulation
DNS	Direct numerical simulation
DoD	Department of Defense
DSRC	DoD Supercomputing Resource Center
ERDC	US Army Engineer Research and Development Center
FDL3DI	AFRL computational fluid dynamics code
HFILES	High-fidelity implicit large-eddy simulation
HOPS	Higher-Order Plasma Solver, AFRL computer code
HPC	High-performance computing
LES	Large-eddy simulation
OVERFLOW	NASA computational fluid dynamics code
QCR	Quadratic constitutive relation
RANS	Reynolds-averaged Navier-Stokes simulation
SBLI	Shock boundary-layer interaction
US3D	Computational fluid dynamics code from University of Minnesota
C_f	Skin-friction coefficient
C_{cr1}	Quadratic constitutive relationship constant
u,v,w	Streamwise, normal, and spanwise velocities
x,y,z	Streamwise, normal, and spanwise coordinates
α	Numerical parameter
δ	Boundary-layer thickness
δ_0	Boundary-layer thickness at the inflow plane
ϕ	Generic dependent variable
η	Kolmogorov length scale